On the generation and modulation of electron spin density in open-shell phosphorus compounds

Dissertation

zur

Erlangung des Doktorgrades (Dr. rer. nat.)

der

Mathematisch-Naturwissenschaftlichen Fakultät

der

Rheinischen Friedrich-Wilhelms-Universität Bonn

vorgelegt von

Philipp Brehm

aus

Siegburg

Bonn, 2023

Angefertigt mit Genehmigung der Mathematisch-Naturwissenschaftlichen Fakultät
der Rheinischen Friedrich-Wilhelms-Universität Bonn

Gutachter/Betreuer: Prof. Dr. Rainer Streubel
Gutachter: Prof. Dr. Olav Schiemann

Tag der Promotion: 20.06.2024
Erscheinungsjahr: 2024

Hiermit versichere ich, dass ich die vorliegende Arbeit unter Einhaltung der Regeln guter wissenschaftlicher Praxis selbständig verfasst, keine anderen als die angegebenen Quellen und Hilfsmittel benutzt und die Zitate kenntlich gemacht habe.

It is so shocking to find out how many people do not believe that they can learn, and how many more believe learning to be difficult.

– Frank Herbert

Publications and conference contributions

Publications

- "*1,3,2-Diheterophospholane complexes: access to new tuneable precursors of phosphanoxyl complexes and P-functional polymers*" P. C. Brehm, A. S. Müller-Feyen, G. Schnakenburg and R. Streubel, *Dalton Trans.* **2022**, *51*, 4400-4405. DOI: 10.1039/D2DT00027J

- "*On metal coordination of neutral open-shell P-ligands focusing on phosphan-oxyls, their electron residence and reactivity*", P. C. Brehm, A. Frontera and R. Streubel, *Chem. Commun.* **2022**, *58*, 6270-6279. DOI: 10.1039/D2CC01302A

- "*Design of transition metal complexes containing a P–E radical motif*" H. Zhu, Z.-W. Qu, S. Grimme, P. C. Brehm and R. Streubel, *Dalton Trans.* **2023**, *52*, 2356-2362. DOI: 10.1039/D2DT04149A

Conference contributions

- Deutsch/Österreichischer Mitarbeiter Workshop MHC-10, Tübingen (Germany), March 15-17th, **2019**, "*TEMPO-substituted phosphane iron complexes as precursors for phosphanoxyl complexes*" (**Oral presentation**).

- European Workshop on Phosphorus Chemistry 2019 EWPC-16, Bristol (United Kingdom), April 24-26th, **2019**, "*The TEMPO-substituted Phosphane Iron(0) Complexes: Precursors for Phosphanoxyl Complexes?*" (**Poster presentation**).

- 13th International Conference on Heteroatom Chemistry, Prague (Czech Republic), June 30th - July 6th, **2019**, "*On the tendency of P-OTEMP substituted complexes to form phosphanoxyl complexes?*" (**Poster presentation**).

- BIGS Summer School 2019, Bonn (Germany), September 10-11th, **2019**, "*TEMPO-substituted Phosphane Iron(0) Complexes: Transient Phosphanoxyl Complexes?*" (**Oral presentation**).

- European Workshop on Phosphorus Chemistry 2020 EWPC-17, Rennes

(France), February 26-28th, **2020**, "*Closing in on stable phosphanoxyl complexes?*" (**Poster presentation**).

- Online Workshop on Phosphorus Chemistry 2021 OWPC-18, Rostock (Germany), March 29-31th, **2021**, "*Inspecting new cyclic diheterophospholane complexes as potential phosphanoxyl complex precursors*" (**Oral presentation**).

- International Conference on Phosphorus Chemistry ICPC-23 (Online), Czestochowa (Poland), July 5-9th, **2021**, "*Generation of novel transient phosphanoxyl complexes from heterophospholane complexes*" (**Poster presentation**).

- Deutsch/Österreichischer Mitarbeiter Workshop MHC-11, Bonn (Germany), March 15-17th, **2021**, "*Phosphanoxyl complexes: differences between group 6 and 8 metal complexes* " (**Oral presentation**).

- PacifiChem 2021 (Online), Honolulu Hawaii (United States of America), December 16-21th, "*Main group radical initiators and their spin density tuning*" (**Poster presentation**).

- 16th International Symposium on Inorganic Ring Systems, Graz (Austria), July 24-29th, **2022**, "*Spin density distribution in 1,3,2-diheterophospholane iron complexes* " (**Oral presentation**).

- American Chemical Society, ACS, Fallmeeting - Sustainability in a Changing World, Chicago/Illinois (United States of America), August 21-25th, **2022**, "*Phosphanoxyl iron complexes – but who is non-innocent?*" (**Poster presentation**).

- BIGS Summer School 2022, Bonn (Germany), September 4-5th, **2022**, "*On the redox chemistry of Lewis base stabilised oxophosphonium adduct: an isolobal approach to phosphanoxyl complexes*" (**Poster presentation**).

- European Workshop on Phosphorus Chemistry 2023 EWPC-19/ 3rd, San Sebastian/Donostia (Spain), **2023**, "*Properties and reactivity of phosphanoxyl adducts* " (**Poster presentation**).

Table of Contents

1. Introduction

1.1. Origin of the term radical

The roots of chemistry go back to early humans, from handling fire in the stone age to metallurgy in the iron and bronze ages. Around the 1st and 2nd century, humankind become more interested in the transformation of matter, rather than in the reaction heat usually used beforehand, this was the beginning of alchemy. In the following centuries, the search for pharmaceutics, the manufacturing of gun powder and the search after the famous 'philosopher stone', to turn any matter into gold, lead to a plethora of discoveries.[1] Among these were the discovery of several minerals and elements, *e.g.*, the isolation of phosphorus by Henning Brandt.[2] For their work alchemist developed tools for distillation, sublimation, extraction etc.,[3,4] however, they lacked a unified language. Different schools of alchemy used different symbols for elements and sometimes even secret codes to protect their knowledge and findings.[5,6] As a consequence, exchange of wisdom was difficult. This issue was recognised only very late in 1782 by de Morveau in his article 'Méthode de nomenclature chimiqué', in which he attempted to generalise the names of elements and compounds in a common chemical language.[7] One suggestion he made was that a compound can be cut into several pieces, which can be transferred from one compound to another. These pieces he called 'radicals' as being the root (lat. radix) of a compound. In 1832 Liebig and Wöhler, working on benzoic acid derivatives, picked up and extending this nomenclature and called the roots of their derivatives benzo-yl.[8] From a modern perspective, these roots are functional groups and the -yl nomenclature, still applied today, is a remnant of these early considerations. However, chemists became intrigued with the idea of isolating such radicals. This led to the work of Bunsen and Frankland, believing that they isolated the cacodyl radical and ethyl radical respectively.[9] Only later it was found that they did not isolate the free 'roots', but their dimeric forms.[10,11] Their failures were in line with the valence theory postulated by Higgins, Frankland and Kekulé. In this theory the isolation of a free radical was not possible, as, *e.g.*, carbon had to have a valence of 4, explaining the isolation of butane instead of the ethyl radical by Frankland. This hampered the attempts to isolate radicals until 1900, when Gomberg synthesised the stable and truly free radical, triphenylmethyl **I**, ironically in the attempt to form its dimer (Figure 1).[12] Since then, the term radical is applied to species having an odd number of electrons. Following Gombergs structural motive, the isoelectronic triarylammoniumyl **II** and -boranidyl **III** ionic radicals were reported in the 1920s.[13,14] Only shortly after Wieland

reported on the discovery of stable aminoxyl (nitroxide) radicals **IV**.[15]
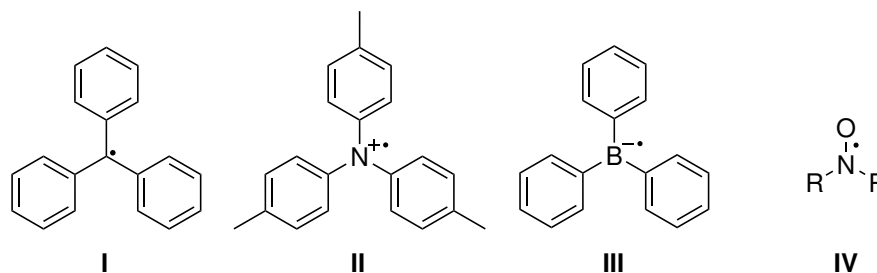
Figure 1: Lewis structures of the first isolated free radical **I** and the related N- and B- ionic radicals **II** and **III**, next to the generalised formula of an aminoxyl **IV**.

1.2. Phosphorus radicals

The newly gained knowledge about radical chemistry sparked a completely new field. In 1957 the first evidence for a phosphorus-based radical as a reactive intermediate was published.[16] Since then, several phosphorus radical species have been postulated, observed or even synthesised. These can be grouped into four compound classes, phosphanyl- **V**, phosphinoyl- **VI**, phosphoniumyl- **VII** and phosphoranyl **VIII** radicals and are derived from their full valence counterparts (Figure 2).[17] The early reports were about phosphoranyl radicals **VIII**, which were generated by the reaction of tertiary phosphanes with *in situ* formed organic radicals, like alkyl, alkoxyl, aminyl or thianyl radicals (Scheme 1).[18,19] After addition of the organic radical to the phosphane, the formed phosphoranyl radical can be observed via electron paramagnetic resonance (EPR). Huge effort was involved to gain knowledge about their structure and today a trigonal bipyramidal structure is assumed in which the unpaired electron resides in an equatorial position. In some cases, tetragonal structures are observed. Usually, these species are rather short-lived and undergoes α- or β-scission, depending on the initially added radical.[17] The β-scission is also known as the free radical Arbuzov reaction resulting in the oxidation of the phosphorus atom,
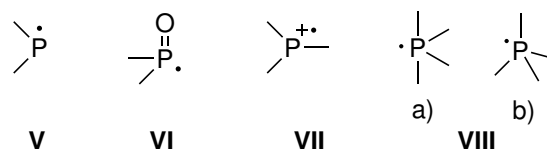
Figure 2: General types of phosphorus-centred radicals, phosphanyl **V**, phosphinoyl **VI**, phosphoniumyl **VII** and trigonal bipyramidal (a) and tetrahedral (b) phosphoranyl **VIII**.
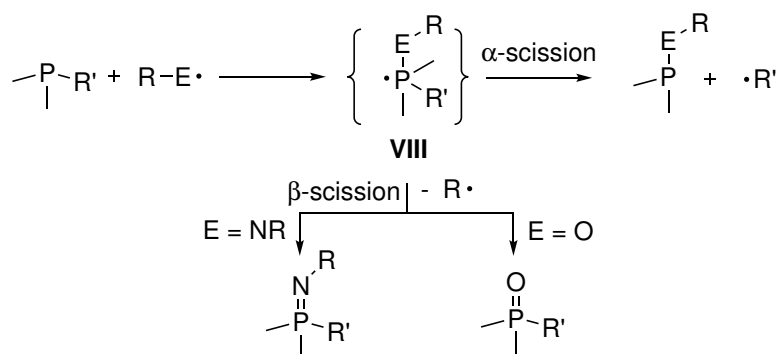
Scheme 1: Generalised formation of phosphoranyl radicals **VIII** and their decomposition pathways via α- or β-scission.

e.g., a phosphane oxide obtained from the reaction of a phosphane with an alkoxyl radical.[17,20,21] Phosphoranyl radicals, as intermediates are still under research today and are widely discussed in photocatalytic processes.[22,23] The exotic phosphoniumyl radicals **VII** were usually electrochemical generated and are highly reactive.[24,25] These radicals are the heavier derivatives of the early on examined ammoniumyl radicals **II**. Only recently, after almost a century, the first derivative having significantly bulky groups was isolated and its structure was obtained from X-ray diffraction studies.[26] Another species, which is in today's focus, are phosphinoyl radicals **VI** (Scheme 2).[27–29] They are generally generated from secondary phosphane oxides via hydrogen abstraction or via irradiation induced α-scission. The latter is commonly used in mono- or bisacyl phosphine oxides (MAPO and BAPO, respectively) and find application as polymerisation initiator, *e.g.*, in dental resins.[30–34] Hydrogen atom transfer from the phosphane oxide as a method to generate **VI** is usually found in olefin phosphorylation reactions (Scheme 2) and allows the synthesis with a
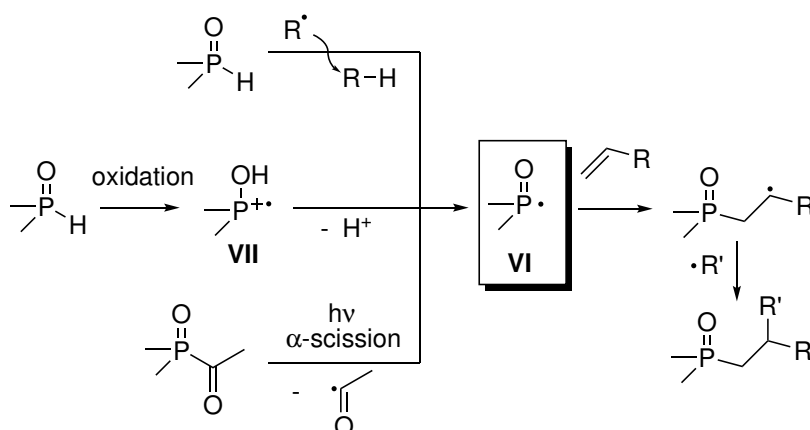
Scheme 2: Synthetic access to phosphinoyl radicals **VI** and addition to an olefine as a common synthetic example.
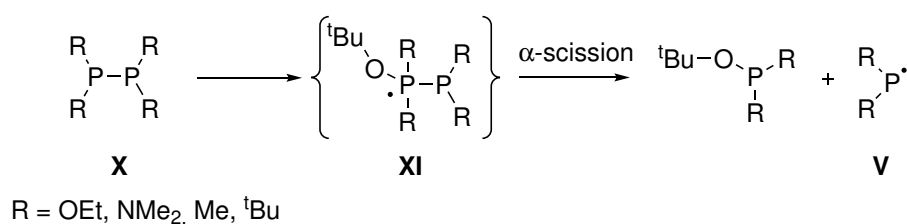
Scheme 3: Generation of phosphanyl radicals **V** in solution via α-scission of *in situ* generated **X**.

large variety of coupling products. Despite the fact that they are commonly used, a stable derivative has yet to be reported. However, plenty of phosphinoyl radicals **VI** have been analysed by EPR.[35–38] The last group in the presented phosphorus-centred radicals are phosphanyl radicals **V** and they were first mentioned in solution as decomposition product from a phosphanyl phosphoranyl radical **XI** (Scheme 3).[39] The reaction of diphosphane **X** with a radical starter yielded **XI**, which underwent α-scission of the P–P bond giving rise to the phosphanyl radicals **V**, which were only detected via EPR. Remarkably only bis-alkoxy and -amino substituted **V** were observed and, hence it was concluded that dialkyl derivatives of **V** were to reactive and thus not observable with EPR techniques. The authors further postulated that a stable unconjugated derivative of **V** can not be prepared. Surprisingly only two years later, in 1976, Lappert was able to disprove this statement by the isolation of a stable dialkylphosphanyl radical.[40] This radical was indeed the first stable heavier main group radical, and the applied concept of kinetic stabilisation via bulky bis(trimethylsilyl)methyl (bisyl) substituents paved the way for more persistent and stable phosphorus radicals (Figure 3).[41–47] Despite that several neutral, cationic and anionic derivatives of **V** are known, they remain scarce which reveals their inherent high reactive character. And several of the isolated species show besides kinetic stabilisation also electronic stabilisation by delocalisation of the unpaired electron. If not sufficiently stabilised a common reaction pathway observed for **V** is a dimerization via radical homocoupling. Indeed, even the first stable phosphanyl radical by Lappert dimerized in the solid state, due to dispersion interactions. 1,3,2-Diazaphospholidinyl radicals were observed by Matsuda and Gudat upon heating a solution of the related diphosphanes (Scheme 4).[48,49] Depending on the size of the substituents the energy necessary for the P–P bond cleavage was reduced, which led to the observation of Dipp substituted 1,3,2-diazaphospholyl radicals already at room temperature in solution. The tendency towards radical formation is correlated with an increasing P–P distance (2.240 − 2.321 Å) in the diphosphanes **X**, which are in the di-azaphospholidines of Gudat much longer than common P–P distances (2.217±0.08 Å).[48] These observations are in line with the higher stability of diamino substituted phosphanyl radicals **V** previously mentioned.

4
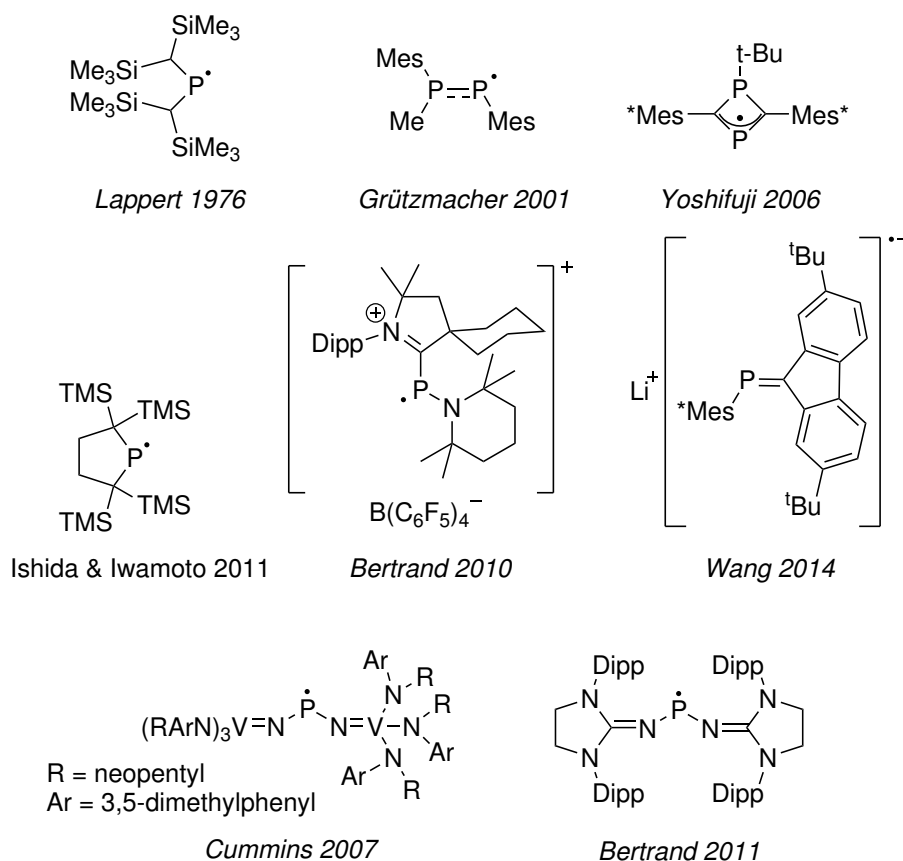
Figure 3: Selection of persistent and stable phosphanyl radicals **V** reported in the literature. TMS = Trimethylsilyl, Mes = 2,4,6,-Trimethylphenyl, Mes* = 2,4,6-Tris(tertbutyl)phenyl, Dipp = 2,6-Diisopropylphenyl.

Despite their high reactivity radicals **V** can be used as synthons in reactions, and under the correct conditions with high selectivity. An *in situ* generated phosphanyl radical by Heurich was trapped with the stable aminoxyl radical (**IV**) 2,2,6,6-tetramethyl-piperidin-1-oxyl (TEMPO). At low temperatures an aminoxylphosphane **XII** was obtained, which rearranged to several P(V) oxide species upon warming (Scheme 5).[50] Theoretical calculations

R = ^{t}Bu, Dmp, Mes, Dipp, 2,6-^{t}Bu(C$_6$H$_4$)
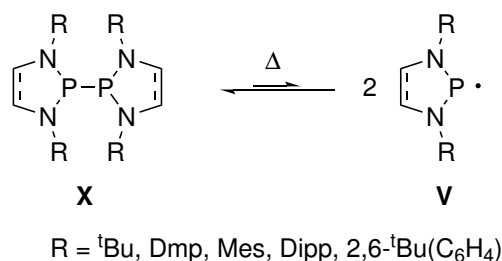
Scheme 4: Equilibrium between (heterocyclic) diphosphanes **X** and their related phosphanyl radicals **V**. Dmp = 2,6-dimethylphenyl.[48]
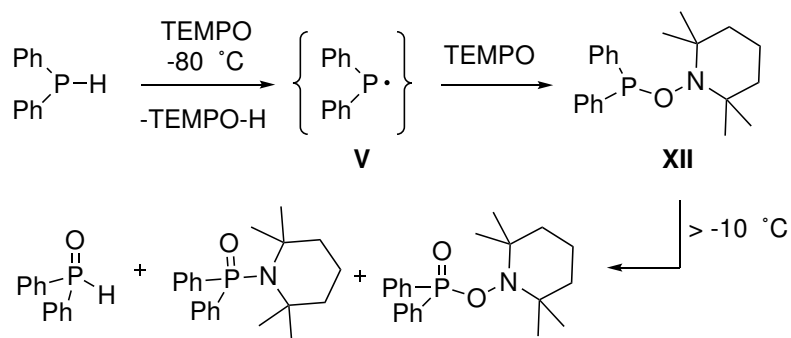
Scheme 5: Synthesis of a thermally unstable aminoxylphosphane **XII** via heterocoupling of a phosphanyl radical **V** with TEMPO.[50]

suggest a homolytic N–O bond cleavage of **XII**. Similar observations were made by Iwamoto reacting the stable cyclic phosphanyl (cf. Figure 3) with TEMPO and 2-azaadamantane-1-oxyl, called AZADO.[51] In a subsequent study by Heurich an aminoxyl diphenylphosphane sulfide **XIII** was synthesised, which showed N–O bond cleavage in THF at elevated temperatures to yield the ammonium thiahypophosphite **XIV**, assumingly via H-abstraction from the solvent by transiently formed radical species (Scheme 6).[50]

Scheme 6: Thermal N–O bond cleavage of aminoxylphosphane sulfide **XIII** to ammonium thiahypophosphite **XIV** by Heurich.[50]

6

1.3. The chemistry of phosphanyl complexes

Early on Cowley recognised the potential of using phosphanyl radicals **V** as ligands in transition metal complexes. Reaction of Lapperts phosphanyl radical with iron (**XV**) and cobalt carbonyls did yield the corresponding metal complexes (Figure 4).[52] This approach also allowed Sunada and Iwamoto to isolate and crystallise the phosphanyl radical coordinated to an iron carbonyl complex **XVI**.[53] In these complexes almost no hyperfine coupling to phosphorus was observed in the EPR experiments and DFT-derived spin density distributions (SDD) show an almost pure metal-centred radical. A general drawback of the access of phosphanyl metal complexes via this method: long-lived radicals **V** are required to allow the coordination to a metal centre in the first place. Another approach was chosen by Geoffroy, he generated phosphanyl complexes **XVII** from phosphane group 6 metal complexes which were already in the metals coordination sphere.[54] After irradiation of a crystalline sample, he detected the phosphanyl complexes in the crystal lattice via EPR. In this case the SDD shows an almost unaltered phosphanyl moiety compared to the free phosphanyl radical **V**. However, no stable complexes of this type were reported until recently when de Bruin and Schneider reported on a phosphanyl osmium complex.[55] In this case the SDD is almost equally shared between the P and the Os atom. In this complex the phosphanyl ligand has 'only' a supermesityl Mes* substitutent which highlights that usually highly reactive radicals such as the latter can be significantly stabilised via metal coordination. An
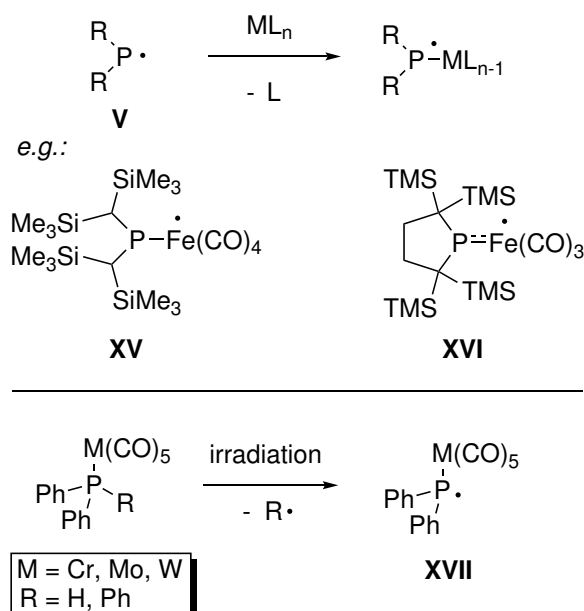
Figure 4: Phosphanyl complexes **XV**-**XVII** generated from stable radicals (top) and in the metal coordination sphere generated radicals (bottom).

Scheme 7: Synthesis of aminoxylphosphane complex **XIX** via radical heterocoupling of TEMPO and phosphanyl complex **XVIII** generated *in situ* by SET of Li/Cl phosphinidenoid complex **XIX**.[58, 59]

extreme case was reported by Streubel, in which the lifetime of a *P*-chloro functionalised phosphanyl tungsten complex **XVII** was long enough to be measured by EPR.[56] This radical was generated by single electron transfer (SET) to a Li/Cl phosphinindenoid complex **XVIII** (Scheme 7).[57] It was possible to obtain further proof for **XVII** by the reaction products with hexafluoroacetone.[60] Trapping reactions of **XVII** with the Gomberg radical **I** were the entry point to the remarkable chemistry of phosphaquinomethane complexes.[61] However, when attempts were made to trap the radical via heterocoupling with a stable aminoxyl radical **IV**, for which TEMPO was chosen, phosphinito complexes **XXII** were obtained instead of the expected aminoxylphosphane complexes **XIX**.[58] The observed product pointed to a cleavage of the N–O bond of an intermediately formed **XIX**, similar to **XIII**. This was in contrast to a previously reported TEMPO-substituted phosphane Au complex by Gates[62] and a BH$_3$ adduct from Heurich, where no such bond cleavage was observed.[50] Nesterov reported that aminoxylphosphane complexes **XIX** show significantly different thermal stability depending on the substitution at the phosphorus atom (Scheme 8).[59] While **XIX** (X = Cl) was detected only by NMR spectroscopy, the F- and H-substituted complexes **XIX** could be isolated.[59] Upon heating **XIX** (X = F) was also transformed to **XXII**, no such behaviour was observed for **XIX** (X = H). Theoretical calculations showed that a N–O homolytic bond cleavage is indeed more favoured than P–O bond breaking in these complexes, in agreement with the observed reaction products.[50, 51] Besides the formed aminyl radical **XXI** in the bond breaking also a transient complex of a P–O containing radical complex **XX** was
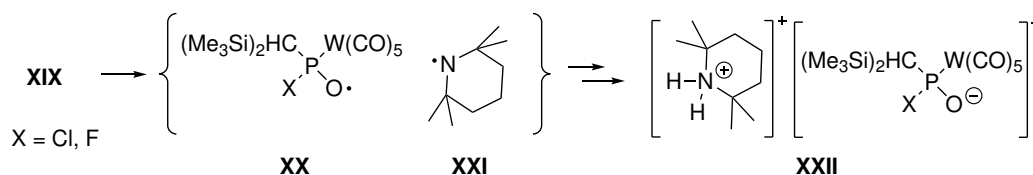
Scheme 8: Formation of postulated transient phosphanoxyl complex **XX** via N–O bond cleavage of **XIX** and the observed final product the phosphinito complex salt **XXII**.

8

assumed. DFT calculations on such a complex **XX** gave an SDD value revealing a mostly metal-centred radical and around 30% oxygen atom contribution and only 10% on phosphorus. The small spin density on phosphorus is in contrast to the SDD usually observed for **VI** being around 50% on the P-atom. As a consequence, these complexes were named phosphanoxyl complexes **XX** in analogy to the lighter uncoordinated homologues, aminoxyl radicals **IV**. As aminoxylphosphane complexes **XIX** proofed to be suitable precursors to transient phosphanoxyl complexes **XX**, access to and properties of **XIX** were further investigated by Heurich. He found that **XIX** can also be prepared via hydrogen abstraction from secondary phosphane complexes and subsequent radical heterocoupling, instead of an initial SET of **XVIII**. Heurich showed that an aminoxyl(diphenyl)phosphane tungsten complex **XIX** is accessible via two different synthetic approaches (Scheme 9).[63] The direct hydrogen abstraction with TEMPO forges **XIX** in high yields (85%) and is superior over an initial deprotonation with a yield of 55%. The same methodology allowed Heurich also the isolation of a TEMPO-1,3,2-diazaphospholidine tungsten complex **XIX**.[64] In this case a third synthetic approach was tested; an initial deprotonation of the secondary phosphane complex and subsequent reaction with the oxoammonium salt [TEMPO]BF$_4$. While this method gave better results than a combination of deprotonation and reaction with TEMPO, also in this case the reaction with two equivalents of TEMPO showed the best outcome. Both complexes **XIX** were investigated towards homolytic N–O bond breaking. The *P*-diphenyl substituted **XIX** remained stable up to temperatures of 50 - 60 °C in toluene, while the N–O bond of the 1,3,2-diazaphospholidine derivative is already cleaved at ambient temperature after two days.[63,64] The nature of the decomposition products of these two *P*-aminoxyl
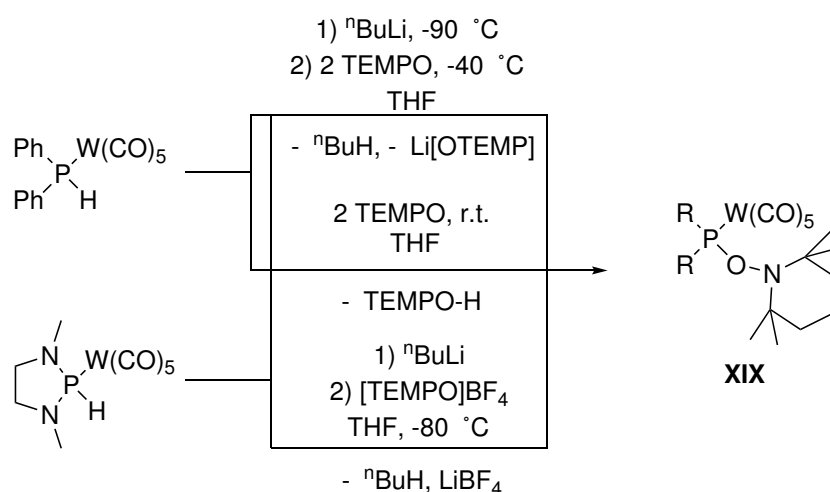
Scheme 9: Formation of isolable aminoxylphosphane complex **XIX** via different synthetic approaches as reported by Heurich.[63,64]
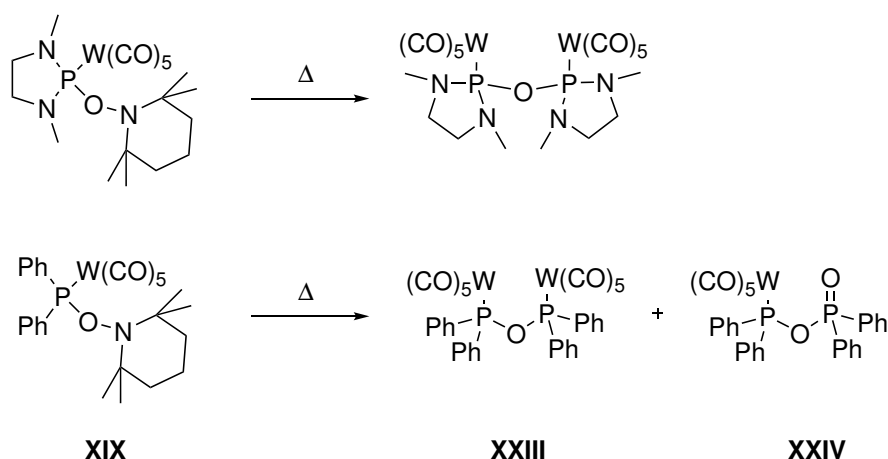
Scheme 10: Reaction products of thermal induces N–O bond cleavage of complexes **XIX**.[64, 65]

complexes **XIX** was also investigated (Scheme 10).[65] Remarkably, none of both complexes showed formation of previously observed phosphinito complex **XXII**. Instead, formal hetero-coupling products **XXIII** of the transient phosphanoxyl complexes **XX** are observed. In the diphenyl derivative a second decomposition pathway was observed, in which the W(CO)$_5$ is liberated in favour of a P–O double bond (**XXIV**).

In the presence of suitable trapping reagents transient generated **XX** reacts via radical het-erocoupling, and several tetreloxylphosphane complexes **XXV** were reported by Heurich (Scheme 11).[65] This reactivity was applied in polymerisation studies, thus allowing the synthesis of end group phosphorylated polystyrene, polymethylacrylate and polyacryloni-trile at noteworthy low temperatures.[63, 66, 67] In *n*-pentane mixing the diphenyl phosphanoxyl complex precursor **XIX** and styrene resulted in polymer formation already at 40 °C and the 1,3,2-diazaphospholidine initiated polymerisation even at ambient temperatures. These activation temperatures are much lower than for commonly used initiators for styrene poly-merisation for which temperatures of 70 - 123 °C are needed.[68, 69]
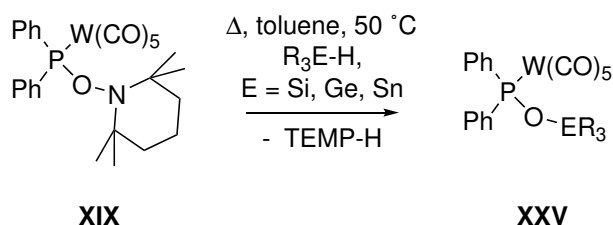
Scheme 11: Trapping reaction of a thermally generated transient phosphanoxyl generated by pre-cursor complex **XIX** with tertiary tetrelanes yielding tetreloxyphosphane complexes **XXV**.[65]
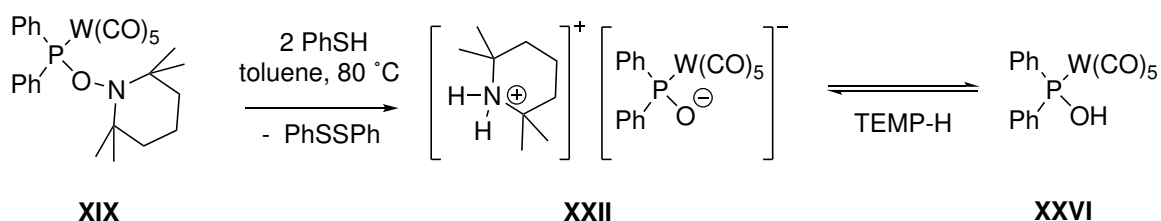
Scheme 12: Formation of an ammonium phosphinito complex **XXII** as trapping product of a phos-phanoxyl complex generated from **XIX** with thiophenol and the equilibrium with the hydroxyphosphane **XXVI**.[66]

In comparison to the *P*-bisyl substituted complexes **XIX** formation of phosphinito complexes **XXII** was never observed as a decomposition pathway, but only if hydrogen atom sources were used as trapping reagents. The reaction of aminoxyl *P*-diphenyl **XIX** with thiophenol allowed the isolation of the diphenylphosphinito complex **XXII** (Scheme 12). Furthermore, via protonation of such this phosphinito complex, it was also possible to isolate the hydroxyphosphane complex **XXVI**, for which it was previously stated by Lorenz to be not accessible in pure form.[70]

The apparent difference in thermal stability depending on the substitution pattern at phosphorus raised the question of the role of the P-bound metal fragment. Heurich and Naz investigated the accessibility of aminoxylphosphane complexes **XXVII** as precursors for phosphanoxyl manganese complexes **XXVIII**, whereby the latter had a relatively electron-rich metal center compared to group 6 $M(CO)_5$ complexes **XX**.[66] Dicarbonyl methylcyclopentadienyl phosphane manganese complexes of secondary phosphanes were deprotonated and reacted with two equivalents of TEMPO at 0 °C (Scheme 13).
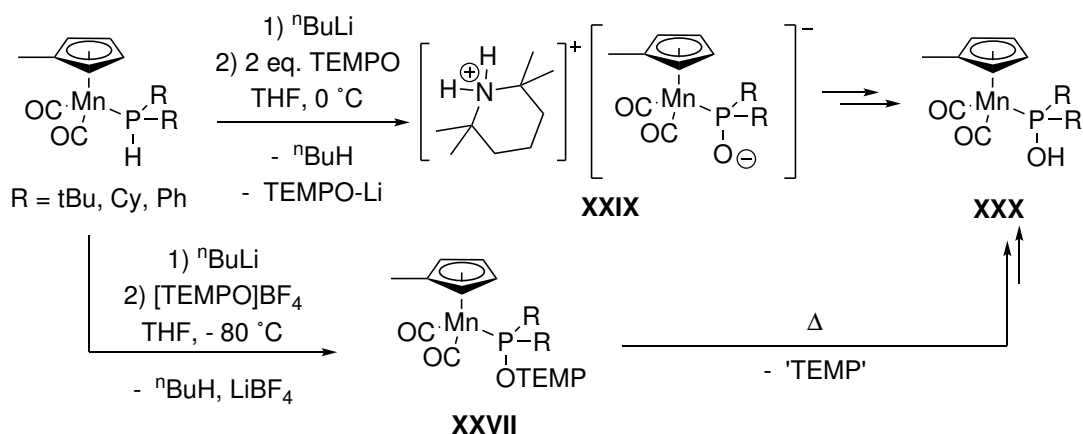
Scheme 13: Reaction scheme for the attempted synthesis of aminoxylphosphane manganese complexes **XXVII** and observed decomposition products **XXIX** and **XXX**.[66]

In this case only the piperidinium phosphinito salts **XXIX** were obtained, which upon purification attempts via column chromatography were converted to the hydroxy phosphane complexes **XXX**. No evidence of an intermediate aminoxylphosphane complex **XXVII** were obtained by the authors. A change in the synthetic protocol to an initial deprotonation and subsequent reaction with the oxoammonium salt [TEMPO]BF$_4$ gave ^{31}P-NMR evidence of **XXVII** next to already formed **XXIX**. All attempts of the authors to isolate **XXVII** failed and in all cases only complex **XXX** was obtained. DFT calculations were used to propose a mechanism in which the hydrogen atom source was the solvent THF.[66]

It was shown that isolated **XXX** could be converted to the phosphinito salt **XXIX** by the addition of the TEMP–H amine in Et$_2$O, but gave **XXX** and TEMP–H back if complex **XXIX** was dissolved in DCM (Scheme 14).
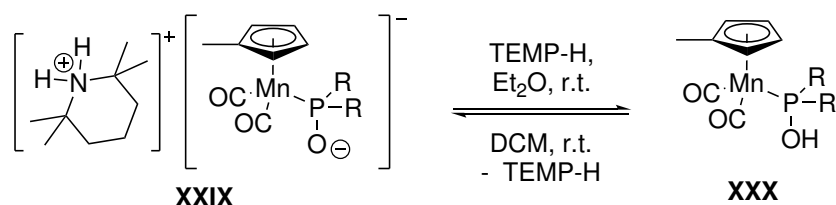
Scheme 14: Solvent depending equilibrium of phosphinito complex **XXIX** and its related hydroxy phosphane complex **XXX** in the presence of the TEMP–H amine.[66]

2. Objectives of this work

This work aims at the synthesis of aminoxylphosphane complexes as suitable precursors for observable phosphanoxyl complexes. So far only a few examples of aminoxylphosphane complexes are known and their chemistry has briefly been touched and, hence, further investigations are required. Furthermore, the effect of the substitution at the phosphorus atom and the nature of the coordinated metal fragment on the formation of transient and not yet directly detected phosphanoxyl complexes are not understood. Therefore, the outline of the presented project is:

- Systematic theoretical investigation on the nature of unligated phosphanoxyls.

- Development of synthetic protocols to access a variety of secondary phosphane tungsten complexes to explore the effects of P-atom substitution on the formation of aminoxylphosphane tungsten complexes.

- Extension to the chemistry of electron rich metal complexes to get insight into the role of the coordinated metal fragment on the spin density distribution, including the influence of co-ligands.

- Targeting compounds with high phosphanoxyl character.

- Contributing to transition metal chemistry and the problem of interplay in case of non-innocent ligands.

3. Theoretical Considerations

Phosphinoyl vs. phosphanoxyl radical character

3.1. Comparison with the lighter homologous aminoxyl radicals

The afore mentioned phosphinoyl radicals **1** (before described as **VI**) are used widely in organic synthesis,[27,29,30,71] mainly in the radical addition to olefins. Noteworthy these radicals react exclusively at the P-centre to form P–C bonds. This is in contrast to aminoxyl (commonly known as nitroxide; before described as **IV**) radicals **2** the lighter homologue of phosphinoyl radicals, in which oxygen-centred reactivity is observed.[72–74] Aminoxyl radicals are surprisingly stable compounds, firstly synthesised in 1845 by Fremy, however, their radical character was only later recognised by Wieland and others in 1914.[15] The trivalent nitrogen atom has a planar environment, however slightly deviating for different cyclic derivatives.[75] The electronic analysis shows an almost 50:50 distribution of the spin density among nitrogen and the oxygen atom which is in line with the single occupation of the π^*(N–O^{exo}) molecular orbital. Structural differences between the two homologues have been noticed already 50 years ago, when a transient phosphinoyl radical was prepared in the crystal lattice of diphenylphosphane oxide by irradiation.[76] Hyperfine coupling parameters and comparison to other, at that time rare, phosphorus-centred radicals, resulted in the conclusion that the generated phosphinoyl radical adopts a pyramidal structure due to larger contribution ($\sim$10%) of the s(P)-orbital (Figure 5).[77] A theoretical study about substituent depending stability of **1** was recently published.[78] However, the question remains if under the right
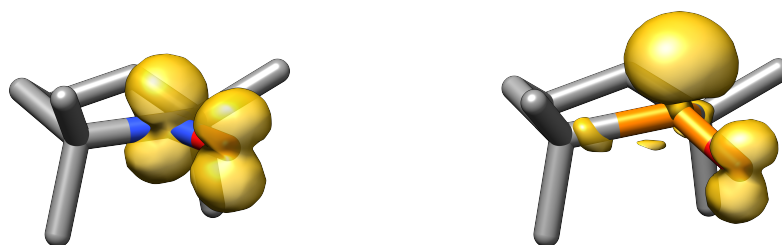
Figure 5: Computed structure and spin density distribution surface of TEMPO **2a** (left) and its phosphorus congener **1a** (right); surface isovalue 0.009.

14

conditions, *e.g.*, a finely selected choice of substituents, a planar environment around the phosphorus atom can be achieved. In analogy to aminoxyl radicals **2** such a radical would be named phosphanoxyl. For this a computational study was now conducted comparing the established 2,2,6,6-tetramethylpiperdin-2-oxyl (TEMPO) aminoxyl radical **2a** with its heavier homologue **1a**. As a level of theory PWPB95-BJD3/def2-QZVPP(CPCM$_{THF}$)//TPSS-BJD3/def2-TZVP(CPCM$_{THF}$) was chosen and is used throughout this work, if not mentioned otherwise. For **1a** a relaxed structure was computed and a phosphanoxyl type with fixed angles **1a'**, thus resembling the situation in TEMPO. As expected from the previous reports **1a** adopts a pyramidal configuration clearly seen by the angle sum $\sum_{\angle}^{P}$ around phosphorus (Table 1).[77] This is accompanied by a P–O^{exo} double bond, with a typical bond length of 1.518 Å and a Mayer bond order (MBO) close to 2. As a result, the spin density distribution (SDD) on P and O^{exo} is 56:21, clearly deviating from the equally shared situation in aminoxyl radicals **2** (Figure 5). Remarkably, **1a'** shows almost identical features, despite the forced planarity. Loewdin reduced molecular orbital population analysis of **1a** shows 2.9% s(P)- and 34.3% p(P)-orbital contribution to the highest single occupied molecular orbital (*h*-SOMO), which is only slightly changed for **1a'** (1.6% s(P)- and 37% p(P)-orbital contribution). In both cases the p(O^{exo})-orbital contributes approximately by the same amount (**1a**: 16%, **1a'**: 15.5%). Comparison of the frontier molecular orbital FMO energies shows that the pyramidalization causes no change in the shape of the FMOs, however a significant stabilisation of the latter (Figure 6). Overall, the relaxed bent structure **1a** is 9.1 kcal mol^{-1} more stable than its phosphanoxyl counterpart **1a'**. Similar consideration regarding **2a** showed, that the same angular situation around the nitrogen atom as around the phosphorus atom in **1a** yield an 'aminoyl' type radical **2a'**. In the *h*-SOMO of **2a** Loewdin reduced molecular orbital population analysis gave almost pure p(N)-orbital contribution (34.8%) and

Table 1: Bond distances (in Å), MBO, angle sums (in °) and Loewdin spin density (in e) and O^{exo} partial charges δ_p(O^{exo}) of **2a** and **2a'** and its related phosphorus radicals **1a** and **1a'**.

	2a	2a'	1a	1a'
d(N–O^{exo})	1.298	1.287	—	—
d(P–O^{exo})	—	—	1.518	1.521
MBO(N–O^{exo})	1.40	1.40	—	—
MBO(P–O^{exo})	—	—	1.87	1.85
$\sum_{\angle}^{N}$	356.13	336.83	—	—
$\sum_{\angle}^{P}$	—	—	336.83	356.13
SDD(N)	0.41	0.39	—	—
SDD(P)	—	—	0.56	0.56
SDD(O^{exo})	0.46	0.50	0.21	0.20
δ_p(O^{exo})	0.02	0.05	−0.09	−0.11

only 0.2% s(N)-orbital mixing paired with 29.4% p(O^{exo})-orbital character. In the bent **2a'** a small increase to 1% s(N)-orbital character and a slight decrease to 33.7% p(N)-orbital contribution, together with 28.5% p(O^{exo})-orbital mixing is observed. While this has no apparent effect on the bond length (N-O^{exo}) and the MBO, the SDD is slightly decreased on the nitrogen atom and increased on the oxygen atom (Table 1). Comparing the energies of both structures shows that the planar **2a** is favoured by 8.5 kcal mol^{-1} over **2a'**. The Loewdin reduced molecular orbital population analysis for **1a** reveals a p(P)- to p(O^{exo})-orbital ratio of 2.1 (and 2.4 for **1a'**), which is almost doubled compared to the p(N)/p(O^{exo}) ratio of 1.2 in the aminoxyl **2a** and the 'aminoyl' **2a'**. Therefore, the almost ideal p-overlap in **2a** and **2a'** is broken in the phosphorus derivatives **1a** and **1a'** yielding a MO of p(P) symmetry mixing with the s(P)-orbital. This effect is present in both, **1a** and **1a'**, and therefore structural independent. From this the P–O^{exo} bond benefits significantly as the double bond character is almost untouched, as seen by the MBO close to 2. Whereas the MBO in **2a** shows a weakening of the N–O^{exo} π-bond.
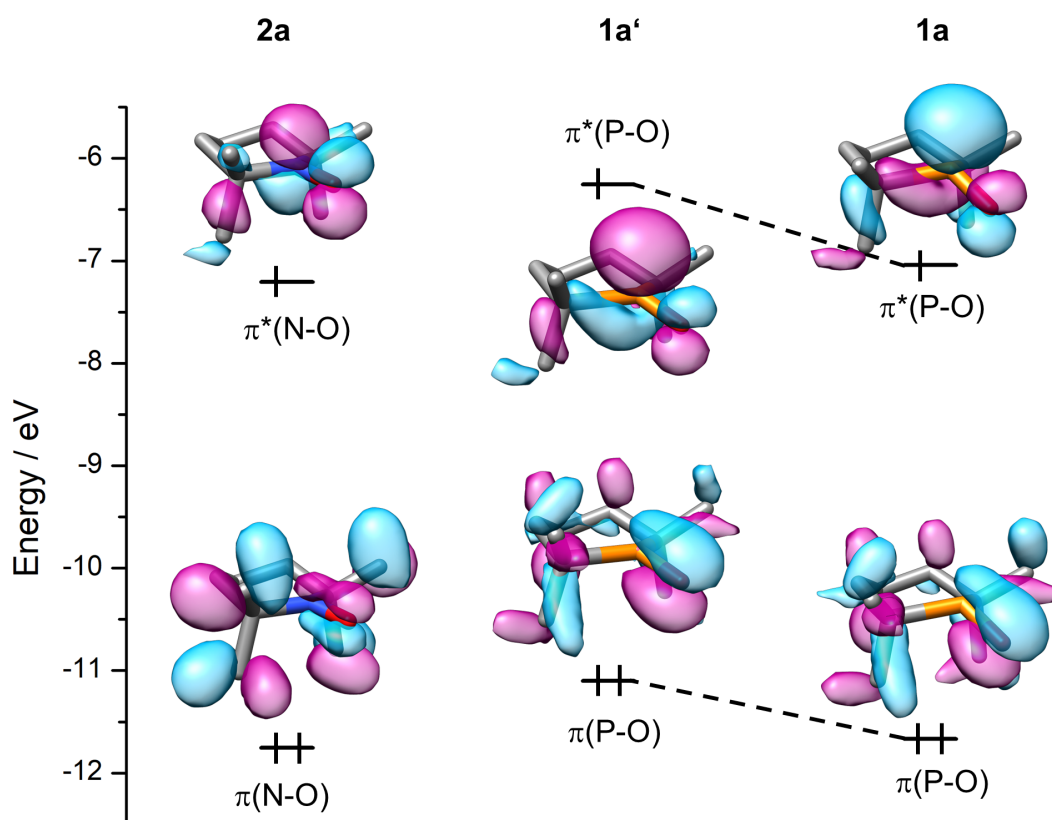
Figure 6: Selected Kohn-Sham FMOs of the radicals **1a**,**1a'** and **2a** with π-symmetry.

16

3.2. Structural comparison with the related ions

Recently the first base-free oxophosphonium **XXXI** salt was isolated and showed a strict planarity around the phosphorus atom, similar as in the well-known oxoammonium salts, *i.e.*, **2a⁺** (Figure 7).[79,80] The origin of this structural feature which is desired for a pure phosphanoxyl like **1a'**, was therefore investigated. For this both analogue structures **1a⁺** and **2a⁺** were computed and showed the expected planar environment around the group 15 element (Table 2). The planarisation of **1a⁺** is accompanied by a shortening of the P–O^{exo} bond and an increase of the MBO, as the π^*(P–O^{exo}) is not populated in **1a⁺**. Similar observations are made for the oxoammonium ion **2a⁺**. Comparison of the π(P/N–O) between the neutral **1a** and **2a**, and the cationic **1a⁺** and **2a⁺** shows that a significant stabilisation is observed for the oxoammonium **2a⁺**, while this effect is smaller in **1a⁺**. From the shape, *e.g.*, the orbital coefficient of the molecular orbitals in **1a⁺** it can be seen, that the P–O bond is significantly polarised, which is also expected due to the increased difference in electronegativity compared to the N–O bond (Figure 8). In addition, the anions **1a⁻** and **2a⁻** were calculated. In
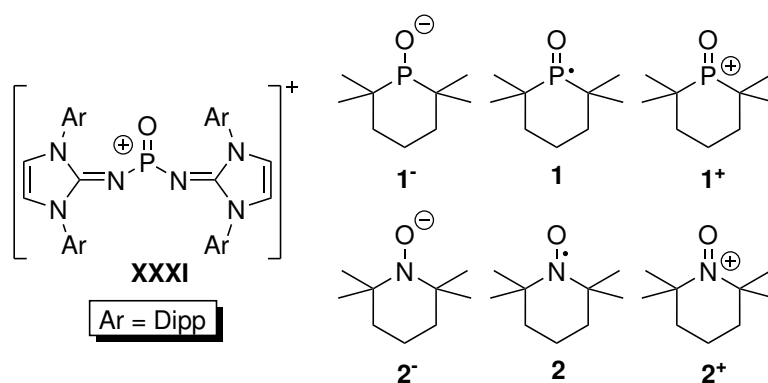
Figure 7: Lewis structures of oxophosphonium ion **XXXI** the phosphinoyl radical **1a**, TEMPO **2a** and their related ions; counter ions are not shown.

Table 2: Bond distances (in Å), MBO, angle sums (in °) and O^{exo} partial charges δ_p of **2a⁺** and **2a⁻** and its related phosphorus radicals **1a⁺** and **1a⁻**.

	2a⁺	**2a⁻**	**1a⁺**	**1a⁻**
d(N–O^{exo})	1.199	1.427	—	—
d(P–O^{exo})	—	—	1.471	1.567
MBO(N–O^{exo})	1.89	0.86	—	—
MBO(P–O^{exo})	—	—	2.16	1.51
$\sum_{\angle}^{N}$	360.0	335.0	—	—
$\sum_{\angle}^{P}$	—	—	359.9	312.9
δ_p(O^{exo})	0.38	−0.39	0.10	−0.28
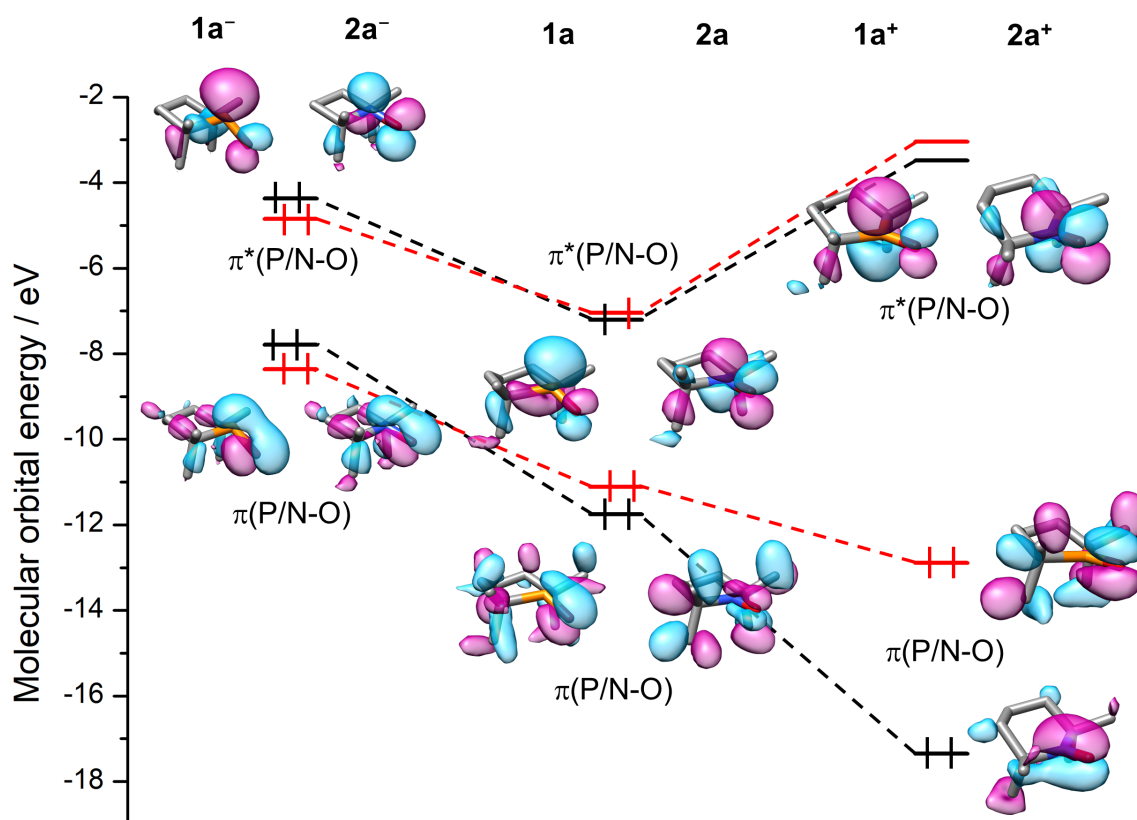
Figure 8: Selected Kohn-Sham FMO diagram (only π-symmetry) of the radicals **1** (red) and **2** (black) and their related ions.

both cases pyramidalization is found for either N and P. The anion **1a⁻** is even more pyramidal than in the phosphinoyl radical **1**. Remarkably, the bond order of the P–O^{exo} is still between double and single bond as seen from the MBO. In contrast in the anion **2a⁻** the MBO for the N–O^{exo} bond is drastically decreased and even lower than 1. The π*(P-O^{exo}) of **1a⁻** is best described as a lone pair at the phosphorus atom with some p(O^{exo})-orbital contribution, this resembles more the shape of the phosphinoyl **1a** than the pure p(P)-orbital in the π*(P–O^{exo}) of the cation **1a⁺**. The situation is inverted for the aminoxyl case. While planarity is found for the oxophosphonium ions, *i.e.*, in **1a⁺** the P–O^{exo} bond is strongly polarised towards the O-atom. This polarisation is kept also throughout the radical **1a** and the anion **1a⁻**, in which it leads to a 'lone-pair' type HOMO (Figure 8). Finally, the unpaired electron is strongly localised on the P-atom (due to the P-polarised π*(P–O^{exo})), rather than on the oxygen atom in **1a**. The smaller difference in electronegativity between N and O allows a stable radical by single occupation of the π*(N–O^{exo}) orbital for aminoxyl radicals **2**.

3.3. α-Substituent effect in TEMPO

As structural changes had only small impacts in the electronic situation of **2a** the question arises if the properties of the N–O bond can otherwise be modified. Therefore, the C-substituents in α-position to the nitrogen atom were replaced by N or O to yield the theoretical 1,3-dimethyl-1,2,3-triazine-2-oxyl **2b** and the 1,3,2-dioxazine-2-oxyl **2c** (Figure 9, Table 3). In comparison to **2a** the N–O^{exo} bond length is shorter in both cases. Remarkably, the calculated structures deviate from planarity around the nitrogen atom. This is especially pronounced for **2c** with an angular sum $\sum_{\angle}^{N}$ of 336.9°, which is the same found for the phosphinoyl radical **1a**, along with an MBO for the N–O^{exo} of 1.7, also comparable with the MBO found for the P–O^{exo} bond in **1a**. Qualitatively, the h-SOMO represents the SDD of **2b** and **2c** in good agreement. Either N and O atoms are involved in the electron delocalisation and make up for 18% (**2b**) and 22% (**2c**) of the SDD. This spin density shared on the α-atoms is mainly taken from the O^{exo} compared to **2a**, while the SDD of the N atom decreases only slightly. Despite the numerically small changes for the nitrogen atom the shape of the SDD around it is affected resembling the SDD of **1a** going from **2a** over **2b** to **2c**. Loewdin reduced molecular orbital population analysis of **2b** shows a strong decrease of the p(N)-orbital contribution to the h-SOMO to 23.1% alongside an increase of the s(N)-orbital mixing to 0.9%. The adjacent nitrogen atoms in **2b** contribute mostly with their
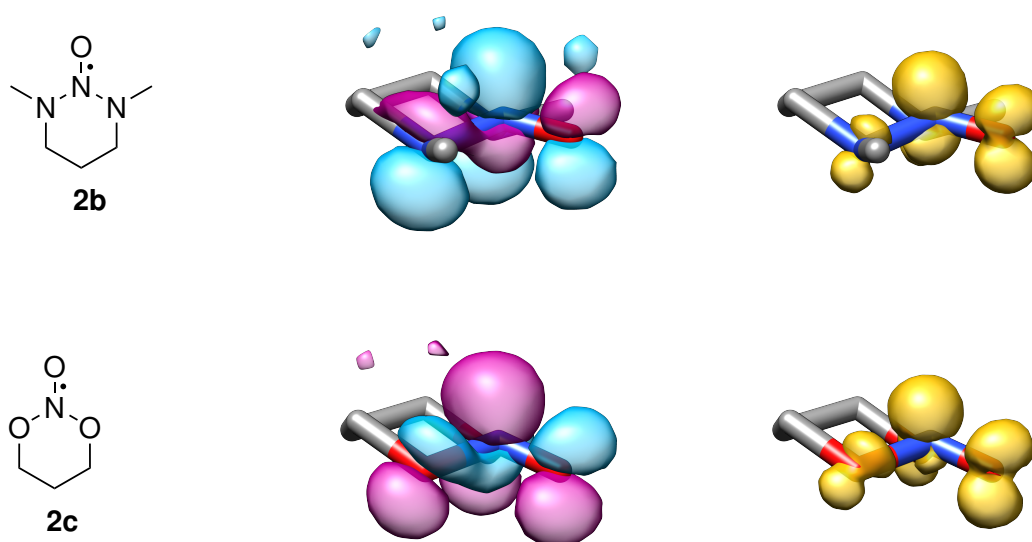
Figure 9: Lewis structure of **2b** and **2c** (left) together with the corresponding h-SOMO (middle) and the spin density (right) distribution.

Table 3: Bond distances (in Å), MBO, angle sums (in °) and Loewdin spin density (in e) and O^{exo} partial charges in theoretical aminoxyl derivatives **2b** and **2c**.

	2b	**2c**
$d(N–O^{exo})$	1.269	1.212
$MBO(N–O^{exo})$	1.45	1.70
$\sum_{\angle}^{N}$	343.1	336.9
$SDD(N)$	0.41	0.36
$SDD(O^{exo})$	0.36	0.39
$SDD(\alpha\text{-}N/O)$	0.09/0.09	0.11/0.11
$\delta_p(O^{exo})$	−0.01	0.09

p(N)-orbitals making up 29.7% of the h-SOMO. The amount of $p(O^{exo})$-orbital character is decreased to 16.7%. The more electronegative substituents in **2c** lead to an even higher s(N)-contribution of 3.2%, while p(N)-orbital is mixed up to 23.6% in the h-SOMO. The O-atoms in α-position contribute to 29.6% and the $p(O^{exo})$-orbital is to 22.5% involved. The initial planar environment of the N-atom in aminoxyl radicals, like **2a**, can be altered by adjacent electronegative substituents, which are able to involve p-type orbitals. This leads to an increase in the s(N)-orbital contribution of the central N-atom to the h-SOMO and finally to pyramidalization. In **2c** the MBO and the angular sum $\sum_{\angle}^{N}$ are even comparable with values found for the phosphinoyl **1a**. Despite the structural changes the SDD in the aminoxyls **2b** and **2c** is still almost equally shared between the central N- and the O^{exo} atom. The mixing of larger amounts of s(N)-orbital into the h-SOMO and therefore in the SDD results in a radical with more σ-type character instead of the almost pure π-type character found in **2a**.

4. Towards P–O containing radical complexes of tungsten

4.1. Theoretical assessment of a family of phosphinoyl radicals

The reported increased thermal instability of 1,3,2-diazaphospholidine complex **XIX**, compared to the diphenyl derivative raised the quest of the effect's origin. To evaluate the steric and electronic effects with respect to stability and reactivity of such complexes a small family was targeted for this study. As a starting point, the hypothetical free phosphinoyl radicals **1d-l** (Figure 10, Table 4) were computed to explore their structures and electronic properties, focusing on the SDD, as similar alternations of the α-substituents led to significant changes of the TEMPO radical **2a**. From these results the best suited framework for the aminoxylphosphane complexes should be determined. The results show that P–O$^{\text{exo}}$ bond lengths range from 1.49 to 1.539 Å. These values fall in between P–O distances observed for **1a$^+$** and **1a$^-$**, with strong double or respectively single bond character. MBOs for the P–O$^{\text{exo}}$ bond span from 1.69 to 1.98. These observations clearly speak for double bonded P–O$^{\text{exo}}$ systems which is in line with the observation previously made for **1a**. Pyramidalization
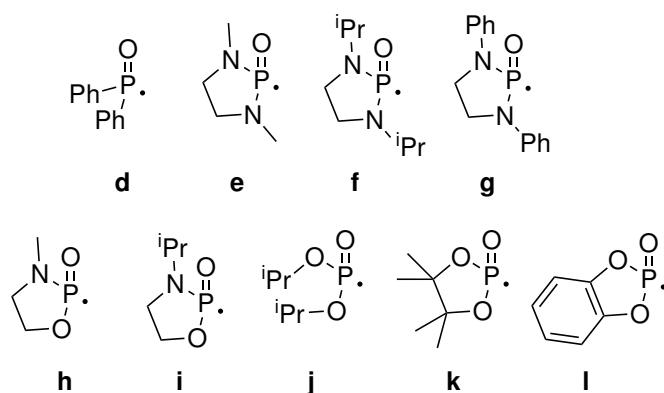
Figure 10: Selection of acyclic and cyclic phospinoyl radicals **1d-l** chosen for DFT investigation

Table 4: P–O bond distances in Å, P-angle sum $\sum_{\measuredangle}^{P}$ in ° and spin density on select atoms in e, in the phosphinoyl radicals **1d-l**.

	1d	**1e**	**1f**	**1g**	**1h**	**1i**	**1j**	**1k**	**1l**
d(P–O$^{\text{exo}}$)	1.507	1.511	1.513	1.506	1.539	1.536	1.497	1.493	1.491
$\sum_{\measuredangle}^{P}$	337.1	329.2	329.6	326.8	287.1	287.5	333.1	329.8	321.1
SDD(P)	0.53	0.55	0.55	0.53	0.01	0.01	0.59	0.59	0.52
SDD(O$^{\text{exo}}$)	0.19	0.16	0.17	0.17	0.09	0.07	0.16	0.18	0.18
SDD(α-N)	—	0.21	0.20	0.19	0.65	0.66	—	—	—
SDD(α-O)	—	—	—	—	0.00	0.01	0.18	0.18	0.22

angles around the P-atom are around 330°, acyclic derivatives **1d** and **1j** show the largest angular sums around phosphorus which is to be expected as they experience no ring strain. An exception is the much smaller angular sum in the 1,3,2-oxazaphospholidinoyl radicals **1h** and **1i**, *i.e.*, around 287° and the longest P–O^{exo} bond distances are observed therein. In addition, the spin density in these systems is heavily distributed on the nitrogen atom and almost no spin is found on the phosphorus atom. Consideration of the FMOs shows a doubly populated lone pair on the P-centre, similar as in the anionic **1a⁻**. The LUMO is an almost pure *p*(N)-orbital, which is found for the spin-down (β-spin) SOMOs but not for the spin-up (α-spin) SOMOs and can be explained as a 'leaking' effect to effort stabilisation. The visualised spin density distribution, as the total difference of α- and β-spins resembles in its form the LUMO, which agrees with the FMO analysis. Overall, **1h** and **1i** are best described with zwitterionic resonance structures with a planar nitrogen and the radical located in the *p*(N)-orbital (Figure 11). The strong planarization of the N-atom is however not exclusive for the 1,3,2-oxazaphospholidinoyl structure, as significant planarity is also found in the 1,3,2-diazaphospholidinoyl radicals **1e-g**. In these, the spin density on the nitrogen atoms adjacent to phosphorus only sums up to ∼10% (similar to the amount on the α-O-atoms the
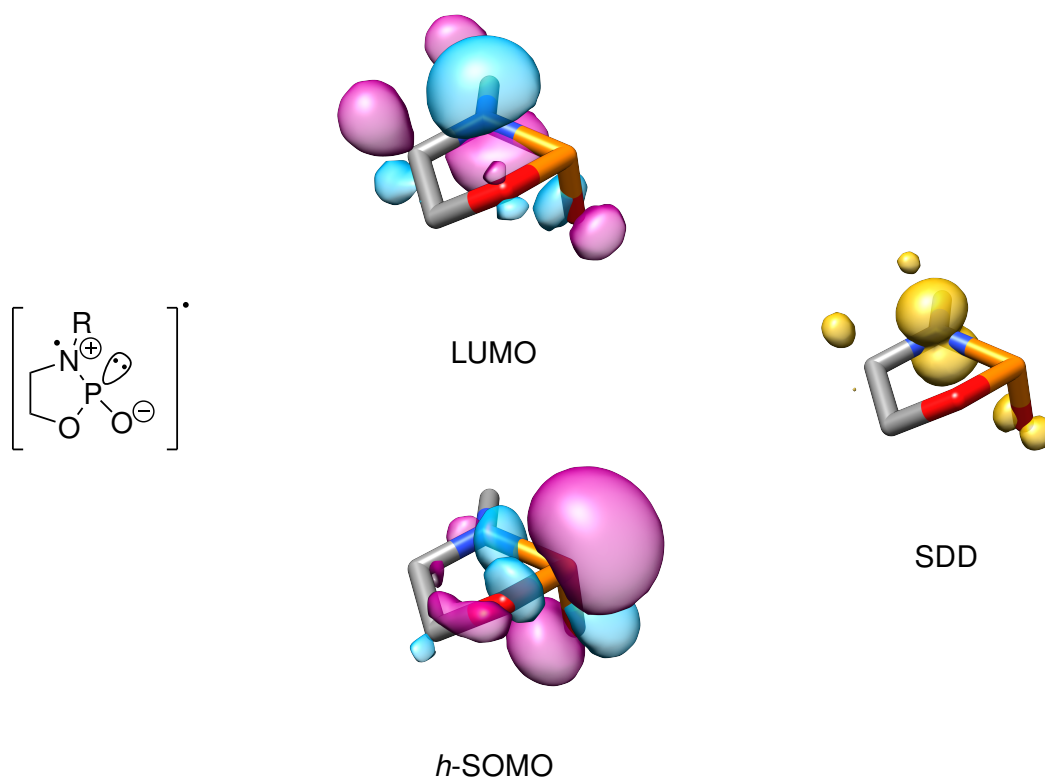
Figure 11: Proposed Lewis structure for **1h,i** along with FMOs and SDD of **1h**.

1,3,2-dioxaphospholanoyl radicals **1j-l**) and hence it can be assumed that the planarity is not directly related to a stronger stabilisation of the unpaired electron. In contrast to the effects described previously for the TEMPO derivatives **2b** and **2c** are the changes in bonding parameters and spin density distribution for the family of phosphinoyl radicals **1** negligibly small for the symmetrical derivatives. Only for the 1,3,2-oxazaphospholidinoyl radicals **1h,i** significant alternations are found as discussed. However, their electronical and structural properties show no similarities with the desired phosphinoyl- or even phosphanoxyl radicals.

4.2. Initial considerations regarding the synthesis of heterocyclic secondary phosphanes

Based on the theoretical results and on the previous experimental studies reported by Heurich,[63,65,67] it was planned to synthesize three parent P-heterocycles **4e,i,k** having a P–H bond, and subsequently convert them into the required pentacarbonyltungsten(0) complexes. Therefore, namely the 1,3-diisopropyl-1,3,2-diazaphosphol-idine complex **6e** as sterically more demanding, the 1,3,2-oxazaphospholidine **6i**, due to the inherently different features in the phosphinoyl radical **2i** and the 1,3,2-dioxaphospholane **6k** complexes were chosen. This set was then probed to evaluate, if electronic changes might occur in the final complex and its related phosphanoxyl complex. Due to the low stability of un-ligated aminoxylphosphanes **XII**, the aminoxylphosphane complexes **XIX** had to be pre-pared already in the coordination sphere of the metal. For this Heurich had used sec-ondary phosphane complex **XXXII**, which were forged by complexation of **4** to a metal fragment and then further reacted to **XIX** (Scheme 15). Hence, access to secondary phosphane complexes **4** is needed. For bisalkyl- and bisaryl-phosphanes **4**, Heurich and Naz showed that free secondary phosphanes can easily react with activated metal frag-ments, *e.g.*, via ligand exchange, to yield the desired secondary phosphane complexes.[50,64] While unligated secondary phosphanes are well known for the mentioned carbon- substi-tuted derivatives, the chemistry of such doubly heteroatom substituted phosphanes E_2PH is less explored, and they were once even considered to be not accessible.[81] In most cases yields are low and formation is not straight forward.[82,83] Even less is known about the five-membered heterocycles with P-H functionality.[48,84] For secondary phosphanes of the 1,3,2-diazaphospholidine family several compounds are reported, however, commonly with large substituents on the 1,3-nitrogen atoms.[85,86] Early attempts to synthesise 1,3,2-diazaphospholidines via reduction with lithium aluminium hydride $Li[AlH_4]$ (LAH) with small substituents gave either poor yields or no product formation.[82] Access of such cyclic phos-phanes was limited to ^{t}Bu substitution (Figure 12). Synthesis of the dimethyl derivative **4e** was achieved by Snow et al. They probed a suitable hydride transfer reagent and found
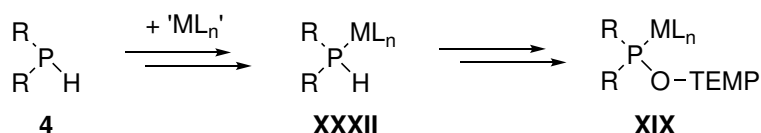
Scheme 15: Synthetic concept of accessing aminoxylphosphane complexes **XIX** from secondary phosphane complexes **XXXII** subsequent to complexation of **4**.
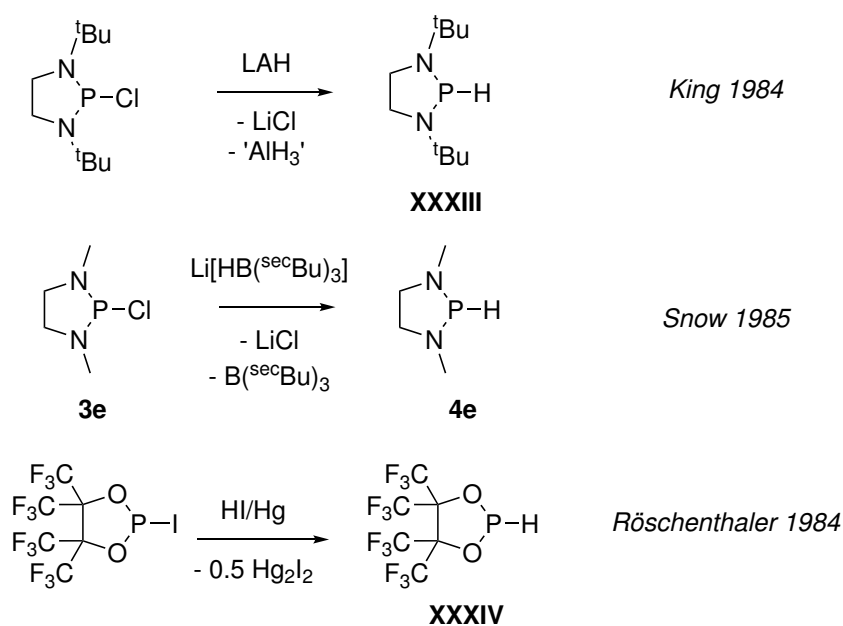
Figure 12: Selected synthesis of secondary 1,3,2-diheterophospholanes **4e**, **XXXIII** and **XXXIV** reported previously in the literature.

Li-selectride Li[HB^{sec}Bu$_3$] to allow for the formation of **4e** at low temperatures, however, they did not report on its isolation and only described its complexation.[87] The importance of the α-substituent can further be assumed as there are no reports on a secondary 1,3,2-oxazaphospholidine, in which the steric bulk is significantly reduced compared to the N,N systems. Only one example of a 1,3,2-dioxaphospholane bearing a P–H unit is reported having a tetrakis(trifluormethyl)pinacol framework **XXXIV**.[88]

4.3. Attempted reduction of 2-chloro-1,3,2-diheterophospholanes via literature protocols

As the unligated (free) phosphanes **4** would allow more convenient transfer to other transition metals in future studies it was tested if the secondary phosphanes **4f,i,k** were accessible via reduction with either LAH oder Li-selectride (Figure 13). The reduction of **3f** with LAH at 0 °C in Et$_2$O yielded a mixture detected via ^{31}P-NMR spectroscopy (Figure 14). Next to two resonances at 110 and 71 ppm several other peaks are present, however, with negligible intensity. The two major signals have a 30:70 ratio. A doublet splitting is observed for the resonance at 71 ppm caused by a scalar $^1J_{P,H}$ coupling of 155 Hz. This resonance is assigned to be the desired secondary phosphane **4f**. It is slightly highfield shifted com-
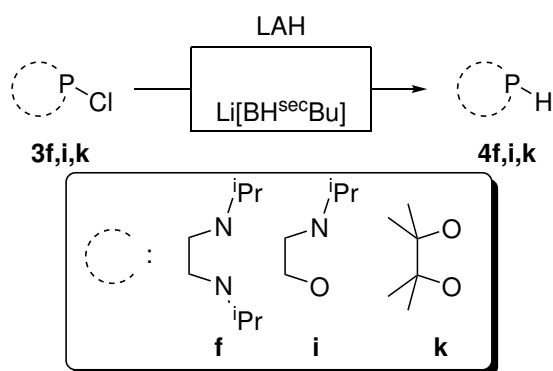
Figure 13: Attempted synthetic routes to access the free secondary phosphanes **4f,i,k** via reduction of **3f,i,k**.

pared to the 1,3-dimethyl-1,3,2-diazaphospholidine **4e** described by Snow et al.[87] with a chemical shift of 97 ppm and a $^1J_{P,H}$ of 150 Hz. The resonance at 110 ppm does not show any resolved couplings and its chemical shift fits to triamino substituted phosphanes which were also reported as side products by King and Snow in the attempts to obtain diamino
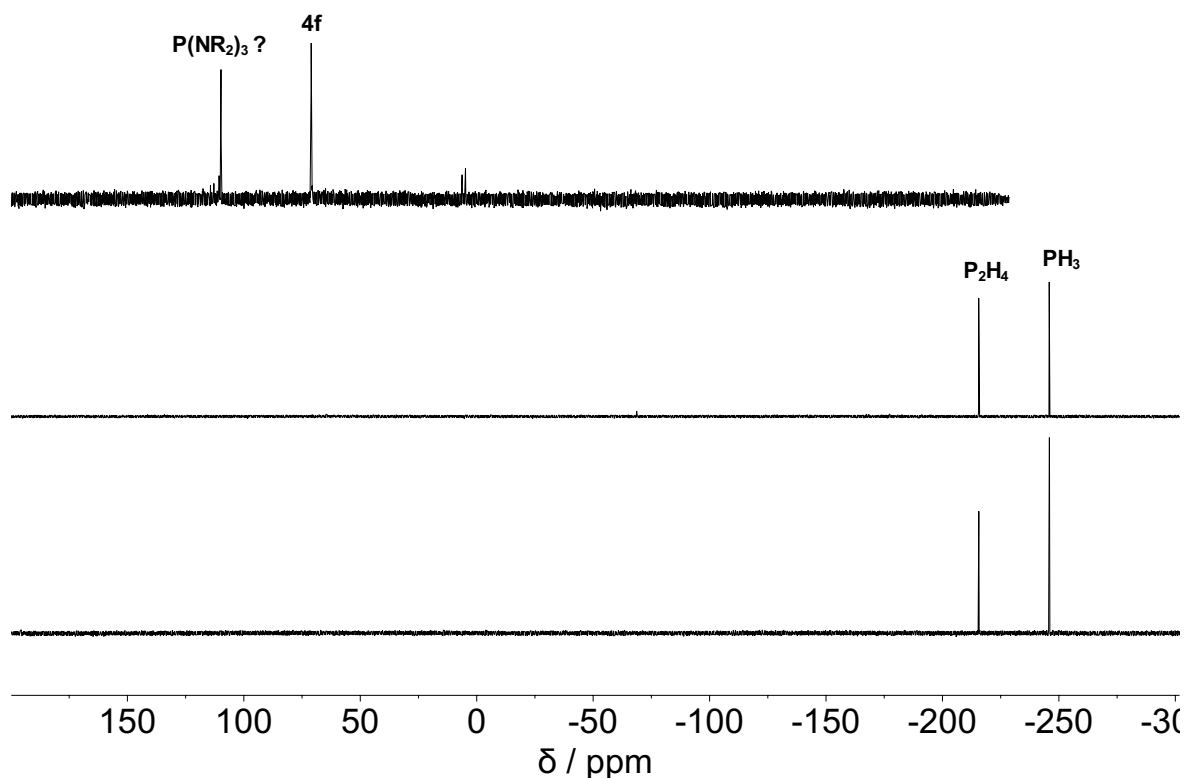
Figure 14: $^{31}P\{^1H\}$-NMR spectra of the attempted reduction with LAH for **3f** (top), **3i** (middle), **3k** (bottom) in Et_2O.

phosphanes with a smaller steric bulk. The reduction of **3i** with LAH at 0 °C in Et_2O yields only fully reduced compounds, *i.e.*, PH_3 ($\delta(^{31}P)$: −246 ppm) and P_2H_4 ($\delta(^{31}P)$: −216 ppm). The reduction of the 1,3,2-dioxaphospholane **3k** with LAH results in the same. It became clear that LAH is not suitable for the reduction of such phosphanes, despite the *^iPr* substituent in **3f** and **3i**. Therefore, the approach reported by Snow was tested. Reduction with Li-selectride of the 2-chlorophosphane **3f** corroborated the assumption of the product formation in the mixture, obtained with LAH, as only one resonance at 71 ppm was observed in the ^{31}P-NMR spectrum (Figure 15). Phosphane **4f** was stable in the mixture at room temperature, even if stirred for prolonged time at such temperatures. However, isolation of **4f** from the reaction mixture was not possible. Under the mild reaction conditions with Li-selectride reduction of **3i** affords a complex product mixture detected by ^{31}P-NMR spectroscopy. Besides two major resonances at 164 and 117 ppm with scalar $^1J_{P,H}$ couplings of 202 and 173 Hz, respectively, the signal of P_2H_4 is also present. While the signal at 117 ppm could be assigned the secondary phosphane **4i** a clear assignment cannot be made. No evidence for the formation of **4k** was found in the reaction mixture of the reduc-
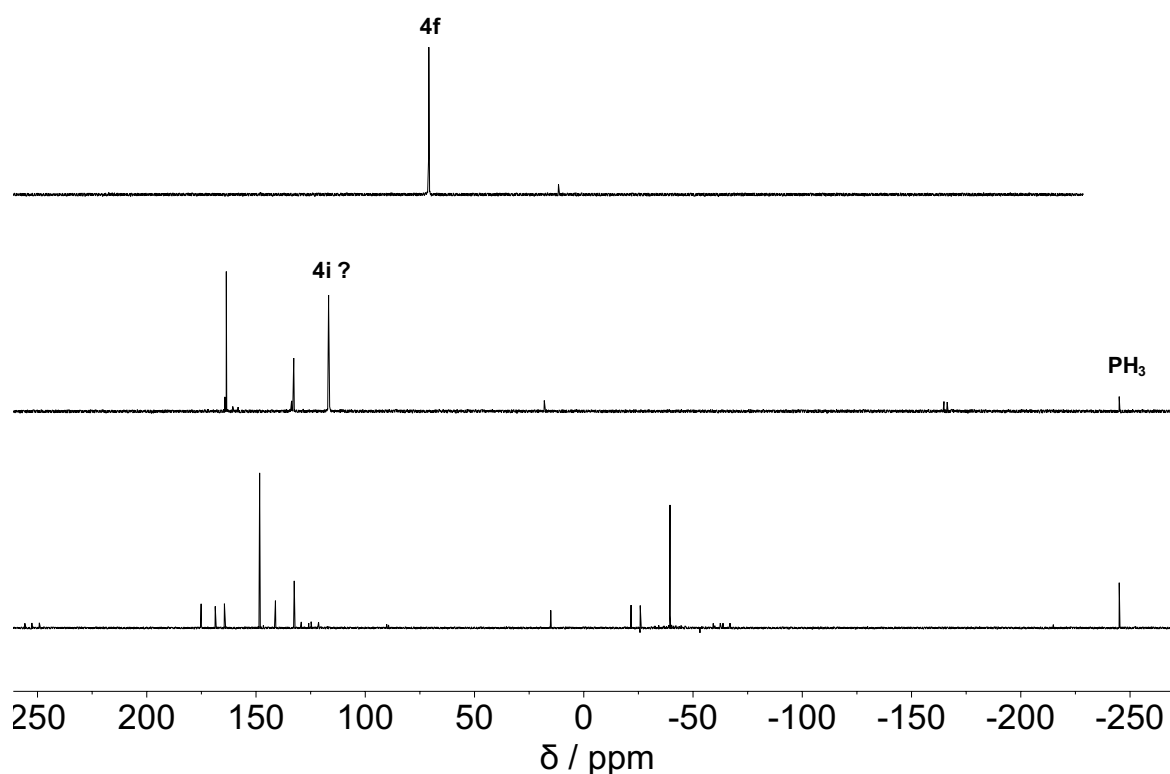
Figure 15: $^{31}P\{^1H\}$-NMR spectra of the reaction solution of the attempted reduction with Li-selectride for **3f** (top), **3i** (middle), **3k** (bottom) in Et_2O.

tion of **3k** with Li-selectride. The reported effect of the size of α-substituents seems to be crucial for the formation of the secondary phosphanes, even under mild conditions. Access to the unligated secondary 1,3,2-diheterophospholanes is therefore only partially possible for derivatives having larger N-substituents in the 1,3,2-diazaphospholidine, but not by the herein described synthetic approaches. Therefore, another method was needed to access the targeted phosphane complexes **6f,i,k**.

4.4. Synthesis of P-heterocyclic tungsten complexes possessing a P–H unit

Despite the frequently used 1,3,2-diazaphospholidine structure, little is reported about complexes still carrying the P–H unit, as many reports focus on structurally related phosphenium complexes.[89,90] Similar coordination chemistry is described for the 1,3,2-oxazaphospholidine motive.[91] However, in this case no complex of such secondary N/O-phosphanes (cyclic and acyclic) is known. And while 1,3,2-dioxaphospholanes are also applied as phosphenium ligands,[92,93] some complexes of the free phosphanes with an intact P–H unit are known.[94]

To access **6f**, the method previously used for **6e**, was used (Scheme 16).[66] For this the chloro-phosphane **3f** was reacted with [W(NCMe)(CO)$_5$] in THF and stirred for 20 h and after purification by filtration over silica **5f** was obtained. The product gave a single resonance at 130 ppm having a $^1J_{W,P}$ coupling of 369 Hz in the ^{31}P$\{^1$H$\}$-NMR spectrum, which is highfield shifted by 30 ppm compared to **3f**. The magnitude of the coupling is at the upper end of the range of $^1J_{W,P}$ coupling constants for trivalent phosphane ligands and originates from the three electronegative substitutents at phosphorus. Reduction with LAH at 0 °C in Et$_2$O yields **6f** in moderate yields after common work-up procedure. The previous discussed reduction study of the free chloro phosphanes **3,i,k** with LAH and Li-selectride suggested less satisfying results for **5i,k** and therefore an alternative method was needed. Remarkably, use of the tetraethylammonium pentacarbonyl hydrido tungstate(0) [NEt$_4$][W(CO)$_5$H]
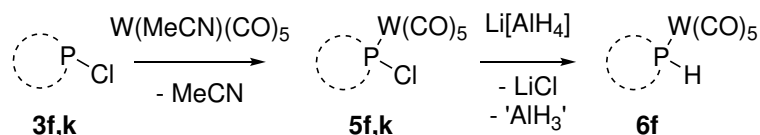
Scheme 16: Complexation of **3f,k** and subsequent synthesis of the cyclic secondary phosphane tungsten complexes **6f** via reduction of **5f**.
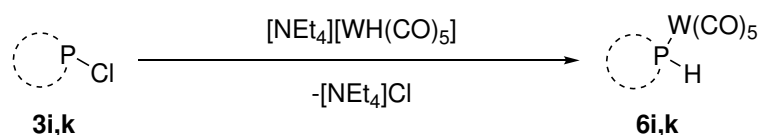
Scheme 17: Synthesis of the cyclic secondary phosphane tungsten complexes **6i,k** via complexation and reduction using the hydrido tungstate salt.

in the reaction with the 2-chloro-1,3,2-diheterophospholanes **3i,k** forged the desired complexes **6i,k** with high selectivity and in moderate to good yields after extraction with Et_2O (Scheme 17). This one step reaction has been previously only scarcely described in the literature.[83] While, the tungstate salt was never used for the reduction of heterocyclic (mono) chlorophosphanes before, similar reactions have been reported for Ta, Mo and Nb complexes; for the latter the reaction mechanism was discussed.[95] The combination of the two synthetic approaches allowed finally the isolation of the secondary heterocyclic phosphane complexes **6f,i,k**. $^{31}P\{^1H\}$-NMR experiments show a singlet for all three compounds which is shifted to lower fields with an increased oxygen content in the five-membered ring (Table 5).

The $^1J_{W,P}$ coupling is increasing from 295 to 325 Hz with higher oxygen content. In the ^{31}P-NMR spectra the signals appear as doublets having large $^1J_{P,H}$ scalar couplings with values of 273, 321 and 350 Hz for **6f**, **6i** and **6k**, respectively. In the ^1H-NMR spectrum the directly bonded P–H resonates at 7.70 for **6f**, at 7.71 and 8.49 ppm, for **6i** and **6k**, respectively. These show satellites from a $^2J_{W,H}$ coupling within the same range as observed for **6e**. These observations agree with the assumption of an increase in *s*-orbital contribution for the P–H bond due to the more electronegative oxygen substituents at the phosphorus atom. Single crystals of the complexes **6f,i** were obtained from saturated *n*-pentane solutions at −30 °C and the molecular structure in the crystal lattice was obtained via X-ray diffraction. Single crystals of **6k** were obtained from an Et_2O solution at −30 °C. However, the result of the measurement showed a 76:24 mixture of **5k** and **6k** in the crystal structure. As the NMR spectra of the used solution of **6k** appeared to be clean, **5k** was synthesised

Table 5: ^{31}P-NMR chemical shifts along scalar coupling constants and the chemical shift of the P–H hydrogen atom in the ^1H-NMR spectrum of **6d-f,i,k** and **5k**. *taken from Ref.[96] **taken from Ref.[64]

	6d*	6e**	6f	6i	6k	5k
$\delta(^{31}P)$ / ppm	−13.6	99.4	78.7	121.0	146.3	146.7
$^1J_{W,P}$ / Hz	231	289	295	305	325	412
$^1J_{P,H}$ / Hz	345	290	273	231	350	—
$\delta(^1H; P–H)$ / ppm	6.83	7.10	7.70	7.71	8.49	—
$^2J_{W,H}$ / Hz	—	17.1	17.4	18.4	22.0	—

to probe for its presence. Therefore, **3k** was reacted with [W(NCMe)(CO)$_5$] in THF and a ^{31}P{^{1}H}-NMR spectrum of the reaction mixture was recorded revealing conversion to **5k** with a chemical shift of 146.7 ppm. Indeed, the chemical shift of **5k** and **6k** are close to isochronic. Repeating the reaction of **3k** with [NEt$_4$][W(CO)$_5$H] to **6k** yielded a pure sample from, which single crystals of **6k** could be grown. The single crystals were analysed by X-ray diffraction and the molecular structure in the crystal was obtained (Figure 16). In general bond lengths are found to be in the expected range compared to reported **6d** and **6e**. However, a clear trend is found for the P–W bond as it is slightly shortened going from **6f** to **6k** (Table 6). If the differences in the P–W bond of **6e** and **6f** are considered, this effect might be due to repulsive forces, as the more sterically demanding ^{i}Pr substituent at the nitrogen atoms forced this deformation. This would be in line with the observation that the bond lengths observed for **6e** and **6i** are similar, despite the differences in the electronic environment of the P-atom. Corroborating the choice of the ^{i}Pr substituent in **6f** as it was selected with the background of observing differences induced by the steric effects. Other bond lengths, like the P–N and P–O bond, are comparable. A deviating pyramidalization of the P-atom, like for **1i** (Table 4) is not observed for the here discussed complexes. However,
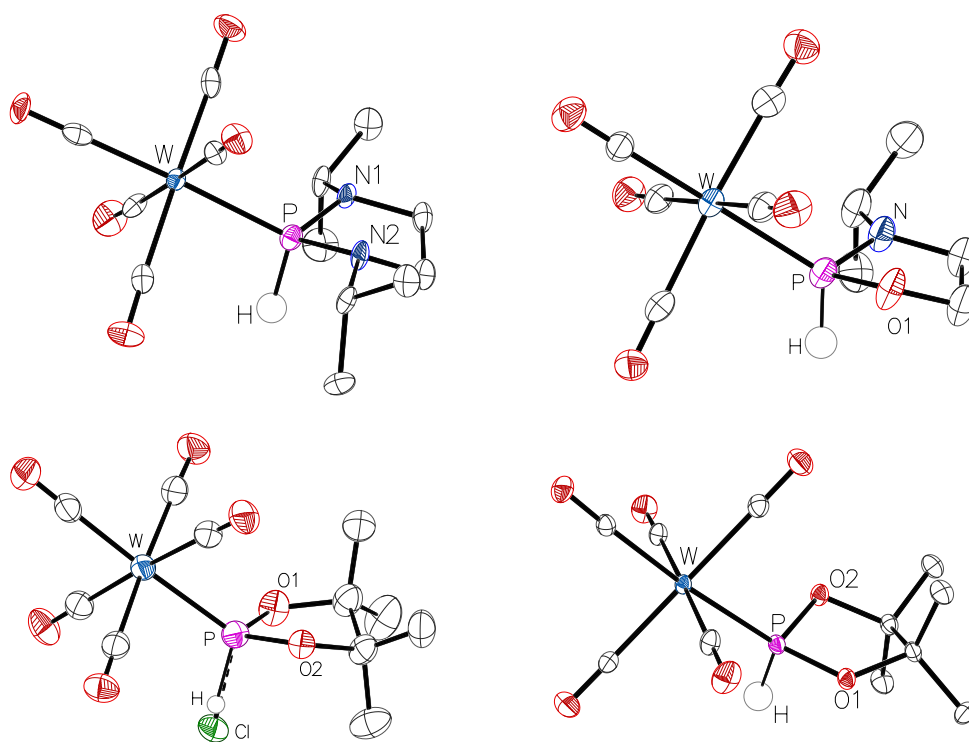
Figure 16: Molecular structure of **6f** (top left), **6i** (top right) and **6k** (bottom left: mixed with 24% **5k**; bottom right: pure **6k**) in the crystal structure; ellipsoids are set at 50% probability level and all hydrogen atoms are omitted for clarity besides directly bound to phosphorus.

Table 6: Selected bond lengths in Å and angle sums in ° of the secondary phosphane $W(CO)_5$ complexes **6d-f,i,k** in the crystal structures obtained by X-ray diffraction. *taken from Ref.[54] **taken from Ref.[64]

	6d*	6e**	6f	6i	6k
d(W–P)	2.5076(4)	2.447(11)	2.46109(10)	2.4452(4)	2.42599(10)
d(P–N)	—	1.68(4)(N1) 1.68(4)(N2)	1.67252(7)(N1) 1.68675(9)(N2)	1.6658(3)	—
d(P–O)	—	—	—	1.6127(2)	1.61360(6)(O1) 1.62172(6)(O2)
$\sum_{\angle}^{P}$	304.8	291.0	305.6	289.9	298.9
$\sum_{\angle}^{N}$	—	352.9(N1) 348.0(N2)	350.1(N1) 345.0(N2)	—	—

the angle sum of **6i** is close to its phosphinoyl derivative **1i**, corroborating the assignment of the phosphane character observed and discussed previously for **1h,i**.

4.5. Synthesis of *P*-OTEMP 1,3,2-diheterophospholane complexes

The successful isolation of the 1,3,2-diheterophospholane complexes **6f,i,k** allowed to conduct further investigations of the formation of the aminoxylphosphane complexes **8f,i,k** and their stability. Heurich and Nesterov described several synthetic routes to access such complexes (cf.Scheme 9, p.9).[58,63] Therefore and firstly, the reaction of **6f** with ⁿBuLi and subsequent reaction with the oxoammonium salt [**2**]BF₄ was investigated (Scheme 18). As the lifetime of the methyl derivative of the 1,3,2-diazaphospholidine complex **8e** was ca. 24 h, the reaction of **6f** was followed via VT-^{31}P{^{1}H}-NMR spectroscopy to detect any temperature sensitive species. After addition of ⁿBuLi at −80 °C, the reaction was allowed to stir for 10 minutes before [**2**]BF₄ was added to the solution. Immediately afterwards the NMR spectra were recorded from −80 °C to r.t. with an increment of 10 °C. At that temperature
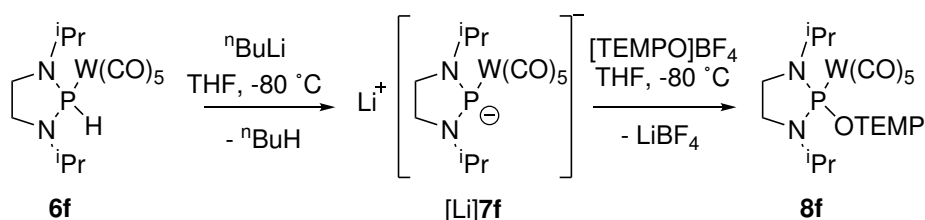
Scheme 18: Attempted synthesis of **8f** via a combination of deprotonation of **6f** with subsequent oxidation of [Li]**7f**.

no selective conversion was observed and only minor signals occurred low field shifted from the starting material. This is in strong contrast to the reports of Heurich about the formation of **8e**, for which he reported a 56% conversion to the product via this route.[66] Upon heating up to room temperature no change was observed, therefore the initial step, the deprotonation by ^{n}BuLi, was investigated. The reaction was repeated without the addition of the [**2**]BF$_4$ salt and followed again by VT-^{31}P{^{1}H}-NMR spectroscopy. A resonance was observed at low temperatures with a chemical shift of 96 ppm which was stable when the reaction mixture had reached room temperature. The resonance showed satellites of a $^1J_{W,P}$ coupling of 289 Hz which is uncommon for phosphanido complexes like [Li]**7f**; normally, coupling constants around 100 Hz are found. The absence of a phosphanido complex was corroborated by the presence of a $^1J_{P,H}$ coupling of 266 Hz in the ^{31}P-NMR spectrum measured at room temperature. To quench a possibly formed anion, methyliodide was added to the reaction mixture but no change was observed in the ^{31}P-NMR spectrum. Hence, **8f** cannot be accessed by this route which had worked for the previously reported aminoxylphosphane tungsten complexes and even in case of the highly reactive cymantren complex **XXVII**. This observation can be explained by the higher hydridic character of the hydrogen atom bound to phosphorus as reported by Gudat et al. for 1,3,2-diazaphospholes. The latter, even react with triflic acid (HOSO$_2$CF$_3$) under dihydrogen formation.[97] Similar effects might be present in the herein reported 1,3,2-diazaphospholidine tungsten complex. As this route was not feasible to access aminoxylphosphane complexes **8** and alternative protocol was used and hence the reaction with two equivalents of TEMPO was tested, already explored by Heurich before (cf. Scheme 9, p.9). The reaction of 1,3,2-diazaphospholidine complex **6f** with two equivalents of TEMPO (Scheme 19) in THF at room temperature yielded a product mixture, with at least five different phosphorus species. The major product showed a very broad resonance at 141.9 ppm and besides small signals at 112.6 and 79.7 ppm, two highfield-shifted resonances at 31.8 and 26.3 ppm. After stirring overnight no resonance besides the highfield-signals were observed. Since the N,N'-dimethyl derivative **8e** was not stable at room temperature for longer than a day, the reaction of **6f** with TEMPO was repeated at 0 °C. Under these conditions the desired *P*-OTEMP complex **8f** was formed selectively and obtained as a bright yellow, temperature sensitive powder after low temperature (−20°C)

6f,i,k **9f,i,k** **8f,i,k**
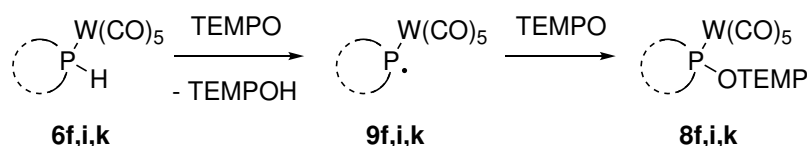
Scheme 19: Synthesis of aminoxylphosphane complexes **8f,i,k** via HAT of **6f,i,k** and subsequent heterocoupling of phosphanyl complex **9f,i,k** with TEMPO.

Table 7: ^{31}P-NMR chemical shifts along scalar $^1J_{W,P}$ coupling constants of complexes **8d-f,i,k**. *taken from Ref.[63] **taken from Ref.[64] *** not detect due to broadness of the signal.

	8d*	8e**	8f	8i	8k
$\delta(^{31}P)$ / ppm	137.9	131.7	142.0	151.0	146.3
$^1J_{W,P}$ / Hz	286.7	341.6	—***	367.0	389.0

column chromatography under argon atmosphere. ^{31}P{^{1}H}-NMR experiments at low temperature showed a broad resonance with a chemical shift of 142 ppm (Table 7), thus underlining the successful formation in the previous attempt at room temperature and the thermal instability of the compound. This chemical shift is slightly shifted to lower fields in comparison to the resonance of the methyl derivative **8e**. Due to the broadness of the signal no ^{183}W satellites could be observed. The molecular structure in the crystal (Figure 17) was obtained via X-ray diffraction analysis of single crystals grown from *n*-pentane solutions.

The P–W bond is elongated to 2.53349(4) Å compared to the secondary phosphane precursor (Table 8). The angle sum around phosphorus is slightly smaller than in **6f**. This stands in contrast to the situation in the *N*-methyl derivative from Heurich **8e**, in which the angular sum is increasing from 291 to 312° upon TEMPO substitution. And while in **6e** and **6f**, both nitrogen atoms in the 1,3,2-diazaphospholidine moiety are almost planar, smaller values for the pyramidalization are found on **8f**. These observations already suggest that the increased steric bulk in **6f** has a significant effect on the bonding and on the electronic situation. It can be assumed that due to the sterically increase the TEMP moiety might be bound weaker than in **8e**, which might be contributing to the lower thermal stability. Since the P–O is longer and the N–O bond is shorter than in **8e**, it appears that the TEMPO unit is slightly weaker bound in **8f**. The N–O distance in the complexes is slightly longer than for TEMPO–H (1.45 Å). The dihedral angle between the N–O and the P–W bond is −8.4°, this is in line with the angle observed for the **8d** derivative of −15.8°. However, for the **8e** derivative an angle of −165.3° is found as the TEMPO moiety is rotated away from the W(CO)$_5$ group in this case. This might also explain the different W-P-O angle of **8f** (121.2°) compared to its methyl derivative **8e** (102.2°), as the W-P-O angle and N-O-P-W dihedral angle (−8.4°) of **8f** aligns with the structural motif of **8d** (W-P-O: 121.7°; N-O-P-W: −15.8°). To get access to the aminoxylphosphane complex **8i**, complex **6i** was reacted with two equivalents of TEMPO at 0 °C to prevent unwanted decomposition. Monitoring the reaction, it became apparent that the reaction progress was very slow, however with high selectivity. If the reaction was carried out at room temperature the reaction time was reduced to 2.5 hours. Surprisingly no decomposition of **8i** was observed under these conditions. **8i** resonated in the ^{31}P{^{1}H}-NMR spectrum at 151 ppm as a singlet with a $^1J_{W,P}$
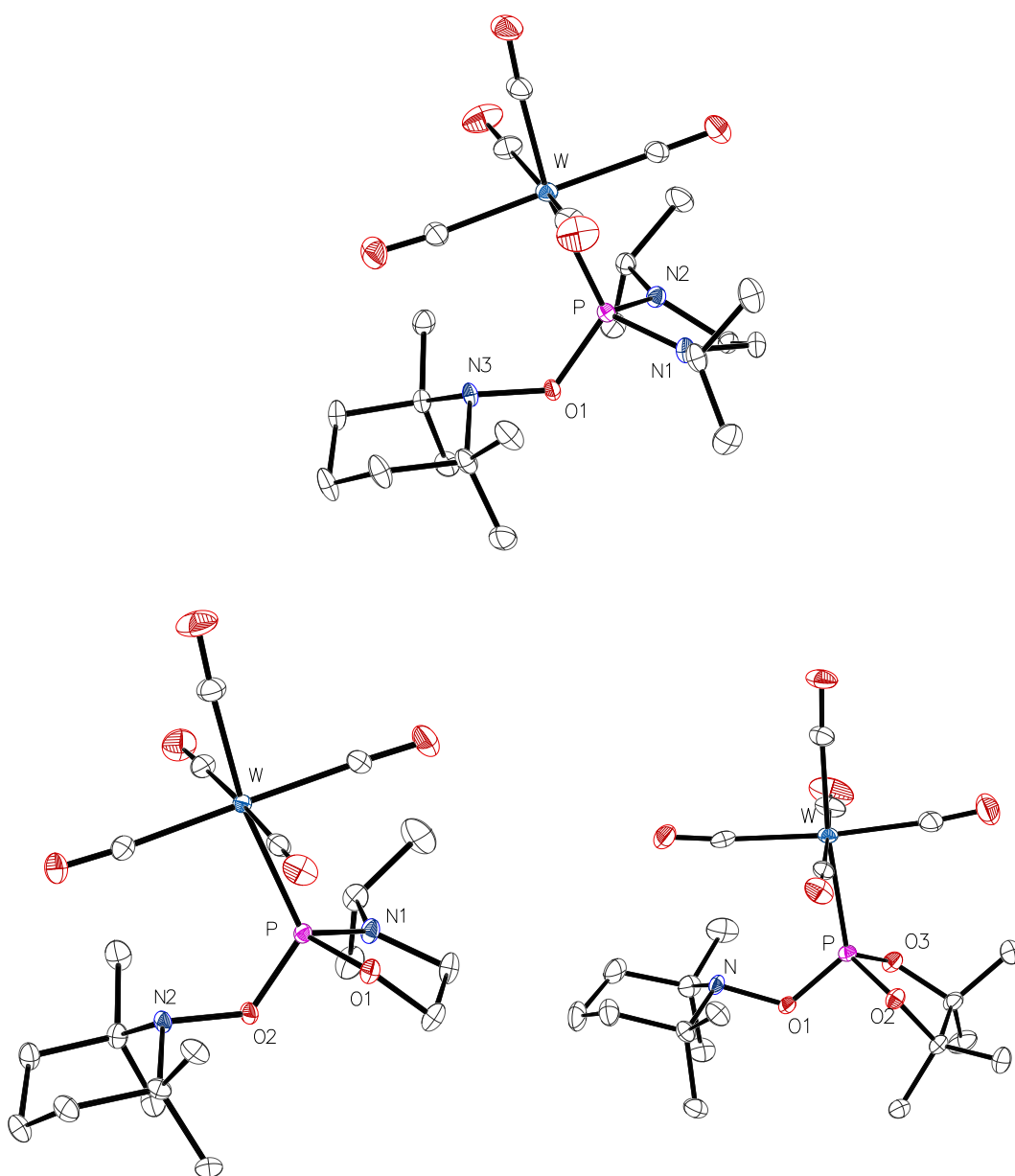
Figure 17: Molecular structure of **8f** (top), **8i** (bottom, left) and **8k** (bottom, right) in the crystal structure; ellipsoids are set at 50% probability level, all hydrogen atoms are omitted for clarity.

coupling of 367 Hz. The $\Delta\delta$(**6i, 8i**) of 30 ppm is much smaller as observed for **8f** ($\Delta\delta$(**6f, 8f**) = 60 ppm). From a saturated *n*-pentane solution single crystals of **8i** were grown and the molecular structure was obtained by X-ray diffraction analysis. No significant deviation from the previously known complexes **8e,f** is observed. However, the P–W bond length of 2.46286(8) Å is shorter and the P–O bond slightly shorter than for **8f** (Table 8). The N–O bond of the aminoxyl moiety is in the same range as for **8f**. The change of bond lengths

Table 8: Selected bond lengths in Å and angle sums in ° of the aminoxylphosphane $W(CO)_5$ complexes **8d-f,i,k** measured in the crystal structures obtained by X-ray diffraction. The $\sum_{\angle}^{N}$ are given only for N-atoms in the 1,3,2-diheterophospholane ring. *from Ref[50] **from Ref[64]

	8d*	8e**	8f	8i	8k
$d(P\text{-}O^{exo})$	1.6392(16)	1.6481(18)	1.65949(5)	1.63311(6)	1.6203(18)
$d(W\text{–}P)$	2.5194(6)	2.5010(7)	2.53349(4)	2.46286(8)	2.4713(6)
$d(N\text{–}O^{exo})$	1.482(3)	1.495(3)	1.47689(3)	1.47353(6)	1.463(2)
$\angle(W\text{-}P\text{-}O)$	121.7	102.2	121.2	124.2	123.7
$\sum_{\angle}^{P}$	299.1	312.1	298.8	296.6	297.3
$\sum_{\angle}^{N}$	—	358.8(N1) 360.0(N2)	357.3(N1) 355.3(N2)	360.0	—

does not affect the angle sum around the phosphorus atom, which is similar as for **8d** and **8f**. The dihedral angle N-O-P-W is $-17.3°$ and tilted away from the ^{i}Pr group at the endocyclic nitrogen atom and towards O2. The N2 atom is planar coordinated with an angular sum of $\sum_{\angle}^{N} = 360°$.

The reaction of 1,3,2-dioxaphospholane complex **6k** with TEMPO did not proceed at 0 °C, and even at room temperature the reaction was slow, thus following the already observed trend in reactivity. After several days full conversion to **8k** was still not achieved and remaining **6k** and an unknown impurity with a ^{31}P-chemical shift of 134 ppm and a $^{1}J_{W,P}$ coupling of 390 Hz was observed. Filtration through Al_2O_3 at $-20°C$ allowed the separation from the starting material. Noteworthy, during the extended reaction time and work-up no sign of decomposition was found. Complex **8k** was assigned to the signal in the $^{31}P\{^{1}H\}$-NMR spectrum with a chemical shift of 162 ppm and a $^{1}J_{W,P}$ coupling of 389 Hz. The shift to lower fields and the increase in the scalar coupling between tungsten and phosphorus is fitting to the trend already observed for **8f** and **8i**. The formation of **8k** was corroborated via X-ray diffraction analysis of single crystals, grown from the Et_2O filtrate (Figure 17). The distance between the W- and P-atom is 2.4713(6) Å, which is slightly longer than for **6k**, but still significantly shorter than for **8f,i**. In comparison to all other aminoxylphosphane complexes the P–O bond lengths is the shortest being 1.6203(18) Å. Furthermore, the shortest N–O bond is also found in **8k** with a value of 1.463(2) Å. This can be explained by the lack of steric repulsion around the P-atom when compared to the nitrogen containing 1,3,2-diheterophospholane complexes **8e,f,i**. This is also in line with the observation that the N-O-P-W plane deviates only by a dihedral angle of $-1.4°$ from planarity. Despite the lack of steric bulk and the high oxygen content the pyramidalization of the phosphorus atom ($\sum_{\angle}^{P} = 297°$) is almost unchanged compared to **8f** and **8i**.

4.6. NMR investigation on the thermal stability of complex 8i

The significantly enhanced thermal stability of **8i** in comparison to **8f** was investigated by various temperature (VT)-NMR spectroscopic experiments. A toluene-$d8$ solution of **8i** was heated from room temperature to 30 °C and then to 100 °C with a 10 °C increment. The VT-^{31}P{^{1}H}-NMR experiment (Figure 18) showed no resonance besides of **8i** throughout the temperature regime of 30 to 80 °C. However, a small decrease of the signal to noise ratio was observed for higher temperatures. At 90 °C the signal of **8i** had disappeared, without the appearance of another resonance. More details could be obtained from the VT-^{1}H-NMR spectrum (Figure 19). Here, already at 50 °C a decrease of the CH$_2$ resonances of the TEMPO moiety was observed, accompanied by a slight low field shift of the *N-^{i}Pr* group and the C$_2$H$_4$ backbone hydrogen atoms of the 1,3,2-oxazaphospholidine moiety. At 70 °C no multiplicity can be assigned to the signals due to the decreased resolution. In agreement with the results of the ^{31}P{^{1}H}-NMR spectrum at 90 °C all resonances belonging to **8i** are
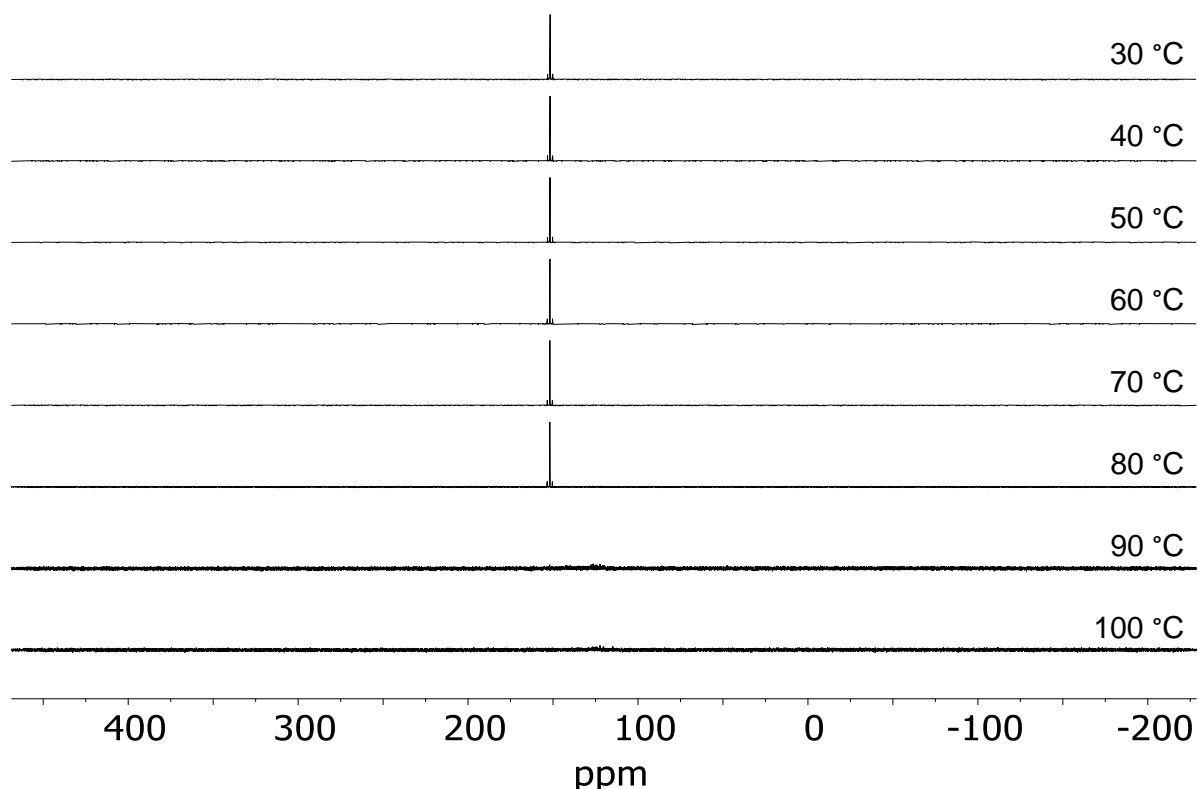
Figure 18: VT-^{31}P{^{1}H}-NMR spectra of the thermolysis of **8i** from 30 °C to 100 °C with an increment of 10 °C in toluene-$d8$.
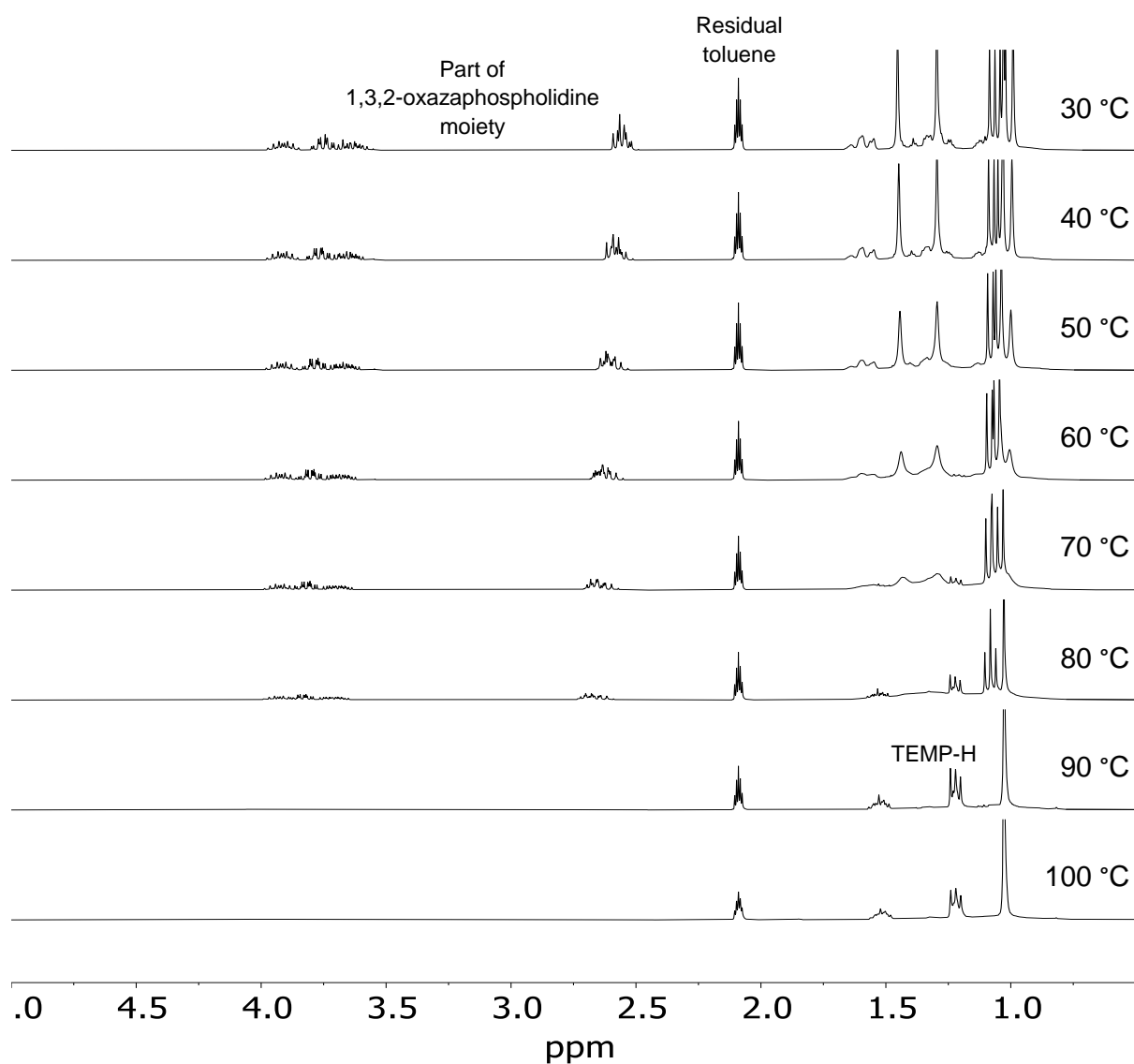
Figure 19: VT-^{1}H-NMR spectra of the thermolysis of **8i** from 30 °C to 100 °C with an increment of 10 °C in toluene-*d*8.

bleached. However, the reminiscent signals can be clearly assigned to the secondary amine TEMP–H. The presence of this amine was also found previously for the diphenyl derivative **8d** (previously also **XIX**) and clearly connected to the formation of a transient phosphanoxyl complex **XX**.[66] Remarkably, no detectable decomposition product of such a species could be observed in this case. A detailed look at the initial NMR spectrum at room temperature already shows traces of the amine pointing to a slow decomposition, already occurring at ambient temperatures. No analytical data could be obtained for the 1,3,2-dioxaphospholane complex **8k** as it could not be separated from the impurity. However, it can be assumed that the thermal stability of **8k** is similar or even higher than that of **8i**, especially as the N–O

bond stabilisation appears to be connected to the presence of oxygen in the five-membered ring.

4.7. DFT analysis of the formation of aminoxylphosphane complexes

4.7.1. Structural and electronic analysis of phosphanyl complexes

To further understand the differences in the formation and the thermal stability of these new *P*-aminoxyl complexes **8** theoretical insight was gained from DFT calculations. Initial calculations focused on the hydrogen abstraction or hydrogen atom transfer (HAT) from the secondary phosphane complexes to TEMPO (**2a**). For this the phosphane complexes **6f,i,k**, their related phosphanyl complexes **9f,i,k** (cf. Scheme 19, p.32) and **2a** as well as TEMPO–H **2a-H** were computed. Qualitatively the calculated structures of the phosphane complexes **6** fit to the ones experimentally observed in the crystal structure. The P–W bond lengths obtained theoretically are longer but a shortening is also observed for higher oxygen content in the ring, in agreement to the experimental trend. The diphenyl derivative **6d** has the longest P–W distance which fits the experimental data. Pyramidalisation angles around the phosphorus atom are in line with the exception of **6d** deviating by 9° towards planarity from the experimentally observed value. For the nitrogen atom in **6i** the angle sum fits to the experiment. The 1,3,2-diazaphospholidine systems, however, adopt in theory a structure with one almost planar nitrogen atom (∼353°) and one with significantly lesser planarity (**6e**: 339°; **6f**: 329°). This deviation might be explained by the superposition of several different configurations, resembling the structure obtained from theory, in the crystal lattice averaging to the experimentally observed values. Structural comparison of the computed phosphanyl complexes proofed to be difficult, as these species are usually highly reactive. Besides the matrix isolated and analysed M(CO)$_5$(PPh$_2$) (M = Cr, Mo, W (**9d**))[98] only recently a stable osmium complex **XXXV** (Figure 20) was described by Bas de Bruin

XXXV **9d**

Figure 20: Lewis structures of the phosphanyl complexes from Bas de Bruin **XXXV**[55] and Geoffroy **9d**.[98] Mes* = 2,4,6-Tris(tertbutyl)phenyl.
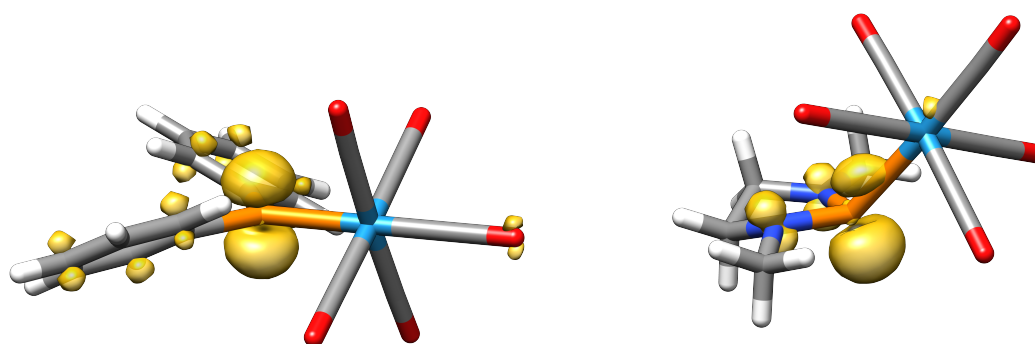
Figure 21: Optimised molecular structure of **9d** (left) and **9e** (right) and the spin density distribution (yellow, isovalue 0.009).

and Schneider.[55] The angle sum found around the P-atom, bearing a hydrogen and Mes* substituent in the osmium complex is 360°, the same angle was found for the calculated structure of the diphenylphosphanyl tungsten complex **9d**. Planarity for $W(CO)_5(PPh_2)$ (**9d**) was already shown by Geoffroy, also by theory and supported by EPR findings.[98] The introduction of heteroatoms as P-substituents leads to deviation from the observed planarity with pyramidalization angles around ∼332° (Figure 21), acyclic heteroatom-containing systems show the same result. In addition, all phosphanyl complexes **9f,i,k** show longer P–W distances than in their secondary phosphane complex precursors **6f,i,k** while for the planar diphenyl derivative **6d** the bond length is found to be shorter. Loewdin spin density distribution analysis shows large contributions on the P-atom, which is ranging from 47% for **9d** to 53% for **9e** and then increasing for higher oxygen content up to 61% in **9k**. Adjacent heteroatoms on the phosphorus make up for 18 to 24% spin density, being highest for the 1,3,2-diazaphospholidinyl systems **9e,f**. The spin density found on the tungsten atom is almost unaltered for the studied systems and the values are around 10%. These findings are well represented by the *h*-SOMOs and the LUMOs. The symmetry of the *h*-SOMOs fit to the spin density distributions, from which the assignment can be made that the unpaired electron resides in the *h*-SOMO for all cases. The molecular orbitals are qualitatively the same for the planar **9d** and the bent heteroatom substituted phosphanyl complexes. Deviation from planarity was already observed in theoretical studies of the highly reactive chlorophosphanyl tungsten complex **XV** (334.2°) bearing the pentamethylcyclopentadienyl (*Cp**) substituent. In the same publication an angle sum of 358.8°was calculated for the bisyl substituted chlorophosphanyl tungsten complex **XV**.[56] These findings were previously not discussed in more detail.

An initial explanation for the deviation from planarity may come from Bent's rule,[99] for which more electronegative substituents favour more p-orbital contribution in the bond making,

thus leading to a more hybridised situation at the phosphorus atom and, hence, pyramidalization. However, this would lead to more s-character for the h-SOMO, in which the unpaired electron is found. From Loewdin reduced spin population analysis it can be seen, that the s-orbital on phosphorus is not more involved for the bent than for the planar situation. Surprisingly, instead the d-orbital contribution is increased to ∼9% for all bent compounds. This might just be an effect of the polarised basis sets (def2-TZVP and def2-QZVPP), and was therefore tested by using a minimal basis set (SV; for the tungsten atom def2-SVP was chosen). However, the lack of d-orbital contribution in the minimal basis set was not compensated with an increase of the s-orbital contribution for the spin population. The significant localisation of the radical in the h-SOMO makes Loewdin orbital population analysis for this MO feasible. The contribution from the phosphorus atom to the h-SOMO for **9d** and **9e** were almost exclusively from p-orbitals, agreeing with the found spin population analysis. And while **9e** utilises some phosphorus s-orbitals, the amount of 1% is negligible and thus not the reason for the pyramidalization. Hence, the bending can not be deduced from the composition of the general orbital shape of the P-atom.

Therefore, the effect of the adjacent atoms on the phosphorus was investigated in more detail by additional calculations of several different P-substitution pattern (Table 9). The parent phosphanyl tungsten complex H_2P-WCO_5 **9m** shows a $\sum_{\angle}^P$ of 343.3°, which almost falls exactly in the middle of planar **9d** and the other 1,3,2-heterodiphospholane complexes investigated in this study. P-alkyl substitution, $e.g.$, dimethylphosphanyl shows almost no change compared to the parent system. The more electronegative CF_3 group causes more pyramidalization of the P-atom. Other electron rich, electronegative substituents like NMe_2, O^iPr and Cl results also in even smaller angle sums, most extreme for O^iPr with 333.1°. All acyclic systems have slightly larger sums than the beforementioned cyclic derivatives, $e.g.$, **9e,f,i,k**, which is to be expected due to the present ring strain. Surprisingly, planarity is only

Table 9: Angle sums around the phosphorus atom in phosphanyl $W(CO)_5$ complexes depending on various substituents R.

R	H	Me	CF$_3$	Ph	Ph(CF$_3$)$_2$	NMe$_2$	O^{i}Pr	Cl
H	343.3	—	—	353.4	354.0	—	—	—
Me		345.0	—	354.2	—	—	—	—
CF$_3$			339.8	—	—	—	—	—
Ph				360.0	—	340.9	—	349.3
Ph(CF$_3$)$_2$					360.0	353.0	—	—
NMe$_2$						337.6	—	343.4
O^{i}Pr							333.1	—
Cl								337.1

observed for the phenyl substituted systems. To explore the strength of this effect, mixed systems were calculated. The results show that substitution of any group investigated in this study by a phenyl group forces the angle sum to increase. This effect is even larger for the 3,5-$(CF_3)_2$-phenyl group, which has an increased σ- and π-acidity compared to the unsubstituted phenyl moiety. Indeed, the dimethylamino(phenyl) and 3,5-$(CF_3)_2$-phenyl P-angular sum differ by $\sim 12°$. As the electronegative alkyl CF_3 group causes the invers effect of the phenyl substituents it can be assumed that the origin of the effect can be found in π-type orbital interaction, rather than being of σ-type.

Hence, frontier molecular analysis was performed for which $(Me_2N)_2P$, Ph_2P and the parent PH_2 complexes **9n,d,m** were chosen as representatives. The complexes were fragmented in the phosphanyl radicals **10n,d,m** (Figure 22) and the $W(CO)_5$ moiety. Some of these fragments (and derivatives) were previously calculated, however, the level of theory was not satisfactory and therefore these fragments were recomputed herein.[100,101] The *h*-SOMO for all three phosphanyl fragments **10n,d,m** is derived from the $p_z(P)$-orbital, either in pure form for the parent PH_2 **10m** or split into π and $\pi*$ molecular orbitals together with orbitals from the adjacent C- or N-atoms. The electron rich diamino phosphanyl **10n** shows a huge splitting by 4.0 eV, while the phenyl substituents **10d** lead to a splitting of only 3.0 eV.
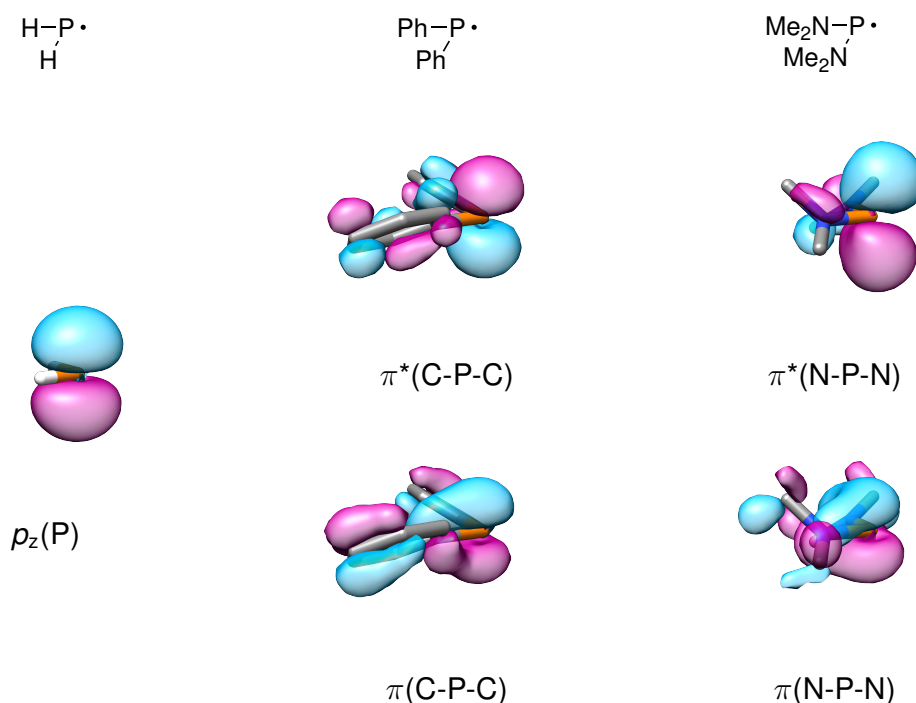
Figure 22: π-symmetric FMO of the phosphanyl fragments PH_2 **10m** (left), PPh_2 **10d** (middle) and $(Me_2N)_2P$ **10n** (right).

The *h*-SOMOs represent the spin density distribution of these fragments very well and can therefore clearly be assigned to the orbitals in which the unpaired electron resides. Their frontier molecular orbitals (FMOs) were then compared to the FMOs of the complexes (Figure 23). In the planar Ph_2P-$W(CO)_5$ **9d** the overlap of the π^*(C-P-C) orbital yields a typical antibonding π^*[(C-P-C)-W] orbital and the bonding π[(C-P-C)-W] counterpart. The slightly bent geometry in H_2P-$W(CO)_5$ **9m** does not allow perfect overlap as in the planar environment of the diphenyl derivative **9d**, qualitatively however, the bonds are similar and can be clearly assigned to an antibonding and bonding π-orbital. In the even more bent bis(dimethylamino)phosphanyl complex **9n** the π[(N-P-N)-W] is only a remnant of the π-bond found for the diphenylphosphanyl complex **9d**. Energetically almost no stabilisation is gained compared to the fragment of the d_z(W) orbital. Remarkably, the bending leads to an overlap of the π^*(N-P-N) orbital with the d_z(W)-orbital, which is of σ-symmetry, and stabilises the otherwise very high lying π^*(N-P-N) significantly.

Similar observations for a 1,3,2-diazaphospholidenium (NHP) group 10 metal complexes were made recently by the group of Thomas.[85, 102] These systems can be compared as the cationic form of the phosphanyl complexes, in which the σ[(N-P-N)-W] orbital is not occupied. To answer the question why the unusual bonding is preferred for electron rich substituents, the not preferred structures of the complexes, planar instead of bent and vice versa (marked with a ') were calculated (Figure 23). Qualitatively the orbitals do not deviate from the situation previously discussed, showing the σ[(N-P-N)-W] type bonding for Ph_2P-$W(CO)_5$ **9d'** and the classical π-bond for the $(Me_2N)_2P$ and H_2P complexes **9n',m'**. While the MO-diagram is almost identical for the parent complex **9m'**, less stabilisation is gained for the π^*[(N-P-N)-W] of the bis(dimethylamino)phosphanyl complex **9n'**, because of its antibonding nature. The π[(N-P-N)-W] of this complex, however, is almost unaffected compared to the bent configuration. The stabilisation of this orbital compared to the individual fragments can be explained by the unfavourable backbonding to the already electron-rich phosphanyl ligand. For the bent configuration isomer of the diphenyl phosphanyl complex **9d'** the π[(C-P-C)-W] is almost unaltered in energy compared to the planar compound. The σ[(N-P-N)-W] is slightly lower in energy than the π^*(C-P-C). In all cases the stabilisation of the π(E-P-E) is almost unaffected by the change of configuration. To evaluate the overall energy gain the absolute energies were compared. In the case of the H_2P-$W(CO)_5$ **9m** the energy difference between bent and planar is only 0.7 kcal mol^{-1}, the diphenyl derivative **9d** has a difference of 1.8 kcal mol^{-1}. For the diaminophosphanyl complex **9n** the bent isomer is energetically favoured by 4.5 kcal mol^{-1}. These values are all rather small and explain why only for **9n** a clear stabilisation can be taken from the MO diagram. It can be
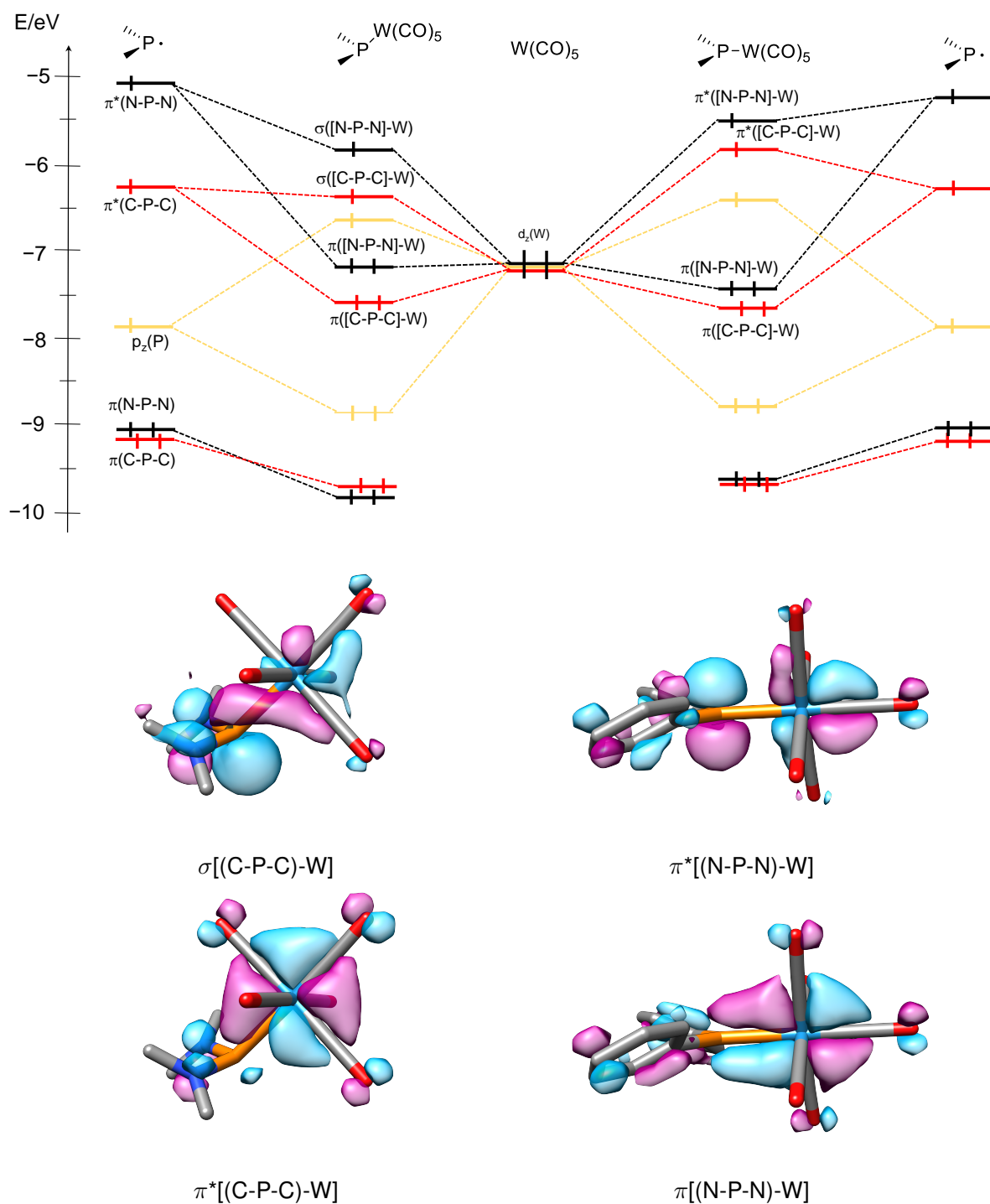
Figure 23: Frontier molecular orbital energy diagram of bent (left) and planar (right) phosphanyl W(CO)$_5$ complexes of PH$_2$ **9m** (yellow), (Me$_2$N)$_2$P **9n** (black), Ph$_2$P **9d** (red) and their related fragments (top). Plotted FMOs resulting from combination of fragment π*-orbital with d_z-(W) as examples for the bent **9n** and planar environment **9d** (bottom).

assumed, that all of these complexes are very flexible in solution under ambient conditions and that their adopted conformation has no significant impact on their reactivity.

4.7.2. Analysis of the formation pathway of *P*-aminoxyl complexes

The formation of all experimentally studied phosphanyl complexes **9f,i,k** is endergonic (Figure 24). HAT from the diphenyl system **6d** is energetically uphill with an increase by Δ_rG of 11.5 kcal mol^{-1}, while the energies for the N containing systems **6f** and **6i** are 7.3 and 6.0 kcal mol^{-1} respectively and slightly higher for the derivative **6e** (8.0 kcal mol^{-1}). 1,3,2-Dioxaphospholan complex **6k** shows the highest Δ_rG being 13.3 kcal mol^{-1}. These values can be related to the homolytic bond dissociation free Gibbs energy (BDG) of the P–H bond (cf. later chapter, Figure 65, p.99). The high BDG of 78 kcal mol^{-1} obtained for the HAT of **6k** could already be part of the difficult formation of the aminoxylphosphane complex **8k**. However, this does not explain the increased temperature needed for the
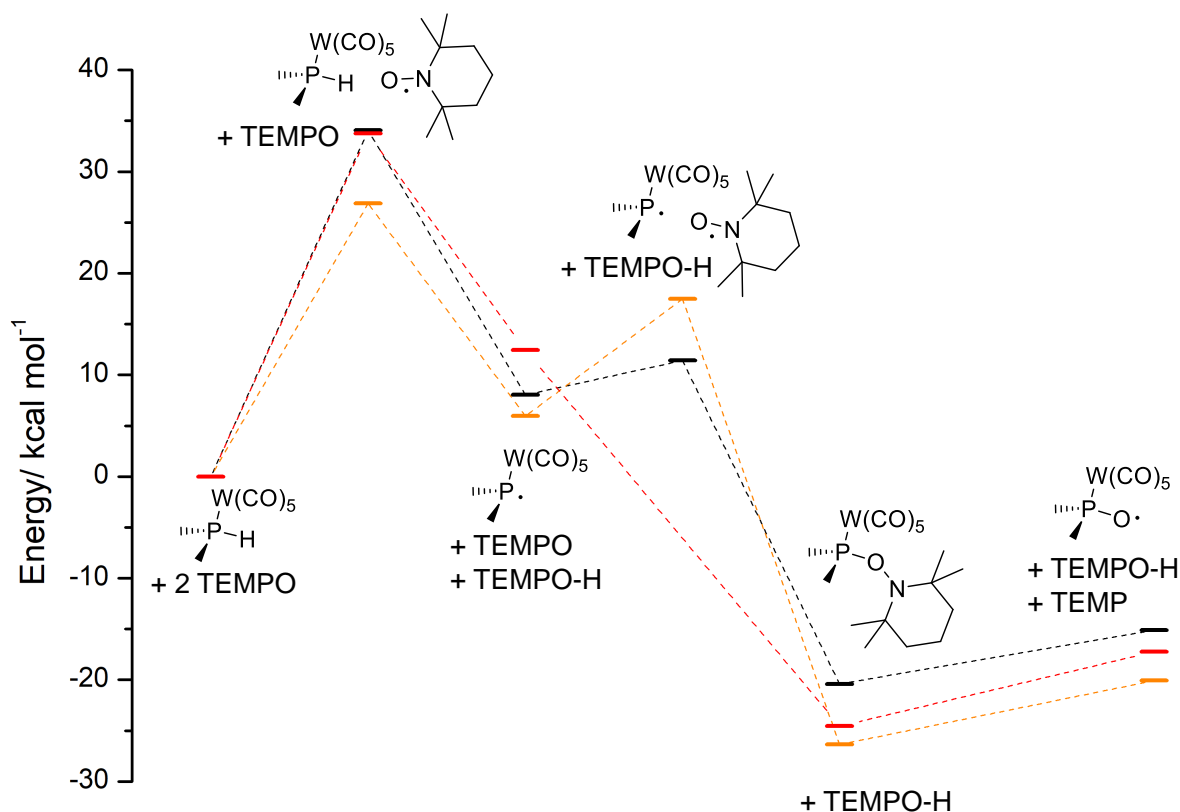
Figure 24: Reaction profile for the formation of phosphanoxyl complexes from the reaction of secondary phosphane complexes **6f** (black), **6i** (orange), **6k** (red) with TEMPO.
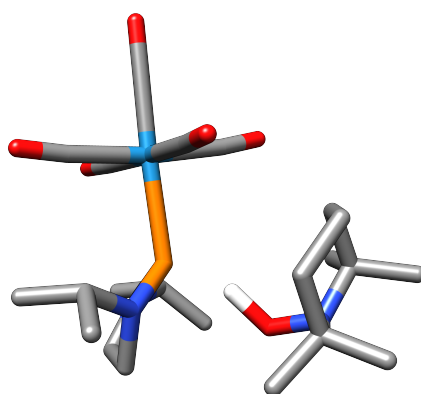
Figure 25: Structure at the transition state (with selected structural parameters) of the HAT from diazapospholidinyl complex **6f** to TEMPO, representative for the HAT for **6i,k**. Selected bond length and angles of **6f** in Å and °, respectively: d(P–W) 2.5703, d(P–H) 1.7352, d(N–O) 1.3684, $\sum_{\angle}^{P}$ 319.2, $\sum_{\angle}^{N}$ 344.7.

conversion from **6i** to **8i**, since the BDG of **8i** is the lowest (70.7 kcal mol^{-1}) for the three studied complexes. Therefore, the transition states of the HAT (Figure 25) were determined, thus yielding the energy of the kinetic barriers. The structures at the transition states fits in between the structures of complex **6f,i,k** and the phosphanyl **9f,i,k**. The results, again, partially contradict the experimentally observed behaviour as the barrier is lowest for the 1,3,2-oxazaphospholidine complex **6i**, then for **6f** and highest for **6k**, 26.9, 33.4 and 34.8 kcal mol^{-1}, respectively. The latter being in good agreement with the observed slow formation of **8k**. To solve the contradiction the second step in the reaction, the homo-coupling of the phosphanyl complexes **9** with TEMPO was computed. The final formation of the aminoxyl-substituted phosphane complexes is exergonic (**8f**: −20.4; **8i**: −26.4; **8k**: −24.5 kcal mol^{-1}). Transition states were only found for **9f** and **9i** (Figure 26), presumably because of the steric repulsion arising from the *N*-substituents, while the dioxaphospholanyl complex **9k** reacts without a barrier to the aminoxylphosphane complex **8k**. The calculated two transition states do not display the same connectivity to the TEMPO unit. The P-atom in the structure at the transition state of **9i** is found over the N–O bond with a P–N distance of 1.986 Å and a P–O distance of 2.163 Å. In the structure at the transition state of **9f** and TEMPO, no close connection between the phosphorus atom and the TEMPO moiety is formed yet (d(P–O) = 2.413 Å). However, the TEMPO is bound via the oxygen atom to one of carbonyl ligands (d(C–O) = 1.662 Å), resulting in the bending of the CO ligand. Remarkably, the angle sum around phosphorus is 356° deviating strongly from the situation discussed for the phosphanyl complex **9f**. The energy barriers for the heterocoupling reaction of **9f** and **9i** are found to be 11.4 and 17.5 kcal mol^{-1}. For the 1,3,2-diazaphospholidine

complex this barrier is only 3.4 kcal mol^{-1} higher in energy than the phosphanyl complex intermediate **9f**. The relative barrier from the 1,3,2-oxazaphospholidine intermediate **9i** to aminoxylphosphane complex **8i** is 9.5 kcal mol^{-1}, isolating the intermediate **9i** energetically between the two transition states, while **9f** easily reacts further to **8f**, explaining the faster proceeding reaction observed experimentally.
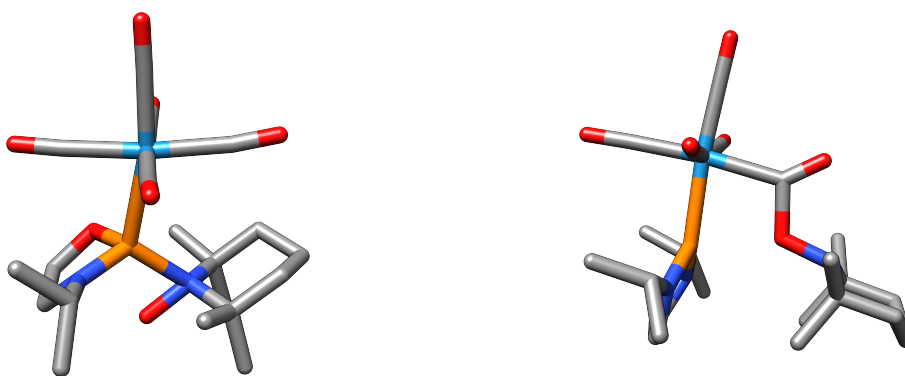
Figure 26: Structure at the transition state of the 1,3,2-oxazaphospholidinyl **9i** (left) and 1,3,2-diazaphospholidinyl complex **9f** (right) in the reaction with TEMPO to the aminoxylphosphane complexes **8i** and **8k**.

To complete the reaction pathway the thermal homolytic N–O bond dissociation was also taken into account (Figure 24). The cleavage proceeds without a barrier in all cases and the BDG of the N–O bonds were calculated to be 5.3, 6.3 and 7.3 kcal mol^{-1} for **8f**, **8i** and **8k**, respectively. Even though these numbers are very similar their trend reflects the experimentally observed thermal stability. The BDG for the methyl derivative **8e** and the previously reported diphenyl derivative **8d** were 6.9 and 15.8 kcal mol^{-1}, which are also in agreement with the experiments, as **8d** can be stored without any decomposition and generates the phosphanoxyl complex **11d** (previously named **XX**) at temperatures around 60 to 80 °C. The presence of heteroatoms adjacent to the P-atom clearly weakens the N–O bond in aminoxylphosphane complexes **8e,f,i** compared to the diphenyl derivative **8d**, suggesting more stable phosphanoxyl complex radicals **11e,f,i**. This electronic effect seems to be most efficient in the 1,3,2-diazaphospholidine complexes **8e,f** and slightly weakened then replacing nitrogen by oxygen as in **8i**. Different steric effects present in **8e,f** causes kinetic differentiation, due to the repulsion of the TEMP unit.

4.7.3. Theoretical investigation on phosphanoxyl tungsten complexes

The transient character of the phosphanoxyl complexes **11** does not allow structure analysis, via, *e.g.*, NMR- or X-ray diffraction, especially if performed at elevated temperatures. The structure and electronic properties were therefore investigated again via DFT calculations (Figure 27). For all studied systems the P–W bond is elongated and ranges between 2.51 Å for **11k** to 2.59 Å for **11f**. Remarkably this observation is accompanied with a large increase in the P–W bond order quantified by the MBO. While in the aminoxyl-substituted phosphane complexes **8f,i,k** values of 0.30 to 0.42 were calculated the phosphanoxyl complexes show values from 0.65 up to 0.8, being even higher than in the phosphanyl complexes **9f,i,k**. Interestingly the values are closer to the MBOs found for the secondary phosphane complexes **6**. Angle sums around phosphorus are in the range of 324 to 330°, which are similar to values found for the phosphanyl complexes **9** and the free phosphinoyl radicals **1**. This is also in good agreement with the change of the P–O^{exo} MBO, which is close to 1.7 (compared to phosphinoyl **1** values of 1.7 to 2.0) and the bond lengths scattered around 1.5 Å, similar to the values observed for the free phosphinoyls **1**. The O-P-W angle in the complexes is increasing for higher oxygen content in the five-membered ring, going from 82.3° (**11f**) over 88.2° (**11i**) to 94.6° (**11k**). While the structural features of the phosphanoxyl complexes **11** and the free radicals **1** are closely related, the spin density distribution reflects the major differences between the two classes of compounds. Spin density on the oxygen atom averages around 18% for the free phosphinoyl ligands **1**, this value is in general increased upon coordination to the W(CO)$_5$ fragment (Figure 27; cf. Table 4, p.21).

SDD:			
W	0.39	0.38	0.46
O	0.24	0.20	0.16
P	0.14	0.10	0.07
N/O	0.05	0.02	0.01
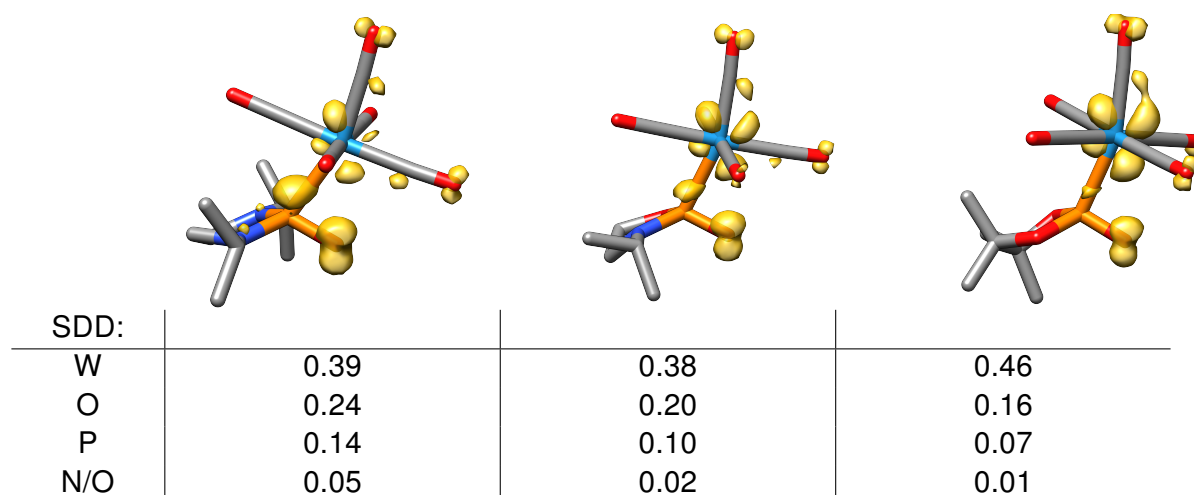
Figure 27: Calculated molecular structures of the phosphanoxyl complexes **11f**, **11i** and **11k** (left to right), the Loewdin spin density distribution for selected atoms in e and the visualised spin density distribution (yellow, isovalue 0.009).

However, it seems that oxygen-substituents at the P-atom dampens this effect or in the case of the 1,3,2-dioxaphospolane complex decreases the spin density on the exocyclic oxygen atom. The most prominent feature in the phosphinoyl radicals **1** is the phosphorus-centred radical character, making up ∼50% of the total spin density. This value is significantly decreased to 6 - 13% in the complexes, being the lowest for the 1,3,2-dioxaphospholanoxyl complex **11k** and highest for the two 1,3,2-diazaphospholidinoxyl complexes **11e** and **11f**. Instead, the major contribution of the spin density is shifted to the metal atom, with values of 32 to 45%. Here again the highest value is observed for the 1,3,2-dioxaphospholanoxyl complex **11k**, followed by the 1,3,2-oxazaphospholdinoxyl complex **11i**. As it can also be seen from the graphical representation of the SDD (Figure 27) leftover spin density is scattered throughout the complexes however adjacent heteroatoms only make up for 5% for 1,3,2-diazaphospholidinoxyl-complexes **11e**, **11f** and for N,O or O,O derivatives **11i** and **11k** less than 2% spin density are found on these atoms. This is remarkable as the free 1,3,2-oxazaphospholidinoyl ligands **1h,i** appeared to be nitrogen-centred radicals, and nothing indicates such a behaviour in the tungsten complex radical **11i**. Noticeable amounts of spin density are found on the carbonyl ligands which are known to be very good π acceptors.

4.8. Summary

The usage of the hydrido tungstate [NEt$_4$][W(CO)$_5$H] is a powerful tool to synthesise secondary heterocyclic phosphane complexes, otherwise difficult to access, bearing directly bound heteroatoms, *e.g.*, N and O. Even limitations originating from little steric bulk in α position to the phosphorus atom, reported previously by King, can be overcome and taken to the extreme of very low kinetic stabilisation in the case of the 1,3,2-dioxaphospholane complex **6k**. The facile reaction of the secondary phosphanes **6f,i,k** with TEMPO yields three new, structurally confirmed aminoxyl substituted phosphane complexes **8f,i,k** to the hitherto scarcely investigated class of compound. Their formation was studied in detail by DFT calculations revealing important milestones in the reaction sequence with TEMPO starting from **6f,i,k**. Despite the absence of significant changes for heteroatom-substituted phosphinoyls **1** their presence affects the synthesis, intermediates and properties of phosphanoxyl complexes **11**. Amino groups stabilise not only the formation of the phosphanyl complexes **9** (by HAT with TEMPO) but also formation of phosphanoxyl complexes **11**, apparent in a weaker N–O bond. The structure of several phosphanyl complexes **9** was discussed revealing a common bent structure, which is amplified by donating substituents adjacent

48

to phosphorus. The opposite is observed for phenyl substituted complexes achieving planarity, which was found for the so far only observed or isolated phosphanyl complexes **9d** and **XXXV**. Phosphanyl complexes **9** undergo heterocoupling with TEMPO (**2**) resulting in the formation of **8** for which two different transition states were found. The lower lying transition state of the 1,3,2-diazaphospholidinyl complex **9f** allows fast formation of the product **8f** even at 0 °C. In contrast, **9i** having a higher barrier for the heterocoupling is only efficiently converted to the product **8i** at ambient temperatures, despite the more energetically favoured phosphanyl complex intermediate **9i**. The absence of steric bulk in **9k** leads to a barrier free formation of **8k**, however, the less stabilised phosphanyl complex **9k** seems to be reason enough to slow the reaction dramatically in contrast to the other cases. DFT analysis of the transient phosphanoxyl complexes **11f,i,k** and the comparison to already reported **11d** and **11e** showed that they are qualitatively the same. In quantitative terms, the spin density on the tungsten atom was increased if more oxygen atoms are bounded to the phosphorus centre, pulling spin density from the ligand. The structure of these phosphanoxyl complexes, considering bond lengths and angles together with MBOs, is best described in a delocalised way within the W-P-O moiety (Figure 28), while the ligand adopts the structure of an uncoordinated phosphinoyl radical **1**. A consequence is that these ligands are in between innocent and non-innocent, and the non-innocent behaviour is increased for higher oxygen content in the heterocycle. Most of the results presented in this chapter have recently been published.[103]
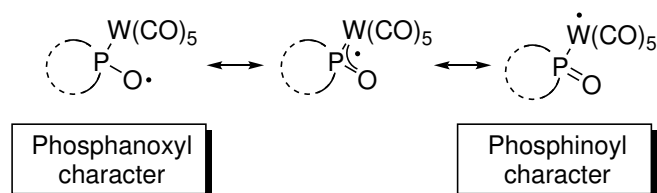
Figure 28: Differenct resonance Lewis structures of phosphanoxyl complexes **11** describing the delocalisated distribution of the electron spin and their expected radical character.

5. Towards P–O containing radical complexes of iron

The small changes observed for the derivatisation of phosphanoxyl tungsten complexes raised again the question of the role of the metal. The significant uptake of spin density of the tungsten atom allows the ligand to behave similarly to a phosphinoyl **1**. An increase in electron density on the metal centre should make such a stabilisation less favoured and might force the system to adopt a phosphanoxyl like structure, along with a significant increase in the spin density distribution on the oxygen atom. However, the small endeavour into the chemistry of phosphanoxyl manganese complexes, being more electron rich, showed that *in situ* formed aminoxylphosphane cymantrene complexes **XXVII** (cf. Scheme 13, p.11) were very reactive. To avoid the potential manifold redox chemistry of manganese, while increasing the valence electrons on the metal, iron(0) complexes were targeted. It had been shown that the tetracarbonyl iron ($FeCO_4$) moiety can tame electron deficient phosphorus species, like the terminal electrophilic phosphinidene iron complex by Lammertsma, especially if combined with a P-bound amino substituent.[106,107] In general the chemistry of phosphane iron complexes is very rich and iron tetracarbonyl complexes of phosphanes have been around for a long time.[108] However, a major contribution to the field of secondary phosphane $Fe(CO)_4$ complexes was done by Treichel et al. introducing several alkyl- and aryl-substituted phosphane complexes (Figure 29, top).[104] Secondary heteroatom-substituted phosphane iron complexes are rare, often limited to certain substituents and complexes containing P–O bonds of that the latter type remained unknown before 2016, when the previously mentioned terminal phosphinidene complex was inserted into secondary amine N–H or O–H bonds of acids and alcohols (Figure 29, bottom).[105] No dialkoxyphosphane complex of the type $[Fe(CO)_4\{HP(OR)_2\}]$ is known today.

Figure 29: Selection of secondary phosphane $Fe(CO)_4$ complexes **12** described by Treichel[104] and the limited synthetic approach to **XXXVII** by Lammertsma.[105]

5.1. Synthesis and reactivity of diphenyl *P*-OTEMP complexes

Initially the aminoxyl(diphenyl)phosphane iron tetracarbonyl complex **17d** was targeted, due to the high stability of its tungsten derivative **8d**. The secondary phosphane complex **12d** is readily accessible from the reaction of diphenylphosphane **4d** with $Fe_2(CO)_9$ (Scheme 20), slightly modified as described by Treichel et al.[104] While **12d** has been synthesised previously, NMR values for this compound are not available in full. The phosphorus nuclei resonates in the ^{31}P-NMR spectrum at 41.5 ppm as a doublet with direct a scalar $^1J_{P,H}$ coupling of 378 Hz. Compared to the free phosphane **4d** ($\delta(^{31}$P$) = -40.3$ ppm) the chemical shift is found at higher frequencies and the scalar coupling is increased in the complex ($^1J_{P,H}$ (**4d**) = 214 Hz),[109] pointing to a higher s-orbital contribution in the P–H bond and higher acidity.

Scheme 20: Modified synthesis of **12d** via complexation of **4d**.

Reaction of **12d** with TEMPO in THF at room temperature yielded a mixture of products (Scheme 21). The ^{31}P{^{1}H}-NMR spectrum of the reaction mixture, if performed and kept stirring at 0 °C for 7 hours, showed three resonances besides left-over starting material (Figure 30). The large amount of remaining starting material can be explained by a very slow reaction of the secondary phosphane complex **12d** with TEMPO at 0 °C. This observation was already observed in the previous described synthesis of **8i,k** and furthermore mentioned by Nesterov for the reaction of TEMPO with the (Bisyl)FP(H)-W(CO)₅ complex, for which he reported that the reaction only occurred above 4 °C.[59] Therefore, the reaction mixture was allowed to warm up to room temperature and stirred for additional two hours (Scheme 21). Subsequent ^{31}P-NMR experiments showed only two remaining signals at

Scheme 21: Formation of **13d** and [TEMPH₂]**14d** from the reaction of the phosphane iron tetracarbonyl complex **12d** with TEMPO at 0 °C to room temperature.

Figure 30: $^{31}P\{^1H\}$-NMR spectrum of the reaction of **12d** with TEMPO in THF kept at 0 °C for 7 hours. Integral values are given below the baseline of the spectrum.

145 and 110 ppm. Repeating the reaction always resulted in similar mixtures with varying ratios of the two resonances. The difference in chemical shift from the starting material **12d** (41.5 ppm) and the small $\Delta\delta(^{31}P)$ of 35 ppm between the two newly observed resonances resembled findings in the chemistry of phosphanoxyl manganese complexes. Therein the attempted synthesis of the aminoxylphosphane complex **XXVII** resulted only in the observation of hydroxyphosphane complex **XXX** and its corresponding base, the phosphinito complex **XXIX** (cf. Scheme 13, p.11). These findings were corroborated via NMR calculations and the $\Delta\delta(^{31}P)$ of **XXX** and **XXIX** was 40.6 ppm (calc. 37.8 ppm). The close proximity of the $\Delta\delta(^{31}P)$ suggested the presence of the acid/base pair **13d** and [TEMPH$_2$]**14d** in the reaction of **12d** with TEMPO (Scheme 21). Addition of TEMP–H to the reaction mixture at ambient temperature resulted in an increased intensity of the 130 ppm resonance. If an excess of amine was added no other resonance besides 130 ppm was observed. These findings agree with the hypothesis of the formation of **13d** and [TEMPH$_2$]**14d** in the reaction. Additionally, a test reaction was performed to synthesise **13d** via hydrolysis of the chloro(diphenyl)phosphane Fe(CO)$_4$ complex **15d**. Despite a very slow reaction of **15d** with
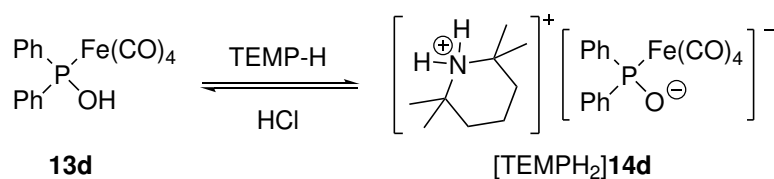
Scheme 22: Transformation of **13d** into [TEMPH$_2$]**14d** and vice versa by addition of the Brønsted base (TEMP–H) or acid (HCl).

water in Et$_2$O, the observed chemical shift in the ^{31}P-NMR spectrum showed only one reso-nance besides **15d** (162.3 ppm) at 143.4 ppm which matches very well with the resonance assumed for **13d**. Otherwise, protonation of [TEMPH$_2$]**14d** with a solution of HCl in Et$_2$O forged **13d** selectively (Scheme 22). The presence of **13d** and [TEMPH$_2$]**14d** were further corroborated by (−)-ESI mass spectrometry, which showed a signal with m/z 368.958 in full agreement for **14d**. Despite the selective transformation of either **13d** and [TEMPH$_2$]**14d** isolation of them was not possible. In the case of **13d**, due to a similar solubility as byprod-ucts, *e.g.*, TEMPO–H and for [TEMPH$_2$]**14d**, which was also remarkably poor soluble in other solvent than THF, due to an unknown impurity. The presence of an assumed inter-mediate aminoxylphosphane complex **17d**, with an apparent low thermal stability, was then probed by the milder approach of an initial deprotonation at −80 °C and further oxidation and heterocoupling with two equivalents of TEMPO (Scheme 23) as an alternative method from Heurich.[63] Addition of TEMPO at −40 °C to a solution of **12d**, previously treated with ^{n}BuLi, led to a colour change from yellow to red. ^{31}P{^{1}H}-NMR experiments of the reaction solution showed an AB-type spin system (62.5, 3.8 ppm) with a $^1J_{P,P}$ of 326 Hz as a major product (74% estimated by NMR integration). This signal is in very good agreement with the formation of the diphosphane iron complex **XXXVIII**, which has already been described in 1973 by Collman.[110] However, these findings are in stark contrast to the results reported for the diphenylphosphane tungsten complex **6d**, for which this approach yielded the desired aminoxylphosphane complex **8d**.

To combine the oxidation and heterocoupling one equivalent of [**2**]BF$_4$ was chosen as
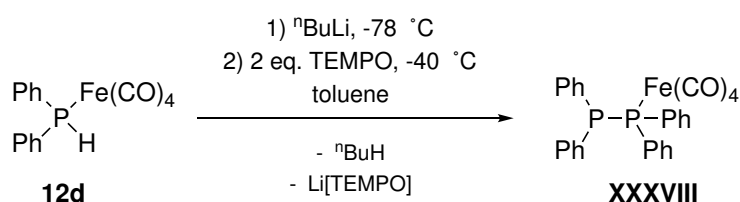
Scheme 23: Synthesis of **XXXVIII** from deprotonation and subsequent oxidation with TEMPO in the attempted synthesis of **17d**.
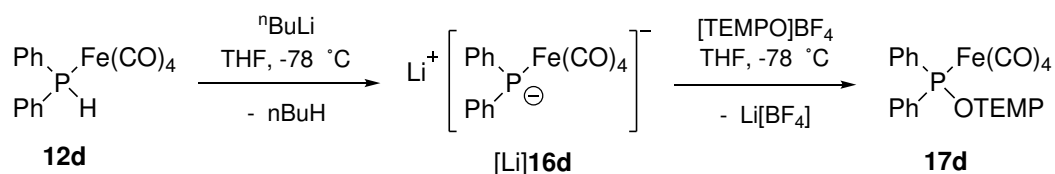
Scheme 24: Synthesis of aminoxylphosphane complex **17d** via deprotonation of **12d** and subsequent SET and heterocoupling with [**2**]BF$_4$.

reagent (Scheme 24), to avoid homocoupling of two intermediate phosphanyl radicals by diffusion processes. The efficiency of the initial deprotonation of **12d** was probed via low temperature ^{31}P-NMR spectroscopy. In the reaction mixture a single resonance is observed at −2.4 ppm with a full width at half maximum (FWHM) of 4 Hz. If the complex is purified by simple washing with *n*-pentane a very broad resonance (FWHM = 740 Hz) at 4.8 ppm is observed in the ^{31}P-NMR spectrum in THF-*d*8. Despite that several salts of **16d** are known, NMR data of these are scarce.[104,111] However, the absence of a direct scalar P–H coupling in the ^{31}P- and ^{1}H-NMR spectrum alongside a resonance at −0.4 ppm in the ^{7}Li{^{1}H}-NMR spectrum corroborates the correct assignment that [Li]**16d** was formed. Furthermore, the deprotonation is very rapid, confirmed by the NMR measurements even at low temperatures. Hence, a suspension of [**2**]BF$_4$ in THF was added five minutes after the addition of ^{n}BuLi to **12d** which led to an immediate color change from yellow to red. The reaction was monitored starting from −70 °C to room temperature by VT-^{31}P-NMR spectroscopy to detect a potential aminoxylphosphane complex **17d** (Figure 31). Remarkably, already at −70 °C only one significant resonance is observable with a chemical shift of 176.5 ppm. This resonance was also present before in the mixture kept at 0 °C, but only in minor amounts (Figure 30). Above temperatures of −30 °C the resonance assigned to [TEMPH$_2$]**14d** at 110 ppm is detected, and between 0 °C and 10 °C this resonance increases notably. At higher temperatures (25 °C) the resonance at 176.5 ppm vanishes completely and, besides the resonance of [TEMPH$_2$]**14d**, two other resonances appear at 164.4 and 145.3 ppm (**13d**). The composition of the reaction mixture at room temperature remains constant over additional 45 minutes. It was therefore concluded, that the aminoxylphosphane complex **17d** is formed at low temperatures and the resonance at 176.5 ppm can be tentatively assigned to it. This strong lowfield shift compared to the phosphane complex **12d** is in good agreement with the previously reported tungsten **8d,e,f,i,k** and manganese aminoxylphosphane complexes **XXVII**.[59,63,65,67] Under strict temperature control during work-up, *e.g.*, removal of solvent at −30 °C, extraction at the same temperature and storage at −80 °C it was possible to obtain a sample of **17d**, with minor impurities and in low yield. Multinu-
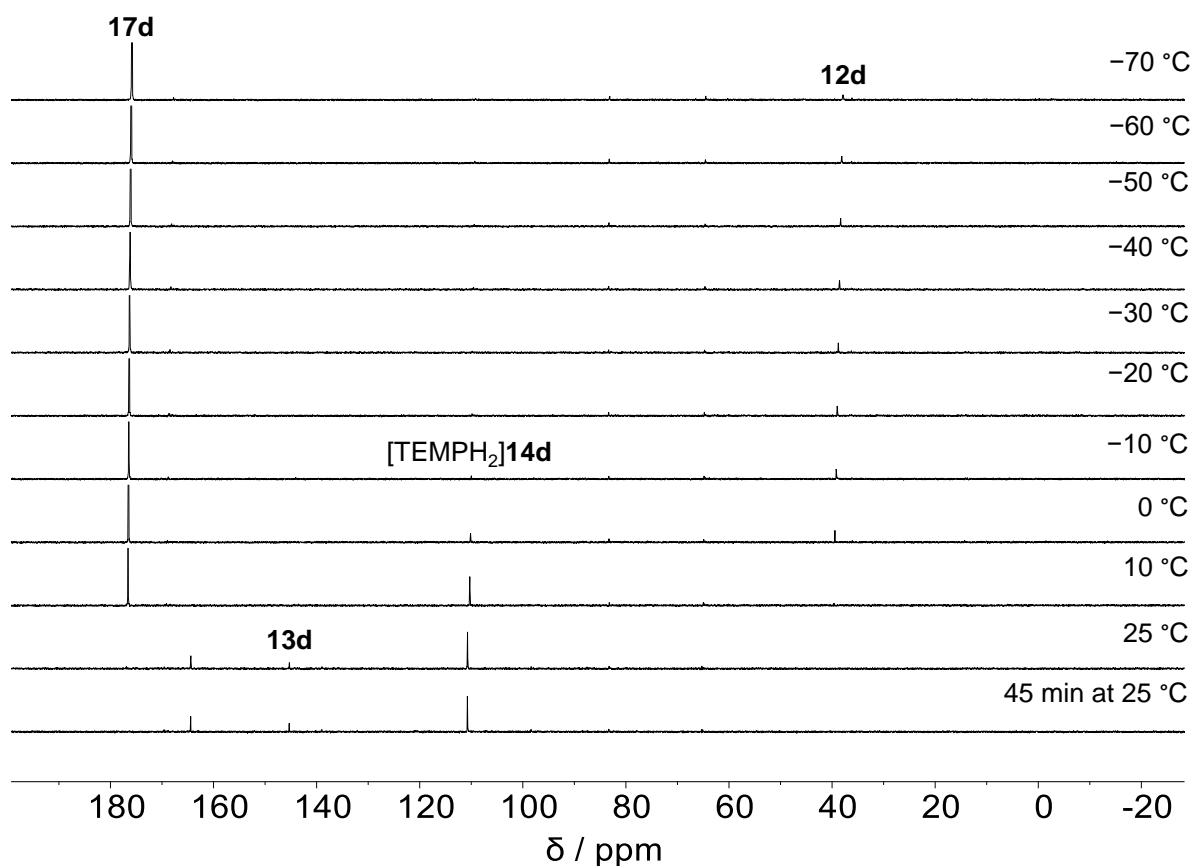
Figure 31: VT-^{31}P{^{1}H}-NMR spectra of the reaction of [Li]**16d** with [**2**]BF$_4$ in THF in the temperature regime $-70\,^{\circ}$C to $25\,^{\circ}$C with an increment of $10\,^{\circ}$C.

clear NMR studies agree with the assignment to aminoxylphosphane complex **17d**. Upon warming up such a solution of purified **17d** in THF an unselective decomposition according to ^{31}P-NMR spectroscopy occurred. ^{1}H-NMR spectroscopy showed evidence of TEMP–H formation in this case, indicating the N–O bond cleavage. Due to thermal sensitivity of **17d** further purification was not possible by common methods and also not by low temperature column chromatography.

The observed final products **13d** and [TEMPH$_2$]**14d** together with the intermediate formed aminoxylphosphane complex **17d** suggest a N–O bond cleavage of the latter resulting in a transient phosphanoxyl iron complex **18d** (Scheme 25). In analogy to the earlier reports of Heurich trapping experiments were conducted, to prove the generation of **18d**.[63] Therefore, a solution of **17d** was prepared by the reaction of **12d** with and ^{n}BuLi and subsequent treatment with [**2**]BF$_4$ at low temperatures. At $-40\,^{\circ}$C ^{n}Bu$_3$SnH was added to the reaction mixture to obtain the stannoxyl phosphane iron complex **19d**, as an analogue of Heurichs

55
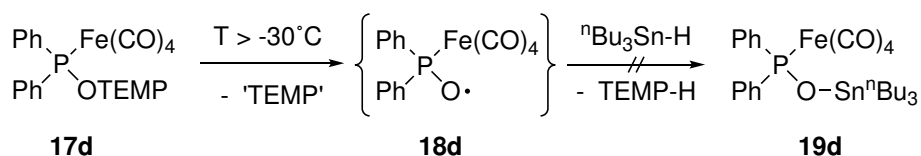
Scheme 25: Assumed formation of phosphanoxyl iron complex **18d** with subsequent trapping attempt with $^nBu_3Sn$–H to form stannoxyl phosphane complex **19d**.

XXIV ($^1J_{Sn,P}$ = 146 - 165 Hz; cf. Scheme 11). The reaction mixture was analysed by ^{31}P-NMR spectroscopy revealing [TEMPH$_2$]**14d** to be the major product next to **13d** and some minor side products, but no evidence for the formation of stannoxyl phosphane complex **19d** was found, especially as no resonance showed coupling of the phosphorus to the ^{117}Sn and/or ^{119}Sn nuclei.

5.2. Synthesis of 1,3,2-diheterophospholane iron(0) complexes

### 5.2.1. Attempted synthesis via common procedures

The differences in thermal stability and decomposition product compared to Heurich's aminoxyl(diphenyl)phosphane tungsten complex **8d** urged to investigate different substitution pattern at the phosphorous atom. The absence of suitable precursors, already discussed for the tungsten compounds, does not allow direct complexation of a secondary phosphanes **4** to the iron carbonyl moiety. Initially the 1,3,2-diazaphospholidine iron complex **12e** was targeted via the stepwise complexation-reduction approach starting from the 2-chlorophosphane **3e** (Scheme 26). Such an approach was taken previously by King in 1984 for ($^iPr_2N)_2$P(H)Fe(CO)$_4$, however, only a low yield of 20% was reported.[112] If the complexation of **3e** with Fe$_2$(CO)$_9$ is carried out in toluene at room temperature a mixture of products is obtained detected by ^{31}P{^{1}H}-NMR spectroscopy with resonances observed at 181 (48%), 192 (37%), 263 (3%) and 291 ppm (12%). The compound with a chemi-
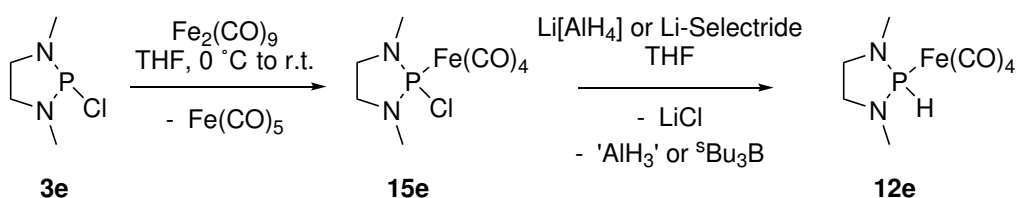

Scheme 26: Reaction scheme for the attempted synthesis of **12e** via step wise complexation-reduction.

cal shift of 192 ppm can be isolated by washing the dried mixture with a Et_2O/petrol ether (60/40) (PE) mixture. While ^{31}P- and ^{1}H-NMR spectra fit to the desired complex **15e**, the carbonyl (CO) resonance at 212 ppm in the ^{13}C{^{1}H}-NMR spectrum shows a triplet with a scalar $^2J_{P,C}$ coupling of 37 Hz and indicates the presence of two chemically identical phosphorus atoms. Further analysis with EI-MS showed m/z peaks being in very good agreement with a suspected double substitution of **3e** to a $FeCO_3$ fragment. However, the observed m/z peaks match with a hydrolysed species, which might have occurred during the preparation of the sample for the MS experiment, pointing to a potential high sensitivity towards air and moisture, as no evidence of P–OH functional groups is observed in the previously recorded NMR spectra. From these experiments the structure was assigned to be compound **20e** (Scheme 27). Attempts of isolating any other compounds from this mixture failed. Therefore, the reaction protocol was changed and THF was used instead of toluene. This led to a significant decrease of side products and only a mixture of **20e** and due the close proximity in chemical shift assumed **15e** (181 ppm) in a ratio of 1:2 was obtained (Scheme 27). From the dried mixture **15e** could be sublimed under mild conditions. The ^{13}C{^{1}H}-NMR spectrum shows a carbonyl signal (213 ppm) with a doublet splitting derived from a scalar $^2J_{P,C}$ of 20 Hz, corroborating the previous assignment of **20e** to the doubly substituted complex. ^{31}P{^{1}H}-NMR spectroscopy also reveals a direct $^1J_{Fe,P}$ coupling with a magnitude of 30 Hz, which lies in the normal range, despite being rarely discussed in the literature.[113] From the sublimate the structure could be obtained via X-ray diffraction analysis (Figure 32) and fits well to the NMR values. Remarkably, a comparison with literature values was difficult as only very few structurally related compounds are known. Best comparison can be drawn between the structure of **15e** and its fluorine derivative.[114] All common bonds are of similar length, the same is observed for common angles. While the bond angle sum around phosphorus ($\sum_{\angle}^{P}$: 301.1°) of the fluoro derivative is also in line with the value of **15e**, the τ_5(Fe) of 0.85 in the fluoro derivative is slightly larger than that of **15e**. For comparison 1,3,2-dioxaphospholane iron complexes **15k,l** were
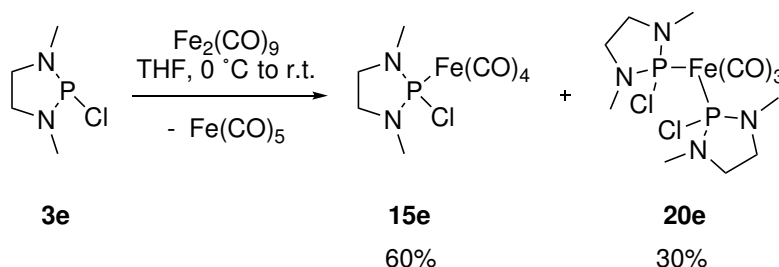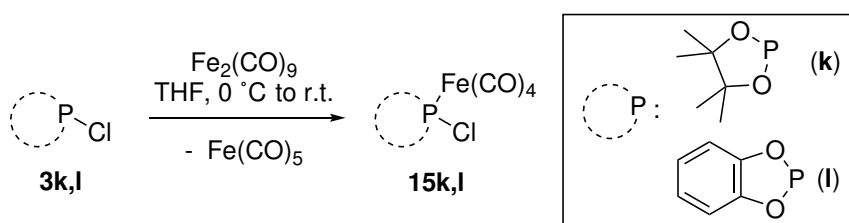

Scheme 27: Complexation of **3e** with $Fe_2(CO)_9$ in THF to yield **15e** and **20e** in a 2:1 ratio derived from ^{31}P-NMR spectroscopy.
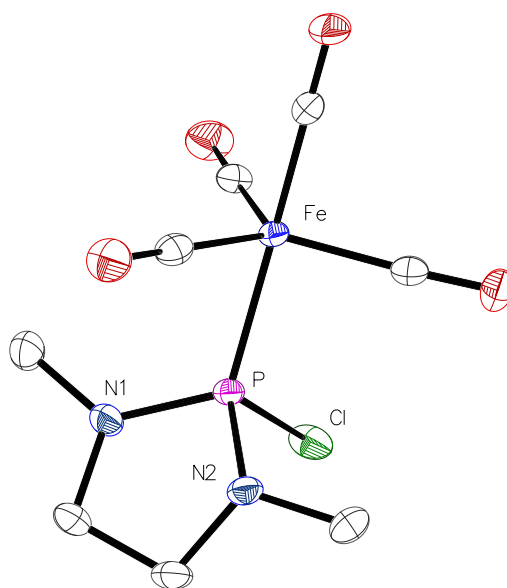
Figure 32: Molecular structure of **15e** in the crystal structure; ellipsoids are set at 50% probability level and all hydrogen atoms are omitted for clarity. Selected bond lengths and angles are given in Å and ° respectively: d(P–Cl) 2.11619(19), d(P–Fe) 2.1726(2), d(P–N1) 1.62989(14), ∡(N1-P-N2) 94.002(9), ∡(Cl-P-Fe) 111.441(7), ∡(N1-P-Cl) 104.736(8), $\sum_{\angle}^{P}$ 301.486; τ_5(Fe) 0.72.

targeted. The chlorophosphanes **3k,l** were treated with $Fe_2(CO)_9$ in THF as before for **3e** (Scheme 28). Both reactions were selective taken from $^{31}P\{^1H\}$-NMR spectra with chemicals shifts of 209.8 ppm (**15l**) and 203.3 ppm (**15k**) with only minor side-products in the low field region. Here, $^1J_{Fe,P}$ of 75 Hz for **15l** and 55 Hz for **15k** were found which is in line with the increasing electronegativity of oxygen over nitrogen compared to the value found in **15e**. Both species show a doublet splitting in the $^{13}C\{^1H\}$-NMR spectrum corroborating mono substitution in both cases. In the EI-MS spectrogram for **15l** a molecular peak is observed at m/z 341.9. Despite that the base peak can be assigned to [**15l**−Fe(CO)$_4$−Cl] no other significant P–Cl fragmentation is observed. To further investigate into the strength


Scheme 28: Complexation of **3k,l** with $Fe_2(CO)_9$ in THF to forge dioxaphospholane complexes **15k** and **15l**.

of the P–Cl bond in **15l**, the complex was treated with $AlCl_3$. However, no reaction was observed which is in stark contrast to non-cyclic bisaminophosphane $Fe(CO)_4$ complexes reported by Cowley.[115] For these systems phosphenium complex formation was observed via chloride abstraction, indicating a stronger P–Cl bond in **15l**. This is supported that initial attempts to reduce **15l** to **12l** with $^nBu_3SnH$ under mild conditions also showed no reactivity of the P–Cl bond. To stabilise a possible reduced form of **15l** *in situ*, the complex was treated with 1,4-bistrimethylsilyl-1,4-diazine **XXXIX** (Scheme 29). The reducing agent **XXXIX** is known in the literature to react with, *e.g.*, dicyclopentadienide titanium dichloride (Cp_2TiCl_2) to yield the pyrazine bridged Ti(III) species and to react with bulky dichlorophosphanes to forge stable diphosphenes.[116,117] The combination would allow formation of pyrazine masked phosphanyl complex **21**. Remarkably, no reaction at all was observed in this case. Also, treatment of **15l** with DIBAL–H resulted in no reaction. Therefore, further reduction was attempted with LAH in Et_2O as applied by Heurich in the synthesis of the 1,3,2-diazaphospholidine tungsten complex **6e**.[66] The reaction was very slow as after 17 hours 76% (estimated from ^{31}P-NMR integration) of the starting material remained. Besides other side-products a resonance with a chemical shift of 228.2 ppm (6% estimated from ^{31}P-NMR) was observed, which showed a $^1J_{P,H}$ of 418 Hz in the coupled ^{31}P-NMR spectrum. This resonance would fit to the desired secondary phosphane complex **12l**. To increase the reaction progress the solvent was changed to THF, however under these reaction conditions an AX-type spin system was formed with high selectivity. In the ^{31}P{^{1}H}-NMR spectrum the resonance signals appear at 311.5 ppm and −10.3 ppm, both having a $^1J_{P,P}$ of 425 Hz. A ^{31}P-NMR experiment shows an additional 184 Hz splitting for the signal ap-
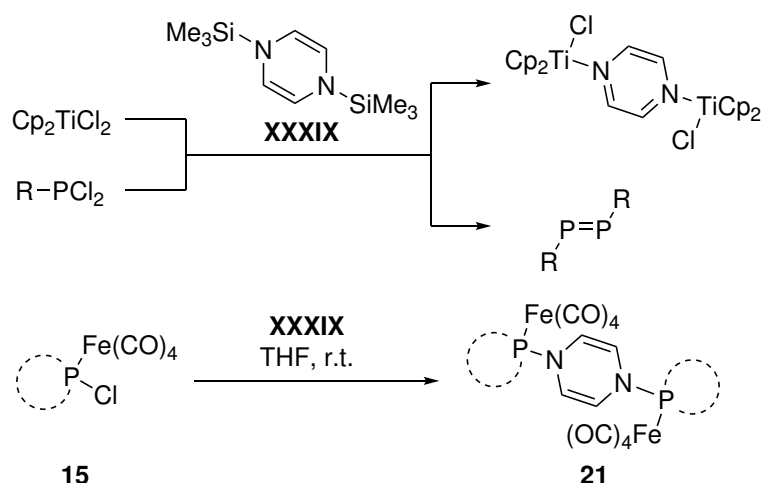

Scheme 29: Reduction of Cp_2TiCl_2 and a bulky dichlorophosphane with **XXXIX** as an example for the reactivity (top). Attempted reaction of chloro phosphane iron complexes **15** with **XXXIX** to forge a masked phosphanyl iron complex **21** (bottom).
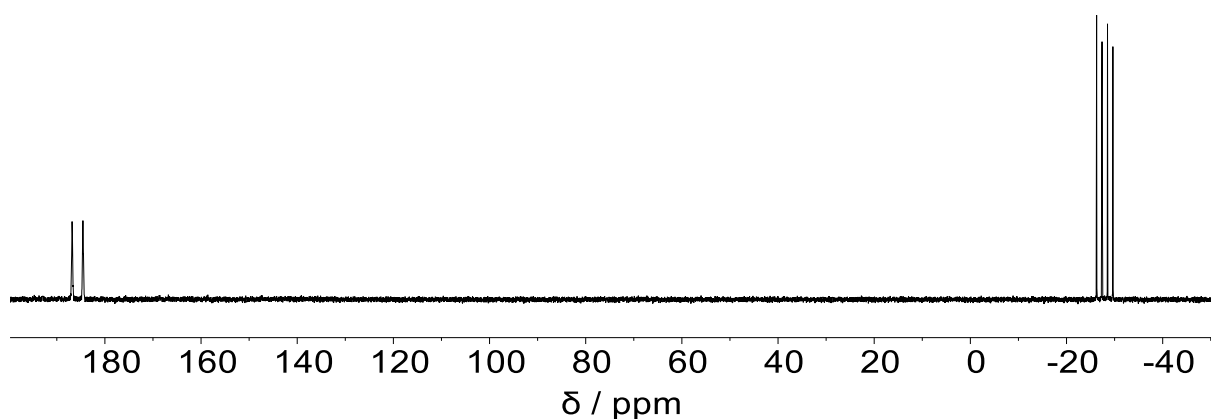
Figure 33: ^{31}P-NMR spectrum of the reaction mixture of **15e** with LAH in THF showing an AX-type spin system assumed to be compound [Li]**22e** or [Li]**22e**^{Fe}.

pearing at −10.3 ppm, originating from a $^1J_{P,H}$ scalar coupling. To probe if this might be an alternative pathway exclusive to the iron complexes the tungsten pentacarbonyl derivative **5l** was synthesised and reacted with LAH in THF. Also in this case, despite more resonances in the high field region, this leads to an AX spin system instead of the complex **6l**. However, showing clear evidence that both phosphorus are still bound to the W(CO)$_5$ fragment due to satellites, arising from $^1J_{W,P}$ coupling. The highfield resonance of the AX spin system shows a fairly low coupling to ^{187}W suggesting an anionic phosphorus. Remarkably, if the reaction is repeated under the same conditions for the iron complex **15e** no simple reduction occurred in contrast to the tungsten derivative **6e** from Heurich. Instead, an AX-type spin system is observed, similar to the one previously discussed; the $\delta(^{31}$P) chemical shifts are 185.7 ppm and −28.0 ppm with a $^1J_{P,P}$ coupling of 366 Hz (Figure 33). Also in this case the highfield resonance (−28.0 ppm) shows an additional $^1J_{P,H}$ of 182 Hz. This coupling can also be found in the ^{1}H-NMR spectrum ($\delta(^1$H): 2.38 ppm; $^1J_{P,H}$ 182.0 Hz; $^2J_{P,H}$ 3.5 Hz) together with one equivalent of resonances of a 1,3,2-diazaphospholidine moiety.
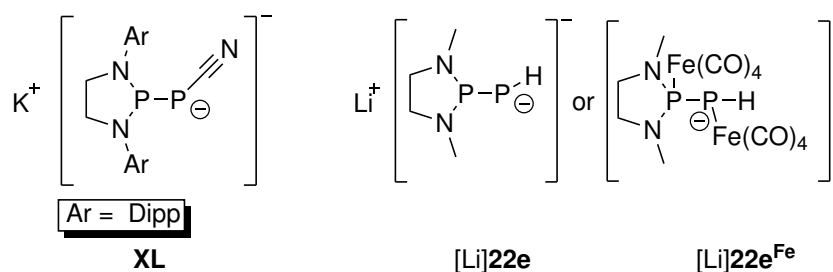

Figure 34: Lewis structures of potassium phosphanyl cyanophosphide **XL** reported by Grütz-macher[118] and the herein assumed lithium phosphanyl phosphanide (complex) [Li]**22e** ([Li]**22e**^{Fe}).

60

This pattern is very much in line with a lithium phosphanyl phosphanide [Li]**22e** and a similar structure **XL** has been published recently by Grützmacher (Figure 34).[118] However, in the here observed case the metal fragments might still be attached [Li]**22e^Fe**. Similar structures can therefore be assumed for the 1,3,2-dioxaphospholane complexes previously discussed. No further investigations were done towards this class of compounds as its chemistry was not further applicable within the scope of the work presented herein.

5.2.2. Application of K[Fe(CO$_4$)H] in the synthesis of secondary heterocyclic phosphane iron(0) complexes

As several common reducing agents did not allow satisfying access of the secondary phosphane iron complexes **12**, the hydrido ferrate K[Fe(CO)$_4$H] was used in analogy to [NEt$_4$][W(CO)$_5$H]. This potassium ferrate salt has been previously used, however only on several occasions to transfer triamino phosphanes P(NR$_2$)$_3$ and also chlorophosphanes **3** to secondary phosphane complex **12**, *e.g.*, **12n** (Scheme 30).[119,120] This is in contrast to results published by Gudat, who showed that cyclic 1,3,2-diazaphospholes **XLI** do not yield a secondary phosphane complex such as **12**, and only the coordination product **XLII** was obtained via salt metathesis and ligand substitution of CO.[121] However, herein all attempted syntheses of secondary iron phosphane complexes **12e,f,h,i,k,l** with K[Fe(CO)$_4$H] were successful and highly selective, and no reactivity as for **XLI** was observed (Scheme 31). The crude products were obtained as yellow to red oils, only **12l** solidified upon stand-ing. Initial attempts to purify the compounds **12e,l** further by column chromatography
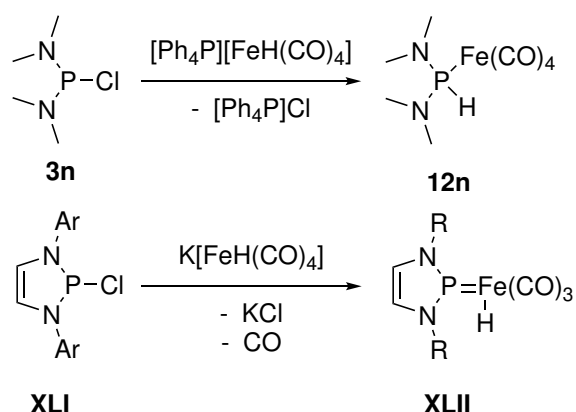
Scheme 30: Reactions of chlorophosphanes **3n** and **XLI** (Ar = Dipp) with the [Fe(CO)$_4$H] anion resulting in the phosphane complex **12n** by Caminade[119] or the phosphenium iron complex **XLII** by Gudat.[121]
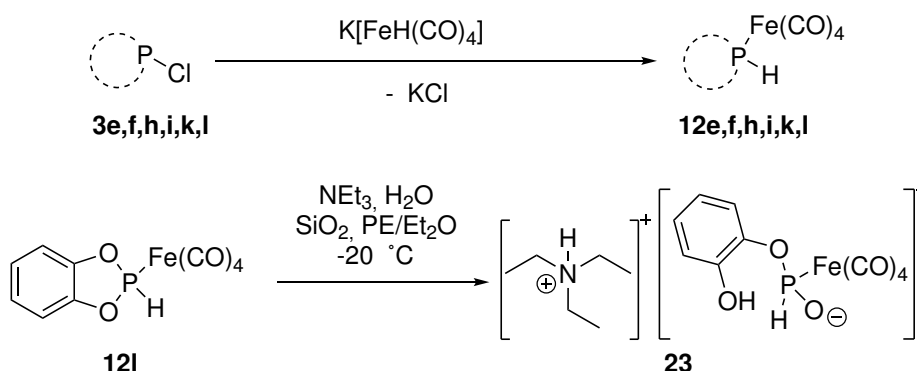
Scheme 31: Synthesis of 1,3,2-diheterophospholane iron complexes **12e,f,h,i,k,l** from chloro phosphane **3e,f,h,i,k,l** via reaction with K[Fe(CO)$_4$H] (top). Ring opening during work-up of **12l** resulting in the phosphinito salt **23**.

with PE(40/60) and either Et$_2$O or DCM showed a significant decrease in yield, *e.g.*, **12e** was obtained in 18% yield and only a negligible amount of **12l** after the column chromatography. This problem could partially be solved by addition of NEt$_3$ to the eluent mixture used in the chromatography, allowing the isolation of **12e,f,h,i,k** in yields above 60%. The 1,3,2-dioxaphospholane complex **12l** could not be purified via this method, as in this case ring opening occurred resulting in **23** (Scheme 31), assumingly due to the basic environment. For all complexes **12e,f,h,i,k,l** a singlet resonance was observed in the ^{31}P{^{1}H}-NMR spectrum (Table 10) which was highfield-shifted compared to the related chlorophosphanes **3** for 1,3,2-diazaphospholidine-based **12e,f** lowfield-shifted for the 1,3,2-dioxaphospholane derivatives **12k,l** and the 1,3,2-oxazaphospholidine derivative **12h** is only slightly lowfield-shifted. These NMR investigations revealed that **12i** is almost isochronous with its chlorophosphane derivative **3i**. From **12e,f,h,i** it can be seen that substitutions of the methyl- to a isopropyl group leads to a more shielded phosphorus centre (shift to higher field) connected with higher electron density on phosphorus due to the increased inductive effect from the *N*-alkyl group. A general observed shift to lower field by an increasing

Table 10: ^{31}P-NMR chemical shifts of **12e,f,h,i,k,l** along scalar coupling constants and the chemical shift of the P–H hydrogen atom in the ^{1}H-NMR spectrum in C$_6$D$_6$. *in THF-*d*8. **not detected due to signal broadening.

12	e	f	h	i	k	l*
$\delta(^{31}$P$)$ / ppm	144.7	125.6	179.4	169.9	196.4	228.7
$\Delta[\delta(^{31}$P$)($**12–3**$)]$ / ppm	−20.9	−34.9	8.8	0.2	19.7	55.0
$^1J_{\text{Fe,P}}$ / Hz	29.9	32.5	—**	32.4	35.0	39.5
$^1J_{\text{P,H}}$ / Hz	357.1	374.5	382.0	374.6	409.3	432.0
$\delta(^1$H; P–H$)$ / ppm	7.10	7.54	7.36	7.54	8.06	8.67

amount of oxygen in the five-membered ring is in line with the high electronegativity of oxygen and therefore less electron density on phosphorus and, hence, deshielding of the latter. For all compounds but **12h** $^1J_{Fe,P}$ couplings were observed ranging from 29.9 to 39.5 Hz. This scalar coupling also increases with higher oxygen content due to the same effect discussed above and in the tungsten derivatives **6**. As expected, in the ^{31}P-NMR spectra of **12e,f,h,i,k,l** a large direct $^1J_{P,H}$ coupling is observed increasing from **12e** to **12l**. Remarkably, the coupling constants show a difference of ca. 60 Hz compared to their W(CO)$_5$-derivatives **6e,i,k** (for **6f** even ∼100 Hz), suggesting a higher s(P)-orbital contribution in the P–H coupling and hence more p(P)-orbital character in the P–Fe bond than in the P–W bond. In the ^{1}H-NMR spectrum the resonance of the P–H hydrogen atom is also moved to lower fields for higher oxygen content (Table 10), which is expected by the previously discussed observations.

As already discussed, compounds **12e,f,h,i,k** were initially obtained as liquids, however upon standing at −30 °C **12k** crystallises. Therefore, X-ray diffraction analysis of crystals of **12k,l** was performed and the molecular structures of **12k,l** were obtained (Figure 35). Whereas the quality of single crystals of **12l** was good, **12k** showed severe disordering and, hence, does not allow for a detailed structure comparison between **12k** and **12l**, but proofs the assumed connectivity. It should be mentioned, again, that 1,3,2-diheterophosphane complexes with a P–H unit are rare, and **12k,l** are the first iron complexes, which does not allow for comparison with literature-known values. However, the distances between P–O1
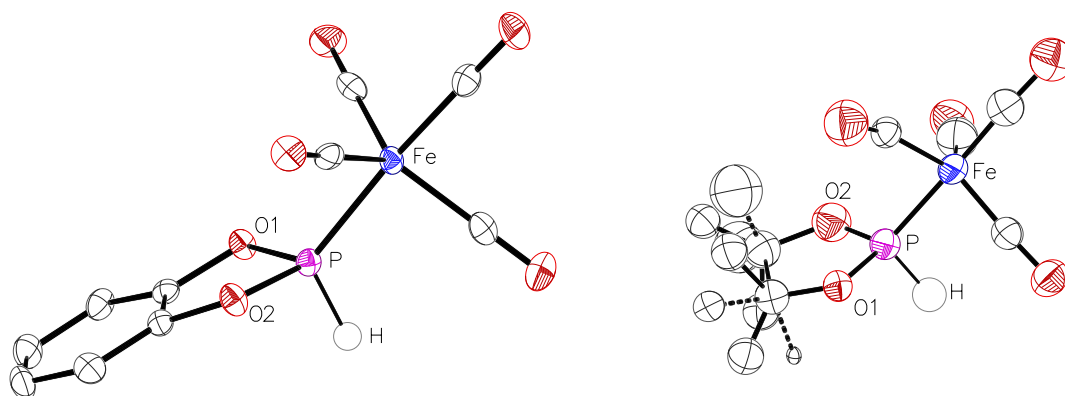
Figure 35: Molecular structures of **12k,l** in the crystal lattice (**12k** right; **12l** left); ellipsoids are set at 50% probability level and all hydrogen atoms, but the P–H, are omitted for clarity besides directly bound to phosphorus. Selected bond lengths and angles of **12l** are given in Å and ° respectively: d(P–Fe) 2.13132(18), d(P–O1) 1.63960(16), d(P–O2) 1.64075(15), ∠(O1-P-O2) 95.889(7), ∠(H-P-Fe) 117.298(4), ∠(O1-P-H) 99.129(4), $\sum_\angle^P$ 297.85; τ_5(Fe) 0.77.

and P–O2 in **12l** are very similar to bond lengths observed in **6k**. A dinuclear iron complex from Shi had also utilised the 1,3,2-dioxaphosphole scaffold as a bridging ligand and the P–O bond lengths, described therein, fit very well to observed distances in **12l**.[122] The iron atom has a τ_5 value of 0.77, which is only slightly larger than that of **15e**.

## 5.3. Synthesis of the first stable aminoxylphosphane iron complex

The successful synthesis of suitable phosphane Fe(CO)$_4$ precursor complexes **12** allowed probing the accessibility of the corresponding aminoxylphosphane complexes **17**. As the attempts to synthesise **17d** showed a low thermal stability of the iron complex, the 1,3,2-dioxaphospholane complex **17l** was targeted initially, as the 1,3,2-dioxaphospholane tungsten complex **8k** possessed higher thermal stability. To prevent decomposition of thermally labile **17l** the deprotonation/oxidation approach was used allowing the potential formation at lower temperatures (Scheme 32). **12l** was deprotonated with ^{n}BuLi in THF at −100 °C and the reaction mixture was analysed by low temperature ^{31}P-NMR spectroscopy at −80 °C. The spectrum showed several resonances, however most prominent was a singlet in the coupled and decoupled mode with a chemical shift of 87.4 ppm (68% by integration) and an AB-type spin system (22%). The latter consisted of two doublets (−49.0 and −58.8 ppm) with a 212 Hz coupling, most probably resulting from a $^1J_{P,P}$ coupling. Another attempt to deprotonated **12l** with substoichiometric amounts of ^{n}BuLi (0.9 eq.) showed a somewhat similar result with a singlet at 92.6 ppm and an AX-type spin system. Chemical shifts and coupling constants are very close to the AX-type spin system observed in the reaction of **15l** with LAH, discussed above in the context of a phosphanyl phosphanides [Li]**22**(Figure 34). However, the highfield-shift and the absence of a $^1J_{P,H}$ suggest that the resonances at 87.4
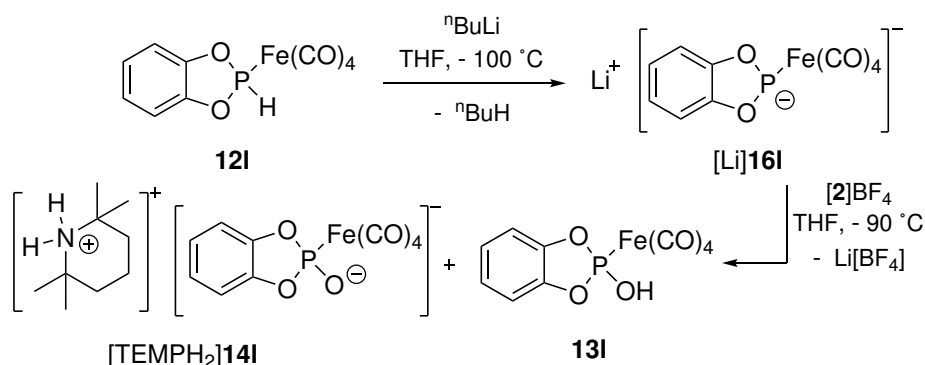
Scheme 32: Attempted synthesis of aminoxylphosphane iron complex **17l** via deprotonation and oxidation of **12l** with ^{n}BuLi and [**2**]BF$_4$.

and 92.6 ppm (differences are assumed to be a concentration effect) arise from the lithium phosphanide complex [Li]**16l**. The full consumption of the starting material **12l**, already at very low temperature, points to a very fast deprotonation. Therefore, deprotonation at −90 °C in THF was repeated, [**2**]BF$_4$ was added after 10 minutes and the reaction followed via *in situ* VT-^{31}P{^{1}H}-NMR spectroscopy (Figure 36). Already at −80 °C a different spectrum is obtained compared to the case without [**2**]BF$_4$. Besides the still present assumed resonance of [Li]**16l**, two other singlets are observed with chemical shifts at 192 ppm and 269 ppm. Additionally, there is an AM-type spin system with chemical shifts of 276 and 181 ppm having a $^1J_{P,P}$ coupling constant of 194 Hz. With increasing temperature
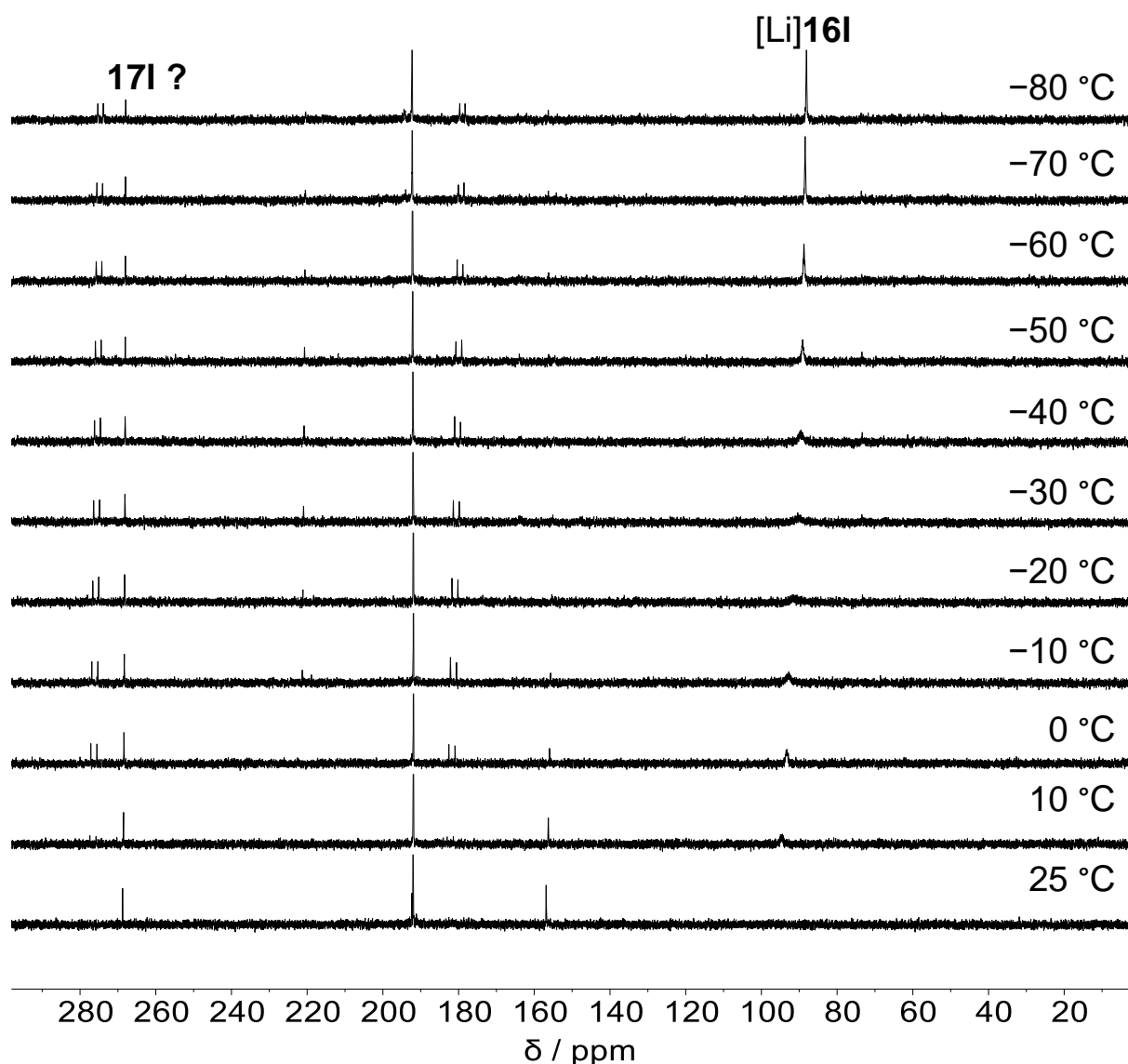
Figure 36: VT-^{31}P{^{1}H}-NMR spectrum of the reaction mixture of [Li]**16l** with [**2**]BF$_4$ in THF.

the resonance of [Li]**16l** is decreasing and, like the AM-type spin system, absent at room temperature. Remaining signals are three singlets with chemical shifts of 276, 192 and 157 ppm (13%, 63% and 24% by integration). The lowfield resonance at 276 ppm might be related to **17l**, however repeating the reaction also led to similar or lower intensity of this signal, and attempts to isolate this compound were unsuccessful. In contrast to the diphenyl derivative **17d** no clean conversion to a single product was observed. Therefore, the reaction with TEMPO was also tested, and here only two signals were observed in the ^{31}P{^{1}H}-NMR spectrum of the reaction mixture at room temperature. Both have been observed before, and their chemical shifts are 192 and 156 ppm (38% and 62%, respectively, by integration). Since both resonances appear at a higher field compared to the starting material and the observed and/or all so far isolated aminoxylphosphane complexes show a lowfield shift, it was assumed that the hydroxyphosphane complex **13l** and its phosphinito salt [TEMPH$_2$]**14l** might have been formed (Scheme 32), somehow analogous to the decomposition of **17d**. Indeed, reaction of the chlorophosphane iron complex **15l** with water in THF initially showed ^{31}P-NMR resonances at 197 and 184 ppm, and after further attempted work-up another resonance at 192 ppm and eventually were completely transformed to a resonance at 153 ppm. This resonance is very close to the already observed ring opening product **23**. Additionally, crystals obtained from this mixture showed to be catechol, corroborating the ring opening and eventually complete cleavage. These findings suggest that **17l** is thermally extremely labile and immediately decomposes to yield **13l** and [TEMPH$_2$]**14l**. An isolation via herein tested methods was not possible.

To check for a possibly stable aminoxylphosphane complex derived from the 1,3,2-diheterophospholane complexes **12e,f,h** the latter were reacted with two equivalents of TEMPO at 0 °C in THF (Scheme 33). Reaction of 1,3,2-oxazaphospholidine complex **12h** showed
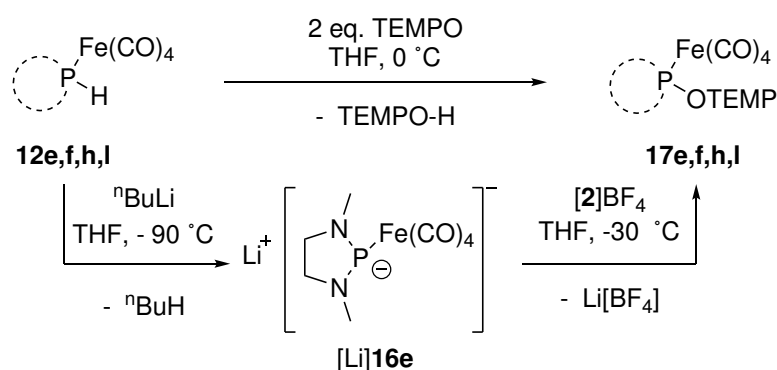
Scheme 33: Attempted synthesis of aminoxylphosphane iron complexes **17e,f,h,l**; additionally, the method via deprotonation followed by oxidation of **12e** with ^{n}BuLi and [**2**]BF$_4$ was examined.

a very clean but slow conversion in the ^{31}P-NMR spectrum to a compound resonating at 178.6 ppm (35% from integration). This is remarkably close to the only other present resonance at 179.1 ppm which was proven to be unreacted starting material through the distinct $^1J_{P,H}$ coupling. It can be assumed that **17h** is resonating at 178.6 ppm despite almost no change in the chemical shift was measured. The latter is remarkable as a significant change in bonding had occurred for the P-atom, but it should be noted that a similar behaviour concerning the chemical shifts of **12h** and **3h** was already observed before (cf. Table 10, p.62). After three hours of further reaction time a ^{31}P{^{1}H}-NMR spectrum was measured and only 10% starting material remained, next to 27% assumed **17h**. The dominant resonance, however, occurs as a singlet at 135 ppm and shows no further coupling. The highfield shift in comparison to the starting material **12h** and assumed **17h** suggest again formation of hydroxyphosphane complex **13h** or the phosphinito complex [TEMPH$_2$]**14h**. However, further reaction time leads to no detectable resonances in the ^{31}P-NMR spectrum. The slow conversion to **17h** even at room temperature mixed with the thermal lability did not allow for the isolation of **17h**. Nevertheless, in comparison to the 1,3,2-dioxaphospholane complex chemistry discussed beforehand, *P*-aminoxyl 1,3,2-oxazaphospholidine complexes such as **17h**, might be in general accessible. An assumed trend towards higher stability with increased nitrogen content in the ring was probed by reacting **12f** with TEMPO. After a reaction time of 10 minutes an NMR sample was prepared and kept at 0 °C. The ^{31}P{^{1}H}-NMR spectrum of this sample showed two major resonances at 106 and 92 ppm (20% and 80%, respectively, by integration). The highfield shift suggests again formation of the corresponding **13f** and [TEMPH$_2$]**14f**. A ^{31}P{^{1}H}-NMR spectrum of the same sample after 1.5 hours showed no resonance at 106 ppm anymore but instead an AM-type spin system with chemical shifts at 151 and 13.7 ppm having a $^2J_{P,P}$ coupling constant of 54.7 Hz. Chemical shifts and the scalar coupling are similar to the phosphinoyl phosphanoxyl tungsten complex **XXIV** (cf. Scheme 10, p.10) from Heurich reported as a decomposition product of **8d**.[67] Hence, it is assumed that herein a phosphinoyl phosphanoxyl iron complex **25f** is formed, however, in only minor amounts (for further discussion: Scheme 35, p.73). The study on the tungsten complexes had shown an increased thermal lability of the diisopropyl derivative **8f** compared to its methyl derivative **8e**. Therefore, **12e** was probed if it might form a reasonable stable aminoxylphosphane complex **17e**. Reaction of **12e** with TEMPO at 0 °C indeed showed a clean conversion to **17e**, according to a ^{31}P{^{1}H}-NMR spectrum obtained from a sample in THF kept at 0 °C. As expected a sharp singlet was observed lowfield-shifted at 165 ppm with a $^1J_{Fe,P}$ coupling constant of 38 Hz. Minor side products are an AM-type spin system (5% estimated by integration) at 158 and 16 ppm with a $^2J_{P,P}$ coupling constant of 60.2 Hz, which is expected to be **25e** (for targeted synthesis: Scheme 35, p.73) and a broad resonance at

120 ppm (4%), which might be hydroxyphosphane **13e** or its phosphinito salt [TEMPH$_2$]**14e**. Further attempts to get a cleaner conversion always showed a similar outcome. However, it was possible to obtain pale yellow single crystals by slowly concentrating the reaction mixture under reduced pressure. X-ray diffraction analysis showed that the assignment to **17e** was correct (Figure 37). The structure is in line with the tungsten derivative of Heurich **8e** and shows in contrast to Heurichs **8d** and in this work presented 1,3,2-diheterophospholane tungsten complexes **8f,i,k** a flipped configuration of the 1,3,2-diazaphospholidine and the TEMPO moiety. Remarkably, the phosphorus nitrogen bonds P–N1 and P–N2 show significantly different lengths but are both longer than in the chlorophosphane complex **15e**. In agreement with an increase in steric bulk of the ligand the P–Fe bond length is also increased compared to **15e**. Furthermore, the pyramidalization of the phosphorus ligand is less pronounced, indicated by an increase in the P-atoms angular sum by $\sim$15°. Despite this, the configuration of the Fe(CO)$_4$ fragment tends to adopt a more trigonal bipyramidal structure as seen by the change in the τ_5 value, which is close to 1. Purification was initially attempted by extensive drying *in vacuo* (high vacuum, 10^{-5} mbar) after extraction with *n*-pentane to remove TEMPO–H. However, at lower temperatures (-10 - 0 °C) it was not possible to remove TEMPO–H effectively. Upon warming up the dry reaction mixture a
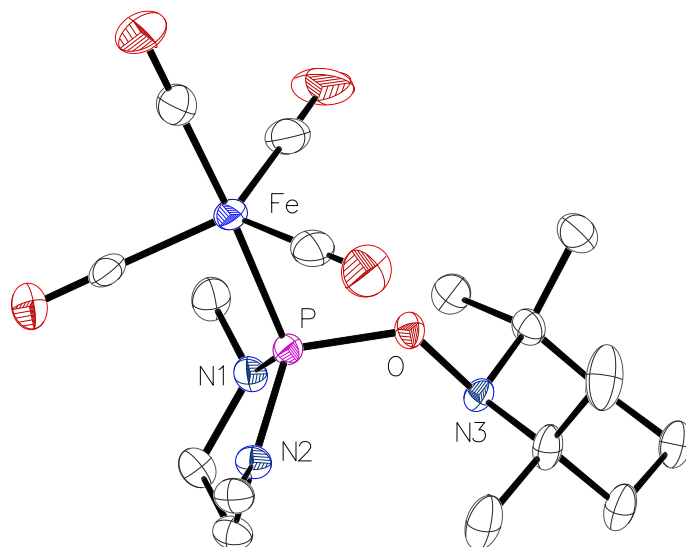

Figure 37: Molecular structure of **17e** in the crystal structure; ellipsoids are set at 50% probability level and all hydrogen atoms are omitted for clarity. Selected bond lengths and angles are given in Å and ° respectively: d(P–O) 1.63059(15), d(P–Fe) 2.20917(17), d(P–N1) 1.67596(13), d(P–N2) 1.64850(13), d(O–N3) 1.48887(12), $\angle$(N1-P-N2) 92.959(6), $\angle$(O-P-Fe) 102.399(7), $\angle$(N1-P-O) 108.890(6), $\angle$(N3-O-P-Fe) 7.6211(8), $\sum_{\angle}^{P}$ 316.114; τ_5(Fe) 0.91.
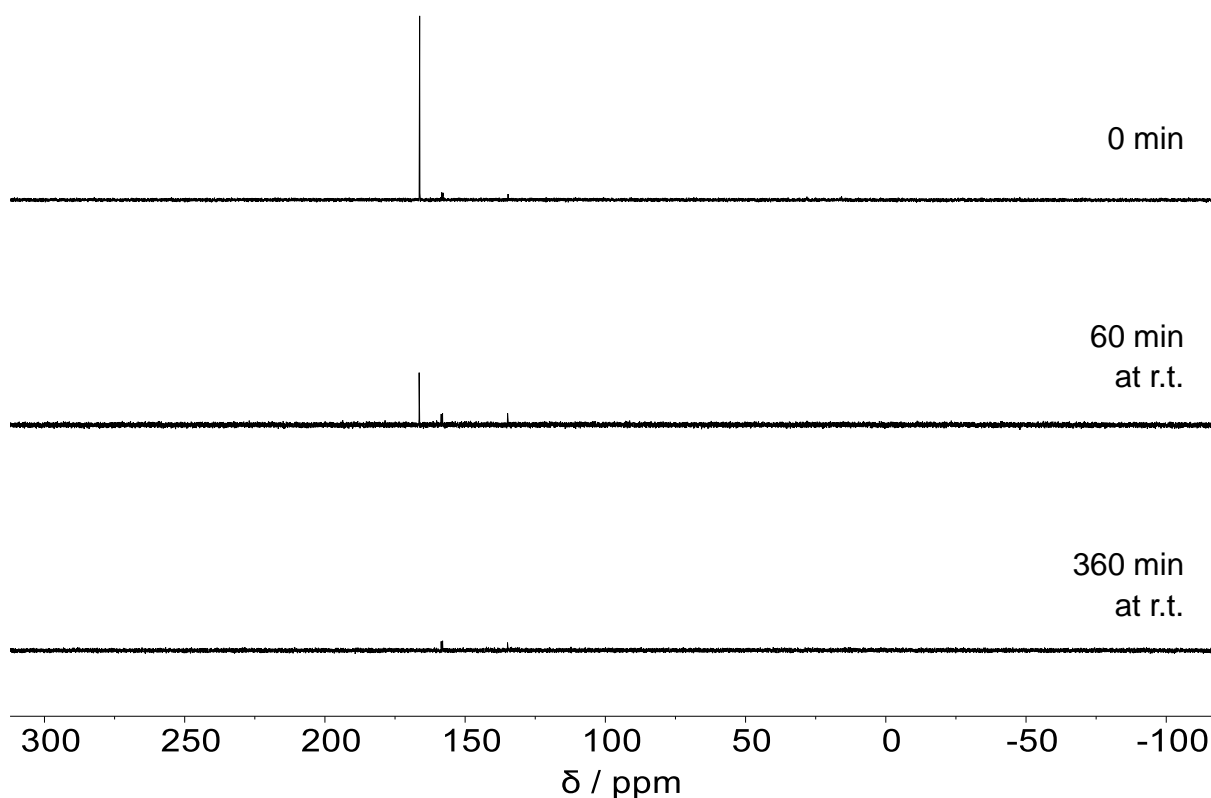
Figure 38: $^{31}P\{^1H\}$-NMR spectrum of the aminoxylphosphane complex **17e** over time at room temperature in THF-d8.

colour change from yellow to dark red was observed. A $^{31}P\{^1H\}$-NMR spectrum in THF of the residue showed no resonances. Therefore, the reaction was repeated and monitored by $^{31}P\{^1H\}$-NMR spectroscopy while warming up (Figure 38). In this case the before mentioned minor side products at 158 and 135 ppm were observed, next to the resonance of **17e**. Already after one hour the intensity of the signal of **17e** was reduced significantly compared to the impurities, without the appearance of any other resonance. After further five hours only the resonances of the impurities were detected. A comparison of the signal to noise ratio showed that the intensity of the other two resonances did not change over time. Remarkably, a similar observation is made in the ^1H-NMR spectrum (THF-d8) (Figure 39). In this case all resonances connected with the 1,3,2-diazaphospholidine moiety of **17e** (2.8 to 3.7 ppm; framed by THF residual resonances) are vanishing. On the other side, changes occur in the highfield region, 1.0 to 1.6 ppm, in which the TEMPO moiety resonances were observed initially. Upon standing, resonances connected to TEMP–H are observed, similar to what was obtained in the thermolysis of **8i**. Similar observations were made if **17e** was synthesised from initial deprotonation of **12e** with subsequent oxidation via [**2**]BF$_4$ at lower
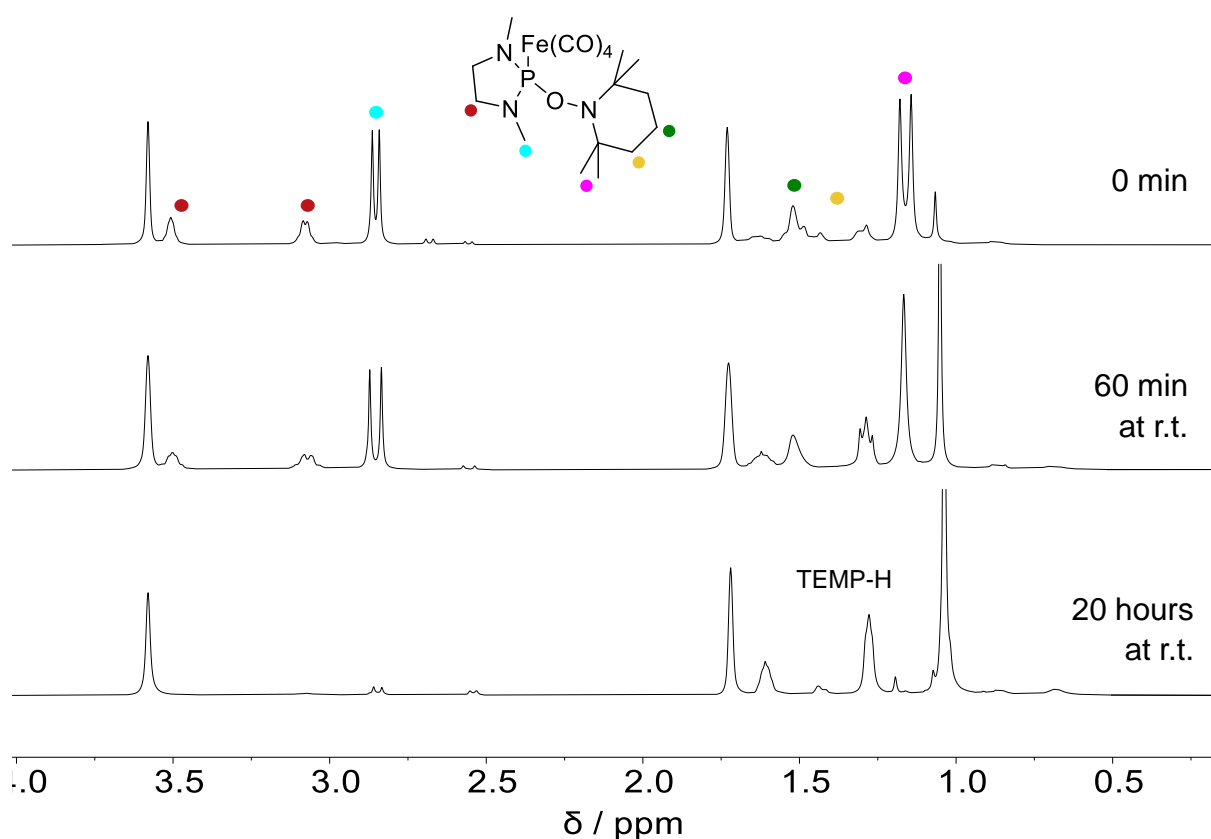
**Figure 39:** ^{1}H-NMR spectrum of the aminoxylphosphane complex **17e** over time at room temperature in THF-d8.

temperatures, ca. $-30\ ^{\circ}$C. This method promised a better separation in the purification process as the product can be simply extracted from the residue and separated from the formed Li[BF$_4$]. However, in these cases, besides the product **17e** only another resonance at 188 ppm in roughly 10% was always observed. Work-up via column chromatography under inert atmosphere and low temperatures (solid phase and receiving flasks) allowed to isolate small amounts of an NMR-pure sample of **17e**. The latter showed the same behaviour at room temperature as the previously discussed mixtures. The presence of TEMP–H suggested N–O bond cleavage and therefore formation of phosphanoxyl complex **18e** (Scheme 36, p.74). Infrared spectra for **12e** and a room temperature warm solution of **17e** show a shift of the the ν(C–O) carbonyl vibration from 1980 cm^{-1} and 1944 cm^{-1} to 2040 cm^{-1} and a very broad signal ranging from 1946-1910 cm^{-1}. The absence of any further reaction products and no precipitation suggested initially a persistent radical species, therefore, EPR and other experiments were performed and will be discussed individually in one of the next chapters.

5.4. Chemistry of the P-OTEMP iron complex 17e

Attempts to trap a potentially persistent radical with commonly used reagents, such as H-donors, like $^nBu_3SnH$ and cyclohexadiene[123] resulted in no observable changes in the mixture. Radical heterocoupling with the Gomberg radical **I** was also unsuccessful. This is in stark contrast to the reactivity of the transient phosphanoxyl tungsten complexes **11d,e**.[63] However, if a solution of **17e**, after warming to room temperature, was treated with **XXXIX** (c.f. Scheme 29, p.59) a weak signal in the $^{31}P\{^1H\}$-NMR spectrum was observed at 151 ppm suggesting successful reduction to **24e** (Scheme 34). In the attempt to isolate the compound via extraction, formation of a side product in minor amounts was observed. The AM-type spin system of this side product had been previously observed and assigned to the phosphinoyl phosphane complex **25e**. Therefore, the reaction was repeated with a fresh cold solution of **17e** in THF to which **XXXIX** was added. In this a mixture of **17e**, **25e** and **24e** was observed and separation proofed to be not possible. To simplify the reaction straightforward reduction was attempted by the addition of $CoCp_2$ to **17e**. In this case a clean conversion to $[CoCp_2]$**14e** was observed after stirring overnight, which could be isolated and purified by simple washing with Et_2O and n-pentane in 60% yield. The ^{31}P-NMR spectrum of $[CoCp_2]$**14e** in MeCN-$d3$ consists of a single resonance with a chemical shift of 110 ppm with a $^3J_{P,H}$ scalar coupling. The ^1H-NMR spectrum shows two multiplets for the CH_2 resonances in the backbone of the 1,3,2-diazaphospholidine and the doublet of the N-CH_3 groups. These resonances appear in a 1:1 ratio with the Cp signal at 5.7 ppm. Diffusion of n-pentane into a DCM solution of $[CoCp_2]$**14e** initiated crystallisation, from which single crystals could be obtained. X-ray diffraction corroborated the assumed
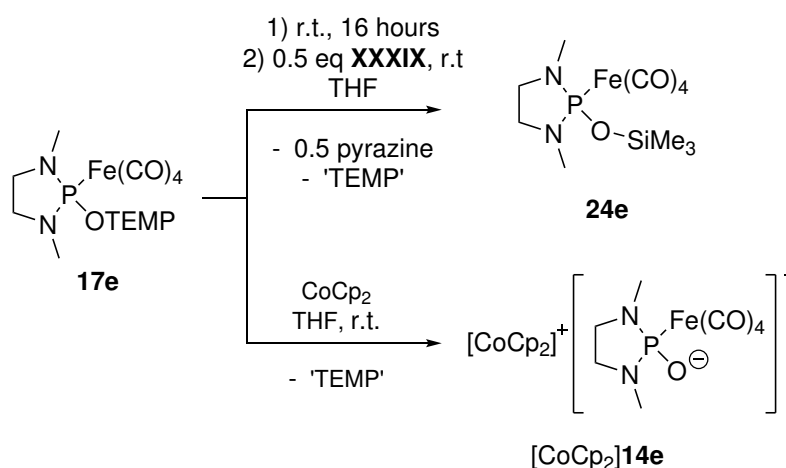
Scheme 34: Synthesis of siloxyphosphane complex **24e** and phosphinito salt $[CoCp_2]$**14e** via reduction of **17e**.
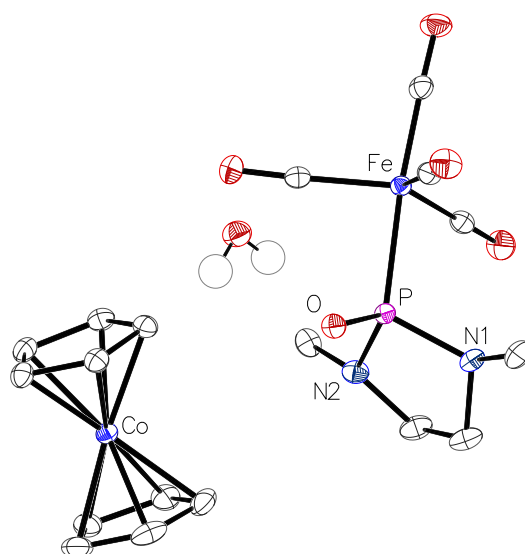
Figure 40: Molecular structure of [CoCp$_2$]**14e** in the crystal structure; ellipsoids are set at 50% probability level and all hydrogen atoms, exceptional for H$_2$O, are omitted for clarity. Selected bond lengths and angles are given in Å and ° respectively: d(P–O) 1.51716(4), d(P–Fe) 2.26487(6), d(P–N1) 1.69834(4), d(P–N2) 1.69936(4), ∡(N1-P-N2) 91.984(3), ∡(O-P-Fe) 113.035, ∡(N1-P-O) 112.924, $\sum_{\angle}^{P}$ 315.283; τ_5(Fe) 0.83.

structure and verified formation of [CoCp$_2$]**14e** (Figure 40). Remarkably, despite that all post reaction transformations were carried out in a glove box, one equivalent of water was found in the crystal lattice. In the 1,3,2-diazaphospholidine moiety of the anion **14e** P–N bond lengths are elongated in comparison to its precursor **17e** and the N-P-N bond angle is slightly smaller. The Fe–P bond is longer and the is O-P-Fe angle increased. Remarkably, the exocyclic P–O bond is significantly shortened which was unexpected. DFT calculations of the anion **14e** yield an MBO of 1.81 (compared to MBO(**17e**): 1.08) suggesting significant multi bond character. These findings are not expected for a phosphinito structure and, therefore, Loewdin charges of **14e** and **17e** were compared to locate the charge in **14e** (Table 11). The most significant changes are observed for the P-atom (0.196 e) and the exocyclic O-atom (0.356 e), some charge can also be found on the nitrogen atoms (0.03 e) and the Fe(CO)$_4$ only takes up 0.05 e of the negative charge. Therefore, the charge analy-

Table 11: Loewdin partial charges in e of **17e** and **14e** for selected atoms. Average values are given for atoms, which appear more than once in the molecule.

	P	O^{exo}	N	Fe	C^{CO}	O^{CO}
17e	0.221	0.253	0.290	−1.769	−0.199	0.435
14e	0.025	−0.103	0.260	−1.776	−0.216	0.403

sis is as expected for a phosphinito complex, like **14e** and does not explain the short P–O bond distance.

The successful isolation of the phosphinito salt [CoCp$_2$]**14e** allowed access to several other previously observed compounds, as it is the nucleophilic synthon of the phosphanoxyl complex **18e**. Initially the synthesis of **24e** was targeted by reacting [CoCp$_2$]**14e** with Me$_3$SiCl in Et$_2$O (Scheme 35). The reaction converged cleanly to a product observed in the ^{31}P{^{1}H}-NMR spectrum with a chemical shift of 147.8 ppm in MeCN-*d*3. This product was isolated by simple filtration and extraction with *n*-pentane in 87% yield as a yellow oil, which darkens over time. Multinuclei NMR experiments, especially ^{29}Si(dept20), proved that the obtained product is the siloxyphosphane iron complex **24e**, after comparison with related P-O-Si motif containing complexes.[124] [CoCp$_2$]**14e** was further used in the reaction with the 2-chloro-1,3,2-diazaphospholidine oxide **26e** to prove the postulated formation of **25e** in previously discussed reactions. A mixture of [CoCp$_2$]**14e** and **26e** in MeCN-*d*3 initially did not react at room temperature. After stirring overnight at 70 °C the ^{31}P{^{1}H}-NMR spectrum of the reaction mixture showed a clean conversion to exactly the AM-type spin system previously assigned to **25e**, with chemical shifts of 158.1 and 15.8 ppm and a scalar $^2J_{P,P}$ coupling of 62 Hz. This proofs that under certain conditions **25e** (and derivatives, *e.g.*, **25f**) is formed in the synthesis and as decomposition products of **17e** (or attempted derivatives, *e.g.*, **17f**), in analogy to the reactivity observed in the tungsten complexes **XIX** from Heurich.
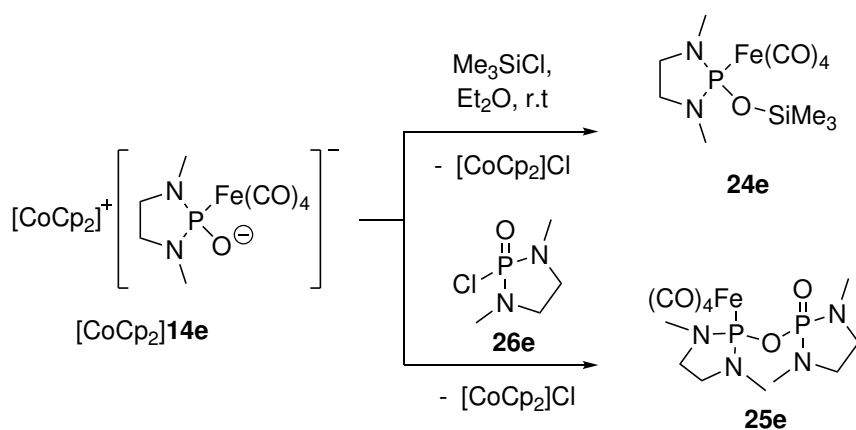

Scheme 35: Synthesis of siloxyphosphane complex **24e** and phosphinoyl phosphane complex **25e** via nucleophilic substitution reactions with [CoCp$_2$]**14**.

73

5.5. Considering a potential persistent iron phosphanoxyl complex

5.5.1. Theoretical assessment

As a lot of phosphorus-centred radicals are usually highly reactive and are rarely isolated, electron paramagnetic spectroscopy (EPR) is a suitable tool to learn about the electronic structure of such species in (frozen) solution. In the context of phosphanoxyl complex chemistry several aspects have to be considered. For the tungsten complexes theory showed a partially delocalised electron spin density over the W-P-O atoms as discussed previously. Therefore, an EPR spectrum of phosphanoxyl complexes could have major contribution from main group element, *e.g.*, phosphorus, oxygen and also metal contribution. This has already been proven to make the interpretation of the EPR spectrum of the transient phosphanoxyl tungsten complex **11d** difficult.[65] Different phosphinoyl radicals **1** have been investigated, g values for these species are reported to be close to 2, *e.g.*, for **1d** a value of 2.0036 was observed.[36,37,76] This is typical for most organic radicals, as spin orbit coupling (SOC) is negligible small. SOC would lead to significant deviation of the observed g value from the g_e value, the value obtained for the free electron. In the case of the metal centre, and especially for iron chemistry SOC has to be taken into account, however depending on the electronic environment, *i.e.*, oxidation state and coordination sphere of the iron atom.[125] The previously discussed observation initially suggested formation of a phosphanoxyl iron complex **18e**, via N-O bond cleavage (Scheme 36). As a starting point the phosphanoxyl iron complex **18e** was computed via DFT. In the calculated neutral doublet minimum structure several features are noteworthy (Figure 41). Firstly, a very short P–O bond, 1.51102 Å compared to the precursor **17e** is found. This is accompanied with an MBO of 1.83 indicating a high double bond character; other bond lengths and angles of the 1,3,2-diazaphospholidine ligand are remarkably unaffected. The Fe–P bond is slightly elongated, which is in line with a decreased MBO (**18e**: 0.79; **17e**: 0.87). Secondly and most surprising, the coordination sphere of the iron atom changed, now adopting a struc-
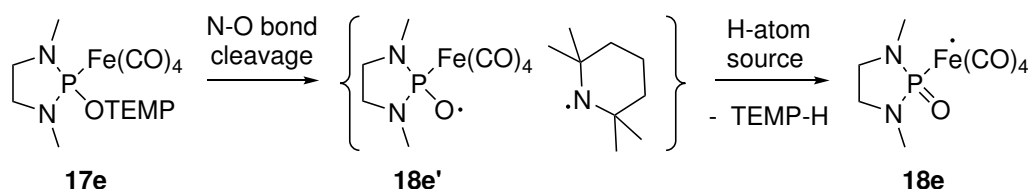

Scheme 36: Assumed formation of phosphanoxyl iron complex **18e** through thermal induced N–O bond cleavage and the structurally unrelaxed cleavage product **18e'**.
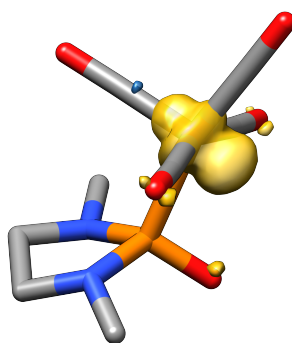
Figure 41: Computed structure of **18e** and its spin density distribution (yellow); all hydrogen atoms are omitted for clarity. Selected bond lengths and angles are given in Å and ° respectively: d(P–O) 1.51102, d(P–Fe) 2.32437, d(P–N1) 1.68633, d(P–N2) 1.68466, $\angle$(N1-P-N2) 92.916, $\angle$(O-P-Fe) 102.450, $\angle$(N1-P-O) 115.834, $\sum_{\angle}^{P}$ 325.157; τ_5(Fe) 0.08. Loewdin spin density on selected atoms in e: Fe 0.97, P -0.01, O 0.02, N 0.01.

ture close to square pyramidal with a τ_5 of 0.08. Spin density distribution analysis showed strong localisation of spin density on the iron atom. The calculations showed further that spin density is mostly found in the $3d$(Fe)- and $4p$(Fe)-orbitals, 85% and 11% respectively. Qualitatively the electron resides in a stereochemically active orbital *cis* to the P-ligand and occupies the open coordination side in the adopted pseudo-octahedral conformation around the iron atom. This is in contrast to the results found for the phosphanoxyl tungsten complexes **11e**. It was therefore tested if a potential structurally unrelaxed phosphanoxyl iron complex **18e'**, having bond lengths and angles like in **17e** also features the iron-centred radical (Figure 42). Indeed, **18e'**, despite having a trigonal bipyramidal coordinated iron atom shows an almost pure iron radical, compared to the phosphanoxyl tungsten complex **11e**, in
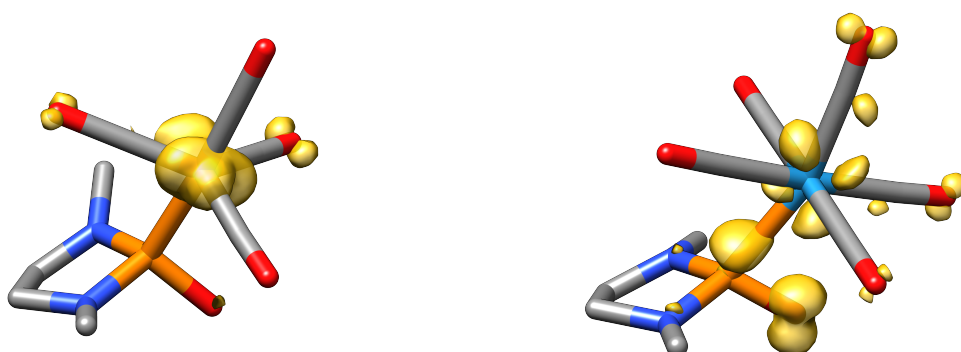
Figure 42: Computed structure of **18e'** (left) and **11e** (right). Spin density distribution given in yellow; all hydrogen atoms are omitted for clarity.

75

which the spin density is much more delocalised. Loewdin spin density distribution of **18e'** is only slightly reduced on the iron atom to 0.92 e, changes on other atoms are negligible small. However, the reorganisation from **18e'** to **18e** amounts to significant 29.9 kcal mol^{-1}.

The bonding between iron and phosphorus was unclear in the means of having a two centre two electron (2c2e)- or a two centre one electron-(2c1e) bond[126] (Figure 43, top). To resolve this the bonding was analysed by FMO analysis. Remarkably, in normal unrestricted (UKS) DFT calculations the *h*-SOMO does not represent the spin density but the formal P-lone pair coordinating to the Fe(CO)$_4$ having only small orbital coefficients on the Fe-atom. Other lower lying MOs show more metal orbital contribution, but are significantly mixed with orbitals of the 1,3,2-diazaphospholidine moiety. This can be explained by a strong interaction and stabilisation of the MO in which the unpaired electron is smeared over several lower lying MOs. To extract the pure expected *h*-SOMO, quasi restricted orbital (QRO) calculations were performed. From these it was possible to obtain the *h*-SOMO which is Fe-centred and shows some backbonding into the π*(CO) orbitals in *cis*-position to the P-ligand (Figure 43, bottom). Furthermore, the calculations revealed that there are two filled SOMOs (α and β) with the same symmetry for a P–Fe bond and, hence, the bond is best described as a 2c2e
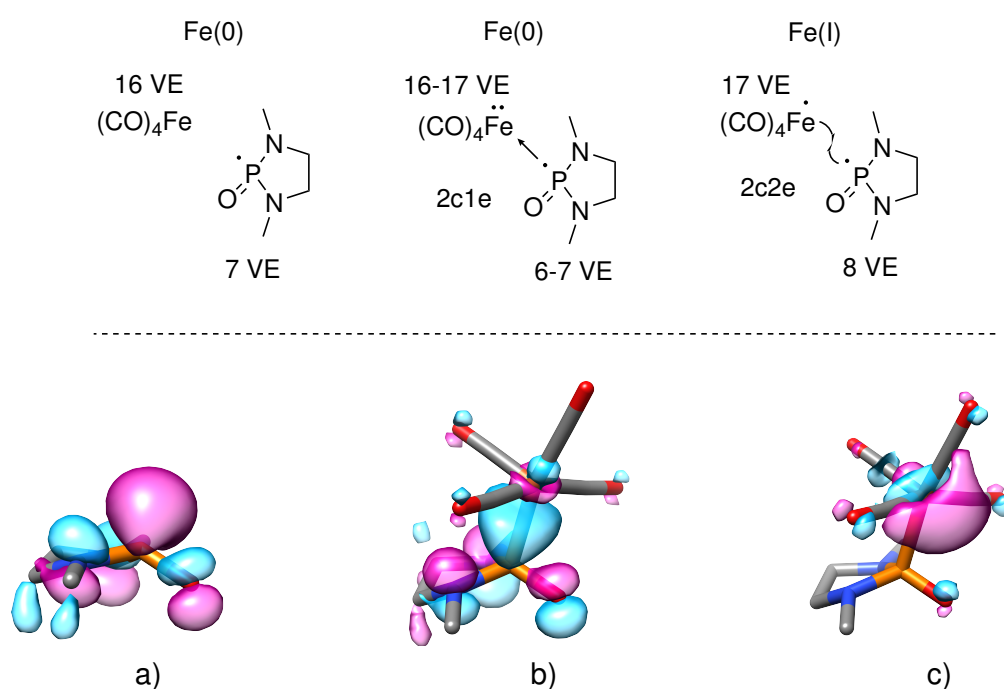
Figure 43: Computed structure of phosphinoyl radical **1e** and *h*-SOMO (bottom, a), phosphanoxyl complex **18e** (QR-KS orbitals) calculations for highest doubly occupied MO (bottom, b) and *h*-SOMO (bottom, c). Lewis fragments, valence electron (VE) number of P and Fe and formal Fe oxidation state in the cases of no interaction (top, left), 2c1e bond (top, middle) and 2c2e bond (top, right).

bond. According to Pauling the element phosphorus is more electronegative than iron and therefore the iron atom is best described to be in the oxidation state +I in **18e**. As a consequence, the phosphorus atom is in the oxidation state +V, in comparison to **17e**, in which the Fe atom was in the oxidation state 0 and phosphorus was +III. From these calculations it can be assumed that **18e** is mostly a metal-centred radical and shows only small or no features of an organic radical.

5.5.2. EPR experiments

For the EPR experiment a solution of **17e** in toluene , obtained from the reaction of **12e** with TEMPO and dried intensively *in vacuo* at 0 °C before redissolving, was allowed to warm to room temperature and was subsequently analysed by continuous wave (CW) X-band EPR spectroscopy. Initially the spectrum was recorded at ambient temperatures and showed no significant resonance, besides a negligible amount of a triplet (1:1:1 intensity) typical for aminoxyl radicals **2**, suggesting a minor contamination with TEMPO. Therefore, the temperature was lowered and spectra were recorded at 200, 170, 150, 120 and 100 K (Figure 44). While at 200 K no significant resonance was observed, a very broad resonance was observed at lower fields at 170 K. At 150 K the signals intensity had significantly increased and two components were resolved. The first peak appears broad at 1054 G (g: 6.40), the second peak with higher intensity resonates at a field of 1580 G (g: 4.27) with a peak-to-peak distance of 94 G. This pattern suggests a rhombic environment for the corresponding spin, however the third peak, expected at higher fields was, if present, not resolved. At lower temperatures the signal was more resolved and showed an additional peak at very low fields, 732 G (g: 9.22), and a shoulder of the central peak at 1388 G (g: 4.86) and a broadening of the signal at 1771 G (g: 3.80).

These g values show significant deviation from the free electron g value g_e and suggest an expected metal centred radical with relative high SOC. Only recently Krossing et al. were able to isolate the $[FeCO_5]^{+\cdot}$ radical cation in the presence of a very bulky weakly coordinating anion.[127] Noteworthy, the iron atom adopts a square pyramidal coordination with a reported τ_5 of 0.05 which is very close to the calculated structure of **18e**. DFT calculations done in this thesis on the $[FeCO_5]^{+\cdot}$ in a doublet state yield a spin density of 0.92 e on the iron atom, which is of the same magnitude as in **18e** and **18e'**. EPR experiments done by Krossing showed a rhombic g-tensor with g = 2.011, 2.059, 2.080. Similar values were also observed by others for square pyramidal tricarbonyl diphosphane

and monocarbonyl tetraphosphane iron(I) complexes[128] along ^{31}P-hyperfine coupling, which is not resolved in the recorded spectrum of spectrum from **17e**. Considering Fe in the oxidation state +I and therefore a d^7-electron configuration such a g-tensor can be expected as several other d^7-system, *e.g.*, Co^{2+} complexes, show similar EPR values.[129–131] These complexes have almost no SOC and are therefore very close to g_e which is in strong contrast to the EPR spectrum obtained for the assumed radical **18e**. However, the values obtained in the experimental spectrum of warmed up **17e** are very similar to values found for several high spin Fe(III) complexes.[132–134] Remarkably, the additional features only observed at lower temperatures (Figure 44) have been discussed in the literature and arise due to an intermediate rhombic character, instead of a pure rhombic character of the paramagnetic species.[134]
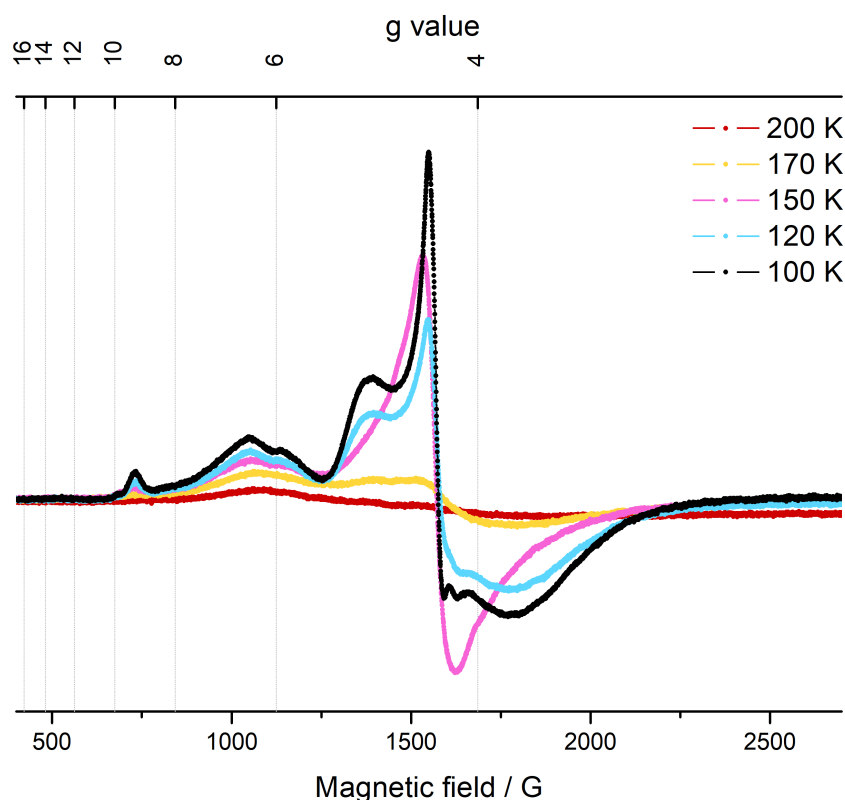
Figure 44: X-band CW-EPR spectrum of a frozen solution of previously warmed to room temperature **17e** in toluene at different temperatures. Every spectrum was averaged over 5 scans, 4 G mod. Amp., 10 dB.

78

5.5.3. ^{57}Fe-Mößbauer experiments

Apparently, after the N–O bond cleavage further oxidation of **18e** occurs. To validate the oxidation state of the Fe atom in the starting complex **17e** and its decomposition products in the mixture Mößbauer spectroscopy was performed in cooperation with Bill from the 'Max-Plank Institut für Energiekonversion' in Mühlheim an der Ruhr. For this freshly prepared and via column chromatography purified **17e** was dissolved in toluene. One part of the yellow solution was immediately added to a Mößbauer sample holder and a X-band EPR tube and frozen in liquid nitrogen. After one hour the remaining solution had turned dark red and an EPR and Mößbauer sample were taken and prepared in the same way, a second EPR sample was taken after 24 hours. All samples were submerged in liquid nitrogen until the measurement was performed. CW X-band EPR spectra of the freshly prepared solution were recorded at 10 and 30 K and reproduced the previously observed EPR spectrum, however in very low intensity. As no resonance at all was expected from this sample, it shows
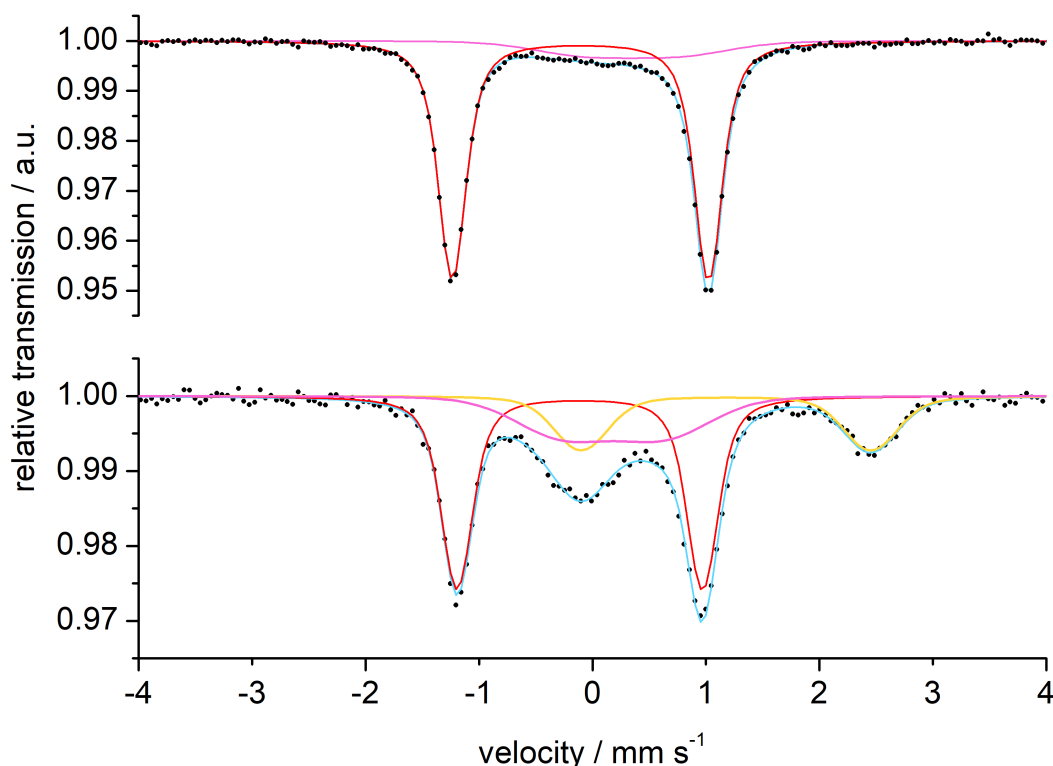

Figure 45: Zero field Mößbauer spectra at 80 K of toluene solution of **17e** (top: directly taken; bottom: one hour at room temperature). Black: Exp. Data; Blue: sum of simulations; Red, yellow, pink: component simulation.

how temperature sensitive **17e** is and it assumingly decomposed partially during purification or sample preparation. Zero-field Mößbauer measurements at 80 K were performed on this sample and predominantly one doublet (86%) was observed with a quadrupole splitting ΔE_q of 2.26 mm s^{-1} and an isomeric shift δ of -0.11 mm s^{-1} (Figure 45). These values are similar to Mößbauer parameters found for $Fe(CO)_5$ ($\Delta E_q = 2.57$; $\delta = -0.085$)[135] or phosphane $Fe(CO)_4$ complexes, *e.g.*, $Fe(CO)_4(P^tBu_3)$ ($\Delta E_q = 2.82$; $\delta = -0.30$)[136] or $Fe(CO)_4(PPh_3)$ ($\Delta E_q = 2.54$; $\delta = -0.31$)[137] and therefore can be assigned to **17e**. This is corroborated further by magnetic Mößbauer measurements done at 0.5 and 1 T at 1.8 K showing that the observed doublet originates from a diamagnetic species. These measurements however also reveal, that the other visible broad signal (14%) with an isomeric shift δ of 0.3 mm s^{-1} originates most probably from iron oxide nanoparticles, which yield different signals depending on composition and size.[138–140] The signal observed here fits well to small nanoparticles ($\sim$5 nm).[141] The EPR spectrum of the 'aged' sample, taken after one hour at room temperature showed one resonance with a g value of 4.3, broader features as previously observed are not detected. The spectrum of the sample taken after 24 hours, however, differed dramatically from the previously recorded, showing broad resonances beyond a g value of 6 (Figure 46). This region can often contain resonances of non-Kramer systems, which have an integer total spin.[142] Measurements were repeated in parallel-mode, which is used to detect resonances from only integer spin system, while
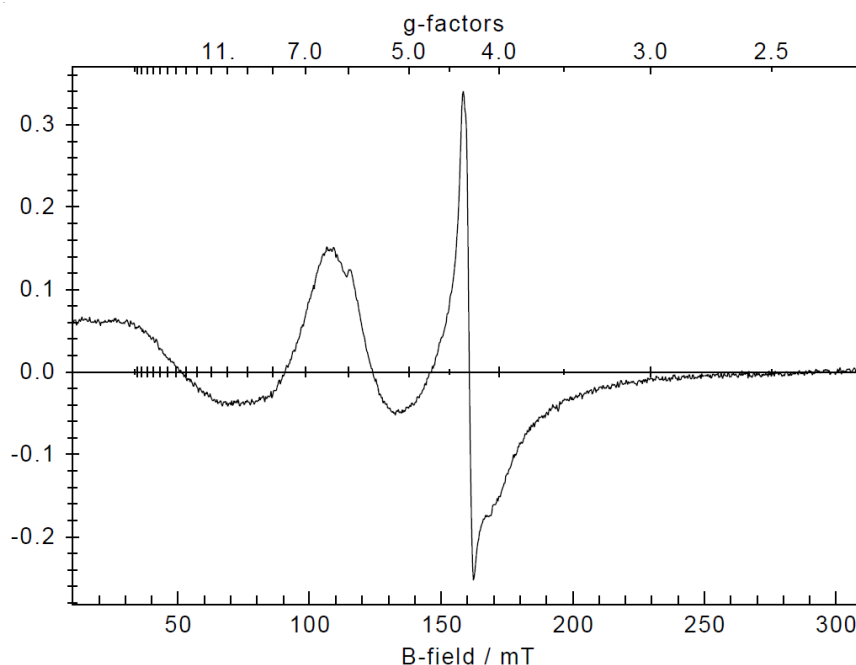
Figure 46: CW X-band EPR spectra of an 'aged' (24 hours at room temperature) solution of **17e** in toluene at 10 K measured in normal mode.
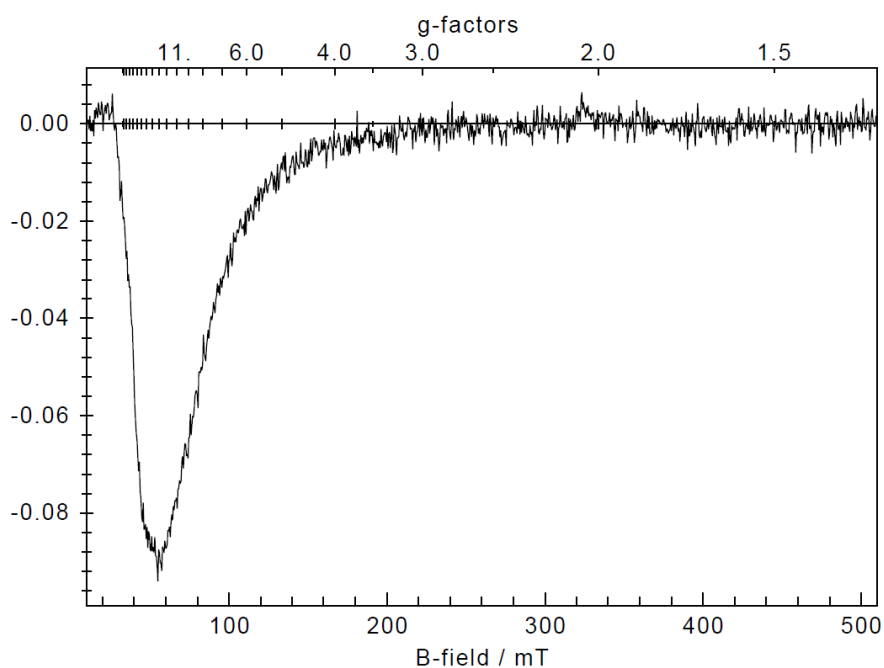
Figure 47: CW X-band EPR spectra of an 'aged' (24 hours at room temperature) solution of **17e** in toluene at 10 K measured in parallel mode.

not exciting any non-integer systems. Indeed, a strong and broad resonance was observed at low fields ($\sim$590 G; g value: $\sim$13), while the previously observed signal at a g value of 4.3 was bleached (Figure 47).[142,143] This is in line with the zero-field Mößbauer spectrum recorded for the one hour 'aged' sample (Figure 45, bottom), in which besides the doublet of **17e** and the assumed nanoparticles signals another doublet is observed. The isomeric shift δ of this signal is -1.18 mm s^{-1} and its quadrupole splitting ΔE_q of 2.55 mm s^{-1} are commonly found in Fe(II) compounds.[144–146] This doublet and the signal of **17e** are roughly in a 1:1 ratio, suggesting 50% conversion. The intensity of the nanoparticle signal is almost unchanged.

5.5.4. Attempt to electrochemical access a P–O containing radical complex

The isolation of the cobaltocenium phosphinito salt [CoCp$_2$]**14e** allowed access to the phosphanoxyl complex **18e** via CV. Therefore, a cyclic voltammogram of a 1 mM solution of [CoCp$_2$]**14e** in a 0.2 M [nBu$_4$N]PF$_6$ THF solution was recorded (Figure 48). The cobaltocenium ion allowed internal referencing to the oxidation potential of Fc/Fc$^+$. As expected, an oxidation event was observed at -255 mV followed by a second oxidation at -110 mV. No return wave was observed, even upon attempted isolation of the first oxidation process. Noteworthy, in scans with a lower voltage limit the oxidation appeared shifted at -310 mV. The initial oxidation is assigned to the formation of **18e**. However, the described observations show that **18e** is not stable under CV conditions at room temperature, even on the CV timescale (50-2000 mV s^{-1}). In the CV experiments **18e** is easily oxidised further, which is in very good agreement with the evidence of Fe in the oxidation states +II and +III, from Mößbauer and EPR spectroscopy. Furthermore, it shows that the presence of *in situ* formed
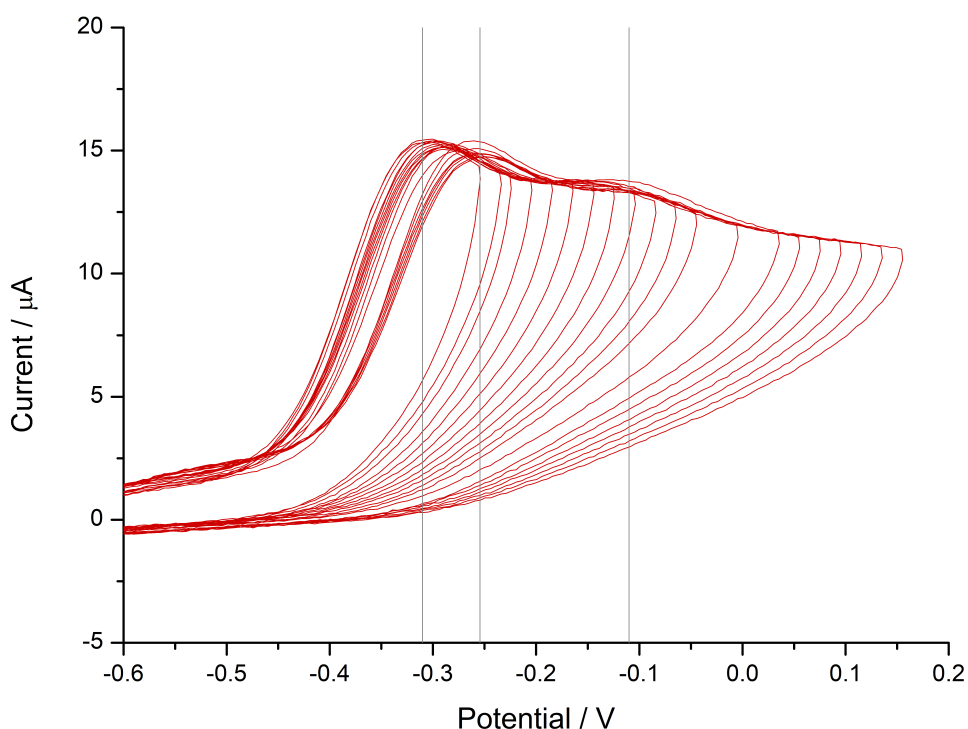

Figure 48: Zoom of the cyclic voltammogram on the oxidative region of [CoCp$_2$]**14e** in THF with different upper scan limits, (scan rate: 200 mV s^{-1}, 0.2 M [nBu$_4$N]PF$_6$, vs. Fc/Fc$^+$ oxidation potential).

TEMP-H in the thermal decomposition of **17e** is not a necessarily factor for the instability of **18e** as it was absent in these electrochemical experiments. While the oxidation process in solution via thermal N–O bond cleavage is unknown, a simple theoretical oxidation product **27** was investigated via DFT (Figure 49). Remarkably, the obtained minimum structure was, regardless of the input structure, always the oxaphosphaferrirane iron(II) complex **27** (the applied nomenclature suggests a three-membered ring, which is discussed in the following). In this unknown structural motif the iron is pseudo-trigonal bipyramidal coordinated,

Figure 49: Lewis formula of the theoretical cationic formal oxaphosphaferriran **27** and its calculated molecular structure and FMO: a) HOMO, b) LUMO, c) HOMO−4 and d) HOMO−10. Selected bond lengths and angles are given in Å and ° respectively: d(P–O) 1.54815, d(P–Fe) 2.22465, d(P–N1) 1.65866, d(P–N2) 1.63573, ∠(N1-P-N2) 96.429, ∠(O-P-Fe) 64.472, ∠(O-Fe-P) 41.891, ∠(N1-P-O) 121.508, $\sum_{\angle}^{P}$ 336.256.

in which one coordination side is bound in a side-on type to the P–O bond. This is in line with a significantly elongated P–O bond distance of 1.548 Å and a MBO(P-O) of 1.48. In contrast the Fe–P bond of **27** is shortened compared to **18e** and similiar to that of **17e**. While the chemistry of side-on coordination iron complexes is well known for alkenes and alkynes,[147,148] side on complexes of heteroatomic π-bonds are scarcely known, *e.g.*, phosphaalkene,[149–151] diphosphenes[152] and a formaldehyde side-on iron complex.[153,154] This coordination mode in **27** is well represented by the HOMO−10. The Fe–P bond can be expressed by two FMOs, the HOMO and HOMO−4, being ligand-centred (HOMO) and metal centred (HOMO−4). Noteworthy, the HOMO−4 qualitative resembles a slipped bond previously discussed in the bent phosphanyl tungsten complexes **9** (cf. Figure 22, p.41). The LUMO of **27** is dominated by the antibonding character of the Fe–O bond. Despite the appearance of significant bonding between Fe and O in the HOMO−10, the MBO of 0.52 suggest only a weak interaction. These results can also be interpreted as a type of coordinative bonding between the negatively polarised oxygen atom and the positively polarised iron atom, represented by the acyclic structure. The atom in molecules (AIM) analysis by Bader shows no bond critical point between iron and oxygen, neither a ring critical point is found for the Fe-P-O three-membered cycle in **27** (Figure 50), the latter has been previously observed for side-on complexes to highly polarised π-bonds and does not necessarily exclude a three-membered ring binding mode.[155–157] This is further supported by the Fe–O distance of 2.092 Å in **27** compared with a proven side-on bound iron formaldehyde complex with a Fe–O bond length of 2.00(1) Å reported by Berke.[153] Furthermore, the reported C-Fe-O bond angle (38.2°) is very similar to the found P-Fe-C angle in the calculated structure of **27**. Commonly only one bond critical point is observed between the metal and the more electropositive element, which fits to the discussed side on complex **27**.

In summary, initial phosphanoxyl iron complexes **18** formation is likely to occur from thermal N–O bond cleavage of aminoxylphosphane iron complexes **17**. In contrast to the tungsten analogues **11**, the spin density is located on the iron atom instead of being shared over the metal, phosphorus and oxygen atoms. While the tungsten complexes can be trapped suggesting a fairly long-life time of **11d,e** the faith of **18e**, generated in the CV, suggest a very short life time for P–O radical iron complexes **18**. The origin of this seems to be the more facile redox chemistry of iron leading to further oxidation observed by CV, EPR and Mößbauer experiments. Initial DFT calculations suggest an oxaphosphaferrirane structure **27** of the oxidised phosphanoxyl complex **18e**, however its presence neither its stability was tested further in this study.
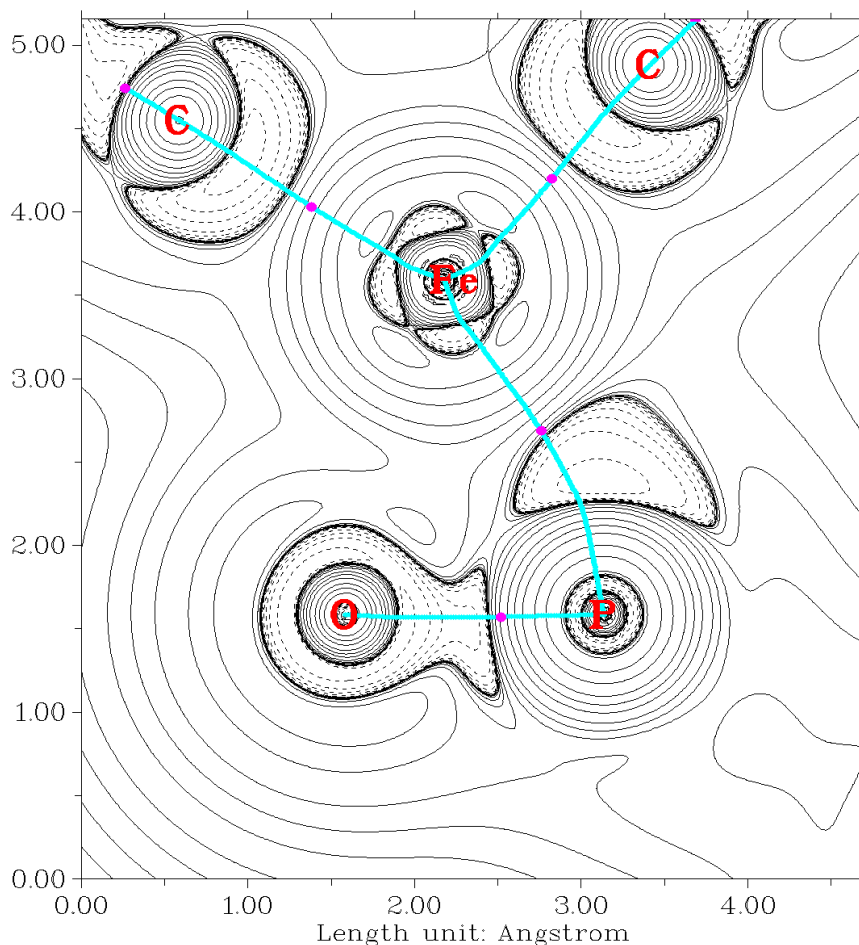
Figure 50: AIM molecular graph of the Laplacian in the Fe-P-O plane showing bond critical points (magenta) and bond paths (cyan lines) of **27**.

5.6. Spin density tuning: combined theory and experiment

During the exploration of the phosphanoxyl iron complex **18e**, several other substitution patterns were investigated which will be presented in the next chapter (p.89). Remarkably, the high spin density on the iron atoms was a common feature to almost all structures. Only 1,3,2-diazaphosphole iron complexes showed a change in the spin density distribution, along with a trigonal bipyramidal coordinated iron. This feature is present in the backbone unsubstituted **18o** as also in the benzo-fused compound **18p** (Figure 51). In **18o** only 6% spin density is found on the Fe atom, while the P and the O atom carry 3% and 2% respectively. The majority of spin density is found on the nitrogen atoms (21% each) and carbon atoms (19%). A similar situation is found in **18p** (Fe: 8%; P: 3%; O: 2%), however, some spin density from the five-membered ring (N: 17% each; C: 12% each) is drawn into the
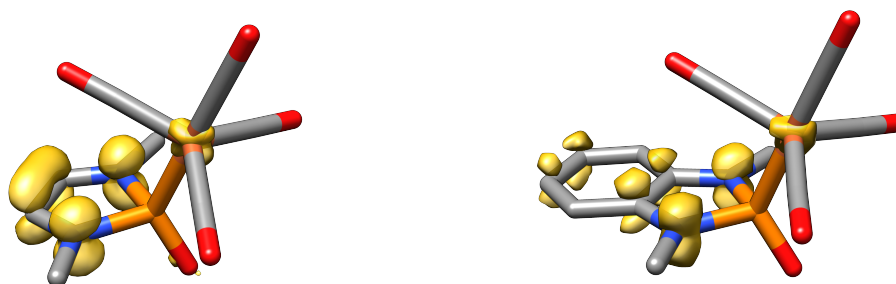
Figure 51: Computed structures of **18o** (left) and **18p** (right). Spin density distribution given in yellow; all hydrogen atoms are omitted for clarity.

annellated benzo moiety (10% each). These drastic differences to the other phosphanoxyl complexes **18** prompted experimental investigations. However, a suitable precursor to **18o**, in the form of the chlorophosphane **3o** is unknown and several attempts via different approaches during this work also failed and therefore, **18p** was targeted. The reaction of *in situ* generated **3p** with K[Fe(CO)$_4$H] in THF proceeds cleanly to the desired product **12p** (Scheme 37), which can be isolated by extraction with *n*-pentane in 60% yield. Further purification via column chromatography with an PE(40/60):Et$_2$O (1:1, +5% NEt$_3$) eluent mixture is possible, however, the yield is decreased significantly and only minor amounts can be obtained. In the ^{31}P{^{1}H}-NMR spectrum a single resonance is observed as a singlet with a chemical shift of 152 ppm and ^{57}Fe satellites from a $^1J_{Fe,P}$ coupling of 33 Hz, similar to the previously reported complexes **12** (cf. Table 10, p.62). This signal shows a doublet of septett splitting in the coupled ^{31}P-NMR spectrum with a scalar coupling constant $^1J_{P,H}$ of 358 Hz and a $^3J_{P,H}$ coupling to the *N*-Me hydrogen atoms of 12 Hz. In the ^{1}H-NMR spectrum the phosphorus-bound H-atom has a chemical shift of 8.94 ppm in THF-*d*8 which is even further lowfield-shifted as in its derivative **12l**, despite the higher electronegativity of oxygen over nitrogen. Single crystals suitable for X-ray diffraction analysis were obtained from a saturated Et$_2$O solution of **12p** at −30 °C (Figure 52). Bond angles and distance are in the
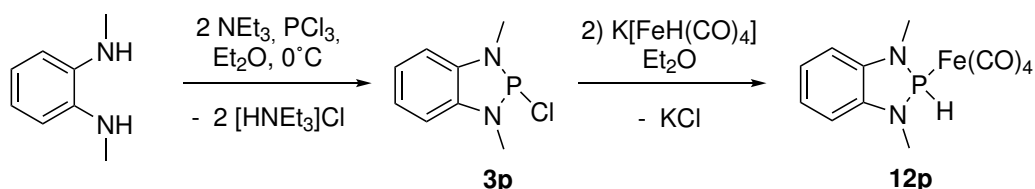

Scheme 37: Synthesis of benz-annulated 1,3,2-diazaphosphole iron complex **12p** via reaction of *in situ* generated **3p** with the potassium hydridoferrate salt.
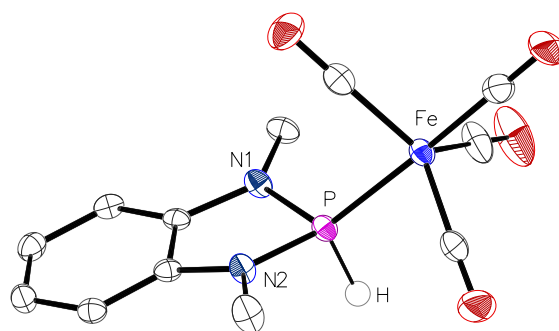
Figure 52: Molecular structure of **12p** in the crystal structure; ellipsoids are set at 50% probability level and non-relevant hydrogen atoms are omitted for clarity. Selected bond lengths and angles are given in Å and $^\circ$ respectively: d(P–Fe) 2.17044(5), d(P–N1) 1.68245(3), d(P–N2) 1.67999(4), $\angle$(N1-P-N2) 91.5403(12), $\angle$(O-P-Fe) 110.8011(7), $\angle$(N1-P-O) 106.515(2), $\sum_{\angle}^{P}$ 301.9266; τ_5(Fe) 0.82.

expected region and comparable to the 1,3,2-dioxophosphole complex **12l** (cf. Figure 35, p.63). In the next step the aminoxylphosphane complex **17p** was targeted. The previous experiments suggest a relatively low thermal stability and therefore initial attempts were made by reacting **12p** with TEMPO at 0 °C in THF. In the ^{31}P{^{1}H}-NMR spectrum of the reaction mixture, taken after one hour reaction time, two resonances were observed, one singlet lowfield-shifted to the starting complex **12p**, with a chemical shift of 164 ppm and another singlet highfield-shifted at 126 ppm; no starting material was observed (Figure 53, top). Direct comparison to the reaction of **12e** suggests that the low field resonance is indeed the desired product **17p**, however, the highfield-shifted resonance is close to the chemical shift of the phosphinito anion resonance **14e** and therefore it is very likely [TEMPH$_2$]**14p**. The reaction was repeated in several organic solvents, *e.g.*, toluene, n-pentane, chlorobenzene, diethyl ether, and despite minor differences the outcome was very similar to the one described above. Hence, **12p** was deprotonated and then reacted with [**2**]BF$_4$ to obtain **17p** at very low temperatures. Even under these conditions a ^{31}P{^{1}H}-NMR spectrum of a sample directly taken from a -30 °C cold reaction mixture, already showed substantial amounts of the highfield resonance. After stirring overnight no resonance for **17p** was observed anymore and only the previously observed resonance at 126 ppm was observed, next to a new singlet resonance at 156 ppm, besides minor side products (Figure 53, bottom). The latter might be assigned as the hydroxyphosphane complex **13p** because of its relative chemical shift to the starting material **12p**.

Despite the theoretical curiosity of the 1,3,2-diazaphospholoxyl complexes **18o,p**, attempts to stabilise such radicals at different temperatures and in different solvents failed experi-
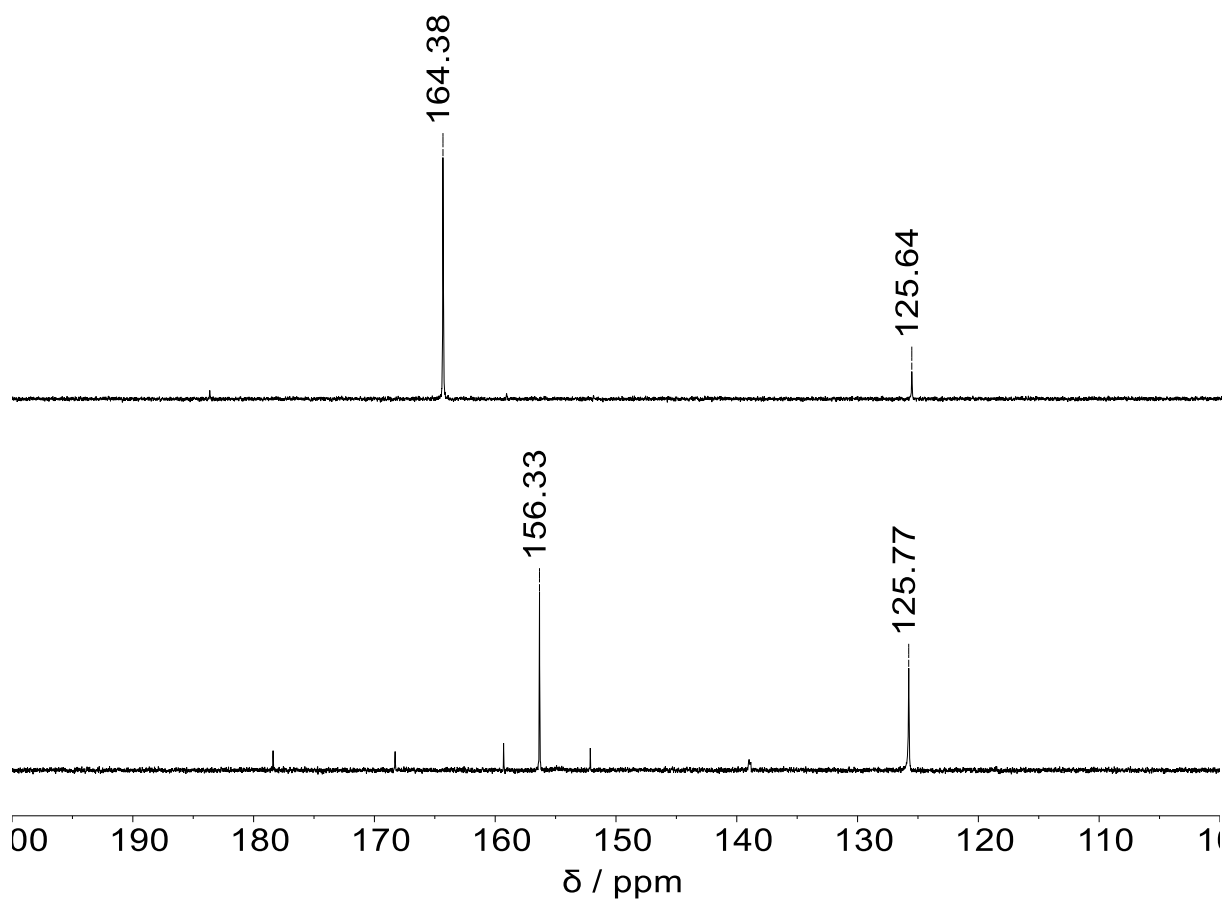
Figure 53: $^{31}P\{^1H\}$-NMR spectrum of the reaction mixture of **12p** with ^{n}BuLi and **2**[BF$_4$] in THF directly measure (top) and after stirring overnight, 12 h (bottom).

mentally. While an assumed aminoxylphosphane complex **17p** is detected via NMR, its follow-up chemistry, probably via an initial N–O bond cleavage, already occurs at low temperatures. This was found to be almost independent from the solvent used in the reaction and made isolation not possible.

5.7. DFT studies on the formation of P–O containing radical complexes

The ambiguous chemistry of the different reported and attempted aminoxylphosphane complexes, namely **8**, **17** and **XXVII** raised questions about its origin. However, their, in most cases, inherent low thermal stability makes an experimentally systematic study difficult. Therefore, a theoretical study was conducted via DFT to gain further insight into this rare class of compounds. For this the formation of the TEMPO phosphane complexes and their N–O bond cleavage was investigated, starting from the secondary phosphane complexes **6**, **12** via the intermediate phosphanyl complexes, similar to the detailed analysis of **6f,i,k** (Figure 24, p.44). Additionally a small set of manganese complexes **28d,e,u** was consid-
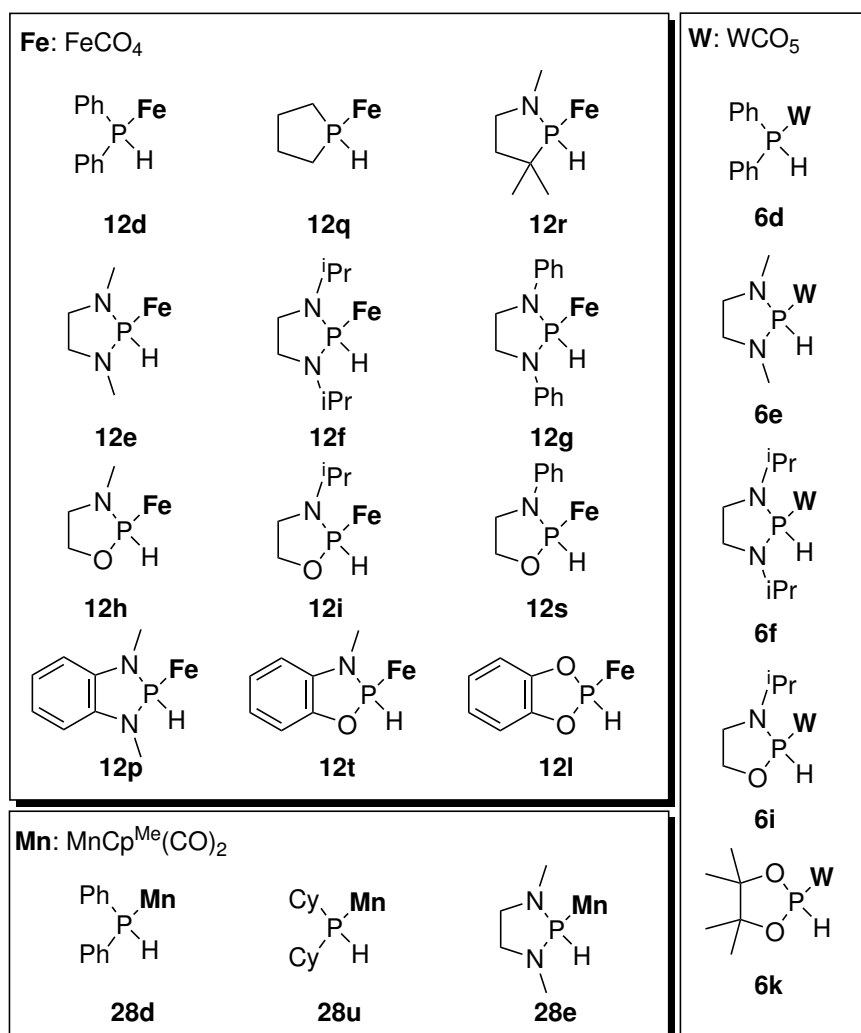
Figure 54: Scope of secondary phosphane complexes as the starting point for the DFT study.

ered to connect the experimental results of Heurich and Rauf Naz with the chemistry of the iron and tungsten complexes (Figure 54). Some complexes had been previously calculated, however on a lower level of theory and were recalculated herein to allow for a better comparability.[50,63–66] For this study no barriers were calculated and only Gibbs free energies are discussed. Besides the already in previous chapters discussed substitution pattern several synthetically not targeted complexes were added to broaden the scope of the study.

Already for the tungsten complexes different temperatures were needed for the reaction between **6** and TEMPO, revealing that already this step is clearly substituent depending (Scheme 38). Therefore, the formation Gibbs free energies were compared for the different substituents based on the directly bonded element to phosphorus (Figure 55). All calculated $\Delta_r G$ are positive, making the formation for all phosphanyl complexes **9,29,30** endergonic. The initial studied tungsten complexes show $\Delta_r G$ values ranging between 6 and 13 kcal mol^{-1}, being the lowest for P–N bond containing complexes, *e.g.* **9i** and **9e,f**. Despite that only three manganese complexes **30** have been calculated, their $\Delta_r G$ values are in all cases higher than for the tungsten complexes **9**. While, the N/N system **30e** shows a smaller $\Delta_r G$ than the carbon system **30u** and **30d**, no trend can be obtained from this due to the small set. In contrast, a clear trend is observed for phosphanyl iron complexes **29**. Minimal $\Delta_r G$ are obtained for nitrogen substituted systems, and this effect is even stronger for N/N systems, *e.g.* **29e-g,p**. Noteworthy, an immense stabilisation is observed for **29p**, which has already been discussed in the context of the phosphanoxyl iron complex **18p**. To evaluate the effect of the steric bulk of the substituent complexes **29e-g** and also their N/O counterparts **29h,i,s** were compared (Figure 56). While all $\Delta_r G$ are lower for the N/N systems than for the N/O, no significant effect is observable among the systems, as their energy differences is in the range of the accuracy of the chosen DFT method. Furthermore, the effect of the metal fragment was investigated for the 1,3-dimethyl-1,3,2-diazaphospholidine (**e**) and the diphenyl (**d**) substitution pattern (Figure 57). In all cases lower $\Delta_r G$ were found for **e** compared to **d**, however the free energies for the **e**-based systems are all very close
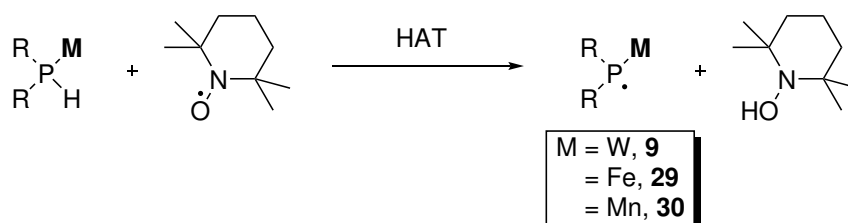

Scheme 38: Initial hydrogen atom transfer reaction from **6, 12, 28** to TEMPO forging phosphanyl complexes **9, 29, 30**.
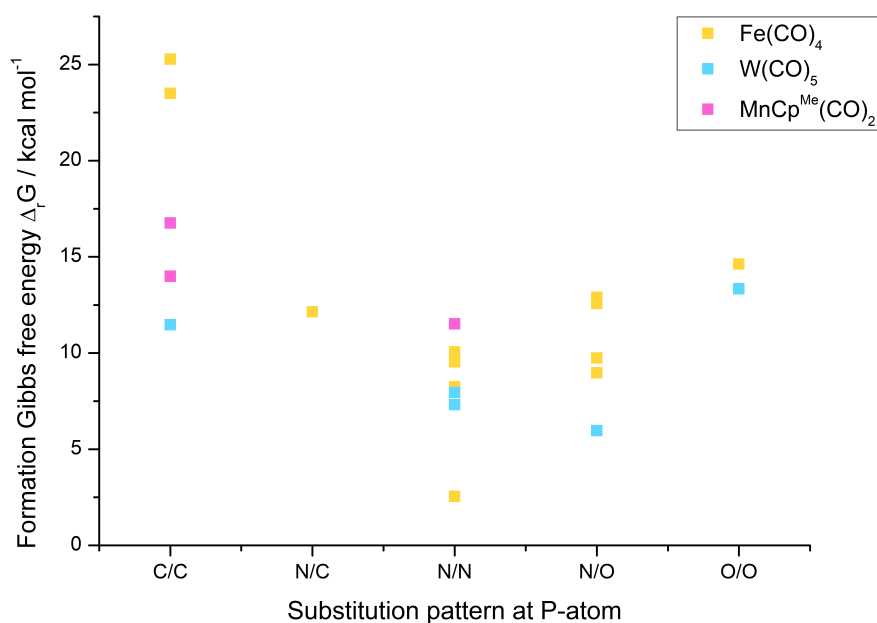
Figure 55: Gibbs free formation energy of the reaction $\Delta_r G$ for phosphanyl complexes **9,29,30** from HAT by TEMPO vs. the directly phosphorus bound element of the substituents.
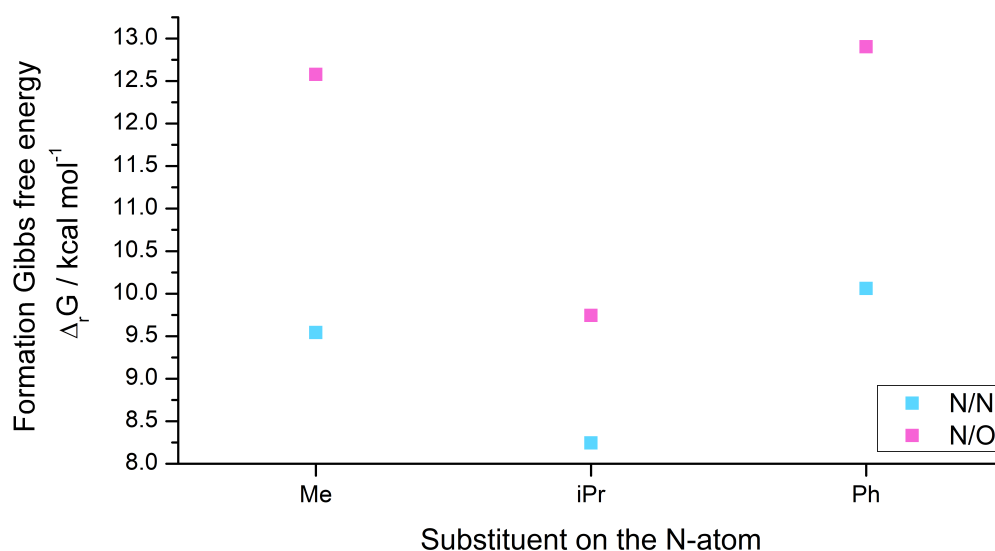

Figure 56: Gibbs free formation energy of the reaction $\Delta_r G$ for phosphanyl complexes **29e-i,s** from HAT by TEMPO vs. substituents on the N-atom in 1,3,2-diazaphospholanyl **29e-g** and 1,3,2-oxazaphospholanyl **29h,i,s** $Fe(CO)_4$ complexes.
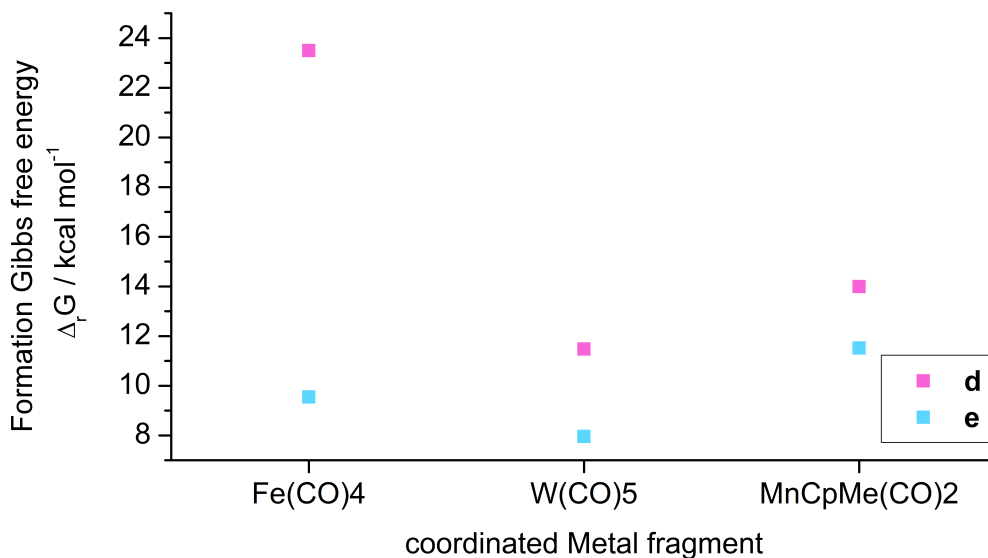
Figure 57: Gibbs free formation energy of the reaction Δ_rG for phosphanyl complexes **9d,e**, **29d,e** and **30d,e** from HAT by TEMPO vs. the coordinated metal fragment.

to each other. While, the calculated Δ_rG values of diphenyl systems **d** of the tungsten and manganese complex are also rather close and show a similar offset to each other as for the **e** derivatives a significant difference is observed for the iron complex. It appears that for the diphenyl system the iron fragment $Fe(CO)_4$ even destabilises the phosphanyl complex **29d**, compared to the other two metals. A similar high Δ_rG is also found for **29q**, suggesting that this is a carbon substituent-based effect rather than an arly vs. alkyl phenomenon.

The same analysis was then conducted on the radical heterocoupling of the phosphanyl complexes with TEMPO (Scheme 39). The Δ_rG for the formation of the aminoxylphosphane complexes are again plotted against the elements in α-position to the P-atom (Figure 58). For the tungsten complexes calculated values are very close to each other, however, slightly
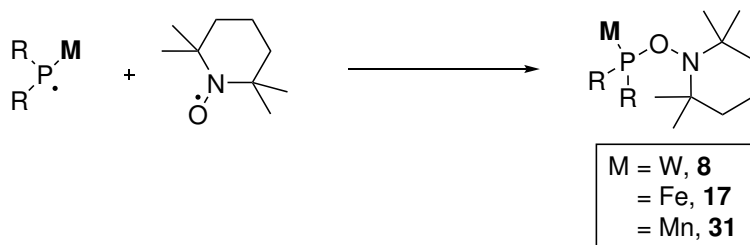
Scheme 39: Heterocoupling of phosphanyl complexes **9, 29, 30** with TEMPO to yield the aminoxylphosphane complexes **8, 17, 31** as a second step in the DFT analysis.
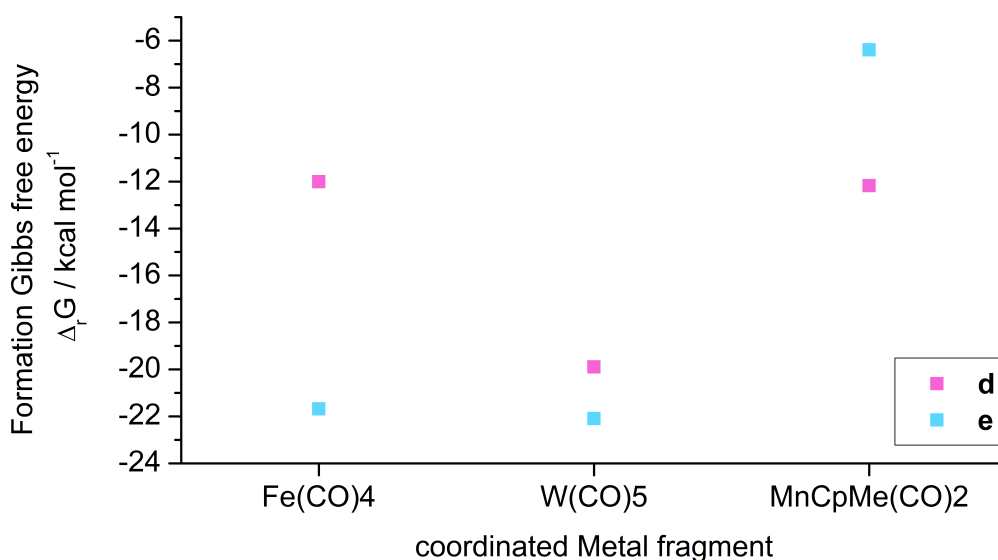
92
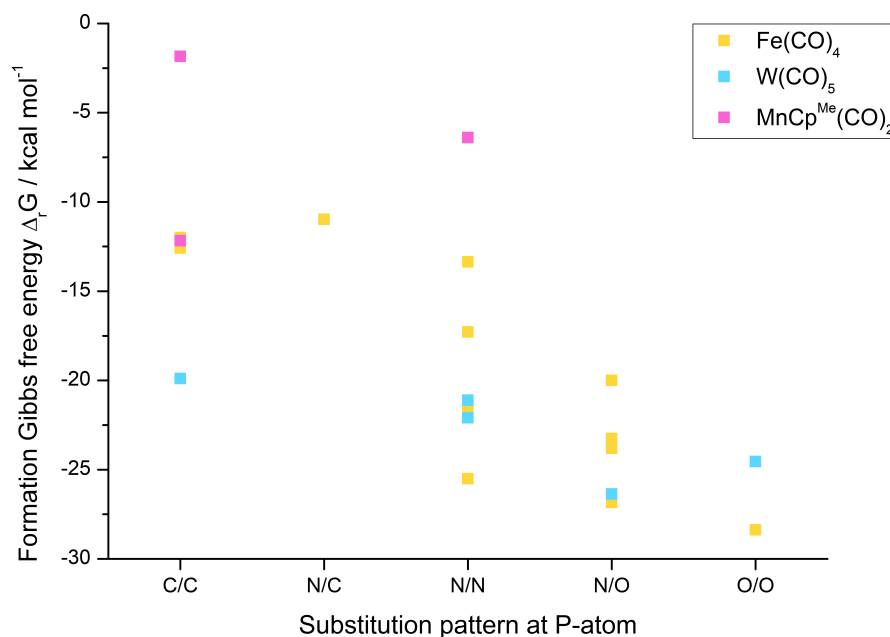
Figure 58: Gibbs free energy of reaction $\triangle_r$G for the heterocoupling between phosphanyl complexes **9,29,30** and TEMPO vs. the directly phosphorus bound element of the substituents.

lower $\triangle_r$G values are observed for oxygen containing system; due to the small set this trend has to be taken with care. In the same manner, the manganese complexes show no trend, but their formation energy is significantly smaller than that of the tungsten and the iron complexes. The latter show more negative $\triangle_r$G values if heteroelements are bound to phosphorus, especially for those having a higher oxygen content. However, the $\triangle_r$G for the iron complexes span over the ranges of manganese and tungsten complexes and therefore show a clear substituent dependency. For the evaluation of the steric effect on the α-position again the N/N and N/O complexes were compared with different substituents on the nitrogen atom (Figure 59). In contrast to the behaviour of the phosphanyl complexes (Figure 55) a significant destabilisation is observed with an increase of the size bound to the N-atoms in the N/N systems **17e-g**. Only a minor change is observed for the N/O systems **17h,i,s**. Therefore, this is clearly assigned to repulsive interaction between the N-atoms substituents and the TEMP moiety, *e.g.*, the four methyl groups. Upon introduction of an oxygen atom, *e.g.*, N/O system, it appears that the system can find a configuration in which this effect is diminished. The investigation into the metal fragment dependency showed significantly different results than for the phosphanyl complexes, discussed above (Figure 60). Similar $\triangle_r$G are found for the iron and tungsten (**e**: Me-N-C$_2$H$_4$-N-Me) based
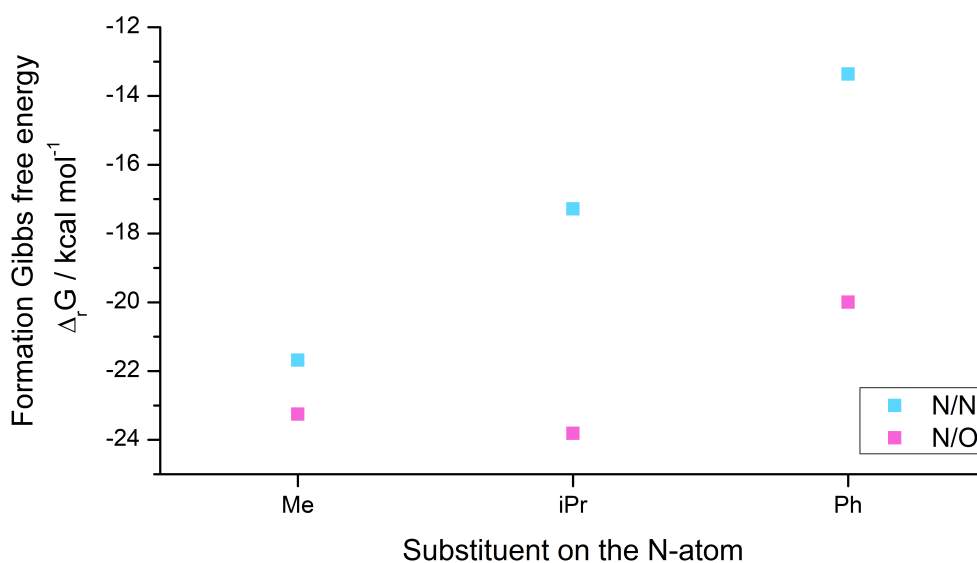
Figure 59: Gibbs free energy of reaction Δ_rG for the heterocoupling between phosphanyl complexes **29e-i,s** and TEMPO vs. substituents on the N-atom in 1,3,2-diazaphospholanyl **29e-g** and 1,3,2-oxazaphospholanyl **29h,i,s** Fe(CO)$_4$ complexes.
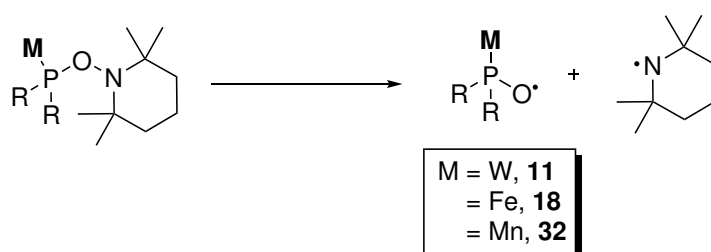

Figure 60: Gibbs free energy of reaction Δ_rG for the heterocoupling between phosphanyl complexes **9d,e**, **29d,e** and **30d,e** and TEMPO vs. the coordinated metal fragment.

complexes, while the related manganese complex is extremely destabilised, *e.g.* roughly 16 kcal mol^{-1} compared to the aforementioned. On the other hand similar Δ_rG values are found for the (**d**: Ph) based system of iron and manganese, which are ~8 kcal mol^{-1} higher

in energy than the tungsten complex. This is in very good agreement with the experiments. Initially, this effect might be attributed to steric effects, since due the long P–W bond the metal fragment tolerates more steric bulk, compare to the Fe and Mn complexes before the repulsion becomes too strong. But remarkably the energetical order of **d** and **e** complexes for manganese is inverted, contradicting the idea of a pure sterically effect.

In the final step the P–O containing radical complex is formed via the already described homolytic N–O bond cleavage under the loss of the TEMP aminyl radical (Scheme 40). Plotting the nature of the directly phosphorus-bound elements against the $\Delta_r G$ values shows again only a strong substituent dependency for the iron complexes (Figure 61). The P–O containing iron complex radicals appear to be significantly more stabilised in the presence of electronegative elements and therefore lowest $\Delta_r G$ values are found for the O/O system **18l**. There is the exception of the indepth discussed **18p**. Because of its so far unique structure and ligand localised SDD, the spin densities on some selected atoms were calculated to evaluate if in general a lower $\Delta_r G$ correlates with a change in the spin density distribution (Table 12). The observed effect in the tungsten complexes has already been discussed in a previous chapter. However, there is no significant change among the different iron and manganese complexes, despite huge electronic differences in the substitution pattern. Remarkably, the Loewdin spin density on the manganese atom in the P–O complex radicals **32** is even higher than that of iron in its complexes **18**. The ligand-based SDD of **18p** was not found for any other complex, despite having an unsaturated backbone in the form of benzannulation in **l** and **t** based complexes. In the attempt to find some delocalisation of the spin in the backbone sulfur-containing systems were also calculated (Figure 62). However, the SDD is found to be the same as for the other P–O containing iron complex radicals.


Scheme 40: Homolytic N–O bond dissociation of the aminoxy phosphane complexes generating the P–O radical complex **11, 18, 32** and the TEMP aminyl radical as the third step in the DFT analysis.
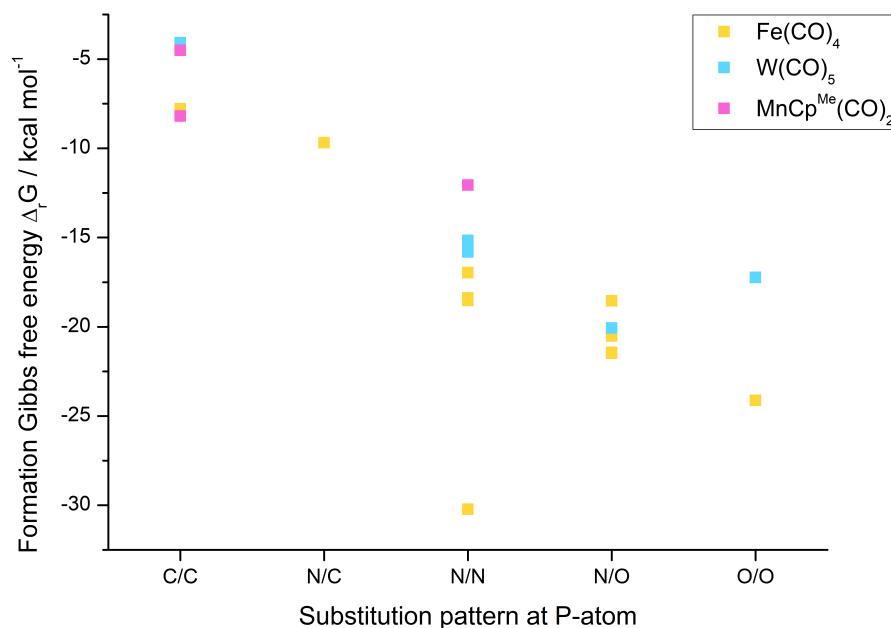
Figure 61: Gibbs free energy of reaction $\Delta_r G$ for formation of the P–O radical complexes **11, 18, 32** vs. the directly phosphorus-bound elements of the substituents.

Table 12: Spin densities in e of selected atoms and groups (L = sum of the large (>0.01) contributions of the *P*-substituent) of the calculated P–O radical complexes **11,18,32**.

	P	O	L	Fe		P	O	L	M
18d	0.01	0.02	0.00	0.94	**18t**	−0.01	0.01	0.00	0.94
18e	−0.01	−0.02	−0.02	0.97	**18v**	−0.01	0.1	0.00	0.93
18f	−0.02	−0.01	0.01	0.93	**18w**	−0.01	0.02	−0.01	0.94
18g	−0.01	0.00	0.00	0.95	**11d**	0.11	0.26	0.02	0.35
18h	−0.01	−0.01	0.01	0.93	**11e**	0.13	0.23	0.04	0.32
18i	−0.01	−0.01	0.01	0.93	**11f**	0.15	0.24	0.05	0.28
18l	0.00	0.01	0.00	0.94	**11i**	0.10	0.20	0.02	0.38
18p	0.03	0.02	0.79	0.08	**11k**	0.07	0.16	0.00	0.46
18q	0.01	0.02	0.00	0.95	**32d**	0.00	−0.01	0.00	1.08
18r	−0.02	−0.03	−0.01	0.96	**32u**	0.00	0.00	0.00	1.09
18s	−0.01	0.01	0.00	0.95	**32e**	0.00	0.00	0.02	1.08
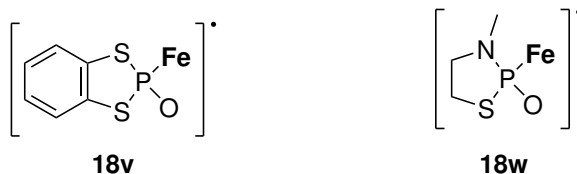
Figure 62: Lewis structure of the phosphanoxyl iron complexes **18v** and **18w**.
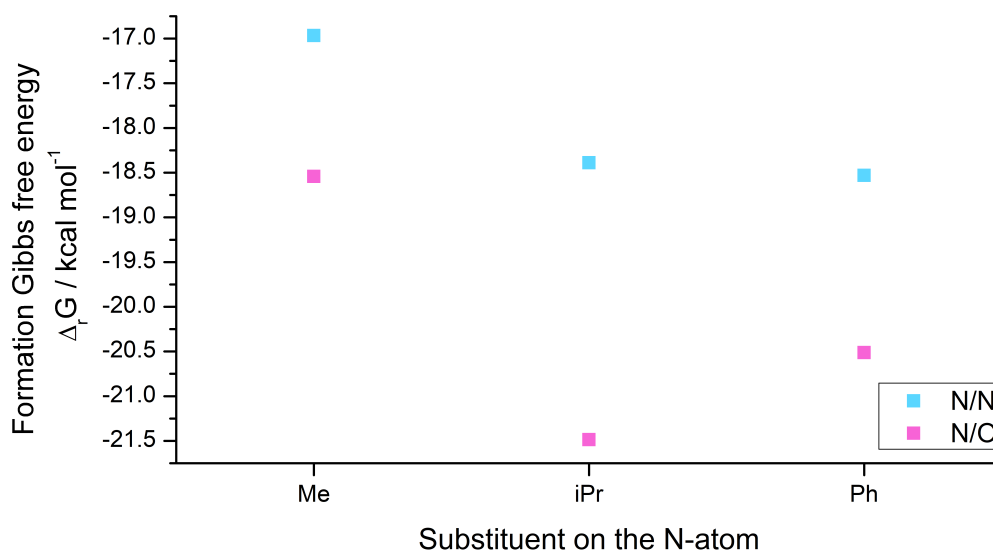
Figure 63: Gibbs free energy of reaction $\triangle_r$G for the formation of the P–O radical complexes **18e-i,s** vs. substituents on the N-atom in diazaphospholidinoxyl **18e-g** and oxazaphospholidinoxyl **18h,i,s** Fe(CO)$_4$ complexes.

In an attempt to find the origin of the higher stability for oxygen-containing P–O containing complex radicals the effect of the N-atom substituent was also investigated in this case (Figure 63). The N/N systems **18e,f,g** appear to be independent from their *N*-substituent as the difference is negligibly small compared to the methods level of accuracy. For the N/O system **18h,i,s** it appears to be the same, having just slightly lower free energies than the N/N system. To complete the comparison the effect of the metal fragment among each other was also conducted for the phosphanoxyl complexes (Figure 64). The Fe(CO)$_4$ fragment seems to stabilise the P–O containing complex radicals very well, as either for **e** and **d** the calculated $\triangle_r$G values are the among the smallest. Corroborating the initial hypothesis that the Fe(CO)$_4$ fragment is able to stabilise such species. An inverted situation is found for the tungsten and the manganese fragments. While the W(CO)$_5$ shows a slightly lower $\triangle_r$G for **e** than the manganese complex, a significantly higher $\triangle_r$G is observed for **d**, with similiar values for manganese and iron complexes of **d**.

While the analysis of the free Gibbs energies of the three different intermediates allows discussion about the stability, the values were not put in relation to each other. The most important $\triangle\triangle_r$G is between the aminoxylphosphane complexes **8,17,31** and the P–O complex radicals **11,18,32**, which is simply the N–O bond cleavage enthalpy BDG. It becomes even more important under the assumption that the N–O bond cleavage proceeds with-
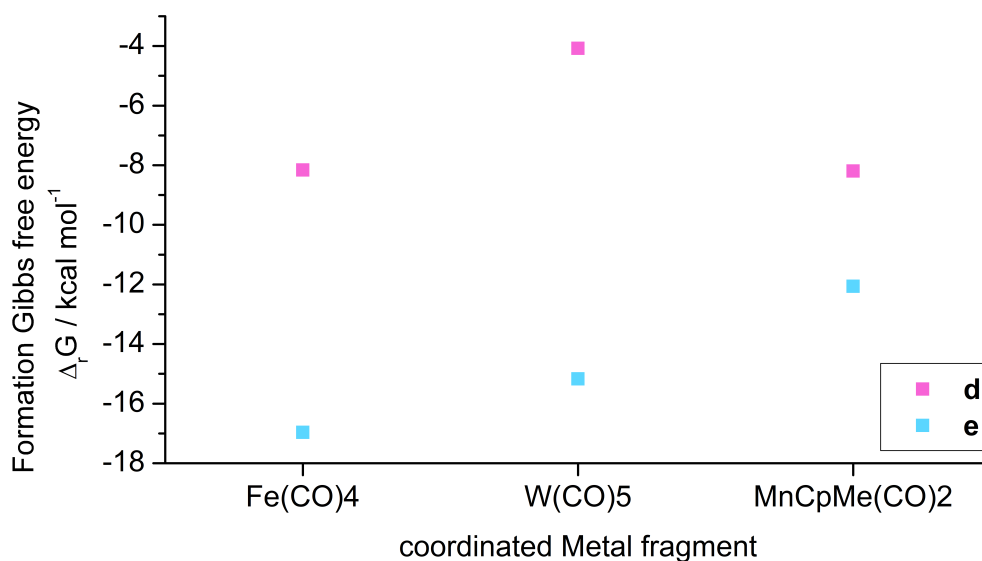
Figure 64: Gibbs free energy of reaction $\Delta_r G$ for the formation of the P–O radical complexes **11d,e**, **18d,e** and **32d,e** vs. the coordinated metal fragment.

out barrier, already observed for the tungsten complexes (cf. Figure 24, p.44). Therefore, the BDG for the chosen scope was analysed in the same way as the simple $\Delta_r G$ of the intermediates beforehand (Figure 65). The calculated values are scattered from -6 to 7 kcal mol^{-1} with one exception having a BDG of 16 kcal mol^{-1}. This value was obtained for the diphenyl tungsten system **8d**, which Heurich focused on due to the high thermal stability of the aminoxylphosphane complex, this is very well reflected in the highly endergonic BDG. In line with this observation, all other tungsten systems are found to have positive and higher BDGs than their related iron or manganese complexes. For several complexes even negative BDGs are obtained, which is related to an exergonic formation of the P–O complex radicals from the aminoxylphosphane complexes. Therefore, it is very likely, that no *P*-aminoxyl complexes can be isolated in these cases. Corroborating the observations in the chemistry of the manganese complexes, for which no aminoxylphosphane complex could be obtained. Again, the effect of the *N*-substituent was investigated (Figure 66). The effect of a larger substituent for the *P*-aminoxyl complexes, which was already discussed (cf. Figure 59, p.94) is reflected here, showing a decrease in the BDG for larger substituents. Again, this effect is slightly smaller for the N/O system than for the N/N systems. Remarkably, this can even lead to negative N–O bond cleavage enthalpies for **f,g,s** and therefore a very unlikely chance of isolating the aminoxylphosphane complexes. These calculations highlight the importance of small *N*-substituent, used throughout this study, to isolate the aminoxylphosphane complexes. The nature of the metal fragment, as experi-

98
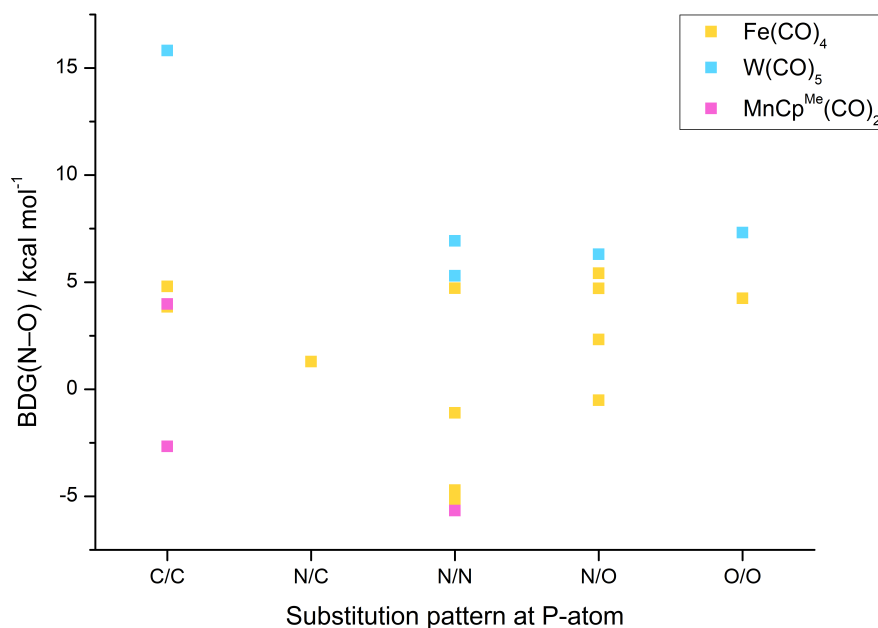
Figure 65: BDG of the N–O bond in aminoxylphosphane complexes **8,17,31** vs. the directly phosphorus bound element of the substituents.
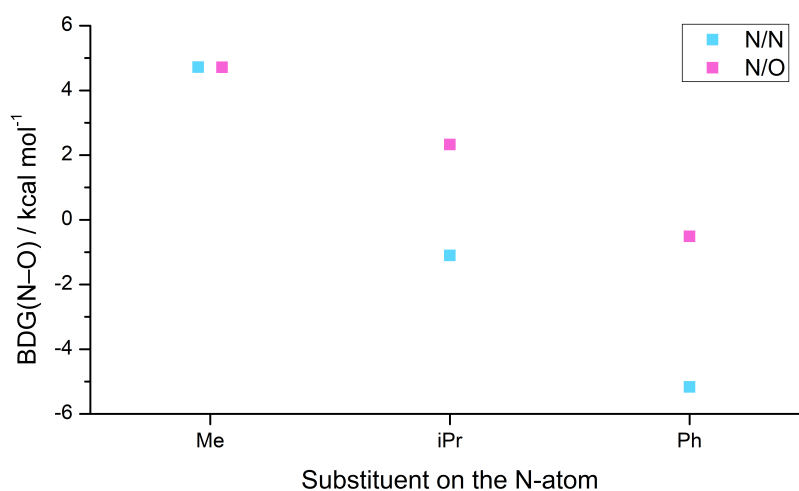
Figure 66: BDG of the N–O bond in aminoxylphosphane complexes **17e-i,s** vs. substituents on the N-atom in aminoxyl 1,3,2-diazaphospholidinoxyl **17e-g** and 1,3,2-oxazaphospholidinoxyl **17h,i,s** $Fe(CO)_4$ complexes.

mentally already observed, also plays an important role. The calculations (Figure 67) show diverging results, on the one hand the BDG obtained manganese and iron (**d**) complexes is
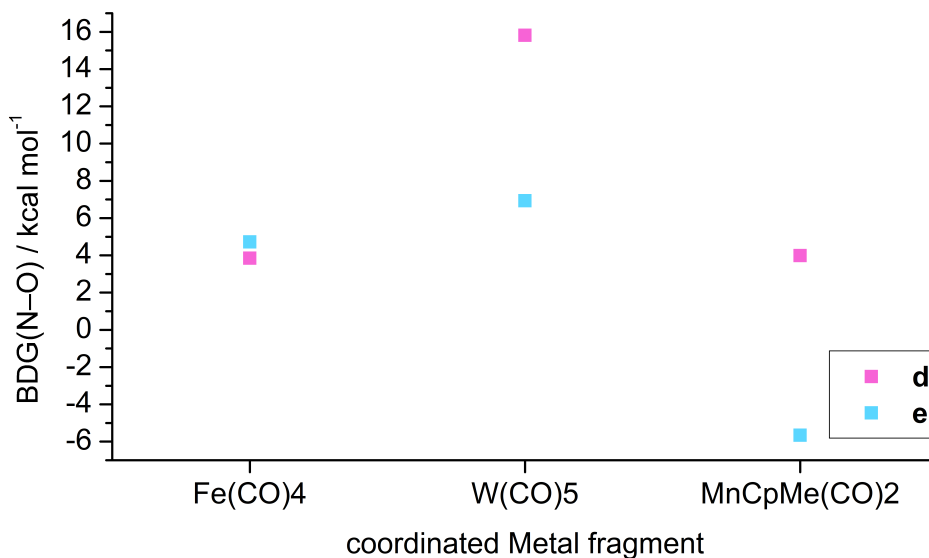
Figure 67: BDG of the N–O bond in aminoxylphosphane complexes **8d,e**, **17d,e** and **31d,e** vs. the coordinated metal fragment.

very similar, but for the tungsten complex the N–O bond is significantly more stable. On the other hand, similar BDGs are found for the iron and tungsten (**e**) complexes, while the N–O bond of the manganese complex is exceptionally weak and even exergonic with a value of -5.7 kcal mol^{-1}.

These calculations show, that the origin for stabilisation of either aminoxylphosphane complexes or phosphanoxyl complexes is still not clear. However, from the combination of the experimental observations and the theoretical analysis some assumption can be made about the stability of the named compounds, especially the aminoxylphosphane complexes. For the initial HAT by TEMPO an important feature of the used secondary phosphane complexes is the presence of heteroatoms bound to phosphorus to stabilise the resulting phosphanyl complexes. As high temperatures should be avoided, since the final aminoxylphosphane complex might be too labile, the HAT should ideally have a very small barrier. The aminoxylphosphane complexes show generally lower Δ_rG for heteroelement substitution on phosphorus and small steric bulk bound to eventual present nitrogen atoms. For the metal fragment the tungsten complexes showed the highest BDG(N–O) suggesting that the W(CO)$_5$ is the best fragment to stabilise the aminoxylphosphane complexes in this study. However, the scope in the present study is rather (too) small, and for a more complete picture several other fragments should be considered in the future.

5.8. Co-ligand effects on P–O containing radical metal complexes

In collaboration with Frontera the effect on the SDD upon variation of the co-ligands was explored (Figure 68).[158] In this study the SDD of phosphanoxyl/phosphinoyl complexes (substitution pattern: **d** and **e**) of iron, tungsten and nickel were analysed. Nickel was chosen as another electron rich first row transition metal to hamper the uptake of a lot of spin density by the metal, thus pushing the spin density onto the ligand. Similar reasoning was applied when one CO ligand was replaced by a PMe$_3$ ligand, to have a less π-acidic ligand and therefore disfavouring a high spin density on the metal. On the other hand a CO ligand was replaced with a CS ligand possessing even higher π-acidity than CO, to draw even more spin density onto the metal, in the cases of tungsten, or for iron complexes to draw even more spin density on the CS ligand itself. This concept was extended to exchange two CO ligands in favour of 2,2'-bipyridine and its heavier homologue 2,2'-biphosphinine possessing higher π-acidity. Bipyridines are known for their non-innocent behaviour and their ability of metal ligand charge transfer (MLCT), and it was expected that the 2,2'-bipyridine can draw significant spin density onto itself in the studied P–O containing radical complexes. Isomers, *facial*/*meridional* for the bipyridine and biphosphinine and *cis*/*trans* for the PMe$_3$ and CS complexes, were also considered to see if different coordination sites have also an effect on the SDD. From the results the complexes can be separated into two groups, delocalised spin density complexes of tungsten **37-40** and very localised spin density com-

R = Ph (**d**), (CH$_2$NMe)$_2$ (**e**)
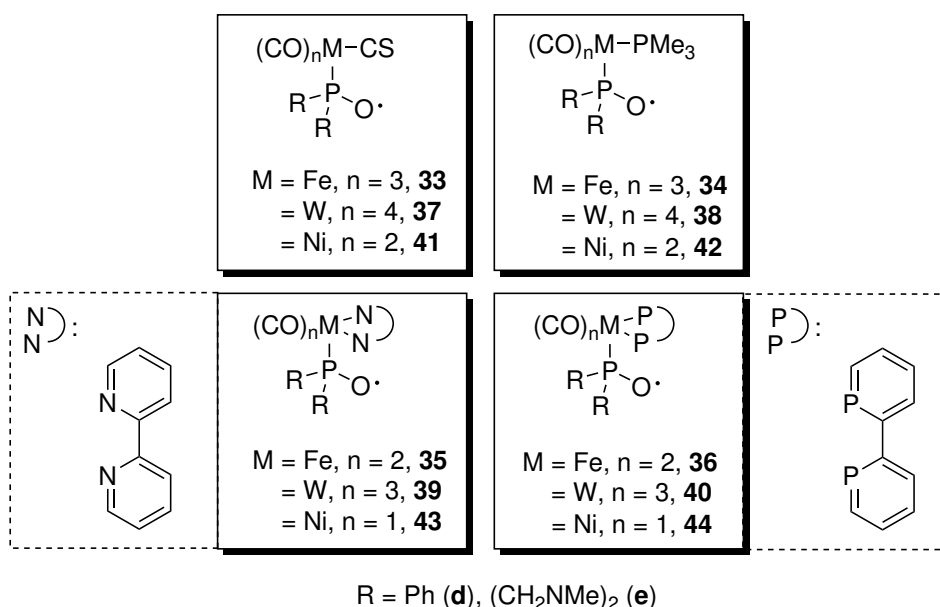
Figure 68: Scope of the DFT investigation on the SDD of P–O radical complexes depending on the co-ligand.

Table 13: Spin densities in e of selected atoms and groups (L = sum of the large contributions in the adduct substituent) of the calculated P–O radical metal complexes. Possible isomers are given as *facial*/(*meridional*); *cis*/(*trans*).

	P	O	L	M		P	O	L	M
33d	−0.01	0.02	0.05	0.93	**33e**	−0.01	0.01	0.04	0.96
	(−0.01)	(0.02)	(0.02)	(0.93)		(−0.01)	(0.02)	(0.00)	(0.97)
34d	0.00	0.02	0.00	1.00	**34e**	0.00	−0.01	0.00	0.99
	(0.00)	(0.02)	(0.02)	(0.93)		(−0.01)	(0.01)	(0.00)	(0.94)
35d	−0.01	−0.01	0.00	1.16	**35e**	−0.01	−0.01	0.02	1.24
	(−0.03)	(−0.01)	(0.08)	(0.92)		(−0.01)	(−0.01)	(−0.06)	(0.98)
36d	0.00	−0.01	0.00	1.08	**36e**	−0.01	−0.01	0.00	1.10
	(−0.01)	(0.02)	(0.12)	(0.88)		(−0.01)	(−0.01)	(0.15)	(0.85)
37d	0.10	0.22	0.23	0.30	**37e**	0.00	0.02	0.12	0.43
	(0.12)	(0.19)	(0.31)	(0.19)		(0.11)	(0.03)	(0.18)	(0.27)
38d	0.07	0.15	0.03	0.49	**38e**	0.09	0.16	0.03	0.45
	(0.07)	(0.15)	(0.05)	(0.48)		(0.07)	(0.15)	(0.05)	(0.47)
39d	0.04	0.02	0.03	0.56	**39e**	0.04	0.01	0.00	0.52
	(0.05)	(0.05)	(0.00)	(0.68)		(0.03)	(0.00)	(0.02)	(0.65)
40d	0.05	0.01	0.06	0.47	**40e**	0.06	0.01	0.00	0.44
	(0.05)	(0.16)	(0.09)	(0.55)		(0.04)	(0.00)	(0.10)	(0.44)
41d	−0.02	0.00	0.05	0.88	**41e**	−0.02	−0.01	0.12	0.81
42d	0.00	0.01	0.02	0.90	**42e**	0.01	0.00	0.03	0.83
43d	0.00	0.01	0.05	1.02	**43e**	0.01	0.01	0.08	1.05
44d	−0.03	0.00	0.15	0.85	**44e**	−0.03	0.00	0.18	0.83

plexes in iron **33-36** and nickel complexes **41-44** (Table 13). The absence of one CO ligand in favour of one of the four probed ligands leads in general to an increase of the spin density on the W centre compared to $W(CO)_5$ phosphanoxyl complexes. The exception are the CS containing complexes *cis*/*trans*-**37d** and *trans*-**37e**, while the *cis*-**37e** isomer shows again an increased spin density on the W-centre. The bipyridine complexes of tungsten **39d,e** show significantly higher spin densities on tungsten, especially the *mer* isomer, with almost no contribution on the P- and O-atom, which was previously not observed in the $W(CO)_5$ complexes. Apparently, the bipyridine ligand is not suitable in this complex to take up spin density and behaves like an innocent ligand. The more π-acidic biphosphinine however is able to take up a maximum of ∼10% of the overall SDD. These observations can also be transferred to the iron and nickel complexes, however, with much higher spin densities on the metal atom itself. The overall result of this study shows, that in the presence of a phosphanoxyl/phosphinoyl ligand other ligands, known to be noninnocent, are almost ineffective in regard of delocalising the spin density distribution. These observations, however, might allow to bulk up such radical complexes to maybe further stabilise them. Therefore, the bisdiphenylphosphanylethylen (dppe) iron(0) complex **45e** was included into the study

(Figure 69). Indeed, the resulting configuration around the Fe-atom resembles the Fe(CO)$_4$ complex **18e**, however, **45e** has a significantly higher τ_5(Fe) value, assumingly due to the steric repulsion of the dppe moiety. Spin density is almost exclusively found on the Fe-atom mimicking the electronic situation of **18e**. From the structure it can clearly be seen that the phenyl substituents are blocking the stereoactive radical on iron from all side, but leaving (only) a small pocket. Hence, this or similar complexes might lead to P–O radical complexes with higher stability.
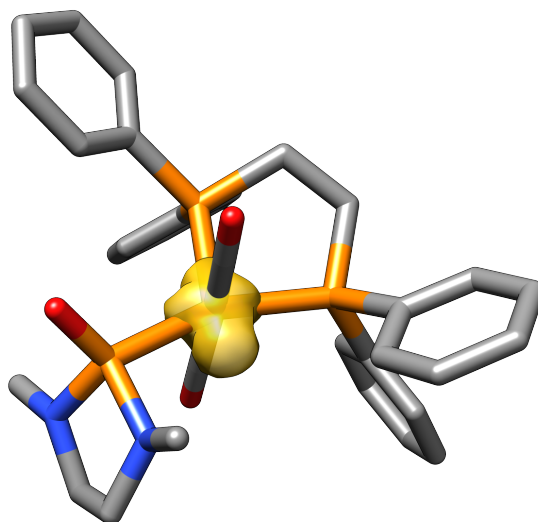
Figure 69: Calculated minimum structure of **45e** with SDD surface (Isovalue: 0.009). τ_5(Fe): 0.27. Selected Loewdin spin densities are given in e: Fe 1.00, P −0.02, O(P-bound) −0.01.

5.9. Theoretical and experimental insight into P–H substituted P–O radical complexes

In collaboration with Zhu and Qu theoretical calculations were performed on the properties of P–O radical complexes having a direct P–H bond **46**, applying the PW6B95-D3/def2-QZVP$_{COSMO-RS(THF)}$//TPSS-D3/def2-TZVP$_{COSMO-RS(THF)}$ level of theory.[159] For this type of P–O radical complexes the general possibility exists to be in an equilibrium with is tautomer, the phosphanyl complex **46'** (Figure 70). This species belongs, somehow, to the category of P-functional phosphanyl complex for which only the *P*-chloro derivative **XV** (cf. Scheme 7, p.8) has been reported. Comparison of the energies of the two isomers showed that actually **46'** is lower in energy by 14.6 kcal mol^{-1}. This is remarkable as phosphanyl complexes previously discussed were always higher in energy than their related P–O radical complexes. However, a significantly high barrier of 31.5 kcal mol^{-1} was found for a potential intramolecular hydrogen shift, yet intermolecular reaction might lead to an efficient transformation to the tautomer **46'** in solution. Mulliken SDD of **46** shows a similar distribution as already found for other phosphanoxyl tungsten complexes in this study, with 0.56 and 0.32 e on the tungsten and the oxygen atom respectively. In the phosphanyl complex **46'** only 0.12 and 0.07 e are found on tungsten and oxygen, while the rest of spin density is localised on the phosphorus atom. In an attempt to gain experimental insight, it was planned to oxidize phosphinito complex **47** to the desired radical species **48** (Scheme 41). As a starting point the phosphinidene imidazole adduct **XLIII**, reported very recently by Biskup[160, 161] was used, having a P-CPh$_3$ instead of a phenyl substituent for more kinetic stabilisation. After hydrolysis of **XLIII** the *P*-hydroxy phosphane complex **XLIV** was obtained and subsequently deprotonated using KO^{t}Bu to forge the phosphinito complex [K]**47**. To increase the solubility the cation was exchanged to tetraphenylphosphonium resulting in the formation of [PPh$_4$]**47**. Following the synthesis, the phosphinito complex was oxidized via CV to observe a potentially formed radical (Figure 71). However, only an irreversible oxidation was observed as a very broad peak at 584 mV. Additionally, there is another peak observed at 149 mV, which is assigned to an unknown impurity. The peak at 584 mV was explored by increasing the upper scan limit stepwise to find potential quasi-reversible conditions, but
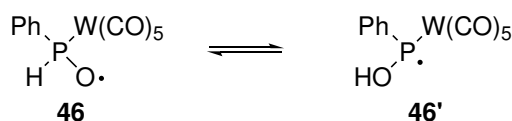
Figure 70: Phosphanoxyl complex **46** and its tautomer the phosphanyl complex **46'**.
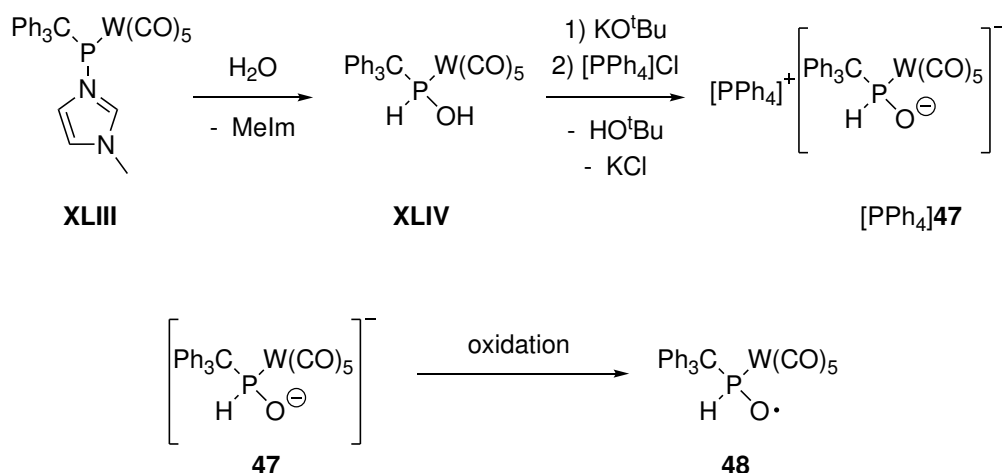
Scheme 41: Synthesis of the phosphinito complex [PPh$_4$]**47** from the methyl imidazole phosphinidene complex adduct **XLIII** by Biskup[160,161] and the planned oxidation to **48**.

none were observed. In contrast to the oxidation of the phosphinito complex [Cp$_2$Co]**14** (cf. Figure 48, p.82) the oxidation potential is shifted to higher values, suggesting a less stabilised radical complex **48**. The absence of a reversible signal with also no return wave at lower potentials, suggested that the radical, formed upon oxidation, is not stable on the CV timescale (scan rates: 50-2000 mV) and also does not react to any CV active species. Therefore, the redox chemistry of **47** was not explored in solution.
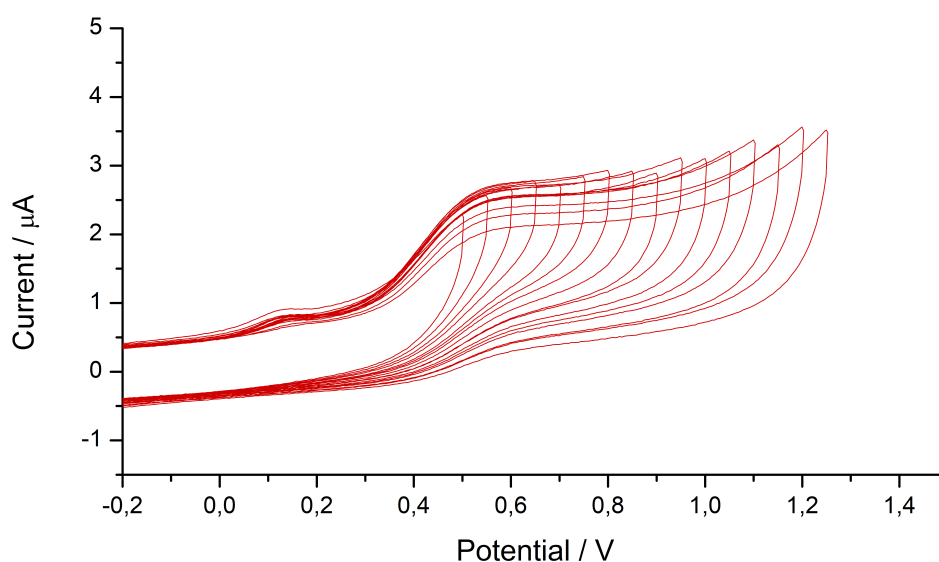
Figure 71: Zoom of the CV on the oxidative region of [PPh$_4$]**47** in MeCN with different upper scan limits, (scan rate: 200 mV s^{-1}, 0.2 M [nBu$_4$N]PF$_6$, vs. Fc/Fc$^+$ oxidation potential).

5.10. DFT analysis on the SDD of P–E containing radical complexes

In a wider perspective the nature of the element E of the radical complexes **11,18,49-54** was investigated in collaboration with Zhu and Qu (Scheme 42).[159] In the study tungsten and iron complexes with the substitution pattern **d** and **e** on the phosphorus atom were analysed regarding their formation free energy from *P*–OTEMP and theoretical *P*–E-TEMP phosphane complexes **8d,17d,e,49'd,e-54'd,e** (E = O, S, NMe, PMe) and the SDD in the final radical complexes **11,18,49d,e-54d,e** (Table 14). The formation of all radicals is endergonic, with the exception of **18d**, however, being only slightly below zero. Noteworthy, the Δ_rG values, which correspond directly to the BDG(N–E), are lowest for E = O, and then increases strongly. The experimentally remarkable stability of **8d** compared to the iron complexes **17d,e** is again reflected in this study (c.f. Figure 65, p.99). For E = S and NMe, similar values are observed, which are 14-27 kcal mol^{-1} larger than for E = O, suggesting a significantly higher stability than their oxygen derivatives. For E = P, Δ_rG values are extremely large and range from 41 to 47 kcal mol^{-1}. Therefore, it can be assumed, that it is very unlikely to access these complexes via a N–P bond cleavage, in analogy to the N–O bond cleavage of aminoxylphosphane complexes. Regardless of their accessibility the SDD of the radicals was analysed. For E = O the results show the same trend as the previously discussed theoretical calculations performed in this work. In all cases going from O to S to NMe to PMe, the spin density on the metal decreases, parallel to an increase on the P-bound E-atom. This even leads to a complete inversion of the SDD of **18e** (O: 0.00 e; Fe: 0.90 e) compared to **54e** (PMe: 0.90 e; Fe: 0.01 e). One noteworthy difference is the different spin density on the S-atom in **52d** (S: 0.31 e) and **52e** (S: 0.03 e), emphasising the effect of different substitution pattern, which might allow fine tuning of the system.
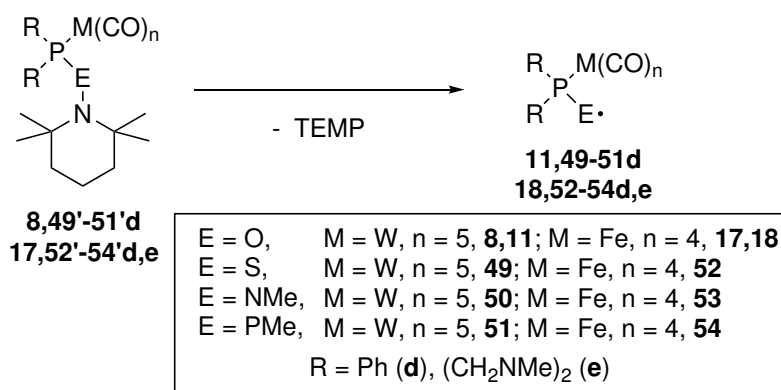
Scheme 42: *P*–E-TEMP tungsten and iron complexes **8,17,49'-54'** and their N–E bond cleavage products the P–E radical complexes **11,18,49-54**.

Table 14: Spin densities in e of selected atoms (E, only O, S, N or P atom, and M) and formation Gibbs free energy $\Delta_r G$ in kcal mol^{-1} of the calculated radical complexes **11,18,49-54**.

	E	M	$\Delta_r G$		E	M	$\Delta_r G$
11d	0.31	0.49	18.9	**11e**	—	—	—
49d	0.48	0.40	32.9	**49e**	—	—	—
50d	0.72	0.13	28.7	**50e**	—	—	—
51d	0.93	0.02	40.8	**51e**	—	—	—
18d	0.09	0.94	−0.4	**18e**	0.00	0.90	0.3
52d	0.31	0.71	20.7	**52e**	0.03	0.90	25.4
53d	0.65	0.29	26.8	**53e**	0.71	0.19	27.4
54d	0.90	0.08	46.1	**54e**	0.91	0.01	47.1

It was further studied if a shift of the metal from the P centre to E is energetically possible (Scheme 43). Therefore, $\Delta_r G$ values and the reaction barriers $\Delta_r G^{\ddagger}$ for the complexes **55-62d** were calculated (Table 15). For the tungsten complexes **55-58d** both $\Delta_r G$ and $\Delta_r G^{\ddagger}$ are rather small. The barrier of the metal shifting increases for E = NMe, PMe, however the $\Delta_r G$ even decreases for **58d**. These observations lead to the conclusion that the transfer of the metal fragment from P and to E is energetically possible, however kinetically the shift is less favoured for E = NMe, PMe, due to increased steric bulk and assumingly larger structural changes in the transition states compared to **55,56d**. High $\Delta_r G$ values are found for the iron complexes **59,60d** making the metal fragment shift less likely in the herein studied P–O radical iron complexes **18** and their related thio derivatives **52**. For E = NMe, PMe (**61,62d**) the calculated $\Delta_r G$ values are very similar to the tungsten complexes, even showing much smaller $\Delta_r G^{\ddagger}$, from which fast equilibria in solution can be assumed. The study shows that

E = O,	M = W, n = 5, **55**; M = Fe, n = 4, **59**
E = S,	M = W, n = 5, **56**; M = Fe, n = 4, **60**
E = NMe,	M = W, n = 5, **57**; M = Fe, n = 4, **61**
E = PMe,	M = W, n = 5, **58**; M = Fe, n = 4, **62**
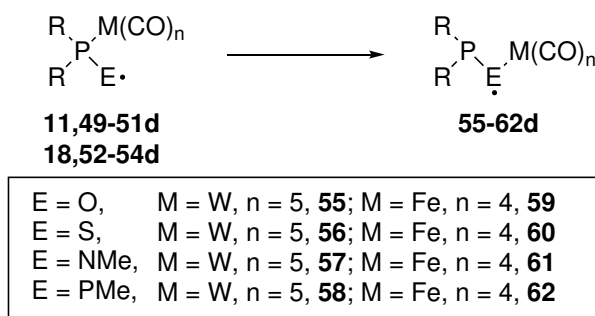
Scheme 43: Metal fragment shift of the iron and tungsten radical complexes **11,18,49-54d**.

Table 15: $\Delta_r G$ and $\Delta_r G^{\ddagger}$ for the metal fragment shift of the P–E radical complexes **11,18,49-54** to yield the P-E–M complexes **55d-62d**.

	55d	56d	57d	58d	59d	60d	61d	62d
$\Delta_r G$	3.7	3.2	3.7	1.3	16.9	7.9	3.6	0.1
$\Delta_r G^{\ddagger}$	3.1	2.0	9.6	11.1	17.4	8.5	3.9	4.6

for very hard elements E, like O, the phosphanoxyl ligand, better described as a phosphinoyl ligand, is extremely innocent. This becomes most apparent in the iron complexes and only if the metal fragment is not able to take up a lot of spin density the SDD is delocalised over M-P-O as found for the tungsten complexes. For the softer elements S, N and P the ligand becomes more noninnocent, keeping the spin density in the ligand framework. It can therefore be assumed that for a phosphanoxyl complex with high spin density on the oxygen atom an electron rich metal fragment should be used, which only acts as a protective group blocking the phosphorus lone pair, allowing reactions at the oxygen atom. The study showed, however, that this might be accompanied with an energetically and kinetically facile metal fragment shift, which would lead again to phosphorus-centred reactivity, which was also observed by Heurich in the decomposition of the phosphanoxyl tungsten complex to **XXIII** (cf. Scheme 10, p.10).

6. Towards P–O containing radical carbene adducts

6.1. Background of *P*-carbene adducts

The calculated high spin density of the previously discussed P–O containing iron complexes **18**, combined with the observed redox processes on the Fe-centre, raised the question if these R_2P–O radical species can be stabilised with less redox active fragments. Therefore, the isolobal concept of Hoffmann was considered. In this concept, summarised in his nobel lecture from 1982, low-valent metal fragments are compared to low-valent main group fragments with respect to their FMOs, the number of valence electrons, their frontier molecular symmetry and the energies of these orbitals.[162] From these situations reactivity aspects can be concluded/assumed. However, this has to be taken with care as a one-to-one relationship is not always fullfilled. As an initial approach to find isolobal pairs the number of valence electrons of the main group and the metal fragment can be compared. In this case the previously experimentally investigated P–O containing radical complex chemistry, namely the $Fe(CO)_4$ and $W(CO)_5$ fragments have 16 valence electrons. The isolobal main group counterpart are therefore 6 valence electron species, such as a chalcogen atom. A carbon-based isolobal species would be a CH_2 fragment, known as carbenes.

The first stable carbene was reported by Bertrand in 1989, followed shortly by Arduengo III in 1991, who synthesised the first stable crystalline carbene.[163,164] Arduengo's carbene had an imidazole-based (1,3-diazole-2-ylidene) scaffold, from which their today commonly used name N-heterocyclic carbenes (NHC for short) originates (Figure 72). In contrast to the parent CH_2, which has a triplet ground state, the N-atoms in the NHC stabilise the singlet ground state making NHC formidable σ-donors and reasonably good π-acceptors.[165] These properties are partly the reasons for their remarkable success as ligands in transition metal chemistry and replace the previously often used phosphane ligands, *e.g.*, in the 2nd generation Grubbs catalyst.[166,167] It was recognised very early that due to their easy access
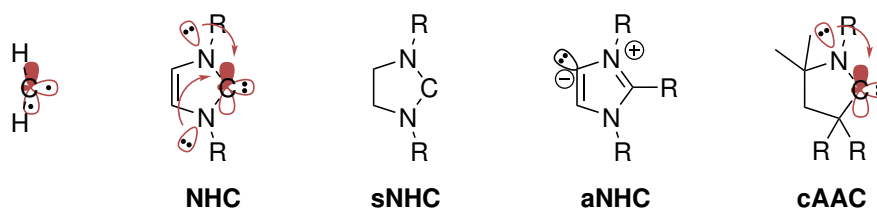
Figure 72: Lewis structures of triplet CH_2 and representatives for NHC, sNHC, aNHC and an cAAC.

an almost limitless variety of derivatives was accessable, which allowed precise fine tuning of the NHC's ligand properties. During the exploration of the NHCs chemistry it was recognise that also the 4- and 5-position of a classical NHC can be turned into carbene centres, the resulting mesoionic carbenes are termed abnormal NHC (aNHC).[168,169] To overcome unwanted reactivity at the 4- or 5-position, NHCs were prepared in which the backbone is saturated (sNHC).[170,171] Another breakthrough was the isolation of cyclic alkyl amino carbenes (cAAC), in which one of the N-atoms is replaced by an alkyl group in an α-position of the carbene centre.[172] It was shown, that cAACs are not only better σ-donors but also significantly more potent π-acceptors.[173] The origin of this is due to the presence of only one N-atom, *i.e.*, the inductive electron withdraw from the sp^2(C) lone pair is diminished and simultaneously the vacant p(C)-orbital is also less stabilised by only one N-lone pair. Especially the increased π-acidity allowed the stabilisation of several low-valent metals.[174]

The overall success of carbenes in transition metal chemistry quickly followed their application in main group chemistry.[173,175–178] Commonly their properties are utilised to stabilise low-valent species, such as silylenes R_2Si, the heavier analogues of carbenes. Even the otherwise highly reactive dihalosilylenes SiX_2 (X = Cl, Br) can be isolated as NHC adducts. However, not only diamagnetic low-valent species can be stabilised, but also NHC adducts of several open-shell main group elements are reported to date.[44,176,179,180] Besides many of the reported radicals are π-radicals also σ-radicals, such as the benzoyl R-C=O radical,[181] can be substantially stabilised. The benzoyl radical can be interpreted as the carbon derivative of the in-depth discussed phosphinoyl radical **1**. Noteworthy, among these open-shell NHC adducts with main group radicals no adduct with a phosphorus radical is reported, the only two examples of a carbene stabilised P-radical are cAAC stabilised phosphanyl radicals reported by Bertrand and Alcarazo.[44,182]

Due to their strong donor abilities, carbenes have also been used to stabilise E=O double bonds, which in the absence of the carbene would dimerise. Hence, early attempts to stabilise silaketones $R_2Si=O$ feature NHC-stabilisation.[183] Similarly, the early chemistry oxophosphonium ions $R_2P=O^+$ developed around NHC stabilised species (Figure 73).[184,185] After an initial example of a thiaphosphonium $R_2P=S^+$ stabilised by the donor molecules dimethylaminopyridine (DMAP) or PMe_3, the approach was transferred to the oxophosphonium chemistry.[186] Masuda reported a pyridine and a NMe_3 stabilised derivative and another NMe_3 adduct was described by Kinjo.[187,188] Chauvin utilised then the strong donor ability of NHCs and isolated the first NHC oxophosphonium adduct salts.[184] Since a base free oxophosphonium was only reported recently,[79] as already discussed (cf. Figure 7, p.17), at the time of Chauvins studies it was necessary to generate the carbene moi-

110
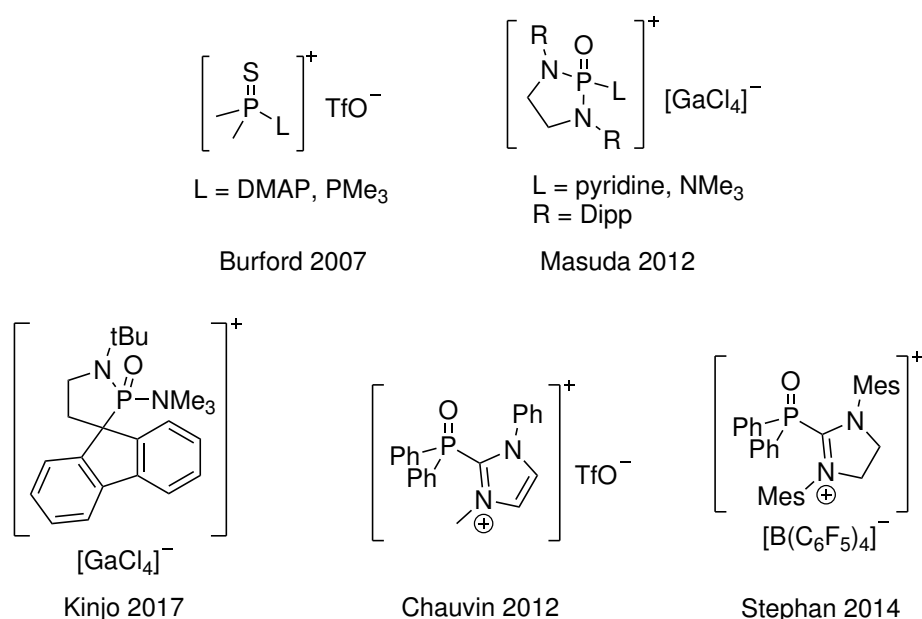
Figure 73: Lewis structures of known thiaphosphonium and oxophosphonium adducts.

ety already bound to the phosphorus atom via N-methylation of a 2-phosphinoyl-imidazol (Scheme 44). This methodology is similar to the approach discussed for the radical ligand complex chemistry (cf. Figure 4, p.7). In the adduct the NHC could be substituted by a bisaminocyclopropenylidene (BAC),[189] which are known to be stronger σ-donors than NHCs (Scheme 45). Furthermore, in the presence of chloride, the P-carbene bond was also cleaved. These observations were interpreted by Chauvin to underline the dative bond character of the P-carbene bond, which was corroborated by DFT calculations.[184] Such substitution reactions were not observed for the pyridine and NMe$_3$ oxophosphonium adducts, suggesting less dative bond character in these derivatives.[187] Reduction of these oxophosphonium carbene adducts, would yield phosphinoyl carbene adducts, which are the
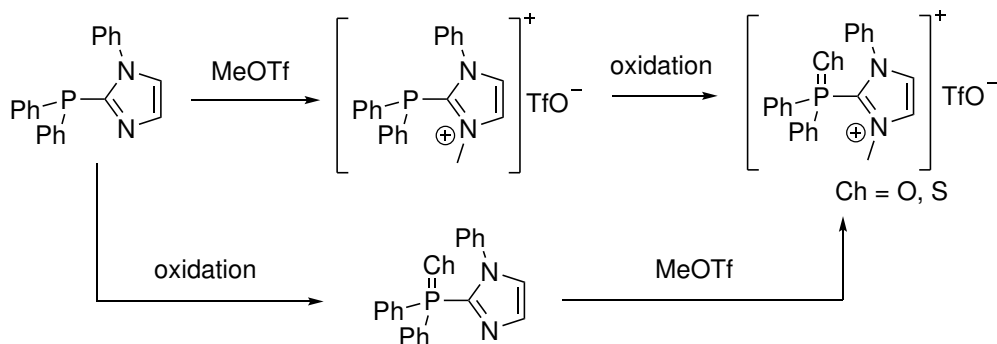
Scheme 44: Synthetic protocol for N-methyl NHC oxophosphonium adducts, reported by Chauvin.[184]
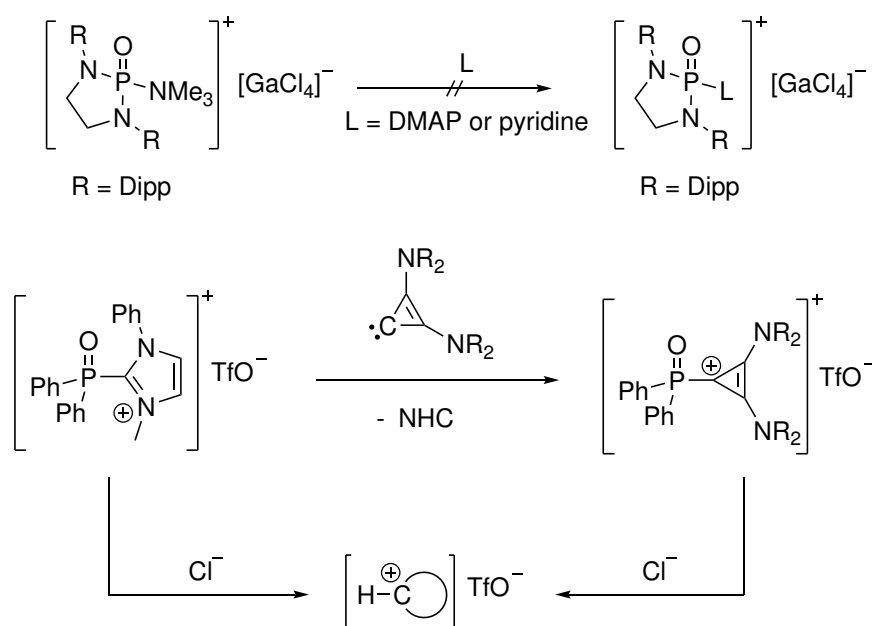
Scheme 45: Attempts of substitution of oxophosphonium adducts, and chloride promoted P-C bond cleavage.[184, 187]

isolobal counterpart to the phosphanoxyl/phosphinoyl metal complexes. An early attempt to generated such species was done by Apeloig in 2007, by irradiating a mixture of the IMes (1,3-dimesityl-imidazol-2-ylidene) NHC and [Hg(P(O)(O^{i}Pr)$_2$)] directly in the EPR spectrometer (Scheme 46).[190] Under these conditions the free phosphinoyl radical **1j** is generated and trapped by IMes. The formed phosphinoyl NHC adduct **63j** shows a doublet in the EPR spectrum arising from a hyperfine coupling between the electron and the ^{31}P nuclei of
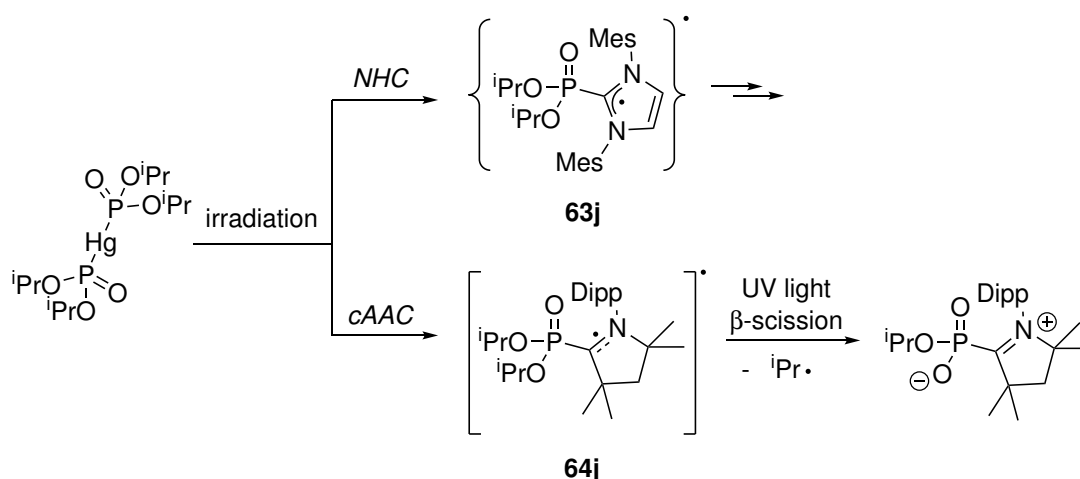
Scheme 46: Synthetic approach to the unstable phosphinoyl NHC adduct **63j** and its stable cAAC derivative **64j** together with the β-scisson product of the latter.[190, 191]

48.7 G, which is in the range of hyperfine couplings observed for free phosphinoyl radicals. Additional hyperfine coupling to the NHCs ^{14}N nuclei proof the adduct structure of **63j**. The radical decayed within 7 seconds without continuous irradiation. Only recently, this system was revisited by Dobrovetsky and by replacement of IMes with the cAAC (1-Dipp-3,3,5,5-tetramethylazolidin-2-ylidene) he was able to isolate the phosphinoyl cAAC adduct **64j**.[191] In the EPR spectrum the hyperfine coupling constant (11.2 G) for the electron and ^{31}P nuclei coupling is significantly smaller than in **63j**. However, reported DFT calculations suggest similar spin density at the phosphorus atom of 3.1% and 4.6%, for **63j** and **64j**, respectively. For the discrepancy of the hyperfine coupling and the DFT calculations the authors considered a different spin-transfer mechanism. However, due to the high π-acidity of cAACs the difference in the observed EPR values is somewhat expected. Under UV-light **64j** undergoes β-scission of the O^{i}Pr substituent. Furthermore, in 2020 Dobrovetsky also recognised the potential of oxophosphonium carbene adducts as precursors to the phosphinoyl radical carbene adducts.[191] He reported the synthesis of a diphenyl oxophosphonium cAAC adduct **XLVII** via oxidation of a phosphenium cAAC adduct **XLV** with ^{t}BuOO^{t}Bu (Scheme 47). High conversation rate was only observed if the reaction was performed under UV light. The *in situ* generated phosphoranyl radical **XLVI**, detected by EPR, undergoes β-scission in analogy to **VIII** and discussed in the introduction for previously observed phosphoranyl radicals (cf. Scheme 1, p.3), forging the oxophosphonium cAAC adduct **XLVII**. Reduction of **XLVII**

Scheme 47: Synthetic approach to the stable phosphinoyl cAAC adduct **64d** via reduction of the oxophosphonium cAAC adduct **XLVII**.[191]

with decamethylcobaltocene (CoCp*$_2$) yielded the first isolable phosphinoyl carbene adduct **64d**. The reported hyperfine coupling of the electron to the ^{31}P-nuclei of 18.2 G is very similar to the value reported for **64j**. However, DFT calculations yield a spin density of only 2% on the P-atom.

The success in isolating a phosphinoyl radical adduct like **64d** can clearly be attributed to the strong σ-donor ability and especially the high π-acidity of cAACs. However, the reported EPR values and also the supporting DFT calculations to **64d** suggest a large carbon-centred radical character, which somehow contradicts the desired target of a phosphinoyl adduct. NHCs on the other hand, due to their weaker π-acidity should leave more radical character on the phosphorus atom. Despite the report of Apeloig, no NHC phosphinoyl adducts such as **63** have been reported so far. Therefore, the synthesis and reduction of NHC oxophosphonium adducts† was investigated and results are described in the following chapter.

6.2. Synthesis of non-bulky NHC oxophosphonium adducts

The facile synthetic approach of Chauvin for NHC oxophosphonium adducts was employed in this study (Scheme 48).[184] Initially the chlorophosphanes **3d,e,f,i** were reacted with *in situ* generated **65** at −78 °C to forge the *N*-methyl imidazolyl phosphanes **66d,e,f**. The reaction of 1,3,2-oxazaphospholidine **3i** with **65** was not selective and yielded multiple products, observed by ^{31}P-NMR spectroscopy. The formation of **66d** is proven by comparison to al-

Scheme 48: Synthetic approach to *N*-Me-imidazolyl phosphane oxides **67d,e,f** having different substitution patterns at the P centre.

---

†This nomenclature is chosen to underline the concept of stabilising the targeted cations and radicals, however, these compounds have a significant imidazol(ium)yl-phosphane character with a delocalised positive charge or unpaired radical distributed over the N-C-N atoms of the imidazol-(ium)yl moiety. However, their adduct properties have been discussed by Chauvin.[184]

ready reported values by Yurchenko and Nishikawa.[192,193] Besides the ^{31}P resonance of **66d** (-30.3 ppm) another resonance at 19.3 ppm is observed in a 80:20 ratio. Comparison with Yurchenko reports suggest that this resonance originates from the corresponding oxide **67d**.[194] Remarkably, this oxidation was not reported by other groups, despite common organic work-up under ambient conditions. However, since the subsequent transformation is the generation of the phosphane oxide **67d** from **66d** no attempts were made to separate the products. Noteworthy, the reaction to **66f** was always accompanied with small amounts (2–4%) of the related secondary phosphane oxide. This impurity could not be separated due to similar solubility and attempts to recrystallise **66f** showed no improvement. Both diazapospholidines **66e,f** were obtained as colourless oils at room temperature, which solidified and partially crystallised if kept at 4 °C. ^{31}P-NMR chemical shifts for **66e,f** in the NMR spectrum appear high field shifted compared to **3e,f** at 86 and 67 ppm, respectively. The similar difference of $\delta(^{31}P)$ by $\sim$20 ppm between the two compound is also observed in the tungsten and iron complexes **6e,f** and **12e,f**. For **66f** single crystals could be obtained and analysed via X-ray diffraction proving the desired connectivity (Figure 74). Despite the manifold derivatives, *i.e.*, reported by Yurchenko, no crystal structure of a bisamino imidazolyl phosphane is known. Comparison of **66f** with the reported structure of **66d** shows no significant changes in the imidazolyl substituent. The P–C5 bond is slightly elongated in **66f** compared to **66d**. Also, bond lengths and angles of the 1,3,2-diazapospholidine moiety are comparable with values obtained for the tungsten complexes **6f** and **8f**. All three phosphanes **66d,e,f** were then oxidised without further purification. Initially **66f** was reacted with
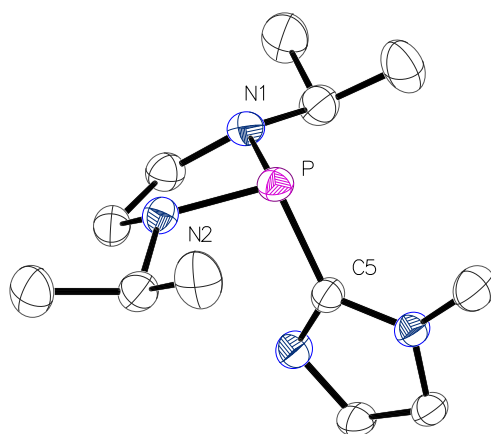
Figure 74: Molecular structure of **66f** in the crystal structure; ellipsoids are set at 50% probability level and all hydrogen atoms are omitted for clarity. Selected bond lengths and angles are given in Å and ° respectively: d(P–C5) 1.86113(13), d(P–N1) 1.70616(13), ∠(N1-P-N2) 91.092(9), ∠(N1-P-C5) 102.703(3); $\sum_{\angle}^{P}$ 296.5, $\sum_{\angle}^{N1}$ 343.6.

mCPBA following the protocol of Chauvin resulting, however, in a mixture of products. Addition of an aqueous solution of H_2O_2 instead forged the phosphane oxides **67d,e,f** with high selectivity. After purification by column chromatography with an eluent mixture of methanol and ethyl acetate, **67d,f** were obtained as colourless oils, which solidify upon standing. Noteworthy, **67e** could only be obtained in minor amounts after column chromatography due to a remarkably insolubility and furthermore collected fractions containing **67e** were also contaminated with *N*-methyl imidazole, suggesting partial decomposition. The phosphane oxides **67d,f** can be stored under ambient conditions without noticeable degradation.

To obtain the IMe$_2$ (1,3-dimethylimidazol-2-ylidene) oxophosphonium adducts **68d,f**, the phosphane oxides **67d,f** were methylated with methyl triflate to generated the NHC fragment already bound to the P-atom (Scheme 49). The methylation is immediate and after evaporation of the solvent and washing with *n*-pentane **68d,f** were obtained as colourless fine powders. The modification at the imidazole substituent has a minor effect on the ^{31}P chemical shift for the diphenyl derivative **68d**, however a stronger impact is observed for **68f** (Table 16). Attempts to crystallise **68d** from a saturated DCM solution, reveals the moisture sensitivity of the NHC oxophosphonium adducts, as X-ray diffraction analysis showed only diphenylphosphinic acid, as the product of the hydrolysed P–C bond. Similar observations were made by Chauvin for the mixed *N*-Ph,*N'*-Me derivative (cf. Scheme 45, p.112).[183] Nevertheless, from single crystals of **68f**, grown from a saturated DCM solution, the structural integrity could be obtained by X-ray diffraction analysis (Figure 75). While sulfides and selenides have been reported, this is the first report of the crystal structure of an NHC oxophosphonium adduct. However, the quality of the crystals obtained was low and bond lengths and angles have to be taken with great care. Still the oxidation of the phosphorus atom leads to significant bond shortening between P–C5 and P–N1/2. The short P–O oxygen bond length is in the expected range for a P–O double bond. Accompanied an increase in the bond angles is found, in line with an increase in s-orbital contribution in all bonds due to the more electronegative oxygen atom bound to phosphorus. The angular sum around
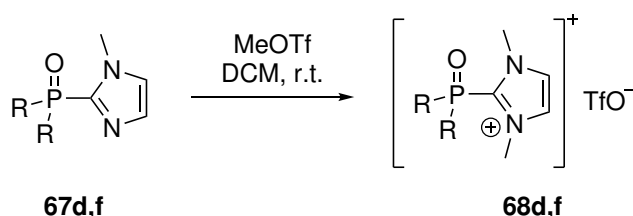
Scheme 49: *N*-methylation of imidazol-2-yl phosphane oxides **67d,f** with MeOTf forging NHC oxophosphonium adducts **68d,f**.

Table 16: ^{31}P-NMR chemical shifts of **66,67,68d,e,f** in a) CDCl$_3$ b) C$_6$D$_6$ c) CD$_2$Cl$_2$.

$\delta(^{31}$P) / ppm	d	e	f
66	-30^a	86^b	67^b
67	18.0^c	19.0^a	12.5^a
68	18.5^c	—	4.4^c
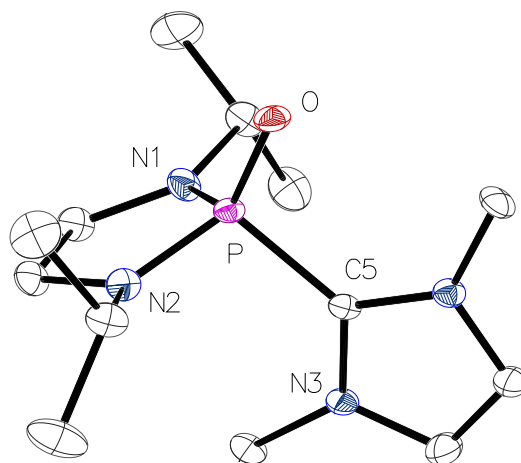
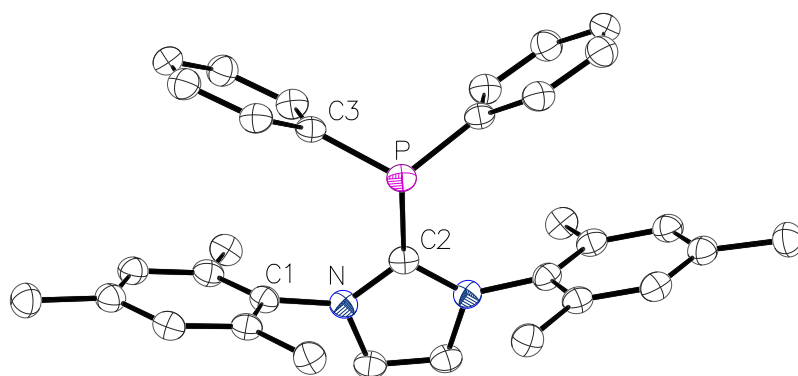**Figure 75:** Molecular structure of **68f** in the crystal structure + OTf; ellipsoids are set at 50% probability level and all hydrogen atoms are omitted for clarity. Selected bond lengths and angles are given in Å and ° respectively: d(P–C5) 1.839(4), d(P–N1) 1.629(3), d(P–O) 1.473(3), ∠(N1-P-N2) 95.63(16), ∠(C5-P-O) 104.90(17), ∠(N1-P-C5) 108.14(17); ∠(N3-C5-P-O) 178.3(3), $\sum_{\angle}^{P}$ 297, $\sum_{\angle}^{N1}$ 360.

the nitrogen atoms of the diazaphospholidine moiety is increased compared to **66f**, having a maximum for N1 with almost 360°, being completely planar. This structural feature is similar to the ones observed in the previously discussed metal complexes.

6.3. Synthesis of bulky NHC oxophosphonium adducts

The facile access to the IMe$_2$ adducts **68**, having no significant steric bulk, relies on the easy methylation of the imidazolyl phosphane oxides **67**. This approach, however, is not possible for commonly used bulky NHCs, such as IMes and therefore the synthetic protocol had to be adjusted. An initial attempt was ligand substitution from the pyridine adducts of oxophosphonium salts similar to the ones reported by Masuda (cf. Figure 73), p.111). It has to be mentioned that ligand substitution was already tried by Masuda on his NEt$_3$ adduct by the better donors pyridine and DMAP, however without success.[187] Since NHCs are known to be much better σ-donors than pyridine and its derivatives, the pyridine adducts

synthesised in this work were probed for a possible substitution with an NHC.

As reported by Masuda the pyridine adducts can also easily be accessed by initial chlorine abstraction from the chlorophosphanes **3d,e,f** with trimethylsilyl triflate and subsequent reaction with pyridine *N*-oxide (Scheme 50).[187] The chlorine abstraction forges the sulfonyl phosphane **69**, which depending on the substituents on the phosphorus atom dissociates in solution to the phosphenium ion.[195,196] Adjacent nitrogen atoms to the P atom stabilise this solvent separated ion pair in contrast to the phenyl substituents in **69d**. Due to their high stability diazaphospholenium ions have already been applied as catalyst in several reactions, *e.g.*, hydroborations of pyridine.[197–199] For the derivative **69f** its presence was also proven in this work by ^{31}P{^{1}H}-NMR spectroscopy, as a broad resonance (FWHM = 78.76 Hz) with a chemical shift at 264 ppm. After formation of **69d,e,f** the compounds were dried *in vacuo* to remove Me$_3$SiCl and then redissolved in DCM before oxidation with pyridine *N*-oxide. After washing with toluene and *n*-pentane the adducts were recrystallised in DCM and Et$_2$O mixtures and obtained in high yields. The ^{31}P{^{1}H}-NMR spectrum of **70d,e,f** in CD$_2$Cl$_2$ shows a single resonance at 45.7, 20.7 and 17.1 ppm respectively. However, the ^{1}H-NMR spectrum of a solution of recrystallised **70d** reveals the presence of another compound with a strongly lowfield shifted resonance at 15.43 ppm. This shift is similar to the N–H hydrogen atom of the lutidinium triflate (14.45 ppm in CD$_2$Cl$_2$) as comparison with the literature shows.[200] The resonance is therefore assigned to the pyridinium triflate, which makes up 33% in the mixture with **70d**. Remarkably, for the 1,3,2-diazaphospholidine adducts **70e,f** no pyridinium salt is observed in the ^{1}H-NMR spectrum. It can be assumed that this is correlated with the higher stability of the phosphenium ions **69e,f** in comparison to **69d**. Similar observations are made in the ESI-mass spectrogram of the **70d,e,f**, in which molecular ion peaks are observed for **70e,f** but not for **70d**, for which only diphenylphosphinic acid based ions are detected. The chloride derivative of **70d** was recently reported by Lee & Lee.[201] Despite
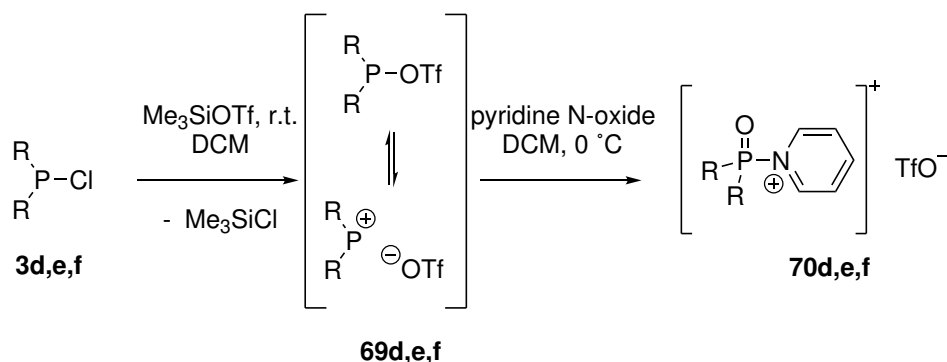
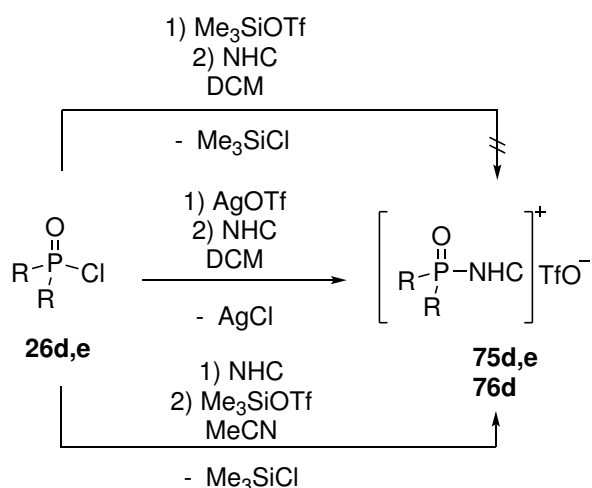**Scheme 50:** Applied procedure for the synthesis of pyridine oxophosphonium adducts **70d,e,f**.

118
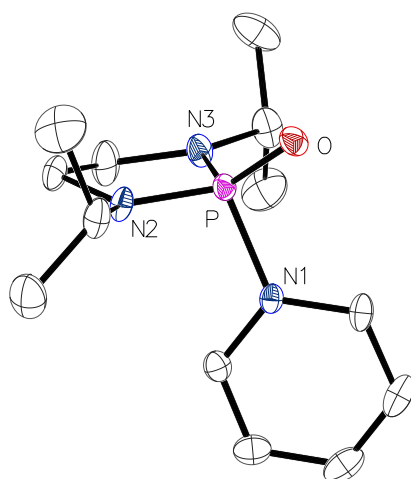
Figure 76: Molecular structure of **70f** in the crystal structure + OTf; ellipsoids are set at 50% probability level and all hydrogen atoms are omitted for clarity. Selected bond lengths and angles are given in Å and ° respectively: d(P–O) 1.46442(12), d(P–N1) 1.81797, d(P–N2) 1.61896(12), d(P–N3) 1.61177(13), ∡(N1-P-N2) 97.147(8), ∡(N1-P-O) 102.304(8), ∡(N3-P-N1) 104.679(8); $\sum_{\angle}^{P}$ 308.9, $\sum_{\angle}^{N3}$ 357.9.

this, X-ray diffraction analysis of single crystals of **70d,f** show the expected connectivity for both compounds. While a satisfying crystal quality was obtained for **70f** (Figure 76), the measured crystals of **70d** were of poor quality and showed two independent molecules in the elementary cell. Bond parameters in **70f** are similar to the reported values of the Dipp derivative by Masuda.[187]

Having the pyridine adducts in hand, substitution reaction with the IMes was attempted (Scheme 51). The reaction of IMes with **70f** in THF at room temperature was followed via ^{31}P{^{1}H}-NMR spectroscopy and immediately a clean conversion to a product with a chemical shift of 14.2 ppm was observed, which has a small $\Delta\delta(^{31}$P) compared to the starting material **70f**. The ^{1}H-NMR spectrum of the product after purification shows resonances of

70f   **71f**
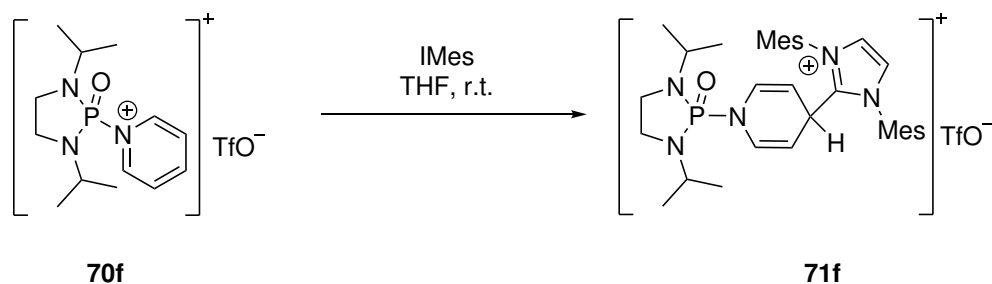
Scheme 51: Addition of IMes to **70f** yielding **71f**, in the attempt of ligand substitution.

119
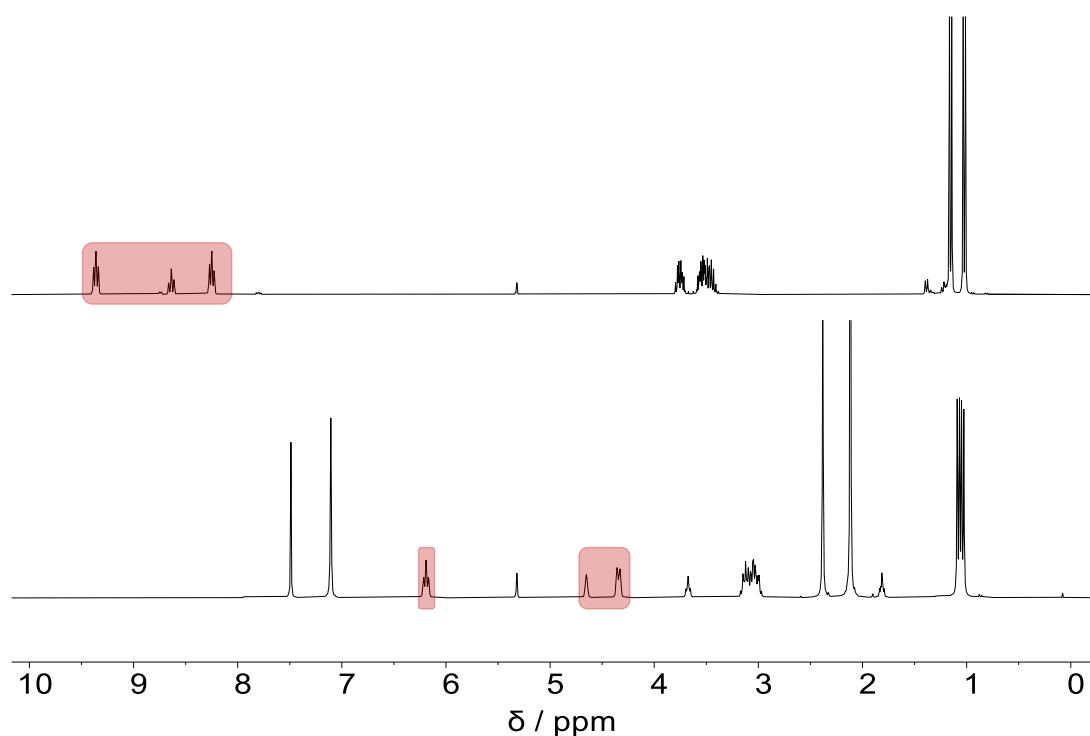
Figure 77: ^{1}H-NMR spectrum of **70f** (top) and **71f** (bottom) in CD_2Cl_2. Highlighted in red are resonances assigned to the pyridine moiety.

the IMes moiety and a set of signals assigned to the pyridine moiety, however, significantly highfield-shifted compared to the resonances of **70f** (Figure 77). Together with ESI-MS results the product was assigned to be **71f**, which is the simple addition product of the IMes to the 4-position of the pyridine in the adduct **70f**. Such reactivity has already been reported for C-substituted pyridinium salts, however this is the first example for a phosphinoyl pyridinium salt.[202] In agreement with the observations by Masuda, substitution of the pyridine does not take place, however the reaction with the strong σ-donor IMes leads to addition probably due to the increased stabilisation of the positive charge by the imidazolium motif. Access to oxophosphonium NHC adducts via substitution of weaker donors by NHCs seems therefore to be not feasible.

Due to the lack of other bulky NHC oxophosphonium adducts, besides the single report of a sNHC (SIMes) by Stephan,[185] different synthetic routes were probed in this work to access such adducts (Scheme 52). For the pyridinium adducts **70** the intermediate formation of phosphenium salts **69** was already presented using Me_3SiOTf, similarly AgOTf can also be used instead. Subsequent reaction with the NHCs IMes or IPr_2Me_2 (1,3-diisopropyl-4,5-dimethyl-imidazol-2-ylidene) forges the NHC phosphenium adducts **73** and **74**, respec-

120
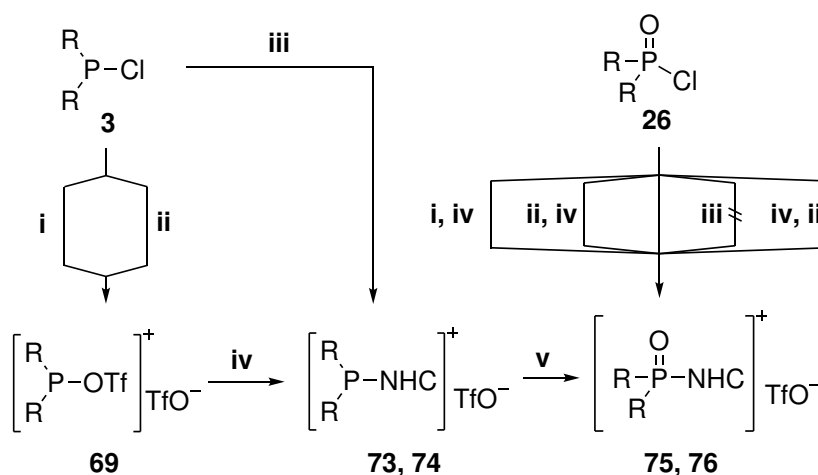
Scheme 52: Conceptional routes, tested in this thesis, for the synthesis of NHC oxophosphonium adducts (bottom right). **i**) AgOTf **ii**) TMSOTf **iii**) [Me$_3$Si-NHC]OTf **iv**) NHC **v**) oxidation.
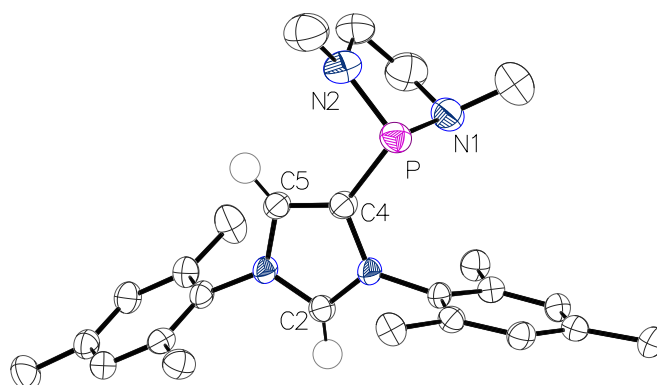
Figure 78: Molecular structure of **72e** in the crystal structure + Cl$^-$; ellipsoids are set at 50% probability level and all hydrogen atoms, but at C2 and C5, are omitted for clarity. Selected bond lengths and angles are given in Å and ° respectively: d(P–C4) 1.8499(5), d(P–N1) 1.6861(6), d(P–N2) 1.61896(12), $\angle$(N1-P-N2) 94.403(18), $\angle$(N1-P-C4) 98.46(2), $\angle$(N3-P-N1) 104.679(8); $\sum_{\angle}^{P}$ 293.8, $\sum_{\angle}^{N1}$ 336.4, $\sum_{\angle}^{N2}$ 356.4.

tively. However, a major drawback of these methods are that the stoichiometry has to be very precise since separation of the products from leftover AgOTf or its NHC complex [Ag(NHC)$_2$]OTf proofed to be difficult. Excess of NHC can also lead to a migration of the R$_2$P moiety away from the 2-position to the backbone of the NHC. This observation was made previously by several authors and during this work in the synthesis of **73e** single crystals of the rearrangement product **72e** were obtained (Figure 78), stressing this issue.[203,204] The chemistry of backbone phosphanylated carbenes was first investigated in 2010[205] and, early on, also Streubel et al. contributed to this field.[206–208]

Table 17: ^{31}P-NMR chemical shifts of chloro phosphanes **3d,e,f** and NHC adducts **73d,e,f** and **74d,e,f** in CD$_2$Cl$_2$.

$\delta(^{31}$P$)$ / ppm	d	e	f
3	82	170	160
73	−7	111	104
74	−28	104	94

Alternatively, 2-trimethylsilyl-imidazolium triflate salts [Me$_3$Si-NHC]OTf can be used to overcome the problem of stoichiometry. This method allowed the synthesis of IMes adducts **73d,e,f** and the smaller IPr$_2$Me$_2$ adducts **74d,e,f** (^{31}P{^{1}H}-NMR values see Table 17). Noteworthy, in all reactions a significant amount of imidazolium triflate was observed as a side product. For the diphenyl substituted **73d** and **74d**, smaller amounts around 5% to 15% are observed, despite their stability towards air and moisture. Recrystallisation can reduce the impurity content to smaller than 2%. This is in stark contrast to the diazaphospholidine based adducts **73,74e,f**. For the isopropyl derivatives **73f** and **74f** the content of imidazolium salt after attempted purification were astonishing 50 and 75%. The smaller methyl derivatives **73e** and **74e** showed less impurity with salt contamination of 19% for both NHC adducts. A similar observation was also made already by Grützmacher using IPr$_2$Me$_2$ to stabilise a phosphiranium ion, there 10% of imidazolium salt were observed as impurity.[209] The formation of the adducts was corroborated by additional HR-(+)-ESI-MS experiments. These NHC adducts show a remarkably high potential for crystallisation. Careful addition of Et$_2$O to a THF solution of the adduct salts leads to immediate formation of crystalline precipitate. X-ray diffraction analysis of these crystals (Figure 79 and 80) allowed to structurally


Figure 79: Molecular structure of **73d** in the crystal structure + OTf$^-$; ellipsoids are set at 50% probability level and all hydrogen atoms are omitted for clarity. Selected bond lengths and angles are given in Å and ° respectively: d(P–C2) 1.84985(8), d(P–C3) 1.82741(5), $\angle$(C1-N-P-C3) −41.3 , $\sum_{\angle}^{P}$ 310.4.
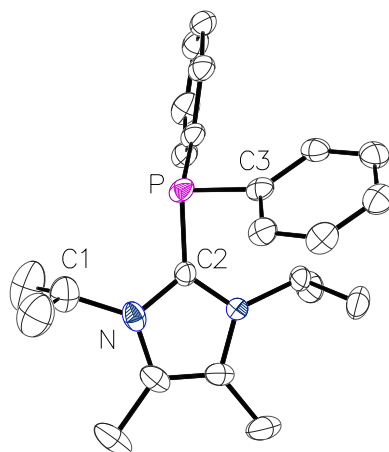
Figure 80: Molecular structure of **74d** in the crystal structure + OTf⁻; ellipsoids are set at 50% probability level and all hydrogen atoms are omitted for clarity. Selected bond lengths and angles are given in Å and ° respectively: d(P–C2) 1.83726(4), d(P–C3) 1.83203(3), ∡(C1-N-P-C3) 140.0, $\sum_{\angle}^{P}$ 312.0.

analyse **73d,e** and **74d**. Comparison to other reported Ph$_2$P-NHC cationic adducts with *N*-aryl substituents, shows that a short P–C2 bond is present in **73d**.[205,206,210] Other bond lengths are in the expected range. A noteworthy feature is the alignment of the phenyl- and mesityl substituents in **73d**, which suggests significant π-interaction equal for both sides of the molecule. Comparison of the C1-N-P-C3 torsion angles of **73d** with the known structures shows that similar values are obtained for mesityl substituted NHCs but in the bigger IDipp (1,3-Dipp-imidazol-2-ylidene) substituted NHCs only one phenyl ring shows an overlap with a Dipp substituent of the NHC with a torsion angle close to 0°. If no π-stacking is possible as in **74d**, the NHC is almost rotated by 90° around the P–C2 bond axis, which also has been reported for other smaller NHC adducts like IMe$_2$ by Alcarazo. The structure of **74d** had been reported earlier by Kuhn as an [AlCl$_4$]⁻ salt.[211] However, slightly different bond lengths are observed, which might be due to the different counter anion and present crystal water in the structure of Kuhn. The quality of the single crystals obtained for **73e** is not sufficient enough to discuss any bonding parameters, however, also there the carbene is oriented similarly to the configuration of **74d**.

In the following step of this concept oxidation of the phosphenium NHC adducts should yield the targeted oxophosphenium adducts (Scheme 53). Despite the several reports of previously discussed phosphenium adducts there are no conceptional reports on oxidation of these. Direct oxidation was only achieved for diphenyl substituted phosphenium adducts by Chauvin and Dobrovetsky, using mCPBA or ^{t}BuOO^{t}Bu (cf. Scheme 44 and 47). Due to

Scheme 53: Oxidation of NHC phosphenium salts **73d,e** and **74d** to the NHC oxophosphonium adducts IMes **75d,e** and IPr$_2$Me$_2$ **76d** and the tested oxidising reagents.

the high content of imidazolium salt in the synthesis of the phosphenium adducts, presumably originating from hydrolysis, the use of mCPBA, because of its acidic nature, was not explored further. Following the report of Dobrovetsky **73d** was reacted with ^{t}BuOO^{t}Bu under brief irradiation with UV light and also without. In both cases a clean conversion to a single product was observed in the ^{31}P{^{1}H}-NMR spectrum of the reaction mixtures. The observed $\delta(^{31}$P) chemical shift of 8 ppm, together with clear evidence from the ^{1}H-NMR spectrum leads to the assignment to be indeed the desired oxophosphonium adduct **75d**, which is also in agreement with Stephans SIMes adduct (Figure 73, $\delta(^{31}$P): 14 ppm).[185] However, the attempted synthesis of the 1,3,2-diazaphospholidine oxophosphonium adduct **75e** via the reaction of **73e** with ^{t}BuOO^{t}Bu led to the formation of species with huge scalar $^1J_{P,H}$ coupling constant of 597 Hz and a chemical shift of 20 ppm. This likely being the secondary phosphane oxide, suggesting a hydrolytic P-NHC bond cleavage. Therefore, other oxidising reagent were tested. The reaction with Me$_3$SiOOSiMe$_3$ did not lead to the formation of the final product and if the mild oxidation reagent N$_2$O is used no reaction is observed. No oxygen transfer is also observed for the reaction of TEMPO with **74d**. Remarkably the usage of iodosylbenzene allows oxidation of **74d** to **76d** which is apparent from a $\delta(^{31}$P) chemical shift of 9 ppm. However, again formation of a significant amount of imidazolium salt (~50%) is observed. This might be the result of hydrolysis since iodosylbenzene is synthesised in aqueous basic solution and precipitates as a polymer. This polymer might encapsule

Scheme 54: Tested synthetic protocols for NHC oxophosphonium adducts **75d,e** and **76d** starting from chloro phosphane oxides **26d,e**.

residual water, which is released upon oxygen transfer to the phosphenium NHC adducts. Therefore, the soluble derivative **XLVIII** reported by Protasiewicz was used (Scheme 53, bottom right).[212] If freshly synthesised this reagent allows clean oxygen transfer without large amounts of imidazolium salt as impurities.

Additional, direct access from the chlorophosphane oxides **26d,e** was tested (Scheme 54). Since chloride abstraction from **3** proved to be easy, chloride abstraction was tested for **26d,e** with AgOTf and also Me$_3$SiOTf. Remarkably no reaction at all was observed between Me$_3$SiOTf and any chlorophosphane oxide **26d,e**. Subsequent addition of IMes to **26d,e** treated with AgOTf in DCM leads to the formation of **75d,e** besides several impurities. Surprisingly, the best results were obtained by reacting **26d,e** with NHC followed by an anion exchange with Me$_3$SiOTf. This method yields the NHC oxophosphonium adducts **75d,e** in high selectivity. The intermediately formed NHC oxophosphonium chloride appears to be stable, which is in contrast to the reports from Chauvin (cf. Scheme 45, p.112). This might be an effect of the increased size of the NHC.

Via the discussed methods it was possible to isolate the oxophosphonium IMes adducts **75d,e**. In the ^{31}P{^{1}H}-NMR spectrum singlets at 8.0 and 8.7 ppm are observed in MeCN-d3, for **75d** and **75e** respectively. In the ^{1}H-NMR of both derivatives the resonances belonging to the IMes moiety have significantly different chemicals shifts (Figure 81). This effect is stronger for the mesityl hydrogen atoms than for the NHC backbone resonances and especially the 3,5-H atoms of the mesityl substituent are highfield shifted by 0.5 ppm from **75e** to **75d**. And while the 2,6-methyl groups are only slightly affected, being 0.05 ppm
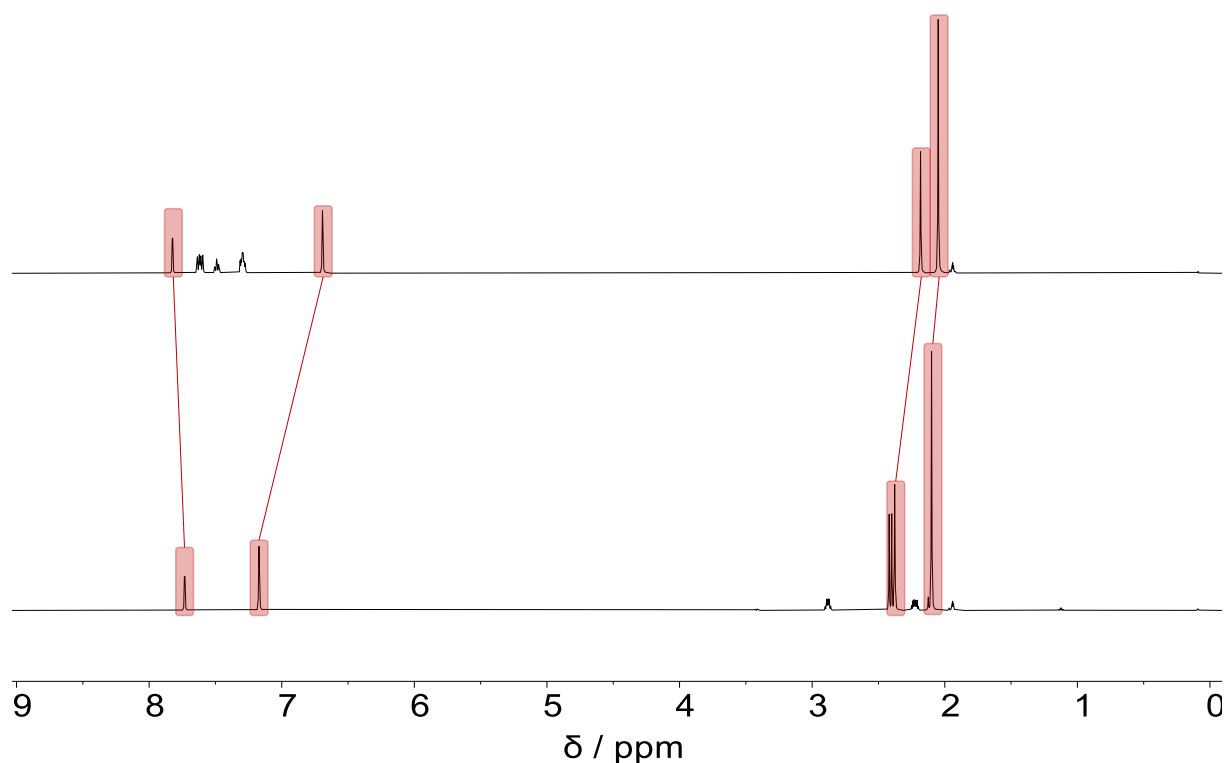
Figure 81: ^{1}H-NMR spectrum of **75d** (top) and **75e** (bottom) in CD_2Cl_2. Highlighted in red are resonances assigned to the IMes moiety.

shifted, the most outskirt 4-methyl group are more shifted by 0.2 ppm. These observations suggest different orientations of the IMes to the oxophosphonium fragment in **75d,e**. Single crystals were obtained from slow diffusion of Et_2O into a MeCN solution of the **75d,e**. The molecular structure of the oxophosphonium adducts in the crystals was obtained by X-ray diffraction analysis (Figure 82 and 83). Comparing the diphenyl systems **73d** and its oxide **75d** no severe changes have occurred upon oxidation. The previously discussed C1-N-P-C3 torsion angle is only slightly altered, but there is still a suitable configuration for positive π-interaction between the phenyl and mesityl substituents. The structure of **75e** shows similar common bond lengths and angles, however, the IMes fragment is rotated with respect to the P–O bond. To quantify this rotation the C1-N-P-O torsion angles of **75d** and **75e** are compared, having a 82° difference. Therefore, it can be concluded that the phenyl substituents are locking in on the observed configuration due to effective π-interactions and without these in **75e** a configuration between carbene and the P-fragment is adopted in which the imidazole-plane and the P–O bond are close to 90° twisted to each other, comparable also with the structure of **74d**.

126
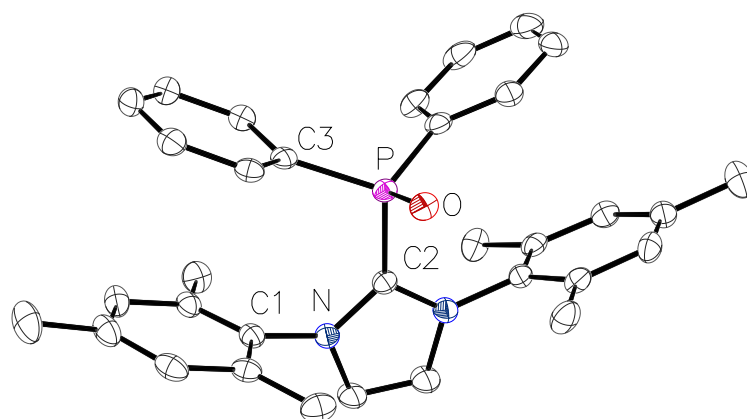
Figure 82: Molecular structure of **75d** in the crystal structure + OTf⁻; ellipsoids are set at 50% probability level and all hydrogen atoms are omitted for clarity. Selected bond lengths and angles are given in Å and ° respectively: d(P–O) 1.481569(14) d(P–C2) 1.85177(2), d(P–C3) 1.801557(16), ∡(C2-P-O) 108.3294(8), ∡(C1-N-P-C3) −26.11150(9), ∡(C1-N-P-O) −26.11150(9), ∡(C1-N-P-O) 86.0686(8).
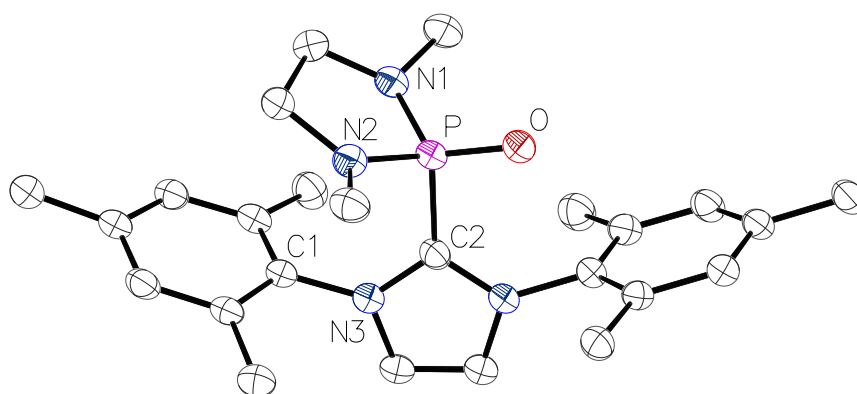
Figure 83: Molecular structure of **75e** in the crystal structure + OTf⁻; ellipsoids are set at 50% probability level and all hydrogen atoms are omitted for clarity. Selected bond lengths and angles are given in Å and ° respectively: d(P–O) 1.46360(3) d(P–C2) 1.85021(4), d(P–N1) 1.62579(4), d(P–N2) 1.61921(4), ∡(N1-P-N2) 95.907(2), ∡(C2-P-O) 103.822(3), ∡(C1-N-P-O) 168.7894(5).

From the insights of the in-depth study to access the NHC oxophosphonium adducts it was also possible to obtain the triflate salt of Dobrovetsky's cAAC adduct **78d** (Scheme 55). Since the reaction of chloro phosphane oxide **26d** and 1-Dipp-3,3-dimethyl-cAAC did not converged completely to **78d**, the cAAC stabilised phosphenium ion **77d** was synthesised as a starting point. The hexafluoroantimonate and the B(C₆F₅)₄ salts of **77d** had already been previously reported by Alcarazo and Dobrovetsky, respectively. Instead of ᵗBuOOᵗBu for further oxidation, in analogy to Dobrovetsky's method, again the monomeric iodosylben-

127
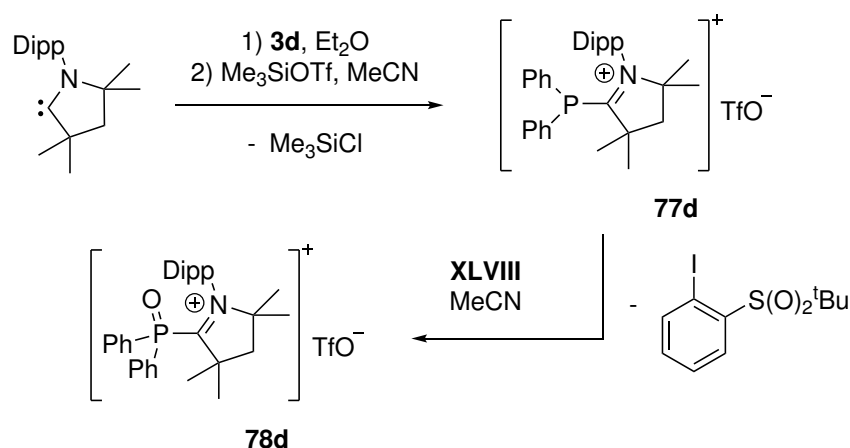
Scheme 55: Synthesis of the oxophosphonium cAAC adduct triflate salt **78d** from oxidation of **77d** with **XLVIII**.

zene **XLVIII** was chosen. After work-up the product is obtained in high yield (94%) and a remarkably clean ^{1}H-NMR spectrum of **78d** can be recorded, in contrast to Dobrovetsky's report in which no yield was given and according to the published ^{1}H-NMR the product was heavily contaminated with difluorobenzene.

6.4. Redox chemistry of NHC oxophosphonium adducts

Having the NHC oxophosphonium adducts **68d,f** and **75d,e** and pyridine adducts **70d,e,f** in hand, the redox properties were investigated by cyclic voltammetry, thus coming back to the initial question if these adducts can stabilise the formal phosphinoyl or phosphanoxyl radical (Scheme 56). As no CV studies were conducted for the cAAC adduct **78d**, yet, this derivative was also included in this study. Remarkably, besides the already discussed reduction of **78d** by Dobrovetsky there are no reports on attempted reduction of any oxophosphonium (adducts) to the current date. To estimate the reduction potentials of the adducts CV experiments were performed. Initially, CVs were recorded for the less bulky IMe$_2$ adducts **68d,f** together with the pyridine adduct **70f** (Figure 84). All three adducts
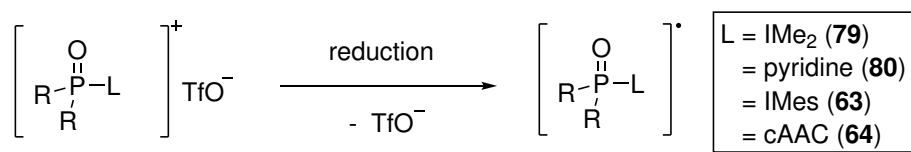
Scheme 56: Reduction of oxophosphonium adducts to the phosphinoyl adducts **63,64,79,80**.

show an irreversible reduction process in the possible redox window of the chosen solvent (Table 18). All three processes are assumed to be one electron transfer events and follow the Randles-Sevcik equation. The processes can be separated into two groups, on the one hand the IMe_2 adducts **68d,f** and on the other hand the pyridine adduct **70f**. The redox potential is therefore mostly determined by the adduct itself, *e.g.* IMe_2 or pyridine, instead of the substitution pattern at the phosphorus atom. Remarkably, while an increase in the scan
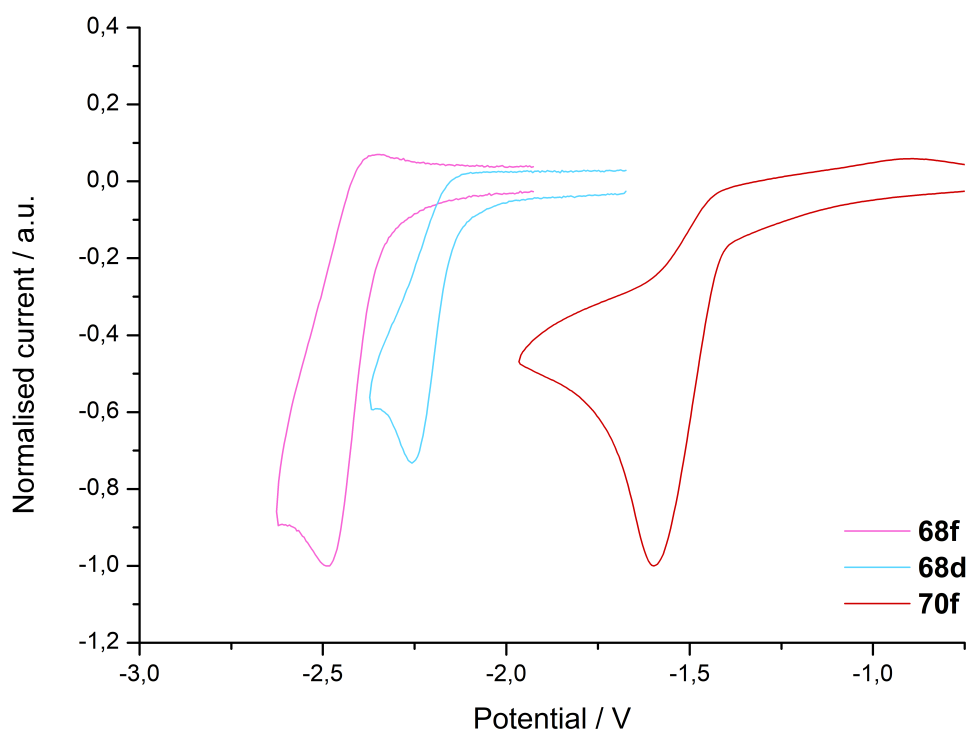
Figure 84: Cyclic voltammogram with normalised current on the isolated reduction processes **68d,f** (in MeCN) and **70f** (in THF), (scan rate: 200 mV s^{-1}, 0.2 M [nBu$_4$N]PF$_6$, vs. Fc/Fc$^+$ oxidation potential).

Table 18: Cathodic E_p^c, anodic potentials E_p^a, peak to peak distance ΔE_p, cathodic I_p^c and anodic I_p^a of the redox processes of the oxophosphonium adducts **68d,f** and **70f** at a scan rate of 200 mV s^{-1} in a MeCN solution of 0.1 M [nBu$_4$N]PF$_6$, referenced vs. Fc/Fc$^+$. *0.2 M [nBu$_4$N]PF$_6$ in THF

	E_p^c / V	E_p^a / V	ΔE_p / mV	I_p^c / μA	I_p^a / μA	$|I_p^a / I_p^c|$
68d	−2.26	—	—	−7.3	—	—
68f	−2.49	−2.37	121	−9.8	0.7	0.07
70f*	−1.60	—	—	−20.9	—	

rate does not change the overall shape of the CV for **68d** and **70f**, a different behaviour is observed for **68f**. While at very low scan rates, *e.g.* 50 and 100 mV s^{-1} only the reduction event is observed, at higher scan rates, starting at 200 mV s^{-1} a small oxidative return peak is observed. This peak recovers only roughly 7% of the current observed for the reduction process for 200 mV s^{-1} but increases to 17% for 1000 mV s^{-1}. This behaviour suggests that the life-time of formed radical **79f** is close to the CV time scale, while **79d** and **80f** are too short-lived to be re-oxidised. However, other main group radicals like a dimesityl boryl Mes$_2$B· radical IMe$_2$ adduct (E_p^c = −1.8 V in DCM) from Gabbai was observed to be stable on the CV time scale, showing the potential of this small NHC to stabilise main group radicals.[213,214] The higher reduction potential compared to **68d,f** suggests that the presence of the phosphinoyl substitutent at the IMe$_2$ hampers the redox potential of the imidazolium moiety.

A drastically different outcome was observed in the reduction of the adducts **75d,e** and **78d** (Figure 85 and Table 19). As expected from the report about the stable radical **64d** by Dobrovetsky the reduction of **78d** showed a significant peak in the return wave for the oxidation of **64d** and a therefore quasi-reversible redox process for **78d**. The reduction appears at an remarkably low potential of −1.05 V, even lower than for **70f**. This in good agreement that the reduction to **78d** with decamethylcobaltocen CoCp*$_2$ proceeded smoothly for the group of Dobrovetsky. At lower potentials the redox processes of **75d,e** are found, however, the difference in the cathodic reduction potential E_p^c of **75d** and **75e** was significantly larger (0.58 V) than previously observed for the IMe$_2$ adducts **68d,f** (0.23 V). Additionally, the current of the peak for the return wave I_p^a of **75d** is much smaller than that for the reduction peak I_p^c and at lower scan rates this becomes more pronounced. This can again be related to a rather short-lived species **63d**, observable in CV. In contrast **75e**, with an even lower reduction potential and closer to its small derivative **68f** shows a well behaved quasi-reversible redox process over scan rates from 50 to 1000 mV s^{-1}. The higher stability compared to **68f** can be clearly attributed to the larger NHC IMes than the IMe$_2$, however, raising the question why **75d** shows not only a shifted reduction potential but foremost a higher instability for its radical **63d**. This might be explained by the previously discussed structural difference. The orientation of the NHC fragment to the P–O bond was found to be similar for **68f** and **75e** and while no structure for **68d** could be obtained it can be assumed that due to missing π-interaction a similar configuration to the aforementioned adducts is present in **68d**, comparable to **74d** (cf. Figure 80, p.123). This would explain the similar reduction potential of these three derivatives. The adduct **75d**, however, shows a different orientation and the also previously discussed NMR data suggest this configuration is also

130
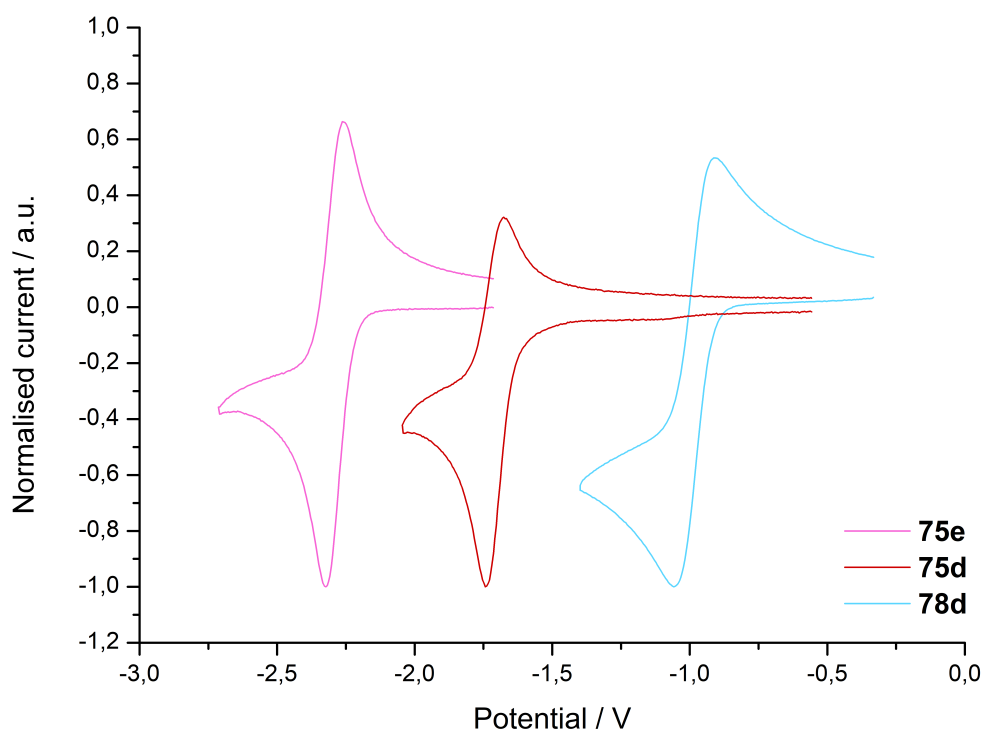
Figure 85: Cyclic voltammogram with normalised current on the isolated reduction processes **75d,e** and **78d** in MeCN, (scan rate: 200 mV s^{-1}, 0.2 M [nBu$_4$N]PF$_6$, vs. Fc/Fc$^+$ oxidation potential).

Table 19: Cathodic E$_p^c$, anodic potentials E$_p^a$, peak to peak distance ΔE$_p$, cathodic I$_p^c$ and anodic I$_p^a$ of the redox processes of the oxophosphonium adducts **75d,e** and **78d** at a scan rate of 200 mV s^{-1} in a MeCN solution of 0.1 M [nBu$_4$N]PF$_6$, referenced vs. Fc/Fc$^+$.

	E$_p^c$ / V	E$_p^a$ / V	ΔE$_p$ / mV	I$_p^c$ / μA	I$_p^a$ / μA	$|$I$_p^a$ / I$_p^c|$
75d	-1.74	-1.68	62	-11.3	5.9	0.53
75e	-2.32	-2.26	65	-12.9	11.0	0.85
78d	-1.05	-0.91	145	-19.8	17.3	0.87

present in solution. Therefore, it can be assumed that the easier reduction of **75d** but also increased instability of the radical **63d** originates from the P-phenyl mesityl π-interaction, locking the NHC-ring plane $\sim$90° rotated with respect to the P–O bond.
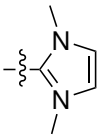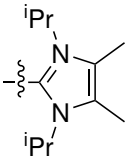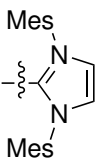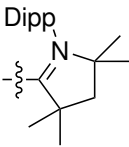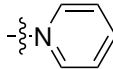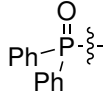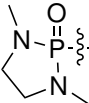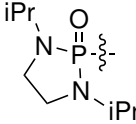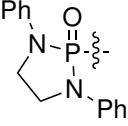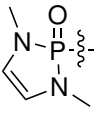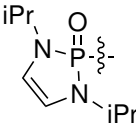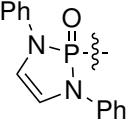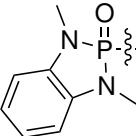
6.5. DFT analysis of cationic and radical P–O containing NHC adducts

The CV experiments were furthermore accompanied by DFT calculations. Optimised structures of the experimentally obtained adducts were general in line with the molecular structures obtained by X-ray diffraction analysis. Furthermore, related structures were calculated which include a series of different substitution pattern for oxophosphonium IMe_2 adducts **68** and their related radicals **79**, and different adduct sets for the diazaphospholidine (**e,f**) and also diphenyl (**d**) substitution (Table 20). From the calculated structures it can also be seen that the $C_{ipso\text{-}IMes}^{NHC}$-$N^{NHC}$-P–O torsion angle of **68d**, for which crystallisation attempts failed, is neither $90°$ nor $180°$, but in between these with a value of $125°$. A similar value, $115°$, is found for the calculated IPr_2Me_2 adduct **76d**, corroborating the effect of π-interaction in the special configuration of **75d**. Additionally, the FMOs were calculated. The LUMOs of the oxophosphonium adducts are of greatest interest for the investigated reduction process. Comparison between the LUMOs of some selected oxophosphoniums adducts (Figure 86) showed that all carbene adducts have qualitatively the same shape and symmetry. Despite being a small effect, the contribution of the P–O oxygen orbitals to the LUMO was higher in the IMe_2 adducts **68d,e** than in the IMes adducts **75d,e** and even less for the cAAC adduct **78d**. This trend is in line with an increase in π-acidity going from NHC to cAACs, as previously mentioned. And since upon reduction the LUMO is populated the higher oxygen contribution suggest that the formed NHC-based radicals have indeed a higher phosphinoyl radical character than the cAAC derivative, as initially postulated. A special case makes the IPr_2Me_2 adducts **76** in which a significant contribution to the LUMO comes one of the phenyl substituents at the phosphorus atom. No contribution of the phosphorus scaffold is however found in the pyridine adducts, *e.g.* **70f**, the LUMO is completely centred on the pyridine substituent, with significant contribution of the C4 atom. This explains the observed reactivity of **70f** with IMes, where addition of the carbene at C4 was observed rather than substitution. In contrast, the computed NMe_3 adduct **82**, inspired by the work of Kinjo, shows almost pure contribution of the phosphorus oxide moiety to the LUMO. Only a negligible amount is found on NMe_3, assuming that a potential radical **83** is less stabilised compared to the other adducts in this study.

In the literature the absolute LUMO energies are often correlated to experimentally obtained reduction potential.[215] Therefore, the reduction potentials E_p^c of the oxophosphonium adducts were plotted against the calculated LUMO energy (Figure 87). It was possible to fit the data to a linear function giving a moderate R^2 value. Noteworthy, the outliers are the pyridine adduct **70f** and the structurally special IMes adduct **75d**, which can be expected,

Table 20: Combination for oxophosphonium adducts and their related radicals investigated in this study. Radicals given in parenthesis.

68d (79d)	**76d** (81d)	**75d** (63d)	**78d** (64d)	**70d** (80d)	**82d** (83d)
68e (79e)	**76e** (81e)	**75e** (63e)	—	**70e** (80e)	—
68f (79f)	—	**75f** (63f)	**78f** (64f)	**70f** (80f)	**82f** (83f)
68g (79g)	—	—	—	—	—
68o (79o)	—	—	—	—	—
68x (79x)	—	—	—	—	—
68y (79y)	—	—	—	—	—
68p (79p)	—	—	—	—	—

133

68e

68d

75e

75d

76d

78d

70f

82d

Figure 86: Structures and LUMOs of selected oxophosphonium addcuts. The counter anion was neglected in these structures.
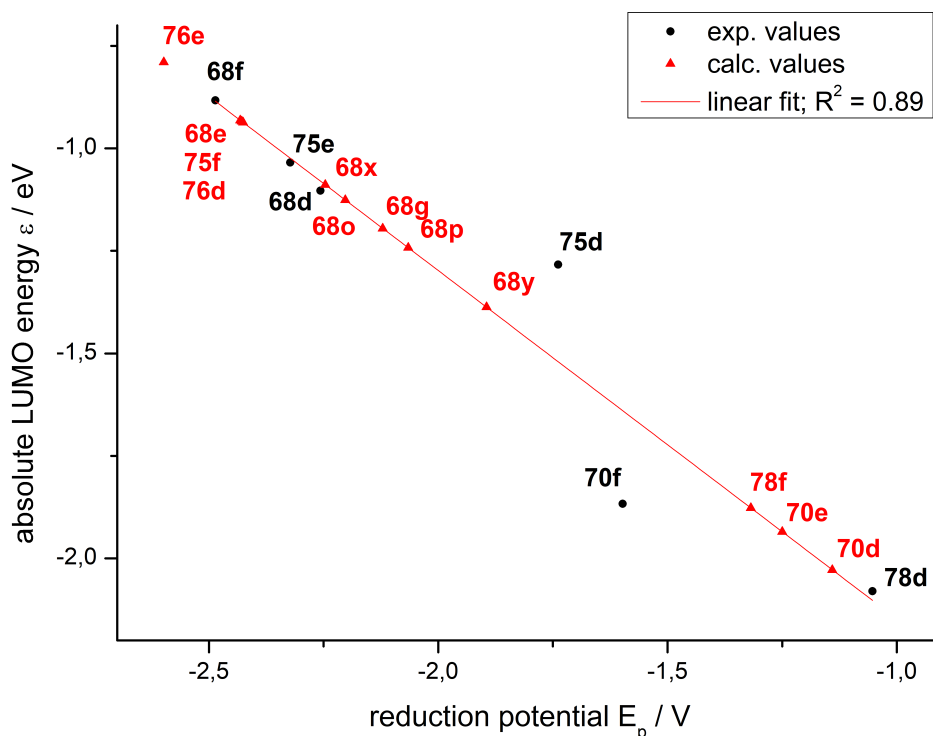
Figure 87: Correlation diagram of the absolute LUMO energy ϵ vs. the reduction potential E_p^c, together with a linear fitting function obtained from the experimental results and extrapolated E_p^c for the theoretically accessed structures.

since the bonding situation between **70f** is clearly different to the other carbene adducts, and the situation of **75d** has also already been discussed in depth. Therefore, it seems carbene adducts yield a good linear correlation between LUMO energies and reduction potential. This justifies extrapolation of the reduction potential for the calculated structures mentioned beforehand. From this it becomes apparent that the reduction potential does only change slightly with respect to the substitution pattern at phosphorus, as all IMe$_2$ adducts **68** cluster together. A similar behaviour is observed for **75** and **76** derivatives and in the same manner pyridine **70** and cAAC adducts **78** are found close to each other. A slight trend inside the group for **68** is the higher reduction potential for an unsaturated backbone in the diazaphosphol moieties, together with the observation that the aromatic phenyl substituent for the diazaphosphol(idines)s in **68g,y** also lowers the reduction potential compared to the alkyl substituted **68e,f,o,x**.

135

Figure 88: Computed structure of the cation **75e** (left) and the related radical **63e** (right). View along the NHC ring plane.

In the next step the corresponding radical species were computed. Structural comparison of the cationic and radical species showed that for all carbene adducts a small bending of the NHC was observed, pushing the phosphorus atom out of the carbenes N-C-N plane (Figure 88). Consideration of the isolobal principle, this structural change is similar to that of the stereoactive radical observed for the Fe(CO)$_4$ complexes **18** (cf. Figure 41, p.75). Otherwise no structurally significant changes were found. For a quantification the reorganisation enthalpies of **68d, 75d, 76d** and **78d** were computed. The values were obtained from the energy difference of the structurally relaxed radicals and the radical still adopting the oxophosphonium adduct structure. The reorganisation enthalpies are rather small and range from 7 and 13 kcal mol^{-1}. Additionally, the reorganisation enthalpy of **75e** was also calculated to see if a different substitution pattern at phosphorus has another effect, however, the computed value of 11 kcal mol^{-1} is in the same range and therefore the structural changes seem to be not severely affected by the substitution pattern at the phosphorus atom. For the pyridine adduct qualitatively no structural change was observed, however, no structure of the radical **83d** could be computed since in all cases a P–NMe$_3$ bond cleavage occurs, corroborating the statement made earlier that NMe$_3$ will not be able to stabilise a phosphinoyl radical sufficiently.

Further insight can be gained from the DFT derived spin densities for the radicals. As expected, the shape of the SDD is very close to the shape of the LUMOs of the adducts (Figure 89). In all calculated derivatives, the major contributions are found on the ligand, *e.g.* carbenes or pyridine. Small spin densities are found on the phosphorus atom and only negligible amounts on the oxygen atom (Table 21). Again, values found for the car-
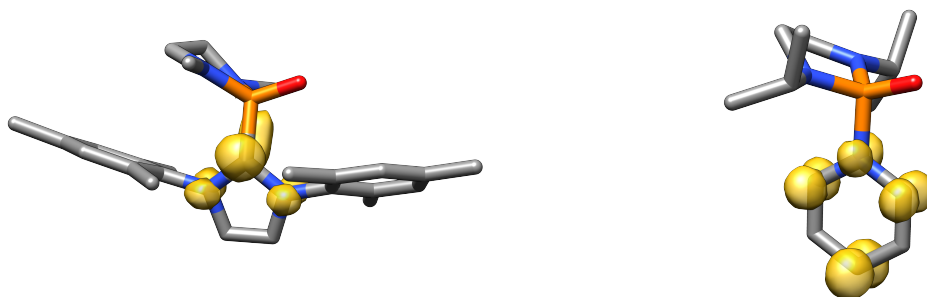
Figure 89: Computed structure and SDD of the radical adduct **63e** (left) representative for the carbene adducts and the pyridine radical adduct **80f** (right).

Table 21: Spin densities in e of selected atoms and groups (L = sum of the large contributions in the adduct substituent) of the calculated 'phosphinoyl' radical adducts.

	P	O	L		P	O	L
79d	0.12	0.00	0.60	**80e**	0.03	0.00	0.86
79e	0.12	0.02	0.67	**80f**	0.03	0.00	0.86
79f	0.10	0.01	0.68	**63d**	0.12	0.01	0.62
79g	0.13	0.01	0.65	**63e**	0.11	0.01	0.66
79o	0.13	0.02	0.66	**63f**	0.10	0.01	0.66
79x	0.11	0.01	0.69	**64d**	0.11	0.01	0.66
79y	0.14	0.02	0.63	**64f**	0.11	0.01	0.66
79p	0.14	0.02	0.64	**81d**	0.12	0.00	0.68
80d	0.03	0.01	0.87	**81e**	0.11	0.01	0.68

bene adducts are remarkably similar to each other with ∼66% of the whole spin density distributed among the N-C2-N atoms. In the pyridine adducts **80d,e,f** around 86% of the spin density are on the pyridine moiety and the phosphorus and oxygen atoms do not take part in the spin delocalisation. It is noteworthy, that also the unsaturated backbone annu-
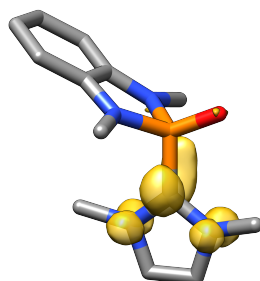
Figure 90: Computed structure and SDD of the radical adduct **79p**.

lated 1,3,2-diazaphospholes **79o,p,x,y** show no different SDD (Figure 90). This stands in contrast to the phosphanoxyl iron complex **18o** and **18p**, for which the SDD was mostly localised on the 1,3,2-diazaphosphole ring and not on the $Fe(CO)_4$ fragment (cf. Figure 51, p.86), revealing the limit of the acceptor properties of the $Fe(CO)_4$ fragment in comparison to common NHCs.

6.6. Attempt to experimentally access P–O containing radical NHC adducts

The strong electronic similarities between all studied carbene adducts raised the question if a phosphinoyl radical NHC adduct can be prepared, in analogy to the cAAC adduct **78d**. The overall similar line shape and similar current ratios between **75e** and **78d** suggest that a stable radical **63e** might be a suitable candidate. Due to very low reduction potential of −2.32 V a stronger reducing agent, than the $CoCp^*_2$ (E_p = −1.91 V in MeCN) had to be used, as it showed no reactivity towards **75e** (Scheme 57). A strong but still mild reducing reagent is the NacNacMg(I) species of Jones, however, reaction of this with **75e** showed no signs of any reaction.[216] Therefore, the reaction with potassium graphite (KC_8) was attempted. Reduction in toluene lead to a mixture of products according to the $^{31}P\{^1H\}$-NMR spectrum with chemical shifts (and contribution to the spectrum) of 112 (77%), 94 (7%) and 23 ppm (16%), which could not be attributed to any literature known compound. If the reaction was carried out in THF, after extraction with *n*-pentane, only the free carbene IMes, was obtained as verified by single crystal X-ray diffraction analysis and ^1H-NMR spectroscopy. This stands in stark contrast to the facile formation of the cAAC adduct **64d** by Dobrovetsky.
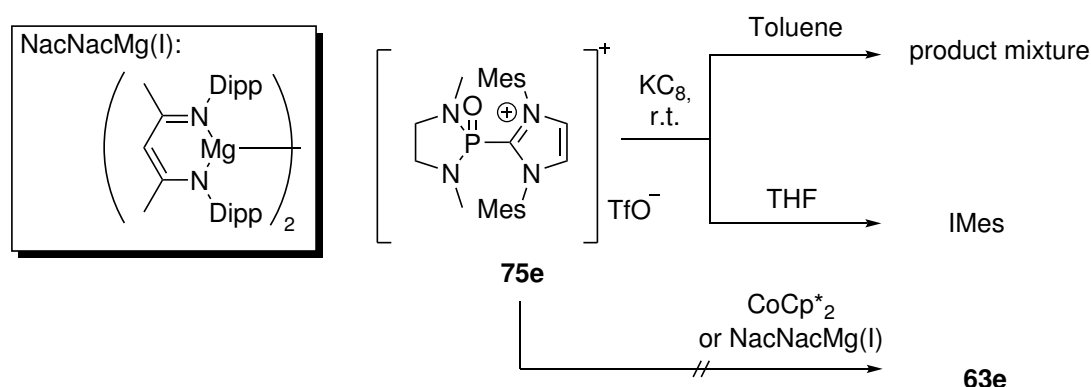
Scheme 57: Attempted synthesis of **63e** by the reduction of **75e** with KC_8, NacNacMg(I) and $CoCp^*_2$.

Together with the very low reduction potential the formation of such NHC adducts might not be energetically favoured and led to P-carbene bond cleavage and generation of the highly reactive free phosphinoyl **1**.

Furthermore, the reduction of the pyridine adduct **70e** with CoCp*$_2$ was tested on a NMR scale (Scheme 58). An immediate reaction was observed and despite a product mixture observed in the ^{1}H-NMR spectrum, two resonances became apparent with chemical shifts of 6.3 and 4.6 ppm. This fits very well to reported 1,1',4,4'-tetrahydro-4,4'-bipyridine structures. However, the reaction was not investigated further and **84e** was not isolated. Indeed, it is known for *N*-pyridinium salts to undergo C-C coupling at the C4 position of the transiently formed radical.[217] This explains the irreversible reduction of **70f** in the CV. In agreement with the FMO analysis of **70** and the obtained SDD for the radical species **80**, these systems should be treated as *N*-phosphinoyl-substituted pyridinium salts, which is lastly corroborated by their reactivity. Hence, these adducts are not well suited for phosphinoyl radical stabilisation.

70e   **80e**   **84e**
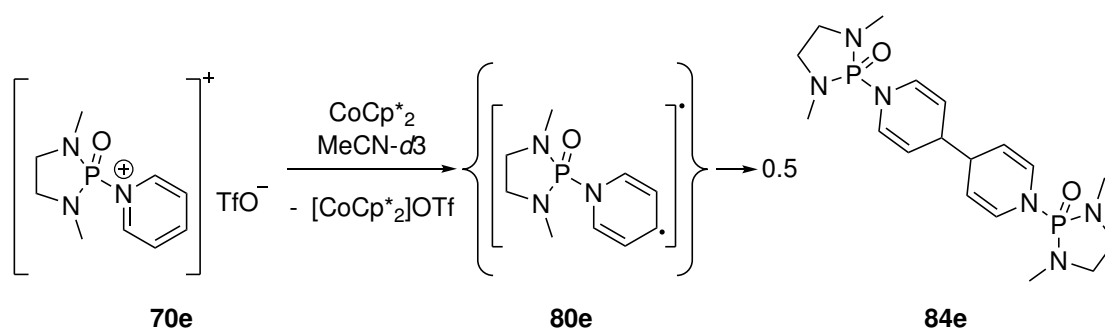
Scheme 58: Reduction of pyridine adduct **70e** to the 4,4'-coupled product **84e** via a transient radical **80e**.

7. Summary

In this thesis the synthesis of aminoxylphosphane tungsten (**8**) and iron complexes (**17**) and the formation of transient P–O containing radical complexes (**11,18**) were systematically studied. Special emphasis was put on the effects of 1,3,2-dihetero-phospholane scaffolds on accessibility, the ease of a thermal homolytic N–O bond cleavage of aminoxylphosphane complexes and the resulting spin density distribution (SDD), supported by state of the art DFT calculations. Furthermore, various co-ligand environments were theoretically studied for the first time as well as attempts to include main group element adducts to phosphorus that are isolobal to the fragments $Fe(CO)_4$ and $W(CO)_5$, *i.e.*, N-heterocyclic carbenes (NHCs) (Figure 91). As a starting point the differences between phosphinoyl, (hypothetical)
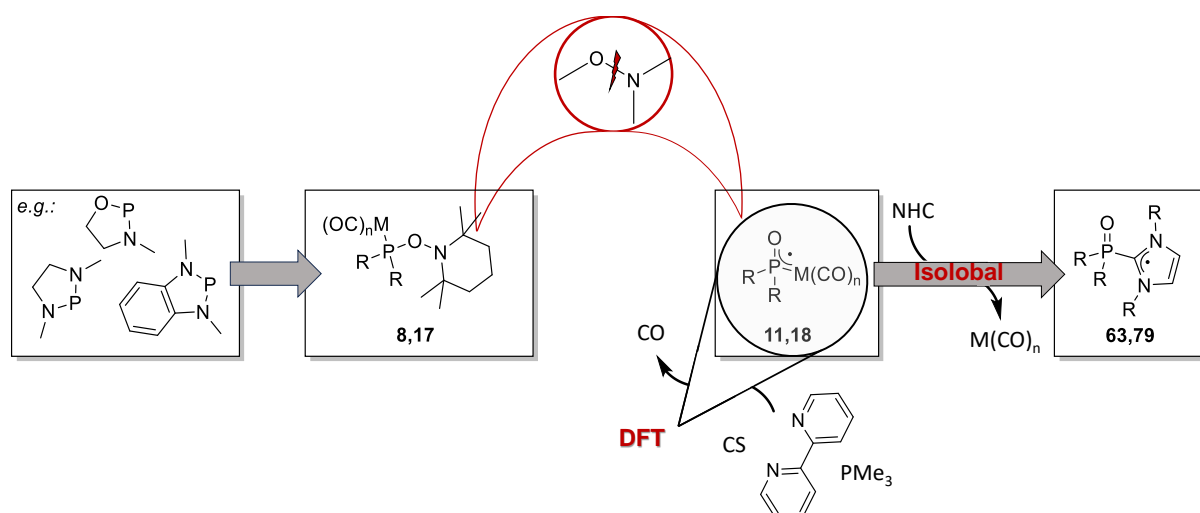
Figure 91: Generalised outline of the contents of this thesis.

phosphanoxyl and aminoxyl radicals (Figure 92) were theoretically investigated focusing on structural and electronic properties. In agreement with earlier results it is clear that the phosphinoyl character is (always) dominating, in the studied systems, due to the higher tendency of phosphorus to involve the energetically higher lying 3p-orbitals into bonding,
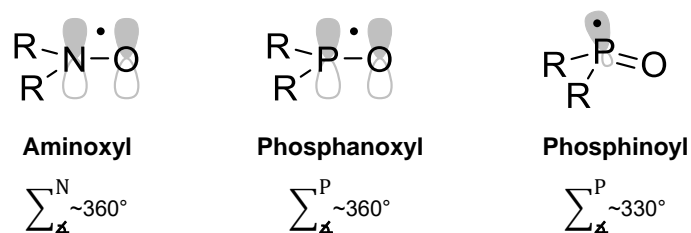
Figure 92: Lewis structures of the aminoxyl, (hypothetical) phosphanoxyl and phosphinoyl radicals.

reserving the 3s-orbitals at the P centre. Coordination of the latter to a metal fragment involves the SOMO of the phosphinoyl radical into bonding and solves this problem (partially), thus allowing phosphanoxyl complex reactivity to come to the fore, first shown by Heurich having the focus largely on the transient tungsten(0) complex [W(CO)$_5$(Ph$_2$PO)] **11d**.

Experimental accessibility of heterocyclic aminoxylphosphane tungsten complexes was explored which led to the isolation of the new complexes **8f,i,k** (Figure 93). For this the new elegant way was applied to use the tungstate salt [NEt$_4$][W(CO)$_5$H] as combined complexation and reducing agent, facilitating the synthesis of otherwise hard to obtain diheteroatom-substituted secondary phosphane complexes **6**. The different substitution pattern of the phosphane ligand allowed comparison of their molecular structures and their thermal stability leading to phosphanoxyl complexes. Double-hybrid DFT calculations (PWBP95-D3/def2-QZVPP) were used to explore the energetical landscape around the phosphanoxyl complexes. From these it was shown that transient species and intermediates react very sensitive on kinetic and electronic changes (Figure 94). Firstly, the
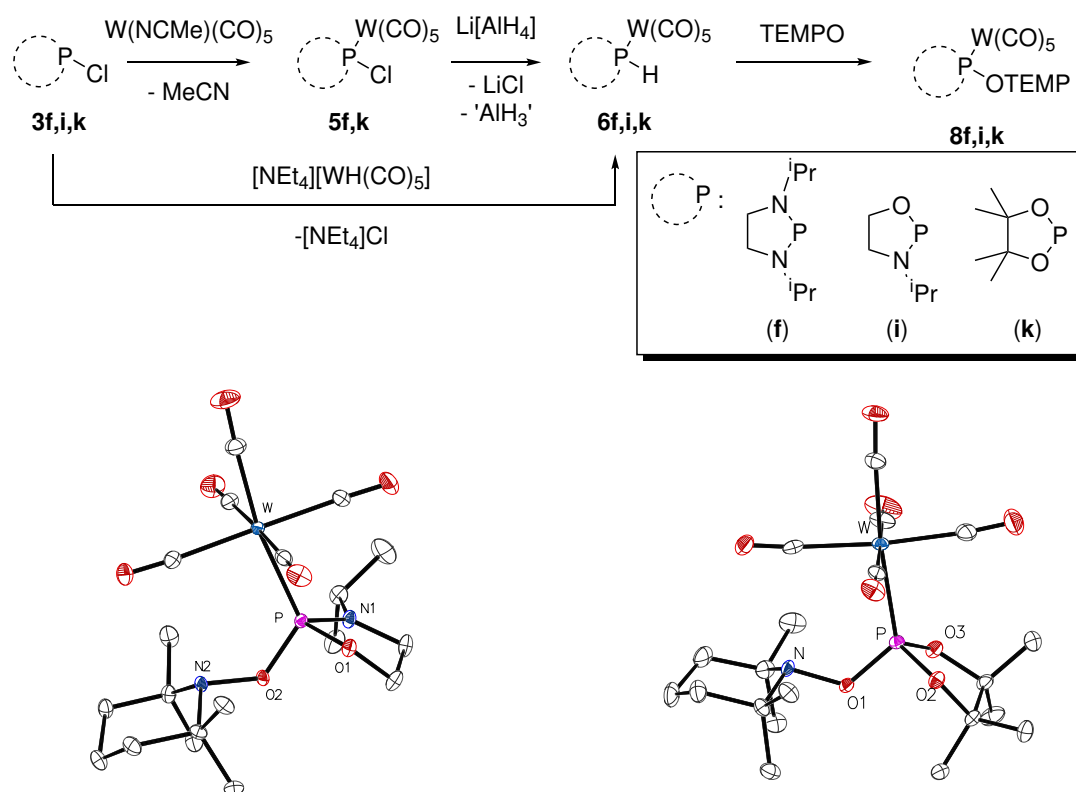
Figure 93: Synthetic protocol used to access the new aminoxylphosphane complexes **8f,i,k**. Structures obtained from single crystal X-ray diffraction are shown for the new mixed 1,3,2-diheterophospholane complexes **8i,k**.
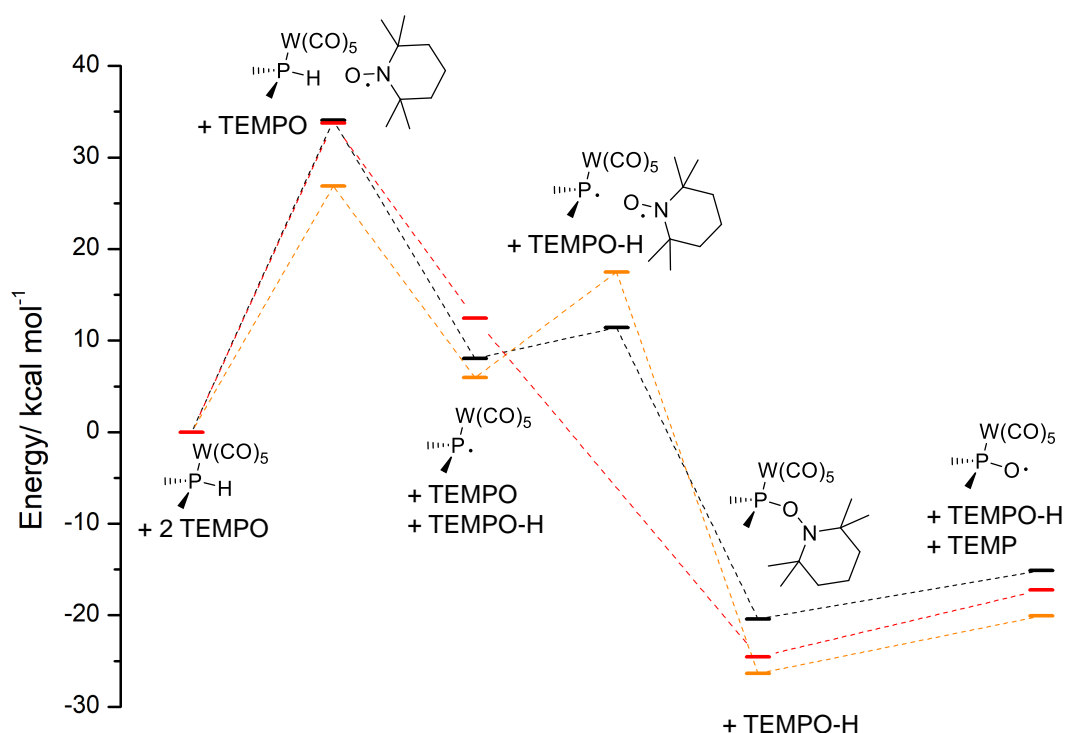
Figure 94: Reaction profile for the formation of phosphanoxyl complexes **11f,i,k** from the reaction of secondary phosphane complexes **6f** (black), **6i** (orange), **6k** (red) with TEMPO.

aminoxylphosphane complexes **8f,i,k** are sensitive towards steric bulk, presumably due to strong repulsion between the *P*-substituents and the TEMPO moiety, resulting in a weak N–O bond. Secondly, oxygen-based *P*-substituents seem to stabilise the aminoxylphosphane tungsten complexes **8i,k**. A trend was observed in the SDD for phosphanoxyl complexes **11**, more oxygen-based *P*-substituents increase the spin density on the tungsten atom, while decreasing the spin density on the phosphorus-based ligand (cf. Figure 27, p.47).[158]

This led to the assumption that in return spin density might be 'pushed' into the ligand, and most likely on the O^{exo}-atom, increasing the phosphanoxyl character of such complexes. The observed tendency in the tungsten complexes should therefore be inverted by an electron rich metal centre. Therefore, in the second part of this thesis the chemistry of aminoxylphosphane Fe(CO)$_4$ complexes **17** was tackled (Figure 95). The previously applied synthetic concept was adopted, using the hydrido ferrate salt K[Fe(CO)$_4$H] for the synthesis of unknown and/or substituent-limited diheteroatom-substituted secondary phosphane iron complexes **12**. Their transformation to aminoxylphosphane iron complexes **17**, however, was mostly unsuccessful as all targeted complexes, partially observed by *in situ* ^{31}P-NMR spectroscopy, were thermally unstable and gave comparable decomposition prod-
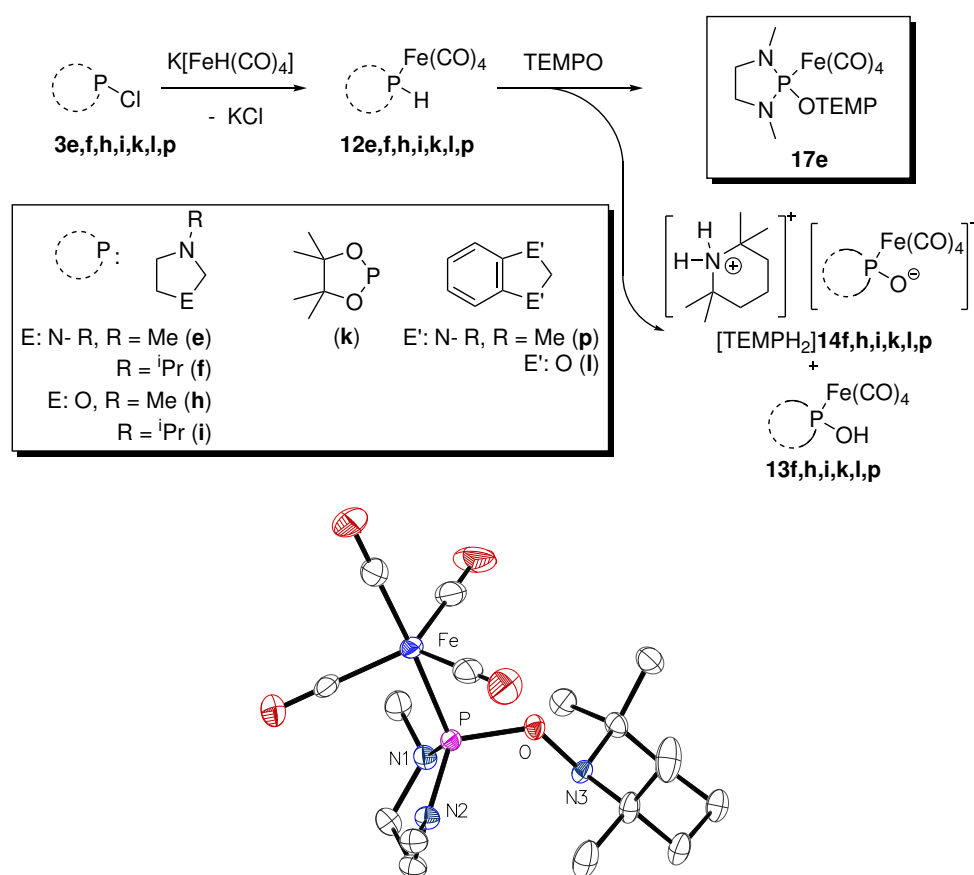
Figure 95: Synthetic protocol used to access the new secondary phosphane complexes **12**, the first aminoxylphosphane iron complexes **17e** and its crystal structure obtained from X-ray diffraction.

ucts **13,14** as the early tungsten complexes from Nesterov and the manganese complexes from Heurich and Naz. However, under strict temperature control it was possible to isolate the first aminoxylphosphane iron complex **17e** and obtain structural proof. The chemistry of the decomposition pathway was investigated and compared to the tungsten derivatives. And while upon warming up NMR evidence was found that N–O bond cleavage occurs, different reaction pathways between tungsten and iron complexes were observed. The aminoxylphosphane iron complex **17e** and its decomposition was therefore analysed by EPR, Mößbauer and CV. Initial EPR experiments gave evidence for a persistent paramagnetic species (Figure 96, left) and these findings were also reproduced in a cooperation with Bill from the Max Planck Institute (Mühlheim a. d. Ruhr). Mößbauer experiments (Figure 96, right) conducted by Bill complimented the EPR experiments and suggest the presence of Fe(II) and Fe(III) containing compounds in the decomposed mixtures. CV experiments further corroborated these results as several irreversible oxidation events occurred, when the iron-centred radical **18e** (Figure 98) was generated from a suitable anionic precursor (cf.
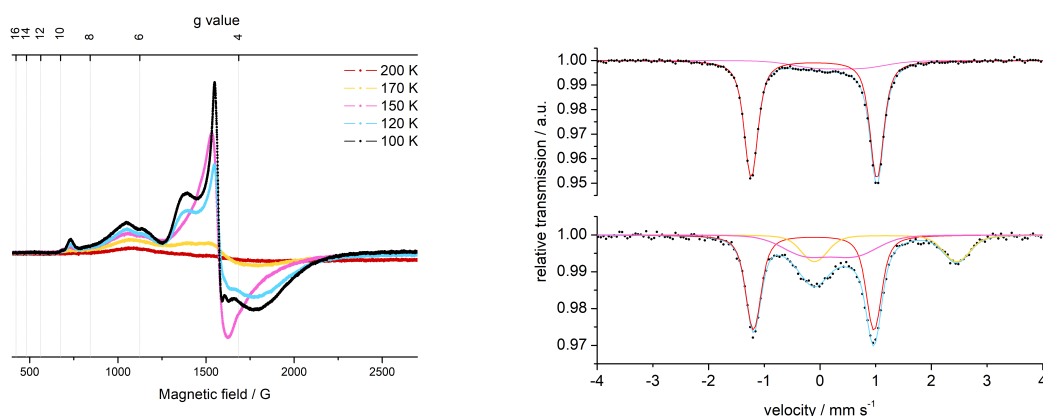
Figure 96: CW X-band EPR spectrum of a frozen solution of decomposed **17e** (left) and frozen solution Mößbauer spectra of **17e** (right, top) and decomposed **17e** (right, bottom) at 80 K.

Figure 48, p.82).

On the assumption of an initially formed transient phosphanoxyl iron radical **18e** DFT calculations were performed. Despite that iron was chosen to increase the spin density on the ligand, the results of the SDD analysis showed that the spin density of the phosphanoxyl complex is concentrated purely on the iron atom and is therefore better described as a phosphinoyl ligand with huge P–O double bond character, in stark contrast to the tungsten derivative **11e** (Figure 97, Figure 98).

phosphanoxyl complex   *phosphinoyl complex*
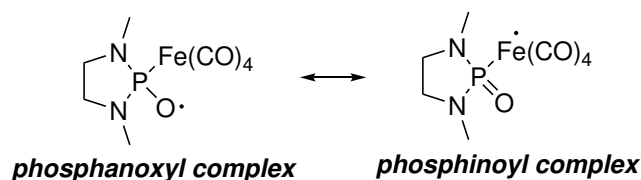
Figure 97: The theoretical P–O containing radical complex **18e** described as a hypothetical phosphanoxyl complex and as a phosphinoyl complex, corroborated by SDD analysis.

This furthermore leads to a structural change of the usually adopted trigonal bipyramidal $Fe(CO)_4L$ complexes to a pseudo octahedral coordination, in which the radical is in a stereoactive position *cis* to the phosphinoyl ligand. In comparison to the recently published stable $[Fe(CO)_5]^+$ radical the phosphinoyl ligand seems to destabilise the complex and to open redox pathways leading to the spectroscopically observed Fe(II/III) species. Further theoretical calculations showed that unsaturated 1,3,2-diazaphosphole complexes, *e.g.*, **18p** (Figure 98, right) are suitable for taking up a large amount of spin density, however a related aminoxylphosphane iron complex **17p** was thermally too unstable to allow for the

144
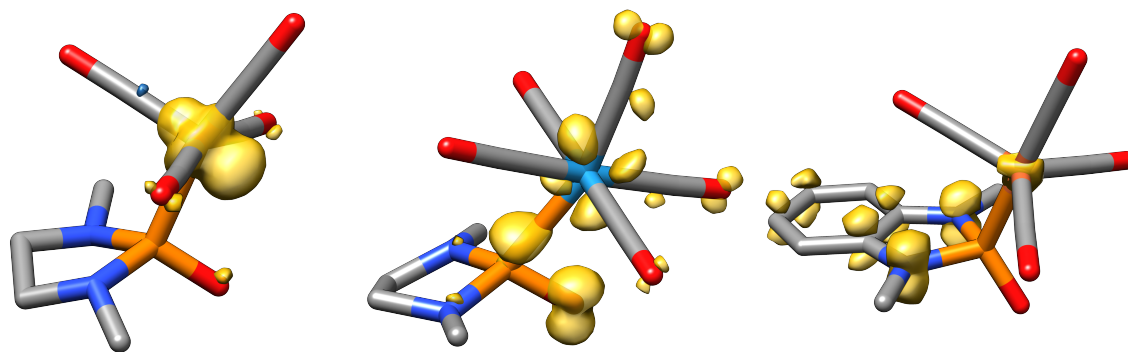
Figure 98: Computed structures of P–O containing radical iron complex **18e** (left), its tungsten derivative **11e** (middle) and the 1,3,2-diazaphosphole iron complex **18p** (right). SDD surface is given in yellow (Isovalue: 0.009).

isolation and decomposition products (presumably **13p** and [TEMPH$_2$]**14p**, cf. Figure 95) were similar to the ones previously observed for the other aminoxylphosphane iron complexes **17**.

Due to the somewhat ambiguous results a larger set of P–O containing radical tungsten **11**, iron **18** and manganese **32** complexes was analysed by DFT (cf. Figure 54, p.89)
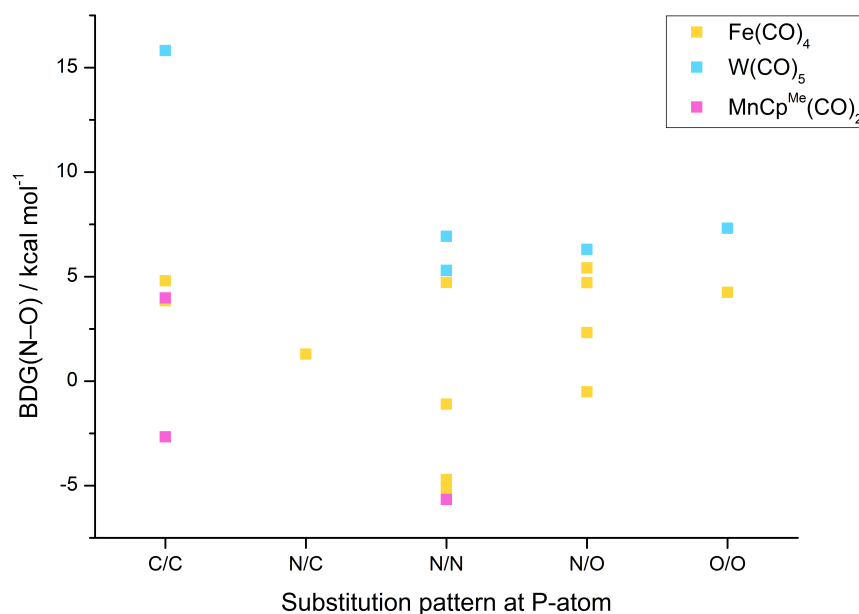
Figure 99: BDG of the N–O bond in aminoxylphosphane complexes **8,17,31** vs. the directly phosphorus bound element of the substituents.

concerning their formation and their SDD to obtain trends regarding stability (Figure 99). The theoretical results fit well to already experimentally observed factors, like high stability for tungsten complexes and the effect of bulky groups for the stability of aminoxylphosphane complexes. While from these results suggestions can be made which complexes might be accessible, no clear trend(s) can be identified to enable predictions. The stability of aminoxylphosphane and phosphanoxyl complexes is very sensitive towards changes and effects of the substitution and the coordinated metal are strongly intertwined.

In a collaboration with Frontera, the unexpected spin density uptake of the iron atom in phosphinoyl complexes was further investigated.[103] A series of iron **33-36**, tungsten **37-40** and nickel **41-44** radical complexes with a phosphinoyl/phosphanoxyl ligand were calculated, in which one or two of the carbonyl ligands were exchanged by σ-donor and also π-acceptor ligands, *i.e.*, PMe$_3$, 2,2'-bipyridine, 2,2'-biphosphinine (cf. Figure 68, p.101). Despite small effects in the tungsten complexes, the spin density of the iron and nickel complexes was almost unaffected by the changes, being still metal-centred.

The relevance of the exocyclic oxygen atom in phosphanoxyl/phosphinoyl complexes was calculated in a collaboration with Hui and Qu, in which also phosphanyl-sulfanyl, phosphanyl-azanyl and diphosphan-2-yl complexes of tungsten **49-51** and iron **52-54** were considered (Figure 100).[159] In contrast to the previous studies this had an immense effect on the SDD of these complexes (cf. Table 14, p.107). Noteworthy, the SDD difference between iron and tungsten P–E radical complexes was lifted for all complexes, besides E = O focused in this thesis. Furthermore, the SDD is shifted from the metal centre to the ligand in the order phosphanyl-sulfanyl, phosphanyl-azanyl and diphosphan-2-yl. The oxygen atom appears to be the exception and is extraordinarily bad in the up-take of spin density, enforcing the
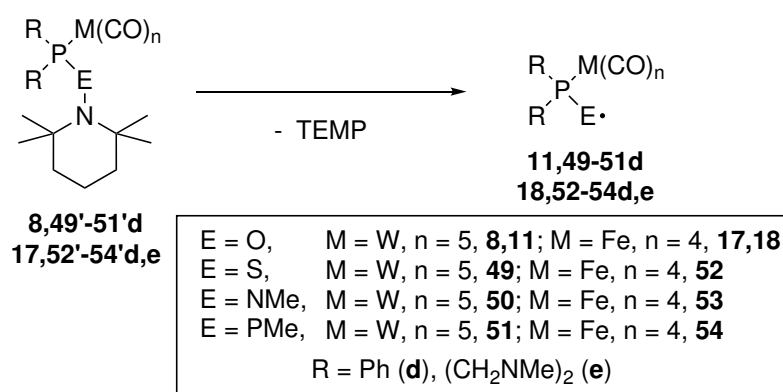
Figure 100: Investigated P–E containing radical tungsten and iron complexes formed by formal N–E bond cleavage in the cooperative study with Zhu and Qu.[159]

metal-centred radical and a highly innocent phosphinoyl ligand.

The problematic redox chemistry of the metal-centred P–O containing radical complexes, *e.g.* Fe (**18**) and Mn (**32**) did not allow isolation of any of these species. In a new conceptual approach and following the isolobal principle the metal fragments were replaced with carbenes. Due to the isolobal exchange carbene-centred radicals are assumed for phosphinoyl carbene adducts. It was shown in the literature that NHC and cAAC are capable to stabilise radical species. During the present study a stable cAAC phosphinoyl adduct **64d** was reported by another group. However, the chemistry of NHC adducts is mostly unknown. For this several oxophosphonium adducts **68d,f** and **75d,e**, as suitable precursors were synthesised thus expanding the portfolio of this rare class of compounds, especially those with large NHCs (Figure 101). Additionally, the protocol for the literature reported cAAC adduct precursor **78d** was optimised, which previously resulted in a poor product quality. Different substitution pattern at the phosphorus atom and different adducts allowed

67d,f   **68d,f**

26d,e   **75d,e**   **73d,e**
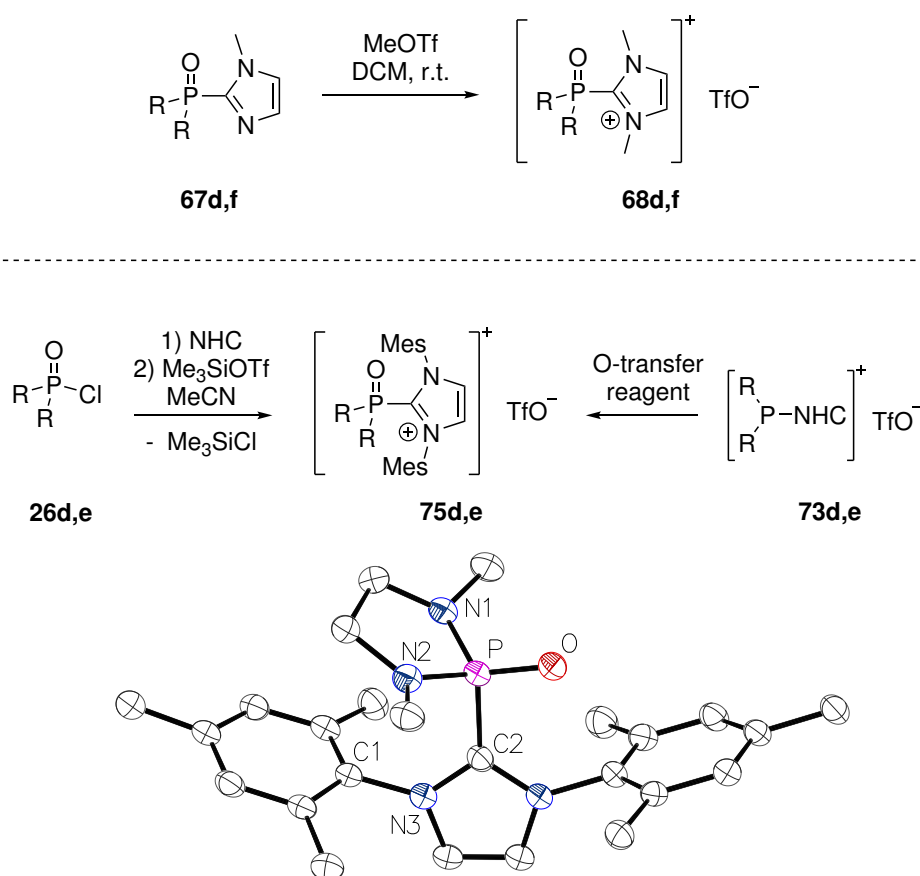
Figure 101: Synthetic strategies used in this thesis to access oxophosphonium NHC adducts **68d,f**, **75d,e**. The X-ray structure of **75e** is given as a representative for these bulky NHC oxophosphonium adducts.
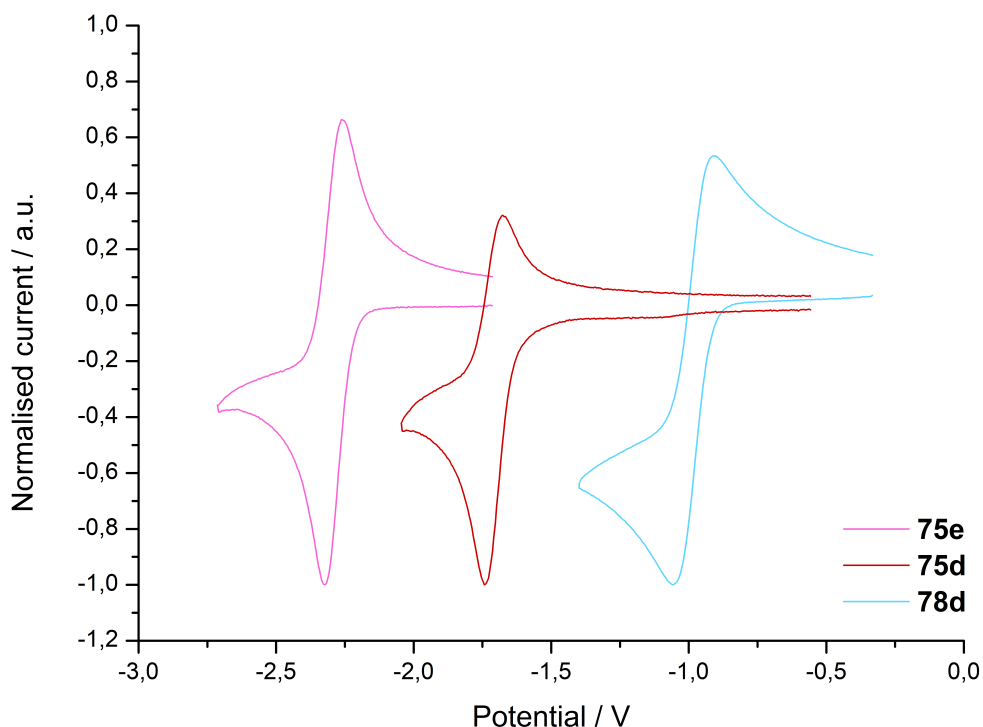
Figure 102: Cyclic voltammogram with normalised current on the isolated reduction processes **75d,e** and **78d** in MeCN, (scan rate: 200 mV s^{-1}, 0.2 M [nBu$_4$N]PF$_6$, vs. Fc/Fc$^+$ oxidation potential).

structural comparison between them. CV studies of the NHC adducts and also the cAAC adduct were conducted, which had previously not been reported. The reduction potentials were correlated to the LUMO energies and gave a good linear fit to which only theoretical studied systems were compared (cf. Figure 87, p.135). The CV study showed that larger NHCs are needed for a quasi-reversible redox process to the paramagnetic phosphinoyl carbene adducts and that much lower potentials are required for the NHC adducts than for the cAAC adduct (Figure 102). Attempts to isolate a phosphinoyl NHC adduct by reduction of the cationic precursor in solution with KC$_8$, CoCp$^*_2$ or a Mg(I) species failed, giving only evidence for a P-C^{NHC} bond cleavage. These results are in strong contrast to the cAAC derivative, suggesting that NHC stabilisation is not efficient enough to support the radical adducts.

SUMMARY

In conclusion, phosphinoyl radicals **1** are very reactive species and only W complexes exhibit partially phosphanoxyl behavior. In contrast, transient Mn, Fe and (calculated) Ni complexes resulted in the formation of metal-centred radical complexes, as estimated by SDD calculations. The latter are largely unreactive towards M-E bond formation. This behaviour is almost co-ligand independent, which might allow isolation of such radical complexes by kinetic stabilisation due to an increased steric bulk shielding the metal-centre. However, investigated bulky NHC P-O containing radical adducts could not been isolated in contrast to reported cAAC derivatives, suggesting that already a small phosphinoyl character destabilises such adducts.

8. Experimental Part

8.1. General working techniques

All reactions were performed, if not stated otherwiseunder dried and deoxygenated argon atmosphere using Schlenk or glovebox techniques. The used argon (>99.998 %) was purified by a system of three columns (deoxygenation by a BTS copper catalyst (BASF PuriStar® R3-15S) at ca. 100 °C, removing moisture with silica gel, phosphorus pentoxide desiccant with indicator (Sicapent®) and calcium chloride). Glassware, spatulae, cannulae as well as filter papers were dried in a compartment dryer at 110 °Cfor at least one hour. Additionally, the glassware was heated with a Teclu burner (up to 1600 °C) or if sensitive with heat gun (up to 550 °C) under active vacuum (<0.03 mbar) flushed with argon and then kept under vacuum for min. 5 to 10 minutes. Sterile syringes were purged with argon three times before use. The solvents were dried by standard procedures by refluxing over proper desiccants under an argon atmosphere (*n*-pentane, petroleum ether 40/65 and toluene over sodium wire (ø = 2 mm); diethyl ether stabilized with 3,5-di-tert-butyl-4-hydroxytoluene (BHT) and tetrahydrofuran over benzophenone and sodium wire) for several days and distilled before use. Alternatively, diethyl ether and toluene were dried using a Mbraun SPS-800 solvent purification system. Transfer of solvents or solutions was achieved by the use of stainless steal cannulae (ø = 2 mm and 4 mm) connecting two glass vessels, one of which was under argon overpressure and the other had a vent (commonly a cannula was used) to the atmosphere. For filtration Schlenk frits or stainless steel cannulae (ø = 1 mm and 2 mm) with Whatmann® Cytiva grade 595 cellulose filter paper or for finer residues Whatman® glass microfiber filters (grade GF/B) or were used. After use, cannulas made of stainless steel were cleaned with acetone, water and diluted hydrochloric acid and glassware by storage in a concentrated solution of potassium hydroxide in ᶦPrOH for at least two days (in the case of glass frits only overnight) and in diluted hydrochloric acid for several hours. Afterwards, the glassware was washed with water, subsequently with demineralised water and acetone. Glass joints were greased with OKS 1112 grease or with PTFE paste (Carl Roth).

8.2. Theoretical methods

All structures were set up with the open-source molecular builder and visualization tool Avogadro 1.2.0.[218] The quantum chemical DFT calculations have been performed using the *ORCA*[219] 4.0.1.2. For optimisation of the structures the TPSS-D3BJ/def2-TZVP + cPCM(THF) level of theory, which combines the TPSS[220] meta-GGA density functional with the BJ-damped DFT-D3[221][222] dispersion correction and the def2-TZVP[223] basis set, using the conductor-like polarisable continuum model (cPCM)[224] solvation model for THF as a solvent (ϵ = 7.25). The density-fitting RI-J (def2/J)[225] approach is used to accelerate the geometry optimization and numerical harmonic frequency calculations. The DFT Grid is set to Grid4, for the final energy FinalGrid5 is chosen (if not mentioned otherwise). The optimized structures are characterised by frequency analysis to identify the nature of located stationary points (no imaginary frequency below -25 cm^{-1} for true minima and only one imaginary frequency (or another below -15 cm^{-1}) for transition states) and to provide thermal corrections (at 298.15 K and 1 atm) according to the modified ideal gas-rigid rotor-harmonic oscillator model. For the calculation of transition states relaxed potential energy surface (PES) were performed along the important bond (breaking or forming) and from the highest energy structure we transition state frequency was taken and the structure was then optimised under the restrain to keep that imaginary vibration. The final free energies in THF are computed on the RI-PWPB95-D3BJ/def2-QZVPP + cPCM(THF), which combines the double-hybrid-meta-GGA PWPB95[226] functional with the BJ-damped DFT-D3 dispersion correction and the def2-QZVPP[223] basis set using the conductor-like polarisable continuum model (cPCM) solvation model for THF as a solvent (ϵ = 7.25). The density-fitting RI-JK (def2/JK)[227] approach is used to accelerate the calculation and the def2-QZVPP/C[228] auxiliary basis set is used. The final reaction Gibbs free energies (Δ_rG) are determined from the electronic single-point energies on the RI-PWPB95-D3BJ/def2-QZVPP + cPCM(THF) level plus the thermal corrections from the TPSS-D3BJ/def2-TZVP + cPCM(THF). The graphical representations of the calculated structures were generated with the free software *UCSF Chimera 1.15*.[229] Atoms in molecules analysis was performed using the free software *MultiWFN*.[230]

8.3. Methods and devices

8.3.1. NMR spectroscopy

NMR spectra were recorded on a Bruker Avance I 300 MHz, Bruker Avance I 400 MHz, Bruker Avance I 500 MHz or Bruker Avance III HD Ascend 500 MHz spectrometer at the NMR department of the University of Bonn and subsequently analyzed by the program Mestrenova 14.2 by *Mestrelab Research S.L.* Obtained ^{1}H- and ^{13}C{^{1}H}-NMR spectra were calibrated against the residual signal of the used deuterated solvents relative to TMS (Tetramethylsilane).[231] Residual peaks given in ppm, MeCN-*d*3: $\delta(^{1}\text{H})$ = 1.940, $\delta(^{13}\text{C})$ = 118.260 or 1.320; C_6D_6: $\delta(^{1}\text{H})$ = 7.160, $\delta(^{13}\text{C})$ = 128.060; $CDCl_3$: $\delta(^{1}\text{H})$ = 7.260, $\delta(^{13}\text{C})$ = 77.160; CD_2Cl_2: $\delta(^{1}\text{H})$ = 5.320, $\delta(^{13}\text{C})$ = 53.840 ; THF-*d*8: $\delta(^{1}\text{H})$ = 3.580 or 1.730, $\delta(^{13}\text{C})$ = 67.570 or 25.370; toluene-*d*8: $\delta(^{1}\text{H})$ = 2.090, $\delta(^{13}\text{C})$ = 20.400. For the heteronuclear NMR spectra the IUPAC recommended method was used. According to which the chemical shift δ of the compound is:

$$\delta = 10^6 \cdot \frac{(\Xi_{\text{sample}} - \Xi_{\text{reference}})}{\Xi_{\text{reference}}}$$

in which Ξ_{sample} is frequency of nucleus relative to the frequency of ^{1}H. The values of Ξ along with the natural abundance and reference are given in Table 22. Deuterated solvents were stored over 10 w% molecular sieve (4 Å) for min. 2 days before usage. The chemical shift (δ) is given in part per million (ppm) and scalar coupling constants $^{n}J_{\text{X,Y}}$ in Hertz (Hz), with n the covalent bonds between the nuclei X and Y, as absolute values neglecting the sign of the gyromagnetic ratio. The multiplicity is described as the following: s = singlet, d = doublet, t = triplet, q = quartet, quint = quintet, sext = sextett, hept = heptet and combinations of these. Coupling to nuclei with a small natural abundance are considered as satellites and denoted with 'sat' in the multiplicities index. For the ^{1}Hinteger numbers *n* are given as *n*H for the

Table 22: Properties of measured NMR-active isotopes used in this work, natural abundance *N*, the frequency factor Ξ, references and the measured spectrometer frequencies relative to the ^{1}Hfrequency, commonly used as a descripter for the NMR-spectrometer.

Isotope	*N* / %	Ξ / %	reference	f_{Mess} / MHz		
				300	400	500
^{1}H	99.989	100.0000	1% SiMe$_4$ (CDCl$_3$)	300.13	400.13	500.13
^{7}Li	92.41	38.8639	10.74 M LiCl (D$_2$O)	116.64		194.37
^{13}C	1.07	25.1450	1 % SiMe$_4$ (CDCl$_3$)	75.48		125.77
^{19}F	100	94.08	CFCl$_3$			470.51
^{29}Si	4.67	19.8672	1% SiMe$_4$ (CDCl$_3$)			99.36
^{31}P	100	40.4807	85 % H$_3$PO$_4$	121.51	161.99	202.48

integral measured relative to other resonances. For complex NMR spectra a combination of 1D- and 2D-NMR experiments (COSY, HSQC, HMBC) are used to assign the resonances. NMR spectra were recorded at a constant temperature of 298 K, if not mentioned otherwise.

8.3.2. EPR spectroscopy

CW-EPR experiments were conducted with an X-Band EPR spectrometer EMXmicro from Bruker, equipped with a super high-quality resonator (SHQ). The spectra were measured at various temperatures, for the low temperature measurements (100-200 K) a variable temperature accessory ER4131VT (Bruker) was used. The spectra were recorded with 19.63 mW (10dB), a modulation frequency of 100 kHz, a moldulation amplitude of 4 G and a time constant of 10.24 ms. Sample solutions were prepared to have a spin concentration of 200-400 μM. EPR spectra recorded at temperatures below 100 K and in parallel mode for the analysis of integer spin paramagnetic systems was performed by Bill from the 'Max-Planck-Institut für Energiekonversion in Mühlheim a. d. Ruhr'.

8.3.3. Mößbauer spectroscopy

The discussed ^{57}Fe-Mößbauer spectra were recorded by Bill and co-workers in collaboration from the 'Max-Planck-Institut für Energiekonversion in Mühlheim a. d. Ruhr'.

8.3.4. Mass spectrometry

Samples were measured by the analytic department of the University of Bonn. Electron impact ionisation (EI) experiments were performed on a Thermo Finnigan MAT 95 XL sector field instrument using an ionisation energy of 70 eV. Calibration and referencing was done using perfluorokerosene (PFK). Electrospray ionisation (ESI) were performed on a Thermo Fisher Scientific Orbitrap XL spectrometer using dichloromethane or acetonitrile as solvents. Air sensitive samples were prepared in a glovebox and sealed in glass vials and only opened shortly before the measurements. Only selected data is given, isotopic patterns are reduced to the isotopomer with the highest mass-to-charge ratio (m/z). No standard deviation for high resolution mass spectra (HRMS) obtained from ESI is given as spectra were recorded only once.

8.3.5. Infrared spectroscopy

ATR-IR spectra were recorded from solid and oils (inside a glovebox at ambient temperatures) in a spectral range from 400-4000 cm^{-1} on a Burker Alpha FTIR spectrometer with a single-reflection ATR unit (Platinum-ART Diamond) or on a Shimadzu IRSpirit FTIR spectrometer with a single-reflection ATR unit (QATR-S). Solution spectra were recorded on a Shimadzu IRSpirit FTIR spectrometer, with stainless steal cells with KBr windows (Omni-Cell SPECAC) seperated by 6 μm with a PTFE spacer (OMNI). The Happ-Genzel function was used for apodisation. The obtained data was analysed with the software *EZ OMNIC 7.3* from *Fisher Scientific* and *LabSolutions IR 2.26* from *Shimadzu*. Intensities of the peaks are given as very strong (vs), strong (s), medium (m) or as weak (w). Broadening of the peaks is marked with a 'br' in the index of the intensity. Only the peaks relevant for the class of compounds are given and if > 1500 cm^{-1}.

8.3.6. Elemental analysis

Elemental analysis was performed on a Elementar Vario Micro analysis device and done in triplicate or more, conducted by technical staff of the University of Bonn. All samples were homogenised and then prepared under glovebox conditions, before weighting on a micoranalytical balance in tin or silver sample containers. For the C,H,N and S content averaged values are given.

8.3.7. Melting point determination

For the melting point determination glass capillaries (ø= 0.1 mm) were filled ∼0.2 mm with homogenised sample under glovebox conditions, and flame-sealed or sealed with grease. Melting points were measured with a *MPmeter* from Toledo or using an determination apparatus after *Tottoli*. Melting points are taken without corrections.

8.3.8. Single crystal X-ray diffraction analysis

Single crystals for the X-ray diffraction measurements were prepared as described. Crystals were then covered under Fomblin and suitable crystals were selected, mounted, mea-

sured and solved by the staff of the analytical department of the University of Bonn. Measurements were performed on a Bruker X8-KappaApex II diffractometer, a Bruker D8 Venture diffractometer, a STOE IPDS-2T diffractometer or a STOE STADIVARI diffractometer, equipped with a low-temperature device (Bruker Kryoflex, Oxford Cryostream 700 series or Oxford Cryostream 800 series) at 100(2) K, 123(2) K or 180(2) K by using graphite monochromated Mo-Kα radiation (λ = 0.71073 Å) or Cu-Kα radiation (λ = 1.54186 Å). Bond parameter analysis was done using the free software *Olex2 1.5*[232]

8.3.9. Cyclic voltammetry

Cyclic voltamorgrams (CV) were measured using the potentio- and galvanostat system called WaveNowXV® of Pine Research in a glovebox at ambient temperatures. Scan rates of 20-10000 mV s^{-1} were applied, however commonly only 50-2000 mV s^{-1} were considered, which gave reasonable shaped CVs. For all CV measurements Pine Research ceramic screen-printed platinum electrodes containing an Ag/AgCl reference electrode were used. These electrodes combine working, counter and reference electrodes on one ceramic plate. As cell a low volume glass cell (V = ~1.2 mL) with a special PTFE insert at the bottom that features a narrow slit for the ceramic screen-printed electrodes was used. Solvents used for the experiments were dried and degassed prior to use. THF was dried over a potassium mirror, recondensed in a Schlenk flask and then degassed (3 *Freeze-Pump-Thaw* cycles). MeCN was dried overnight over CaH_2 and then distilled on P_4O_{10}, from which it was quickly distilled on molecular sieve (3 Å) and then degassed (3 *Freeze-Pump-Thaw* cycles). Experiments were performed with [$^nBu_4N$]PF_6 as electrolyte (previously dried at 80 °C under reduced pressure (<0.02 mbar) for 24 h). The concentration of the electrolyte was 0.2 M in THF, and 0.1 M in MeCN. The analyte solution was prepared with a concentration of 1 mM. After background scans on the electrolyte solution were measured to identify the anodic and cathodic limits with respect to the nominal voltage of the solid silver reference, the analyte was added. Next, open circuit potential measurements were performed to establish the starting potential of the cyclic voltammetry experiments. Careful cyclic voltammetry scans were then measured in the anodic and cathodic directions to encounter the most accessible processes, and only after these were investigated thoroughly, further scans to higher positive and negative potentials were measured. At the end of the measurements internal references were added (Cp_2Fe or [Cp_2Co]PF_6) to the same concentration as the analyte. The ferrocene/ferrocenium redox couple was set to 0 V, in agreement with the IUPAC recommendations.[233] CV spectra were plotted using the software *OriginPro*

8G of OriginLab.

8.4. Waste Disposal

Laboratory chemical waste was disposed according to the 'Gefahstoffverordnung' (Gef-StoffV). Chemical waste was neutralised/quenched if reactive and then separated into individual containers for organic solvents, solids, filter and filtration media and heavy metal waste. Syringes and cannulae were separated from eachother. The collected waste containers were submitted to the department *4.2 Arbeits- und Umweltschutz of the University of Bonn*.

8.5. Used chemicals

Chemical	CAS	producer
1,3,-Diisopropylthiourea	2986-17-6	Sigma-Aldrich
2-(^{t}Butylperoxy)-2-methylpropane	110-05-4	Sigma-Aldrich
Acetonitrile	75-05-8	VWR
Acetonitrile-*d*3	2206-26-0	Deutero GmbH
		Sigma-Aldrich
Aluminium oxide 90 neutral	1344-28-1	Merck
C_6D_6	1076-43-3	Deutero GmbH
		Sigma-Aldrich
Butane-2,3-dione	431-03-8	Sigma-Aldrich
Catechol	120-80-9	AlfaAesar (Thermo Fisher Scientific)
Cobaltocen	1277-43-6	abcr
Cobaltocenium hexafluorophosphate	12427-42-8	Sigma-Aldrich
Chloroform-*d*1	865-49-6	Deutero GmbH
		Sigma-Aldrich
Decamethylcobaltocen	74507-62-3	Sigma-Aldrich
Dichloromethane	75-09-2	Sigma-Aldrich
Dichloromethane-*d*2	1665-00-5	Deutero GmbH
		Sigma-Aldrich
Diethylether	60-29-7	VWR
Diiron nonacarbonyl	15321-51-4	abcr
Ethyl acetate	141-78-6	Juli.O GmbH
Ferrocen	102-54-5	Acros
Graphite	7782-42-5	Fisher Scientific
Hydrogen peroxide	772-84-1	ThGeyer
Iodine	7553-56-2	VWR
Iron pentacarbonyl	236-670-8	Sigma-Aldrich
Methanol	811-98-3	Fisher Scientific
Methyl trifluormethanesulfonate	333-27-7	Merck
^{n}BuLi	109-72-8	Acros
N-isopropylaminoethanol	109-56-8	TCI
N-methylaminoethanol	109-83-1	Aldrich

156

N-methyl imidazole	616-47-7	AlfaAesar
N,N'-dimethylethylenediamine	110-70-3	TCI
N,N'-diisopropylethylenediamine	4013-94-9	TCI
n-Pentane	109-66-0	VWR
Ortho-difluorbenzene	367-11-3	abcr
Ortho-phenylenediamine	95-54-5	AlfaAesar (Thermo Fisher Scientific)
Peroxybis(trimethylsilane)	5796-98-5	Fluorochem
Petrol ether (40/65)	64742-49-0	Juli.O GmbH
Pinacol	76-09-5	Fluorochem
Phosphorus trichloride	7719-122	Acros
Phosphoryltrichloride	10025-87-3	Acros
Potassium	7440-09-7	Riedel de Haen
Pyrazine	290-37-9	Fluorochem
Pyridine N-oxide	694-59-7	Merck
Silica gel 60	7631-86-9	Merck
Sodium	7440-23-5	Sigma-Aldrich
Sodium hydroxide	1310-73-2	VWR
Sodium hypochlorite	7681-52-9	Roth
^{t}BuLi	594-19-4	Acros
TEMPO	2564-83-2	Fluorochem
Tetrabutylammonium hexafluorophosphate	3109-63-5	AlfaAesar (Thermo Fisher Scientific)
Tetrachloromethane	56-23-5	Acros
Tetrafluoroboric acid (aqueous)	16872-11-0 Sigma-Aldrich	
Tetrahydrofuran-*d*8	1693-74-9	Deutero GmbH
		Sigma-Aldrich
Tetrahydrofurane	203-726-8	VWR
Tetraphenylphosphonium bromide	2751-90-8	Sigma-Aldrich
Thiophenol	108-98-5	—*
Toluene	108-88-3	VWR
Toluene-*d*8	2037-26-5	Deutero GmbH
		Sigma-Aldrich
Triethylamine	121-44-8	Sigma-Aldrich
Trimethylsilyl chloride	75-77-4	Acros
Trimethylsilyl trifluormethanesulfonate	27607-77-8	Acros
Tungsten hexacarbonyl	14040-11-0	abcr

8.6. List of compound abbreviations
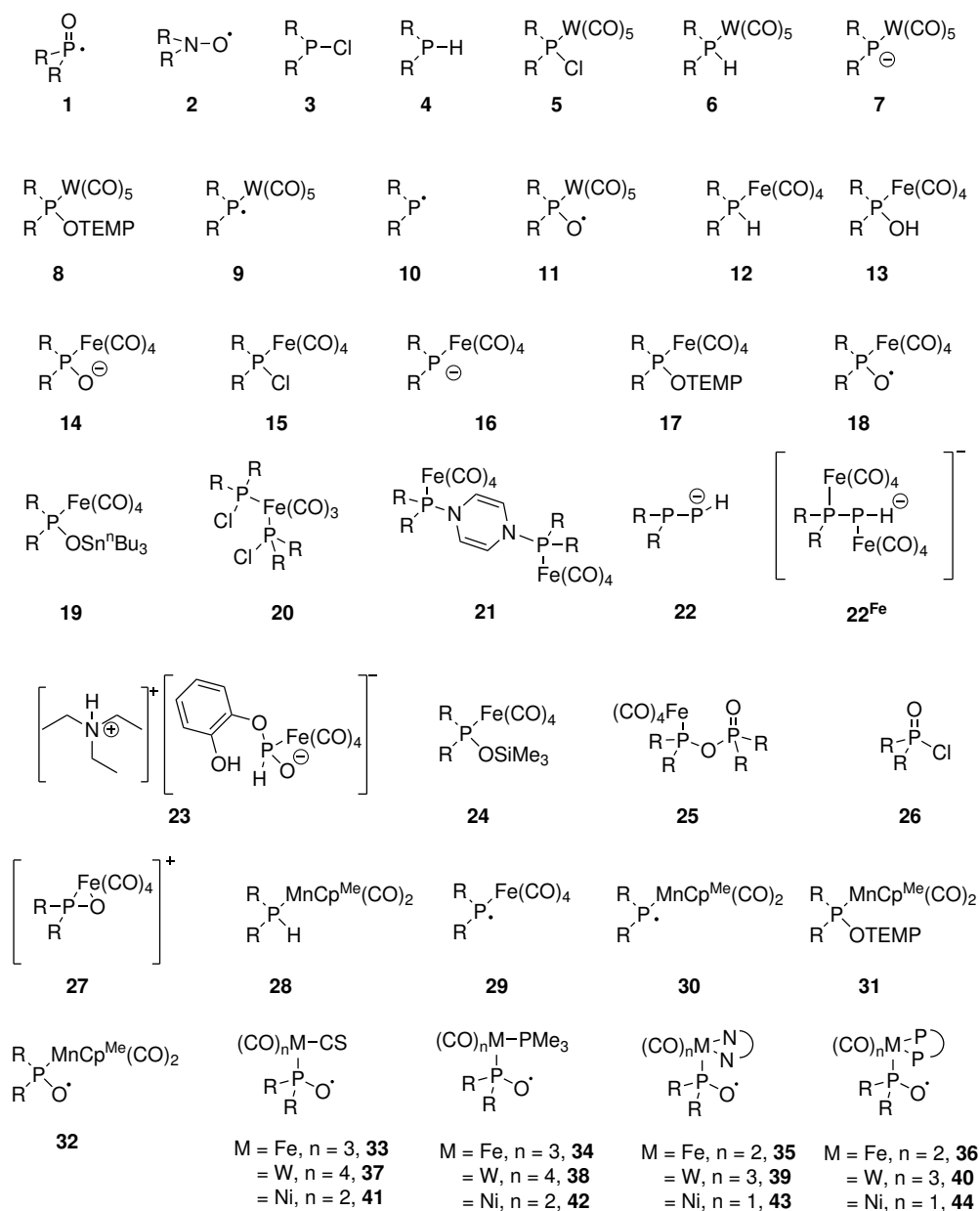
Figure 103: Part 1.: Numbering abbreviation of the compounds presented in this work.
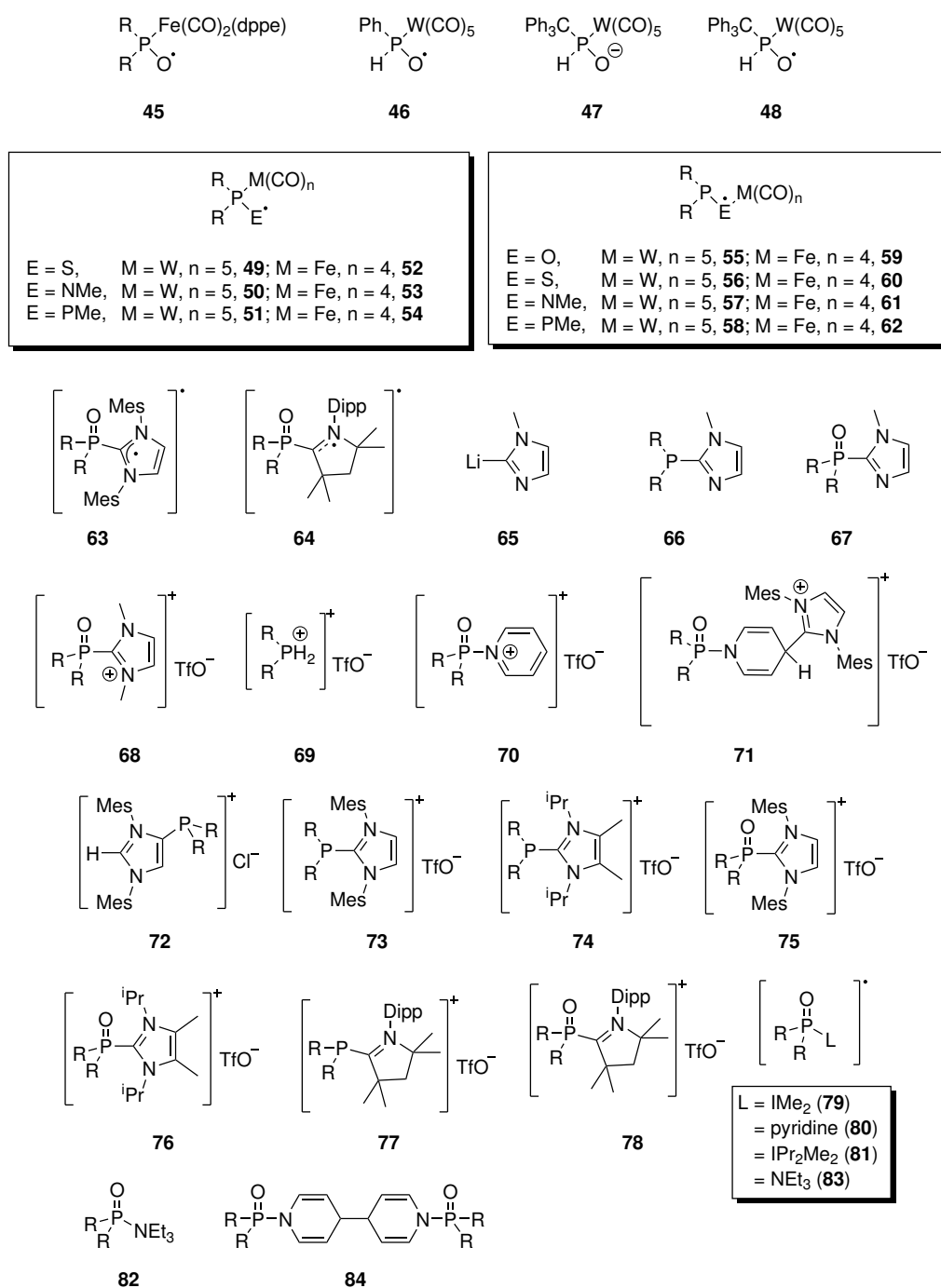
Figure 104: Part 2.:Numbering abbreviation of the compounds presented in this work.
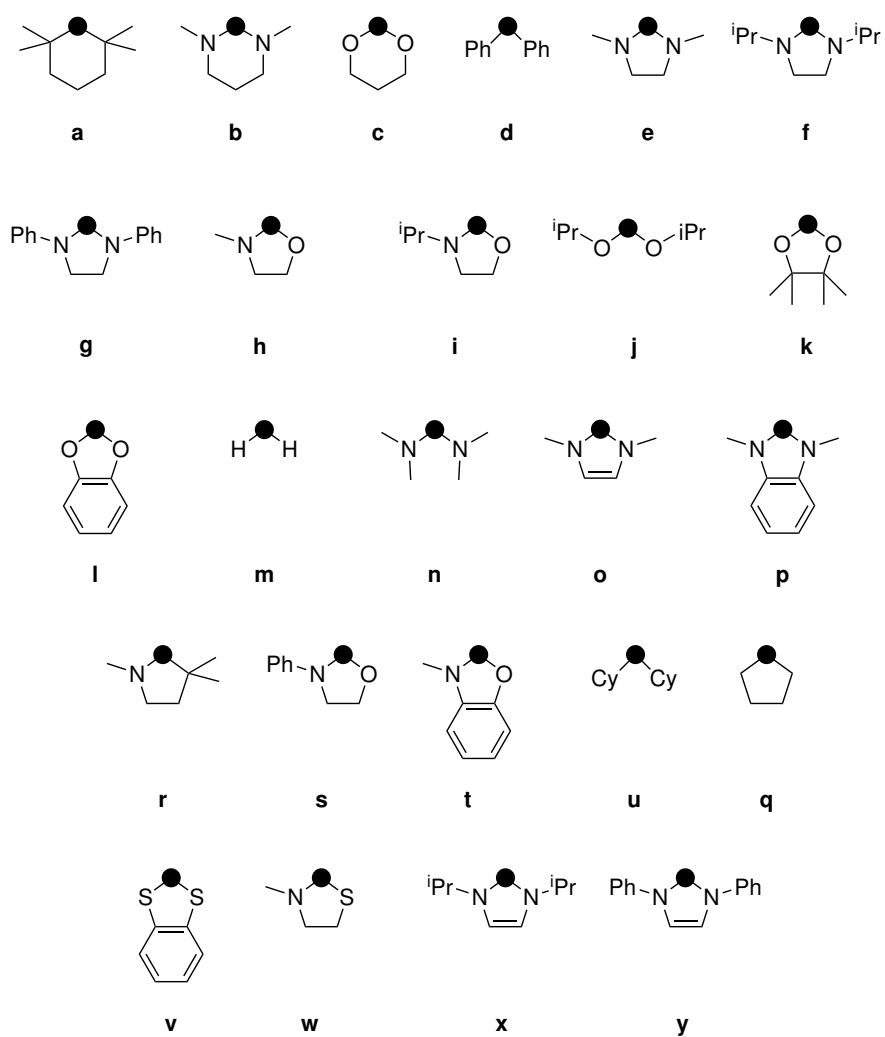
Figure 105: Suffix used for the indication of the substitution pattern (for R) at the P-atom in the described compounds.

8.7. Synthetic protocols and characterisation

Following compounds were synthesised according to literature procedures:

- Chlorophosphanes **3e,f,h,k,l**[203, 234–237]

- Chlorophosphane oxide **26e**[238]

- [**2**]BF$_4$[239]

- [NEt$_4$][W(CO)$_5$H][240]

- K[Fe(CO)$_4$H][241]

- IMes[242]

- IPr$_2$Me$_2$[243]

- cAAC[172]

- Iodosylbenzene **XLVIII**[244]

- (NacNacMg)$_2$[245]

8.7.1. Synthesis of 2-chloro-3-isopropyl-1,3,2-oxazaphospholidine (3i)
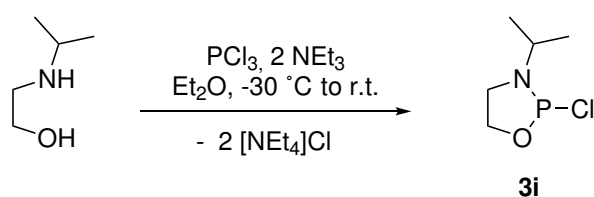
3i has been described in the literature (according to the database SciFinder^n), published by Nuretdinova, O. N. and Gaidukova, N. M. in Zhurnal Obshchei Khimii in 1998. Access is however very limited. Hence the synthesis of **3i** is described in the following.

Synthesis: To a dried 250 mL three-necked round bottom flask with vacuum adapter and two 50 mL dropping funnels, 50 mL Et$_2$O were added. In one of the dropping funnels 25 mL of Et$_2$O, 7 mL of NEt$_3$ (50 mmol, 1 eq.) and 5.75 mL (50 mmol, 1 eq.) of N-isopropyl-2-aminoethanol were mixed. The second dropping funnel was filled with 25 mL of Et$_2$O and

4.4 mL (50 mmol, 1 eq.) of PCl$_2$. The flask was cooled to $-30\ °$C in a cooling bath and kept at this temperature for the duration of the addition. While stirring, the two solutions were simultaneously added dropwise. After 30 minutes the addition was completed. To the reaction mixture 7 mL of NEt$_3$ (50 mmol, 1 eq.) in 20 mL of Et$_2$O were added dropwise. The reaction mixture was stirred for 30 minutes, after which the cooling bath was removed. The precipitated salt was filtered off through a frit (P3) and washed eight times with 20 mL of Et$_2$O each. The solvent was removed from the filtrate under reduced pressure (26 mbar, 25 °C), and the crude product was obtained as yellow oil. The crude product was distilled (T: 130 °C, b.p.: 107-108 °C, 21 mbar) to obtain the pure product as a colourless liquid.

Reaction code: AMF-10, 23m3a053.20

Molecular formula: C$_5$H$_{11}$ClNOP

Molecular weight: 167.58 g mol^{-1}

Yield: 3.165 g, 38 %. In the accessible literature's abstract yields ranging from 21-42% are reported.

Boiling point: 107-108 °C at 21 mbar

^{1}H-NMR (300.1 MHz, 298 K, CDCl$_3$): 4.47 (s$_{br}$, 2H, OCH$_2$), 3.51 (m, 1H, CH^{i}Pr$_2$), 3.21 (m, 2H, NCH$_2$), 1.33 (d, $^2J_{H,H}$ = 6.4 Hz, 6 H, CH$_3$)

^{31}P{^{1}H}-NMR (121.5 MHz, 298 K, CDCl$_3$): 168.4 (s).

8.7.2. Synthesis of [pentacarbonyl(2-chloro-1,3-diisopropyl-1,3,2-diazaphospholidine-κP)tungsten(0)] (5f)

3f   **5f**
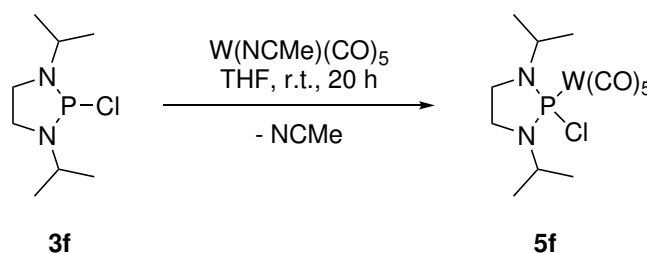
Synthesis: In a dried 100 mL Schlenk tube 2.19 g (6 mmol, 1 eq.) W(NCMe)(CO)$_5$ were dissolved in 15 mL of THF. A solution of 0.92 g (4.4 mmol, 0.73 eq.) **3f** in 10 mL of THF was added via a transfer cannula and rinsed two times with 5 mL of THF. The reaction was stirred for 20 h. After removing the solvent at reduced pressure (3·10^{-2} mbar) the crude product was extracted with three times 15 mL of *n*-pentane. The *n*-pentane solution was

filtered through silica (ø= 2 cm, h = 1.5 cm) and the solid phase was washed with additional 90 mL of *n*-pentane. The product was obtained as a yellow solid.

Reaction code: PB-321, 40t4a072.21

Molecular formula: $C_{13}H_{18}ClN_2O_5PW$

Molecular weight: 532.56 g mol^{-1}

Yield: 0.61 g, 26%

Melting point: 125 °C

Elemental analysis:

calculated (%) C 29.32 H 3.41 N 5.26 , found (%) C 29.26 H 3.52 N 5.26

MS: (EI, 70 eV, selected data): m/z (%) = 532.0 (0.2) [M]$^{+\bullet}$, 516.0 (3) [M-CO]$^{+\bullet}$, 497.0 (10) [M-3CO]$^{+\bullet}$, 469.0 (6) [M-4CO]$^{+\bullet}$, 441.0 (5) [M-6CO]$^{+\bullet}$, 173.2 (100) [M-W(CO)$_6$]$^{+\bullet}$.

IR: (ATR diamond, selected data): $\tilde{\nu}$ in cm^{-1} = 2971 (w, ν(C-H)), 2938 (w, ν(C-H)), 2883 (w, ν(C-H)), 2078 (w, ν(C=O)), 1902 (vs, ν(C=O)).

^{1}H-NMR: (500 MHz, 298 K, C_6D_6): 4.06 – 3.96 (m, 2H, CH(iPr)2), 2.70 – 2.65 (m, 2H, CH$_2$), 2.50 – 2.43 (m, 2H, CH2), 1.08 (d, $^3J_{H,H}$ = 6.6 Hz, 6H, CH$_3$), 0.93 (d, $^3J_{H,H}$ = 6.8 Hz, 6H, CH$_3$).

^{13}C{^{1}H}-NMR: (125.8 MHz, 298 K, C_6D_6): 198.8 (d$_{sat}$, $^2J_{P,C}$= 42 Hz, $^1J_{W,C}$ = 141 Hz, trans-CO), 195.9 (d$_{sat}$, $^2J_{P,C}$ = 9 Hz, $^1J_{W,C}$ = 126 Hz, cis-CO), 46.2 (d, $^2J_{P,C}$ = 12 Hz, CH(iPr)2), 40.2 (d, $^2J_{P,C}$ = 6 Hz, CH$_2$), 21.3 (d, $^3J_{P,C}$ = 12 Hz, CH$_3$), 18.6 (s, CH$_3$).

^{31}P-NMR: (202.5 MHz, 298 K, C_6D_6): 130.9 (s$_{sat}$, $^1J_{W,P}$ = 369 Hz, $^2J_{P,C}$ = 42 Hz)

8.7.3. Synthesis of [pentacarbonyl(1,3-diisopropyl-1,3,2-diazaphospholidine-κP)tungsten(0)] (6f)

5f **6f**
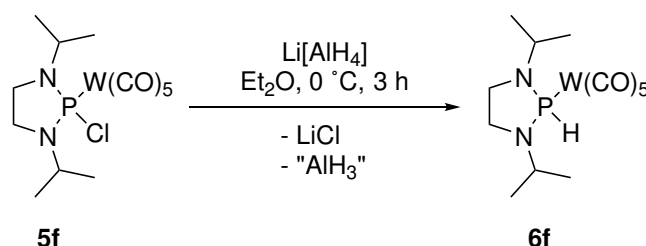
Synthesis: In a dried 100 mL Schlenk tube 0.53 g (1 mmol, 1 eq.) of **5f** were dissolved in 10 mL of Et$_2$O. The solution was cooled in an ice bath and a cooled suspension of 38.0 mg (1 mmol, 1 eq.) of Li[AlH$_4$] in 5 mL of Et$_2$O was added with a transfer cannula, which was rinsed two times with 15 mL of Et$_2$O. The mixture was allowed to warm to room temperature

and after 3 h the solvent was removed under reduced pressure ($3 \cdot 10^{-2}$ mbar). The product was extracted five times with 10 mL of *n*-pentane. After removing the solvent at reduced pressure ($3 \cdot 10^{-2}$ mbar) the product was obtained as a bright yellow solid.

Reaction code: AMF-21, AMF-38, 29m3a055.20

Crystallographic code: GXray6366

Molecular formula: $C_{13}H_{19}N_2O_5PW$

Molecular weight: 498.12 g mol^{-1}

Yield: 0.34 g, 69%

Melting point: 69 °C

Elemental analysis:

calculated (%) C 31.35 H 3.84 N 5.62 , found (%) C 31.31 H 3.65 N 5.65

MS: (EI, 70 eV, selected data): m/z (%) = 498.1 (0.5) [M]$^{+\bullet}$, 441.1 (0.5) [M-H-3CO]$^{+\bullet}$, 173.2 (100) [M-HW(CO)$_5$]$^{+\bullet}$

IR (ATR diamond) $\tilde{\nu}$ in cm^{-1}: = 2974 (w, ν(C-H)), 2935 (w, ν(C-H)), 2878 (w, ν(C-H)), 2368 (w, ν(P-H)), 2072 (w, ν(C=O)), 1893 (vs, ν(C-H))

^{1}H-NMR: (300 MHz, 298 K, C_6D_6): 7.70 (d$_{sat}$, $^1J_{P,H}$ = 272.9 Hz, $^2J_{W,H}$ = 17.4 Hz, 1H, P-H), 3.78 – 3.65 (m, 2H, CH(^{i}Pr)2), 2.66 – 2.55 (m, 2H, CH$_2$), 2.36 – 2.29 (m, 2H, CH$_2$), 1.00 (d, $^3J_{H,H}$ = 6.6 Hz, CH$_3$), 0.83 (d, $^3J_{H,H}$ = 6.6 Hz, CH$_3$).

^{13}C{^{1}H}-NMR: (76 MHz, 298 K, C_6D_6): 198.9 (d, $^2J_{P,C}$ = 26 Hz, trans-CO), 196.2 (d$_{sat}$, $^2J_{P,C}$ = 9 Hz, $^1J_{W,C}$ = 125 Hz, cis-CO), 45.2 (d, $^2J_{P,C}$ = 11 Hz, CH(^{i}Pr)2), 41.6 (d, $^2J_{P,C}$ = 5 Hz, CH$_2$), 21.1 (d, $^3J_{P,C}$ = 11 Hz, CH$_3$), 17.3 (d, $^3J_{P,C}$ = 2.0 Hz, CH$_3$)

^{31}P{^{1}H}-NMR: (122 MHz, 298 K, C_6D_6): 78.7 (s$_{sat}$, $^1J_{W,H}$ = 295 Hz)

^{31}P-NMR: (122 MHz, 298 K, C_6D_6): 78.7 (dm$_{sat}$, $^1J_{P,H}$ = 273 Hz, $^1J_{W,H}$ = 295 Hz)

8.7.4. Synthesis of [pentacarbonyl(3-isopropyl-1,3,2-oxazaphospholidine-κP)tungsten(0)] (6i)

3i　　　　　　　　　　　　　**6i**
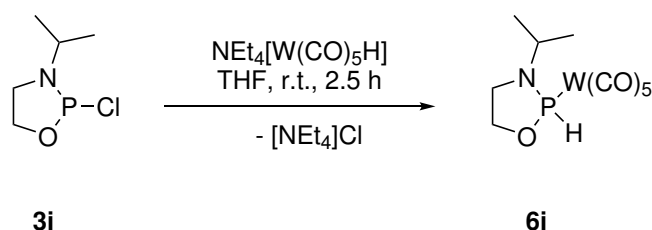
Synthesis: In a 100 mL Schlenk tube 0.45 g (1 mmol, 1 eq.) NEt$_4$[W(CO)$_5$H] were suspended in 15 mL of THF. While stirring, a solution of 0.17 g (1.04 mmol, 1.05 eq.) **3i** in

5 mL of THF was added with a transfer canula, which was rinsed with 5 mL of THF after addition. After 2.5 hours the solvent was removed under reduced pressure ($3 \cdot 10^{-2}$ mbar). The product was extracted from the sticky yellow residue by extraction with five times 10 mL of Et_2O. After removing the solvent from the filtrate under reduced pressure ($3 \cdot 10^{-2}$ mbar) the product was obtained as an off-white powder.

Reaction code: PB-269, 31p5a004.20, 29m3a055.20, 21m3b009.21

Crystallographic code: GXray6449

Molecular formula: $C_{10}H_{12}NO_6PW$

Molecular weight: 457.02 g mol^{-1}

Yield: 0.19 g, 41.5%

Melting point: 91 °C

Elemental analysis:

calculated (%) C 26.28 H 2.65 N 3.06 , found (%) C 25.96 H 3.24 N 2.89

MS: (EI, 70 eV, selected data): m/z = 457.0 $[M]^{+\bullet}$, 429.0 $[M-CO]^{+\bullet}$, 399.0 $[M-3CO-2H]^{+\bullet}$, 371.0 $[M-4CO-2H]^{+\bullet}$, 343.0 $[M-5CO-2H]^{+\bullet}$, 132.1 $[M-H-WCO_5]^{+\bullet}$

IR (ATR diamond) $\tilde{\nu}$ in cm^{-1}: 2963 (w, ν(C-H)), 2216 (w, ν(P-H)), 2076 (w, ν(C=O)), 1880 (vs, ν(C=O))

^{1}H-NMR: (500 MHz, 298 K, C_6D_6): 7.71 (d_{sat}, $^1J_{P,H}$ = 321 Hz, $^2J_{W,H}$ = 18.4 Hz, 1H, PH), 3.72 – 3.6 (m, 1H, CH^{i}Pr2), 3.46 – 3.39 (m, 1H, OCH$_2$), 3.37 – 3.32 (m, 1H, OCH$_2$), 2.36 – 2.28 (m, 1H, NCH$_2$), 2.06 – 2.00 (m, 1H, NCH$_2$), 0.89 (d, $^3J_{H,H}$ = 6.6 Hz, 3H, CH$_3$), 0.72 (d, $^3J_{H,H}$ = 6.6 Hz, 3H, CH$_3$)

^{13}C{^{1}H}-NMR: (126 MHz, 298 K, C_6D_6): 198.7 (d_{sat}, $^2J_{P,C}$ = 28.1 Hz, $^1J_{W,C}$ = 138 Hz, trans-CO), 195.6 (d_{sat}, $^2J_{P,C}$ = 9 Hz, $^1J_{W,C}$ = 125 Hz, cis-CO), 69.1 (d, $^2J_{P,C}$ = 10 Hz, OCH$_2$), 45.6 (d, $^2J_{P,C}$ = 11 Hz, CH^{i}Pr2), 41.1 (s, NCH$_2$), 21.6 (d, $^3J_{P,C}$ = 8 Hz, CH$_3$), 19.4 (d, $^3J_{P,C}$ = 4 Hz, CH$_3$);

^{31}P{^{1}H}-NMR: (203 MHz, 298 K, C_6D_6): 121 (s_{sat}, $^1J_{W,P}$ = 305 Hz)

^{31}P-NMR: (203 MHz, 298 K, C_6D_6): 121 (dm_{sat}, $^1J_{P,H}$ = 321 Hz, $^1J_{W,P}$ = 305 Hz)

8.7.5. Synthesis of [pentacarbonyl(4,4,5,5-tetramethyl-1,3,2-dioxaphospholane-κP)tungsten(0)] (6k)
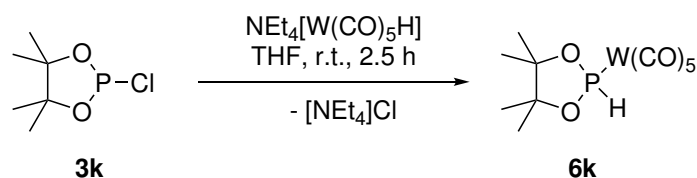
Synthesis: In a 100 mL Schlenk tube 0.69 g (1.51 mmol, 1 eq.) $NEt_4[W(CO)_5H]$ were suspended in 15 mL of THF. While stirring a solution of 0.29 g (1.59 mmol, 1.05 eq.) **3k** in 5 mL of THF was added with a transfer canula, which was rinsed with two times with 2.5 mL of THF after addition. After 1.5 hours the solvent was removed under reduced pressure ($3 \cdot 10^{-2}$ mbar). The product was extracted from the sticky yellow residue by extraction with five times 10 mL of Et_2O. The solvent was removed under reduced pressure to give the pure product as an off-white powder. To increase the yield the residue from the filtration was purified via column chromatography (SiO_2, argon, -20 °C, ø= 1 cm, h = 10 cm, petrol ether (40/65) with 2.5 % NEt3). The product was obtained in the first fraction. After removing the solvent under reduced pressure ($3 \cdot 10^{-2}$ mbar) the product was obtained as an off-white powder.

Reaction code: AMF-7, 22p5a042.20

Crystallographic code: GXray6538

Molecular formula: $C_{11}H_{13}O_7PW$

Molecular weight: 472.03 g mol^{-1}

Yield: 0.27 g, 38.6%

Melting point: 63 °C

Elemental analysis:

calculated (%) C 27.99 H 2.78 , found (%) C 28.00 H 2.91

MS: (EI, 70 eV, selected data): m/z = 472.0 [M]$^{+\bullet}$, 444.0 [M-CO]$^{+\bullet}$, 416.0 [M-3CO]$^{+\bullet}$;

IR (ATR diamond) $\tilde{\nu}$ in cm^{-1}: 2993 (w, ν(C-H)), 2280 (w, ν(P-H)), 2076 (w, ν(C=O)), 1906 (vs, ν(C=O))

^{1}H-NMR: (500 MHz, 298 K, C_6D_6): 8.49 (d$_{sat}$, $^1J_{P,H}$ = 349.7 Hz, $^2J_{W,H}$ = 22 Hz, 1H, PH), 0.96 (s, 3H, CH_3) 0.75 (s, 6H, CH_3)

^{13}C{^{1}H}-NMR: (126 MHz, 298 K, C_6D_6): 198.6 (d$_{sat}$, $^2J_{P,C}$ = 30.7 Hz, $^1J_{W,C}$ = 137 Hz, trans-CO), 195.3 (d$_{sat}$, $^2J_{P,C}$ = 9 Hz, $^1J_{W,C}$ = 125 Hz, cis-CO), 87.0 (d, $^2J_{P,C}$ = 6 Hz, (Me$_2$CO), 24.5 (d, $^3J_{P,C}$ = 5 Hz, CH_3), 21.5 (d, $^3J_{P,C}$ = 4 Hz, CH_3)

^{31}**P{^{1}H}-NMR**: (203 MHz, 298 K, C_6D_6): 146.3 (s$_{sat}$, $^1J_{W,P}$ = 325 Hz)

^{31}**P-NMR**: (203 MHz, 298 K, C_6D_6): 146.3 (d$_{sat}$, $^1J_{P,H}$ = 350 Hz, $^1J_{W,P}$ = 325 Hz)

8.7.6. Synthesis of [pentacarbonyl(1,3-diisopropyl-2-(2,2,6,6-tetramethylpiperidin-1-oxyl)-1,3,2-diazaphospholidine-κP)tungsten(0)] (8f)
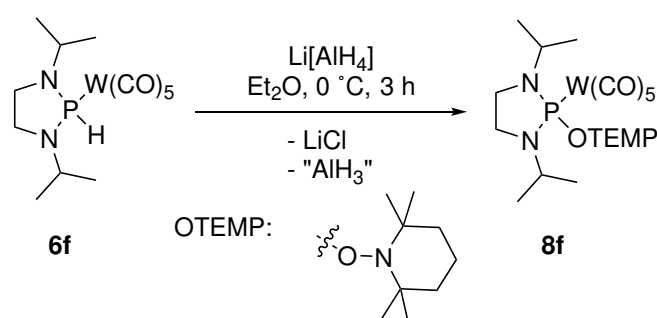
Synthesis: In a 100 mL Schlenk tube 0.4 g (0.80 mmol, 1 eq.) **6f** were dissolved in 15 mL of Et_2O. The colourless solution was cooled with an ice bath and with a transfer cannula a solution of 0.25 g (1.60 mmol, 2 eq.) TEMPO in 5 mL of Et_2O was added. After addition the cannula was rinsed with 5 mL of Et_2O. After 3 hours the solvent was removed under reduced pressure ($3 \cdot 10^{-2}$ mbar). The obtained yellow solid was purified via column chromatography (Al_2O_3, argon, $-20\ ^\circ$C, ø= 3 cm, h = 4 cm, petrol ether (40/65)). After the first fraction (50 mL petrol ether) the product was obtained in the second fraction (20 mL PE, 30 mL PE with 20% Et_2O, 55 mL PE with 50% Et_2O and 35 mL PE: Et_2O (1:1). All solutions had to be kept cold at around 0 $^\circ$C. After removing solvent under reduced pressure ($3 \cdot 10^{-2}$ mbar) and 0 $^\circ$C the product was obtained as a thermal labile yellow powder.

Reaction code: AMF-42, 35m3mTT2.20

Crystallographic code: GXray6371

Molecular formula: $C_{22}H_{36}N_3O_6PW$

Molecular weight: 653.36 g mol^{-1}

Yield: N/A (due to thermal instability of the product)

Elemental analysis:

calculated (%) C 40.44 H 5.55 N 6.43 , found (%) C 41.05 H 5.98 N 6.07

MS: N/A (due to thermal instability of the product)

IR (ATR diamond) $\tilde{\nu}$ in cm^{-1}: N/A (due to thermal instability of the product)

^{1}**H-NMR**: (300 MHz, 298 K, CDCl$_3$): 4.07- 3.93 (m, 2H, CH^{i}Pr2), 3.29 – 3.21 (m, 2H

NCH$_2$), 3.12 – 3.02 (m, 2H, NCH$_2$), 1.61 – 1.45 (m, 6H, CH$_2$-CH$_2$-CH$_2$), 1.26 (s, 6H, CCH$_3$ (TEMP-moiety)), 1.23 (d, $^3J_{H,H}$ = 6.6 Hz, 6H, N-CH(CH$_3$)$_2$), 1.15 (d, $^3J_{H,H}$ = 6.5 Hz, 6H, N-CH(CH$_3$)$_2$), 1.07 (s, 6H, CCH$_3$ (TEMP-moiety))

^{13}C{^{1}H}-NMR: (76 MHz, 298 K, CDCl$_3$): 198.8 (d, $^2J_{P,C}$ = 32 Hz, trans-CO), 198.4 (d, $^2J_{P,C}$ = 9 Hz, cis-CO), 61.0 (d, $^3J_{P,C}$ = 2 Hz, NC(CH$_2$)(CH$_3$)$_2$ (TEMP-moiety)), 46.1 (d, $^2J_{P,C}$ = 14 Hz, CH^{i}Pr2), 41.1 (d, $^2J_{P,C}$ = 3 Hz, N-CH$_2$), 40.0 (s, CH$_2$-CH$_2$-CH$_2$), 33.2 (NC(CH$_2$)(CH$_3$)$_2$ (TEMP-moiety)), 21.7 (d, $^3J_{P,C}$ = 2 Hz, NCH(CH$_3$)$_2$), 20.9 (s, NC(CH$_2$)(CH$_3$)$_2$ (TEMP-moiety)), 20.8 (d, $^3J_{P,C}$ = 5 Hz, NCH(CH$_3$)$_2$), 16.8 (s, CH$_2$-CH$_2$-CH$_2$ (TEMP-moiety))

^{31}P{^{1}H}-NMR: (122 MHz, 298 K, CDCl$_3$): : 140.6 (br. s)

8.7.7. Synthesis of [pentacarbonyl(3-isopropyl-2-(2,2,6,6-tetramethylpiperidin-1-oxyl)-1,3,2-oxazaphospholidine-κP)tungsten(0)] (8i)
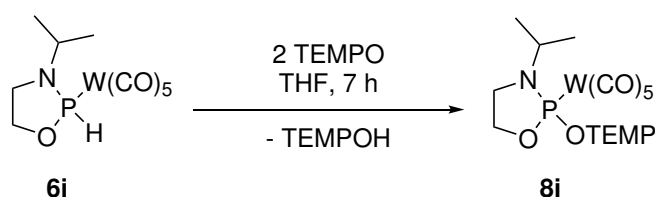
Synthesis: In a 10 mL Schlenk tube 122 mg (0.27 mmol, 1 eq.) **6i** was dissolved in 3 mL THF. A solution of 84 mg (0.53 mmol, 2 eq.) TEMPO in 1 mL of THF was added to the solution of **6i** with a transfer cannula. The cannula was rinsed with 1 mL of THF. The reaction mixture was stirred for 7 hours and all volatiles were removed under reduced pressure (4·10^{-2} mbar) to obtain the product as a beige powder.

Reaction code: PB-211, 49p5a042.20
Crystallographic code: GXray6459
Molecular formula: C$_{19}$H$_{29}$N$_2$O$_7$PW
Molecular weight: 612.26 g mol^{-1}
Yield: 0.16 g, 97 %
Elemental analysis:
calculated (%) C 37.27 H 4.77 N 4.58 , found (%) C 37.62 H 5.22 N 4.53
MS: (EI, 70 eV, selected data): m/z = 612.2 [M]$^{+\bullet}$, 456.0 [M-TEMPO]$^{+\bullet}$, 428.0 [M-TEMPO-CO]$^{+\bullet}$, 140.1 [TEMP]$^{+\bullet}$, 132.1 [M-TEMPO-W(CO)5]$^{+\bullet}$, 126.1 [TEMP-N]$^{+\bullet}$
IR (ATR diamond) $\tilde{\nu}$ in cm^{-1}: fehlt

¹H-NMR: (500 MHz, 298 K, THF-*d*8): 4.35 – 4.26 (m, 2H, OCH₂), 3.95 (dh, $^3J_{P,H}$ = 10.3 Hz, $^3J_{H,H}$ = 6.6 Hz, NCH^{i}Pr2), 3.37 – 3.27 (m, 1H, NCH₂) 3.20 – 3.10 (m, 1H, NCH₂), 1.69 – 1.51 (m , 5H, CH₂-CH₂-CH₂ (TEMP-moiety)), 1.41 (s, 3H, NC(CH₂)(CH₃)₂), 1.33 (d, $^3J_{H,H}$ = 6.7 Hz, 3H, NCH(CH₃)₂), 1.32 (s, 3H, NC(CH₂)(CH₃)₂), 1.27 (d, $^3J_{H,H}$ = 6.6 Hz, 3H, NCH(CH₃)₂), 1.18 (s, 3H, NC(CH₂)(CH₃)₂), 1.14 (s, 3H, NC(CH₂)(CH₃)₂)

¹³C{¹H}-NMR: (126 MHz, 298 K, THF-*d*8): 199.6 (d$_{sat}$, $^2J_{P,C}$ = 37 Hz, $^1J_{W,C}$ = 140 Hz, trans-CO), 198.0 (d$_{sat}$, $^2J_{P,C}$ = 9 Hz, $^1J_{W,C}$ = 126 Hz, cis-CO), 67.8 (d, $^2J_{P,C}$ = 9 Hz, OCH₂), 62.6 (d, $^2J_{P,C}$ = 5 Hz, NC(CH₂)(CH₃)₂), 62.0 (s, NC(CH₂)(CH₃)₂), 45.3 (d, $^2J_{P,C}$ = 13 Hz, NCH(CH₃)₂), 41.2 (s, NC(CH₂)(CH₃)₂), 41.1 (s, NC(CH₂)(CH₃)₂), 40.4 (s, NCH₂), 34.3 (s, NC(CH₂)(CH₃)₂), 33.81 (s, NC(CH₂)(CH₃)₂), 22.1 (s, NCH(CH₃)₂), 21.5 (s, NC(CH₂)(CH₃)₂), 21.4 (s, NC(CH₂)(CH₃)₂), 20.9 (d, $^3J_{P,C}$ = 7 Hz, NCH(CH₃)₂)

³¹P-NMR: (203 MHz, 298 K, THF-*d*8): 151.0 (s$_{sat}$, $^1J_{W,P}$ = 366.7 Hz)

8.7.8. Synthesis of [pentacarbonyl(4,4,5,5-tetramethyl-2-(2,2,6,6-tetramethylpiperidin-1-oxyl)-1,3,2-dioxaphospholane-κP)tungsten(0)] (8k)
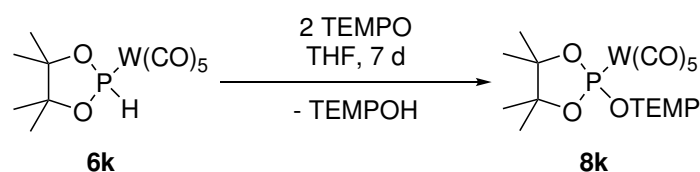
Synthesis: In a 10 mL Schlenk tube 99 mg (0.21 mmol, 1 eq.) **6k** was dissolved in 6 mL of THF. A solution of 71 mg (0.44 mmol, 2.1 eq.) TEMPO in 2 mL of THF was added to the solution of **6k** with a transfer cannula. The cannula was rinsed twice with 1 mL of THF. The solution was stirred for a week until a mixture of presumably 8k, **6k** and an unknown complex were formed in a ratio of 7:1.5:1. Via column chromatography (SiO₂, argon, -20 °C, ø= 2 cm, h = 10 cm, Et₂O) **6k** was removed from the mixture. From a saturated Et₂O solution at 4 °C single crystals were grown.

Reaction code: PB-230, 05t4a097.21

Crystallographic code: GXray6587

Molecular formula: C₂₀H₃₀NO₈PW

Molecular weight: 627.27 g mol⁻¹

Yield: 88% contribution in the reaction mixture (estimated by ³¹P-NMR signal integration)

³¹P{¹H}-NMR: (162 MHz, 298 K, THF): 161.9 (s$_{sat}$, $^1J_{W,P}$ = 387.8 Hz, 8k), 146.1 (s$_{sat}$, $^1J_{W,P}$ =

325 Hz, 6k), 131.1(s_{sat}, $^1J_{W,P}$ = 391.5 Hz)

8.7.9. Synthesis of [tetracarbonyl(diphenylphosphane-κP)iron(0)] (12d)
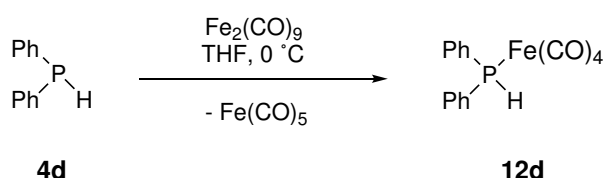
The synthesis of **12d** was slightly modified from the procdeure described by Treichel et al.[104]

Synthesis: In a 250 mL Schlenk flask 3.83 g $Fe_2(CO)_9$ were suspended in 40 mL THF at 0 °C. In a 100 mL Schlenk tube 1.92 mL **4d** were dissolved in 40 mL THF at 0 °C and then added to the $Fe_2(CO)_9$ suspension via a transfer canula. After the addition the canula was rinsed once with 10 mL precooled THF. Then the ice bath was removed and the mixture was stirred for 3 hours at room temperature after which the solvent was removed. The crude residue was loaded on a low temperature column (h = 5 cm, ø= 5 cm, SiO_2, PE:Et_2O, −20 °C) under inert conditions. The pure product was obtained in the fraction with an eluent mixture (PE:Et_2O, 110:5). The following fractions, with higher Et_2O content, contained the disubstituted complex. After evaporation of the solvent under reduced pressure ($3 \cdot 10^{-2}$ mbar) the product was obtained as a hazelnut brown powder.
The analtical data fits to previously reported values by Treichel.

Reaction code: PB-165
Yield: 2.35 g, 63%; Lit.-value:[104] 68%.

8.7.10. Synthesis of [tetracarbonyl(2-chloro-1,3-dimethyl-1,3,2-diazaphospholidine-κP)iron(0)] (15e)
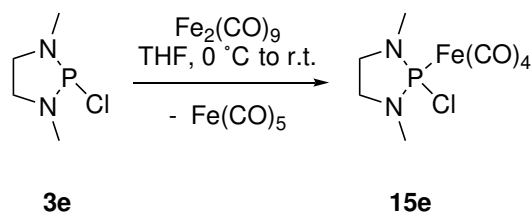
Synthesis: In a 250 mL Schlenk flask 2.25 g $Fe_2(CO)_9$ were suspended in 85 mL THF at 0 °C. In a 50 mL Schlenk tube 1.013 g **3e** were dissolved in 10 mL THF at 0 °C and then added to the $Fe_2(CO)_9$ suspension with a syringe. After the addition the syringe was rinsed twice with 2.5 mL THF. Then the ice bath was removed and the dark red mixture was stirred for 2.5 hours at room temperature after which the solvent was removed. The product was then sublimed from the crude residue on a cold finger at 0 °C under a pressure of $8 \cdot 10^{-2}$ mbar. The yield could be increased if the Schlenk flask was heated to 40 °C and the pressure was reduced to $4 \cdot 10^{-2}$ mbar. The product was obtained as yellow needles in moderate yields.

Reaction code: PB-107, 34ta022.19

Crystallographic code: GXray6677

Molecular formula: $C_8H_{10}N_2O_4PClFe$

Molecular weight: : 320.45 g mol^{-1}

Yield: 0.82 g, 39%

Melting point: 69 °C

Elemental analysis:

calculated (%) C 29.99 H 3.15 N 8.74 , found (%) C 30.00 H 3.33 N 8.55

MS: (EI, 70 eV, selected data): m/z = 558.0 [2M-Cl-CO+O]$^{+\bullet}$, 530.0 [2M-Cl-2CO+O]$^{+\bullet}$, 502.0 [2M-Cl-3CO+O]$^{+\bullet}$, 474.0 [2M-Cl-4CO+O]$^{+\bullet}$, 418.0 [2M-Cl-6CO+O]$^{+\bullet}$, 362.1 [2M-Cl-8CO+O]$^{+\bullet}$, 306.1 [2M-Cl-8CO-Fe+O]$^{+\bullet}$, 318.9 [M-H]$^{+\bullet}$, 285.0 [M-Cl]$^{+\bullet}$, 257.0 [M-Cl-CO]$^{+\bullet}$, 229.0 [M-Cl-2CO]$^{+\bullet}$, 201.0 [M-Cl-3CO]$^{+\bullet}$, 117.1 [M-Cl-Fe-4CO]$^{+\bullet}$.

IR (ATR diamond) $\tilde{\nu}$ in cm^{-1}: 2859 (w, ν(C-H)), 2058 (s, ν(C=O)), 1978 (w, ν(C=O)), 1928 (vs, ν(C=O))

^{1}H-NMR: (400 MHz, 298 K, THF-d8): 3.45 − 3.34 (m, 2H, C_2H_4), 3.28 − 3.22 (m, 2H, C_2H_4) 2.84 (d, $^3J_{P,H}$ = 16.9 Hz, 6H, N-CH$_3$).

^{13}C{^{1}H}-NMR: (101 MHz, 298 K, THF-d8): 213.4 (d, $^2J_{P,C}$ = 20 Hz, CO), 51.3 (d, $^2J_{P,C}$ =

6 Hz, N-CH$_3$), 33.0 (d, $^2J_{P,C}$ = 8 Hz, C$_2$H$_4$).

^{31}P-NMR: (203 MHz, 298 K, THF-d8): 182.0 (s$_{sat}$, $^1J_{Fe,P}$ = 47 Hz).

8.7.11. Synthesis of [tetracarbonyl(2-chloro-2H-benzo[4,5-c]-1,3,2-dioxaphospholane-κP)iron(0)] (15l)

3l   **15l**
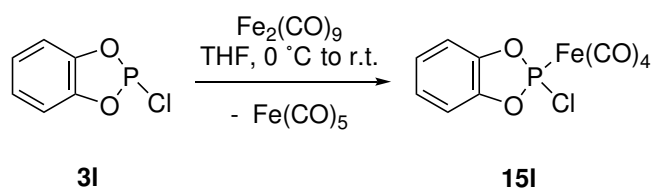
Synthesis: In a 250 mL Schlenk flask 2.537 g Fe$_2$(CO)$_9$ were suspended in 30 mL THF at 0 °C. In a 50 mL Schlenk tube 1.510 g **3l** were dissolved in 50 mL THF at 0 °C and then added to the Fe$_2$(CO)$_9$ suspension with a transfer canula. After the addition the canula was rinsed twice with 10 mL THF. Then the ice bath was removed and the dark red mixture was stirred for 1.5 hours at room temperature after which the solvent was removed. The product was obtained in 95% yield estimated from ^{31}P{^{1}H}-NMR spectroscopy. Attempts to purify the crude product via common-work-up was not possible. Inert column chromatography (h = 4 cm, ø= 1 cm, Al$_2$O$_3$, PE, −20 °C) allowed the isolation of **15l** however in negligible amounts. Vacuum distillation (Oil bath: 140 °C, Thermometer: N.A., Pressure: 5·10^{-3} mbar) allowed the isolation of **15l** as an orange oil, but also in this case only small amounts were obtained as decomposition occurs at these temperatures.

Reaction code: PB-78, PB-85; 33m3b018.19
Molecular formula: C$_{10}$H$_4$O$_6$PClFe
Molecular weight: : 342.40 g mol^{-1}
Yield: 94% (estimated from ^{31}P{^{1}H}-NMR)
MS: (EI, 70 eV, selected data): m/z = 341.9 [M]$^+$, 313.9 [M-CO], 285.9 [M-2CO], 257.9 [M-3CO], 229.9 [M-4CO], 139 [M-Fe-4CO-Cl]
^{1}H-NMR: (300 MHz, 298 K, C$_6$D$_6$): 6.66 (m, 2H, benzo), 6.53 (m, 2H, benzo)
^{13}C{^{1}H}-NMR: (76 MHz, 298 K, C$_6$D$_6$): 210.6 (d, $^2J_{P,C}$ = 16 Hz, CO), 145.4 (d, $^2J_{P,C}$ = 8 Hz, benzo(C^{ipso-O}), 124.8 (s, benzo(C^{meta}), 113.5 (d, $^2J_{P,C}$ = 7 Hz, benzo(C^{ortho}
^{31}P-NMR: (122 MHz, 298 K, C$_6$D$_6$): 210.5 (s$_{sat}$, $^1J_{Fe,P}$ = 74 Hz)

8.7.12. Synthesis of [tetracarbonyl(2-chloro-4,5-dimethyl-1,3,2-dioxaphospholane-κP)iron(0)] (15k)
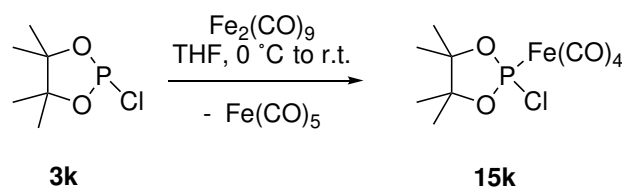
Synthesis: In a 250 mL Schlenk flask 99.2 g Fe$_2$(CO)$_9$ were suspended in 2.5 mL THF at 0 °C. In a 50 mL Schlenk tube 51 mg **3k** were dissolved in 2.5 mL THF at 0 °C and then added to the Fe$_2$(CO)$_9$ suspension with a transfer canula. After the addition the canula was rinsed twice with 1.5 mL THF. Then the ice bath was removed and the orange mixture was stirred for 1.5 hours at room temperature after which the solvent was removed. The product was obtained in quantitative yield estimated from ^{31}P{^{1}H}-NMR spectroscopy.

Reaction code: PB-92; 24m3a047.19, 24t4a093.19, 24p5a028.19
Molecular formula: C$_{10}$H$_{12}$O$_6$PClFe
Molecular weight: : 350.47 g mol^{-1}
Yield: 98% (estimated from ^{31}P{^{1}H}-NMR)
^{1}H-NMR: (400 MHz, 298 K, THF-d8): 1.39 (s, 6H, 2xCH$_3$), 1.30 (s, 6H, 2xCH$_3$)
^{13}C{^{1}H}-NMR: (126 MHz, 298 K, THF-d8): 211.3 (d, $^2J_{P,C}$ = 22 Hz, CO), 92.5 (d, $^2J_{P,C}$ = 7.1 Hz, Me$_2$C-O)), 25.2 (d, $^2J_{P,C}$ = 6 Hz, H3C-), 24.5 (d, $^2J_{P,C}$ = 3 Hz, H3C-)
^{31}P-NMR: (162 MHz, 298 K, THF-d8): 202.6 (s$_{sat}$, $^1J_{Fe,P}$ = 55 Hz).

8.7.13. Synthesis of [tetracarbonyl(1,3-dimethyl-1,3,2-dioxaphospholane-κP)iron(0)] (12e)
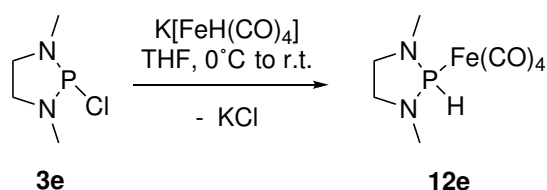
Synthesis: In a 500 mL Schlenk flask 4.058 g K[Fe(CO)$_4$H]] were dissolved in 180 mL THF at 0 °C. In a 100 mL Schlenk tube 3.120 g **3e** were dissolved in 40 mL THF at 0

°C and then added to the K[Fe(CO)$_4$H]] suspension with a transfer canula. After the addition the canula was rinsed twice with 10 mL THF. Then the ice bath was removed and the mixture was stirred for 1 hour at room temperature after which the solvent was removed. The crude product was extracted from the residue with 60 mL (30+15+15 mL) n-pentane and then the red filtrate was dried to become a red oil. After further purification via inert column chromatography (h = 10 cm, ø= 4.5 cm, SiO$_2$ PE (5% NEt$_3$), −20 °C) from which the first fraction and also the second (PE:Et$_2$O, 1:1 + 5% NEt$_3$) contained product and were combined. After solvent removal under reduced pressure (3·10^{-2} mbar) the product was obtained as a red oil in good yield.

Reaction code: PB-133/239; 42p5a004.19, 10p5a032.18

Molecular formula: C$_8$H$_{11}$O$_4$N$_2$PFe

Molecular weight: 286.00 g mol^{-1}

Yield: 4.225 g, 76%

Elemental analysis:

calculated (%) C 33.60 H 3.88 N 9.79 , found (%) C 33.41 H 3.99 N 9.78

MS: (EI, 70 eV, selected data): m/z = 285.9 [M]$^{+\bullet}$, 257.9 [M-CO]$^{+\bullet}$, 229.9 [M-2CO]$^{+\bullet}$, 201.9 [M-3CO]$^{+\bullet}$, 173.9 [M-4CO]$^{+\bullet}$, 117.0 [M-Fe-4CO-H]$^{+\bullet}$

IR: (toluene solution) $\tilde{\nu}$ in cm^{-1} 3027 (m, C-H), 2054 (s, P-H), 1980 (s(br) CO), 1944 (vs(br), CO)

^{1}H-NMR: (500 MHz, 298 K, THF-d8): 7.47 (d, $^1J_{P,H}$ = 357 Hz, 1H), 3.28 − 3.20 (m, 2H, backbone-C$_2$H$_4$), 3.13 − 3.07 (m, 2H, C$_2$H$_4$), 2.75 (d, $^1J_{P,H}$ = 14.4 Hz, 6H, 2xN-Me)

^{13}C{^{1}H}-NMR: (126 MHz, 298 K, THF-d8): 214.02 (d, $^2J_{P,C}$ = 21 Hz, CO), 53.62 (d, $^2J_{P,C}$ = 3 Hz, C$_2$H$_4$), 34.58 (d, $^2J_{P,C}$ = 7 Hz, N-CH$_3$)

^{31}P{^{1}H}-NMR: (162 MHz, 298 K, THF-d8): 144.1 (s$_{sat}$, $^1J_{Fe,P}$ = 29 Hz)

^{31}P-NMR: (162 MHz, 298 K, THF-d8): 144.0 (dm, $^1J_{P,H}$ = 358 Hz)

8.7.14. Synthesis of [tetracarbonyl(1,3-(1-methylethyl)-1,3,2-diazaphospholidine-κP)iron(0)] (12f)
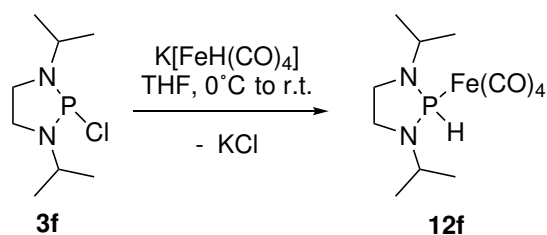
Synthesis: In a 100 mL Schlenk flask 1.3450 g K[Fe(CO)$_4$H] were dissolved in 30 mL THF at 0 °C. In a 25 mL Schlenk tube 1.088 g **3f** were dissolved in 25 mL THF at 0 °C and then added to the K[Fe(CO)$_4$H] suspension with a transfer canula. After the addition the canula was rinsed with 10 mL THF. Then the ice bath was removed and the yellow-brown mixture was stirred for 1.5 hours at room temperature after which the solvent was removed. The crude product was extracted from the residue with 50 mL (30+10+10 mL) *n*-pentane and the filtrate was dried to become a red oil. After further purification via inert column chromatography (h = 11 cm, ø= 4.5 cm, SiO$_2$ PE (2.5% NEt$_3$), −20 °C) from which the first fraction (PE, 2.5% NEt$_3$) contained product. After removal of solvent and drying under reduced pressure (3·10^{-2} mbar) the product was obtained as a red-orange oil in moderate yield.

Reaction code: PB-146, AMF-5; 22p5a007.20

Molecular formula: C$_{12}$H$_{19}$O$_4$N$_2$PFe

Molecular weight: : 342.11 g mol^{-1}

Yield: 1.627 g, 67%

Elemental analysis:

calculated (%) C 42.13 H 5.60 N 8.11 , found (%) C 41.83 H 5.65 N 8.14

MS: (EI, 70 eV, selected data): m/z = 342.0 [M]$^{+\bullet}$, 314.0 [M-CO]$^{+\bullet}$, 286.0 [M-2CO]$^{+\bullet}$, 258.0 [M-3CO]$^{+\bullet}$, 230.0 [M-4CO]$^{+\bullet}$, 173.1 [M-Fe-4CO-H]$^{+\bullet}$.

IR (ATR diamond) $\tilde{\nu}$ in cm^{-1}: (2970, 2934, 2872) (m, ν(C-H)), 2187 (w, ν(P-H)), 2048 (vs, ν(C=O)), 1971 (w, ν(C=O)), 1919 (vs, ν(C=O))

^{1}H-NMR: (500 MHz, 298 K, THF-*d*8): 7.84 (d, $^1J_{P,H}$ = 344 Hz, 1H), 3.92 (m ,2H, C$_2$H$_4$), 3.24 (m, 2H, C$_2$H$_4$), 1.23 (d, $^3J_{H,H}$ = 6.5 Hz, 6H, 2xCH$_3$), 1.15 (d, $^3J_{H,H}$ = 6.5 Hz, 6H, 2xCH$_3$).

^{13}C{^{1}H}-NMR: (125.78 MHz, 298 K, THF-*d*8): 214.5 (d, $^2J_{P,C}$ = 21 Hz, CO), 46.1 (d, $^2J_{P,C}$ = 9 Hz, C$_2$H$_4$), 42.3 (s, CH(Me)2), 21.6 (d, $^3J_{P,C}$ = 7 Hfz, CH$_3$), 19.8 (d, $^3J_{P,C}$ = 3 Hz, CH$_3$).

^{31}P{^{1}H}-NMR: (203 MHz, 298 K, THF-*d*8): 124.4 (s$_{sat}$, $^1J_{Fe,P}$ = 30 Hz).

^{31}P-NMR: (203 MHz, 298 K, THF-*d*8): 124.4 (dm, $^1J_{P,H}$ = 344 Hz).

8.7.15. Synthesis of [tetracarbonyl(3-methyl-1,3,2-oxazaphospholidine-κP)iron(0)] (12h)
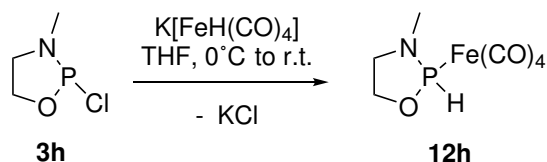
Synthesis: In a 100 mL Schlenk flask 1.565 g K[Fe(CO)$_4$H] were dissolved in 20 mL THF at 0 °C. In a 25 mL Schlenk tube 1.102 g **3h** were dissolved in 10 mL THF at 0 °C and then added to the K[Fe(CO)$_4$H] suspension with a transfer canula. After the addition the canula was rinsed with 5 mL THF. Then the ice bath was removed and the yellow-brown mixture was stirred for 18 hours at room temperature after which the solvent was removed. The crude product was extracted from the residue with 40 mL (20+10+10 mL) *n*-pentane and the filtrate was dried to become a red oil. After further purification via inert column chromatography (h = 11 cm, ø= 4.5 cm, SiO$_2$ PE:Et$_2$O (2.5% NEt$_3$), −20 °C) from which the first (PE, 2.5% NEt$_3$) and second (PE:Et$_2$O, 2:1 ,2.5% NEt$_3$) fraction contained product. After removal of solvent and drying under reduces pressure (3·10^{-2} mbar) the product was obtained as an orange oil in bad yield.

Reaction code: PB-551, AMF-9; PCB230221p5a010, PCB230217t4a035,
40m3a032.21

Molecular formula: C$_7$H$_8$O$_5$NPFe

Molecular weight: : 272.96 g mol^{-1}

Yield: 0.657 g, 32%

Elemental analysis:

calculated (%) C 30.80 H 2.95 N 5.13 , found (%) C 31.59 H 3.39 N 5.14

IR (ATR diamond) $\tilde{\nu}$ in cm^{-1}: 2906 (m, ν(C-H)), 2250 (w, ν(P-H)), 2057 (s, ν(C=O)), 1972 (vs, ν(C=O))

^{1}H-NMR: (400 MHz, 298 K, C$_6$D$_6$): 7.34 (d, $^1J_{P,H}$ = 382 Hz, 1H), 3.52 − 3.39 (m(br), 1H, O-CH$_2$), 3.29 − 3.21 (m(br), 1H, O-CH$_2$), 2.23 (d, $^3J_{P,H}$ = 13.7 Hz, 3H, N-CH$_3$), 2.23 (m(br), 1H, N-CH$_2$), 2.03 − 1.94 (m(br), 1H, N-CH$_2$)

^{13}C{^{1}H}-NMR: (126 MHz, 298 K, C$_6$D$_6$): 212.5 (d, $^2J_{P,C}$ = 22 Hz, CO), 68.0 (s, O-CH$_2$), 50.8 (s, N-CH$_2$), 32.0 (s, N-CH$_3$)

^{31}P{^{1}H}-NMR: (203 MHz, 298 K, C$_6$D$_6$): 179.4 (s)

^{31}P-NMR: (203 MHz, 298 K, C$_6$D$_6$): 179.4 (d, $^1J_{P,H}$ = 382 Hz).

8.7.16. Synthesis of [tetracarbonyl(3-(1-methylethyl)-1,3,2-oxazaphospholidine-κP)iron(0)] (12i)
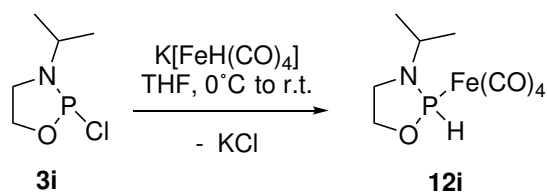
Synthesis: In a 100 mL Schlenk flask 1.473 g K[Fe(CO)$_4$H] were dissolved in 20 mL THF at 0 °C. In a 25 mL Schlenk tube 1.031 g **3i** were dissolved in 10 mL THF at 0 °C and then added to the K[Fe(CO)$_4$H] suspension with a transfer canula. After the addition the canula was rinsed with 5 mL THF. Then the ice bath was removed and the yellow-brown mixture was stirred for 18 hours at room temperature after which the solvent was removed. The crude product was extracted from the residue with 40 mL (20+10+10 mL) *n*-pentane and the filtrate was dried to become a red oil. After further purification via inert column chromatography (h = 11 cm, ø= 4.5 cm, SiO$_2$ PE (2.5% NEt$_3$), −20 °C) from which the first fraction (PE, 2.5% NEt$_3$) contained product. After removal of solvent and drying under reduces pressure (3·10^{-2} mbar) the product was obtained as an orange oil in moderate yield.

Reaction code: PB-552, PCB230303p5a034

Molecular formula: C$_9$H$_{12}$O$_5$NPFe

Molecular weight: : 301.01 g mol^{-1}

Yield: 1.002 g, 47%

Elemental analysis:

calculated (%) C 35.91 H 4.02 N 4.65 , found (%) C 36.47 H 4.31 N 4.67

^{1}H-NMR: (500 MHz, 298 K, C$_6$D$_6$): 7.54 (d, $^1J_{P,H}$ = 375 Hz, 1H, P-H), 3.70 (dhept, $^3J_{P,H}$ = 9.2 Hz, $^3J_{H,H}$ = 6.7 Hz, 1H, CHMe$_2$), 3.44 (pent, $^3J_{H,H}$ = 8.4 Hz 1H, O-CH$_2$), 3.38 − 3.29 (m, 1H, O-CH$_2$), 2.46 − 2.30 (m, 1H, N-CH$_2$), 2.04 (m, 1H, N-CH$_2$), 0.88 (d, $^3J_{H,H}$ = 6.7 Hz, 3H, CH$_3$), 0.71 (d, $^3J_{H,H}$ = 6.7 Hz, 3H, CH$_3$)

^{13}C{^{1}H}-NMR: (126 MHz, 298 K, C$_6$D$_6$): 212.3 (d, $^2J_{P,C}$ = 22 Hz, CO), 67.5 (d, $^2J_{P,C}$ = 10 Hz, O-CH$_2$), 44.5 (d, $^2J_{P,C}$ = 9.1 Hz, N-CH$_2$), 40.1 (d, $^2J_{P,C}$ = 2.1 Hz, N-CHMe$_2$), 20.9 (d, $^2J_{P,C}$ = 7.7 Hz, CH$_3$), 19.0 (d, $^2J_{P,C}$ = 7.7 Hz, CH$_3$)

^{31}P{^{1}H}-NMR: (203 MHz, 298 K, C$_6$D$_6$): 169.9 (s$_{sat}$, $^1J_{Fe,P}$ = 32 Hz)

^{31}P-NMR: (203 MHz, 298 K, C$_6$D$_6$): 169.9 (dm, $^1J_{P,H}$ = 375 Hz).

8.7.17. Synthesis of [tetracarbonyl(4,4,5,5-tetramethyl-1,3,2-dioxaphospholane-κP)iron(0)] (12k)

3k   **12k**
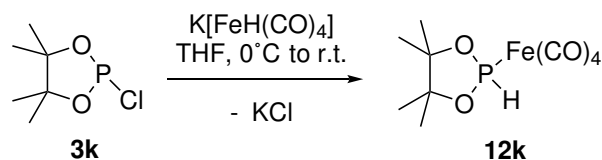
Synthesis: In a 100 mL Schlenk flask 1.045 g K[Fe(CO)$_4$H] were dissolved in 20 mL THF at 0 °C. In a 25 mL Schlenk tube 947 mg **3k** were dissolved in 5 mL THF at 0 °C and then added to the K[Fe(CO)$_4$H] suspension with a transfer canula. After the addition the canula was rinsed with 5 mL THF. Then the ice bath was removed and the yellow-brown mixture was stirred for 1 hour at room temperature after which the solvent was removed. The crude product was extracted from the residue with 30 mL (10+10+10 mL) *n*-pentane and the filtrate was dried to become a red oil. After further purification via inert column chromatography (h = 11 cm, ø= 4.5 cm, SiO$_2$ PE:Et$_2$O (2.5% NEt$_3$), −20 °C) from which the first fraction (PE, 2.5% NEt$_3$) contained product. After removal of solvent and drying under reduces pressure (3·10^{-2} mbar) the product was obtained as an orange oil in low yield.

Reaction code: PB-546, PCB230221p5a008

Crystallographic code: GXray6326g

Molecular formula: C$_{10}$H$_{13}$O$_6$PFe

Molecular weight: : 316.03 g mol^{-1}

Yield: 445 mg, 28%

Melting point: 37 °C

Elemental analysis:

calculated (%) C 38.01 H 4.15 , found (%) C 39.30 H 4.55

MS: (EI, 70 eV, selected data): m/z = 316.0 [M]$^{+\bullet}$, 288.0 [M-CO]$^{+\bullet}$, 260.0 [M-2CO]$^{+\bullet}$, 232.0 [M-3CO]$^{+\bullet}$, 204 [M-4CO]$^{+\bullet}$.

IR (ATR diamond) $\tilde{\nu}$ in cm^{-1}: 2985 (m, ν(C-H)), 2321 (w, ν(P-H)), 2056 (s, ν(C=O)), 1988 (m, ν(C=O)), 1925 (vs, ν(C=O))

^{1}H-NMR: (500 MHz, 298 K, C$_6$D$_6$): 8.06 (d, $^1J_{P,H}$ = 409 Hz, 1H, P-H), 0.95 (s, 6H, C(CH$_3$)$_2$), 0.70 (s, C(CH$_3$)$_2$).

^{13}C{^{1}H}-NMR: (126 MHz, 298 K, C$_6$D$_6$): 212.43 (d, $^2J_{P,C}$ = 23 Hz, CO), 88.1 (d, $^2J_{P,C}$ = 6 Hz, C2Me4), 24.4 (d, $^3J_{P,C}$ = 5 Hz, C$_2$(CH$_3$)4), 21.7 (d, $^3J_{P,C}$ = 4 Hz, C$_2$(CH$_3$)4)

^{31}P{^{1}H}-NMR: (203 MHz, 298 K, C$_6$D$_6$): 196.4 (s$_{sat}$, $^1J_{Fe,P}$ = 36 Hz)

^{31}**P-NMR**: (203 MHz, 298 K, C_6D_6): 196.4 (d, $^1J_{P,H}$ = 409 Hz).

8.7.18. Synthesis of [tetracarbonyl(2H-benzo[4,5-c]-1,3,2-dioxaphospholane-κP)iron(0)] (12l)
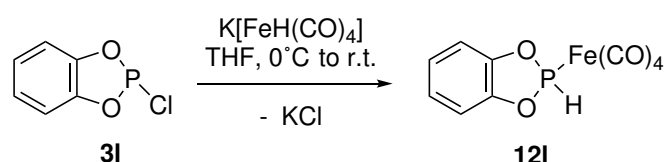
Synthesis: In a 100 mL Schlenk flask 425 mg K[Fe(CO)$_4$H] were dissolved in 10 mL THF at 0 °C. In a 25 mL Schlenk tube 400 mg **3l** were dissolved in 3 mL THF at 0 °C and then added to the K[Fe(CO)$_4$H] suspension with a transfer canula. After the addition the canula was rinsed twice with 3.5 mL THF. Then the ice bath was removed and the yellow-brown mixture was stirred for 2.5 hours at room temperature after which the solvent was removed. The crude product was extracted from the residue with 60 mL (15+10+10+10+10+5 mL) *n*-pentane and the red filtrate was dried to become a yellow beige solid. The product can be recrystallized from a saturated *n*-pentane solution, however an impurity (2 – 5%) with a δd(^{31}P) chemical shift of 192 ppm was still observed. Further attempts to purify the crude product via inert column chromatography (h = 11 cm, ø= 4.5 cm, SiO$_2$ PE:Et$_2$O (2.5% NEt$_3$), −20 °C) lead to hydrolysis (**23** in only small yields. If under the same conditions NEt$_3$ is not used nothing is collected in several fractions for several PE:Et$_2$O ratios.

Reaction code: PB-138, 43p5a021.19

Crystallographic code: GXray6173f

Molecular formula: $C_{10}H_5O_6PFe$

Molecular weight: : 307.96 g mol^{-1}

Yield: 505 mg, 82% (crude product, after solvent removal; 2% impurity)

MS: (EI, 70 eV, selected data): m/z (%) 307.9 [M]$^{+\bullet}$, 279.9 [M-CO]$^{+\bullet}$, 251.9 [M-2CO]$^{+\bullet}$, 223.9 [M-3CO]$^{+\bullet}$, 196.0 [M-4CO]$^{+\bullet}$

IR (ATR diamond) $\tilde{\nu}$ in cm^{-1}: 2985 (m, ν(C-H)), 2321 (w, ν(P-H)), 2056 (s, ν(C=O)), 1988 (m, ν(C=O)), 1925 (vs, ν(C=O))

^{1}**H-NMR**: (500 MHz, 298 K, C_6D_6): 8.67 (d, $^1J_{P,H}$ = 432 Hz, 1H, P-H), 7.26 – 7.21 (m, 2H, C_6H_4), 7.12 – 7.07 (m, 2H, C_6H_4)

^{13}**C{^{1}H}-NMR**: (126 MHz, 298 K, THF-*d8*): 211.6 (d, $^2J_{P,C}$ = 22 Hz, CO), 148.1 (d, 2 $^4J_{P,C}$ = 6 Hz, C_6H_4), 125.3 (s, C_6H_4), 114.1 (d, 2 $^4J_{P,C}$ = 7 Hz, C_6H_4)

^{31}**P{^{1}H}-NMR**: (203 MHz, 298 K, THF-d8): 228.7 (s$_{sat}$, $^1J_{Fe,P}$ = 40 Hz)

^{31}**P-NMR**: (203 MHz, 298 K, THF-d8): 228.7 (d, $^1J_{P,H}$ = 432 Hz).

8.7.19. Synthesis of [tetracarbonyl(1,3-dimethyl-2H-benzo[4,5-c]-1,3,2-diazaphosphole-κP)iron(0)] (12p)
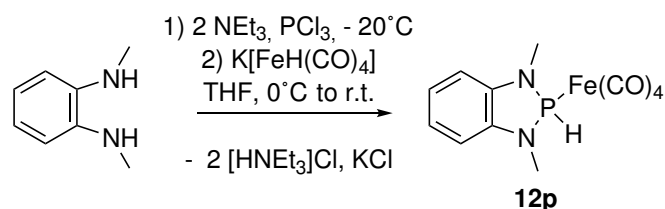
Synthesis: In a three necked 250 mL round bottom flask, equipped with a dropping funnel and a vacuum adapter, 1.034 g freshly prepared 1,2-dimethylaminobenzol was dissolved in 10 mL Et$_2$O and 2.1 mL NEt$_3$ were added. The dropping funnel was charged with 7.5 mL Et$_2$O and 0.66 mL PCl3. The round bottom flask was cooled to 0 °C in an ice bath and the PCl$_3$ solution was added dropwise to the diaminobenzene over the period of 20 minutes. After the addition was completed the dropping funnel was rinsed with 3 mL Et$_2$O. The mixture was stirred for 1.5 hours at 0 °C, after which the formed colourless suspension was filtered through a glass filter (P3) and the residue was washed four times (20+10+30+20 mL) with Et$_2$O. The solvent was removed from the filtrate under reduced pressure (100 mbar) at room temperature. And the residual colourless powder was suspended in 20 mL THF and added via a transfer canula to a cooled (0 °C) solution of 1.577 mg K[Fe(CO)$_4$H] in 30 mL THF in a 100 mL Schlenk tube. After addition the canula was rinsed with 20 mL THF. The reaction mixture was stirred at rom temperature for 30 minutes after which the solvent was removed under reduced pressure (3·10^{-2} mbar). After thorough drying the product was extracted from the red residue with 100 mL n-pentane. Removal of the solvent under reduced pressure (3·10^{-2} mbar) gives a red-brown powder in moderate yield. Further purification via column chromatography (h = 10 cm, ø= 1 cm, SiO$_2$, PE:Et$_2$O (2.5% NEt$_3$), −20 °C) is possible however leads to a decrease of the yield below 10%.

Reaction code: PB-272, 21m3a028.21

Crystallographic code: GXray6753

Molecular formula: C$_{12}$H$_{11}$O$_4$N$_2$PFe

Molecular weight: : 333.98 g mol^{-1}

Yield: 1.515 mg, 59%

Melting point: 131 °C

Elemental analysis:

calculated (%) C 43.15 H 3.32 N 8.39 , found (%) C 42.58 H 3.33 N 8.27

MS: (EI, 70 eV, selected data): m/z (%) 333.9 [M]$^{+\bullet}$, 305.9 [M-CO]$^{+\bullet}$, 277.9 [M-2CO]$^{+\bullet}$, 249.9 [M-3CO]$^{+\bullet}$, 249.9 [M-3CO]$^{+\bullet}$, 222.0 [M-4CO]$^{+\bullet}$, 182.0 [M-4CO-Fe+O]$^{+\bullet}$ 165 [M-4CO-Fe-H]$^{+\bullet}$.

IR (ATR diamond) $\tilde{\nu}$ in cm^{-1}: 2932(m, ν(C-H)), 2052 (m, ν(P-H)), 2029 (m, ν(C=O)), 1910 (vs, ν(C=O))

^{1}H-NMR: (300 MHz, 298 K, THF-$d8$): 8.94 (d, $^1J_{P,H}$ = 358.4 Hz, 1H, P-H), 6.58 – 6.68 (m, 4H, C$_6$H$_4$), 3.10 (d, $^3J_{P,H}$ = 11.9 Hz, 6H, N-CH$_3$).

^{13}C{^{1}H}-NMR: (76 MHz, 298 K, THF-$d8$): 212.1 (d, $^2J_{P,C}$ = 20 Hz, CO), 138.8 (d, $^XJ_{P,C}$ = 2 Hz, C$_6$H$_4$), 119.9 (s, C$_6$H$_4$), 107.9 (d, $^XJ_{P,C}$ = 5 Hz, C$_6$H$_4$), 28.0 (d, $^2J_{P,C}$) = 9 Hz, N-CH$_3$)

^{31}P{^{1}H}-NMR: (122 MHz, 298 K, THF-$d8$): 151.8 (s$_{sat}$, $^1J_{Fe,P}$ = 33 Hz)

^{31}P-NMR: (122 MHz, 298 K, THF-$d8$): 151.8 (dhept, $^1J_{P,H}$ = 356 Hz, $^3J_{P,H}$ = 12 Hz).

8.7.20. Synthesis of triethylammonium[tetracarbonyl([2-hydroxy-phenoxyl]-phosphinito-κP)ferrate(0)] (23)
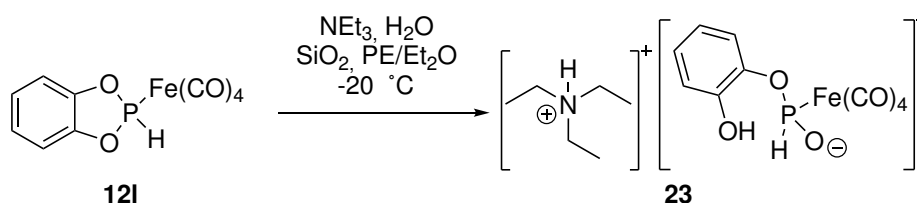
Synthesis: **12l** was synthesized from 904 mg of **3l** and 1.060 g K[Fe(CO)$_4$H]. The crude product was charged on an inert colum for purification (h = 11 cm, ø= 4.5 cm, SiO$_2$ PE:Et$_2$O (2.5% NEt$_3$), −20 °C). An initial yellow band on the column stopped, after one third the height and could only be eluted with THF(2.5% NEt$_3$). After removing the solvent from this fraction a colourless solid was obtained in very low yield.

Reaction code: PB-547, PCB230221p5a009

Molecular formula: C$_{16}$H$_{22}$O$_7$PNFe

Molecular weight: : 427.17 g mol^{-1}

Yield: 80 mg, 4%

Elemental analysis:

calculated (%) C 44.99 H 5.19 N 3.28 , found (%) C 45.43 H 5.29 N 3.36

¹H-NMR: (500 MHz, 298 K, C_6D_6): 10.66 (s(br), 1H, O-H), 9.34 (s(br), 1H, N-H), 8.87 (d, $^1J_{P,H}$ = 414 Hz, 1H, P-H), 7.34 (dt, $^3J_{H,H}$ = 8 Hz, $^3J_{H,H}$ = 1.6 Hz, 1H, C6H4), 7.17 (dd, $^2J_{H,H}$ = 8 Hz, $^3J_{H,H}$ = 1.6 Hz, 1H, C6H4), 6.91 (m, $^XJ_{P,H}$ = 9.4 Hz, $^3J_{H,H}$ = 1.6 Hz, 1H, C6H4), 6.73 – 6.69 (m, 1H, C6H4), 1.96 (q, $^3J_{H,H}$ = 7.3 Hz, 6H, N-CH₂-Me), 0.51 (t, $^3J_{H,H}$ = 7.3 Hz, 9H, N-CH₂-CH₃)

¹³C{¹H}-NMR: (126 MHz, 298 K, THF-$d8$): 215.7 (d, $^2J_{P,C}$ = 23 Hz, CO), 149.3 (d, $^3J_{P,C}$ = 4 Hz, HO-C6H4), 145.3 (d, $^3J_{P,C}$ = 16 Hz, P-O-C6H4), 125.85 (d, $^XJ_{P,C}$ = 1.7 Hz, C6H4), 123.30 (d, $^XJ_{P,C}$ = 4.3 Hz, C6H4), 120.74 (d, $^XJ_{P,C}$ = 1.6 Hz, C6H4), 118.24 (d, $^XJ_{P,C}$ = 1.6 Hz, C6H4), 45.50 (s, N-CH₂-Me), 8.06 (s, N-CH₂-CH₃).

³¹P{¹H}-NMR: (203 MHz, 298 K, THF-$d8$): 159.3 (s_{sat}, $^1J_{Fe,P}$ = 28 Hz)

³¹P-NMR: (203 MHz, 298 K, THF-$d8$): 159.3 (d, $^1J_{P,H}$ = 414 Hz)

8.7.21. Synthesis of [tetracarbonyl(2-(2,2,6,6-tetramethylpiperidin-N-oxyl)-1,3-dimethyl-1,3,2-diazaphospholidine-κP)iron(0)] (17e)

12e   **17e**
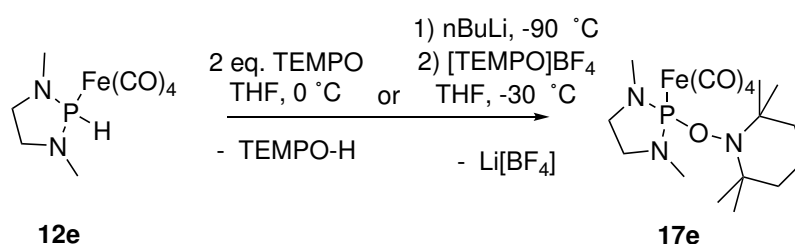
Synthesis:

Method 1: In a 100 mL Schlenk flask 222 mg of **12e** were dissolved in 10 mL THF and cooled to 0 °C. In a 10 mL Schlenk tube 245 mg TEMPO were dissolved in 4 mL THF and cooled to 0 °C. The TEMPO solution was added to 13e via a transfer canula, which was rinsed after addition with 3 mL THF. The walls of reaction vessel were also rinsed with 3 mL THF. The reaction mixture was stirred for 1.5 hours at 0 °C, after which the solvent was removed at 0 °C. Eventually, the orange residue starts to crystallise. The crystals were dissolved and the solution was filtered with 60 mL (20+20+10+10 mL) *n*-pentane. The filtrate was concentrated to 20 mL, subsequent slow evaporation of solvent led to formation of crystalline product in high yield.

Method 2: In a 100 mL Schlenk flask 272 mg of **12e** were dissolved in 10 mL THF and cooled to −90 °C. Then 0.38 mL ⁿBuLi (c = 2.5 M) were added dropwise with a syringe to the stirred solution. The reaction mixture was allowed to warm to −50 °C. In a 100 mL

Schlenk flask 231 mg [TEMPO][BF$_4$] was suspended in 10 mL THF and cooled to -50 °C. Then the reaction mixture was added to the [TEMPO][BF$_4$] suspension via a transfer canula, after addition the canula was rinsed with 2 mL THF. The reaction mixture was allowed to warm up to -10 °C at which point the solvent was removed at the same temperature. The orange, partially crystalline, residue was then dissolved in *n*-pentane and charged on an inert column (h = 4 cm, ø= 3 cm, SiO$_2$ PE (2.5% NEt$_3$), -20 °C). In the process of column chromatography, the solvent have to be precooled and all receiving flasks have to be kept at or below 0 °C at all time. The product was obtained in the first fraction (PE (2.5% NEt$_3$)). After evaporation of the solvent under reduced pressure ($3 \cdot 10^{-2}$ mbar) the product was obtained as orange-colorless crystals. ^{31}P-NMR spectroscopy shows a 2% impurity ($\delta(^{31}$P): 188 ppm).

Reaction code: PB-142, 43p5a022.19

Crystallographic code: GSTR693

Molecular formula: C$_{17}$H$_{28}$O$_5$PN$_3$Fe

Molecular weight: : 441.25 g mol^{-1}

Yield: Method 1: 342 mg ,96%; Method 2: 198 mg, 47%.

MS: (EI, 70 eV, selected data): m/z = 558.0 [2M-CO-O]$^{+\bullet}$, 529.9 [2M-2CO-O]$^{+\bullet}$, 502.0 [2M-3CO-O]$^{+\bullet}$, 474.0 [2M-4CO-O]$^{+\bullet}$, 418.0 [2M-6CO-O]$^{+\bullet}$, 390.0 [2M-7CO-O]$^{+\bullet}$, 362.0 [2M-8CO-O]$^{+\bullet}$, 117.1 [M-Fe-4CO-OTEMP]

IR: (toluene solution) $\tilde{\nu}$ in cm^{-1} 2040, 1946-1910 (s, very broad ν(C=O)

^{1}**H-NMR**:(500 MHz, 273 K, THF-*d*8) 3.53 – 3.48 (m, 2H, C$_2$H$_4$), 3.12 – 3.02 (m, 2H, C$_2$H$_4$), 2.85 (d, $^3J_{P,H}$ = 11.1 Hz, 6H, N-CH$_3$), 1.68 – 1.58 (m, 2H, TEMPO-(4-CH$_2$)), 1.56 – 1.41 (m, 4H, TEMPO-(3,5-CH$_2$)), 1.18 (s, 6H, TEMPO-(2xCH$_3$)), 1.14 (s, 6H, TEMPO-(2xCH$_3$)).

^{13}**C-NMR**:(126 MHz, 173 K, THF-*d*8) 214.9 (d, $^2J_{P,C}$ = 23 Hz, CO), 62.8 (d, $^2J_{P,C}$ = 2.4 Hz,), 52.9 (s, C$_2$H$_4$), 41.7 (s, TEMPO-(4 CH$_2$)), 36.88 (d, $^2J_{P,C}$ = 14 Hz, N-CH$_3$), 35.3 (s, TEMPO-(2xCH$_3$)), 20.9 (s, TEMPO-(2xCH$_3$)), 17.9 (s, TEMPO-(3,5-CH$_2$)).

^{31}**P{^{1}H}-NMR**:(203 MHz, 273 K, THF-*d*8) 165.1 (s$_{sat}$, $^1J_{Fe,P}$ = 39 Hz).

^{31}**P**:(203 MHz, 273 K, THF-*d*8) 165.1 (m(br)).

8.7.22. Synthesis of
[tetracarbonyl(1,3-dimethyl-2-oxo-1,3,2-diazaphospholidine-κP)iron(0)] (18e)
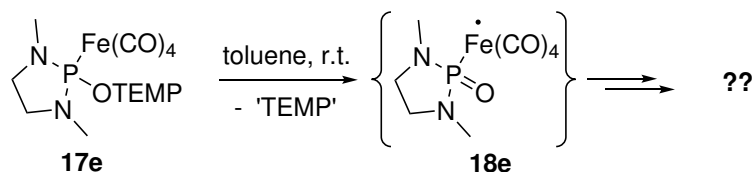
For the EPR and Mößbauer measurements **17e** was dissolved in dry (over a potassium mirror), recondensed and degased (via freeze-pump-thaw cycles) toluene to the desired concentration (EPR: ~400 μM, Mößbauer: 1 mM). These samples were kept at room temperature for several hours, upon a gradual darkening in colour to red was observed. Samples were frozen in liquid nitrogen if in the ^{31}P-NMR spectrum no trace of **17e** were detected.

8.7.23. Synthesis of [tetracarbonyl((2,2,6,6-tetramethylpiperidin-N-oxyl)-
diphenylphosphane-κP)iron(0)] (17d)
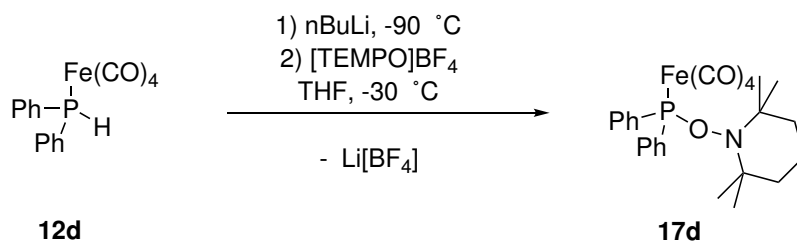
Synthesis: In a 100 mL Schlenk flask 200 mg of **12d** were dissolved in 15 mL THF and cooled to -95 °C. Then 0.39 mL ^{n}BuLi (c = 1.6 M) were added dropwise with a syringe to the stirred solution. The reaction mixture was allowed to warm to -50 °C. In a 100 mL Schlenk flask 137 mg [TEMPO][BF$_4$] was suspended in 5 mL THF and cooled to -50 °C. Then the reaction mixture was added to the [TEMPO][BF$_4$] suspension via a transfer canula, after addition the canula was rinsed with 3 mL THF. The reaction mixture was kept at -80 °C for 1.5 hours and then was allowed to warm up to -35 °C at which point the solvent was removed at the same temperature. The product was then extracted from the residue with 80 mL (20+10+20+20+10 mL) cold (-30 °C) n-pentane and the solvent was removed from the filtrate at the same temperature.

Reaction code: PB-153, 03m3mTT2.20

Molecular formula: C$_{25}$H$_{28}$O$_5$PNFe

184

Molecular weight: : 509.32 g mol^{-1}

Yield: N/A (due to thermal instability)

^{1}H-NMR:(300 MHz, 193 K, THF-d8) 7.80 (m, 4H, C_6H_5), 7.49 (m, 6H, C_6H_5), 1.63 − 1.45 (m, 2H, TEMPO-(4-CH_2)), 1.38 − 1.17 (m, 4H, TEMPO-(3,5-CH_2)), 0.98 − 0.81 (m, 12H, TEMPO-(4xCH_3)); signals 1.63 − 1.45 and 1.38 − 1.17 are overlapping with residual n-pentane resonances.

^{31}P{^{1}H}-NMR: (122 MHz, 193 K, THF-d8) 175.5 (s).

8.7.24. Synthesis of [biscyclopentadienylcobalt(II)][tetracarbonyl(1,3,2-diazaphospholidinito-κP)iron(0)] ([CoCp$_2$]14e)

12e → [CoCp$_2$]**14e**
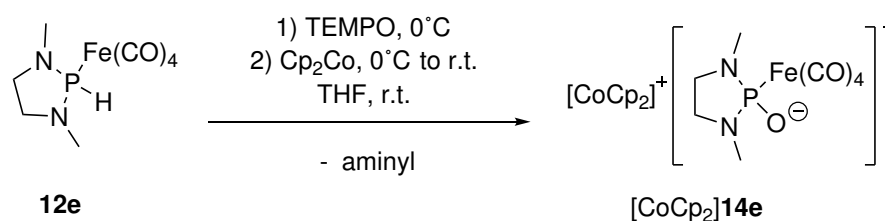
Synthesis: In a 100 mL Schlenk flask 516 mg of **12e** were dissolved in 20 mL THF and cooled to 0 °C. Then 557 mg TEMPO dissolved in 5 mL and cooled to 0 °C were added with a transfer canula to the stirred solution of **12e**. The reaction mixture was kept at 0 °C and stirred for 2 hours, after which the solvent was removed at 0 °C and further dried for 2 hours under reduced pressure (3·10^{-2} mbar) and at 0 °C. The residue was dissolved in precooled (0 °C) 10 mL THF and then added via a transfer canula to a suspension of 337 mg CoCp$_2$ in 5 mL THF and the canula was rinsed twice with 2 mL THF. After 24 hours the solution was filtered and the residue was washed with 3 mL THF. After evaporation of the solvent from the filtrate, the residue was washed with twice 2.5 mL Et$_2$O to obtain the product as an olive-green powder in moderate yield.

Reaction code: PB-557, PCB230322m3a020, PCB230411p5a001

Crystallographic code: GXray6821f

Molecular formula: C$_{18}$H$_{20}$O$_5$PN$_2$CoFe

Molecular weight: : 490.12 g mol^{-1}

Yield: 518 mg, 60%

Melting point: 175 °C

Elemental analysis:

calculated (%) C 44.11 H 4.11 N 5.72 , found (%) C 43.35 H 4.36 N 5.85

MS: ((−)-ESI): m/z 602.944 [2M+H]⁻, 300.968 [M]⁻, 272.973 [M-CO]⁻, 244.978 [M-2CO]⁻;
((+)-ESI): m/z 189.011 [CoCp$_2$]⁺

IR (ATR diamond) $\tilde{\nu}$ in cm⁻¹: 3000-2800 (w, ν(C-H)), 2018 (s, ν(C=O)), 1925 (m, ν(C=O)), 1876 (vs, ν(C=O))

¹H-NMR: (300 MHz, 298 K, MeCN-$d3$): 5.69 (s, 10H, 2xC5H5), 3.13 – 3.01 (m, 2H, C$_2$H$_4$), 2.98 – 2.86 (m, 2H, C$_2$H$_4$), 2.63 (d, $^3J_{P,H}$ = 11.3 Hz, 6H, N-CH$_3$).

¹³C{¹H}-NMR: (126 MHz, 298 K, MeCN-$d3$): 219.4 (d, $^2J_{P,C}$ = 21 Hz, CO), 85.9 (s, C5H5), 51.4 (s, C$_2$H$_4$), 34.7 (d, $^2J_{P,C}$ = 6 Hz, N-CH$_3$).

³¹P{¹H}-NMR: (202 MHz, 298 K, MeCN-$d3$): 109.5 (s(br)).

8.7.25. Synthesis of [tetracarbonyl(1,3-dimethyl-2-trimethylsiloxyl-1,3,2-diazaphospholidine-κP)iron(0)] (24e)
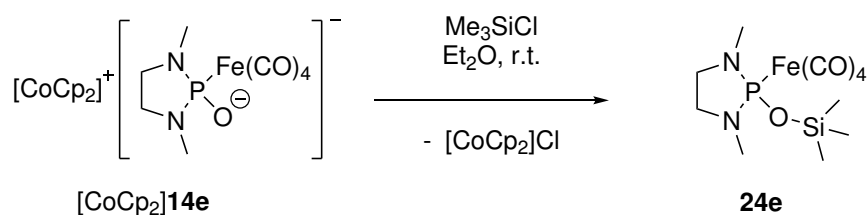
Synthesis: In a 10 mL Schlenk tube 108 mg [CoCp$_2$]**14e** were partially dissolved in 5 mL Et$_2$O and 0.03 mL Me$_3$3SiCl was added and the solution was stirred for 1 hour. Then the solution was filtered and the solvent was removed under reduced pressure. Extraction with 10 mL (4+3+3 mL) n-pentane and subsequent drying resulted in a pale-yellow solid in good yield.

Reaction code: PB-582, PCB230411p5a003

Molecular formula: C$_{11}$H$_{19}$N$_2$PO$_5$SiFe

Molecular weight: 374.19 g mol⁻¹

Yield: 71 mg, 87%

¹H-NMR: (500 MHz, 298 K, MeCN-$d3$): 3.28 – 3.19 (m, 2H, C$_2$H$_4$), 3.13 – 3.05 (m, 2H, C$_2$H$_4$), 2.75 (d, $^3J_{P,C}$ = 12.9 Hz, 6H, N-CH$_3$), 0.20 (s, 6H, O-Si(CH$_3$)^3).

¹³C{¹H}-NMR: (126 MHz, 298 K, MeCN-$d3$): 215.2 (d, $^2J_{P,C}$ = 24 Hz, CO), 51.6 (d, $^2J_{P,C}$ = 2 Hz, C$_2$H$_4$), 33.8 (d, $^2J_{P,C}$ = 9 Hz, N-CH$_3$).

²⁹Si(dept20)-NMR: (99 MHz, 298 K, MeCN-$d3$): 15.1 (d, $^2J_{P,Si}$ = 23.0 Hz, P-O-Si).

^{31}**P{^{1}H}-NMR**: (122 MHz, 298 K, MeCN-*d*3): 147.7 (s$_{sat}$, $^1J_{Fe,P}$ = 39 Hz, $^2J_{P,Si}$ = 23 Hz).

8.7.26. Synthesis of [tetracarbonyl(1,3-dimethyl-2-(1,3-dimethyl-2-oxo-1,3,2-diazaphospholidin-2-oxyl)-1,3,2-diazaphospholidine-κP)iron(0)] (25e)
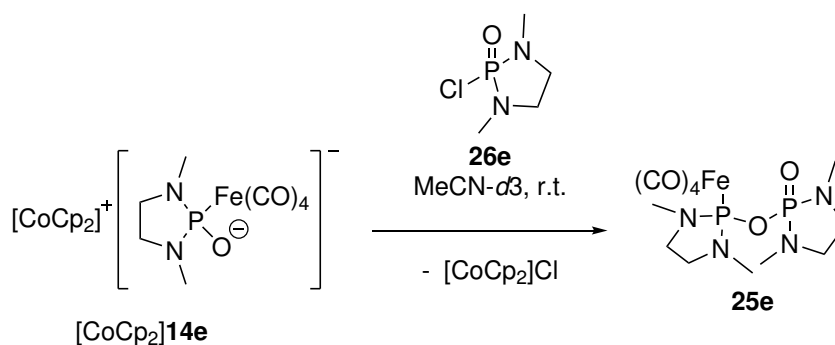
Synthesis: In a Young-NMR tube 22 mg [CoCp$_2$]**14e** were partially dissolved in 0.5 mL MeCN-*d*3 and 8 mg **26e** was added and the solution was heated for 2 hours at 70 °C until full conversion was observed.

Reaction code: PB-564, PCB230312m3a058

Molecular formula: C$_{12}$H$_{20}$N$_4$P$_2$O$_6$Fe

Molecular weight: 434.11 g mol^{-1}

Yield: quant. estimated from ^{1}H- and ^{31}P{^{1}H}-NMR spectra.

HR-MS: ((+)-ESI): m/z (%)) C$_{12}$H$_{21}$N$_2$PO$_3$ calc.: 435.0280, found: 435.0279.

^{1}**H-NMR**: (300 MHz, 298 K, MeCN-*d*3): 3.55 − 3.42 (m, 2H, C$_2$H$_4$), 3.19 − 3.03 (m, 4, C$_2$H$_4$), 2.83 (d, $^3J_{P,C}$ = 13.3 Hz, N-CH$_3$), 2.54 (d, $^3J_{P,C}$ = 13.3 Hz, C$_2$H$_4$), 2.40 − 2.39 (m, C$_2$H$_4$ N-CH$_3$).

^{31}**P{^{1}H}-NMR**: (122 MHz, 298 K, MeCN-*d*3): 158.1 (d, $^2J_{P,P}$ = 62 Hz, P-Fe), 15.8 (d, $^2J_{P,P}$ = 62 Hz, P=O).

8.7.27. Synthesis of [2,2,6,6-tetramethylpiperidinium][tetracarbonyl-(diphenylphosphinito-κP)ferrate(0)]([TEMPH$_2$]14d)

12d → [TEMPH$_2$]**14d**
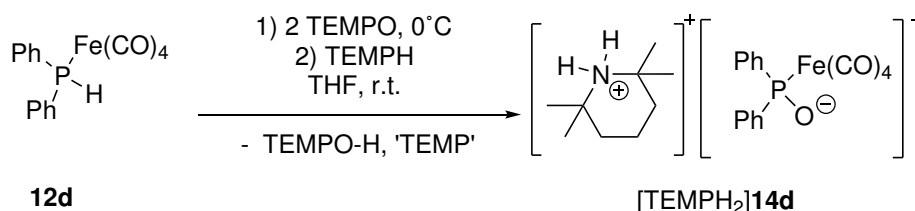
Synthesis: In a 100 mL Schlenk flask 357 mg **12d** was dissolved in 20 mL THF and cooled to 0 °C. In a 20 mL Schlenk tube 315 mg TEMPO were dissolved in 10 mL THF, cooled to 0 °C and added to the solution of 13d via a transfer canula, which was rinsed with 10 mL THF. The reaction mixture was allowed to stir for 1.5 hours, after which the mixture was warmed to room temperature. After 2 days the solvent was removed and the residue dried under reduced pressure (3·10^{-2} mbar) for 4 hours. To the solid 10 mL THF were added and 0.6 mL of the free amine TEMPH were added. After 3 days the reaction was complete (checked by ^{31}P-NMR spectroscopy) and the solvent was removed. The residue was washed with 40 mL (20+10+10 mL) of *n*-pentane and dried for 3 hours under reduced pressure (3·10^{-2} mbar).

Reaction code: PB-98, 29p5a025.19

Molecular formula: C$_{25}$H$_{30}$O$_5$PNFe

Molecular weight: : 511.34 g mol^{-1}

Yield: 130 mg, 25%

MS: ((+)-ESI): m/z 368.9 [M]$^+$, 340.9 [M-CO]$^+$, 257.0 [M-4CO]$^+$; ((+)-ESI): m/z 142.159 [TEMPH$_2$]$^+$

IR (ATR diamond) $\tilde{\nu}$ in cm^{-1}: 3598 (w, ν(N-H)), 3053 (w, ν(C-H)), 2025 (m, ν(C=O)), 1908 (vs, ν(C=O))

^{1}H-NMR: (500 MHz, 298 K, THF-$d8$): 7.71 (s(br), 4H, P-C$_6$H$_5$), 7.24 (s(br), 6H, P-C$_6$H$_5$), 5.70 & 5.45 (s, 1H, N-H), 1.65 (s(br), 2H, TEMPO-4-CH$_2$), 1.46 (s(br), 4H, TEMPO-3,5-CH$_2$), 1.24 (s(br), 12H, 4xTEMPO-CH$_3$).

^{13}C{^{1}H}-NMR: (126 MHz, 298 K, MeCN-$d3$): 216.6 (d, $^2J_{P,C}$ = 18 Hz, CO), 148.3 (d, $^1J_{P,C}$ = 49 Hz, *ipso*(P-C$_6$H$_5$)) 137.2 (s, P-C$_6$H$_5$), 130.3 (d, $^XJ_{P,C}$ = 10 Hz, P-C$_6$H$_5$), 128.1 (s, P-C$_6$H$_5$), 126.9 (d, $^XJ_{P,C}$ = 10 Hz, P-C$_6$H$_5$), 36.1 (s), 28.1 (s), 16.7 (s).

^{31}P{^{1}H}-NMR: (202 MHz, 298 K, MeCN-$d3$): 109.5 (s(br)).

8.7.28. Synthesis of [tetraphenylphosphonium][(triphenylmethylphosphinito-κP)tungstate(0)] ([PPh$_4$]47)
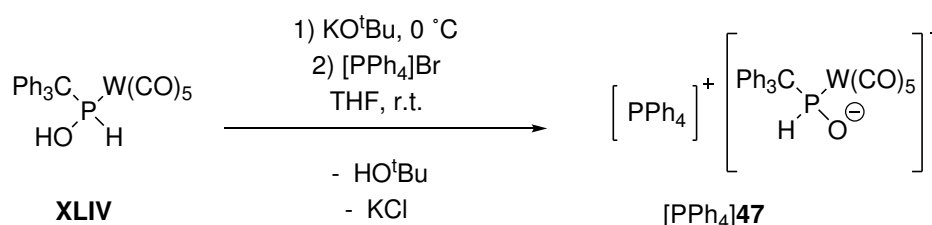
Synthesis: In a 10 mL Schlenk tube 50 mg **XLIV** were dissolved in 3 mL THF and cooled to 0 °C. After the addition of 9 mg KO^{t}Bu as a solid, the reaction mixture was stirred for 1 hour. Then 34 mg of [PPh$_4$]Br were added as a solid and the reaction was stirred for 24 hours, after which the precipitate was filtered off through a glass filter and the solvent was removed from the filtrate under reduced pressure (3·10^{-2} mbar). The colourless residue was washed three times with 5 mL Et$_2$O and the product was obtained as a colourless powder in moderate yield.

Reaction code: PB-542, PCB230207p5a021, PCB230206m3a026

Molecular formula: C$_{48}$H$_{36}$O$_6$P$_2$W

Molecular weight: : 954.60 g mol^{-1}

Yield: 33 mg, 43%

Elemental analysis:

calculated (%) C 60.39 H 3.80 , found (%) C 60.27 H 3.95

MS: ((+)-ESI): m/z 615.021 [M]$^+$, 587.026 [M-CO]$^+$, 559.031 [M-2CO]$^+$, 531.023 [M-3CO]$^+$ 305.200 [H-IMes]$^+$; ((−)-ESI): m/z 149.1 [OTf]$^-$

HR-MS ((+)-ESI): m/z C$_{24}$H$_{16}$PO$_6$W calc. 615.0203, found 615.0209.

^{1}H-NMR: (500 MHz, 298 K, MeCN-d3): 8.39 (d, $^1J_{P,H}$ = 293.3 Hz, 1H, P-H), 7.94 − 7.88 (m, 4H), 7.77 − 7.71 (m, 8H), 7.71 − 7.64 (m, 8H), 7.48 − 7.39 (m, 6H), 7.28 − 7.19 (m, 6H), 7.19 − 7.14 (m, 3H).

^{13}C{^{1}H}-NMR: (126 MHz, 298 K, MeCN-d3): 205.1 (s(br), trans-CO), 201.0 (s(br), cis-CO), 147.6 (s), 136.4 (d, $^XJ_{P,C}$ = 3 Hz), 135.7 (d, $^XJ_{P,C}$ = 10 Hz), 131.6 (d, $^XJ_{P,C}$ = 6 Hz), 131.3 (d, $^XJ_{P,C}$ = 13 Hz), 128.3 (s), 126.5 (s), 118.9 (d, $^1J_{P,C}$ = 90 Hz, *ipso*(P-C$_6$H$_5$)).

^{31}P{^{1}H}-NMR: (122 MHz, 298 K, MeCN-d3): 85.8 (s$_{sat}$, $^1J_{W,P}$ = 255 Hz, H-P-W(CO)5), 23.0 (s, PPh4).

^{31}P-NMR: (122 MHz, 298 K, MeCN-d3): 85.8 (d$_{sat}$, $^1J_{P,H}$ = 294, $^1J_{W,P}$ = 255 Hz, H-P-

W(CO)5), 23.0 (s(br), PPh4).

8.7.29. Synthesis of (1-methylimidazol-2-yl)diphenylphosphane (66d)
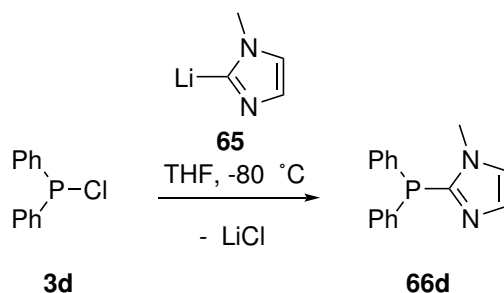
66d has previously been synthesised by Nishikawa et al. in the same manner, however the reaction outcome from the synthesis in this work differed and is therefore described in the following:

Synthesis: In a 250 mL Schlenk tube 2.17 mL N-methylimidazole were dissolved in 25 mL THF and cooled to $-80\,°C$. After addition of 10.9 mL ^{n}BuLi (c = 2.5 M in hexane) the reaction mixture was allowed to stir for 1 hour, while warming up to $-60\,°C$, before a solution of 5 mL **3d** in 5 mL THF was added dropwise via a transfer canula. After 16 hours the solvent was removed under reduced pressure ($3·10^{-2}$ mbar). To the residue 25 mL Et_2O and 10 mL H_2O were added and stirred for 5 minutes. The phases were separated with a separatory funnel and the aqueous phase was washed three times with 10 mL Et_2O. The organic phases were collected and dried over $MgSO_4$ for 5 minutes. The solvent was removed on a rotary evaporator ($40\,°C$, 700 mbar) and a colourless oil was obtained. ^{31}P-NMR spectroscopy shows that 80% of **66d** were contained in the oil alongside 20% of its oxide **67d**, which was not reported by Nishikawa.

The analytical data of **66d** fits to the report of Nishikawa.[192]

8.7.30. Synthesis of 1,3-dimethyl-2-(1-methylimidazol-2-yl)-1,3,2-diazaphospholidine (66e)
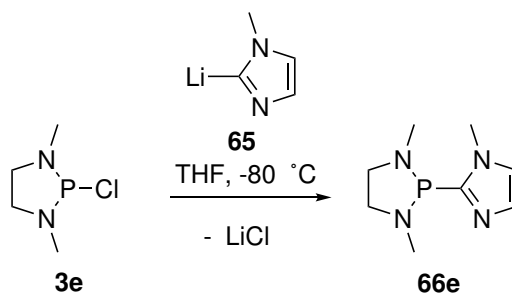
Synthesis: In a 25 mL Schlenk tube 0.4 mL N-methylimidazole were dissolved in 7.5 mL THF and cooled to $-80\ ^{\circ}$C. After addition of 2 mL ^{n}BuLi (c = 2.5 M in hexane) the reaction mixture was allowed to stir for 50 minutes, before a solution of 771 mg **3e** in 2.5 mL THF was added via a transfer canula and the canula was rinsed with 2 mL THF. After 16 hours the solvent was removed under reduced pressure (20 mbar) at 30 $^{\circ}$C. The product was extracted with 20 mL (15+5+5 mL) Et$_2$O and 2x5 mL DCM to yield a colourless wax, which was used without further purification in 90% purity.

Reaction code: PB-320, 39m3a046.21

Molecular formula: C$_8$H$_{15}$N$_4$P

Molecular weight: : 198.21 g mol^{-1}

Yield: 869 mg, 90% (estimated from ^{31}P-NMR spectroscopy)

MS: (ESI, 70 eV, selected signals): m/z 213.1 [M+O-H]$^{+\bullet}$, 213.1 [M]$^{+\bullet}$, 117.1 [M-C$_4$N$_2$H$_5$]$^{+\bullet}$, 82.0 [C$_4$N$_2$H$_5$].

^{1}**H-NMR**: (300 MHz, 298 K, C$_6$D$_6$): 7.25 (d, $^{3}J_{H,H}$ = 1 Hz, 1H, C$_2$H$_2$), 6.32 (t, $^{3}J_{H,H}$ = 1 Hz, $^{4}J_{P,H}$ = 1 Hz, 1H, C$_2$H$_2$), 3.59 – 3.44 (m, 2H, C$_2$H$_4$), 3.16 (s, 3H, imidazole N-CH$_3$), 3.01 – 2.84 (m, 2H, C$_2$H$_4$), 2.65 (d, $^{3}J_{P,H}$ = 15.3 Hz, 6H, 2xP-N-CH$_3$).

^{31}**P{^{1}H}-NMR**: (122 MHz, 298 K, C$_6$D$_6$): 84.3 (s).

8.7.31. Synthesis of 1,3-diisopropyl-2-(1-methylimidazol-2-yl)-1,3,2-diazaphospholidine (66f)
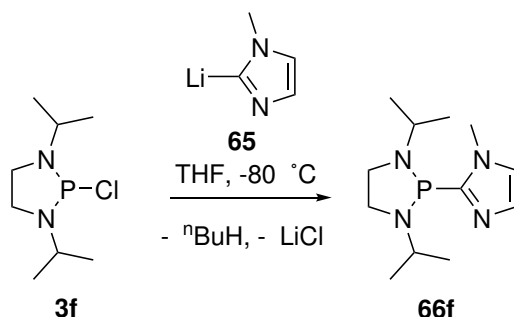
Synthesis: In a 25 mL Schlenk tube 0.81 mL N-methylimidazole were dissolved in 10 mL THF and cooled to $-80\,°C$. After addition of 4.1 mL ^{n}BuLi (c = 2.5 M in hexane) the reaction mixture was allowed to stir for 1 hour, before a solution of 2.133 g **3f** in 3 mL THF was added via a transfer canula and the canula was rinsed twice with 5 mL THF. After 21 hours the solvent was removed under reduced pressure ($3 \cdot 10^{-2}$ mbar) room temperature. The residue was washed with 3x20 mL n-pentane and then extracted with 3x20 mL toluene to yield a colourless oil after evaporation of the solvent under reduced pressure ($3 \cdot 10^{-2}$ mbar), which in the fridge (4 °C) crystallised and was used without further purification in 99% purity.

Reaction code: PB-304, 33p5b032.21

Crystallographic code: GXray6620_pl

Molecular formula: $C_{12}H_{23}N_4P$

Molecular weight: 254.32 g mol^{-1}

Yield: 1.974 g, 78%

MS: (ESI, 70 eV, selected signals): m/z (%) 254.2 [M]$^{+\bullet}$, 171.2 [M-2H-methylimidazole]$^{+\bullet}$.

^{1}H-NMR: (500 MHz, 298 K, CDCl$_3$): 7.09 (d, $^3J_{H,H}$ = 1.1 Hz, 1H, C$_2$H$_2$), 6.80 (t, $^3J_{H,H}$ = 1.1 Hz, $^4J_{P,H}$ = 1.1 Hz, 1H, C$_2$H$_2$), 3.84 (s, 3H, imidazole N-CH$_3$), 3.43 − 3.36 (m, 2H, C$_2$H$_4$), 3.26 − 2.13 (m, 4H, C$_2$H$_4$ & N-CHMe$_2$), 1.16 (d, $^2J_{H,H}$ = 6.4 Hz, 6H, 2xN-CH(CH$_3$)$_2$), 1.13 (d, $^2J_{H,H}$ = 6.4 Hz, 6H, 2xN-CH(CH$_3$)$_2$).

^{31}P{^{1}H}-NMR: (122 MHz, 298 K, CDCl$_3$): 66.9 (s).

8.7.32. Synthesis of 1,3-dimethyl-2-(1-methylimidazol-2-yl)-1,3,2-diazaphospholidine P-oxide (67e)

66e → **67e**
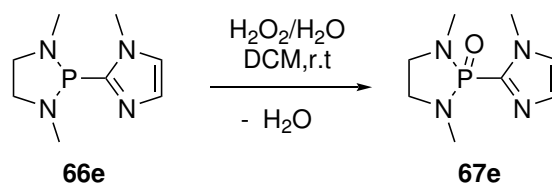
Synthesis: In a 25 mL Schlenk tube 225 mg **66e** were dissolved in 10 mL DCM to which 0.12 mL of a 30% H_2O_2 aqueous solution was added dropwise with a syringe. After addition a colourless solid precipitated and the solution was stirred for 17 hours. After solvent removal under reduces pressure ($3 \cdot 10^{-2}$ mbar) and drying for 2 hours a colourless gel was obtained. Purification was attempted via column chromatography (h = 15 cm, ø= 3 cm, SiO_2, MeOH:Ethylacetate (1:3)), and product containing fractions (in low yield) were contaminated with 20% N-methylimidazole from hydrolysis. And was therefore not used further.

Reaction code: PB-325, 45m3a005.21
Molecular formula: $C_8H_{15}N_4PO$
Molecular weight: 241.21 g mol^{-1}
Yield: —
MS (EI, 70 eV, selected signals): m/z (%) 213.1 [M+O]$^{+\bullet}$, 198.1 [M]$^{+\bullet}$, 82.0 [methyl-imidazole+H]$^{+}$.
^{1}H-NMR: (300 MHz, 298 K, CDCl$_3$): 7.07 (dd, $^4J_{P,H}$ = 1.6 Hz , $^3J_{H,H}$ = 1.0 Hz, 1H, C$_2$H$_2$), 6.90 (dd, $^3J_{H,H}$ = 1.0 Hz, $^4J_{P,H}$ = 2.3 Hz, 1H, C$_2$H$_2$), 3.93 (s, 3H, imidazole N-CH3), 3.25 (s, 2H, C$_2$H$_4$), 3.22 (s, 2H, C$_2$H$_4$), 2.45 (d, $^3J_{P,H}$ = 10.4 Hz, 6H, 2xP-N-CH$_3$).
^{31}P{^{1}H}-NMR: (122 MHz, 298 K, CDCl$_3$): 19.0 (s).

8.7.33. Synthesis of 1,3-dimethyl-2-(1-methylimidazol-2-yl)-1,3,2-diazaphospholidine P-oxide (67e)

66f → **67f**
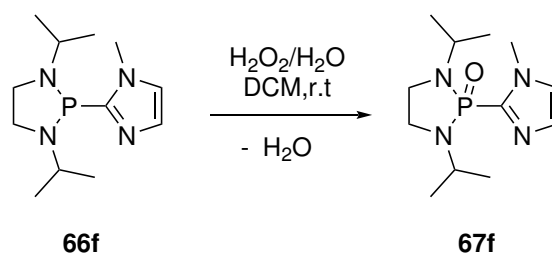
Synthesis: In a 25 mL Schlenk tube 486 mg **66f** were dissolved in 10 mL DCM to which 0.19 mL of a 30% H_2O_2 aqueous solution was added dropwise with a syringe. After addition a colourless solid precipitated and the solution was stirred for 2 hours. After solvent removal under reduces pressure ($3 \cdot 10^{-2}$ mbar) and drying for 2 hours a colourless oil was obtained. Purification of the crude product via column chromatography (h = 10 cm, ø= 2 cm, SiO_2, MeOH:Ethylacetate (2:8)) resulted a colourless gel in good yield.

Reaction code: PB-307, 45m3a005.21

Molecular formula: $C_{12}H_{23}N_4PO$

Molecular weight: 270.32 g mol^{-1}

Yield: 462 mg, 89%

MS: (EI, 70 eV, selected signals): m/z (%) 270.1 $[M]^{+\bullet}$, 255.1 $[M-CH_3]^{+\bullet}$, 227.1 $[M-{}^iPr]^{+\bullet}$, 185.0 $[M-2(C_3H_7+H]^{+\bullet}$.

^{1}H-NMR: (300 MHz, 298 K, CDCl$_3$): 7.19 (dd, $^4J_{P,H}$ = 1.3 Hz , $^3J_{H,H}$ = 1.3 Hz, 1H, C$_2$H$_2$), 6.96 (dd, $^3J_{H,H}$ = 1.0 Hz, $^4J_{P,H}$ = 2.2 Hz, 1H, C$_2$H$_2$), 4.05 (s, 3H, imidazole N-CH$_3$), 3.48 – 3.26 (m, 6H, C$_2$H$_4$ & 2xN-CHMe$_2$), 1.14 (d, $^3J_{H,H}$ = 6.6 Hz, 6H, 2xP-N-CH(CH$_3$)), 0.99 (d, $^3J_{H,H}$ = 6.6 Hz, 6H, 2xP-N-CH(CH$_3$)).

^{31}P{^{1}H}-NMR: (122 MHz, 298 K, CDCl$_3$): 12.5 (s).

8.7.34. Synthesis of [(1,3-dimethylimidazolium-2-yl)diphenylphosphane oxide] triflate (68d)

67d   **68d**
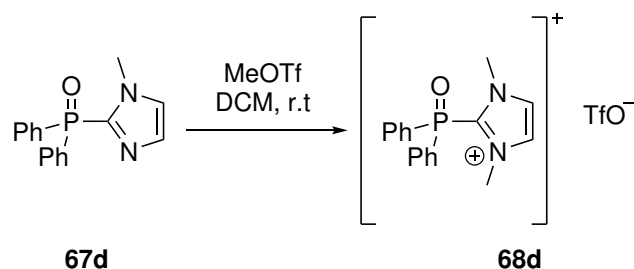
Synthesis: In a 100 mL Schlenk tube 1.826 g **67d** were dissolved in 30 mL DCM to which 0.73 mL MeOTf was added dropwise with a syringe and the reaction mixture was stirred for 2 hours. Then the solvent was removed under reduces pressure ($3 \cdot 10^{-2}$ mbar) to give a sticky residue. The residue was stirred in and washed with 50 mL Et$_2$O and 70 mL (25+25+10+10 mL) *n*-pentane, then dried to give a colourless powder in almost quantitative yield.

Reaction code: PB-310, 41p5a002.21

Molecular formula: $C_{18}H_{18}N_2PO_4SF_3$

Molecular weight: 446.38 g mol^{-1}

Yield: 2.728 g, 94%

Melting point: 126 °C

Elemental analysis:

calculated (%) C 48.43 H 4.06 N 6.28 S 7.18 , found (%) C 48.48 H 4.16 N 6.21 S 7.19

MS: ((+)-ESI): m/z (%) 441.082 [Ph$_2$P(O)OP(O)Ph$_2$+Na]$^+$, 419.100
[Ph$_2$P(O)OP(O)Ph$_2$+H]$^+$, 297.118 [M]$^+$, 219.059 [Ph$_2$P(O)OH+H]$^+$; ((−)-ESI): m/z (%) 148.9
[OTf]$^-$.

^{1}H-NMR: (500 MHz, 298 K, CD$_2$Cl$_2$): 7.82 – 7.73 (m, 6H, P-C$_6$H$_5$), 7.72 (d, $^4J_{P,H}$ = 1.8 Hz,
2H, C$_2$H$_2$), 7.70 – 7.65 (m, 4H, P-C$_6$H$_5$), 3.71 (s, 6H, 2x imidazolium N-CH$_3$).

^{13}C{^{1}H}-NMR: (126 MHz, 298 K, CD$_2$Cl$_2$): 138.8 (d, $^1J_{P,C}$ = 94 Hz, P-CN$_2$), 135.3 (d, $^XJ_{P,C}$ =
3 Hz, P-C$_6$H$_5$), 132.3 (d, $^XJ_{P,C}$ = 11 Hz, P-C$_6$H$_5$), 130.5 (d, $^XJ_{P,C}$ = 14 Hz, P-C$_6$H$_5$), 128.3
(d, $^3J_{P,C}$ = 4 Hz, C$_2$H$_2$), 127.6 (d, $^1J_{P,C}$ = 115 Hz, *ipso*-P-C$_6$H$_5$), 121.2 (q, $^1J_{F,C}$ = 321 Hz,
S-CF$_3$), 39.1 (s, imidazolium N-CH$_3$).

^{19}F{^{1}H}-NMR: (471 MHz, 298 K, CD$_2$Cl$_2$): −79.0 (s).

^{31}P{^{1}H}-NMR: (202 MHz, 298 K, CD$_2$Cl$_2$): 18.5 (s).

8.7.35. Synthesis of [1,3-diisopropyl-2-(1,3-dimethylimidazolium-2-yl)-1,3,2-diazaphospholidine *P*-oxide] triflate (68e)

67f   **68f**
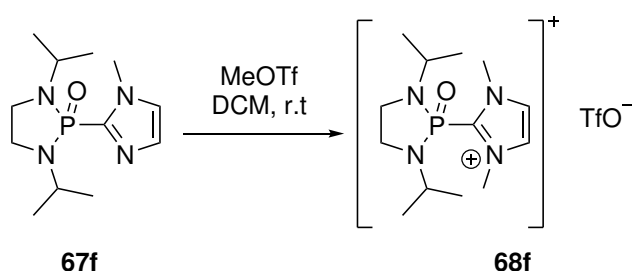
Synthesis: In a 25 mL Schlenk tube 117 mg **67f** were dissolved in 5 mL DCM to which
0.45 mL MeOTf was added dropwise with a syringe and the reaction mixture was stirred for
1 hours. Then the solvent was removed under reduces pressure (3·10^{-2} mbar) to give a
colourless oil, which crystallised under scratching the glass walls of the flask. The residue
was stirred in and washed with 3x5 mL Et$_2$O and 2x4 mL *n*-pentane, then dried to give a
colourless powder in quantitative yield.

Reaction code: PB-324, 40c5a049.21

Crystallographic code: GXray6707k

Molecular formula: $C_{14}H_{26}N_4PO_4SF_3$

Molecular weight: 434.41 g mol^{-1}

Yield: quant .

Melting point: 172 °C

Elemental analysis:

calculated (%) C 38.71 H 6.03 N 12.90 S 7.38 , found (%) C 38.46 H 5.89 N 12.70 S 7.26

MS: ((+)-ESI): m/z (%) 285.186 [M]$^+$; ((−)-ESI): m/z (%) 148.9 [OTf]$^-$

^{1}H-NMR: (500 MHz, 298 K, CD$_2$Cl$_2$): 7.67 (d, $^4J_{P,H}$ = 2.3 Hz, 2H, C$_2$H$_2$), 4.09 (s, 6H, 2x imidazolium N-CH$_3$), 3.59 – 3.50 (m, 2H, C$_2$H$_4$), 3.50 – 3.35 (m, 4H, C$_2$H$_4$ & 2xN-CHMe$_2$), 1.17 (d, $^3J_{H,H}$ = 6.6 Hz, 6H, 2xP-N-CH(CH$_3$)), 1.11 (d, $^3J_{H,H}$ = 6.6 Hz, 6H, 2xP-N-CH(CH$_3$)).

^{13}C{^{1}H}-NMR: (126 MHz, 298 K, CD$_2$Cl$_2$): 139.5 (d, $^1J_{P,C}$ = 174 Hz, P-CN$_2$), 127.3 (d, $^3J_{P,C}$ = 6 Hz, C$_2$H$_2$) 121.3 (q, $^1J_{F,C}$ = 321 Hz, S-CF$_3$), 46.7 (d, $^2J_{P,C}$ = 6 Hz, N-CH(Me)2), 40.3 (d, $^2J_{P,C}$ = 14 Hz, C$_2$H$_4$), 38.9 (s, imidazolium N-CH$_3$), 21.31 (d, $^3J_{P,C}$ = 2 Hz, N-CH(CH$_3$)$_2$), 21.11 (d, $^3J_{P,C}$ = 4 Hz, N-CH(CH$_3$)$_2$).

^{19}F{^{1}H}-NMR: (470 MHz, 298 K, CD$_2$Cl$_2$): −79.0 (s).

^{31}P{^{1}H}-NMR: (202 MHz, 298 K, CD$_2$Cl$_2$): 4.5.

8.7.36. Synthesis of [pyridiniumyldiphenylphosphane P-oxide] triflate (70d)
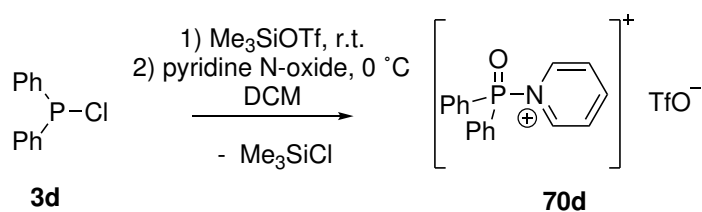
Synthesis: In a 25 mL Schlenk tube 356.6 mg **3d** were dissolved in 8 mL DCM to which 0.29 mL Me$_3$SiOTf was added dropwise with a syringe and the reaction mixture was stirred for 1 hours in a glove box. All volatiles were removed under reduces pressure (3·10^{-2} mbar) to give a colourless oil. The oil was dissolved in 5 mL DCM, cooled to 0 °C and a solution of 150 mg pyridine N-oxide in 3 mL DCM was added. After evaporation of the solvent under reduces pressure (3·10^{-2} mbar) a colourless precipitate was dissolved in just enough DCM and a few drops of Et$_2$O were added and the solution was kept cooled at 4 C to recrystallize the product in moderate yield. However, pyridinium triflate co-crystalized alongside (33%).

Reaction code: PB-437, 21p5a003.22

Crystallographic code: GXray6900f

Molecular formula: $C_{18}H_{15}NPO_4SF_3$

Molecular weight: 429.35 g mol^{-1}

Yield: 452 mg, 65% (33% contamination of pyridinium triflate)

MS: ((+)-ESI): m/z (%) 441.077 [Ph$_2$P(O)OP(O)Ph$_2$+Na]$^+$, 419.095 [Ph$_2$P(O)OP(O)Ph$_2$+H]$^+$, 247.088, 219.057 [Ph$_2$P(O)OH+H]$^+$; ((−)-ESI): m/z (%) 149.1 [OTf]$^-$.

^{1}H-NMR: (500 MHz, 298 K, CD$_2$Cl$_2$): 9.06 (d, $^XJ_{P,H}$ = 6 Hz, 2H, NC$_5$H$_5$), 8.70 − 8.66 (m, 2H, 4-C-H in NC$_5$H$_5$), 8.21 (t, $^XJ_{P,H}$ = 7 Hz, 2H, NC$_5$H$_5$), 8.00 − 7.90 (m, 4H, P-C$_6$H$_5$), 7.91 − 7.81 (m, 2H, 4-C-H in P-C$_6$H$_5$), 7.71 (m, 4H, P-C$_6$H$_5$). Pyridinium triflate: 15.43 (s, 1H, N-H), 9.06 (d, $^XJ_{P,H}$ = 6 Hz, 2H, NC$_5$H$_5$), 8.70 − 8.66 (m, 2H, 4-C-H in NC$_5$H$_5$), 8.21 (t, $^XJ_{P,H}$ = 7 Hz, 2H, NC$_5$H$_5$).

^{13}C{^{1}H}-NMR: (126 MHz, 298 K, CD$_2$Cl$_2$): 149.1 (s, NC$_5$H$_5$), 143.68 (s, NC$_5$H$_5$), 136.47 (s, NC$_5$H$_5$), 133.40 (d, $^XJ_{P,C}$ = 12 Hz, P-C$_6$H$_5$), 130.55 (d, $^XJ_{P,C}$ = 14 Hz, P-C$_6$H$_5$), 129.03 (s, P-C$_6$H$_5$), 123.52 (d, $^1J_{P,C}$ = 121 Hz, P-C$_6$H$_5$), 121.09 (q, $^1J_{F,C}$ = 320 Hz, S-CF$_3$).

^{19}F{^{1}H}-NMR: (470 MHz, 298 K, CD$_2$Cl$_2$): −79.0 (s).

^{31}P{^{1}H}-NMR: (202 MHz, 298 K, CD$_2$Cl$_2$): 45.7 (s).

8.7.37. Synthesis of [1,3-dimethyl-2-(pyridiniumyl)-1,3,2-diazaphospholidine P-oxide] triflate (70e)
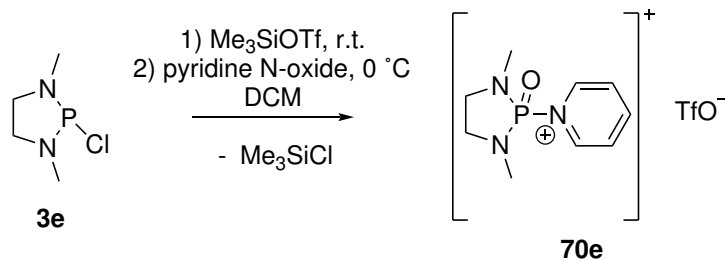
Synthesis: In a 25 mL Schlenk tube 302 mg **3e** were dissolved in 6 mL DCM to which 0.38 mL Me$_3$SiOTf was added dropwise with a syringe and the reaction mixture was stirred for 15 minutes in a glove box. All volatiles were removed under reduces pressure ($3 \cdot 10^{-2}$ mbar) to give a colourless oil. The oil was dissolved in 5 mL DCM, cooled to 0 °C and a solution of 188 mg pyridine N-oxide in 2 mL DCM was added to stir for 1 hour. After evaporation of the solvent under reduces pressure ($3 \cdot 10^{-2}$ mbar) the colourless residue was washed with 2x2 mL toluene and 3x3 mL *n*-pentane and after drying was obtained as a colourless powder.

Reaction code: PB-544, PCB230213p5a002

Molecular formula: C$_{10}$H$_{15}$N$_3$PO$_4$SF$_3$

Molecular weight: 361.28 g mol^{-1}

Yield: 674 mg, 94%

Melting point: 151 °C

Elemental analysis:

calculated (%) C 33.25 H 4.19 N 11.63 S 8.87 , found (%) C 33.46 H 4.21 N 11.66 S 9.26

MS: ((+)-ESI): m/z (%) 212.095 [M]$^+$, 133.053 [M-NC$_5$H$_5$]$^+$; ((−)-ESI): m/z (%) 149.1 [OTf]$^-$.

HR-MS: ((+)-ESI): m/z (%) C$_9$H$_{15}$N$_3$PO calc. 212.0947, found 212.0950.

^{1}H-NMR: (500 MHz, 298 K, MeCN-*d*3): 9.03 − 9.97 (m, 2H, NC$_5$H$_5$), 8.69 − 8.63 (m, 1H, 4-C-H in NC$_5$H$_5$), 8.17 − 8.11 (m, 2H, NC$_5$H$_5$), 3.55 (s, 2H, C$_2$H$_4$), 3.53 (s, 2H, C$_2$H$_4$), 2.59 (d, $^3J_{P,H}$ ´= 10.6 Hz, N-CH$_3$).

^{13}C{^{1}H}-NMR: (126 MHz, 298 K, MeCN-*d*3): 149.6 (d, $^XJ_{P,C}$ = 2 Hz, NC$_5$H$_5$), 145.8 (d, $^XJ_{P,C}$ = 3 Hz, NC$_5$H$_5$), 129.5 (d, $^XJ_{P,C}$ = 5 Hz, NC$_5$H$_5$), 123.4 (q, $^1J_{F,C}$ = 321 Hz, S-CF$_3$), 47.0 (d, $^2J_{P,C}$ = 15 Hz, C$_2$H$_4$) 30.9 (d, $^3J_{P,C}$ = 6 Hz, N-CH$_3$).

^{19}F{^{1}H}-NMR: (470 MHz, 298 K, MeCN-*d*3): −79.3 (s).

^{31}P{^{1}H}-NMR: (202 MHz, 298 K, MeCN-*d*3): 20.7 (s).

EXPERIMENTAL PART

8.7.38. Synthesis of [1,3-diisopropyl-2-(pyridiniumyl)-1,3,2-diazaphospholidine P-oxide] triflate (70f)
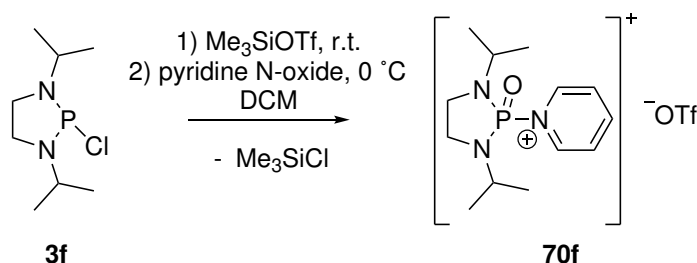
Synthesis: In a 25 mL Schlenk tube 235 mg **3f** were dissolved in 6 mL DCM to which 0.2 mL Me$_3$SiOTf was added dropwise with a syringe and the reaction mixture was stirred for 1 hours in a glove box. All volatiles were removed under reduces pressure ($3 \cdot 10^{-2}$ mbar) to give a colourless oil. The oil was dissolved in 7 mL DCM, cooled to 0 °C and a solution of 105 mg pyridine N-oxide in 1.5 mL DCM was added to stir for 1 hour. After evaporation of the solvent under reduces pressure ($3 \cdot 10^{-2}$ mbar) the colourless residue was washed with 5 mL toluene and *n*-pentane each. Subsequently the solid was dissolved in just enough DCM and a few drops of Et$_2$O were added and the solution was kept cooled at 4 °C to recrystallize the product in almost quantitative yield.

Reaction code: PB-435, 20p5a055.22

Crystallographic code: GXray6901f

Molecular formula: C$_{14}$H$_{23}$N$_3$PO$_4$SF$_3$

Molecular weight: 417.38 g mol^{-1}

Yield: 447 mg, 95%

Melting point: 212 °C

MS: ((+)-ESI): m/z (%) 268.157 [M]$^+$, 189.115 [M-NC$_5$H$_5$]$^+$; ((−)-ESI): m/z (%) 149.1 [OTf]$^-$.

^{1}H-NMR: (500 MHz, 298 K, CD$_2$Cl$_2$): 9.42 − 9.31 (m, 2H, NC$_5$H$_5$), 8.67 − 8.60 (m, 1H, 4-C-H in NC$_5$H$_5$), 8.29 − 8.21 (m, 2H, NC$_5$H$_5$), 3.80 − 3.69 (m, 2H, C$_2$H$_4$), 3.59 − 3.52 (m, 2H, C$_2$H$_4$), 3.47 (dsept, 2H, $^3J_{P,H}$ = 11.4 Hz, $^3J_{H,H}$ ´ = 6.6 Hz, N-CHMe$_2$), 1.15 (d, $^3J_{H,H}$ ´ = 6.6 Hz, N-CH(CH$_3$)$_2$), 1.02 (d, $^3J_{H,H}$ ´ = 6.6 Hz, N-CH(CH$_3$)$_2$).

^{13}C{^{1}H}-NMR: (126 MHz, 298 K, CD$_2$Cl$_2$): 148.7 (d, $^XJ_{P,C}$ = 2 Hz, NC$_5$H$_5$), 145.6 (d, $^XJ_{P,C}$ = 3 Hz, NC$_5$H$_5$), 129.1 (d, $^XJ_{P,C}$ = 5 Hz, NC$_5$H$_5$), 121.3 (q, $^1J_{F,C}$ = 321 Hz, S-CF$_3$), 46.8 (d, $^2J_{P,C}$ = 5 Hz, N-CHMe$_2$), 39.8 (d, $^XJ_{P,C}$ = 16 Hz, C$_2$H$_4$) 21.1 (d, $^3J_{P,C}$ = 3 Hz, N-CH(CH$_3$)$_2$), 20.5 (d, $^3J_{P,C}$ = 3 Hz).

^{19}F{^{1}H}-NMR: (470 MHz, 298 K, CD$_2$Cl$_2$): −79.0 (s).

^{31}P{^{1}H}-NMR: (202 MHz, 298 K, CD$_2$Cl$_2$): 17.1 (s).

8.7.39. Synthesis of [1,3-diisopropyl-2-(4-(1,3-bis(2,4,6-(trimethylphenyl)imidazolium-2-ylpyridinyl)-1,3,2-diazaphospholidine P-oxide] triflate (71f)
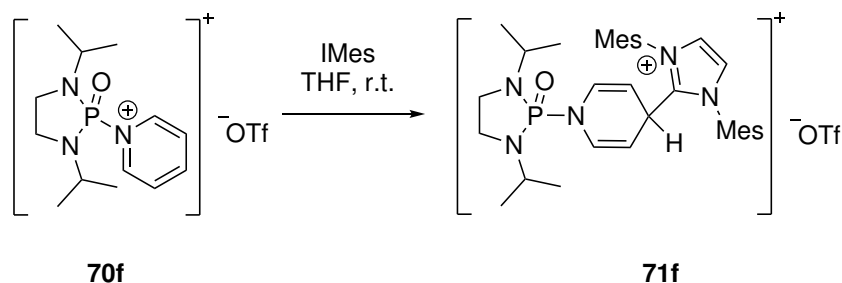
Synthesis: In a 10 mL Schlenk tube 30 mg **70f** were dissolved in 1 mL THF to which 23 mg IMes in 1 mL THF was added dropwise with a syringe and the reaction mixture was stirred for 15 minutes in a glove box. The Schlenk tube was taken out of the glove box and the solvent was removed. The residue, a yellow-brownish foam, was suspended in 3 mL Et_2O and DCM was added dropwise to the suspension until the solution became clear. After the solution turned clear, it turns briefly turbid again and further stirring breaks this emulsion into two phases. The mixture was kept at $-40\ °C$ overnight. The upper layer was removed with a syringe and the denser layer, a brown oil, was washed with 2x4 mL *n*-pentane and then a mixture of 2x3 mL a mixture of THF/Et_2O (1:10), gradually changing the oil into a solid. After the washing the product was obtained as a colourless powder in good yield.

Reaction code: PB-442, 21m3a053.22

Molecular formula: $C_{35}H_{47}N_5PO_4SF_3$

Molecular weight: 721.82 g mol^{-1}

Yield: 43 mg, 83%

Elemental analysis:

calculated (%) C 58.24 H 6.56 N 9.70 S 4.44 , found (%) C 57.87 H 6.54 N 9.28 S 4.19

MS: ((+)-ESI): m/z (%) 572.350 [M]$^+$, 268.157 [M-IMes]$^+$, 189.115 [M-IMes-NC$_5$H$_5$]$^+$; ((−)-ESI): m/z (%) 149.1 [OTf]$^-$.

^{1}H-NMR: (300 MHz, 298 K, CD_2Cl_2): 7.49 (s, 2H, C_2H_2), 7.11 (s, 4H, *meta*-N-$C_6H_2Me_3$), 6.19 (m, 2H, *ortho*-NC$_5$H$_5$), 4.65 (m, 1H, *para*-NC$_5$H$_5$), 4.34 (m, 2H, *meta*-NC$_5$H$_5$), 3.20 − 2.94 (m, 6H, C_2H_4 & N-CHMe$_2$), 2.38 (s, 6H, 2x*para*-C6H2(CH$_3$)3), 2.12 (s, 12H, 2x*ortho*-C6H2(CH$_3$)3).

^{13}C{^{1}H}-NMR: (126 MHz, 298 K, CD_2Cl_2): 147.0 (s, CN$_2$), 142.19 (s, NC$_5$H$_5$), 134.8 (s, NC$_5$H$_5$), 130.9 − 129.9 (m, N-$C_6H_2Me_3$), 125.2 (d, $^XJ_{P,C}$ = 2 Hz, *ipso*(N-$C_6H_2Me_3$)), 121.4

(q, $^1J_{F,C}$ = 321 Hz, S-CF$_3$), 95.5 – 94.8 (m, NC$_5$H$_5$), 45.1 – 44.1 (m, N-CHMe$_2$), 39.3 (d, $^2J_{P,C}$ = 14 Hz, C$_2$H$_4$), 32.71 (s, *ortho*-(N-C$_6$H$_2$(CH$_3$)3)), 21.3 (d, $^3J_{P,C}$ = 1 Hz, N-CH(CH$_3$)$_2$), 18.0 (d, $^3J_{P,C}$ = 1 Hz, N-CH(CH$_3$)$_2$).

^{31}P{^{1}H}-NMR: (122 MHz, 298 K, CD$_2$Cl$_2$): 14.2 (s).

8.7.40. Synthesis of [1,3-bis(2,4,6-trimethylphenyl)imidazolium-2-yl(diphenyl)phosphane] triflate (73d)

3d   **73d**
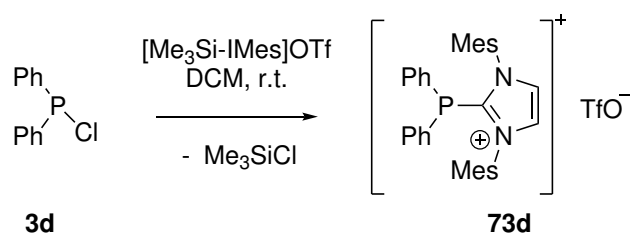
Synthesis: In a 10 mL Schlenk tube 162 mg **3d** were dissolved in 5 mL DCM and 258 mg [Me$_3$Si-IMes]OTf was added as a solid at once. After 40 minutes the solvent was removed under reduced pressure and the residue was washed with 15 mL (10+2.5+2.5 mL) *n*-pentane and dried. The colourless solid was recrystallised from a THF/Et$_2$O(1:5) mixture and obtained in good yield as colourless airstable crystals.

Reaction code: PB-484, 38t4b063.22

Crystallographic code: GXray7072

Molecular formula: C$_{34}$H$_{34}$N$_2$PO$_3$SF$_3$

Molecular weight: 638.69 g mol^{-1}

Yield: 239 mg, 76% (+10% H-IMesOTf)

Melting point: 143 °C

Elemental analysis:

calculated (%) C 63.94 H 5.37 N 4.39 S 5.02 , found (%) C 63.49 H 5.49 N 4.23 S 5.07

MS: ((+)-ESI): m/z (%) 489.244 [M]$^+$, 305.200 [H-IMes]$^+$; ((−)-ESI): m/z (%) 149.1 [OTf]$^-$.

HR-MS: ((+)-ESI): m/z (%) C$_{33}$H$_{34}$N$_2$PO calc. 489.2454, found 489.2444.

^{1}H-NMR: (400 MHz, 298 K, CD$_2$Cl$_2$): 7.62 (s, 2H, C$_2$H$_2$), 7.39 – 7.25 (m, 6H, P-C$_6$H$_5$), 7.22 – 7.15 (m, 4H, P-C$_6$H$_5$), 6.74 (s, 4H, *meta*-N-C$_6$H$_2$Me$_3$), 2.23 (s, 6H, *para*-C$_6$H$_2$Me$_3$), 2.02 (s, 12H, *ortho*-C$_6$H$_2$Me$_3$).

^{13}C{^{1}H}-NMR: (126 MHz, 298 K, CD$_2$Cl$_2$): 148.2 (d, $^1J_{P,C}$ = 65 Hz, CN$_2$), 142.1 (s, N-C$_6$H$_2$Me$_3$), 135.4 (d, $^1J_{P,C}$ = 26 Hz, P-C$_6$H$_5$), 134.4 (s, N-C$_6$H$_2$Me$_3$), 131.7 (d, $^XJ_{P,C}$ =

2 Hz, P-C$_6$H$_5$), 131.1 (s, N-C$_6$H$_2$Me$_3$), 130.3 (s, N-C$_6$H$_2$Me$_3$), 129.2 (d, $^XJ_{P,C}$ = 10 Hz, P-C$_6$H$_5$), 127.8 (d, $^XJ_{P,C}$ = 2 Hz, P-C$_6$H$_5$), 126.9 (d, $^XJ_{P,C}$ = 6 Hz, P-C$_6$H$_5$), 21.1 (s, *para*-(N-C6H2(CH$_3$)3), 18.4 (d, $^4J_{P,C}$ = 4 Hz, *ortho*-(N-C6H2(CH$_3$)3)).

^{31}P{^{1}H}-NMR: (202 MHz, 298 K, MeCN-*d*3): −7.1 (s).

8.7.41. Synthesis of [1,3-dimethyl-2-(1,3-bis(2,4,6-trimethylphenyl)imidazolium-2-yl)-1,3,2-diazaphospholidine] triflate (73e)
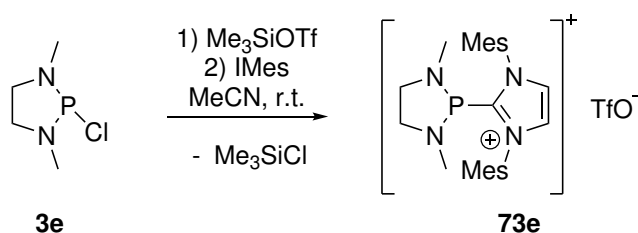
Synthesis: In a 10 mL Schlenk tube 177 mg **3e** were dissolved in 5 mL MeCN to which 0.19 mL Me$_3$SiOTf was added with a syringe and the reaction mixture was stirred for 30 minutes in a glove box. After which 323 mg IMes in 2 mL MeCN was added dropwise to the solution. The Schlenk tube was taken out of the glove box and the solvent was removed. The residue washed with 4x4 mL Et$_2$O and dried (3·10^{-2} mbar) to obtained the product as a colourless solid in good yield.

Reaction code: PB-581, PCB230411p5a002

Crystallographic code: GXray7078

Molecular formula: C$_{26}$H$_{34}$N$_4$PO$_3$SF$_3$

Molecular weight: 570.61 g mol^{-1}

Yield: 556 mg, 84%

Melting point: 158 °C

MS: ((+)-ESI): m/z (%) 437.246 [M+O]$^+$, 421.251 [M]$^+$, 305 [H-IMes]$^+$; ((−)-ESI): m/z (%) 149.1 [OTf]$^-$.

^{1}H-NMR: (500 MHz, 298 K, MeCN-*d*3): 7.52 (s, 2H, C$_2$H$_2$), 7.18 (s, 4H, *meta*-N-C$_6$H$_2$Me$_3$), 2.86 − 2.79 (m, 2H, C$_2$H$_4$), 2.71 − 2.66 (m, 2H, C$_2$H$_4$), 2.36 (s, 6H, 2x *para*-C6H2(CH$_3$)3), 2.11(s, 12H, 2x *ortho*-C6H2(CH$_3$)3), 2.10 (d, $^3J_{P,H}$ = 14.3.

^{13}C{^{1}H}-NMR: (126 MHz, 298 K, CD$_2$Cl$_2$): 155.4 (d, $^2J_{P,C}$ = 111 Hz, CN$_2$), 141.9 (s, C$_6$H$_2$Me$_3$), 135.5 (s, C$_6$H$_2$Me$_3$), 130.6 (s, C$_6$H$_2$Me$_3$), 126.7 (d, $^2J_{P,C}$ = 3 Hz, C$_6$H$_2$Me$_3$), 122.2 (q, $^1J_{F,C}$ = 321 Hz, S-CF$_3$), 55.7 (d, $^2J_{P,C}$ = 8 Hz, C$_2$H$_4$), 37.4 (d, $^2J_{P,C}$ = 35 Hz, N-CH$_3$), 21.2 (s, *ortho*-(N-C6H2(CH$_3$)3)), 18.0 (d, $^XJ_{P,C}$ = 4 Hz, *para*-(N-C6H2(CH$_3$)3)).

^{19}F{^{1}H}-NMR: (470 MHz, 298 K, MeCN-d3): −79.4 (s).

^{31}P{^{1}H}-NMR: (202 MHz, 298 K, MeCN-d3): 110.9 (s).

8.7.42. Synthesis of [1,3-bisdiisopropyl-4,5-dimethyl-imidazolium-2-yl(diphenyl)phosphane] triflate (74d)

3d   **74d**
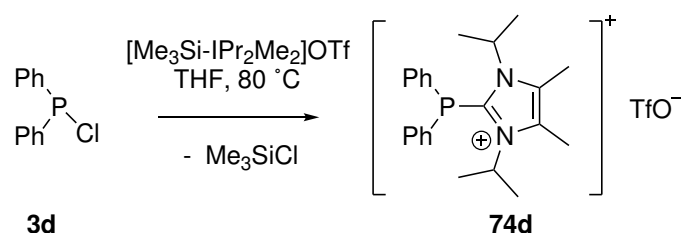
Synthesis: In a 10 mL Schlenk tube 418 mg [Me$_3$Si-IPr$_2$Me$_2$]OTf were dissolved in 5 mL THF and 0.35 mL **3d** were added dropwise. The Schlenk tube was sealed with a glass stopper and heated to 80 °C in an oil bath for 50 minutes, before the mixture was concentrated to 1 mL and n-pentane was added until the solution become slightly turbid. The solution was then cooled to −40 °C upon, after 30 minutes, crystals were obtained, which were washed with a mixture of THF:n-pentane (1:2). The crystals were then dried (3·10^{-2} mbar) to obtained the air stable colourless product in moderate yield.

Reaction code: PB-486/493, 39t4a038.22, 42m3a017.22

Crystallographic code: GXray7079

Molecular formula: C$_{24}$H$_{30}$N$_2$PO$_3$SF$_3$

Molecular weight: 514.54 g mol^{-1}

Yield: 270 mg, 51%

Melting point: 173 °C

Elemental analysis:

calculated (%) C 56.02 H 5.88 N 5.44 S 6.23 , found (%) C 55.90 H 5.99 N 5.46 S 6.08

^{1}H-NMR: (300 MHz, 298 K, MeCN-d3): 7.59 − 7.42 (m, 10H, 2xP-C$_6$H$_5$), 5.05 (sbr, 2H, 2xN-CHMe$_2$), 2.38 (s, 6H, C$_2$(CH$_3$)$_2$), 1.32 (sbr, 12H, N-CH(CH$_3$)$_2$).

^{13}C{^{1}H}-NMR: (101 MHz, 298 K, CD$_2$Cl$_2$): 132.1 (d, $^3J_{P,C}$ = 19 Hz, C$_2$Me$_2$), 131.0 (s, P-C$_6$H$_5$), 130.2 (s, P-C$_6$H$_5$), 129.0 (d, $^XJ_{P,C}$ = 9 Hz, P-C$_6$H$_5$), 121.5 (q, $^1J_{F,C}$ = 321 Hz, S-CF$_3$), 53.7 (s, N-CHMe$_2$) 21.2 (s, N-CH(CH$_3$)$_2$), 11.1 (s, C$_2$(CH$_3$)$_2$).

^{31}P{^{1}H}-NMR: (122 MHz, 298 K, MeCN-d3): −28.0 (s).

8.7.43. Synthesis of [2-(1,3-bisdiisopropyl-4,5-dimethyl-imidazolium-2-yl)-1,3-dimethyl-1,3,2-diazaphospholidine] triflate (74e)
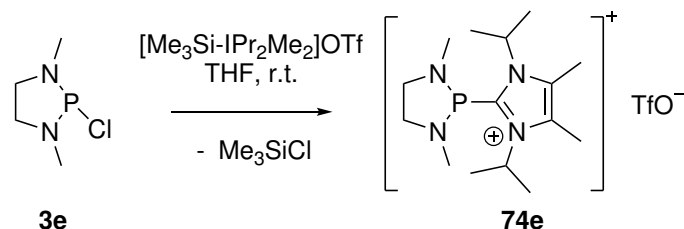
Synthesis: In a 100 mL Schlenk tube 395 mg **3e** were dissolved in 15 mL THF and 803 mg [Me$_3$Si-IPr$_2$Me$_2$]OTf was added as a solid in small portions. After 17 hours all volatiles were removed under reduced pressure and the residual pale-yellow sticky mass was washed with 3x7 mL *n*-pentane and dried. The product obtained as a colourless powder and a 20% contamination with [H-IPr$_2$Me$_2$]OTf.

Reaction code: PB-477, 38p5b006.22

Molecular formula: C$_{16}$H$_{30}$N$_4$PO$_3$SF$_3$

Molecular weight: 446.47 g mol^{-1}

Yield: 712 mg, 80% (+20% H-IPr$_2$Me$_2$ OTf estimated from ^{1}H-NMR spectroscopy)

^{1}H-NMR: (500 MHz, 298 K, CD$_2$Cl$_2$): 5.34 (sept, $^3J_{H,H}$ = 7 Hz, N-CHMe$_2$), 3.28 (m, 2H, C$_2$H$_4$), 3.13 (m, 2H, C$_2$H$_4$), 2.79 (d, $^3J_{P,H}$ = 14.8 Hz, N-CH$_3$), 2.34 (s, 6H, C$_2$(CH$_3$)$_2$), 1.58 (d, $^3J_{H,H}$ = 7.1 Hz, 12H, N-CH(CH$_3$)$_2$). H-IPr$_2$Me$_2$ OTf: 8.85 (s, 1H, H-CN$_2$), 4.47 (sept, $^3J_{H,H}$ = 6.8 Hz, 2H, N-CHMe$_2$), 2.34 (s, 6H, C$_2$(CH$_3$)$_3$), 1.58 (d, $^3J_{H,H}$ = 6.8 Hz, 12H, N-CH(CH$_3$)$_2$).

^{13}C{^{1}H}-NMR: (126 MHz, 298 K, CD$_2$Cl$_2$): 147.79 (d, $^1J_{P,C}$ = 144.2 Hz, CN$_2$), 129.63 (d, $^3J_{P,C}$ = 3.2 Hz, C$_2$Me$_2$), 121.40 (q, $^1J_{F,C}$ = 321.3 Hz, S-CF$_3$), 54.67 (d, J = 9.0 Hz, N-CHMe$_2$), 50.83 (d, $^2J_{P,C}$ = 14.3 Hz, C$_2$H$_4$), 36.15 (d, $^2J_{P,C}$ = 26.1 Hz, N-CH$_3$), 21.66 (s, N-CH(CH$_3$)$_2$), 11.20 (s, C$_2$(CH$_3$)$_2$).

^{31}P{^{1}H}-NMR: (202 MHz, 298 K, CD$_2$Cl$_2$): 103.6 (s).

8.7.44. Synthesis of [2-(1,3-bisdiisopropyl-4,5-dimethyl-imidazolium-2-yl)-1,3-di(1-methylethyl)-1,3,2-diazaphospholidine] triflate (74f)

3f **74f**
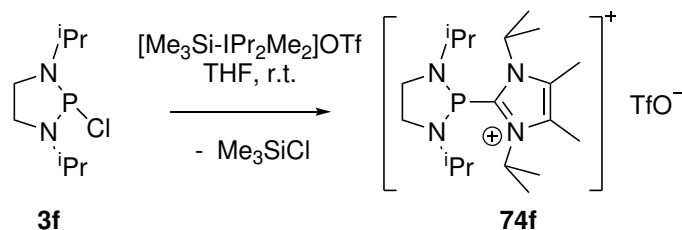
Synthesis: In a 50 mL Schlenk tube 194 mg **3f** were dissolved in 15 mL THF and 376 mg [Me$_3$Si-IPr2Me$_2$]OTf was added as a solid at once. After 1 hour all volatiles were removed under reduced pressure and the residue was washed with 10 mL (5+3+2 mL) *n*-pentane and dried. The colourless solid was obtained as a colourless powder and with a 200% contamination of [H-IPr$_2$Me$_2$]OTf.

Reaction code: PB-474, 36t4b063.22
Molecular formula: C$_{20}$H$_{38}$N$_4$PO$_3$SF$_3$
Molecular weight: 502.58 g mol^{-1}
Yield: 293 mg (200% H-IPr$_2$Me$_2$ OTf)
^{1}H-NMR: (400 MHz, 298 K, CD$_2$Cl$_2$): 5.73 – 5.56 (m, 2H, carbene N-CHMe$_2$), 3.42 (dsept, $^3J_{P,H}$ = 9.4 Hz, $^3J_{H,H}$ = 6.5 Hz, 2H, P-N-CHMe$_2$), 3.36 – 3.24 (m, 2H, C$_2$H$_4$), 3.23 – 3.12 (m, 2H, C$_2$H$_4$), 2.35 (s, 6H, C$_2$(CH$_3$)$_2$), 1.57 (d, $^3J_{H,H}$ = 6.8 Hz, 12H, carbene N-CH(CH$_3$)$_2$), 1.18 (d, $^3J_{H,H}$ = 6.4 Hz, 6H, P-N-CH(CH$_3$)$_2$), 1.16 (d, $^3J_{H,H}$ = 6.4 Hz, 6H, P-N-CH(CH$_3$)$_2$).
^{31}P{^{1}H}-NMR: (202 MHz, 298 K, MeCN-*d*3): 94.1 (s).

8.7.45. Synthesis of [1,3-bis(2,4,6-trimethylphenyl)imidazolium-2-yl(diphenyl)phosphane P-oxide] triflate (75d)

26d **75d**
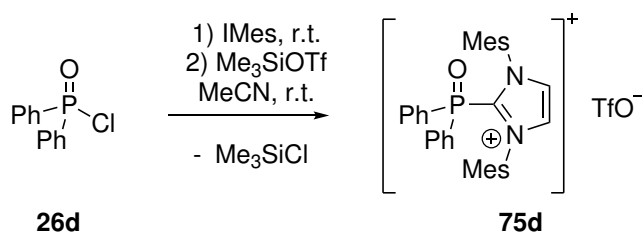
Synthesis: In a 10 mL Schlenk tube 168 mg **26d** were dissolved in 5 mL MeCN and 216 mg

205

IMes was added as a solid at once. After 2 hours 0.13 mL Me$_3$SiOTf were added and the reaction was stirred for further 30 minutes before all volatiles were removed under reduced pressure and the residue was washed with a mixture of THF/Et$_2$O (1:2) and dried to obtain the product as a colourless powder in good yield. Single crystals can be grown from slow diffusion of Et$_2$O into a saturated MeCN solution of **75d**.

Other reaction protocols discussed in this work are usually contaminated with [H-IMes]OTf and are therefore not reported here.

Reaction code: PB-567, PCB230314p5a018

Crystallographic code: GXray7032

Molecular formula: C$_{34}$H$_{34}$N$_2$PO$_4$SF$_3$

Molecular weight: 654.69 g mol^{-1}

Yield: 347 mg, 75%

Melting point: >260 °C

Elemental analysis:

calculated (%) C 62.38 H 5.23 N 4.28 S 4.90 , found (%) C 62.28 H 5.47 N 4.18 S 4.78

MS: ((+)-ESI): m/z (%) 505.241 [M]$^+$, 489.245 [M-O]$^+$, 305.201 [H-IMes]$^+$; ((−)-ESI): m/z (%) 148.9 [OTf]$^-$.

HR-MS: ((+)-ESI): m/z (%)) C$_{33}$H$_{34}$N$_2$PO$_3$ calc.: 505.2403, found: 505.2400.

^{1}H-NMR: (500 MHz, 298 K, MeCN-d3): 7.82 (d, $^4J_{P,H}$ = 1.7 Hz, 2H, C$_2$H$_2$), 7.65 − 7.59 (m, 4H, P-C$_6$H$_5$), 7.52 − 7.46 (m, 2H, *para*-P-C$_6$H$_5$), 7.33 − 7.26 (m, 4H, P-C$_6$H$_5$), 6.69 (s, 4H, N-C$_6$H$_2$Me$_3$), 2.18 (s, 6H, *para*-N-C$_6$H$_2$(CH$_3$)$_3$), 2.05 (s, 12H, *ortho*-N-C$_6$H$_2$(CH$_3$)$_3$).

^{13}C{^{1}H}-NMR: (126 MHz, 298 K, CD$_2$Cl$_2$): 142.74 (s, N-C$_6$H$_2$Me$_3$), 142.54 (d, $^1J_{P,C}$ = 85 Hz, P-CN$_2$), 135.74 (s, N-C$_6$H$_2$Me$_3$), 134.29 (d, $^XJ_{P,C}$ = 3 Hz, P-C$_6$H$_5$), 131.77 (d, $^XJ_{P,C}$ = 10 Hz, P-C$_6$H$_5$), 131.51 (s, N-C$_6$H$_2$Me$_3$), 130.40 (s, *meta*-N-C$_6$H$_2$Me$_3$), 129.89 (d, $^XJ_{P,C}$ = 13.3 Hz, P-C$_6$H$_5$), 129.35 (d, $^4J_{P,C}$ = 3.1 Hz, C$_2$H$_2$), 127.34 (d, $^1J_{P,C}$ = 114.4 Hz, *ipso*-P-C$_6$H$_5$), 122.20 (q, $^1J_{F,C}$ = 321 Hz, S-CF$_3$), 20.95 (s, *para*-N-C$_6$H$_2$(CH$_3$)$_3$), 18.25 (s, *ortho*-N-C$_6$H$_2$(CH$_3$)$_3$).

^{19}F{^{1}H}-NMR: (471 MHz, 298 K, MeCN-d3): −79.3 (s).

^{31}P{^{1}H}-NMR: (202 MHz, 298 K, MeCN-d3): −7.1 (s).

8.7.46. Synthesis of [2-(1,3-bis(2,4,6-trimethylphenyl)imidazolium-2-yl)-1,3-dimethyl-1,3,2-diazaphospholidine-2-oxide] triflate (75e)
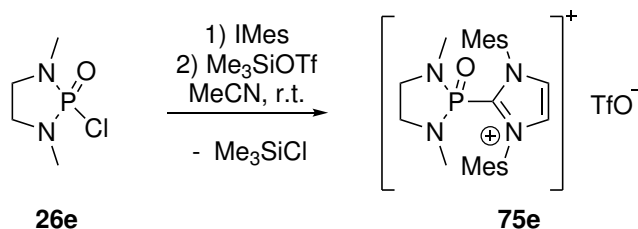
Synthesis: In a 10 mL Schlenk tube 111 mg **26e** were dissolved in 5 mL MeCN and 200 mg IMes was added as a solid at once. After 2 hours 0.12 mL Me_3SiOTf were added and the reaction was stirred for further 30 minutes before all volatiles were removed under reduced pressure and the residue was washed with a mixture of THF/Et_2O (1:2) and dried to obtain the product as a colourless powder in moderate yield. Single crystals can be grown from slow diffusion of Et_2O into a saturated MeCN solution of **75e**.

Reaction code: PB-566, PCB230314p5a019

Crystallographic code: GXray6975

Molecular formula: $C_{26}H_{34}N_4PO_4SF_3$

Molecular weight: 586.61 g mol^{-1}

Yield: 200 mg, 52%

Melting point: 242 °C

Elemental analysis:

calculated (%) C 53.24 H 5.84 N 9.55 S 5.47, found (%) C 52.99 H 6.17 N 9.49 S 5.49

MS: ((+)-ESI): m/z (%) 437.246 [M]$^+$, 305.201 [H-IMes]$^+$; ((−)-ESI): m/z (%) 148.9 [OTf]$^-$.

^{1}H-NMR: (500 MHz, 298 K, MeCN-$d3$): 7.73 (d, $^4J_{P,H}$ = 2.1 Hz, 2H, C_2H_2), 7.17 (s, 4H, N-$C_6H_2Me_3$), 2.92 − 2.82 (m, 2H, C_2H_4), 2.41 (d, $^3J_{P,H}$ = 9.9 Hz, 6H, N-CH_3), 2.38 (s, 6H, *para*-N-$C_6H_2(CH_3)_3$), 2.27 − 2.18 (m, 2H, C_2H_4), 2.10 (s, 12H, *ortho*-N-$C_6H_2(CH_3)_3$).

^{13}C{^{1}H}-NMR: (126 MHz, 298 K, CD_2Cl_2): 143.90 (d, $^1J_{P,C}$ = 170 Hz, P-CN_2), 142.14 (s, N-$C_6H_2Me_3$), 135.50 (s, N-$C_6H_2Me_3$), 133.61 (s, N-$C_6H_2Me_3$), 130.40 (s, *meta*-N-$C_6H_2Me_3$), 128.66 (d, 4J = 5.5 Hz, C_2H_2), 122.19 (q, $^1J_{F,C}$ = 321 Hz, S-CF_3), 47.01 (d, $^2J_{P,C}$ = 15 Hz, C_2H_4), 32.49 (d, $^2J_{P,C}$ = 6 Hz, N-CH_3), 21.19 (s, *para*-N-$C_6H_2(CH_3)_3$), 17.86 (s, *ortho*-N-$C_6H_2(CH_3)_3$).

^{19}F{^{1}H}-NMR: (471 MHz, 298 K, MeCN-$d3$): −79.3 (s).

^{31}P{^{1}H}-NMR: (202 MHz, 298 K, MeCN-$d3$): 8.7 (s).

8.7.47. Synthesis of

[1,3-bisdiisopropyl-4,5-dimethyl-imidazolium-2-yl(diphenyl)phosphane
P-oxide] triflate (76d)
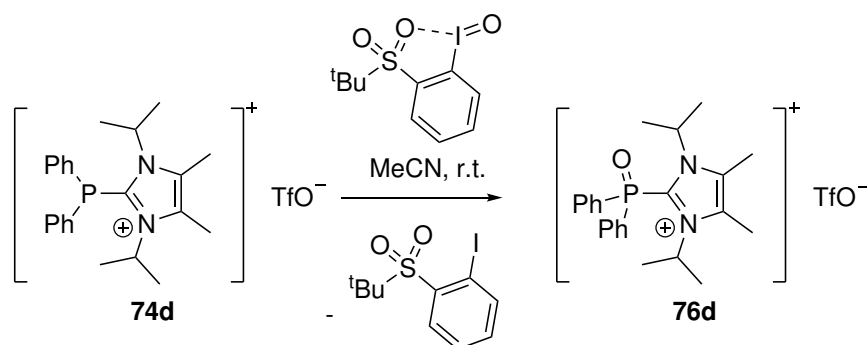
Synthesis: In a 10 mL Schlenk tube 160 mg **74d** were dissolved in 3 mL MeCN and 19 mg of the iodosylbenzene **XLVIII** were added as a solid at once. The reaction was stirred for 16 hours and the solvent was removed under reduced pressure. The residue was dissolved in 1 mL THF and Et$_2$O was added dropwise until a formed precipitate just dissolved again and the solution was kept in the fridge overnight. Formed crystals were filtered from the supernatant and washed with 2x1 mL Et$_2$O before drying. The product was obtained as colourless crystals, which had crystallised with 15% of **74d**.

Other methods, which were discussed in this thesis have been applied to obtained **76d**, but failed.

Reaction code: PB-579, PCB230323p5a057

Molecular formula: C$_{24}$H$_{30}$N$_2$PO$_4$SF$_3$

Molecular weight: 530.54 g mol^{-1}

Yield: 83 mg, 50%

Melting point: 177 °C

^{1}H-NMR: (300 MHz, 298 K, MeCN-*d*3): 7.84 − 7.75 (m, 6H, P-C$_6$H$_5$), 7.72 − 7.62 (m, 4H, P-C$_6$H$_5$), 5.27 (m, 2H, 2xN-CHMe$_2$), 2.39 (s, 6H, C$_2$(CH$_3$)$_2$), 1.27 (d, $^3J_{H,H}$ = 7.0 Hz, 12H, N-CH(CH$_3$)$_2$).

^{13}C{^{1}H}-NMR: (126 MHz, 298 K, MeCN-*d*3): 135.4 (d, $^4J_{P,C}$ = 3 Hz, P-C$_6$H$_5$), 134.11 (s, C$_2$Me$_2$), 133.0 (d, $^XJ_{P,C}$ = 11 Hz, P-C$_6$H$_5$), 132.80, 131.23, 130.83 (d, $^XJ_{P,C}$ = 13 Hz, P-C$_6$H$_5$), 130.60 (d, J = 6.4 Hz), 130.28 (d, $^1J_{P,C}$ = 114.9 Hz, *ipso*-(P-C$_6$H$_5$)), 130.02 (d, J = 8.4 Hz), 122.20 (q, $^1J_{F,C}$ = 321 Hz, S-CF$_3$), 53.67 (s, N-CHMe$_2$), 20.70 (s, N-CH(CH$_3$)$_2$), 11.59 (s, C$_2$(CH$_3$)$_2$).

^{19}F{^{1}H}-NMR: (471 MHz, 298 K, MeCN-*d*3): −79.3 (s).

^{31}**P{^{1}H}-NMR**: (122 MHz, 298 K, MeCN-*d*3): −22.2 (s).

8.7.48. Synthesis of [2-(1-(2,6-(1-methylethyl)phenyl)-3,3,5,5-tetramethyl-azolidinium)diphenylphosphane oxide] triflate (78d)
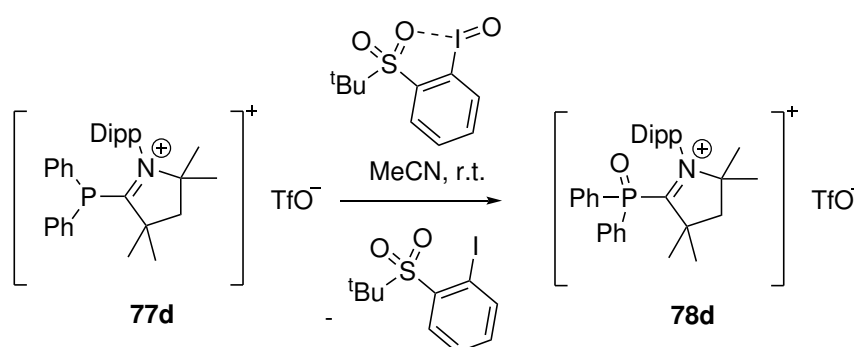
Synthesis: In a 10 mL Schlenk tube 97 mg **77d** were dissolved in 5 mL MeCN. To the bright yellow solution 84 mg of the iodosylbenzene **XLVIII** were added as a solid at once. After the addition the solution immediately becomes colourless and is stirred for 16 hours over night. The solvent is removed and thoroughly dried and subsequently washed twice with 5 mL Et$_2$O and a drop of THF. Final washing of the colourless solid with 3x2 mL *n*-pentane yields the product in good yield.

Reaction code: PB-575, PCB230318t5a036
Molecular formula: C$_{33}$H$_{41}$NPO$_4$SF$_3$
Molecular weight: 635.72 g mol^{-1}
Yield: 84 mg, 85%
^{1}**H-NMR**: (500 MHz, 298 K, MeCN-*d*3): 7.86 − 7.80 (m, 2H, *para*-P-C$_6$H$_5$), 7.80 − 7.72 (m, 4H, P-C$_6$H$_5$), 7.72 − 7.65 (m, 4H, P-C$_6$H$_5$), 7.53 (m, 1H, *para*-CHDipp), 7.42 − 7.38 (m, 2H,*meta*-CHDipp), 2.68 (hept, $^3J_{H,H}$ = 6.5 Hz, 2H, -CHMe$_2$), 2.56 (s, 2H, CH$_2$), 1.52 (s, 6H, P-C-C(CH$_3$)$_2$,), 1.38 (d, 3JH;H = 6.4 Hz, 6H, -CH(CH$_3$)$_2$), 1.26 (s, 6H, N-CMe$_2$), 1.00 (d, $^3J_{H,H}$ = 6.5 Hz, 6H, -CH(CH$_3$)$_2$).
^{31}**P{^{1}H}-NMR**: (162 MHz, 298 K, MeCN-*d*3): 24.5 (s).

9. References

[1] W. Newman, *Atoms and Alchemy: Chymistry and the experimental Origins of the Scientific Revolution*, The University of Chicago Press, **2006**.

[2] J. Wisniak, *Indian J. Chem. Techn.* **2005**, *12*, 108–122.

[3] U. Veronesi, M. Martinón-Torres, *Angew. Chem. Int. Ed.* **2018**, *57*, 7346–7350.

[4] R. G. W. Anderson, *Instruments and Experimentation in the History of Chemistry*, MIT Press, **2000**.

[5] F. Lüdy-Tenger, *Alchemistische und chemische Zeichen*, Gesellschaft für Geschichte der Pharmazie, **1928**.

[6] M. Pereira, *Speculum.* **1999**, *74*, 336–356.

[7] G. de Morveau, A. L. Lavoisier, L. Berthollet, A. F. de Fourcroy, *Méthode de nomenclature chimique*, Paris, **1787**.

[8] J. Liebig, *Ann. Chim.* **1838**.

[9] E. Frankland, *Q. J. Chem. Soc.* **1850**, *2*, 263–296.

[10] D. Seyferth, *Organometallics* **2001**, *20*, 2940–2955.

[11] D. Seyferth, *Organometallics* **2001**, *20*, 1488–1498.

[12] M. Gomberg, *J. Am. Chem. Soc.* **1900**, *22*, 757–771.

[13] E. Krause, H. Polack, *Ber. Dtsch. Chem. Ges.* **1926**, *59*, 777–785.

[14] E. Weitz, H. W. Schwechten, *Ber. Dtsch. Chem. Ges.* **1926**, *59*, 2307–2314.

[15] H. Wieland, M. Offenbächer, *Ber. Dtsch. Chem. Ges.* **1914**, *47*, 2111–2115.

[16] F. Ramirez, N. McKelvie, *J. Am. Chem. Soc.* **1957**, *79*, 5829–5830.

[17] S. Marque, P. Tordo, in *Top. Curr. Chem.*, volume 250, pages 43–76, **2005**.

[18] W. G. Bentrude, *Acc. Chem. Res.* **1982**, *15*, 117–125.

[19] C. Walling, R. Rabinowitz, *J. Am. Chem. Soc.* **1959**, *81*, 1243–1249.

[20] K. B. Mullah, W. G. Bentrude, *J. Org. Chem.* **1991**, *56*, 7218–7224.

[21] K. P. Dockery, W. G. Bentrude, *J. Am. Chem. Soc.* **1997**, *119*, 1388–1399.

[22] J. A. Rossi-Ashton, A. K. Clarke, W. P. Unsworth, R. J. Taylor, *ACS Catal.* **2020**, *10*, 7250–7261.

[23] J. Maddigan-Wyatt, J. F. Hooper, *Adv. Synth. Catal.* **2021**, *363*, 924–936.

[24] R. L. Powell, C. D. Hall, *J. Am. Chem. Soc.* **1969**, *91*, 5403–5404.

[25] B. Merzougui, Y. Berchadsky, P. Tordo, G. Gronchi, *Electrochim. Acta* **1997**, *42*, 2445–2453.

[26] X. Pan, X. Chen, T. Li, Y. Li, X. Wang, *J. Am. Chem. Soc.* **2013**, *135*, 3414–3417.

[27] J. M. Barks, B. C. Gilbert, A. F. Parsons, B. Upeandran, *Tetrahedron Lett.* **2001**, *42*, 3137–3140.

[28] D. Chen, Z. Wu, Y. Yao, C. Zhu, *Org. Chem. Front.* **2018**, *5*, 2370–2374.

[29] J. Liu, H.-Z. Xiao, Q. Fu, D.-G. Yu, *Chem. Synth.* **2021**, *9*, 1–52.

[30] J. P. Fisher, M. D. Timmer, T. A. Holland, D. Dean, P. S. Engel, A. G. Mikos, *Biomacromolecules* **2003**, *4*, 1327–1334.

[31] S. Benedikt, J. Wang, M. Markovic, N. Moszner, K. Dietliker, A. Ovsianikov, H. Grützmacher, R. Liska, *J. Polym. Sci., Part A: Polym. Chem.* **2016**, *54*, 473–479.

[32] I. Kunio, E. Takeshi, *Dent. Mater. J.* **2010**, *29*, 481–501.

[33] A. Kowalska, J. Sokolowski, K. Bociong, *Polymers* **2021**, *13*, 470.

[34] D. Darvasiová, Z. Barberiková, A. Eibel, M. Schmallegger, G. Gescheidt, M. Zalibera, D. Neshchadin, *Polym. Chem.* **2017**, *8*, 6943–6947.

[35] S. Jockusch, V. I. Koptyug, P. F. McGarry, G. W. Sluggett, N. J. Turro, D. M. Watkins, *J. Am. Chem. Soc.* **1997**, *119*, 11495–11501.

[36] G. W. Sluggett, P. F. McGarry, V. I. Koptyug, N. J. Turro, *J. Am. Chem. Soc.* **1996**, *118*, 7367–7372.

[37] S. Jockusch, N. J. Turro, *J. Am. Chem. Soc.* **1998**, *120*, 11773–11777.

[38] G. W. Sluggett, C. Turro, M. W. George, I. V. Koptyug, N. J. Turro, *J. Am. Chem. Soc.* **1995**, *117*, 5148–5153.

[39] D. Griller, B. P. Roberts, A. G. Davies, K. U. Ingold, *J. Am. Chem. Soc.* **1974**, *96*, 554–556.

[40] M. J. S. Gynane, A. Hudson, M. F. Lappert, P. P. Power, *J. Chem. Soc., Chem. Commun.* **1976**, pages 623–624.

[41] S. Loss, A. Magistrato, L. Cataldo, S. Hoffmann, M. Geoffroy, U. Röthlisberger, H. Grützmacher, *Angew. Chem. Int. Ed.* **2001**, *40*, 723–726.

[42] S. Ito, M. Kikuchi, M. Yoshifuji, A. J. Arduengo, T. A. Konovalova, L. D. Kispert, *Angew. Chem. Int. Ed.* **2006**, *45*, 4341–4345.

[43] S. Ishida, F. Hirakawa, T. Iwamoto, *J. Am. Chem. Soc.* **2011**, *133*, 12968–12971.

[44] O. Back, M. A. Celik, G. Frenking, M. Melaimi, B. Donnadieu, G. Bertrand, *J. Am. Chem. Soc.* **2010**, *132*, 10262–10263.

[45] P. Agarwal, N. A. Piro, K. Meyer, P. Müller, C. C. Cummins, *Angew. Chem. Int. Ed.* **2007**, *46*, 3111–3114.

[46] O. Back, B. Donnadieu, M. von Hopffgarten, S. Klein, R. Tonner, G. Frenking, G. Bertrand, *Chem. Sci.* **2011**, *2*, 858–861.

[47] X. Pan, X. Wang, Y. Zhao, Y. Sui, X. Wang, *J. Am. Chem. Soc.* **2014**, *136*, 9834–9837.

[48] O. Puntigam, D. Förster, N. A. Giffin, S. Burck, J. Bender, F. Ehret, A. D. Hendsbee, M. Nieger, J. D. Masuda, D. Gudat, *Eur. J. Inorg. Chem.* **2013**, *4*, 2041–2050.

[49] B. S. Huchenski, K. N. Robertson, A. W. Speed, *Eur. J. Org. Chem.* **2020**, *2020*, 5140–5144.

[50] T. Heurich, Z. W. Qu, S. Nožinović, G. Schnakenburg, H. Matsuoka, S. Grimme, O. Schiemann, R. Streubel, *Chem. - Eur. J.* **2016**, *22*, 10102–10110.

[51] S. Ishida, F. Hirakawa, T. Iwamoto, *Chem. Lett.* **2015**, *44*, 94–96.

[52] A. H. Cowley, R. A. Kemp, J. C. Wilburn, *J. Am. Chem. Soc.* **1982**, *104*, 331–332.

[53] Y. Sunada, S. Ishida, F. Hirakawa, Y. Shiota, K. Yoshizawa, S. Kanegawa, O. Sato, H. Nagashima, T. Iwamoto, *Chem. Sci.* **2016**, *7*, 191–198.

[54] B. Ndiaye, S. Bhat, A. Jouaiti, T. Berclaz, G. Bernardinelli, M. Geoffroy, *J. Phys. Chem. A* **2006**, *110*, 9736–9742.

[55] J. Abbenseth, D. Delony, M. C. Neben, C. Würtele, B. de Bruin, S. Schneider, *Angew. Chem. Int. Ed.* **2019**, *58*, 6338–6341.

[56] A. Özbolat Schön, M. Bode, G. Schnakenburg, A. Anoop, M. van Gastel, F. Neese, R. Streubel, *Angew. Chem. Int. Ed.* **2010**, *49*, 6894–6898.

[57] A. Schmer, P. Junker, A. Espinosa Ferao, R. Streubel, *Acc. Chem. Res.* **2021**.

[58] V. Nesterov, S. Schwieger, G. Schnakenburg, S. Grimme, R. Streubel, *Organometallics* **2012**, *31*, 3457–3459.

[59] V. Nesterov, Z.-W. Qu, G. Schnakenburg, S. Grimme, R. Streubel, *Chem. Commun.* **2014**, *50*, 12508–12511.

[60] C. M. García, A. Bauzá, G. Schnakenburg, A. Frontera, R. Streubel, *Chem. Commun.* **2017**, *53*, 933–936.

[61] P. Junker, J. M. Villalba Franco, G. Schnakenburg, V. Nesterov, R. T. Boere, Z. W. Qu, R. Streubel, *Dalton Trans.* **2020**, *49*, 13544–13548.

[62] P. W. Siu, S. C. Serin, I. Krummenacher, T. W. Hey, D. P. Gates, *Angew. Chem. Int. Ed.* **2013**, *52*, 6967–6970.

[63] T. Heurich, V. Nesterov, G. Schnakenburg, Z.-W. Qu, S. Grimme, K. Hazin, D. P. Gates, M. Engeser, R. Streubel, *Angew. Chem. Int. Ed.* **2016**, *55*, 14439–14443.

[64] T. Heurich, Z.-W. Qu, R. Kunzmann, G. Schnakenburg, M. Engeser, S. Nožinović, R. Streubel, *Chem. - Eur. J.* **2018**, *24*, 6473–6478.

[65] T. Heurich, Z.-W. Qu, G. Schnakenburg, Y. NejatyJahromy, O. Schiemann, S. Grimme, R. Streubel, *Organometallics* **2017**, *36*, 2877–2883.

[66] T. Heurich, N. R. Naz, Z.-W. Qu, G. Schnakenburg, R. Streubel, *Organometallics* **2018**, *37*, 3670–3677.

[67] T. Heurich, *Dissertation* **2017**, *University of Bonn*.

[68] M. K. Georges, R. P. N. Veregin, P. M. Kazmaier, G. K. Hamer, *Macromolecules* **1993**, *26*, 2987–2988.

[69] V. Sciannamea, J. Catala, R. Jerome, C. Jérôme, C. Detrembleur, *J. Polym. Sci., Part A: Polym. Chem.* **2009**, *47*, 1085–1097.

[70] C. Zeiher, W. Hiller, I.-P. Lorenz, *Chem. Ber.* **1985**, *118*, 3127–3134.

[71] A. Santini, I. T. Gallegos, C. M. Felix, *Primary dental journal* **2013**, *2*, 30–33.

[72] A. R. Forrester, R. H. Thomson, *Nature* **1964**, *203*, 74–75.

[73] L. Tebben, A. Studer, *Angew. Chem. Int. Ed.* **2011**, *50*, 5034–5068.

[74] J. P. Lomont, S. C. Nguyen, C. B. Harris, *J. Am. Chem. Soc.* **2013**, *135*, 11266–11273.

[75] R. G. Hicks, *Stable Radicals*, John Wiley & Sons, Ltd, Chichester, UK, **2010**.

[76] M. Geoffroy, E. A. Lucken, *Mol. Phys.* **1971**, *22*, 257–262.

[77] M. Guerra, *Chem. Phys. Lett.* **1995**, *237*, 61–64.

[78] P. Kaymak, M. Yang, Z. Benkő, *Dalton Trans.* **2023**, *52*, 13930–13945.

[79] M. A. Wünsche, T. Witteler, F. Dielmann, *Angew. Chem. Int. Ed.* **2018**, *57*, 7234–7239.

[80] Y. Yonekuta, K. Oyaizu, H. Nishide, *Chem. Lett.* **2007**, *36*, 866–867.

[81] G. Huttner, H.-D. Müller, *Angew. Chem.* **1975**, *87*, 596–597.

[82] R. B. King, N. D. Sadanani, P. M. Sundaram, *J. Chem. Soc., Chem. Commun.* **1983**, page 477.

[83] H. Westermann, M. Nieger, E. Niecke, J. P. Majoral, A. M. Caminade, R. Mathieu, E. Irmer, *Organometallics* **1989**, *8*, 244–249.

[84] R. B. King, P. M. Sundaram, *J. Org. Chem.* **1984**, *49*, 1784–1789.

[85] L. K. Oliemuller, C. E. Moore, C. M. Thomas, *Inorg. Chem.* **2022**, *61*, 19440–19451.

[86] J. Zhang, J. Yang, J. Cheng, *Angew. Chem. Int. Ed.* **2019**, *58*, 5983–5987.

[87] S. S. Snow, D. X. Jiang, R. W. Parry, *Inorg. Chem.* **1985**, *24*, 1460–1463.

[88] G.-V. Röschenthaler, R. Bohlen, W. Storzer, *Phosphorus Chemistry* **1981**, pages 443–446.

[89] S. Burck, J. Daniels, T. Gans-Eichler, D. Gudat, K. Nättinen, M. Nieger, *Z. anorg. allg. Chem.* **2005**, *631*, 1403–1412.

[90] L. D. Hutchins, E. N. Duesler, R. T. Paine, *Organometallics* **1984**, *3*, 399–403.

[91] H. Nakazawa, Y. Yamaguchi, T. Mizuta, K. Miyoshi, *Organometallics* **1995**, *14*, 4173–4182.

[92] W. Malisch, K. Hindahl, K. Grün, W. Adam, F. Prechtl, W. S. Sheldrick, *J. Organomet. Chem.* **1996**,

509, 209–214.

[93] E. Groß, K. Jörg, K. Fiederling, A. Göttlein, W. Malisch, R. Boese, *Angew. Chem-ger. Edit.* **1984**, *96*, 705–706.

[94] S. Challet, J. C. Leblanc, C. Moïse, *Phosphorus, Sulfur, Silicon Relat. Elem.* **1994**, *97*, 95–102.

[95] G. I. Nikonov, Y. K. Grishin, D. A. Lemenovskii, N. B. Kazennova, L. G. Kuzmina, J. A. Howard, *J. Organomet. Chem.* **1997**, *547*, 183–198.

[96] Y. X. Ng, F. Mathey, *Angew. Chem. Int. Ed.* **2013**, *52*, 14140–14142.

[97] D. Gudat, A. Haghverdi, M. Nieger, *Angew. Chem. Int. Ed.* **2000**, *39*, 3084–3086.

[98] B. Ndiaye, S. Bhat, A. Jouaiti, T. Berclaz, G. Bernardinelli, M. Geoffroy, *J. Phys. Chem. A* **2006**, *110*, 9736–9742.

[99] H. A. Bent, *Chem. Rev.* **1961**, *61*, 275–311.

[100] N. A. Giffin, A. D. Hendsbee, T. L. Roemmele, M. D. Lumsden, C. C. Pye, J. D. Masuda, *Inorg. Chem.* **2012**, *51*, 11837–11850.

[101] H. Takano, H. Katsuyama, H. Hayashi, W. Kanna, Y. Harabuchi, S. Maeda, T. Mita, *Nat. Commun.* **2022**, *13*.

[102] B. Pan, Z. Xu, M. W. Bezpalko, B. M. Foxman, C. M. Thomas, *Inorg. Chem.* **2012**, *51*, 4170–4179.

[103] P. C. Brehm, A. S. Müller-Feyen, G. Schnakenburg, R. Streubel, *Dalton Trans.* **2022**, *51*, 4400–4405.

[104] P. M. Treichel, W. K. Dean, W. M. Douglas, *Inorg. Chem.* **1972**, *11*, 1609–1615.

[105] J. B. M. Wit, G. B. de Jong, M. Schakel, M. Lutz, A. W. Ehlers, J. C. Slootweg, K. Lammertsma, *Organometallics* **2016**, *35*, 1170–1176.

[106] J. B. Wit, G. T. Van Eijkel, M. Schakel, K. Lammertsma, *Tetrahedron* **2000**, *56*, 137–141.

[107] A. W. Ehlers, E. J. Baerends, K. Lammertsma, *J. Am. Chem. Soc.* **2002**, *124*, 2831–2838.

[108] T. A. Manuel, *Inorg. Chem.* **1963**, *2*, 854–858.

[109] R. Batchelor, T. Birchall, *J. Am. Chem. Soc.* **1982**, *104*, 674–679.

[110] J. P. Collman, R. G. Komoto, W. O. Siegl, *J. Am. Chem. Soc.* **1973**, *95*, 2389–2390.

[111] W. Petz, F. Weller, *Z. Naturforsch. B* **1996**, *51*, 715–721.

[112] R. B. King, W. K. Fu, *Inorg. Chem.* **1986**, *25*, 2384–2389.

[113] R. Benn, A. Rufińska, *Magn. Reson. Chem.* **1988**, *26*, 895–902.

[114] D. W. Bennett, R. J. Neustadt, R. W. Parry, F. W. Cagle, *Acta Crystallogr. B.* **1978**, *34*, 3362–3364.

[115] A. H. Cowley, R. A. Kemp, *Chem. Rev.* **1985**, *85*, 367–382.

[116] T. Saito, H. Nishiyama, H. Tanahashi, K. Kawakita, H. Tsurugi, K. Mashima, *J. Am. Chem. Soc.* **2014**, *136*, 5161–5170.

[117] L. P. Ho, A. Nasr, P. G. Jones, A. Altun, F. Neese, G. Bistoni, M. Tamm, *Chem. Eur. J.* **2018**, *24*, 18922–18932.

[118] Z. Li, J. E. Borger, F. Müller, J. R. Harmer, C. Su, H. Grützmacher, *Angew. Chem. Int. Ed.* **2019**, *58*, 11429–11433.

[119] J. J. Brunet, R. Chauvin, O. Diallo, F. Kindela, P. Leglaye, D. Neibecker, *Coord. Chem. Rev.* **1998**, *178-180*, 331–351.

[120] J.-J. Brunet, R. Chauvin, O. Diallo, B. Donnadieu, J. Jaffart, D. Neibecker, *J. Organomet. Chem.* **1998**, *570*, 195–200.

[121] B. Stadelmann, J. Bender, D. Förster, W. Frey, M. Nieger, D. Gudat, *Dalton Trans.* **2015**, *44*, 6023–6031.

[122] Y. C. Shi, Y. Shi, W. Yang, *J. Organomet. Chem.* **2014**, *772*, 131–138.

[123] A. Baschieri, R. Amorati, L. Valgimigli, L. Sambri, *J. Org. Chem.* **2019**, *84*, 13655–13664.

[124] R. Kunzmann, Y. Omatsu, G. Schnakenburg, A. Espinosa Ferao, T. Yanagisawa, N. Tokitoh, R. Streubel, *Chem. Commun.* **2020**, *56*, 3899–3902.

[125] M. J. Graham, J. M. Zadrozny, M. Shiddiq, J. S. Anderson, M. S. Fataftah, S. Hill, D. E. Freedman, *J. Am. Chem. Soc.* **2014**, *136*, 7623–7626.

[126] D. W. O. De Sousa, M. A. C. Nascimento, *Phys. Chem. Chem. Phys.* **2019**, *21*, 13340–13357.

[127] J. M. Rall, M. Schorpp, M. Keilwerth, M. Mayländer, C. Friedmann, M. Daub, S. Richert, K. Meyer, I. Krossing, *Angew. Chem. Int. Ed.* **2022**, *61*.

[128] J. H. MacNeil, A. C. Chiverton, S. Fortier, M. C. Baird, R. C. Hynes, A. J. Williams, K. F. Preston, T. Ziegler, *J. Am. Chem. Soc.* **1991**, *113*, 9834–9842.

[129] S. A. Cockle, *Biochem. J.* **1974**, *137*, 587–596.

[130] F. Kennedy, H. Hill, T. A. Kaden, B. L. Vallee, *Biochem. Biophys. Res. Commun.* **1972**, *48*, 1533–1539.

[131] A. A. Pavlov, J. Nehrkorn, Y. A. Pankratova, M. Ozerov, E. A. Mikhalyova, A. V. Polezhaev, Y. V. Nelyubina, V. V. Novikov, *Phys. Chem. Chem. Phys.* **2019**, *21*, 8201–8204.

[132] Y. Zang, J. Kim, Y. Dong, E. C. Wilkinson, E. H. Appelman, L. Que, *J. Am. Chem. Soc.* **1997**, *119*, 4197–4205.

[133] R. Krzyminiewski, Z. Kruczynski, B. Dobosz, A. Zajac, A. Mackiewicz, E. Leporowska, S. Folwaczna, *Appl. Magn. Reson.* **2011**, *40*, 321–330.

[134] J. T. Weisser, M. J. Nilges, M. J. Sever, J. J. Wilker, *Inorg. Chem.* **2006**, *45*, 7736–7747.

[135] R. H. Herber, W. R. Kingston, G. K. Wertheim, *Inorg. Chem.* **1963**, *2*, 153–158.

[136] J. Ensling, P. Gütlich, L. Rösch, *Z. Naturforsch. B* **1975**, *30*, 850–853.

[137] R. L. Collins, R. Pettit, *J. Chem. Phys.* **1963**, *39*, 3433–3436.

[138] V. K. Sharma, Z. Homonnay, T. Nishida, J.-M. Greneche, *J. Mater. Res.* **2023**, *38*, 925–936.

[139] S. Kubuki, Y. Watanabe, K. Akiyama, M. Ristić, S. Krehula, Z. Homonnay, E. Kuzmann, T. Nishida, in *AIP Conference Proceedings*, AIP Publishing LLC, **2014** pages 134–141.

[140] J.-C. Jumas, M. Womes, R. Alcántara, P. Lavela, J. L. Tirado, *Hyperfine Interact.* **2008**, *183*, 1–5.

[141] H.-Y. Hah, *Dissertation* **2018**, *The University of Tennessee, Knoxville*.

[142] M. P. Hendrich, P. G. Debrunner, *Biophys. J.* **1989**, *56*, 489–506.

[143] S. J. Yoo, H. C. Angove, B. K. Burgess, M. P. Hendrich, E. Münck, *J. Am. Chem. Soc.* **1999**, *121*, 2534–2545.

[144] A. J. Hofmann, C. Jandl, C. R. Hess, *Eur. J. Inorg. Chem.* **2020**, *2020*, 499–505.

[145] T. H. Moss, A. B. Robinson, *Inorg. Chem.* **1968**, *7*, 1692–1694.

[146] T. Birchall, N. N. Greenwood, J. A. McCleverty, *Nature* **1967**, *215*, 625–626.

[147] B. W. Roberts, J. Wong, *J. Chem. Soc., Chem. Commun.* **1977**, page 20.

[148] H. D. Murdoch, E. Weiss, *Helv. Chim. Acta* **1963**, *46*, 1588–1594.

[149] A. Marinetti, L. Ricard, F. Mathey, *Organometallics* **1990**, *9*, 788–793.

[150] R. Appei, C. Casser, F. Knoch, *J. Organomet. Chem.* **1985**, *297*, 21–26.

[151] A.-M. Caminade, J.-P. Majoral, R. Mathieu, Y. Y. C. Y. L. Ko, *J. Chem. Soc., Chem. Commun.* **1987**, page 639.

[152] R. Mathieu, A. M. Caminade, J. P. Majoral, S. Attali, M. Sanchez, *Organometallics* **1986**, *5*, 1914–1916.

[153] H. Berke, W. Bankhardt, G. Huttner, J. v. Seyerl, L. Zsolnai, *Chem. Ber.* **1981**, *114*, 2754–2768.

[154] F. Delbecq, P. Sautet, *J. Am. Chem. Soc.* **1992**, *114*, 2446–2455.

[155] P. Macchi, *Coordination Chemistry Reviews* **2003**, *238–239*, 383–412.

[156] C. Foroutan-Nejad, S. Shahbazian, R. Marek, *Chem. Eur. J.* **2014**, *20*, 10140–10152.

[157] A. N. Desnoyer, W. He, S. Behyan, W. Chiu, J. A. Love, P. Kennepohl, *Chem. Eur. J.* **2019**, *25*, 5259–5268.

[158] P. C. Brehm, A. Frontera, R. Streubel, *Chem. Commun.* **2022**, *58*, 6270–6279.

[159] H. Zhu, Z.-W. Qu, S. Grimme, P. C. Brehm, R. Streubel, *Dalton Trans.* **2023**, *52*, 2356–2362.

[160] D. Biskup, G. Schnakenburg, R. T. Boeré, A. Espinosa Ferao, R. K. Streubel, *Nat. Commun.* **2023**, *14*.

[161] D. Biskup, G. Schnakenburg, R. T. Boeré, A. Espinosa Ferao, R. Streubel, *Dalton Trans.* **2023**, *52*, 13781–13786.

[162] R. Hoffmann, *Angew. Chem. Int. Ed.* **1982**, *21*, 711–724.

[163] A. Igau, A. Baceiredo, G. Trinquier, G. Bertrand, *Angew. Chem.* **1989**, *101*, 617–618.

[164] A. J. Arduengo, R. L. Harlow, M. Kline, *J. Am. Chem. Soc.* **1991**, *113*, 361–363.

[165] X.-F. Zhang, M.-J. Sun, Z.-X. Cao, *Theor. Chem. Acc.* **2016**, *135*, 163.

[166] F. Glorius, *N-Heterocyclic Carbenes in Transition Metal Catalysis*, volume 21 of *Topics in Organometallic Chemistry*, Springer Berlin Heidelberg, Berlin, Heidelberg, **2007**.

[167] S. Díez-González, N. Marion, S. P. Nolan, *Chem. Rev.* **2009**, *109*, 3612–3676.

[168] Vivancos, C. Segarra, M. Albrecht, *Chem. Rev.* **2018**, *118*, 9493–9586.

[169] R. H. Crabtree, *Coord. Chem. Rev.* **2013**, *257*, 755–766.

[170] S. Fantasia, J. L. Petersen, H. Jacobsen, L. Cavallo, S. P. Nolan, *Organometallics* **2007**, *26*, 5880–5889.

[171] R. L. Lord, H. Wang, M. Vieweger, M.-H. Baik, *J. Organomet. Chem.* **2006**, *691*, 5505–5512.

[172] V. Lavallo, Y. Canac, C. Präsang, B. Donnadieu, G. Bertrand, *Angew. Chem. Int. Ed.* **2005**, *44*, 5705–5709.

[173] M. Soleilhavoup, G. Bertrand, *Acc. Chem. Res.* **2015**, *48*, 256–266.

[174] S. Kumar Kushvaha, A. Mishra, H. W. Roesky, K. Chandra Mondal, *Chem. Asian J.* **2022**, *17*.

[175] S. Kundu, S. Sinhababu, V. Chandrasekhar, H. W. Roesky, *Chem. Sci.* **2019**, *10*, 4727–4741.

[176] C. D. Martin, M. Soleilhavoup, G. Bertrand, *Chem. Sci.* **2013**, *4*, 3020–3030.

[177] K. Breitwieser, H. Bahmann, R. Weiss, D. Munz, *Angew. Chem. Int. Ed.* **2022**, *61*.

[178] Y. J. Lin, W. C. Liu, Y. H. Liu, G. H. Lee, S. Y. Chien, C. W. Chiu, *Nat. Commun.* **2022**, *13*, 1–8.

[179] H. Song, E. Pietrasiak, E. Lee, *Acc. Chem. Res.* **2022**, *55*, 2213–2223.

[180] T. Taniguchi, *Chem. Soc. Rev.* **2021**, *50*, 8995–9021.

[181] P. J. Krusic, P. Meakin, *Chem. Phys. Lett.* **1973**, *18*, 347–350.

[182] L. Gu, Y. Zheng, E. Haldón, R. Goddard, E. Bill, W. Thiel, M. Alcarazo, *Angew. Chem. Int. Ed.* **2017**, *56*, 8790–8794.

[183] Y. Xiong, S. Yao, M. Driess, *J. Am. Chem. Soc.* **2009**, *131*, 7562–7563.

[184] C. Maaliki, C. Lepetit, C. Duhayon, Y. Canac, R. Chauvin, *Chem. Eur. J.* **2012**, *18*, 16153–16160.

[185] M. H. Holthausen, M. Mehta, D. W. Stephan, *Angew. Chem. Int. Ed.* **2014**, *53*, 6538–6541.

[186] J. J. Weigand, N. Burford, D. Mahnke, A. Decken, *Inorg. Chem.* **2007**, *46*, 7689–7691.

[187] A. D. Hendsbee, N. A. Giffin, Y. Zhang, C. C. Pye, J. D. Masuda, *Angew. Chem-ger. Edit.* **2012**, *124*, 10994–10998.

[188] J. Cui, Y. Li, R. Ganguly, R. Kinjo, *Inorg. Chim. Acta* **2017**, *460*, 2–7.

[189] V. Lavallo, Y. Canac, B. Donnadieu, W. W. Schoeller, G. Bertrand, *Science* **2006**, *312*, 722–724.

[190] B. Tumanskii, D. Sheberla, G. Molev, Y. Apeloig, *Angew. Chem. Int. Ed.* **2007**, *46*, 7408–7411.

[191] Y. Livshits-Kritsman, B. Tumanskii, G. Ménard, R. Dobrovetsky, *Chem. Commun.* **2020**, *56*, 1341–1344.

[192] M. Abdul Jalil, T. Yamada, S. Fujinami, T. Honjo, H. Nishikawa, *Polyhedron* **2001**, *20*, 627–633.

[193] A. P. Marchenko, H. N. Koidan, A. N. Huryeva, V. E. Zarudnitskii, A. A. Yurchenko, A. N. Kostyuk, *J. Org. Chem.* **2010**, *75*, 7141–7145.

[194] A. A. Tolmachev, A. A. Yurchenko, A. S. Merculov, M. G. Semenova, V. E. Zarudnitskii, V. V. Ivanov, A. M. Pinchuk, *Heteroat. Chem.* **1999**, *10*, 585–597.

[195] N. Burford, P. Losier, C. Macdonald, V. Kyrimis, P. K. Bakshi, T. S. Cameron, *Inorg. Chem.* **1994**, *33*, 1434–1439.

[196] V. A. Jones, S. Sriprang, M. Thornton-Pett, T. P. Kee, *J. Organomet. Chem.* **1998**, *567*, 199–218.

[197] T. Hynes, E. N. Welsh, R. McDonald, M. J. Ferguson, A. W. H. Speed, *Organometallics* **2018**, *37*, 841–844.

[198] T. Lundrigan, E. N. Welsh, T. Hynes, C.-H. Tien, M. R. Adams, K. R. Roy, K. N. Robertson, A. W. H. Speed, *J. Am. Chem. Soc.* **2019**, *141*, 14083–14088.

[199] A. W. H. Speed, *Chem. Soc. Rev.* **2020**, *49*, 8335–8353.

[200] J. J. Curley, R. G. Bergman, T. D. Tilley, *Dalton Trans.* **2012**, *41*, 192–200.

[201] M. E. Ul, N. K. Dey, A. K. Guha, C.-K. Kim, B.-S. Lee, H.-W. Lee, *Bull. Korean Chem. Soc.* **2007**, *28*, 1797–1802.

[202] P. W. Antoni, T. Bruckhoff, M. M. Hansmann, *J. Am. Chem. Soc.* **2019**, *141*, 9701–9711.

[203] J. Ruiz, A. F. Mesa, *Chem. Eur. J.* **2012**, *18*, 4485–4488.

[204] J. Ruiz, A. F. Mesa, D. Sol, *Organometallics* **2015**, *34*, 5129–5135.

[205] D. Mendoza-Espinosa, B. Donnadieu, G. Bertrand, *J. Am. Chem. Soc.* **2010**, *132*, 7264–7265.

[206] P. K. Majhi, S. C. Serin, G. Schnakenburg, D. P. Gates, R. Streubel, *Eur. J. Inorg. Chem.* **2014**, *2014*, 4975–4983.

[207] P. K. Majhi, G. Schnakenburg, A. J. Arduengo, R. Streubel, *Aust. J. Chem.* **2015**, *68*, 1282.

[208] N. R. Naz, G. Schnakenburg, Z. Kelemen, D. Gál, L. Nyulászi, R. T. Boeré, R. Streubel, *Dalton Trans.* **2021**, *50*, 689–695.

[209] M. Flores-Jarillo, V. Salazar-Pereda, F. J. Ruiz-Mendoza, A. Alvarez-Hernández, O. R. Suarez-Castillo,

D. Mendoza-Espinosa, *Inorg. Chem.* **2018**, *57*, 28–31.

[210] N. Kuhn, J. Fahl, D. Bläser, R. Boese, *Z. Anorg. Allg. Chem.* **1999**, *625*, 729–734.

[211] D. Macikenas, E. Skrzypczak-Jankun, J. D. Protasiewicz, *J. Am. Chem. Soc.* **1999**, *121*, 7164–7165.

[212] C. W. Chiu, F. P. Gabbaï, *Angew. Chem. Int. Ed.* **2007**, *46*, 1723–1725.

[213] T. Matsumoto, F. P. Gabbai, *Organometallics* **2009**, *28*, 4252–4253.

[214] S. J. Bonyhady, C. Jones, S. Nembenna, A. Stasch, A. J. Edwards, G. J. McIntyre, *Chem. Eur. J.* **2010**, *16*, 938–955.

[215] J. Conradie, *J. Phys. Conf. Ser.* **2015**, *633*, 012045.

[216] Z. Han, R. Kortlever, H. Y. Chen, J. C. Peters, T. Agapie, *ACS Cent. Sci.* **2017**, *3*, 853–859.

[217] J. Krysiak, C. Lyon, A. Baceiredo, H. Gornitzka, M. Mikolajczyk, G. Bertrand, *Chem. - Eur. J.* **2004**, *10*, 1982–1986.

[218] M. D. Hanwell, D. E. Curtis, D. C. Lonie, T. Vandermeersch, E. Zurek, G. R. Hutchison, *J. Cheminf.* **2012**, *4*.

[219] F. Neese, F. Wennmohs, U. Becker, C. Riplinger, *J. Chem. Phys.* **2020**, *152*.

[220] J. Tao, J. P. Perdew, V. N. Staroverov, G. E. Scuseria, *Phys. Rev. Lett.* **2003**, *91*, 146401.

[221] S. Grimme, S. Ehrlich, L. Goerigk, *J. Comput. Chem.* **2011**, *32*, 1456–1465.

[222] S. Grimme, J. Antony, S. Ehrlich, H. Krieg, *J. Chem. Phys.* **2010**, *132*.

[223] F. Weigend, R. Ahlrichs, *Phys. Chem. Chem. Phys.* **2005**, *7*, 3297.

[224] V. Barone, M. Cossi, *J. Phys. Chem. A* **1998**, *102*, 1995–2001.

[225] F. Weigend, *Phys. Chem. Chem. Phys.* **2006**, *8*, 1057.

[226] L. Goerigk, S. Grimme, *J. Chem. Theory Comput.* **2010**, *7*, 291–309.

[227] F. Weigend, *J. Comput. Chem.* **2007**, *29*, 167–175.

[228] A. Hellweg, C. Hättig, S. Höfener, W. Klopper, *Theor. Chem. Acc.* **2007**, *117*, 587–597.

[229] E. F. Pettersen, T. D. Goddard, C. C. Huang, G. S. Couch, D. M. Greenblatt, E. C. Meng, T. E. Ferrin, *J. Comput. Chem.* **2004**, *25*, 1605–1612.

[230] T. Lu, F. Chen, *J. Comput. Chem.* **2011**, *33*, 580–592.

[231] H. E. Gottlieb, V. Kotlyar, A. Nudelman, *J. Org. Chem.* **1997**, *62*, 7512–7515.

[232] O. V. Dolomanov, L. J. Bourhis, R. J. Gildea, J. A. K. Howard, H. Puschmann, *J. Appl. Crystallogr.* **2009**, *42*, 339–341.

[233] R. S. Stojanovic, A. M. Bond, *Anal. Chem.* **1993**, *65*, 56–64.

[234] D. Breen, A. R. Kennedy, C. J. Suckling, *Org. Biomol. Chem.* **2009**, *7*, 178–186.

[235] S. E. Denmark, H. Stadler, R. L. Dorow, J. H. Kim, *J. Org. Chem.* **1991**, *56*, 5063–5079.

[236] A. S. Jones, C. McGuigan, R. T. Walker, *J. Chem. Soc., Perkin Trans. 1* **1985**, page 199.

[237] A. Tromelin, E. D. Manouni, R. Burgada, *Phosphorus, Sulfur, Silicon Relat. Elem.* **1986**, *27*, 301–312.

[238] K. Utvary, V. Gutmann, C. Kemenater, *J. Inorg. Nucl. Chem.* **1965**, *1*, 75–76.

[239] S. H. Wood, S. Etridge, A. R. Kennedy, J. M. Percy, D. J. Nelson, *Chem. Eur. J.* **2019**, *25*, 5574–5585.

[240] T. Imamoto, *Sci. Synth.* **2003**, *2*.

[241] Y. Takegami, Y. Watanabe, H. Masada, I. Kanaya, *Bull. Chem. Soc. Jpn.* **1967**, *40*, 1456–1458.

[242] A. J. Arduengo, R. Krafczyk, R. Schmutzler, H. A. Craig, J. R. Goerlich, W. J. Marshall, M. Unverzagt, *Tetrahedron* **1999**, *55*, 14523–14534.

[243] S. J. Ryan, S. D. Schimler, D. C. Bland, M. S. Sanford, *Organic Letters* **2015**, *17*, 1866–1869.

[244] A. D. Cardenal, A. Maity, W.-Y. Gao, R. Ashirov, S.-M. Hyun, D. C. Powers, *Inorg. Chem.* **2019**, *58*, 10543–10553.

[245] J. Hicks, M. Juckel, A. Paparo, D. Dange, C. Jones, *Organometallics* **2018**, *37*, 4810–4813.

I. Abbreviations

Ar	Aryl	$^i Pr$	iso-propyl
			1-methyl-ethyl
AIM	Atoms in molecules	KS	Kohn-Sham
AZADO	2-azaadamantane-1-oxyl	LAH	Lithium aluminium hydride
BAPO	bisacyl phosphine oxide	LUMO	lowest unoccupied molecular orbital
BDG	bond dissociation free Gibbs energy	MAPO	monoacyl phosphine oxide
Bisyl	bis(trimethylsilyl)methyl	MBO	mayer bond order
cAAC	cyclic alkyl amino carbenes	mCPBA	meta-chloroperoxybenzoic acid
Cp	cyclopentadienyl	Me	methyl
Cp*	pentamethylcyclopentadienyl	MeCN	Acetonitrile
CV	cyclo voltammetry/voltammogram	mer	meridional
CW	continuous wave	Mes	2,4,6-Trimethylphenyl
DCM	dichlormethane	Mes*	2,4,6-Tri(tertbutyl)phenyl
	methylene chloride		2,4,6-Tris(1,1-(dimethyl)ethyl)phenyl
DFT	Density functional theory	$^n Bu$	n-butyl
NacNac	1,3-Diketimine ligand	NHC	N-heterocyclic carbenes
DIBAL–H	diisobutylaluminium hydride	NMR	nuclear magnetic resonance
Dipp	2,4-Di(isopropyl)phenyl	PE	petrol ether
	2,4-Di(1-(methyl)ethyl)phenyl		
Dmp	2,6-dimethylphenyl	QRO	quasi-restricted orbital
Dppe	bisdiphenylphosphanylethylen	SET	single electron transfer
EI	electron ionisation	SDD	spin density distribution
EPR	electron paramagnetic resonance	SOMO	single occupied molecular orbital
SOC	spin orbit coupling	$^t Bu$	tert-butyl
			1,1-dimethylethyl
ESI	electrospray ionisation	TEMPH₂	2,2,6,6-Tetramethylpiperinium cation
Et	ethyl	TEMPO	2,2,6,6-Tetramethylpiperin-1-oxyl
fac	facial	TEMP–H	2,2,6,6-Tetramethylpiperin
Fc/Fc⁺	Ferrocen/Ferrocenium	THF	tetrahydrofurane
FMO	frontier molecular orbitals	Trilfate (OTf⁻)	trifluoromethanesulfonate
FWHM	full width at half maximum	UKS	unrestricted Kohn-Sham
HAT	Hydrogen atom transfer	UV	ultra violet
HOMO	highest occupied molecular orbital	VT	various temperature
h-SOMO	highest single occupied molecular orbital		
IDipp	1,3-Bis(2,6-diisopropylphenyl)imidazole-2-ylidene		
IMe₂	1,3-dimethylimidazole-2-ylidene		
IMes	1,3-Bis(2,4,6-trimethylphenyl)imidazole-2-ylidene		

II. Crystallographic data
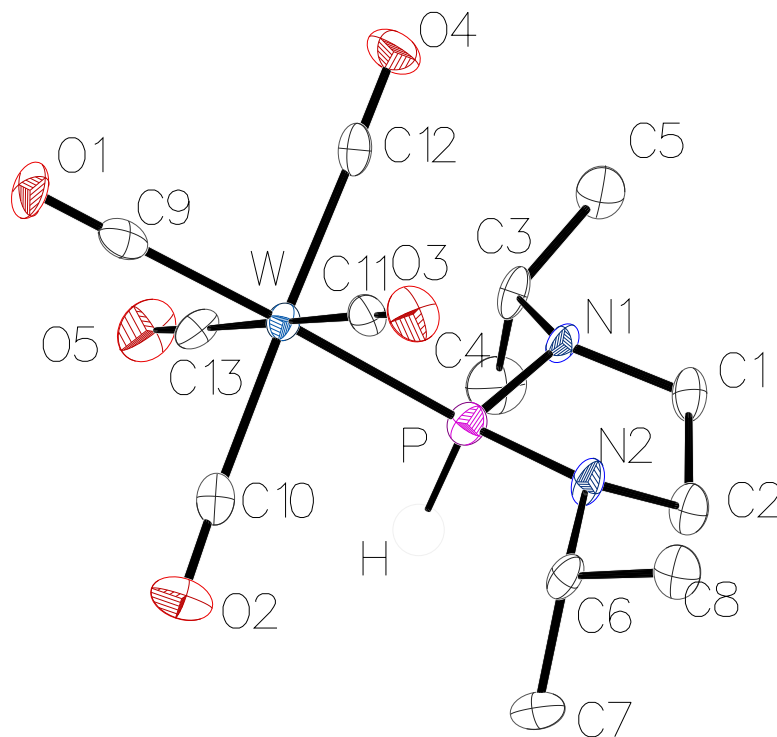
Figure 106: Molecular structure of **6f** in the crystal obtained by X-ray diffraction.

Table 25: Crystal data and structure refinement for **6f**.

Identification code	GSTR696,AMF-38 // GXray6366
Crystal Habitus	clear colourless plate
Device Type	STOE IPDS-2T
Empirical formula	C13H19N2O5PW
Moiety formula	C13 H19 N2 O5 P W
Formula weight	498.12
Temperature/K	123.0
Crystal system	orthorhombic
Space group	P212121
a/Å	8.3463(4)
b/Å	9.9319(5)
c/Å	21.1509(13)
$\alpha/°$	90
$\beta/°$	90
$\gamma/°$	90
Volume/Å^3	1753.30(16)
Z	4
ρ_{calc} g/cm^3	1.887
μ/mm^{-1}	6.701

F(000)	960.0
Crystal size/mm^3	0.12 × 0.1 × 0.06
Absorption correction	integration
Tmin; Tmax	0.3226; 0.5198
Radiation	MoKα (λ = 0.71073)
2Θ range for data collection/°	5.246 to 53.994°
Completeness to theta	0.997
Index ranges	-10 ≤ h ≤ 10, -12 ≤ k ≤ 12, -21 ≤ l ≤ 26
Reflections collected	9246
Independent reflections	3768 [Rint = 0.0402, Rsigma = 0.0830]
Data/restraints/parameters	3768/0/207
Goodness-of-fit on F2	0.641
Final R indexes [I≥2σ (I)]	R1 = 0.0230, wR2 = 0.0314
Final R indexes [all data]	R1 = 0.0347, wR2 = 0.0327
Largest diff. peak/hole / e Å^{-3}	0.73/-0.67
Flack parameter	-0.011(9)

Table 26: Bond Lengths for **6f**.

Atom	Atom	Length/Å	Atom	Atom	Length/Å
W	P	2.4611(18)	O4	C12	1.154(8)
W	C9	2.015(7)	O5	C13	1.142(8)
W	C10	2.055(8)	N1	C1	1.483(8)
W	C11	2.036(7)	N1	C3	1.476(9)
W	C12	2.025(8)	N2	C2	1.485(9)
W	C13	2.048(7)	N2	C6	1.486(8)
P	N1	1.687(5)	C1	C2	1.529(9)
P	N2	1.673(5)	C3	C4	1.509(10)
O1	C9	1.148(7)	C3	C5	1.546(10)
O2	C10	1.140(9)	C6	C7	1.523(10)
O3	C11	1.143(7)	C6	C8	1.525(8)

Table 27: Bond Angles for **6f**.

Atom	Atom	Atom	Length/Å	Atom	Atom	Atom	Angle/°
C9	W	P	176.19(18)	C3	N1	P	119.8(5)
C9	W	C10	90.5(3)	C3	N1	C1	119.3(5)
C9	W	C11	90.8(2)	C2	N2	P	107.1(4)
C9	W	C12	90.1(3)	C2	N2	C6	117.8(5)
C9	W	C13	87.5(3)	C6	N2	P	120.2(4)
C10	W	P	88.99(19)	N1	C1	C2	107.2(6)
C11	W	P	92.90(18)	N2	C2	C1	103.8(6)
C11	W	C10	86.8(3)	N1	C3	C4	114.1(6)
C11	W	C13	178.0(3)	N1	C3	C5	108.6(5)
C12	W	P	90.60(19)	C4	C3	C5	109.8(6)
C12	W	C10	177.1(3)	N2	C6	C7	114.1(5)
C12	W	C11	90.4(3)	N2	C6	C8	109.2(6)
C12	W	C13	90.7(3)	C7	C6	C8	113.1(6)
C13	W	P	88.79(19)	O1	C9	W	178.4(6)
C13	W	C10	92.2(3)	O2	C10	W	176.7(6)
N1	P	W	121.2(2)	O3	C11	W	177.9(8)
N2	P	W	121.8(2)	O4	C12	W	179.1(6)

223

| N2 | P | N1 | 92.5(3) | O5 | C13 | W | 177.3(6) |
| C1 | N1 | P | 111.0(4) | | | | |
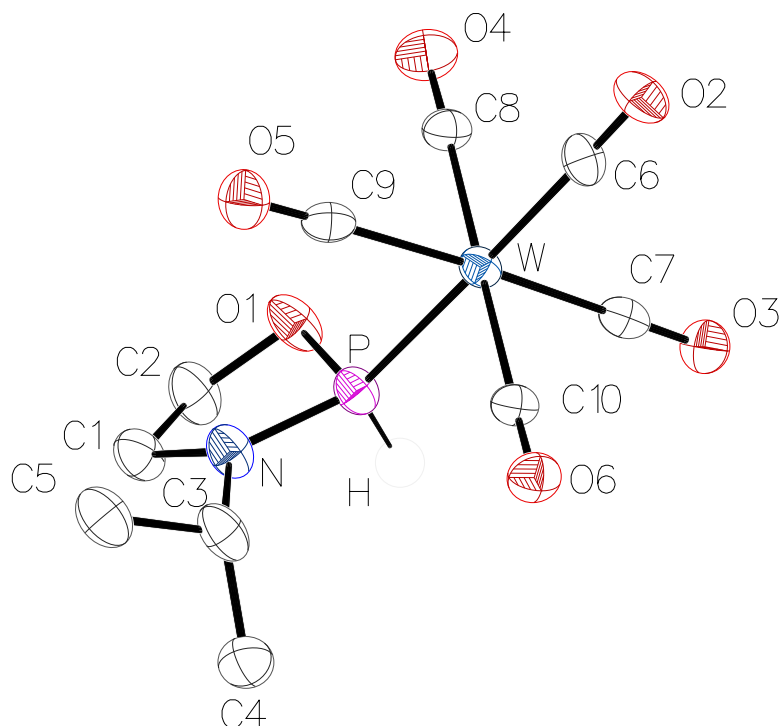
Figure 107: Molecular structure of **6i** in the crystal obtained by X-ray diffraction.

Table 28: Crystal data and structure refinement for **6i**.

Identification code	GSTR708, PB-208 // GXray6449
Crystal Habitus	clear colourless block
Device Type	STOE IPDS-2T
Empirical formula	C10H12NO6PW
Moiety formula	C10 H12 N O6 P W
Formula weight	457.03
Temperature/K	123
Crystal system	monoclinic
Space group	P21/n
a/Å	6.5169(11)
b/Å	18.469(4)
c/Å	12.033(2)
α/°	90
β/°	102.349(13)
γ/°	90
Volume/Å^3	1414.8(4)
Z	4
ρ_{calc} g/cm^3	2.146
μ/mm^{-1}	8.297
F(000)	864.0
Crystal size/mm^3	0.15 × 0.12 × 0.08
Absorption correction	integration
Tmin; Tmax	0.0104; 0.0396

Radiation	MoKα (λ = 0.71073)
2Θ range for data collection/°	5.61 to 55.994°
Completeness to theta	0.993
Index ranges	-8 ≤ h ≤ 5, -24 ≤ k ≤ 22, -15 ≤ l ≤ 15
Reflections collected	7225
Independent reflections	3401 [Rint = 0.0378, Rsigma = 0.0518]
Data/restraints/parameters	3401/0/177
Goodness-of-fit on F2	0.876
Final R indexes [I≥2σ (I)]	R1 = 0.0268, wR2 = 0.0542
Final R indexes [all data]	R1 = 0.0433, wR2 = 0.0566
Largest diff. peak/hole / e Å^{-3}	1.32/-1.63

Table 29: Bond Lengths for **6i**.

Atom	Atom	Length/Å	Atom	Atom	Length/Å
W	P	2.4451(13)	O3	C7	1.150(6)
W	C6	2.022(5)	O4	C8	1.131(7)
W	C7	2.042(5)	O5	C9	1.130(7)
W	C8	2.053(5)	O6	C10	1.126(6)
W	C9	2.066(5)	N	C1	1.471(6)
W	C10	2.061(5)	N	C3	1.461(7)
P	O1	1.613(4)	C1	C2	1.519(8)
P	N	1.666(4)	C3	C4	1.526(9)
O1	C2	1.450(6)	C3	C5	1.527(8)
O2	C6	1.146(6)			

Table 30: Bond Angles for **6i**.

Atom	Atom	Atom	Length/Å	Atom	Atom	Atom	Angle/°
C6	W	P	177.32(15)	O1	P	N	94.6(2)
C6	W	C7	91.07(19)	N	P	W	121.27(16)
C6	W	C8	90.8(2)	C2	O1	P	109.0(4)
C6	W	C9	92.4(2)	C1	N	P	111.2(3)
C6	W	C10	89.2(2)	C3	N	P	123.7(4)
C7	W	P	88.06(13)	C3	N	C1	120.8(4)
C7	W	C8	90.3(2)	N	C1	C2	106.0(4)
C7	W	C9	176.6(2)	O1	C2	C1	107.8(4)
C7	W	C10	89.4(2)	N	C3	C4	113.4(5)
C8	W	P	86.72(14)	N	C3	C5	110.0(5)
C8	W	C9	89.5(2)	C4	C3	C5	111.4(5)
C8	W	C10	179.7(2)	O2	C6	W	179.0(5)
C9	W	P	88.52(14)	O3	C7	W	179.7(5)
C10	W	P	93.38(14)	O4	C8	W	178.7(5)
C10	W	C9	90.8(2)	O5	C9	W	178.3(5)
O1	P	W	115.83(15)	O6	C10	W	177.6(4)
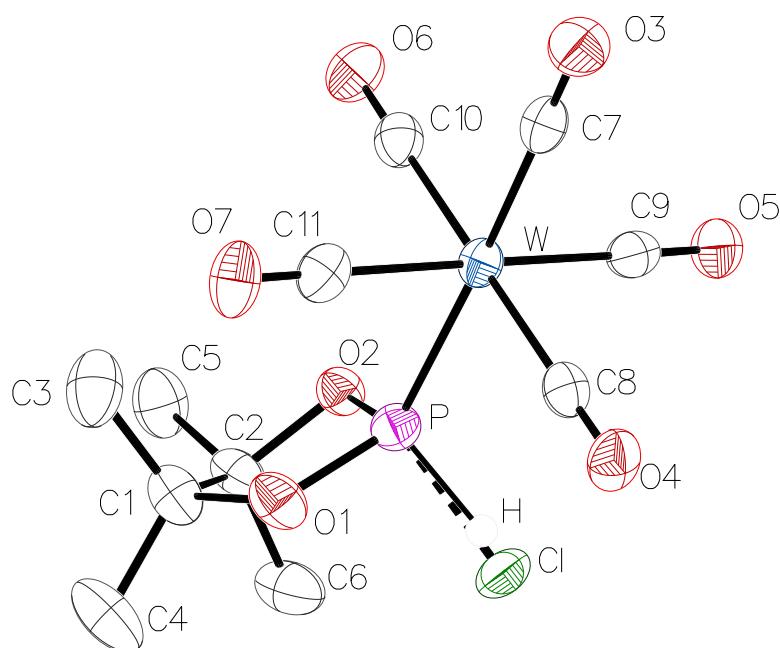
Figure 108: Molecular structure of **5/6k** in the crystal obtained by X-ray diffraction.

Table 31: Crystal data and structure refinement for **5/6k**.

Identification code	AMF-46 // GXray6371
Crystal Habitus	clear colourless plate
Device Type	STOE IPDS-2T
Empirical formula	C11H12.77Cl0.23O7PW
Moiety formula	C11 H12.77 Cl0.23 O7 P W
Formula weight	480.13
Temperature/K	123
Crystal system	monoclinic
Space group	P21/c
a/Å	10.5582(4)
b/Å	12.6072(3)
c/Å	12.6533(5)
α/°	90
β/°	113.537(3)
γ/°	90
Volume/Å^3	1544.14(10)
Z	4
ρ_{calc} g/cm^3	2.065
μ/mm^{-1}	7.650
F(000)	911.0
Crystal size/mm^3	0.48 × 0.12 × 0.04
Absorption correction	integration
Tmin; Tmax	0.0281; 0.1048
Radiation	MoKα (λ = 0.71073)
2Θ range for data collection/°	5.306 to 51.99°
Completeness to theta	0.999

227

Index ranges	-13 ≤ h ≤ 13, -15 ≤ k ≤ 13, -15 ≤ l ≤ 15	
Reflections collected	17722	
Independent reflections	3027 [Rint = 0.0426, Rsigma = 0.0268]	
Data/restraints/parameters	3027/1/199	
Goodness-of-fit on F2	0.890	
Final R indexes [I≥2σ (I)]	R1 = 0.0157, wR2 = 0.0316	
Final R indexes [all data]	R1 = 0.0235, wR2 = 0.0325	
Largest diff. peak/hole / e Å^{-3}	0.59/-0.88	

Table 32: Bond Lengths for **5/6k**.

Atom	Atom	Length/Å	Atom	Atom	Length/Å
W	P	2.4224(8)	O3	C7	1.143(4)
W	C7	2.024(3)	O4	C8	1.133(4)
W	C8	2.051(3)	O5	C9	1.137(4)
W	C9	2.049(3)	O6	C10	1.135(4)
W	C10	2.050(3)	O7	C11	1.135(4)
W	C11	2.057(3)	C1	C2	1.549(4)
Cl	P	2.013(5)	C1	C3	1.525(5)
P	O1	1.608(2)	C1	C4	1.513(5)
P	O2	1.606(2)	C2	C5	1.505(5)
O1	C1	1.475(4)	C2	C6	1.517(4)
O2	C2	1.474(4)			

Table 33: Bond Angles for **5/6k**.

Atom	Atom	Atom	Length/Å	Atom	Atom	Atom	Angle/°
C7	W	P	177.45(9)	O2	P	O1	96.92(12)
C7	W	C8	90.96(13)	C1	O1	P	111.72(18)
C7	W	C9	91.20(12)	C2	O2	P	110.75(18)
C7	W	C10	90.90(12)	O1	C1	C2	104.3(2)
C7	W	C11	90.76(12)	O1	C1	C3	106.5(3)
C8	W	P	89.65(9)	O1	C1	C4	107.1(3)
C8	W	C11	91.42(13)	C3	C1	C2	112.9(3)
C9	W	P	91.28(8)	C4	C1	C2	114.3(3)
C9	W	C8	89.89(13)	C4	C1	C3	111.0(3)
C9	W	C10	88.01(13)	O2	C2	C1	102.7(2)
C9	W	C11	177.62(12)	O2	C2	C5	106.3(3)
C10	W	P	88.58(9)	O2	C2	C6	108.0(3)
C10	W	C8	177.22(12)	C5	C2	C1	114.7(3)
C10	W	C11	90.61(13)	C5	C2	C6	110.9(3)
C11	W	P	86.74(9)	C6	C2	C1	113.5(3)
Cl	P	W	117.59(12)	O3	C7	W	179.2(3)
O1	P	W	119.43(9)	O4	C8	W	179.4(3)
O1	P	Cl	97.26(15)	O5	C9	W	178.8(3)
O2	P	W	117.33(8)	O6	C10	W	178.9(3)
O2	P	Cl	104.56(15)	O7	C11	W	178.4(3)
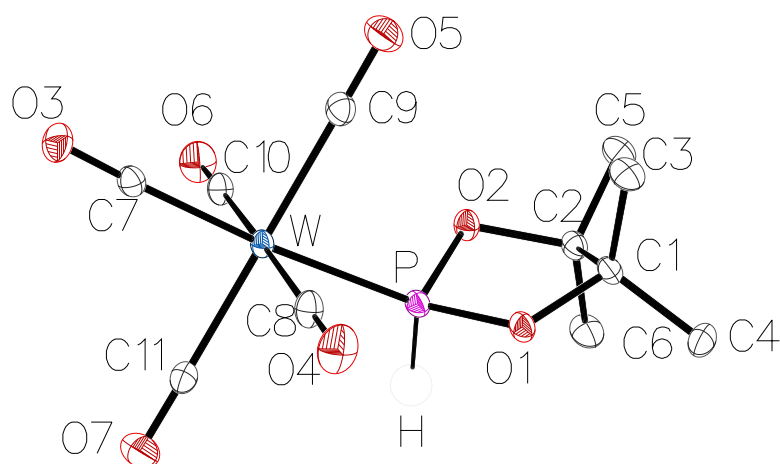
Figure 109: Molecular structure of **6k** in the crystal obtained by X-ray diffraction.

Table 34: Crystal data and structure refinement for **6k**.

Identification code	GSTR721, PB-213 // GXray6538
Crystal Habitus	clear light yellow block
Device Type	STOE IPDS-2T
Empirical formula	C11H13O7PW
Moiety formula	C11 H13 O7 P W
Formula weight	472.03
Temperature/K	123
Crystal system	triclinic
Space group	P-1
a/Å	7.0371(3)
b/Å	10.1674(4)
c/Å	10.6647(4)
$\alpha/°$	99.282(3)
$\beta/°$	101.783(3)
$\gamma/°$	91.016(3)
Volume/Å^3	736.17(5)
Z	2
ρ_{calc} g/cm^3	2.129
μ/mm^{-1}	7.980
F(000)	448.0
Crystal size/mm^3	0.14 × 0.12 × 0.12
Absorption correction	integration
Tmin; Tmax	0.1271; 0.3962
Radiation	MoKα (λ = 0.71073)
2Θ range for data collection/°	5.922 to 55.988°
Completeness to theta	0.999
Index ranges	-9 $\leq$ h $\leq$ 8, -13 $\leq$ k $\leq$ 13, -14 $\leq$ l $\leq$ 14
Reflections collected	25605
Independent reflections	3563 [Rint = 0.0583, Rsigma = 0.0238]
Data/restraints/parameters	3563/0/190
Goodness-of-fit on F2	1.167
Final R indexes [I$\geq$2σ (I)]	R1 = 0.0147, wR2 = 0.0347

Final R indexes [all data]   R1 = 0.0156, wR2 = 0.0350
Largest diff. peak/hole / e Å^{-3} 1.47/-0.80

Table 35: Bond Lengths for **6k**.

Atom	Atom	Length/Å	Atom	Atom	Length/Å
W	P	2.4260(6)	O3	C7	1.139(3)
W	C7	2.026(2)	O4	C8	1.140(3)
W	C8	2.042(2)	O5	C9	1.134(3)
W	C9	2.048(2)	O6	C10	1.137(3)
W	C10	2.050(2)	O7	C11	1.135(3)
W	C11	2.054(2)	C1	C2	1.564(3)
P	O1	1.6217(16)	C1	C3	1.520(3)
P	O2	1.6136(15)	C1	C4	1.513(3)
O1	C1	1.476(2)	C2	C5	1.516(3)
O2	C2	1.474(3)	C2	C6	1.519(3)

Table 36: Bond Angles for **6k**.

Atom	Atom	Atom	Length/Å	Atom	Atom	Atom	Angle/°
C7	W	P	175.76(6)	C2	O2	P	109.49(12)
C7	W	C8	91.60(9)	O1	C1	C2	103.97(15)
C7	W	C9	88.57(9)	O1	C1	C3	106.93(17)
C7	W	C10	90.70(9)	O1	C1	C4	107.61(16)
C7	W	C11	90.57(9)	C3	C1	C2	113.11(17)
C8	W	P	90.52(7)	C4	C1	C2	113.73(19)
C8	W	C9	89.79(9)	C4	C1	C3	110.88(18)
C8	W	C10	176.96(9)	O2	C2	C1	102.70(16)
C8	W	C11	88.88(9)	O2	C2	C5	106.41(17)
C9	W	P	87.77(7)	O2	C2	C6	109.01(16)
C9	W	C10	92.25(9)	C5	C2	C1	114.54(16)
C9	W	C11	178.40(8)	C5	C2	C6	110.13(18)
C10	W	P	87.31(7)	C6	C2	C1	113.43(18)
C10	W	C11	89.11(9)	O3	C7	W	178.12(19)
C11	W	P	93.14(7)	O4	C8	W	178.5(2)
O1	P	W	120.36(6)	O5	C9	W	178.2(2)
O2	P	W	115.41(6)	O6	C10	W	178.67(19)
O2	P	O1	96.57(8)	O7	C11	W	178.3(2)
C1	O1	P	112.07(12)				
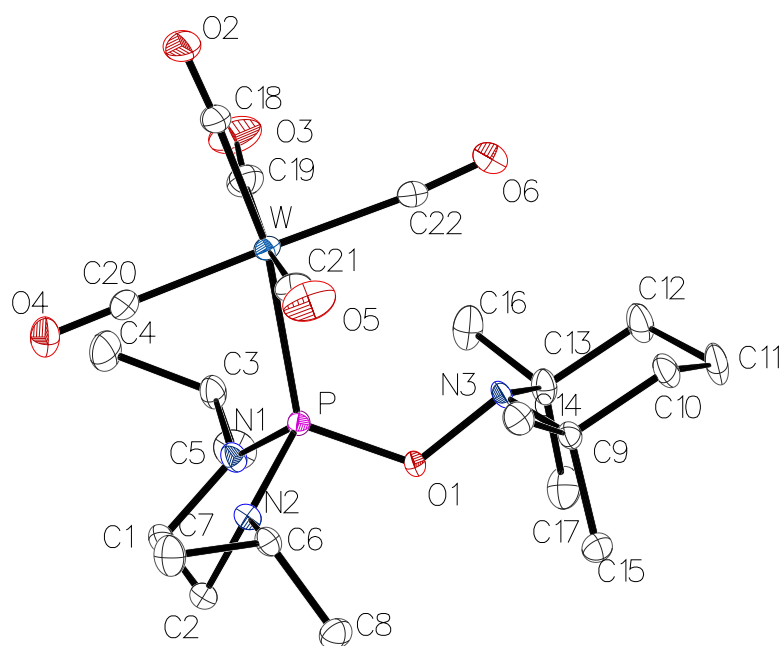
Figure 110: Molecular structure of **8f** in the crystal obtained by X-ray diffraction.

Table 37: Crystal data and structure refinement for **8f**.

Identification code	GSTR707, AMF-42 // GXray6448
Crystal Habitus	clear colourless block
Device Type	STOE IPDS-2T
Empirical formula	C22H36N3O6PW
Moiety formula	C22 H36 N3 O6 P W
Formula weight	653.36
Temperature/K	123
Crystal system	monoclinic
Space group	P21/n
a/Å	12.1269(3)
b/Å	10.9786(2)
c/Å	20.1204(5)
α/°	90
β/°	102.575(2)
γ/°	90
Volume/Å^3	2614.50(11)
Z	4
ρ_{calc} g/cm^3	1.660
μ/mm^{-1}	4.519
F(000)	1304.0
Crystal size/mm^3	0.25 × 0.15 × 0.1
Absorption correction	integration
Tmin; Tmax	0.3373; 0.6122
Radiation	MoKα (λ = 0.71073)
2Θ range for data collection/°	5.566 to 55.994°
Completeness to theta	0.999

Index ranges	-14 ≤ h ≤ 16, -14 ≤ k ≤ 14, -26 ≤ l ≤ 26		
Reflections collected	36816		
Independent reflections	6301 [Rint = 0.0622, Rsigma = 0.0333]		
Data/restraints/parameters	6301/5/306		
Goodness-of-fit on F2	0.982		
Final R indexes [I≥2σ (I)]	R1 = 0.0185, wR2 = 0.0380		
Final R indexes [all data]	R1 = 0.0240, wR2 = 0.0391		
Largest diff. peak/hole / e Å^{-3}	0.79/-1.00		

Table 38: Bond Lengths for **8f**.

Atom	Atom	Length/Å	Atom	Atom	Length/Å
W	P	2.5335(5)	N2	C2	1.467(2)
W	C18	1.991(2)	N2	C6	1.467(2)
W	C19	2.048(2)	N3	C9	1.494(3)
W	C20	2.042(2)	N3	C13	1.506(2)
W	C21	2.040(2)	C1	C2	1.508(3)
W	C22	2.059(2)	C3	C4	1.530(3)
P	O1	1.6595(15)	C3	C5	1.533(3)
P	N1	1.6842(16)	C6	C7	1.527(3)
P	N2	1.6749(16)	C6	C8	1.523(3)
O1	N3	1.4770(18)	C9	C10	1.541(3)
O2	C18	1.148(3)	C9	C14	1.526(3)
O3	C19	1.138(3)	C9	C15	1.537(3)
O4	C20	1.136(3)	C10	C11	1.522(3)
O5	C21	1.141(3)	C11	C12	1.514(3)
O6	C22	1.137(3)	C12	C13	1.534(3)
N1	C1	1.468(2)	C13	C16	1.527(3)
N1	C3	1.481(3)	C13	C17	1.537(3)

Table 39: Bond Angles for **8f**.

Atom	Atom	Atom	Length/Å	Atom	Atom	Atom	Angle/°
C18	W	P	169.33(6)	C9	N3	C13	117.12(16)
C18	W	C19	84.92(9)	N1	C1	C2	105.08(15)
C18	W	C20	89.09(8)	N2	C2	C1	103.71(15)
C18	W	C21	85.58(9)	N1	C3	C4	112.74(16)
C18	W	C22	92.20(8)	N1	C3	C5	110.06(18)
C19	W	P	95.65(7)	C4	C3	C5	110.30(18)
C19	W	C22	86.81(9)	N2	C6	C7	110.43(17)
C20	W	P	80.25(6)	N2	C6	C8	112.64(16)
C20	W	C19	93.65(9)	C8	C6	C7	110.67(18)
C20	W	C22	178.67(8)	N3	C9	C10	107.38(15)
C21	W	P	94.69(6)	N3	C9	C14	107.58(16)
C21	W	C19	169.05(9)	N3	C9	C15	116.07(15)
C21	W	C20	91.62(8)	C14	C9	C10	107.02(15)
C21	W	C22	88.14(9)	C14	C9	C15	108.30(16)
C22	W	P	98.46(6)	C15	C9	C10	110.12(17)
O1	P	W	121.20(5)	C11	C10	C9	113.45(16)
O1	P	N1	103.84(7)	C12	C11	C10	108.16(18)
O1	P	N2	103.43(8)	C11	C12	C13	113.61(18)
N1	P	W	117.33(6)	N3	C13	C12	106.67(15)

232

N2	P	W	114.79(6)	N3	C13	C16	107.12(17)
N2	P	N1	91.52(8)	N3	C13	C17	115.58(17)
N3	O1	P	120.81(11)	C12	C13	C17	111.60(18)
C1	N1	P	113.41(12)	C16	C13	C12	107.60(18)
C1	N1	C3	116.36(15)	C16	C13	C17	107.93(17)
C3	N1	P	125.49(13)	O2	C18	W	177.14(19)
C2	N2	P	112.88(12)	O3	C19	W	173.3(2)
C2	N2	C6	117.49(15)	O4	C20	W	179.0(2)
C6	N2	P	126.91(12)	O5	C21	W	174.16(19)
O1	N3	C9	106.65(13)	O6	C22	W	175.25(19)
O1	N3	C13	106.26(13)				
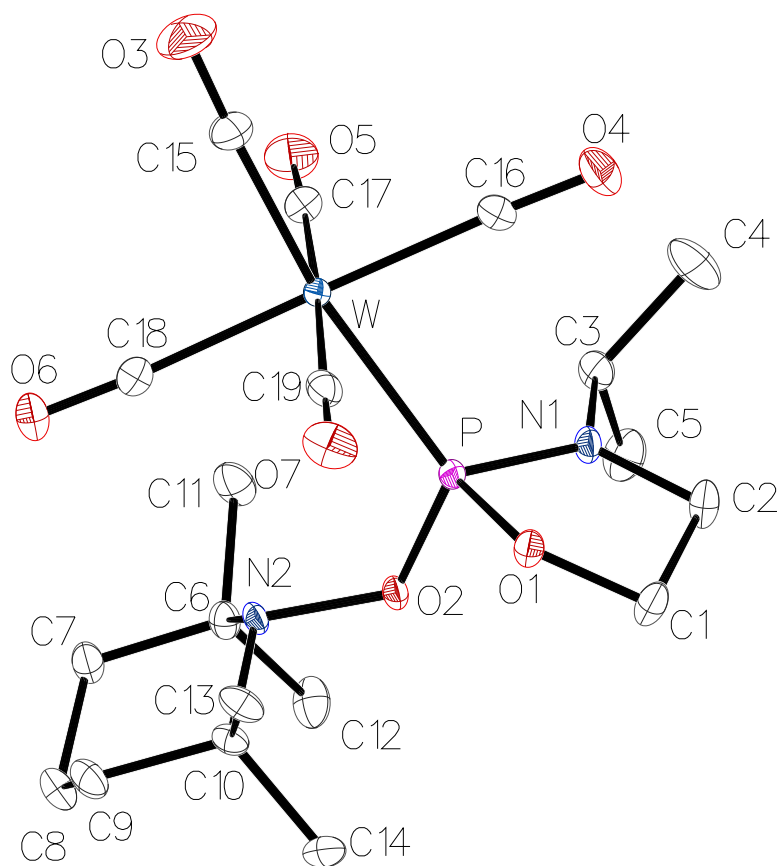
Figure 111: Molecular structure of **8i** in the crystal obtained by X-ray diffraction.

Table 40: Crystal data and structure refinement for **8i**.

Identification code	GSTR709, PB-211 // GXray6459
Crystal Habitus	clear colourless block
Device Type	STOE IPDS-2T
Empirical formula	C19H29N2O7PW
Moiety formula	C19 H29 N2 O7 P W
Formula weight	612.26
Temperature/K	100
Crystal system	triclinic
Space group	P-1
a/Å	8.2932(3)
b/Å	10.1104(3)
c/Å	15.3182(5)
α/°	73.319(2)
β/°	74.659(3)
γ/°	71.740(3)
Volume/Å^3	1146.66(7)
Z	2
ρ_{calc} g/cm^3	1.773

μ/mm^{-1}	5.148
F(000)	604.0
Crystal size/mm^3	0.3 × 0.15 × 0.12
Absorption correction	integration
Tmin; Tmax	0.3164; 0.6833
Radiation	MoKα (λ = 0.71073)
2Θ range for data collection/°	5.482 to 55.996°
Completeness to theta	0.999
Index ranges	-10 ≤ h ≤ 10, -13 ≤ k ≤ 13, -20 ≤ l ≤ 20
Reflections collected	19824
Independent reflections	5540 [Rint = 0.0643, Rsigma = 0.0395]
Data/restraints/parameters	5540/0/277
Goodness-of-fit on F2	1.018
Final R indexes [I≥2σ (I)]	R1 = 0.0175, wR2 = 0.0418
Final R indexes [all data]	R1 = 0.0197, wR2 = 0.0423
Largest diff. peak/hole / e Å^{-3}	1.10/-1.90

Table 41: Bond Lengths for **8i**.

Atom	Atom	Length/Å	Atom	Atom	Length/Å
W	P	2.4629(5)	N1	C2	1.465(3)
W	C15	2.021(2)	N1	C3	1.464(3)
W	C16	2.021(3)	N2	C6	1.505(2)
W	C17	2.048(2)	N2	C10	1.504(2)
W	C18	2.070(3)	C1	C2	1.523(3)
W	C19	2.054(2)	C3	C4	1.524(4)
P	O1	1.6274(14)	C3	C5	1.529(3)
P	O2	1.6331(15)	C6	C7	1.524(3)
P	N1	1.6647(18)	C6	C11	1.532(3)
O1	C1	1.447(2)	C6	C12	1.541(3)
O2	N2	1.473(2)	C7	C8	1.520(3)
O3	C15	1.140(3)	C8	C9	1.518(3)
O4	C16	1.141(3)	C9	C10	1.535(3)
O5	C17	1.137(3)	C10	C13	1.533(3)
O6	C18	1.134(3)	C10	C14	1.538(3)
O7	C19	1.133(3)			

Table 42: Bond Angles for **8i**.

Atom	Atom	Atom	Length/Å	Atom	Atom	Atom	Angle/°
C15	W	P	170.50(8)	O2	N2	C10	107.51(14)
C15	W	C16	89.09(10)	C10	N2	C6	118.01(16)
C15	W	C17	89.28(9)	O1	C1	C2	105.69(16)
C15	W	C18	90.78(10)	N1	C2	C1	103.91(17)
C15	W	C19	90.96(9)	N1	C3	C4	111.69(19)
C16	W	P	82.01(6)	N1	C3	C5	111.46(18)
C16	W	C17	93.18(9)	C4	C3	C5	110.8(2)
C16	W	C18	177.84(8)	N2	C6	C7	107.34(16)
C16	W	C19	89.17(9)	N2	C6	C11	106.29(17)
C17	W	P	94.50(6)	N2	C6	C12	115.29(17)
C17	W	C18	88.97(9)	C7	C6	C11	108.36(17)
C17	W	C19	177.64(9)	C7	C6	C12	110.69(18)

235

C18	W	P	97.98(6)	C11	C6	C12	108.60(18)
C19	W	P	85.62(6)	C8	C7	C6	113.71(17)
C19	W	C18	88.68(9)	C9	C8	C7	108.06(18)
O1	P	W	109.81(5)	C8	C9	C10	113.92(18)
O1	P	O2	103.79(8)	N2	C10	C9	107.37(16)
O1	P	N1	93.25(8)	N2	C10	C13	107.14(16)
O2	P	W	124.21(6)	N2	C10	C14	114.88(17)
O2	P	N1	99.59(8)	C9	C10	C14	111.42(18)
N1	P	W	120.91(6)	C13	C10	C9	107.21(17)
C1	O1	P	110.59(12)	C13	C10	C14	108.48(17)
N2	O2	P	119.47(11)	O3	C15	W	177.3(3)
C2	N1	P	113.71(13)	O4	C16	W	177.44(19)
C3	N1	P	125.75(15)	O5	C17	W	177.4(2)
C3	N1	C2	120.54(17)	O6	C18	W	175.73(19)
O2	N2	C6	104.38(14)	O7	C19	W	178.7(2)
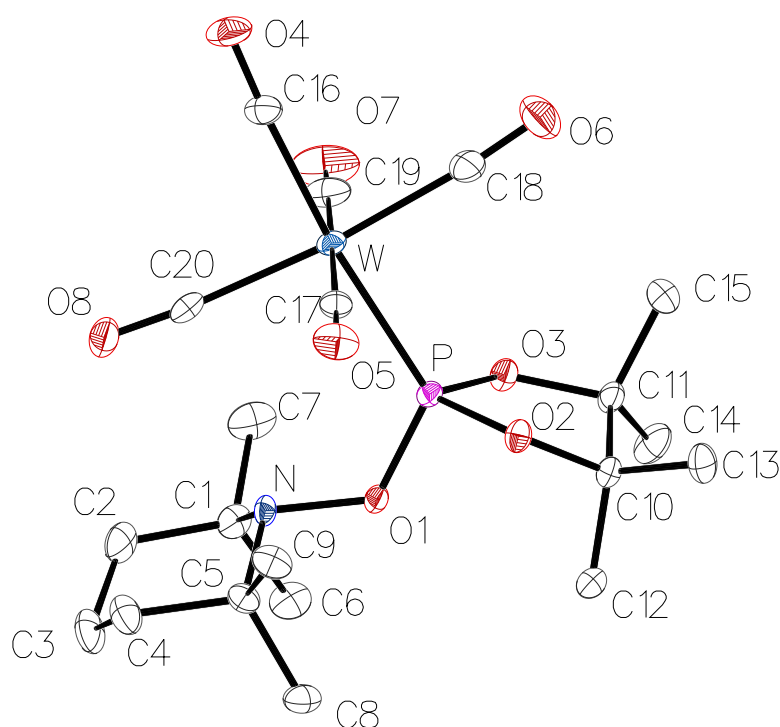
Figure 112: Molecular structure of **8k** in the crystal obtained by X-ray diffraction.

Table 43: Crystal data and structure refinement for **8k**.

Identification code	GSTR722, PB-242.EI // GXray6587
Crystal Habitus	clear yellowish colourless block
Device Type	STOE IPDS-2T
Empirical formula	C20H30NO8PW
Moiety formula	C20 H30 N O8 P W
Formula weight	627.27
Temperature/K	123
Crystal system	monoclinic
Space group	P21/n
a/Å	11.1040(2)
b/Å	14.0762(2)
c/Å	15.5766(3)
α/°	90
β/°	93.904(2)
γ/°	90
Volume/Å^3	2429.01(7)
Z	4
ρ_{calc} g/cm^3	1.715
μ/mm^{-1}	4.864
F(000)	1240.0
Crystal size/mm^3	0.25 × 0.21 × 0.18
Absorption correction	integration
Tmin; Tmax	0.4419; 0.8542

Radiation	MoKα (λ = 0.71073)	
2Θ range for data collection/°	5.24 to 55.998°	
Completeness to theta	0.999	
Index ranges	-14 ≤ h ≤ 13, -18 ≤ k ≤ 18, -20 ≤ l ≤ 20	
Reflections collected	38270	
Independent reflections	5876 [Rint = 0.0550, Rsigma = 0.0258]	
Data/restraints/parameters	5876/0/288	
Goodness-of-fit on F2	1.043	
Final R indexes [I≥2σ (I)]	R1 = 0.0243, wR2 = 0.0598	
Final R indexes [all data]	R1 = 0.0280, wR2 = 0.0611	
Largest diff. peak/hole / e Å^{-3}	3.05/-1.74	

Table 44: Bond Lengths for **8k**.

Atom	Atom	Length/Å	Atom	Atom	Length/Å
W	P	2.4713(6)	O8	C20	1.142(3)
W	C16	2.016(3)	N	C1	1.501(3)
W	C17	2.035(3)	N	C5	1.498(3)
W	C18	2.032(3)	C1	C2	1.540(4)
W	C19	2.049(3)	C1	C6	1.535(4)
W	C20	2.051(3)	C1	C7	1.530(4)
P	O1	1.6203(18)	C2	C3	1.514(5)
P	O2	1.6084(18)	C3	C4	1.520(4)
P	O3	1.6130(18)	C4	C5	1.543(4)
O1	N	1.463(2)	C5	C8	1.535(4)
O2	C10	1.475(3)	C5	C9	1.528(3)
O3	C11	1.472(3)	C10	C11	1.558(3)
O4	C16	1.142(3)	C10	C12	1.521(4)
O5	C17	1.144(3)	C10	C13	1.518(3)
O6	C18	1.143(4)	C11	C14	1.518(4)
O7	C19	1.134(4)	C11	C15	1.522(4)

Table 45: Bond Angles for **8k**.

Atom	Atom	Atom	Length/Å	Atom	Atom	Atom	Angle/°
C16	W	P	174.37(8)	C6	C1	C2	111.3(2)
C16	W	C17	91.67(10)	C7	C1	C2	108.8(2)
C16	W	C18	84.39(11)	C7	C1	C6	108.1(2)
C16	W	C19	91.33(11)	C3	C2	C1	113.7(2)
C16	W	C20	89.06(11)	C2	C3	C4	109.3(2)
C17	W	P	88.79(7)	C3	C4	C5	112.7(2)
C17	W	C19	176.76(10)	N	C5	C4	105.5(2)
C17	W	C20	87.83(10)	N	C5	C8	116.4(2)
C18	W	P	90.00(8)	N	C5	C9	107.0(2)
C18	W	C17	89.53(11)	C8	C5	C4	111.2(2)
C18	W	C19	91.99(13)	C9	C5	C4	108.1(2)
C18	W	C20	172.86(11)	C9	C5	C8	108.2(2)
C19	W	P	88.35(8)	O2	C10	C11	103.06(18)
C19	W	C20	91.00(12)	O2	C10	C12	109.0(2)
C20	W	P	96.57(7)	O2	C10	C13	106.2(2)
O1	P	W	123.67(7)	C12	C10	C11	113.3(2)
O2	P	W	114.09(7)	C13	C10	C11	114.0(2)

O2	P	O1	102.20(10)	C13	C10	C12	110.7(2)
O2	P	O3	95.97(9)	O3	C11	C10	104.01(18)
O3	P	W	117.25(7)	O3	C11	C14	107.0(2)
O3	P	O1	99.08(10)	O3	C11	C15	106.9(2)
N	O1	P	119.93(14)	C14	C11	C10	114.0(2)
C10	O2	P	111.50(14)	C14	C11	C15	110.6(2)
C11	O3	P	113.26(15)	C15	C11	C10	113.7(2)
O1	N	C1	105.38(18)	O4	C16	W	176.7(2)
O1	N	C5	105.96(17)	O5	C17	W	178.3(2)
C5	N	C1	118.3(2)	O6	C18	W	174.9(3)
N	C1	C2	105.8(2)	O7	C19	W	179.6(3)
N	C1	C6	115.7(2)	O8	C20	W	174.3(2)
N	C1	C7	107.0(2)				
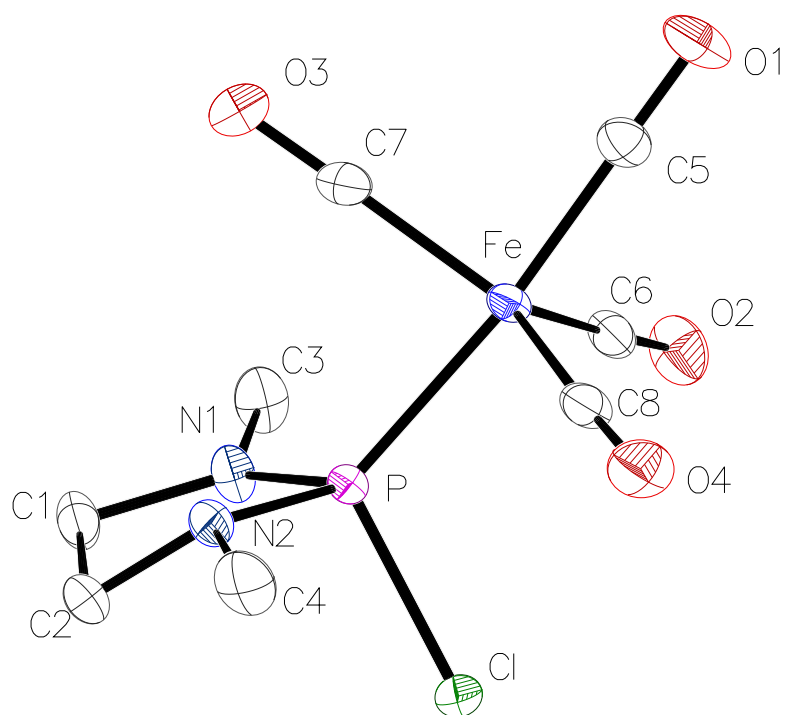
Figure 113: Molecular structure of **15e** in the crystal obtained by X-ray diffraction.

Table 46: Crystal data and structure refinement for **15e**.

Identification code	GSTR739, PB-107 // GXraymo
Crystal Habitus	clear light yellow block
Device Type	STOE STADIVARI
Empirical formula	C8H10ClFeN2O4P
Moiety formula	C8 H10 Cl Fe N2 O4 P
Formula weight	320.45
Temperature/K	120.0
Crystal system	monoclinic
Space group	Pc
a/Å	6.9354(6)
b/Å	6.4697(10)
c/Å	14.1938(17)
$\alpha/°$	90
$\beta/°$	97.364(8)
$\gamma/°$	90
Volume/Å^3	631.62(14)
Z	2
ρ_{calc} g/cm^3	1.685
μ/mm^{-1}	1.534
F(000)	324.0
Crystal size/mm^3	0.2 × 0.15 × 0.12
Absorption correction	multi-scan
Tmin; Tmax	1.0000; 1.0000
Radiation	MoKα (λ = 0.71073)

2Θ range for data collection/°	5.788 to 61.59°
Completeness to theta	1.000
Index ranges	-9 ≤ h ≤ 9, -9 ≤ k ≤ 9, -20 ≤ l ≤ 20
Reflections collected	14397
Independent reflections	3349 [Rint = 0.0155, Rsigma = 0.0151]
Data/restraints/parameters	3349/2/156
Goodness-of-fit on F2	1.049
Final R indexes [I≥2σ (I)]	R1 = 0.0189, wR2 = 0.0420
Final R indexes [all data]	R1 = 0.0210, wR2 = 0.0429
Largest diff. peak/hole / e Å^{-3}	0.25/-0.28
Flack parameter	-0.004(6)

Table 47: Bond Lengths for **15e**.

Atom	Atom	Length/Å	Atom	Atom	Length/Å
Fe	P	2.1726(6)	O2	C6	1.138(3)
Fe	C5	1.799(2)	O3	C7	1.136(3)
Fe	C6	1.795(2)	O4	C8	1.140(3)
Fe	C7	1.796(2)	N1	C1	1.458(3)
Fe	C8	1.800(3)	N1	C3	1.449(3)
Cl	P	2.1162(8)	N2	C2	1.470(3)
P	N1	1.630(2)	N2	C4	1.456(3)
P	N2	1.653(2)	C1	C2	1.519(4)
O1	C5	1.129(3			

Table 48: Bond Angles for **15e**.

Atom	Atom	Atom	Length/Å	Atom	Atom	Atom	Angle/°
C5	Fe	P	172.89(9)	N2	P	Fe	120.71(8)
C5	Fe	C8	89.35(11)	N2	P	Cl	102.75(8)
C6	Fe	P	93.53(8)	C1	N1	P	113.94(16)
C6	Fe	C5	92.85(11)	C3	N1	P	127.21(17)
C6	Fe	C7	117.02(11)	C3	N1	C1	117.8(2)
C6	Fe	C8	113.22(12)	C2	N2	P	109.15(15)
C7	Fe	P	83.85(8)	C4	N2	P	121.19(17)
C7	Fe	C5	90.45(11)	C4	N2	C2	115.2(2)
C7	Fe	C8	129.70(11)	N1	C1	C2	105.46(19)
C8	Fe	P	91.02(8)	N2	C2	C1	104.70(19)
Cl	P	Fe	111.44(3)	O1	C5	Fe	179.6(3)
N1	P	Fe	120.37(8)	O2	C6	Fe	178.0(2)
N1	P	Cl	104.74(8)	O3	C7	Fe	178.3(2)
N1	P	N2	94.00(10)	O4	C8	Fe	177.1(2)
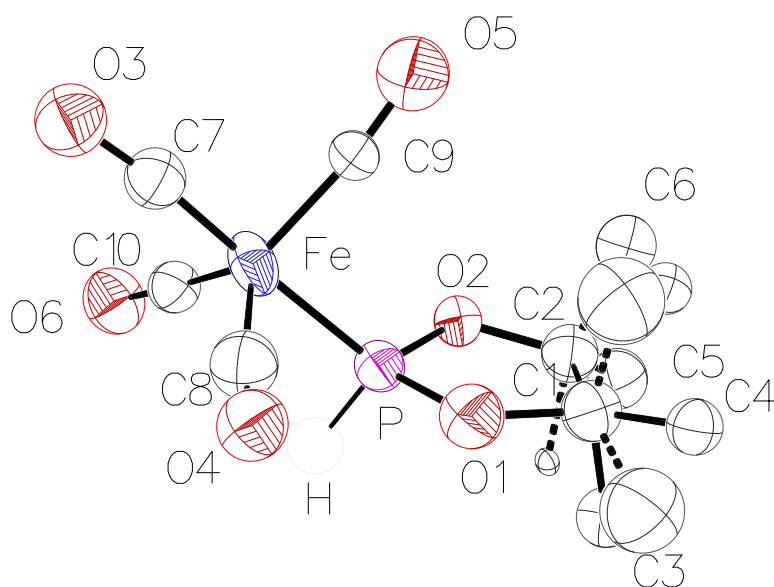
Figure 114: Molecular structure of **12k** in the crystal obtained by X-ray diffraction.

Table 49: Crystal data and structure refinement for **12k**.

Identification code	GSTR696, AMF-7 // GXray6326g
Crystal Habitus	clear colourless plate
Device Type	Bruker X8-KappaApexII
Empirical formula	C10H13FeO6P
Moiety formula	C10 H13 Fe O6 P
Formula weight	316.02
Temperature/K	100
Crystal system	orthorhombic
Space group	Pca21
a/Å	13.446(6)
b/Å	15.062(7)
c/Å	13.536(6)
α/°	90
β/°	90
γ/°	90
Volume/Å^3	2741(2)
Z	8
ρ_{calc} g/cm^3	1.531
mu/mm$^{\text{textminus}1}$	1.231
F(000)	1296.0
Crystal size/mm^3	0.19 × 0.18 × 0.04
Absorption correction	empirical
Tmin; Tmax	0.4966; 0.7460
Radiation	MoKα (λ = 0.71073)
2Θ range for data collection/°	2.704 to 55.986°
Completeness to theta	1.000
Index ranges	-17 ≤ h ≤ 17, -19 ≤ k ≤ 19, -17 ≤ l ≤ 17
Reflections collected	35422

Table 50: Bond Lengths for **12k**.

Atom	Atom	Length/Å	Atom	Atom	Length/Å
Fe'	P'	2.158(9)	Fe	C7	1.68(4)
Fe'	C7'	1.87(3)	Fe	C8	1.82(5)
Fe'	C8'	1.72(3)	Fe	C9	1.77(3)
Fe'	C9'	1.90(6)	Fe	C10	1.71(3)
Fe'	C10'	1.70(3)	P	O1	1.55(2)
P'	O1'	1.53(2)	P	O2	1.558(19)
P'	O2'	1.63(2)	O1	C1	1.52(4)
O1'	C1'	1.52(3)	O2	C2	1.41(4)
O2'	C2'	1.36(3)	O3	C7	1.33(5)
O3'	C7'	1.05(3)	O4	C8	1.07(4)
O4'	C8'	1.19(4)	O5	C9	1.23(4)
O5'	C9'	1.04(5)	O6	C10	1.24(4)
O6'	C10'	1.28(4)	C1	C2	1.61(5)
C1'	C2'	1.496(14)	C1	C3	1.501(15)
C1'	C3'	1.505(14)	C1	C4	1.494(15)
C1'	C4'	1.501(14)	C1	C3S	1.496(14)
C1'	C3T	1.506(14)	C1	C4S	1.513(14)
C1'	C4T	1.517(14)	C2	C5	1.29(6)
C2'	C5'	1.602(14)	C2	C6	1.512(14)
C2'	C6'	1.498(10)	C2	C5S	1.508(14)
Fe	P	2.131(9)	C2	C6S	1.493(14)

Table 51: Bond Angles for **12k**.

Atom	Atom	Atom	Length/Å	Atom	Atom
C7'	Fe'	P'	176.6(10)	C7	Fe
C7'	Fe'	C9'	92.8(18)	C8	Fe
C8'	Fe'	P'	86.1(11)	C9	Fe
C8'	Fe'	C7'	90.6(14)	C9	Fe
C8'	Fe'	C9'	124(2)	C10	Fe
C9'	Fe'	P'	88.3(15)	C10	Fe
C10'	Fe'	P'	87.8(11)	C10	Fe
C10'	Fe'	C7'	94.7(14)	O1	P
C10'	Fe'	C8'	122.9(14)	O1	P
C10'	Fe'	C9'	112(2)	O2	P
O1'	P'	Fe'	120.8(9)	C1	O1
O1'	P'	O2'	96.4(12)	C2	O2
O2'	P'	Fe'	119.1(9)	O1	C1
C1'	O1'	P'	115.0(18)	C3	C1
C2'	O2'	P'	111.3(17)	C3	C1

C2'	C1'	O1'	100.2(18)	C4	C1
C2'	C1'	C3'	99.8(11)	C4	C1
C2'	C1'	C4'	145(4)	C4	C1
C2'	C1'	C3T	99.9(12)	C3S	C1
C2'	C1'	C4T	105.2(13)	C3S	C1
C3'	C1'	O1'	93.1(16)	C3S	C1
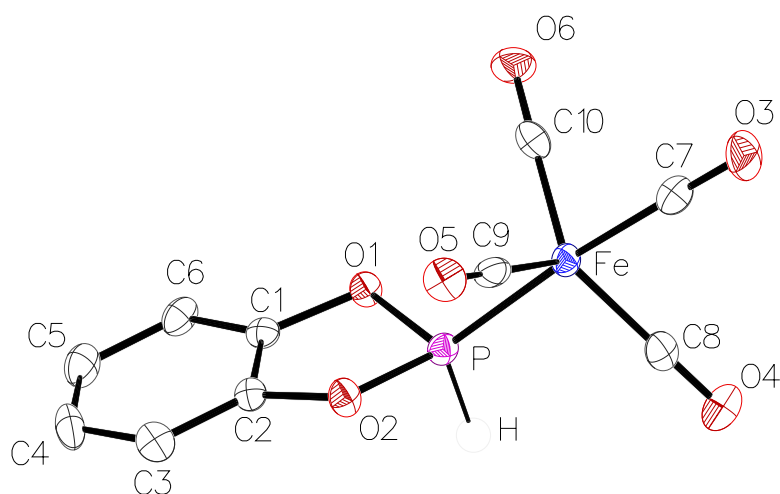
Figure 115: Molecular structure of **12l** in the crystal obtained by X-ray diffraction.

Table 52: Crystal data and structure refinement for **12l**.

Identification code	GSTR686, PB-138 // GXray6173f
Crystal Habitus	clear colourless plate
Device Type	Bruker X8-KappaApexII
Empirical formula	C10H5O6PFe
Moiety formula	C10 H5 Fe O6 P
Formula weight	307.96
Temperature/K	100
Crystal system	orthorhombic
Space group	Pca21
a/Å	16.151(2)
b/Å	10.4300(12)
c/Å	6.8190(8)
α/°	90
β/°	90
γ/°	90
Volume/Å^3	1148.7(2)
Z	4
ρ_{calc} g/cm^3	1.781
μ/mm^{-1}	1.467
F(000)	616.0
Crystal size/mm^3	0.35 × 0.26 × 0.08
Absorption correction	empirical
Tmin; Tmax	0.5417; 0.7461
Radiation	MoKα (λ = 0.71073)
2Θ range for data collection/°	7.572 to 50.46°
Completeness to theta	0.995
Index ranges	-18 $\leq$ h $\leq$ 19, -12 $\leq$ k $\leq$ 12, -8 $\leq$ l $\leq$ 5
Reflections collected	7821
Independent reflections	1918 [Rint = 0.0646, Rsigma = 0.0551]
Data/restraints/parameters	1918/1/166
Goodness-of-fit on F2	1.024

Table 53: Bond Lengths for **12l**.

Atom	Atom	Length/Å	Atom	Atom	Length/Å
Fe	P	2.1313(15)	O4	C8	1.145(6)
Fe	C7	1.809(6)	O5	C9	1.153(6)
Fe	C8	1.798(5)	O6	C10	1.137(7)
Fe	C9	1.801(6)	C1	C2	1.393(7)
Fe	C10	1.812(6)	C1	C6	1.366(9)
P	O1	1.640(4)	C2	C3	1.366(7)
P	O2	1.641(4)	C3	C4	1.402(8)
O1	C1	1.397(6)	C4	C5	1.375(8)
O2	C2	1.400(6)	C5	C6	1.400(7)
O3	C7	1.142(7)			

Table 54: Bond Angles for **12l**.

Atom	Atom	Atom	Length/Å	Atom	Atom	Atom	Angle/°
C7	Fe	P	175.15(19)	C2	C1	O1	112.0(4)
C7	Fe	C10	93.0(3)	C6	C1	O1	126.3(5)
C8	Fe	P	87.95(17)	C6	C1	C2	121.6(5)
C8	Fe	C7	89.0(3)	C1	C2	O2	111.8(4)
C8	Fe	C9	129.1(3)	C3	C2	O2	126.0(5)
C8	Fe	C10	117.5(3)	C3	C2	C1	122.2(5)
C9	Fe	P	88.84(18)	C2	C3	C4	116.7(5)
C9	Fe	C7	90.1(3)	C5	C4	C3	121.1(5)
C9	Fe	C10	113.4(3)	C4	C5	C6	121.8(6)
C10	Fe	P	91.75(18)	C1	C6	C5	116.7(7)
O1	P	Fe	119.51(15)	O3	C7	Fe	179.1(5)
O1	P	O2	95.9(2)	O4	C8	Fe	177.8(7)
O2	P	Fe	118.29(15)	O5	C9	Fe	179.5(5)
C1	O1	P	108.3(3)	O6	C10	Fe	178.9(6)
C2	O2	P	108.3(3)				
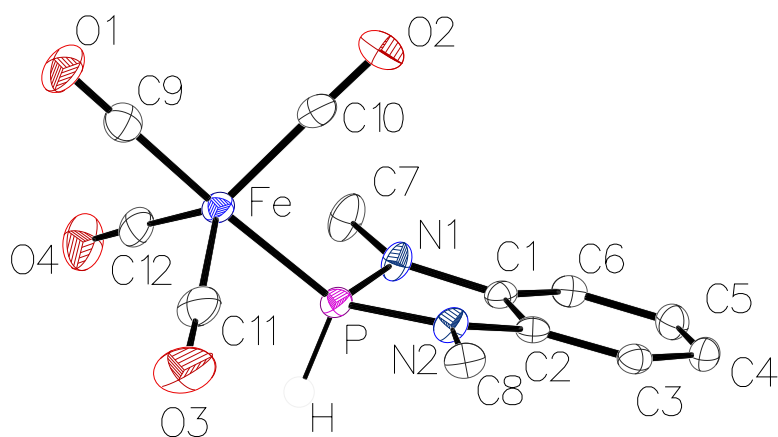
Figure 116: Molecular structure of **12p** in the crystal obtained by X-ray diffraction.

Table 55: Crystal data and structure refinement for **12p**.

Identification code	GSTR744, PB-272 // GXray6753
Crystal Habitus	clear brownish colourless block
Device Type	STOE IPDS-2T
Empirical formula	C12H11FeN2O4P
Moiety formula	C12 H11 Fe N2 O4 P
Formula weight	334.05
Temperature/K	123
Crystal system	trigonal
Space group	R-3
a/Å	19.0115(5)
b/Å	19.0115(5)
c/Å	20.4834(6)
α/°	90
β/°	90
γ/°	120
Volume/Å^3	6411.6(4)
Z	18
ρ_{calc} g/cm^3	1.557
μ/mm^{-1}	1.183
F(000)	3060.0
Crystal size/mm^3	0.12 × 0.1 × 0.09
Absorption correction	integration
Tmin; Tmax	0.6213; 0.9091
Radiation	MoKα (λ = 0.71073)
2Θ range for data collection/°	5.334 to 50.5°
Completeness to theta	0.999
Index ranges	-22 $\leq$ h $\leq$ 22, -22 $\leq$ k $\leq$ 22, -24 $\leq$ l $\leq$ 24
Reflections collected	20708
Independent reflections	2584 [Rint = 0.1008, Rsigma = 0.0473]
Data/restraints/parameters	2584/0/187
Goodness-of-fit on F2	0.940
Final R indexes [I$\geq$2σ (I)]	R1 = 0.0236, wR2 = 0.0547
Final R indexes [all data]	R1 = 0.0332, wR2 = 0.0563

Largest diff. peak/hole / e Å⁻³   0.40/-0.32

Table 56: Bond Lengths for **12p**.

Atom	Atom	Length/Å	Atom	Atom	Length/Å
Fe	P	2.1704(5)	N1	C1	1.405(2)
Fe	C9	1.800(2)	N1	C7	1.458(2)
Fe	C10	1.789(2)	N2	C2	1.400(2)
Fe	C11	1.784(2)	N2	C8	1.460(2)
Fe	C12	1.799(2)	C1	C2	1.407(2)
P	N1	1.6800(15)	C1	C6	1.375(3)
P	N2	1.6824(15)	C2	C3	1.380(2)
O1	C9	1.139(2)	C3	C4	1.397(3)
O2	C10	1.151(2)	C4	C5	1.383(3)
O3	C11	1.145(2)	C5	C6	1.397(3)
O4	C12	1.143(3)			

Table 57: Bond Angles for **12p**.

Atom	Atom	Atom	Length/Å	Atom	Atom	Atom	Angle/°
C9	Fe	P	176.71(7)	C2	N2	C8	120.88(14)
C10	Fe	P	87.06(6)	C8	N2	P	126.11(12)
C10	Fe	C9	90.55(9)	N1	C1	C2	110.67(15)
C10	Fe	C12	127.65(9)	C6	C1	N1	128.27(15)
C11	Fe	P	90.03(6)	C6	C1	C2	120.99(16)
C11	Fe	C9	93.13(9)	N2	C2	C1	111.18(15)
C11	Fe	C10	120.60(10)	C3	C2	N2	128.10(15)
C11	Fe	C12	111.53(10)	C3	C2	C1	120.65(16)
C12	Fe	P	88.54(6)	C2	C3	C4	118.23(16)
C12	Fe	C9	91.13(8)	C5	C4	C3	120.92(16)
N1	P	Fe	120.98(5)	C4	C5	C6	120.92(17)
N1	P	N2	91.54(7)	C1	C6	C5	118.26(16)
N2	P	Fe	120.50(6)	O1	C9	Fe	179.8(2)
C1	N1	P	111.37(11)	O2	C10	Fe	178.44(17)
C1	N1	C7	121.22(15)	O3	C11	Fe	178.7(2)
C7	N1	P	126.14(13)	O4	C12	Fe	177.9(2)
C2	N2	P	111.49(11)				

248
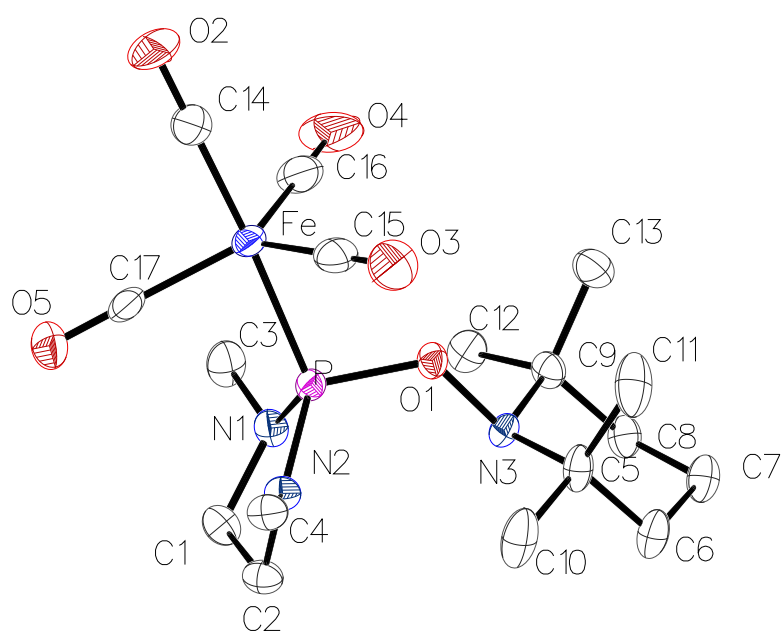
Figure 117: Molecular structure of **17e** in the crystal obtained by X-ray diffraction.

Table 58: Crystal data and structure refinement for **17e**.

Identification code	GSTR693, PB-142 // GXraymatrixa-new
Crystal Habitus	clear light brown plate
Device Type	STOE IPDS-2T
Empirical formula	C17H28FeN3O5P
Moiety formula	C17 H28 Fe N3 O5 P
Formula weight	441.24
Temperature/K	123
Crystal system	triclinic
Space group	P-1
a/Å	8.9054(7)
b/Å	9.8984(8)
c/Å	12.7846(10)
α/°	71.066(6)
β/°	81.708(6)
γ/°	84.096(6)
Volume/Å^3	1052.94(15)
Z	2
ρ_{calc} g/cm^3	1.392
μ/mm^{-1}	0.823
F(000)	464.0
Crystal size/mm^3	0.15 × 0.1 × 0.03
Absorption correction	empirical
Tmin; Tmax	0.5415; 0.8309
Radiation	MoKα (λ = 0.71073)
2Θ range for data collection/°	5.408 to 50.496°
Completeness to theta	0.975

Index ranges	$-9 \leq h \leq 10$, $-10 \leq k \leq 11$, $-15 \leq l \leq 15$	
Reflections collected	10956	
Independent reflections	10956 [Rint = 0.0460, Rsigma = 0.0616]	
Data/restraints/parameters	10956/0/251	
Goodness-of-fit on F2	0.947	
Final R indexes [I≥2σ (I)]	R1 = 0.0481, wR2 = 0.1067	
Final R indexes [all data]	R1 = 0.0726, wR2 = 0.1139	
Largest diff. peak/hole / e Å^{-3}	0.50/-0.47	

Table 59: Bond Lengths for **17e**.

Atom	Atom	Length/Å	Atom	Atom	Length/Å
Fe	P	2.2092(12)	N1	C3	1.466(5)
Fe	C14	1.787(5)	N2	C2	1.462(5)
Fe	C15	1.797(5)	N2	C4	1.453(5)
Fe	C16	1.783(5)	N3	C5	1.512(4)
Fe	C17	1.790(4)	N3	C9	1.502(5)
P	O1	1.631(2)	C1	C2	1.513(5)
P	N1	1.676(3)	C5	C6	1.532(6)
P	N2	1.649(3)	C5	C10	1.521(6)
O1	N3	1.489(4)	C5	C11	1.538(6)
O2	C14	1.143(6)	C6	C7	1.507(6)
O3	C15	1.145(5)	C7	C8	1.520(5)
O4	C16	1.147(6)	C8	C9	1.534(5)
O5	C17	1.141(5)	C9	C12	1.528(5)
N1	C1	1.467(5)	C9	C13	1.537(6)

Table 60: Bond Angles for **17e**.

Atom	Atom	Atom	Length/Å	Atom	Atom	Atom	Angle/°
C14	Fe	P	177.06(15)	O1	N3	C9	105.7(3)
C14	Fe	C15	93.0(2)	C9	N3	C5	115.7(3)
C14	Fe	C17	91.92(19)	N1	C1	C2	105.8(3)
C15	Fe	P	88.78(14)	N2	C2	C1	104.4(3)
C16	Fe	P	89.60(16)	N3	C5	C6	105.4(3)
C16	Fe	C14	91.7(2)	N3	C5	C10	107.8(3)
C16	Fe	C15	115.6(2)	N3	C5	C11	115.9(4)
C16	Fe	C17	121.8(2)	C6	C5	C11	111.8(3)
C17	Fe	P	85.14(13)	C10	C5	C6	108.0(4)
C17	Fe	C15	122.2(2)	C10	C5	C11	107.7(4)
O1	P	Fe	102.40(10)	C7	C6	C5	113.6(4)
O1	P	N1	108.89(15)	C6	C7	C8	109.1(3)
O1	P	N2	114.27(14)	C7	C8	C9	113.6(3)
N1	P	Fe	121.83(12)	N3	C9	C8	106.4(3)
N2	P	Fe	116.91(12)	N3	C9	C12	107.4(3)
N2	P	N1	92.96(16)	N3	C9	C13	116.4(3)
N3	O1	P	122.9(2)	C8	C9	C13	111.6(3)
C1	N1	P	112.6(3)	C12	C9	C8	107.4(3)
C3	N1	P	122.6(3)	C12	C9	C13	107.3(4)
C3	N1	C1	112.5(3)	O2	C14	Fe	178.7(5)
C2	N2	P	113.8(2)	O3	C15	Fe	179.7(4)
C4	N2	P	127.9(3)	O4	C16	Fe	179.2(4)

| C4 | N2 | C2 | 118.0(3) | O5 | C17 | Fe | 179.6(4) |
| O1 | N3 | C5 | 106.4(3) | | | | |
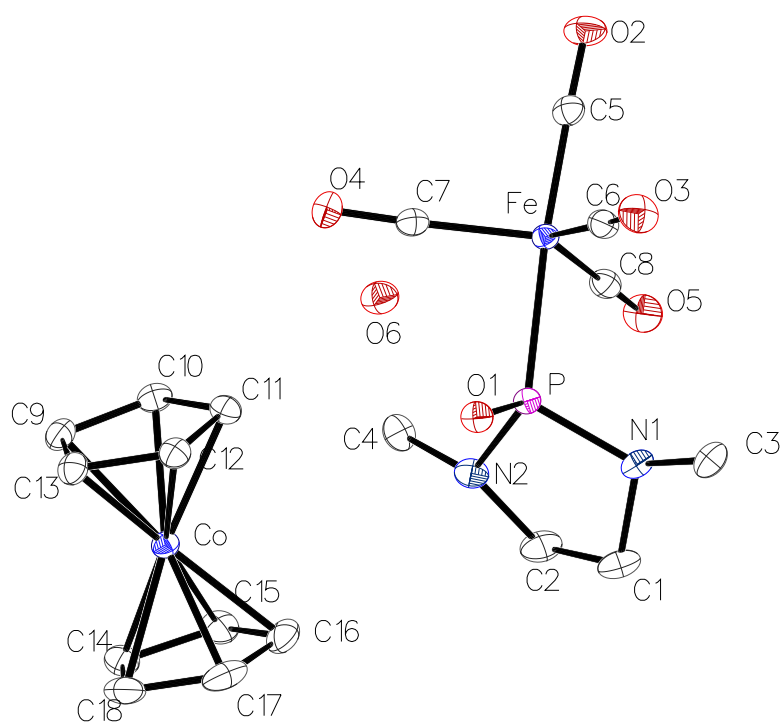
Figure 118: Molecular structure of CoCp$_2$**14e** in the crystal obtained by X-ray diffraction.

Table 61: Crystal data and structure refinement for CoCp$_2$**14e**.

Identification code	GSTR749, PB-360 // GXraymo_6821f
Crystal Habitus	clear yellow plate
Device Type	Bruker D8 Venture
Empirical formula	C18H22CoFeN2O6P
Moiety formula	C8 H10 Fe N2 O5 P, C10 H10 Co, H2 O
Formula weight	508.12
Temperature/K	100.0
Crystal system	monoclinic
Space group	P21/c
a/Å	11.4035(4)
b/Å	15.0426(6)
c/Å	11.8895(5)
α/°	90
β/°	95.853(2)
γ/°	90
Volume/Å^3	2028.87(14)
Z	4
ρ_{calc} g/cm^3	1.664
μ/mm-1	1.649
F(000)	1040.0
Crystal size/mm^3	0.36 × 0.19 × 0.07
Absorption correction	empirical
Tmin; Tmax	0.6222; 0.7460

Radiation	MoKα (λ = 0.71073)	
2Θ range for data collection/°	4.38 to 60.002°	
Completeness to theta	0.996	
Index ranges	-16 $\leq$ h $\leq$ 16, -21 $\leq$ k $\leq$ 21, -16 $\leq$ l $\leq$ 16	
Reflections collected	44248	
Independent reflections	5901 [Rint = 0.0414, Rsigma = 0.0226]	
Data/restraints/parameters	5901/0/267	
Goodness-of-fit on F2	1.038	
Final R indexes [I$\geq$2σ (I)]	R1 = 0.0204, wR2 = 0.0529	
Final R indexes [all data]	R1 = 0.0216, wR2 = 0.0538	
Largest diff. peak/hole / e Å^{-3}	0.41/-0.25	

Table 62: Bond Lengths for CoCp$_2$**14e**.

Atom	Atom	Length/Å	Atom	Atom	Length/Å
Fe	P	2.2649(3)	Co	C11	2.0370(11)
Fe	C5	1.7853(11)	Co	C12	2.0346(10)
Fe	C6	1.7834(11)	Co	C13	2.0301(11)
Fe	C7	1.7866(11)	Co	C14	2.0396(11)
Fe	C8	1.7843(11)	Co	C15	2.0459(11)
P	O1	1.5172(8)	Co	C16	2.0318(11)
P	N1	1.6983(9)	Co	C17	2.0184(12)
P	N2	1.6994(9)	Co	C18	2.0230(11)
O2	C5	1.1496(14)	C9	C10	1.4242(16)
O3	C6	1.1501(14)	C9	C13	1.4300(15)
O4	C7	1.1488(14)	C10	C11	1.4266(15)
O5	C8	1.1507(14)	C11	C12	1.4234(15)
N1	C1	1.4629(14)	C12	C13	1.4250(15)
N1	C3	1.4525(14)	C14	C15	1.4231(17)
N2	C2	1.4670(15)	C14	C18	1.4224(18)
N2	C4	1.4560(14)	C15	C16	1.4202(18)
C1	C2	1.5148(18)	C16	C17	1.4218(19)
Co	C9	2.0314(11)	C17	C18	1.4254(19)
Co	C10	2.0388(11)			

Table 63: Bond Angles for CoCp$_2$**14e**.

Atom	Atom	Atom	Length/Å	Atom	Atom	Atom	Angle/°
C5	Fe	P	174.93(4)	C16	Co	C11	106.17(5)
C5	Fe	C7	94.82(5)	C16	Co	C12	118.69(5)
C6	Fe	P	85.86(3)	C16	Co	C14	68.94(5)
C6	Fe	C5	95.46(5)	C16	Co	C15	40.76(5)
C6	Fe	C7	111.81(5)	C17	Co	C9	155.39(5)
C6	Fe	C8	125.34(5)	C17	Co	C10	160.46(5)
C7	Fe	P	89.21(3)	C17	Co	C11	122.06(5)
C8	Fe	P	84.42(3)	C17	Co	C12	104.06(5)
C8	Fe	C5	90.84(5)	C17	Co	C13	118.34(5)
C8	Fe	C7	121.66(5)	C17	Co	C14	69.10(5)
O1	P	Fe	113.04(3)	C17	Co	C15	68.81(5)
O1	P	N1	112.92(4)	C17	Co	C16	41.10(6)
O1	P	N2	110.38(5)	C17	Co	C18	41.30(6)
N1	P	Fe	111.37(3)	C18	Co	C9	120.99(5)

253

N1	P	N2	91.98(5)	C18	Co	C10	157.79(5)
N2	P	Fe	115.50(3)	C18	Co	C11	159.12(5)
C1	N1	P	110.00(8)	C18	Co	C12	122.01(5)
C3	N1	P	119.83(7)	C18	Co	C13	105.60(5)
C3	N1	C1	115.05(9)	C18	Co	C14	40.99(5)
C2	N2	P	112.36(8)	C18	Co	C15	68.86(5)
C4	N2	P	122.15(7)	C18	Co	C16	69.31(5)
C4	N2	C2	113.98(9)	C10	C9	Co	69.80(6)
N1	C1	C2	103.71(9)	C10	C9	C13	107.88(9)
N2	C2	C1	104.74(9)	C13	C9	Co	69.34(6)
O2	C5	Fe	177.42(10)	C9	C10	Co	69.24(6)
O3	C6	Fe	177.97(10)	C9	C10	C11	108.08(10)
O4	C7	Fe	177.92(10)	C11	C10	Co	69.44(6)
O5	C8	Fe	178.99(11)	C10	C11	Co	69.58(6)
C9	Co	C10	40.96(5)	C12	C11	Co	69.45(6)
C9	Co	C11	69.11(4)	C12	C11	C10	108.01(10)
C9	Co	C12	69.19(4)	C11	C12	Co	69.63(6)
C9	Co	C14	108.98(5)	C11	C12	C13	108.11(10)
C9	Co	C15	126.74(5)	C13	C12	Co	69.31(6)
C9	Co	C16	162.93(5)	C9	C13	Co	69.43(6)
C10	Co	C14	123.29(5)	C12	C13	Co	69.64(6)
C10	Co	C15	109.62(5)	C12	C13	C9	107.92(10)
C11	Co	C10	40.98(4)	C15	C14	Co	69.85(6)
C11	Co	C14	158.15(5)	C18	C14	Co	68.88(7)
C11	Co	C15	121.81(5)	C18	C14	C15	107.90(11)
C12	Co	C10	68.96(4)	C14	C15	Co	69.38(6)
C12	Co	C11	40.93(4)	C16	C15	Co	69.08(6)
C12	Co	C14	160.41(5)	C16	C15	C14	108.28(11)
C12	Co	C15	155.57(5)	C15	C16	Co	70.15(7)
C13	Co	C9	41.23(4)	C15	C16	C17	107.81(11)
C13	Co	C10	69.09(5)	C17	C16	Co	68.94(7)
C13	Co	C11	69.08(5)	C16	C17	Co	69.96(7)
C13	Co	C12	41.05(4)	C16	C17	C18	108.16(11)
C13	Co	C14	124.75(5)	C18	C17	Co	69.52(7)
C13	Co	C15	163.01(5)	C14	C18	Co	70.13(7)
C13	Co	C16	154.03(5)	C14	C18	C17	107.84(11)
C14	Co	C15	40.77(5)	C17	C18	Co	69.17(7)
C16	Co	C10	124.96(5)				
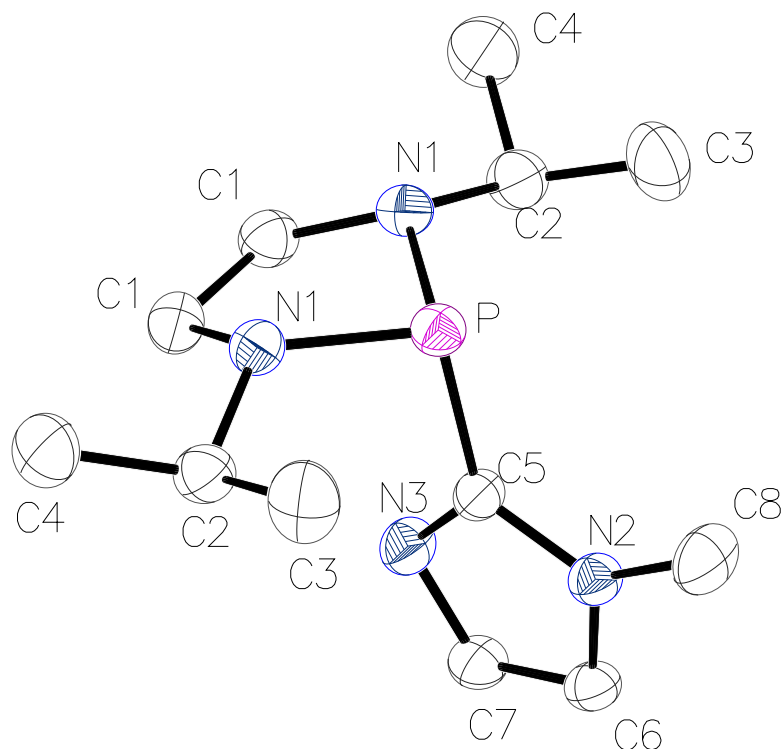
Figure 119: Molecular structure of **66f** in the crystal obtained by X-ray diffraction.

Table 64: Crystal data and structure refinement for **66f**.

Identification code	GSTR727, PB-298 // GXray6620_pl
Crystal Habitus	clear colourless plate
Device Type	STOE IPDS-2T
Empirical formula	C12H23N4P
Moiety formula	C12 H23 N4 P
Formula weight	254.31
Temperature/K	180
Crystal system	orthorhombic
Space group	Pnma
a/Å	10.7908(13)
b/Å	13.5065(14)
c/Å	9.7719(8)
$\alpha/°$	90
$\beta/°$	90
$\gamma/°$	90
Volume/Å^3	1424.2(3)
Z	4
ρ_{calc} g/cm^3	1.186
μ/mm^{-1}	0.180
F(000)	552.0
Crystal size/mm^3	0.33 × 0.3 × 0.12
Absorption correction	integration

Tmin; Tmax	0.8859; 0.9707
Radiation	MoKα (λ = 0.71073)
2Θ range for data collection/°	5.624 to 56.026°
Completeness to theta	0.999
Index ranges	-12 $\leq$ h $\leq$ 14, -17 $\leq$ k $\leq$ 17, -12 $\leq$ l $\leq$ 11
Reflections collected	7367
Independent reflections	1791 [Rint = 0.0735, Rsigma = 0.0728]
Data/restraints/parameters	1791/0/95
Goodness-of-fit on F2	0.828
Final R indexes [I$\geq$2σ (I)]	R1 = 0.0390, wR2 = 0.0871
Final R indexes [all data]	R1 = 0.0708, wR2 = 0.0929
Largest diff. peak/hole / e Å^{-3}	0.48/-0.39

Table 65: Bond Lengths for **66f**.

Atom	Atom	Length/Å	Atom	Atom	Length/Å
P	N11	1.7062(15)	N2	C8	1.458(3)
P	N1	1.7062(15)	N3	C5	1.322(3)
P	C5	1.861(2)	N3	C7	1.367(3)
N1	C1	1.473(2)	C1	C11	1.520(3)
N1	C2	1.476(2)	C2	C3	1.522(3)
N2	C5	1.374(3)	C2	C4	1.516(3)
N2	C6	1.366(3)	C6	C7	1.357(4)

1+X,3/2-Y,+Z

Table 66: Bond Angles for **66f**.

Atom	Atom	Atom	Length/Å	Atom	Atom	Atom	Angle/°
N11	P	N1	91.09(10)	N1	C1	C11	108.10(9)
N1	P	C5	102.70(8)	N1	C2	C3	110.59(16)
N11	P	C5	102.70(8)	N1	C2	C4	110.56(16)
C1	N1	P	111.04(11)	C4	C2	C3	109.91(16)
C1	N1	C2	114.02(14)	N2	C5	P	121.91(17)
C2	N1	P	118.52(12)	N3	C5	P	127.68(18)
C5	N2	C8	127.3(2)	N3	C5	N2	110.4(2)
C6	N2	C5	107.4(2)	C7	C6	N2	105.5(2)
C6	N2	C8	125.2(2)	C6	C7	N3	111.0(2)
C5	N3	C7	105.6(2)				

1+X,3/2-Y,+Z
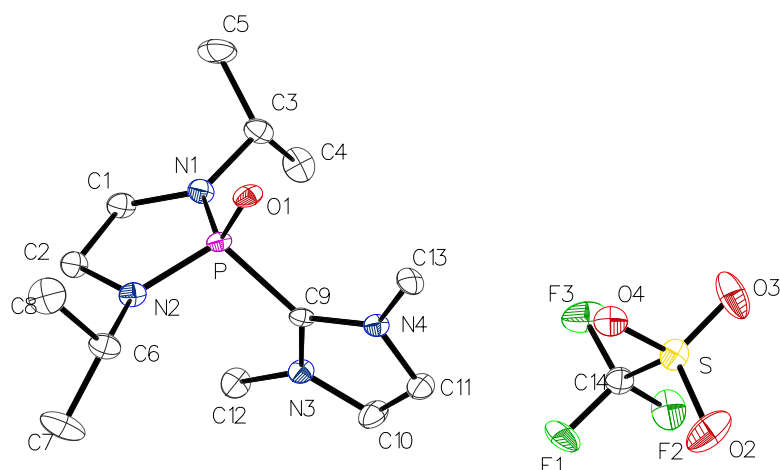
Figure 120: Molecular structure of **68f** in the crystal obtained by X-ray diffraction.

Table 67: Crystal data and structure refinement for **68f**.

Identification code	GSTR762, PB-324 // GXraycu_6707k
Crystal Habitus	clear colourless plate
Device Type	Bruker D8 Venture
Empirical formula	C14H26N4O4F3PS
Moiety formula	C F3 O3 S, C13 H26 N4 O P
Formula weight	434.42
Temperature/K	100.0
Crystal system	monoclinic
Space group	P21/n
a/Å	12.4801(15)
b/Å	12.4523(15)
c/Å	13.0447(15)
α/°	90
β/°	99.065(6)
γ/°	90
Volume/Å^3	2001.9(4)
Z	4
ρ_{calc} g/cm^3	1.441
μ/mm-1	2.703
F(000)	912.0
Crystal size/mm^3	0.16 × 0.15 × 0.11
Absorption correction	empirical
Tmin; Tmax	0.2768; 0.7543
Radiation	CuKα (λ = 1.54178)
2Θ range for data collection/°	9.116 to 135.478°
Completeness to theta	0.959
Index ranges	-11 $\leq$ h $\leq$ 14, -14 $\leq$ k $\leq$ 14, -15 $\leq$ l $\leq$ 15
Reflections collected	14125
Independent reflections	3471 [Rint = 0.0756, Rsigma = 0.0690]
Data/restraints/parameters	3471/0/250
Goodness-of-fit on F2	1.468
Final R indexes [I$\geq$2σ (I)]	R1 = 0.1285, wR2 = 0.3185

Table 68: Bond Lengths for **68f**.

Atom	Atom	Length/Å	Atom	Atom	Length/Å
S	O2	1.431(4)	N2	C6	1.477(5)
S	O3	1.441(4)	N3	C9	1.341(5)
S	O4	1.442(3)	N3	C10	1.376(6)
S	C14	1.828(5)	N3	C12	1.475(6)
F1	C14	1.334(5)	N4	C9	1.350(5)
F2	C14	1.340(5)	N4	C11	1.375(5)
F3	C14	1.326(5)	N4	C13	1.476(6)
P	O1	1.473(3)	C1	C2	1.543(5)
P	N1	1.620(3)	C3	C4	1.538(6)
P	N2	1.629(3)	C3	C5	1.517(6)
P	C9	1.839(4)	C6	C7	1.526(6)
N1	C1	1.461(5)	C6	C8	1.520(7)
N1	C3	1.486(5)	C10	C11	1.343(7)
N2	C2	1.467(5)			

Table 69: Bond Angles for **68f**.

Atom	Atom	Atom	Length/Å	Atom	Atom	Atom	Angle/°
O2	S	O3	114.9(3)	C2	N2	C6	121.4(3)
O2	S	O4	115.1(2)	C6	N2	P	120.9(3)
O2	S	C14	103.9(2)	C9	N3	C10	109.6(3)
O3	S	O4	114.4(2)	C9	N3	C12	126.6(3)
O3	S	C14	103.1(2)	C10	N3	C12	123.8(4)
O4	S	C14	103.2(2)	C9	N4	C11	109.2(3)
F1	C14	S	112.2(3)	C9	N4	C13	129.1(3)
F1	C14	F2	106.9(4)	C11	N4	C13	121.6(3)
F2	C14	S	111.5(3)	N1	C1	C2	107.0(3)
F3	C14	S	111.0(3)	N2	C2	C1	106.9(3)
F3	C14	F1	107.6(4)	N1	C3	C4	111.1(3)
F3	C14	F2	107.5(3)	N1	C3	C5	111.2(4)
O1	P	N1	119.25(17)	C5	C3	C4	111.6(3)
O1	P	N2	121.97(17)	N2	C6	C7	110.2(4)
O1	P	C9	104.90(17)	N2	C6	C8	111.8(3)
N1	P	N2	95.63(16)	C8	C6	C7	112.0(4)
N1	P	C9	108.14(17)	N3	C9	P	126.2(3)
N2	P	C9	105.85(17)	N3	C9	N4	106.7(3)
C1	N1	P	115.0(2)	N4	C9	P	127.0(3)
C1	N1	C3	122.2(3)	C11	C10	N3	107.0(4)
C3	N1	P	122.6(3)	C10	C11	N4	107.4(4)
C2	N2	P	114.0(2)				
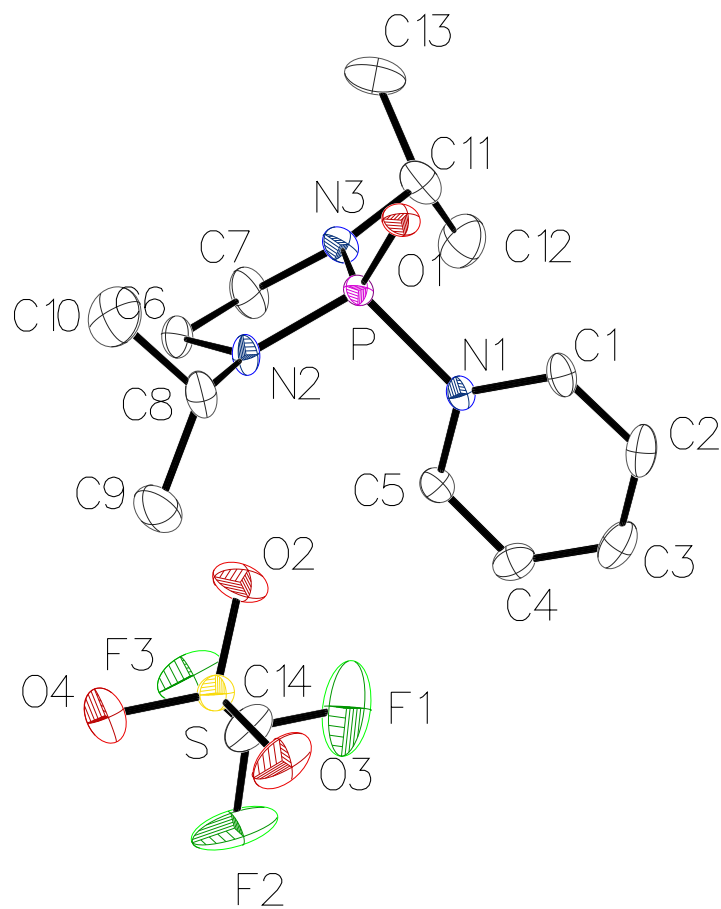
Figure 121: Molecular structure of **70f** in the crystal obtained by X-ray diffraction.

Table 70: Crystal data and structure refinement for **70f**.

Identification code	GSTR767, PB-435 // GXraycu_6901f
Crystal Habitus	clear colourless plate
Device Type	Bruker D8 Venture
Empirical formula	C14H23F3N3O4PS
Moiety formula	C F3 O3 S, C13 H23 N3 O P
Formula weight	417.38
Temperature/K	100.0
Crystal system	monoclinic
Space group	P21/n
a/Å	8.9810(11)
b/Å	19.055(2)
c/Å	22.949(3)
α/°	90
β/°	97.262(4)
γ/°	90
Volume/Å^3	3895.8(8)
Z	8

ρ_{calc} g/cm^3	1.423
μ/mm^{-1}	2.742
F(000)	1744.0
Crystal size/mm^3	0.22 × 0.21 × 0.04
Absorption correction	empirical
Tmin; Tmax	0.5359; 0.7536
Radiation	CuKα (λ = 1.54178)
2Θ range for data collection/°	7.766 to 135.496°
Completeness to theta	0.997
Index ranges	-10 $\leq$ h $\leq$ 10, -22 $\leq$ k $\leq$ 22, -25 $\leq$ l $\leq$ 27
Reflections collected	66277
Independent reflections	7042 [Rint = 0.0464, Rsigma = 0.0268]
Data/restraints/parameters	7042/0/477
Goodness-of-fit on F2	1.023
Final R indexes [I$\geq$2σ (I)]	R1 = 0.0319, wR2 = 0.0811
Final R indexes [all data]	R1 = 0.0340, wR2 = 0.0819
Largest diff. peak/hole / e Å^{-3}	0.40/-0.40

Table 71: Bond Lengths for **70f**.

Atom	Atom	Length/Å	Atom	Atom	Length/Å
S	O2	1.4356(13)	C3	C4	1.389(3)
S	O3	1.4313(14)	C4	C5	1.376(2)
S	O4	1.4303(14)	C6	C7	1.523(2)
S	C14	1.825(2)	C8	C9	1.514(3)
F1	C14	1.320(3)	C8	C10	1.521(3)
F2	C14	1.320(2)	C11	C12	1.514(3)
F3	C14	1.332(2)	C11	C13	1.518(3)
S'	O2'	1.4452(12)	P'	O1'	1.4644(11)
S'	O3'	1.4420(12)	P'	N1'	1.8180(12)
S'	O4'	1.4399(12)	P'	N2'	1.6190(12)
S'	C14'	1.8157(17)	P'	N3'	1.6118(13)
F1'	C14'	1.325(2)	N1'	C1'	1.3531(19)
F2'	C14'	1.337(3)	N1'	C5'	1.3587(19)
F3'	C14'	1.348(2)	N2'	C6'	1.4754(19)
P	O1	1.4634(11)	N2'	C8'	1.4723(19)
P	N1	1.8090(13)	N3'	C7'	1.4766(18)
P	N2	1.6120(13)	N3'	C11'	1.4824(19)
P	N3	1.6156(13)	C1'	C2'	1.380(2)
N1	C1	1.3535(19)	C2'	C3'	1.381(2)
N1	C5	1.3543(19)	C3'	C4'	1.393(2)
N2	C6	1.4765(19)	C4'	C5'	1.372(2)
N2	C8	1.474(2)	C6'	C7'	1.538(2)
N3	C7	1.462(2)	C8'	C9'	1.523(2)
N3	C11	1.473(2)	C8'	C10'	1.527(2)
C1	C2	1.380(2)	C11'	C12'	1.519(2)
C2	C3	1.380(3)	C11'	C13'	1.522(2)

Table 72: Bond Angles for **70f**.

Atom	Atom	Atom	Length/Å	Atom	Atom	Atom	Angle/°

260

O2	S	C14	102.44(9)	C1	C2	C3	119.82(15)
O3	S	O2	116.06(9)	C2	C3	C4	119.38(15)
O3	S	C14	103.93(9)	C5	C4	C3	119.21(15)
O4	S	O2	113.97(9)	N1	C5	C4	120.78(14)
O4	S	O3	115.31(10)	N2	C6	C7	106.44(12)
O4	S	C14	102.52(9)	N3	C7	C6	106.30(13)
F1	C14	S	112.23(15)	N2	C8	C9	110.48(15)
F1	C14	F3	107.34(18)	N2	C8	C10	111.21(15)
F2	C14	S	111.85(15)	C9	C8	C10	111.90(16)
F2	C14	F1	106.09(18)	N3	C11	C12	111.89(14)
F2	C14	F3	107.55(16)	N3	C11	C13	109.94(15)
F3	C14	S	111.46(13)	C12	C11	C13	111.74(15)
O2'	S'	C14'	103.26(9)	O1'	P'	N1'	102.30(6)
O3'	S'	O2'	115.09(7)	O1'	P'	N2'	120.07(6)
O3'	S'	C14'	103.52(8)	O1'	P'	N3'	124.01(7)
O4'	S'	O2'	114.44(7)	N2'	P'	N1'	107.06(6)
O4'	S'	O3'	115.52(7)	N3'	P'	N1'	104.70(6)
O4'	S'	C14'	102.51(8)	N3'	P'	N2'	97.15(6)
F1'	C14'	S'	112.54(14)	C1'	N1'	P'	120.29(10)
F1'	C14'	F2'	107.64(16)	C1'	N1'	C5'	120.48(12)
F1'	C14'	F3'	107.36(16)	C5'	N1'	P'	119.23(10)
F2'	C14'	S'	110.74(13)	C6'	N2'	P'	112.48(10)
F2'	C14'	F3'	107.42(17)	C8'	N2'	P'	124.54(10)
F3'	C14'	S'	110.91(12)	C8'	N2'	C6'	121.90(12)
O1	P	N1	103.36(6)	C7'	N3'	P'	113.04(10)
O1	P	N2	123.33(7)	C7'	N3'	C11'	120.94(12)
O1	P	N3	120.62(7)	C11'	N3'	P'	123.97(10)
N2	P	N1	105.34(6)	N1'	C1'	C2'	120.49(13)
N2	P	N3	97.07(7)	C1'	C2'	C3'	119.71(14)
N3	P	N1	105.31(6)	C2'	C3'	C4'	119.15(14)
C1	N1	P	119.62(11)	C5'	C4'	C3'	119.55(14)
C1	N1	C5	120.59(13)	N1'	C5'	C4'	120.60(13)
C5	N1	P	119.75(10)	N2'	C6'	C7'	105.90(12)
C6	N2	P	112.41(10)	N3'	C7'	C6'	106.40(12)
C8	N2	P	122.70(10)	N2'	C8'	C9'	112.21(13)
C8	N2	C6	121.57(12)	N2'	C8'	C10'	110.35(13)
C7	N3	P	112.60(11)	C9'	C8'	C10'	111.34(14)
C7	N3	C11	122.81(13)	N3'	C11'	C12'	110.05(13)
C11	N3	P	123.17(10)	N3'	C11'	C13'	111.31(12)
N1	C1	C2	120.22(15)	C12'	C11'	C13'	112.01(14)
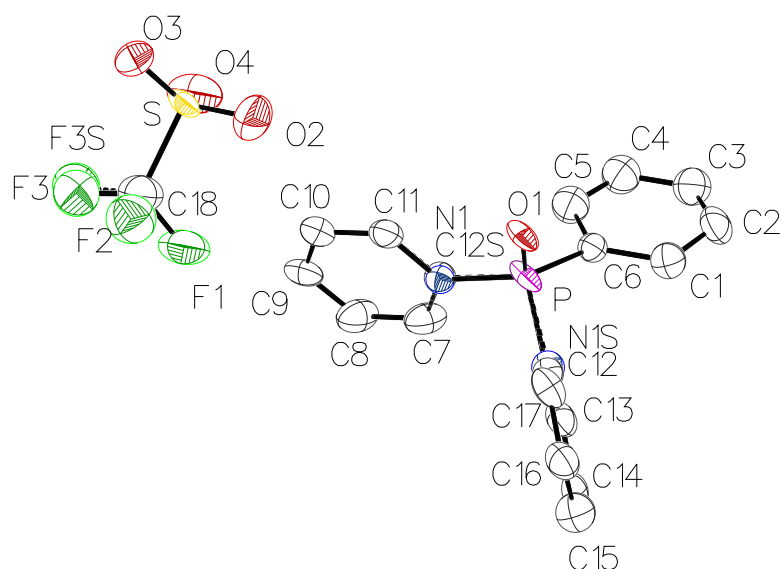
Figure 122: Molecular structure of **70d** in the crystal obtained by X-ray diffraction.

Table 73: Crystal data and structure refinement for **70d**.

Identification code	GSTR774, PB-437 // GXraycu_6900f
Crystal Habitus	clear colourless plate
Device Type	Bruker D8 Venture
Empirical formula	C18H15F3NO4PS
Moiety formula	C F3 O3 S, C17 H15 N O P
Formula weight	429.34
Temperature/K	100.0
Crystal system	orthorhombic
Space group	Pca21
a/Å	39.972(2)
b/Å	11.0784(8)
c/Å	8.4502(5)
$\alpha/°$	90
$\beta/°$	90
$\gamma/°$	90
Volume/Å^3	3742.0(4)
Z	8
ρ_{calc} g/cm^3	1.524
μ/mm^{-1}	2.856
F(000)	1760.0
Crystal size/mm^3	0.09 × 0.06 × 0.02
Absorption correction	empirical
Tmin; Tmax	0.5221; 0.7536
Radiation	CuKα (λ = 1.54178)
2Θ range for data collection/°	4.422 to 135.466°
Completeness to theta	0.998
Index ranges	-47 ≤ h ≤ 47, -13 ≤ k ≤ 13, -10 ≤ l ≤ 10
Reflections collected	101525

Table 74: Bond Lengths for **70d**.

Atom	Atom	Length/Å	Atom	Atom	Length/Å
S	O2	1.450(15)	C14	C15	1.3900
S	O3	1.416(11)	C15	C16	1.3900
S	O4	1.365(15)	C16	C17	1.3900
S	C18	1.82(2)	C1	C2	1.40(2)
F1	C18	1.36(2)	C2	C3	1.33(2)
F2	C18	1.40(3)	C3	C4	1.37(3)
F3	C18	1.17(4)	C4	C5	1.37(2)
F3S	C18	1.383(14)	P'	O1'	1.467(10)
S'	O2'	1.436(16)	P'	N'	1.742(9)
S'	O3'	1.53(2)	P'	C6'	1.792(9)
S'	O4'	1.319(17)	P'	C6'S	1.747(16)
S'	C18'	1.721(19)	P'	N'S	1.776(17)
F1'	C18'	1.25(3)	P'	C12D	1.747(13)
F2'	C18'	1.51(3)	N'	C1'	1.3900
F3'	C18'	1.24(2)	N'	C5'	1.3900
P	O1	1.482(11)	C1'	C2'	1.3900
P	C12S	1.791(9)	C1'	C6'S	1.39(2)
P	C12	1.870(18)	C2'	C3'	1.3900
P	C6	1.767(15)	C3'	C4'	1.3900
P	N1	1.783(17)	C4'	C5'	1.3900
P	N1S	1.755(9)	C5'	C6'S	1.38(2)
C12S	C11	1.3900	C6'	C7'	1.3900
C12S	C7	1.3900	C6'	C11'	1.3900
C11	C10	1.3900	C7'	C8'	1.3900
C11	N1	1.404(19)	C7'	N'S	1.434(19)
C10	C9	1.3900	C8'	C9'	1.3900
C9	C8	1.3900	C9'	C10'	1.3900
C8	C7	1.3900	C10'	C11'	1.3900
C7	N1	1.39(2)	C11'	N'S	1.36(2)
C12	C13	1.34(2)	C12D	C13'	1.41(2)
C12	C17	1.33(2)	C12D	C17'	1.365(19)
C6	C1	1.44(2)	C13'	C14'	1.44(2)
C6	C5	1.43(2)	C14'	C15'	1.43(3)
N1S	C13	1.3900	C15'	C16'	1.31(3)
N1S	C17	1.3900	C16'	C17'	1.36(2)
C13	C14	1.3900			

Table 75: Bond Angles for **70d**.

Atom	Atom	Atom	Length/Å	Atom	Atom	Atom	Angle/°

O2	S	C18	102.6(10)	C17	N1S	P	117.1(6)
O3	S	O2	113.5(9)	C12	C13	C14	115.6(9)
O3	S	C18	104.0(9)	N1S	C13	C14	120.0
O4	S	O2	112.8(11)	C15	C14	C13	120.0
O4	S	O3	120.9(9)	C14	C15	C16	120.0
O4	S	C18	99.8(10)	C17	C16	C15	120.0
F1	C18	S	113.6(14)	C12	C17	C16	115.7(9)
F1	C18	F2	100.8(16)	C16	C17	N1S	120.0
F1	C18	F3S	112(2)	C2	C1	C6	115.2(14)
F2	C18	S	109.3(14)	C3	C2	C1	121.3(16)
F3	C18	S	116(2)	C2	C3	C4	125.3(17)
F3	C18	F1	124(2)	C5	C4	C3	117.1(17)
F3	C18	F2	88(3)	C4	C5	C6	120.1(16)
F3S	C18	S	107.5(19)	O1'	P'	N'	108.5(6)
F3S	C18	F2	114(2)	O1'	P'	C6'	116.3(7)
O2'	S'	O3'	105.7(11)	O1'	P'	C6'S	108.9(7)
O2'	S'	C18'	109.3(11)	O1'	P'	N'S	114.7(7)
O3'	S'	C18'	92.7(13)	O1'	P'	C12D	113.6(6)
O4'	S'	O2'	122.0(12)	N'	P'	C6'	106.7(6)
O4'	S'	O3'	109.1(13)	N'	P'	C12D	106.4(6)
O4'	S'	C18'	113.8(11)	C6'S	P'	N'S	107.7(8)
F1'	C18'	S'	120.4(16)	C6'S	P'	C12D	104.7(8)
F1'	C18'	F2'	97(2)	C12D	P'	C6'	104.8(6)
F2'	C18'	S'	102.9(18)	C12D	P'	N'S	106.6(7)
F3'	C18'	S'	120.3(16)	C1'	N'	P'	120.6(6)
F3'	C18'	F1'	114.8(19)	C1'	N'	C5'	120.0
F3'	C18'	F2'	91(2)	C5'	N'	P'	119.4(6)
O1	P	C12S	112.7(6)	N'	C1'	C2'	120.0
O1	P	C12	107.0(7)	C2'	C1'	C6'S	119.7(8)
O1	P	C6	116.2(6)	C1'	C2'	C3'	120.0
O1	P	N1	112.9(7)	C2'	C3'	C4'	120.0
O1	P	N1S	107.1(6)	C3'	C4'	C5'	120.0
C6	P	C12S	107.9(6)	C4'	C5'	N'	120.0
C6	P	C12	106.0(7)	C6'S	C5'	C4'	119.9(8)
C6	P	N1	108.7(7)	C7'	C6'	P'	121.5(6)
N1	P	C12	105.3(9)	C7'	C6'	C11'	120.0
N1S	P	C12S	107.2(7)	C11'	C6'	P'	117.4(6)
N1S	P	C6	105.2(6)	C6'	C7'	C8'	120.0
C11	C12S	P	115.0(6)	C8'	C7'	N'S	119.3(8)
C11	C12S	C7	120.0	C9'	C8'	C7'	120.0
C7	C12S	P	125.0(6)	C8'	C9'	C10'	120.0
C12S	C11	C10	120.0	C11'	C10'	C9'	120.0
C10	C11	N1	120.1(8)	C10'	C11'	C6'	120.0
C11	C10	C9	120.0	N'S	C11'	C10'	121.2(8)
C8	C9	C10	120.0	C1'	C6'S	P'	120.0(11)
C9	C8	C7	120.0	C5'	C6'S	P'	119.5(11)
C8	C7	C12S	120.0	C5'	C6'S	C1'	120.2(13)
N1	C7	C8	120.5(8)	C7'	N'S	P'	119.8(11)
C13	C12	P	118.2(12)	C11'	N'S	P'	120.5(11)
C17	C12	P	113.1(12)	C11'	N'S	C7'	119.3(14)
C17	C12	C13	128.6(16)	C13'	C12D	P'	127.2(11)
C1	C6	P	119.9(11)	C17'	C12D	P'	119.4(11)
C5	C6	P	118.8(11)	C17'	C12D	C13'	113.4(14)

264

C5	C6	C1	120.8(14)	C12D	C13'	C14'	118.8(15)
C11	N1	P	114.7(11)	C15'	C14'	C13'	121.6(16)
C7	N1	P	125.9(11)	C16'	C15'	C14'	117.4(19)
C7	N1	C11	119.3(13)	C15'	C16'	C17'	120.1(19)
C13	N1S	P	122.8(6)	C12D	C17'	C16'	128.5(17)
C13	N1S	C17	120.0				
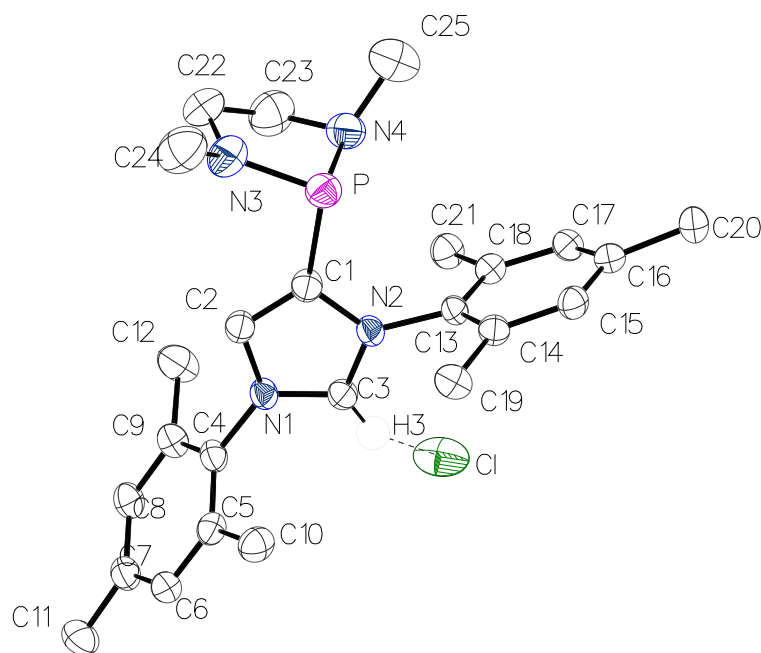
Figure 123: Molecular structure of **72e** in the crystal obtained by X-ray diffraction.

Table 76: Crystal data and structure refinement for **72e**.

Identification code	GSTR775, PB-402 // GXray6887
Crystal Habitus	clear light yellow block
Device Type	STOE IPDS2T
Empirical formula	C25H34ClN4P
Moiety formula	Cl, C25 H34 N4 P
Formula weight	456.98
Temperature/K	123(2)
Crystal system	monoclinic
Space group	P21/c
a/Å	21.062(10)
b/Å	16.194(4)
c/Å	15.444(5)
α/°	90
β/°	105.86(3)
γ/°	90
Volume/Å^3	5067(3)
Z	8
ρ_{calc} g/cm^3	1.198
μ/mm^{-1}	0.233
F(000)	1952.0
Crystal size/mm^3	0.21 × 0.12 × 0.09
Absorption correction	integration
Tmin; Tmax	0.7744; 0.9639
Radiation	MoKα (λ = 0.71073)
2Θ range for data collection/°	3.72 to 55.998°

Completeness to theta	0.998
Index ranges	$-27 \leq h \leq 27, -19 \leq k \leq 21, -18 \leq l \leq 20$
Reflections collected	41637
Independent reflections	12210 [Rint = 0.0756, Rsigma = 0.0817]
Data/restraints/parameters	12210/555/573
Goodness-of-fit on F2	0.966
Final R indexes [I$\geq$2σ (I)]	R1 = 0.0558, wR2 = 0.1530
Final R indexes [all data]	R1 = 0.1007, wR2 = 0.1682
Largest diff. peak/hole / e Å^{-3}	0.77/-0.59

Table 77: Bond Lengths for **72e**.

Atom	Atom	Length/Å	Atom	Atom	Length/Å
P	N3	1.682(2)	P'	N3'	1.660(2)
P	N4	1.6860(11)	P'	N4'	1.696(3)
P	C1	1.850(2)	P'	C1'	1.868(2)
N1	C2	1.383(3)	N1'	C2'	1.382(3)
N1	C3	1.334(3)	N1'	C3'	1.332(3)
N1	C4	1.4586(11)	N1'	C4'	1.4584(11)
N2	C1	1.400(3)	N2'	C1'	1.391(3)
N2	C3	1.325(3)	N2'	C3'	1.333(3)
N2	C13	1.4588(11)	N2'	C13'	1.4596(11)
N3	C22	1.4592(12)	N3'	C22'	1.4587(12)
N3	C24	1.4587(11)	N3'	C24'	1.4572(11)
N4	C23	1.4613(11)	N4'	C23'	1.4585(11)
N4	C25	1.4605(11)	N4'	C25'	1.4586(11)
C1	C2	1.354(3)	C1'	C2'	1.351(3)
C4	C5	1.396(3)	C4'	C5'	1.394(3)
C4	C9	1.384(3)	C4'	C9'	1.393(3)
C5	C6	1.385(3)	C5'	C6'	1.393(3)
C5	C10	1.507(3)	C5'	C10'	1.509(3)
C6	C7	1.391(3)	C6'	C7'	1.387(3)
C7	C8	1.391(3)	C7'	C8'	1.384(3)
C7	C11	1.511(3)	C7'	C11'	1.517(3)
C8	C9	1.390(3)	C8'	C9'	1.397(3)
C9	C12	1.511(3)	C9'	C12'	1.509(3)
C13	C14	1.394(3)	C13'	C14'	1.399(3)
C13	C18	1.396(3)	C13'	C18'	1.392(3)
C14	C15	1.384(3)	C14'	C15'	1.391(4)
C14	C19	1.508(3)	C14'	C19'	1.498(3)
C15	C16	1.394(3)	C15'	C16'	1.378(4)
C16	C17	1.382(3)	C16'	C17'	1.388(3)
C16	C20	1.513(3)	C16'	C20'	1.508(3)
C17	C18	1.383(3)	C17'	C18'	1.390(3)
C18	C21	1.500(3)	C18'	C21'	1.501(3)
C22	C23	1.514(4)	C22'	C23'	1.488(5)

Table 78: Bond Angles for **72e**.

Atom	Atom	Atom	Length/Å	Atom	Atom	Atom	Angle/°
N3	P	N4	94.40(11)	N3'	P'	N4'	94.41(12)
N3	P	C1	100.95(12)	N3'	P'	C1'	99.76(13)

267

N4	P	C1	98.46(11)	N4'	P'	C1'	97.38(12)
C2	N1	C4	127.09(19)	C2'	N1'	C4'	125.00(18)
C3	N1	C2	109.40(17)	C3'	N1'	C2'	109.29(17)
C3	N1	C4	123.46(19)	C3'	N1'	C4'	125.48(19)
C1	N2	C13	124.22(18)	C1'	N2'	C13'	123.09(18)
C3	N2	C1	109.92(18)	C3'	N2'	C1'	110.18(17)
C3	N2	C13	125.85(19)	C3'	N2'	C13'	126.50(19)
C22	N3	P	113.26(18)	C22'	N3'	P'	111.97(19)
C24	N3	P	123.4(2)	C24'	N3'	P'	126.8(2)
C24	N3	C22	119.8(2)	C24'	N3'	C22'	121.2(3)
C23	N4	P	107.43(17)	C23'	N4'	P'	110.0(2)
C25	N4	P	114.91(18)	C25'	N4'	P'	119.8(2)
C25	N4	C23	114.1(2)	C25'	N4'	C23'	119.0(3)
N2	C1	P	122.02(17)	N2'	C1'	P'	121.71(16)
C2	C1	P	132.23(19)	C2'	C1'	P'	132.70(19)
C2	C1	N2	105.6(2)	C2'	C1'	N2'	105.6(2)
C1	C2	N1	107.4(2)	C1'	C2'	N1'	107.7(2)
N2	C3	N1	107.6(2)	N1'	C3'	N2'	107.2(2)
C5	C4	N1	117.73(19)	C5'	C4'	N1'	118.25(19)
C9	C4	N1	118.64(19)	C9'	C4'	N1'	118.07(19)
C9	C4	C5	123.62(18)	C9'	C4'	C5'	123.66(17)
C4	C5	C10	122.3(2)	C4'	C5'	C10'	121.5(2)
C6	C5	C4	117.1(2)	C6'	C5'	C4'	116.5(2)
C6	C5	C10	120.5(2)	C6'	C5'	C10'	121.9(2)
C5	C6	C7	121.6(2)	C7'	C6'	C5'	122.1(2)
C6	C7	C8	118.8(2)	C6'	C7'	C11'	120.8(2)
C6	C7	C11	119.8(2)	C8'	C7'	C6'	119.2(2)
C8	C7	C11	121.4(2)	C8'	C7'	C11'	119.9(2)
C9	C8	C7	121.9(2)	C7'	C8'	C9'	121.4(2)
C4	C9	C8	116.9(2)	C4'	C9'	C8'	117.1(2)
C4	C9	C12	121.6(2)	C4'	C9'	C12'	122.8(2)
C8	C9	C12	121.5(2)	C8'	C9'	C12'	120.1(2)
C14	C13	N2	118.08(19)	C14'	C13'	N2'	118.62(19)
C14	C13	C18	123.80(17)	C18'	C13'	N2'	117.33(18)
C18	C13	N2	118.04(19)	C18'	C13'	C14'	123.94(18)
C13	C14	C19	121.8(2)	C13'	C14'	C19'	121.9(2)
C15	C14	C13	117.4(2)	C15'	C14'	C13'	115.7(2)
C15	C14	C19	120.8(2)	C15'	C14'	C19'	122.4(2)
C14	C15	C16	121.0(2)	C16'	C15'	C14'	122.8(2)
C15	C16	C20	120.1(2)	C15'	C16'	C17'	119.1(2)
C17	C16	C15	118.9(2)	C15'	C16'	C20'	121.0(2)
C17	C16	C20	120.9(2)	C17'	C16'	C20'	119.8(2)
C16	C17	C18	122.9(2)	C16'	C17'	C18'	121.3(2)
C13	C18	C21	121.8(2)	C13'	C18'	C21'	122.8(2)
C17	C18	C13	115.8(2)	C17'	C18'	C13'	117.1(2)
C17	C18	C21	122.5(2)	C17'	C18'	C21'	120.1(2)
N3	C22	C23	105.7(2)	N3'	C22'	C23'	107.3(2)
N4	C23	C22	109.4(2)	N4'	C23'	C22'	111.2(3)
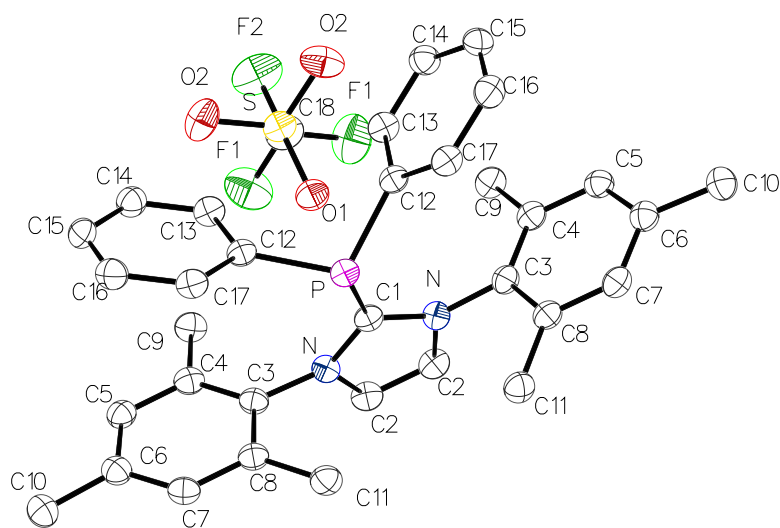
Figure 124: Molecular structure of **73d** in the crystal obtained by X-ray diffraction.

Table 79: Crystal data and structure refinement for **73d**.

Identification code	GSTR786, PB-500 // GXray7072
Crystal Habitus	clear colourless plate
Device Type	STOE STADIVARI
Empirical formula	C34H34F3N2O3PS
Moiety formula	C F3 O3 S, C33 H34 N2 P
Formula weight	638.66
Temperature/K	100
Crystal system	monoclinic
Space group	P21/m
a/Å	8.2686(3)
b/Å	17.0761(6)
c/Å	11.3358(4)
α/°	90.00
β/°	103.944(3)
γ/°	90.00
Volume/Å^3	1553.40(10)
Z	2
ρ_{calc} g/cm^3	1.365
μ/mm^{-1}	1.89
F(000)	668.0
Crystal size/mm^3	0.15 × 0.1 × 0.05
Absorption correction	multi-scan
Tmin; Tmax	0.5517; 0.8549
Radiation	CuKα (λ = 1.54186)
2Θ range for data collection/°	8.036 to 140.952°
Completeness to theta	0.998
Index ranges	-10 ≤ h ≤ 10, -7 ≤ k ≤ 20, -13 ≤ l ≤ 13
Reflections collected	20257
Independent reflections	3046 [Rint = 0.0546, Rsigma = 0.0307]
Data/restraints/parameters	3046/0/211

Goodness-of-fit on F2	1.055
Final R indexes [I≥2σ (I)]	R1 = 0.0473, wR2 = 0.1202
Final R indexes [all data]	R1 = 0.0603, wR2 = 0.1310
Largest diff. peak/hole / e Å^{-3}	0.47/-0.47

Table 80: Bond Lengths for **73d**.

Atom	Atom	Length/Å	Atom	Atom	Length/Å
S	O1	1.441(2)	C3	C8	1.407(3)
S	O2	1.4371(18)	C4	C5	1.389(3)
S	O21	1.4371(18)	C4	C9	1.512(3)
S	C18	1.832(3)	C5	C6	1.398(3)
F1	C18	1.327(3)	C6	C7	1.398(3)
F2	C18	1.335(4)	C6	C10	1.500(3)
P	C1	1.850(3)	C7	C8	1.377(3)
P	C121	1.827(2)	C8	C11	1.510(3)
P	C12	1.827(2)	C12	C13	1.401(3)
N	C1	1.353(2)	C12	C17	1.394(3)
N	C2	1.389(3)	C13	C14	1.379(3)
N	C3	1.446(3)	C14	C15	1.385(3)
C2	C21	1.338(5)	C15	C16	1.386(3)
C3	C4	1.396(3)	C16	C17	1.387(3)

^{1}+X,1/2-Y,+Z

Table 81: Bond Angles for **73d**.

Atom	Atom	Atom	Length/Å	Atom	Atom	Atom	Angle/°
O1	S	C18	102.98(14)	C4	C3	N	119.74(18)
O21	S	O1	114.81(8)	C4	C3	C8	122.4(2)
O2	S	O1	114.81(8)	C8	C3	N	117.72(18)
O21	S	O2	114.81(16)	C3	C4	C9	122.9(2)
O21	S	C18	103.58(9)	C5	C4	C3	117.36(18)
O2	S	C18	103.58(9)	C5	C4	C9	119.68(19)
F11	C18	S	111.44(17)	C4	C5	C6	122.3(2)
F1	C18	S	111.44(17)	C5	C6	C10	121.0(2)
F11	C18	F1	107.4(3)	C7	C6	C5	117.7(2)
F11	C18	F2	107.48(19)	C7	C6	C10	121.24(19)
F1	C18	F2	107.48(19)	C8	C7	C6	122.56(19)
F2	C18	S	111.3(2)	C3	C8	C11	121.9(2)
C121	P	C1	102.24(8)	C7	C8	C3	117.52(19)
C12	P	C1	102.24(8)	C7	C8	C11	120.55(18)
C12	P	C121	105.95(13)	C13	C12	P	125.87(16)
C1	N	C2	109.24(18)	C17	C12	P	115.59(15)
C1	N	C3	127.40(17)	C17	C12	C13	118.5(2)
C2	N	C3	122.54(17)	C14	C13	C12	120.5(2)
N1	C1	P	126.25(12)	C13	C14	C15	120.5(2)
N	C1	P	126.25(12)	C14	C15	C16	119.7(2)
N	C1	N1	106.6(2)	C15	C16	C17	120.0(2)
C21	C2	N	107.44(12)	C16	C17	C12	120.7(2)

^{1}+X,1/2-Y,+Z
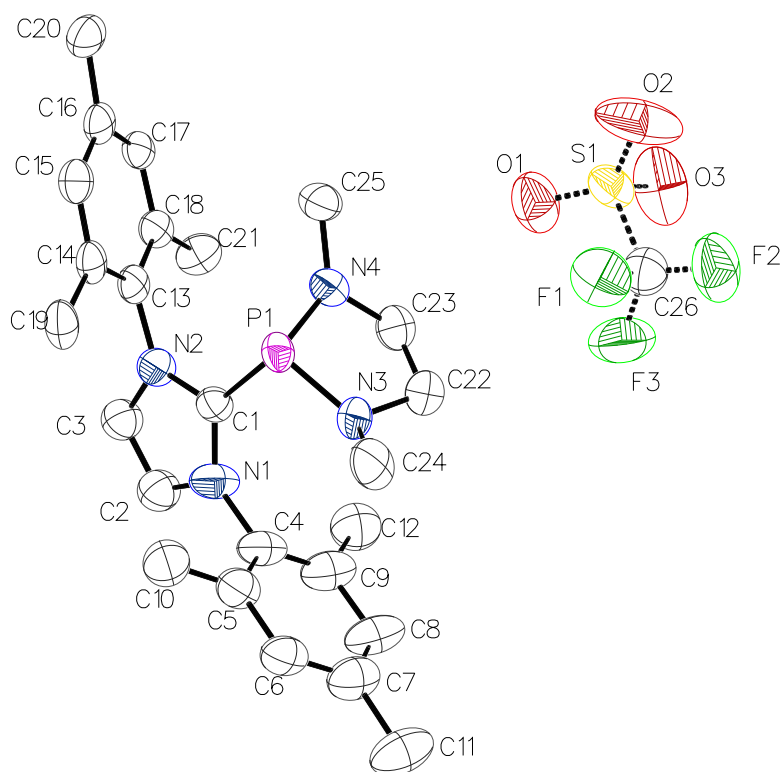
Figure 125: Molecular structure of **73e** in the crystal obtained by X-ray diffraction.

Table 82: Crystal data and structure refinement for **73e**.

Identification code	GSTR787, PB-506 // GXray7078
Crystal Habitus	clear colourless plate
Device Type	STOE STADIVARI
Empirical formula	C108H144F12N16O13P4S4
Moiety formula	4(C F3 O3 S), 3(C25 H34 N4 P), C25 H31 N4 P, C4 H8 O
Formula weight	2351.48
Temperature/K	100
Crystal system	monoclinic
Space group	P21/c
a/Å	30.6956(3)
b/Å	12.22180(15)
c/Å	33.6249(3)
α/°	90.00
β/°	112.5923(7)
γ/°	90.00
Volume/Å^3	11646.53(20)
Z	4
ρ_{calc} g/cm^3	1.343
μ/mm^{-1}	1.989
F(000)	4960.0
Crystal size/mm^3	0.21 × 0.13 × 0.08

Table 83: Bond Lengths for **73e**.

Atom	Atom	Length/Å	Atom	Atom	Length/Å
P1	N3	1.6694(19)	C16B	C20B	1.493(3)
P1	N4	1.647(2)	C17B	C18B	1.397(3)
P1	C1	1.910(2)	C18B	C21B	1.500(3)
N1	C1	1.352(3)	C22B	C23B	1.441(4)
N1	C2	1.363(3)	P1C	N3C	1.687(3)
N1	C4	1.449(3)	P1C	N4C	1.667(3)
N2	C1	1.328(2)	P1C	C1C	1.973(2)
N2	C3	1.381(3)	P1T	N3T	1.460(3)
N2	C13	1.453(3)	P1T	N4T	1.587(6)
N3	C22	1.461(4)	P1T	C1C	1.766(3)
N3	C24	1.466(4)	N1C	C1C	1.329(3)
N4	C23	1.468(4)	N1C	C2C	1.291(7)
N4	C25	1.432(4)	N1C	C2T	1.429(5)
C2	C3	1.356(3)	N1C	C4C	1.452(3)
C4	C5	1.392(4)	N2C	C1C	1.361(3)
C4	C9	1.393(4)	N2C	C3C	1.200(7)
C5	C6	1.395(3)	N2C	C3T	1.438(5)
C5	C10	1.474(5)	N2C	C13C	1.446(3)
C6	C7	1.399(4)	N3C	C22C	1.444(4)
C7	C8	1.373(5)	N3C	C24C	1.430(6)
C7	C11	1.513(4)	N3T	C22T	1.466(4)

Table 84: Bond Angles for **73e**.

Atom	Atom	Atom	Length/Å	Atom	Atom	Atom	Angle/°
N3	P1	C1	98.76(10)	C23B	C22B	N3B	108.85(19)
N4	P1	N3	93.29(11)	C22B	C23B	N4B	109.9(2)
N4	P1	C1	101.69(11)	N3C	P1C	C1C	100.02(12)
C1	N1	C2	109.86(18)	N4C	P1C	N3C	95.20(14)
C1	N1	C4	129.3(2)	N4C	P1C	C1C	104.17(13)
C2	N1	C4	120.8(2)	N3T	P1T	N4T	86.5(2)
C1	N2	C3	108.97(19)	N3T	P1T	C1C	93.18(17)
C1	N2	C13	124.78(19)	N4T	P1T	C1C	106.8(3)
C3	N2	C13	126.25(16)	C1C	N1C	C2T	111.4(2)
C22	N3	P1	113.64(18)	C1C	N1C	C4C	125.46(19)
C22	N3	C24	115.9(2)	C2C	N1C	C1C	108.3(4)
C24	N3	P1	120.4(2)	C2C	N1C	C4C	124.5(4)
C23	N4	P1	110.58(19)	C2T	N1C	C4C	122.7(2)
C25	N4	P1	128.0(2)	C1C	N2C	C3T	109.3(2)
C25	N4	C23	121.0(2)	C1C	N2C	C13C	127.5(2)
N1	C1	P1	130.35(14)	C3C	N2C	C1C	108.9(4)
N2	C1	P1	122.33(17)	C3C	N2C	C13C	121.6(4)
N2	C1	N1	107.15(19)	C3T	N2C	C13C	122.8(2)
C3	C2	N1	106.3(2)	C22C	N3C	P1C	110.8(3)
C2	C3	N2	107.58(19)	C24C	N3C	P1C	121.2(2)
C5	C4	N1	117.9(2)	C24C	N3C	C22C	119.3(3)
C5	C4	C9	123.2(2)	P1T	N3T	C22T	120.6(3)

C9	C4	N1	119.0(2)	P1T	N3T	C24T	110.8(3)
C4	C5	C6	116.5(3)	C22T	N3T	C24T	116.1(4)
C4	C5	C10	122.3(2)	C23C	N4C	P1C	113.3(2)
C6	C5	C10	121.1(3)	C23C	N4C	C25C	115.1(3)
C5	C6	C7	122.2(3)	C25C	N4C	P1C	128.14(18)
C6	C7	C11	120.0(3)	C23T	N4T	P1T	124.5(3)
C8	C7	C6	119.0(2)	C25T	N4T	P1T	120.2(4)
C8	C7	C11	121.0(3)	C25T	N4T	C23T	110.4(4)
C7	C8	C9	121.3(3)	N1C	C1C	P1C	120.25(16)
C4	C9	C8	117.7(3)	N1C	C1C	P1T	118.64(18)
C4	C9	C12	124.0(2)	N1C	C1C	N2C	106.93(19)
C8	C9	C12	118.3(3)	N2C	C1C	P1C	130.52(17)
C14	C13	N2	119.0(2)	N2C	C1C	P1T	127.96(17)
C18	C13	N2	118.6(2)	N1C	C2C	C3C	104.8(5)
C18	C13	C14	122.4(2)	C3T	C2T	N1C	105.0(3)
C13	C14	C19	121.4(2)	N2C	C3C	C2C	108.1(6)
C15	C14	C13	117.0(2)	C2T	C3T	N2C	106.5(3)
C15	C14	C19	121.6(2)	C5C	C4C	N1C	118.29(17)
C14	C15	C16	123.5(2)	C5C	C4C	C9C	123.0(2)
C15	C16	C17	117.3(2)	C9C	C4C	N1C	118.63(16)
C15	C16	C20	121.9(2)	C4C	C5C	C6C	117.70(19)
C17	C16	C20	120.8(2)	C4C	C5C	C10C	121.2(2)
C18	C17	C16	122.0(2)	C6C	C5C	C10C	121.11(18)
C13	C18	C21	121.3(2)	C7C	C6C	C5C	122.20(18)
C17	C18	C13	117.8(2)	C6C	C7C	C8C	118.9(2)
C17	C18	C21	120.9(2)	C6C	C7C	C11C	120.61(19)
N3	C22	C23	105.7(2)	C8C	C7C	C11C	120.5(2)
N4	C23	C22	107.0(3)	C7C	C8C	C9C	121.13(19)
N3A	P1A	C1A	98.32(10)	C4C	C9C	C12C	122.6(2)
N4A	P1A	N3A	94.14(10)	C8C	C9C	C4C	116.97(17)
N4A	P1A	C1A	102.85(9)	C8C	C9C	C12C	120.41(19)
C1A	N1A	C2A	109.8(2)	C14C	C13C	N2C	118.18(17)
C1A	N1A	C4A	126.01(18)	C14C	C13C	C18C	123.7(2)
C2A	N1A	C4A	123.81(17)	C18C	C13C	N2C	117.89(18)
C1A	N2A	C3A	109.43(19)	C13C	C14C	C15C	116.31(19)
C1A	N2A	C13A	127.08(16)	C13C	C14C	C19C	122.8(2)
C3A	N2A	C13A	123.4(2)	C15C	C14C	C19C	120.9(2)
C22A	N3A	P1A	110.73(17)	C16C	C15C	C14C	122.43(19)
C24A	N3A	P1A	121.07(15)	C15C	C16C	C20C	120.99(18)
C24A	N3A	C22A	117.9(2)	C17C	C16C	C15C	118.7(2)
C23A	N4A	P1A	113.23(17)	C17C	C16C	C20C	120.33(17)
C25A	N4A	P1A	124.87(18)	C16C	C17C	C18C	121.69(17)
C25A	N4A	C23A	118.40(18)	C13C	C18C	C17C	117.14(18)
N1A	C1A	P1A	121.62(17)	C13C	C18C	C21C	121.6(2)
N1A	C1A	N2A	106.76(17)	C17C	C18C	C21C	121.24(17)
N2A	C1A	P1A	130.58(14)	N3C	C22C	C23C	105.6(2)
C3A	C2A	N1A	106.7(2)	N3T	C22T	C23T	105.5(2)
C2A	C3A	N2A	107.4(3)	N4C	C23C	C22C	106.9(3)
C5A	C4A	N1A	117.6(2)	N4T	C23T	C22T	94.8(3)
C5A	C4A	C9A	123.3(2)	O1	S1	O3	115.50(9)
C9A	C4A	N1A	119.12(19)	O1	S1	C26	102.64(10)
C4A	C5A	C6A	117.3(2)	O2	S1	O1	115.01(12)
C4A	C5A	C10A	122.3(2)	O2	S1	O3	115.05(11)
C6A	C5A	C10A	120.33(19)	O2	S1	C26	103.51(11)

273

C7A	C6A	C5A	120.6(2)	O3	S1	C26	102.47(10)
C6A	C7A	C11A	119.2(2)	F1	C26	S1	113.04(17)
C8A	C7A	C6A	120.2(2)	F1	C26	F2	107.33(15)
C8A	C7A	C11A	120.6(3)	F1	C26	F3	105.37(19)
C7A	C8A	C9A	121.1(3)	F2	C26	S1	111.00(16)
C4A	C9A	C12A	121.4(2)	F2	C26	F3	108.4(2)
C8A	C9A	C4A	117.4(2)	F3	C26	S1	111.42(13)
C8A	C9A	C12A	121.2(3)	O1A	S1A	O3A	107.00(17)
C14A	C13A	N2A	117.76(18)	O1A	S1A	C26A	107.18(16)
C14A	C13A	C18A	123.3(2)	O2A	S1A	O1A	128.83(17)
C18A	C13A	N2A	118.86(19)	O2A	S1A	O3A	101.20(19)
C13A	C14A	C15A	116.90(19)	O2A	S1A	C26A	106.25(16)
C13A	C14A	C19A	124.3(2)	O3A	S1A	C26A	103.84(16)
C15A	C14A	C19A	118.8(2)	F1A	C26A	S1A	107.6(2)
C14A	C15A	C16A	122.0(2)	F2A	C26A	S1A	115.4(3)
C15A	C16A	C20A	120.2(2)	F2A	C26A	F1A	104.1(3)
C17A	C16A	C15A	118.76(19)	F2A	C26A	F3A	117.2(3)
C17A	C16A	C20A	121.0(2)	F3A	C26A	S1A	111.9(2)
C18A	C17A	C16A	120.88(19)	F3A	C26A	F1A	98.3(3)
C13A	C18A	C21A	121.06(18)	O1B	S1B	O3B	101.5(2)
C17A	C18A	C13A	118.0(2)	O1B	S1B	C26B	115.8(2)
C17A	C18A	C21A	120.86(18)	O2B	S1B	O1B	114.0(2)
N3A	C22A	C23A	107.15(19)	O2B	S1B	O3B	121.0(2)
N4A	C23A	C22A	106.32(17)	O2B	S1B	C26B	114.20(19)
N3B	P1B	N4B	94.57(9)	O3B	S1B	C26B	87.5(2)
N3B	P1B	C1B	102.40(8)	F1B	C26B	S1B	100.0(2)
N4B	P1B	C1B	95.07(8)	F1B	C26B	F2B	102.54(19)
C1B	N1B	C2B	109.31(13)	F1B	C26B	F3B	97.4(3)
C1B	N1B	C4B	126.03(13)	F2B	C26B	S1B	98.8(2)
C2B	N1B	C4B	124.13(15)	F3B	C26B	S1B	101.2(2)
C1B	N2B	C3B	109.69(14)	F3B	C26B	F2B	148.8(3)
C1B	N2B	C13B	124.16(13)	O1C	S1C	C26C	100.3(2)
C3B	N2B	C13B	125.39(12)	O2C	S1C	O1C	112.6(2)
C22B	N3B	P1B	112.64(14)	O2C	S1C	C26C	106.9(2)
C24B	N3B	P1B	126.46(17)	O3C	S1C	O1C	109.2(2)
C24B	N3B	C22B	119.07(17)	O3C	S1C	O2C	116.5(2)
C23B	N4B	P1B	107.71(16)	O3C	S1C	C26C	110.1(3)
C25B	N4B	P1B	118.14(18)	F1C	C26C	S1C	109.9(4)
C25B	N4B	C23B	119.3(2)	F1C	C26C	F2C	113.6(4)
N1B	C1B	P1B	130.33(11)	F1C	C26C	F3C	107.2(4)
N2B	C1B	P1B	123.96(13)	F2C	C26C	S1C	100.6(3)
N2B	C1B	N1B	105.68(13)	F3C	C26C	S1C	111.5(3)
C3B	C2B	N1B	107.93(16)	F3C	C26C	F2C	114.0(5)
C2B	C3B	N2B	107.37(14)	O1S	S1S	O2S	117.2(2)
C5B	C4B	N1B	118.35(15)	O1S	S1S	O3S	108.5(2)
C5B	C4B	C9B	123.47(16)	O1S	S1S	C26S	102.0(2)
C9B	C4B	N1B	118.09(17)	O2S	S1S	C26S	97.6(2)
C4B	C5B	C6B	117.48(16)	O3S	S1S	O2S	120.8(2)
C4B	C5B	C10B	123.26(16)	O3S	S1S	C26S	108.0(2)
C6B	C5B	C10B	119.26(18)	F1S	C26S	S1S	111.9(3)
C7B	C6B	C5B	121.17(19)	F1S	C26S	F2S	101.2(3)
C6B	C7B	C11B	119.92(19)	F1S	C26S	F3S	117.0(4)
C8B	C7B	C6B	119.74(17)	F2S	C26S	S1S	110.1(3)
C8B	C7B	C11B	120.34(18)	F2S	C26S	F3S	118.1(4)

274

C7B	C8B	C9B	121.85(18)	F3S	C26S	S1S	98.8(2)
C4B	C9B	C12B	121.91(16)	O1T	S1T	O2T	116.4(4)
C8B	C9B	C4B	116.27(18)	O1T	S1T	O3T	113.8(4)
C8B	C9B	C12B	121.82(17)	O1T	S1T	C26T	106.0(2)
C14B	C13B	N2B	117.71(17)	O2T	S1T	C26T	100.5(2)
C18B	C13B	N2B	119.38(16)	O3T	S1T	O2T	115.8(3)
C18B	C13B	C14B	122.90(16)	O3T	S1T	C26T	101.4(2)
C13B	C14B	C19B	122.14(16)	F1T	C26T	S1T	110.83(9)
C15B	C14B	C13B	117.64(18)	F1T	C26T	F2T	110.21(13)
C15B	C14B	C19B	120.21(17)	F1T	C26T	F3T	98.65(9)
C14B	C15B	C16B	121.12(18)	F2T	C26T	S1T	114.72(5)
C15B	C16B	C20B	120.36(19)	F3T	C26T	S1T	116.40(8)
C17B	C16B	C15B	118.89(18)	F3T	C26T	F2T	104.75(16)
C17B	C16B	C20B	120.7(2)	C27	O4	C30	102.7(3)
C16B	C17B	C18B	122.38(19)	O4	C27	C28	112.6(2)
C13B	C18B	C17B	116.95(17)	C27	C28	C29	90.4(2)
C13B	C18B	C21B	122.98(16)	C30	C29	C28	106.5(3)
C17B	C18B	C21B	120.01(18)	O4	C30	C29	104.2(3)
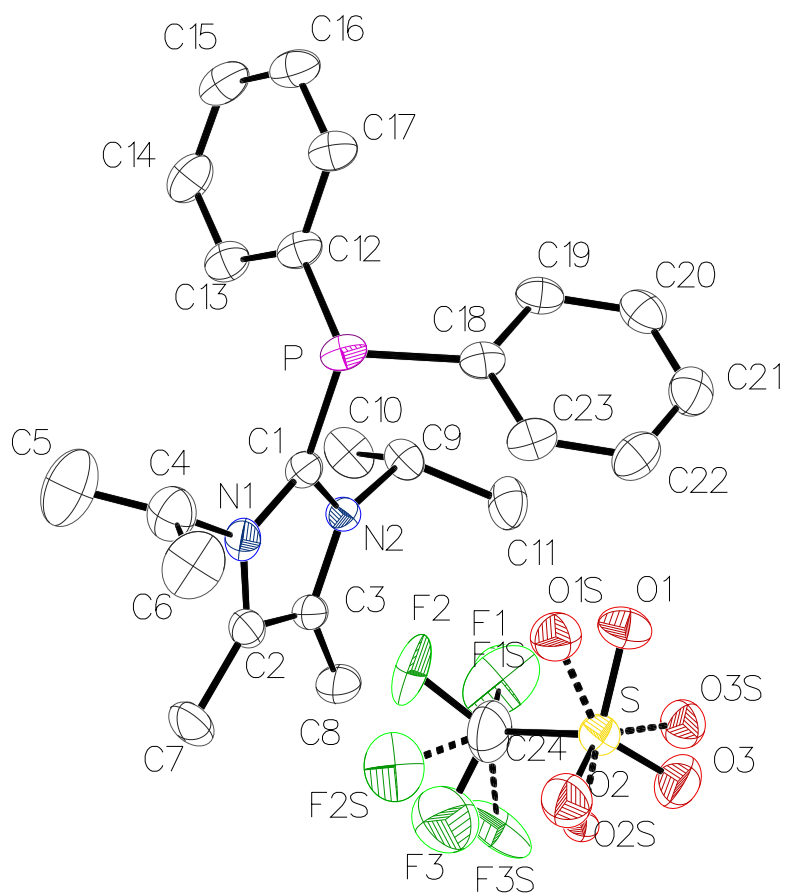
Figure 126: Molecular structure of **74d** in the crystal obtained by X-ray diffraction.

Table 85: Crystal data and structure refinement for **74d**.

Identification code	GSTR788, PB-504 // GXray7079
Crystal Habitus	clear colourless block
Device Type	STOE STADIVARI
Empirical formula	C24H30F3N2O3PS
Moiety formula	C F3 O3 S, C23 H30 N2 P
Formula weight	514.54
Temperature/K	100
Crystal system	monoclinic
Space group	C2/c
a/Å	14.8036(4)
b/Å	11.83898(20)
c/Å	28.3555(8)
α/°	90
β/°	90.8725(22)
γ/°	90
Volume/Å^3	4969.00(21)
Z	8

ρ_{calc} g/cm^3		1.376
μ/mm^{-1}		2.22
F(000)		2160.0
Crystal size/mm^3		0.35 × 0.26 × 0.17
Absorption correction		multi-scan
Tmin; Tmax		0.3143; 0.4169
Radiation		CuKα (λ = 1.54186)
2Θ range for data collection/°		6.234 to 141.442°
Completeness to theta		0.998
Index ranges		-13 $\leq$ h $\leq$ 18, -14 $\leq$ k $\leq$ 11, -34 $\leq$ l $\leq$ 33
Reflections collected		30607
Independent reflections		4727 [Rint = 0.0260, Rsigma = 0.0159]
Data/restraints/parameters		4727/390/369
Goodness-of-fit on F2		1.052
Final R indexes [I$\geq$2σ (I)]		R1 = 0.0604, wR2 = 0.1566
Final R indexes [all data]		R1 = 0.0660, wR2 = 0.1624
Largest diff. peak/hole / e Å^{-3}		0.95/-0.83

Table 86: Bond Lengths for **74d**.

Atom	Atom	Length/Å	Atom	Atom	Length/Å
S	O1	1.439(3)	N2	C9	1.493(3)
S	O1S	1.467(10)	C2	C3	1.363(4)
S	O2	1.436(4)	C2	C7	1.494(4)
S	O2S	1.404(7)	C3	C8	1.491(4)
S	O3	1.458(3)	C4	C5	1.445(5)
S	O3S	1.396(7)	C4	C6	1.452(5)
S	C24	1.795(4)	C9	C10	1.527(4)
F1	C24	1.251(8)	C9	C11	1.522(4)
F1S	C24	1.377(9)	C12	C13	1.392(4)
F2	C24	1.428(5)	C12	C17	1.408(4)
F2S	C24	1.368(7)	C13	C14	1.397(4)
F3	C24	1.280(5)	C14	C15	1.382(5)
F3S	C24	1.509(7)	C15	C16	1.379(5)
P	C1	1.837(3)	C16	C17	1.387(4)
P	C12	1.821(3)	C18	C19	1.396(4)
P	C18	1.832(3)	C18	C23	1.396(4)
N1	C1	1.357(3)	C19	C20	1.388(4)
N1	C2	1.376(4)	C20	C21	1.382(4)
N1	C4	1.501(4)	C21	C22	1.386(5)
N2	C1	1.351(3)	C22	C23	1.385(4)
N2	C3	1.384(3)			

Table 87: Bond Angles for **74d**.

Atom	Atom	Atom	Length/Å	Atom	Atom	Atom	Angle/°
O1	S	O3	112.6(2)	C3	N2	C9	127.3(2)
O1	S	C24	108.11(19)	N1	C1	P	120.75(19)
O1S	S	C24	85.4(4)	N2	C1	P	130.30(19)
O2	S	O1	114.1(2)	N2	C1	N1	107.0(2)
O2	S	O3	114.6(2)	N1	C2	C7	124.6(3)
O2	S	C24	105.2(2)	C3	C2	N1	107.4(2)

O2S	S	O1S	114.6(5)	C3	C2	C7	128.0(3)
O2S	S	C24	103.4(4)	N2	C3	C8	125.4(3)
O3	S	C24	100.83(19)	C2	C3	N2	106.9(2)
O3S	S	O1S	116.5(6)	C2	C3	C8	127.7(3)
O3S	S	O2S	123.9(6)	C5	C4	N1	112.7(3)
O3S	S	C24	102.2(4)	C5	C4	C6	123.9(4)
F1	C24	S	116.7(6)	C6	C4	N1	115.8(3)
F1	C24	F2	100.3(6)	N2	C9	C10	110.6(2)
F1	C24	F3	114.9(6)	N2	C9	C11	111.8(2)
F1S	C24	S	116.5(9)	C11	C9	C10	113.6(2)
F1S	C24	F3S	91.5(11)	C13	C12	P	124.0(2)
F2	C24	S	105.7(3)	C13	C12	C17	118.8(2)
F2S	C24	S	120.0(4)	C17	C12	P	116.6(2)
F2S	C24	F1S	121.9(10)	C12	C13	C14	119.8(3)
F2S	C24	F3S	86.6(5)	C15	C14	C13	120.6(3)
F3	C24	S	113.5(3)	C16	C15	C14	120.2(3)
F3	C24	F2	103.4(4)	C15	C16	C17	119.8(3)
F3S	C24	S	105.2(3)	C16	C17	C12	120.8(3)
C12	P	C1	105.21(12)	C19	C18	P	125.8(2)
C12	P	C18	106.55(13)	C19	C18	C23	119.0(3)
C18	P	C1	100.17(11)	C23	C18	P	115.2(2)
C1	N1	C2	109.3(2)	C20	C19	C18	120.0(3)
C1	N1	C4	122.8(3)	C21	C20	C19	120.4(3)
C2	N1	C4	127.4(2)	C20	C21	C22	120.1(3)
C1	N2	C3	109.3(2)	C23	C22	C21	119.8(3)
C1	N2	C9	123.2(2)	C22	C23	C18	120.6(3)

278
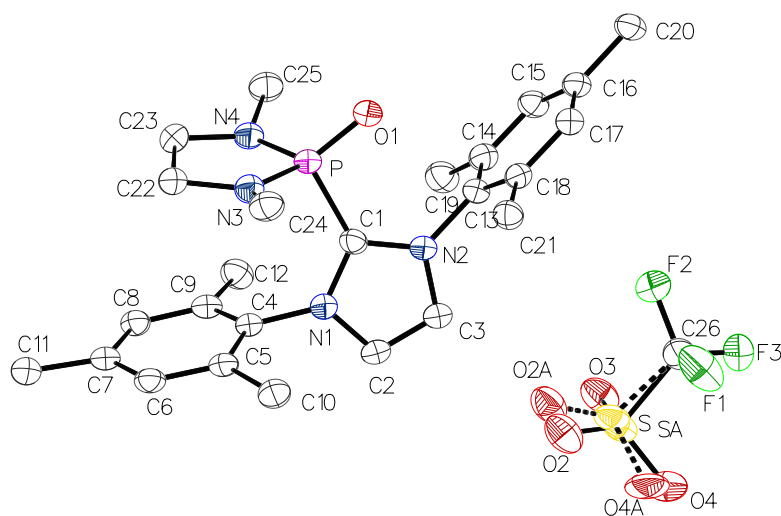
Figure 127: Molecular structure of **75e** in the crystal obtained by X-ray diffraction.

Table 88: Crystal data and structure refinement for **75e**.

Identification code	GSTR779, PB-455.K // GXray6975
Crystal Habitus	clear colourless plate
Device Type	Stadivari
Empirical formula	C26H34F3N4O4PS
Moiety formula	C25 H34 N4 O P, C F3 O3 S
Formula weight	586.60
Temperature/K	100
Crystal system	monoclinic
Space group	P21/n
a/Å	7.5298(2)
b/Å	23.2491(9)
c/Å	16.3263(4)
α/°	90
β/°	99.150(2)
γ/°	90
Volume/Å^3	2821.73(15)
Z	4
ρ_{calc} g/cm^3	1.381
μ/mm^{-1}	2.071
F(000)	1232.0
Crystal size/mm^3	0.6 × 0.4 × 0.04
Absorption correction	multi-scan
Tmin; Tmax	0.1991; 0.2745
Radiation	CuKα (λ = 1.54186)
2Θ range for data collection/°	9.38 to 141.02°
Completeness to theta	0.992
Index ranges	-9 $\leq$ h $\leq$ 6, -27 $\leq$ k $\leq$ 27, -19 $\leq$ l $\leq$ 16
Reflections collected	23820
Independent reflections	5266 [Rint = 0.0390, Rsigma = 0.0291]
Data/restraints/parameters	5266/18/389

Goodness-of-fit on F2			1.027			
Final R indexes [I≥2σ (I)]			R1 = 0.0495, wR2 = 0.1268			
Final R indexes [all data]			R1 = 0.0627, wR2 = 0.1368			
Largest diff. peak/hole / e Å^{-3}			0.47/-0.40			

Table 89: Bond Lengths for **75e**.

Atom	Atom	Length/Å	Atom	Atom	Length/Å
P	O1	1.4636(17)	C9	C12	1.507(3)
P	N3	1.619(2)	C13	C14	1.397(3)
P	N4	1.626(2)	C13	C18	1.386(3)
P	C1	1.850(2)	C14	C15	1.393(3)
N1	C1	1.366(3)	C14	C19	1.503(4)
N1	C2	1.380(3)	C15	C16	1.392(4)
N1	C4	1.443(3)	C16	C17	1.399(3)
N2	C1	1.345(3)	C16	C20	1.501(3)
N2	C3	1.381(3)	C17	C18	1.394(3)
N2	C13	1.457(3)	C18	C21	1.500(3)
N3	C22	1.465(3)	C22	C23	1.543(3)
N3	C24	1.456(3)	S	O2	1.449(12)
N4	C23	1.469(3)	S	O3	1.374(14)
N4	C25	1.465(3)	S	O4	1.423(12)
C2	C3	1.351(3)	S	C26	1.895(16)
C4	C5	1.396(3)	F1	C26	1.337(3)
C4	C9	1.394(3)	F2	C26	1.332(3)
C5	C6	1.391(3)	F3	C26	1.331(3)
C5	C10	1.507(3)	O3	SA	1.459(6)
C6	C7	1.393(3)	C26	SA	1.799(8)
C7	C8	1.396(3)	O4A	SA	1.444(5)
C7	C11	1.505(3)	SA	O2A	1.445(5)
C8	C9	1.394(3)			

Table 90: Bond Angles for **75e**.

Atom	Atom	Atom	Length/Å	Atom	Atom	Atom	Angle/°
O1	P	N3	120.10(11)	C14	C13	N2	117.0(2)
O1	P	N4	120.52(10)	C18	C13	N2	119.0(2)
O1	P	C1	103.82(10)	C18	C13	C14	124.0(2)
N3	P	N4	95.91(10)	C13	C14	C19	123.0(2)
N3	P	C1	107.95(10)	C15	C14	C13	116.6(2)
N4	P	C1	107.80(11)	C15	C14	C19	120.3(2)
C1	N1	C2	109.7(2)	C16	C15	C14	122.1(2)
C1	N1	C4	126.19(19)	C15	C16	C17	118.4(2)
C2	N1	C4	124.1(2)	C15	C16	C20	120.9(2)
C1	N2	C3	110.23(19)	C17	C16	C20	120.7(2)
C1	N2	C13	127.19(19)	C18	C17	C16	121.9(2)
C3	N2	C13	122.1(2)	C13	C18	C17	116.9(2)
C22	N3	P	114.86(16)	C13	C18	C21	121.8(2)
C24	N3	P	124.66(18)	C17	C18	C21	121.2(2)
C24	N3	C22	119.3(2)	N3	C22	C23	106.7(2)
C23	N4	P	114.15(16)	N4	C23	C22	106.88(19)
C25	N4	P	122.63(18)	O2	S	C26	100.2(9)

280

C25	N4	C23	117.9(2)	O3	S	O2	116.3(10)
N1	C1	P	127.37(17)	O3	S	O4	112.9(9)
N2	C1	P	126.66(17)	O3	S	C26	101.7(7)
N2	C1	N1	105.9(2)	O4	S	O2	118.1(9)
C3	C2	N1	107.1(2)	O4	S	C26	104.3(10)
C2	C3	N2	107.2(2)	F1	C26	S	113.3(4)
C5	C4	N1	118.8(2)	F1	C26	SA	110.9(3)
C9	C4	N1	118.1(2)	F2	C26	S	116.9(4)
C9	C4	C5	122.9(2)	F2	C26	F1	107.0(2)
C4	C5	C10	121.8(2)	F2	C26	SA	110.6(3)
C6	C5	C4	117.4(2)	F3	C26	S	105.9(5)
C6	C5	C10	120.8(2)	F3	C26	F1	107.2(2)
C5	C6	C7	121.7(2)	F3	C26	F2	105.9(2)
C6	C7	C8	118.7(2)	F3	C26	SA	114.8(3)
C6	C7	C11	121.3(2)	O3	SA	C26	102.9(3)
C8	C7	C11	120.0(2)	O4A	SA	O3	117.1(4)
C9	C8	C7	121.6(2)	O4A	SA	C26	101.8(4)
C4	C9	C8	117.3(2)	O4A	SA	O2A	114.8(4)
C4	C9	C12	121.8(2)	O2A	SA	O3	112.9(4)
C8	C9	C12	120.8(2)	O2A	SA	C26	105.0(4)
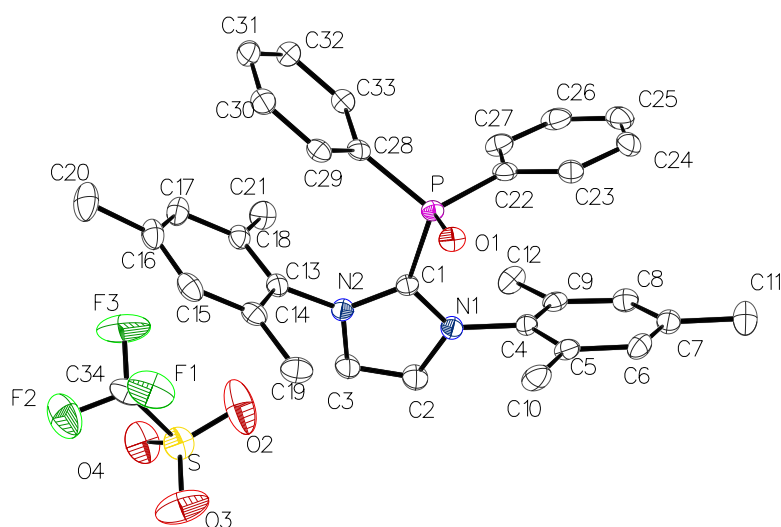
Figure 128: Molecular structure of **75d** in the crystal obtained by X-ray diffraction.

Table 91: Crystal data and structure refinement for **75d**.

Identification code	GSTR781, PB-487 // GXray7032
Crystal Habitus	clear colourless plank
Device Type	STOE STADIVARI
Empirical formula	C34H34F3N2O4PS
Moiety formula	C F3 O3 S, C33 H34 N2 O P
Formula weight	654.66
Temperature/K	100
Crystal system	orthorhombic
Space group	P212121
a/Å	13.5333(2)
b/Å	14.1436(2)
c/Å	16.6085(2)
α/°	90
β/°	90
γ/°	90
Volume/Å^3	3179.03(8)
Z	4
ρ_{calc} g/cm^3	1.368
μ/mm^{-1}	1.885
F(000)	1368.0
Crystal size/mm^3	0.35 × 0.2 × 0.1
Absorption correction	multi-scan
Tmin; Tmax	0.4765; 0.5482
Radiation	CuKα (λ = 1.54186)
2Θ range for data collection/°	8.212 to 141.728°
Completeness to theta	1.000
Index ranges	-15 $\leq$ h $\leq$ 16, -17 $\leq$ k $\leq$ 15, -20 $\leq$ l $\leq$ 16
Reflections collected	98447
Independent reflections	6046 [Rint = 0.0313, Rsigma = 0.0126]
Data/restraints/parameters	6046/0/412

Goodness-of-fit on F2		1.036	
Final R indexes [I≥2σ (I)]		R1 = 0.0313, wR2 = 0.0769	
Final R indexes [all data]		R1 = 0.0332, wR2 = 0.0783	
Largest diff. peak/hole / e Å^{-3}		0.30/-0.43	
Flack parameter		-0.009(5)	

Table 92: Bond Lengths for **75d**.

Atom	Atom	Length/Å	Atom	Atom	Length/Å
S	O2	1.427(3)	C7	C11	1.503(4)
S	O3	1.432(3)	C8	C9	1.390(4)
S	O4	1.423(2)	C9	C12	1.510(3)
S	C34	1.816(3)	C13	C14	1.396(4)
F1	C34	1.323(4)	C13	C18	1.390(4)
F2	C34	1.327(4)	C14	C15	1.392(4)
F3	C34	1.326(4)	C14	C19	1.504(4)
P	O1	1.4816(17)	C15	C16	1.389(4)
P	C1	1.852(2)	C16	C17	1.394(4)
P	C22	1.800(3)	C16	C20	1.509(4)
P	C28	1.802(3)	C17	C18	1.396(4)
N1	C1	1.353(3)	C18	C21	1.511(4)
N1	C2	1.380(3)	C22	C23	1.398(4)
N1	C4	1.450(3)	C22	C27	1.406(4)
N2	C1	1.356(3)	C23	C24	1.392(4)
N2	C3	1.382(3)	C24	C25	1.388(4)
N2	C13	1.444(3)	C25	C26	1.383(4)
C2	C3	1.351(4)	C26	C27	1.386(4)
C4	C5	1.397(3)	C28	C29	1.404(3)
C4	C9	1.395(4)	C28	C33	1.399(3)
C5	C6	1.397(4)	C29	C30	1.387(4)
C5	C10	1.506(4)	C30	C31	1.390(4)
C6	C7	1.385(4)	C31	C32	1.384(4)
C7	C8	1.395(4)	C32	C33	1.388(4)

Table 93: Bond Angles for **75d**.

Atom	Atom	Atom	Angle/°	Atom	Atom	Atom	Angle/°
O2	S	O3	115.6(2)	C6	C7	C11	120.5(2)
O2	S	C34	102.92(17)	C8	C7	C11	120.7(2)
O3	S	C34	103.05(16)	C9	C8	C7	121.6(2)
O4	S	O2	114.04(16)	C4	C9	C12	122.1(2)
O4	S	O3	115.57(18)	C8	C9	C4	117.5(2)
O4	S	C34	103.10(15)	C8	C9	C12	120.4(2)
F1	C34	S	112.5(2)	C14	C13	N2	117.7(2)
F1	C34	F2	106.7(3)	C18	C13	N2	118.6(2)
F1	C34	F3	106.5(3)	C18	C13	C14	123.7(2)
F2	C34	S	111.1(2)	C13	C14	C19	122.1(2)
F3	C34	S	111.9(2)	C15	C14	C13	116.8(2)
F3	C34	F2	107.8(3)	C15	C14	C19	121.0(2)
O1	P	C1	108.33(10)	C16	C15	C14	121.8(2)
O1	P	C22	113.39(12)	C15	C16	C17	119.0(2)
O1	P	C28	111.27(11)	C15	C16	C20	120.5(3)

283

C22	P	C1	103.76(11)	C17	C16	C20	120.5(3)
C22	P	C28	111.01(11)	C16	C17	C18	121.5(2)
C28	P	C1	108.68(11)	C13	C18	C17	116.9(2)
C1	N1	C2	109.7(2)	C13	C18	C21	121.7(2)
C1	N1	C4	128.6(2)	C17	C18	C21	121.4(2)
C2	N1	C4	121.8(2)	C23	C22	P	116.7(2)
C1	N2	C3	109.9(2)	C23	C22	C27	119.6(2)
C1	N2	C13	126.7(2)	C27	C22	P	123.6(2)
C3	N2	C13	123.2(2)	C24	C23	C22	120.0(3)
N1	C1	P	125.68(18)	C25	C24	C23	119.8(3)
N1	C1	N2	106.2(2)	C26	C25	C24	120.6(3)
N2	C1	P	127.97(18)	C25	C26	C27	120.3(3)
C3	C2	N1	107.5(2)	C26	C27	C22	119.7(3)
C2	C3	N2	106.8(2)	C29	C28	P	115.49(19)
C5	C4	N1	119.5(2)	C33	C28	P	124.41(19)
C9	C4	N1	117.3(2)	C33	C28	C29	119.9(2)
C9	C4	C5	123.1(2)	C30	C29	C28	119.7(2)
C4	C5	C10	123.7(2)	C29	C30	C31	120.2(2)
C6	C5	C4	116.8(2)	C32	C31	C30	120.1(3)
C6	C5	C10	119.6(2)	C31	C32	C33	120.6(3)
C7	C6	C5	122.2(2)	C32	C33	C28	119.5(2)
C6	C7	C8	118.7(2)				

III. List of Figures

285

286

287

IV. List of Schemes

291

V. List of Tables

293

295